Radiative effects of Saharan dust layer on the marine atmosphere

Mohammed Shabeeb Abed
University of Leeds
School of Earth and Environment

Submitted in accordance with the requirements for the degree of Doctor of Philosophy
June 2020

Acknowledgements

First and foremost, I would like to thank my supervisor Dr Steven Dobbie for his support and help during my studies. I would also like to thank Michelle Lesnianski and other staff in the School of Earth and Environment who guide and help me throughout my PhD.

Thank you to Phil Rosenberg for his collaborative assistance about providing me the physical processes for generating dust size distributions. Thanks to Richard Rigby for his assistance with all computer issues. I am also grateful to Alex Rap for providing me radiation code that was required for the development of dust and water vapour radiative effects. I would also thank Claire Ryder for her information about dust optics in this work.

This work used the Large Eddy-Model from UK-Met Office with using datasets taken from FENNEC flights and the European Centre for Medium-Range Weather Forecasts (ECMWF). I would like to thank them for providing me data and access to the model for this work. I would also like to thank Chris Reed for his supporting to get CIP data from flight observations.

This work was funded by the Iraqi Government, with support by the official representative of the Iraqi Ministry of Higher Education and Scientific Research in the UK. I would like to thank them for making this work possible.

On a personal note. I would like to thank my family and my friends for their support throughout this work.

Abstract

Millions of tonnes of dust annually are advected from Africa across the Atlantic Ocean. Very significant impacts on marine atmospheric structure develop including well-mixed Saharan aerosol layers (SAL) by mechanisms not fully understood.

In this research, the marine structure was investigated using the UKMO LEM based on FENNEC aircraft-based observations. Surprisingly, FENNEC observations showed that water vapour had significantly elevated levels in all the dusty SAL layers. LEM simulations with offline radiative heating showed that water vapour radiative effects were dominant in influencing the marine atmospheric structure rather than dust. Well-mixed potential temperature layers are created in approximately eight hours most effectively by longwave radiation interacting with elevated water vapour of the SAL. Other factors had little or no impact, such as shortwave radiation or wind shear. Once formed, the layers could last for long periods of a week or more even with radiative interactions disabled. Differential CAPE/CIN analyses indicated stability was enhanced below the SAL and strong CAPE throughout the SAL.

A new bin resolved hybrid Lagrangian-Eulerian 1-D transport model including 1st-order turbulence closure forced by ECMWF reanalysis was developed to estimate the levels of dust across the Atlantic. Transported dust was found to be most sensitive to fall velocity with strong dependence on kinematic viscosity, dust density, refractive index (through determining dust mass from observations) and somewhat on particle shape. Dust amounts predicted in the Caribbean were not enough to maintain well-mixed layers, however, water vapour radiative effects were, for the cases studied.

This research found radiative heating rates of elevated water vapour, beyond background levels, was dominant in determining the impacted SAL marine potential temperature structures. This work will ensure water vapour is targeted as key to the SAL structures, which will be important for future work understanding dust transport and downwind weather impacts of SALs.

Contents

Contents

List of Figures

List of tables

List of acronyms

ACE	Aerosol Characterization Experiment
AERONET	AERosol RObotic NETwork
AMMA	African Monson Multidisciplinary Analysis
AOD	Aerosol Optical Depth
ARM	Atmospheric Radiation measurement
ATW	African Trade Wind
BADC	British Atmospheric Data Centre
BOA	Bottom Of Atmosphere
BOMEX	Barbados Oceanographically Meteorological Experiment
CAPE	Convective Available Potential Energy
CAS	Cloud and Aerosol Spectrometer
CCN	Cloud Condensation Nuclei
CDL	Configuration Definition Language
CDP	Cloud Droplet Probe
CERES	Clouds and the Earth's Radiant Energy System
CIMSS	Cooperative Institute for Meteorological Satellite Studies
CIN	Convective Inhibition
LCL	Lifted Condensation Level
CO2	Carbon Dioxide
CStoDConverter	Converter Software from Scattering to Diameter
DALR	Dry Adiabatic Lapse Rate
DHR	Dust Heating Rates
AI	Aerosol Index
DLW	Dust Long Wave
DMT	Droplet Measurement Technologies
DODO	Dust Outflow Deposition to the Ocean
DRE	Direct Radiative Effect
DSW	Dust Short Wave
DT	Dust Total
ECMWF	European Centre for Medium-Range Weather Forecasts
EL	Equilibrium Level
ESSA	Environmental Science Services Administration
FAAM	Facility for Airborne Atmospheric Measurements

FLIP	Floating Instrument Platform
GERB	Geostationary Earth Radiation Budget
GERBILS	Geostationary Earth Radiation Budget Inter-comparison of Longwave and Shortwave Radiation
GOES	Geostationary Operational Environmental Satellite
GOM	Gulf of Mexico
HYSPLIT	Hybrid Single-Particle Lagrangian Integrated Trajectory
IOP	Intensive Observational Period
IR	Infrared
IRE	Indirect Radiative Effect
ISAP	International Standard Atmosphere Properties
ITCZ	Inter-tropical convergence zone
KTS	Knots unit
LIDAR	Light Detection and Ranging
LPDM	Lagrangian Particle Dispersion Model
LEM	Large-Eddy Model
LW	Long Wave
MACR	Monte Carlo Aerosol Cloud Radiation
MA	Marine Atmosphere
MAL	Marine Aerosol Layer
MBL	Marine Boundary Layer
MCSs	Mesoscale convective systems
MDR	Main Development Region
METEOSAT	Geostationary Meteorological Satellite
MieConScat	Mie Conversion Software for Scattering
MISR	Multi-angle imaging spectroradiometer
MMR	Mass Mixing Ratio
MODIS	Moderate Resolution Imaging Spectroradiometer
MOSRS	Met Office Science Repository Service
NASA	National Aeronautics and Space Administration
NCAR	National Centre for Atmospheric Research
NERC	Natural Environment Research Council
NetCDF	Network Common Data Form
NOAA	National Oceanic and Atmospheric Administration
OPC	Optical Particle Counter
O3	Ozone
PCASP	Passive Cavity Aerosol Spectrometer Particles

PDF	Probability Density Function
PMS	Particle Measurement System
PRIDE	Puerto Rico Dust Experiment
RH	Relative Humidity
RegCM4	Reginal Climate Model
S	Stratus cloud
SABL	Saharan Atmospheric Boundary Layer
SAL	Saharan Air Layer
SALR	Saturated Adiapatic Lapse Rate
SALTRACE	Saharan Aerosol Long-Range Transport and Aerosol–Cloud-Interaction Experiment
SAMUM-2	Saharan Mineral Dust Experiment 2
SC	Saharan coast
SD	Standard Deviation
SDRE	Semi-Direct Radiative Effect
SF	Scaling factor
SHADE	Saharan Dust Experiment
SID2H	Small Ice Detector 2H
SW	Short Wave
SZA	Solar Zenith Angle
TOA	Top Of Atmosphere
TOMS	Total Ozone Mapping Spectrometer
TC	Tropical Cyclone
TCWV	Total Column Water Vapor
UKAE-146	British Aerospace Aircraft
UKMO	United Kingdom Met Office
UTC	Coordinated Universal Time
WAM	West African Monsoon
WHO	World Health Organisation
WRF-Chem	Weather Research and Forcasting model
WNA	western north Atlantic
ZLCL	Lifted Condensation Level
ZLFC	Level of Free Convection
ZLNB	Level of Neutral Buoyancy

1 Chapter 1: Introduction, Literature Review and Research Aims

1.1 Introduction

Arid and semi-arid land surfaces are mainly responsible for the production of atmospheric dust observed around the globe (Yue et al., 2017). It is known that the sources of atmospheric dust are mostly distributed across a band of arid (Sahara) and semi-arid (north Africa) regions that extend across the globe, including the Americas and from the west coast of north Africa to central Africa as well as the Far East (Goudie and Middleton, 2001; Goudie and Middleton, 2006; Kellogg and Griffin, 2007; Cabello et al., 2016). Dust from the land in these regions can enter the atmosphere depends on many factors: the strength of the surface wind and the properties of the land surface such as soil type, soil moisture, etc. As presented by the World Health Organization (WHO, 1999), dust is compost of small dry and solid particles created from land soil. When dust is lifted into the atmosphere, it can be transported by wind, in some instances traveling, thousands of kilometres over land and oceans (Bergametti et al., 1989; Tegen et al., 1994; Prospero et al., 1996; Prospero and Peter, 2003; Giménez et al., 2010; Lemaître et al., 2010; Doronzo et al., 2015). Dust can be intensively emitted to the atmosphere from land sources via dust-storms which are a common phenomenon in this region (Wang et al., 2017). For instance, figure (1.1) shows the extent of dust lifted into the air that is carried by wind from north west Africa. This heavy dust was observed over land in African by instruments of the African Monsoon Multidisciplinary Analysis (AMMA) campaign.

It is well documented that atmospheric dust from desert sources can be transported on a global scale and the most active sources of atmospheric dust are in north Africa, the Middle East and Asian regions. The land surface of these regions is characterized by arid, dry, hot regions which are significant dust sources, as dust particles from the land of these regions can be easily eroded by weather factors such as wind, and thus lifted into the atmosphere. Moreover, these dry regions are significant producers of dust on a global scale because they have harsh environmental conditions represented by a lack of precipitation, and they therefore have droughts frequently.

Figure 1. 1. Intensive Saharan dust (dust storm) over the African land observed by African Monsoon Multidisciplinary Analysis (AMMA) campaign.

Airborne dust in the atmosphere mainly consists of mineral dust that can be internally mixed with other aerosols or minerals such as quartz, feldspar, clay, carbonates, sulphates, and iron (Knippertz and Stuutz, 2014). Moreover, the existence of dust particles in the atmosphere plays an important role in the atmosphere because dust particles can impact on air quality, land or ocean fertilization and atmospheric radiation. When dust is lifted in large amounts from land to the atmosphere, quantification of atmospheric dust is needed. Previous studies such as Schutz et al., (1981), Tanaka and Chiba, (2006), Engelstaedter et al., (2006), Koren et al., (2006), Huneeus et al., (2011), and Torge et al., (2011) show that the annual emission of Saharan dust is roughly 1600 T g/year, which is about half of global dust emission of 3000 T g/year. This implies that the Saharan dust is responsible for providing dust into the atmosphere more than other regions (Rosenfeld et al., 2001; Cuesta et al., 2009; Huang et al., 2014; Allen et al., 2015). In figure (1.2), the global index of dust particles from Total Ozone Mapping Spectrometer (TOMS) satellite confirms that most dust from desert areas is generated from north Africa compared to other locations, where it is clearly shown that the red area in this figure (i.e. figure 1.2) refers to the high contribution of dust coming from the northern part of Africa. Based on above, it is clear that large amounts of dust are entering the atmosphere during outbreaks from the continent of Africa and extending over large regions of the globe and affecting not only radiation but also having a key role in fertilisation of distant lands and oceans, so it is important to understand how the dust interacts and modifies the marine atmosphere as it is transported which is the focus of this thesis.

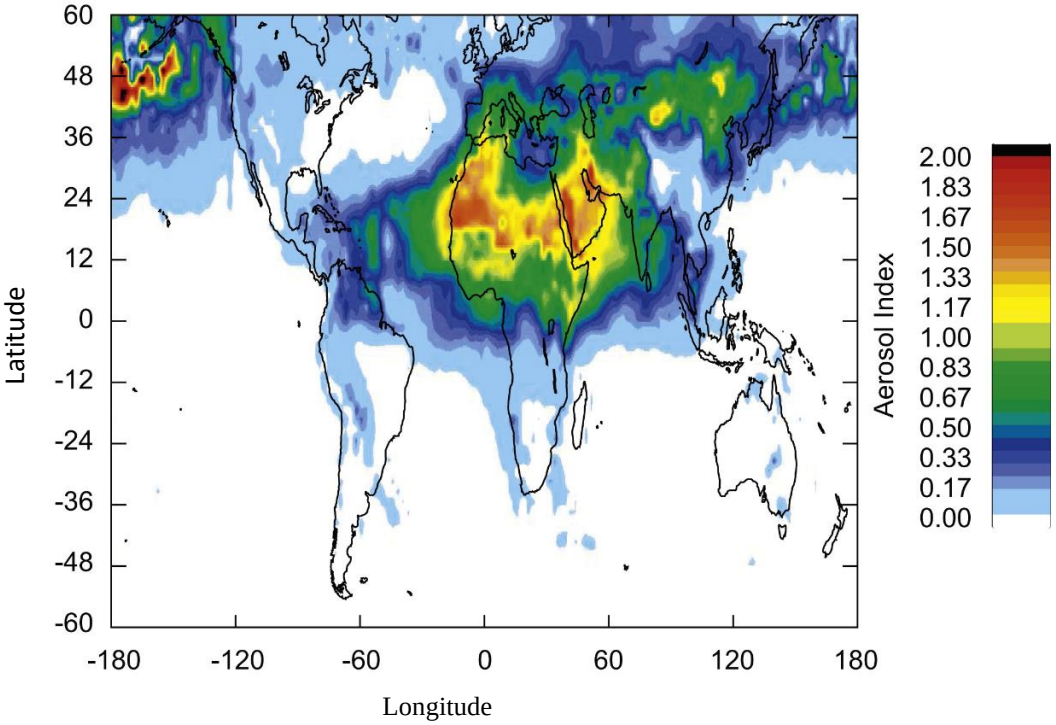

Figure 1. 2. Aerosol Index (AI) calculated by TOMS satellite from the desert land regions in the globe. The coloured vertical bar on the left shows the strength of atmospheric dust globally. Figure is taken from Hu and Sokhi, (2009).

1.2 Meteorological systems affecting west Africa

1.2.1 African land: atmospheric structure, dust and wind systems

The atmospheric structure in the continent of Africa is affected by various atmospheric constituents such winds, dust-aerosols, clouds, humidity, temperature, pressure, and radiation. In this research, it is important to understand atmospheric profiles over both the African land and marine environment and which factors influence dust transportation. The meteorological winds over west Africa are a key factor for determining the transportation of Saharan dust, since dust can be transported away from its sources, exceeding 5000 km or more over the Atlantic. The climatology of wind systems over Africa can be characterised by three main systems: the Inter-Tropical Convergence Zone (ITCZ), African Trade Wind (ATW) and African Easterly Jet (AEJ).

The ITCZ, which is at or near the equator, is associated with the location where the sun is at its zenith at mid-day and is the location where the maximum solar flux can reach the surface on cloud free days. It is the location where the southeast and northeast trade winds converge, and air ascends by convection, usually resulting in clouds, and the convergence and ascent establishes the Hadley circulation (Broccoli et al., 2006). Figure (1.3) shows the surface position

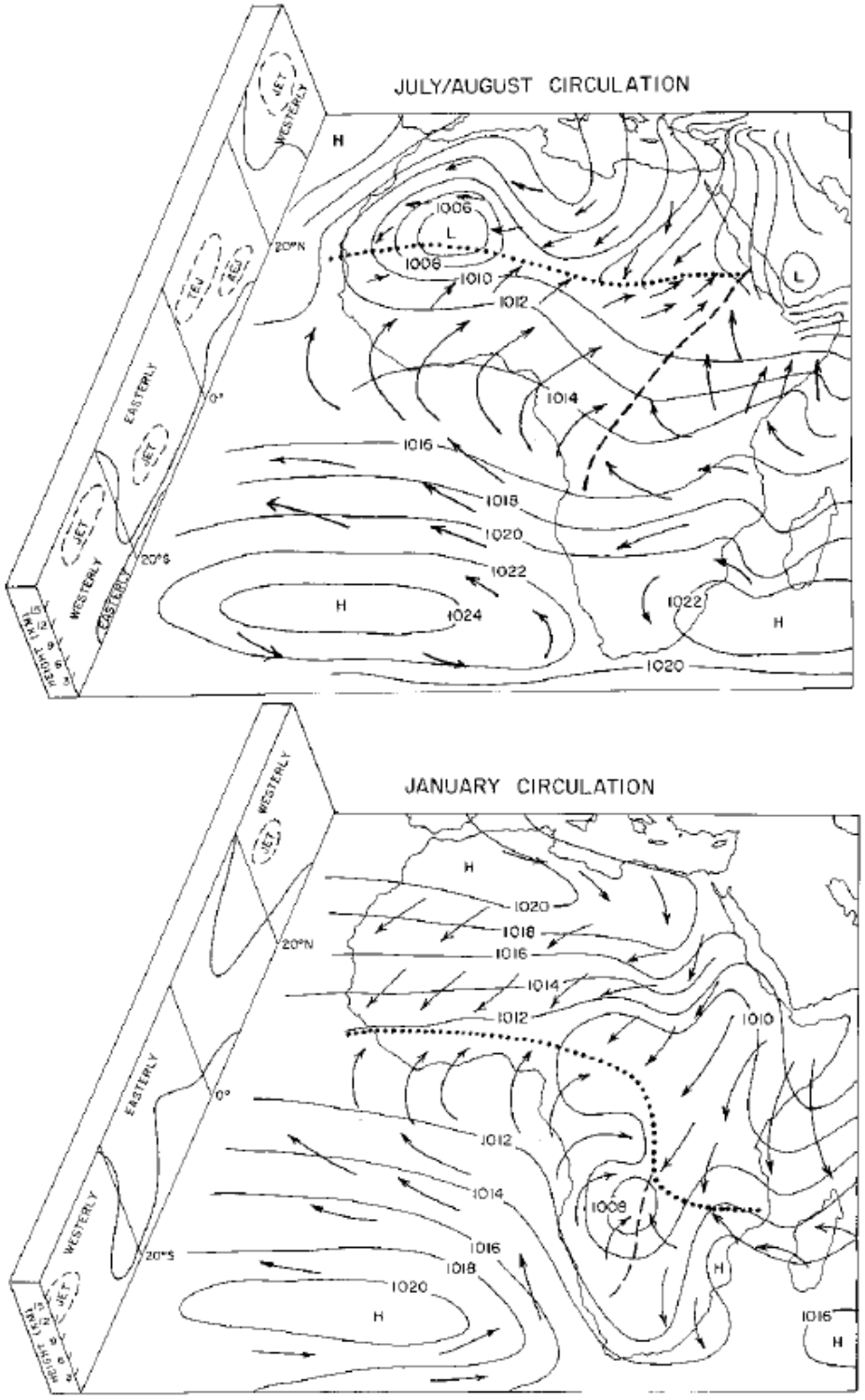

Figure 1. 3. Wind system associated with the ITCZ over Africa during January and July-August. The top plot shows the atmospheric circulation over Africa in July-August, while the atmosphere circulation over Africa in January is shown in the plot on the bottom. Arrows show the direction of wind, e.g. ATW and AEJ with height. Dotted line indicates the location of the ITCZ over the continent of Africa. The schematic block on the left of each plot shows vertical easterlies at tropical latitude and easterlies at subtropical regions with height in units of km. Pressure (mb) is indicated by solid lines. Figure is taken from Mbourou et al. (1997).

of the ITCZ, winds and pressure over the African continent during the summer (top panel) and winter (bottom panel) seasons. The ITCZ is where the ATWs of the northern and southern (southeast and northeast winds convergent) hemispheres are convergent. Maximum heating occurs in the transition zone between the dry air (Harmattan wind) and moist air (monsoon flow). Between February and June, the ITCZ shifts to the north and then it returns to the south around December.

The energy available to drive the ITCZ can be accounted for through net balance of radiative fluxes assuming a steady-state atmosphere by using the following equation (Bischoff and Schneider, 2016):

$$F = (SW_a - LW_e) - OE \qquad \text{Eq. (1)}$$

Where, F is the vertically integrated energy flux in the atmosphere, $(SW_a - LW_e)$ is the difference between absorbed short-wave (SW) and emitted long-wave (LW) radiation and OE is oceanic energy at the surface. The OE is the amount of energy that is absorbed and retained by the ocean, F is the energy available for the atmosphere. This equation explains the net energy input to the atmosphere in a column, where the net energy over land is different from that over ocean since the ocean surface is able to absorb energy from the surface and retain it more than land surface. Thus, transported energy in the atmosphere in equation 1 describes the difference between SW and LW net fluxes term and oceanic energy at the surface.

The ITCZ is important for understanding the climatology of west Africa. The ITCZ is represented by a low pressure system and so significant precipitation is associated with it along with seasonal variations of both temperature and precipitation. In west Africa, the rainy season takes place between June and September, while a dry season occurs during rest of the year (Nicklin, 2011). The ITCZ is associated with high equatorial solar heating which causes the air to be lifted up and links the convergent trade winds in both northern and southern hemispheres. Therefore, ascending air along this ITCZ globally produces high cloudiness, frequent thunderstorms and heavy rainfall. The location of the ITCZ is important also for the West African Monsoon (WAM), since the WAM is characterized by summer rainfall over the continent and winter drought and this can be affected by the location of the ITCZ (Janicot et al., 2015). In addition, rainfall over west Africa is controlled by the advection of moisture from the Gulf of Guinea in the low altitudes of the atmosphere as well as the African monsoon that develops over this part of the African land during the northern spring and summer (Sultan and Janicot, 2003). The position of the ITCZ can seasonally vary and it correlates generally to the thermal equator. Also, the ITCZ propagates poleward more prominently over land than over water, and over the northern hemisphere more than over the southern hemisphere since water has a much higher heat capacity than land. In July and August, over the Atlantic and Pacific, the ITCZ is between 5 and 15 degrees north of the equator, but further north over the African land and Asia.

In January, over the Atlantic, the ITCZ generally resides no further south than the equator but extends much further south over south America.

WAM is the major circulation affecting Africa that transports air in the south-westerly direction from the Atlantic (Gulf of Guinea) to the continent of Africa due to differences of sea-surface temperature and atmospheric conditions over African land. Figure (1.4) displays the positions of different types of African winds such as the AEJ and the Tropical East Jet (TEJ). The Inter Tropical Discontinuity (ITD) is shown as the dashed blue line in figure (1.4), represented as the meeting location of the Harmattan and the monsoon flows. Figure (1.4) also depicts the intensive easterly winds, where the AEJ is indicated by the yellow tube. The AEJ is characterized by strong variability of rain over the Sahel. Other winds such as TEJ (light blue arrow) and Sub-Tropical Westerly Jet, TWJ (dark blue tube at the top of this figure), are located at the upper levels of the west African atmosphere, where they are developed by convection process.

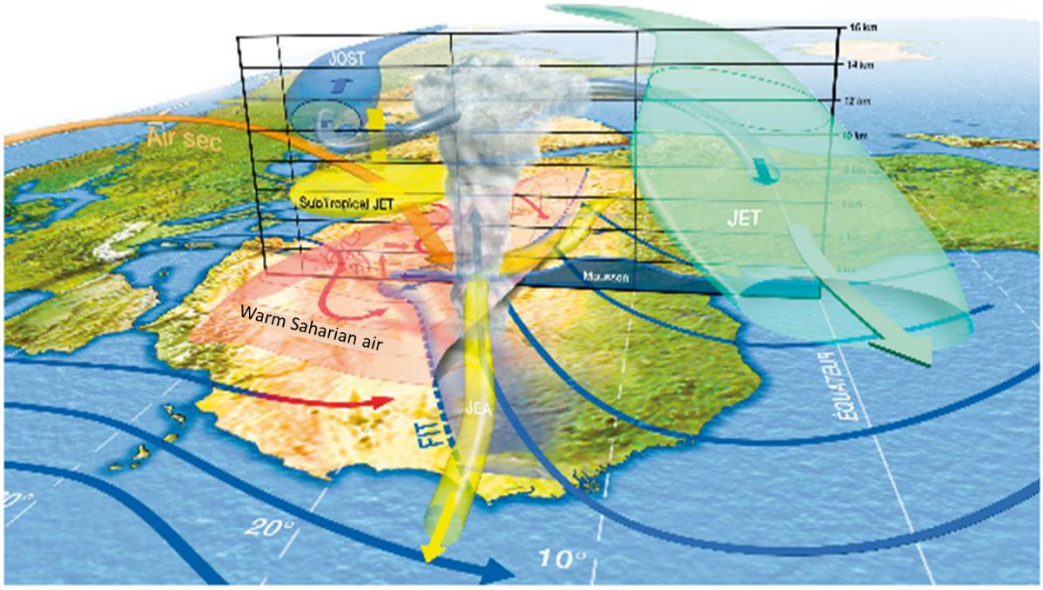

Figure 1. 4. Three-dimensional schematic view of the WAM over west Africa. TEJ (shown by green arrow) indicate to Inter-Tropical Discontinuity (ITD) and Tropical Easterly Jet, TEJ (green arrow), respectively. Yellow arrow indicates the Jet from East Africa (JEA). Red arrow stands for warm Saharian air and orange arrow denote to Air sec (dry air). Figure is taken from Lafore et al. (2010

To the north of the ITCZ, the ATW (Harmattan) is generated from the Hadley circulation and has a south-easterly direction due to the Coriolis effects of the Earth's rotation (Mbourou et al., 1997). This wind blows from north-east to south-west (easterlies) carrying dust from the Sahara toward the Guinea coast of Africa. During this transport, the dust can mix up to 7 km or more due to convection (Marsham et al., 2013). Thus, most of the Saharan dust is transported by upper-level-winds. The AEJ is a strong wind located above the ATW at about 600-700 hPa, which is generated from the vertical inversion of meridional thermal gradient in the middle troposphere between Chad and Senegal (Fontaine and Janicot, 1992). The AEJ wind is responsible for carrying

dust far from the western coastline of Africa long distances towards the Caribbean. This strong wind containing the dust can affect the African Easterly Waves (AEW) over the Atlantic, where the AEWs flow along the AEJ toward the west from the continent of Africa (Nicklin, 2011).

Dust can be transported at any time in the year, but the strongest transport is during the summer and spring. Most of dust is transported by the AEJ which controls dust transportation over the Atlantic. The schematic diagram (1.5) depicts the influence of the AEJ on dust transportation between land and the Atlantic through presenting a vertical cross-section of the Saharan Heat Low (SHL), which is represented as a region over Africa with low pressure. The yellow shaded region is the Saharan air layer (SAL) transported over the Atlantic mainly by the AEJ, while grey shaded regions indicate peak rainfall. The panel below presents the meridional variations in the potential temperature (θ) and equivalent potential temperature (θ_e), see the caption of figure 1.5. Lines in the figure highlight typical meridional variations in potential temperature (θ) for the atmospheric boundary layer, where it is characterized by significant gradient increases of θ with heights between the Sahara and Guinea coasts. For this region, the AEJ is situated as shown in the yellow shaded area in the diagram above. The solid line below (inside the box) this diagram shows the moist static energy equivalent potential temperature (θ_e). Equivalent potential temperature diminishes north of 10 °N, while θ continues to increase, as the boundary layer is characterized by a dry layer north of the core of the ITCZ. At low altitudes, the south westerlies from the Atlantic produce most of the humidity for the WAM, while polewards of this, north-easterlies advect relatively drier Saharan air into the rainy region. Interestingly, dust transportation toward Europe is sometimes caused by the intense cyclones that pass over the African land from the west of the Mediterranean towards Europe (Moulin et al., 1997; Engelstaedter et al., 2006; Zhao et al., 2010).

To conclude, dust is potentially affected by multiple wind systems after being lifted from the surface. Dust is transported by easterlies from the north-east to the south-west coasts of the African continent. The mechanism of dust transportation over land is usually controlled by different winds compared to over the Atlantic, where dust is influenced by the strong AEJ over the Atlantic. This wind can act as a supporting factor to transport dust far distances from the African coastline. In the next section, I discuss the general properties of dust that are important for investigating the radiative effects of African dust over the Atlantic, particularly in the study region of the Canary Islands and Caribbean.

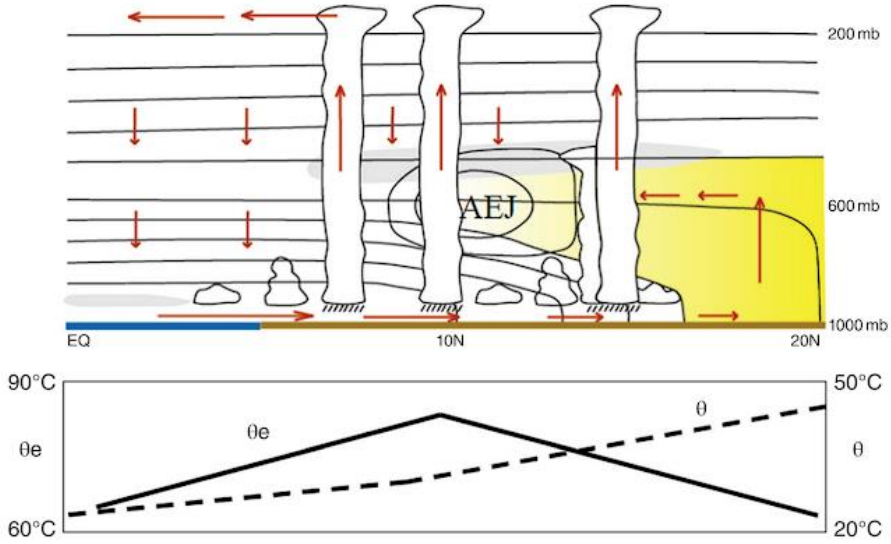

Figure 1. 5. Schematic diagram shows the atmospheric structure over west Africa and the Atlantic as vertical cross-section from south to north. The diagram on top panel explains the mechanism of dust transportation associated with shallow monsoon layer. This moist layer (i.e. low monsoon layer) is located beneath the dryness of the SAL and contributes to intersect the dust layer above it. Shallow monsoon air is characterized by strong convective inhibition (CIN) because of dust layer. The monsoon is located just to the south of the AEJ. Grey shaded areas in the top diagram present maximum precipitation. Panel below highlights the structure of potential temperature (dashed line) for typical meridional variations in the potential temperature of atmospheric boundary layer (θ), where it is characterized by increasing θ with height and linked to AEJ. Solid line shows moist static energy equivalent potential temperature (θe). Equivalent potential temperature initialises to diminish north of 10◦N, while θ continues to increase as the boundary layer is characterized by dry layer north of the core of the ITCZ. This figure is taken from lebel et al. (2010).

1.3 General properties of dust

1.3.1 Dust emission

Dust from arid and semi-arid regions can be lifted into the atmosphere through boundary layer surface winds. This is typically represented in models when the wind friction velocity (u*) exceeds a certain threshold value, in which the threshold value depends on the size distribution and texture of the land soil. This parameter not only controls whether the dust will be lifted, but also the amount that is lifted. The definition of u* can be expressed by the following equation,

$$u(z) = \frac{u^*}{vo} \ln\left(\frac{z}{L_0}\right) \qquad \text{Eq. (2)}$$

Where $u(z)$ is the wind velocity at an altitude z above the surface, vo is the von Karman constant, and L_0 is the aerodynamic roughness length. The equation above is related to neutral conditions, where u^* can be proportional to shear stress (s), which has a potential impact on the entire dust sizes (Parker and Diop-Kane, 2017). Shear stress can be expressed by

$$s = \rho_a u^{*2} \qquad \text{Eq. (3)}$$

Where ρ_a the density of air (kg/m^3). So, to produce dust particles a significant wind stress is needed. This is along with the source function, which depends on the ability of soil to release the particles of dust and, therefore, allowing dust to be transported into the atmosphere. Dust emission, especially from the Sahara Desert, can be investigated by using the Lagrangian Particle Dispersion Model, LPDM (Sodemann et al., 2015), as shown by the following formula

$$F = c * f * (u - u_t) * u^2 \qquad \text{Eq. (4)}$$

Where F is the total mass flux in units of $\mu g/m^2.s$, c is a dimensional factor value, which equals 0.7 $\mu g.\frac{s^2}{m^5}$, f is a fraction for bare-soil surface at each 0.25˚x 0.25˚grid box, u is surface wind velocity at 10 m, and u_t is the threshold velocity in units of m/s.

The process of dust uplift and transport from the land surface is modelled numerically. It has been shown that to model dust emissions correctly it needs to capture the process on a small scale (with dust height about 1m from the surface) using saltation and sand blasting processes (Astitha et al., 2012, ACP). However, for the large-scale, it has been shown by Parker and Diop-Kane (2017) that the determination of input data (data taken from observations) in the modelling of dust emission is conditionally related to surface properties such as seasonal vegetation and soil type. The challenges in specifying the required observational data for dust modelling is particularly strong in semi-arid land such as the north Africa region. Simulating dust emissions based on using campaign measurements (including Bodele Dust Expermint, BoDEx, AMMA and FENNEC) provides appropriate information in specifying the spatio-temporal variation of dust emission over the Sahara.

To understand dust emission better, a schematic diagram figure (1.6) shows that the effects of saltation bombardment as well as surface wind on dust-soil particles lifts dust particles into the atmosphere, depending on the size and shape of dust particles. For dust particles ranging between 70-500 μm in size, the dust particles will emit from the surface depending on forces such as particle cohesion, which makes particles either stick to each other or not, thereby affectings how much is released into the atmosphere. Dust of sizes less than 20 μm in diameter can be transported long distances by winds in the atmosphere. In contrast, large particles with sizes about 20 and up to 100 μm or more can either be suspended in the atmosphere but only for much shorter periods and will sediment to the ground quickly. Sometimes, the fallen dust particles contribute to modifying the saltation process.

Dust emission is controlled by the threshold values between the drag near the surface and the gravitational inertia of particle sizes. When the value of drag exceeds the inertia of dust with sizes greater than about 60 to 80 μm, these particles will move horizontally. As these sizes move downwind, small sizes of silt and clay particles will separate from large dust particles. However, these disaggregated particles will not be emitted into the atmosphere due to cohesive and gravitational forces, which are larger than aerodynamic entrainment. Thus, these forces will make the separated dust particles stick together, rather than being released into the atmosphere. Due to

these processes, it is major challenge to model dust emission. The most straight forward approach is to consider dust emission from the land surface when the wind friction velocity exceeds a threshold value.

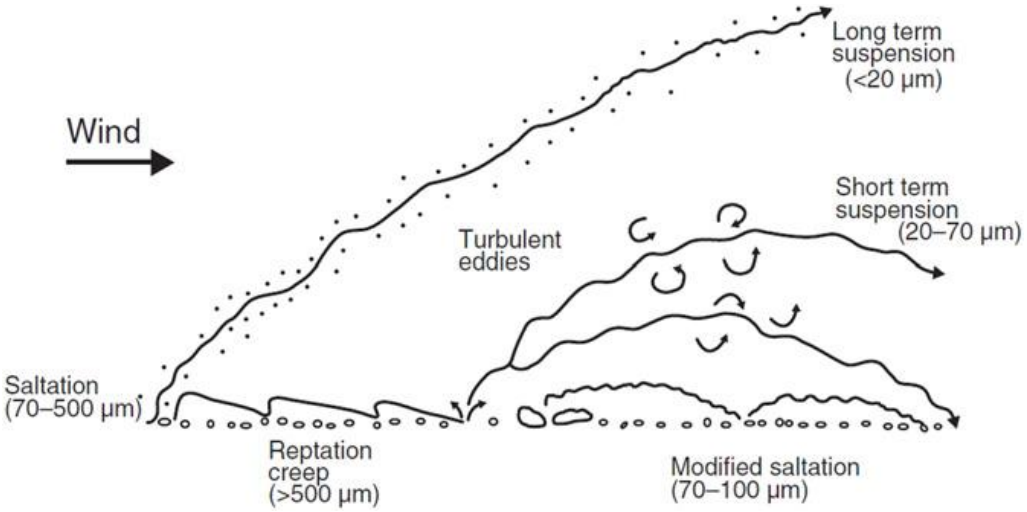

Figure 1. 6. Schematic diagram of ways for dust to transport into the atmosphere. Dust emits from land surface by the saltation bombardment process corresponding to specific meteorological conditions of the land surface. Dust sizes have kinetic energy as they hit the ground. As these particles hit the ground, they will transfer their kinetic energy to the surface particles. Not all particles that get hit by particles will be emitted to the atmosphere, where this depends on the forces between particles to make them release to the atmosphere due to cohesive and gravitational forces. The figure is taken from Astitha et al. (2012, ACP) and Kok et al. (2012).

The major challenge of simulating dust emission is related to the correction factor (f_{drag}) of different surfaces (i.e. rough and smooth surfaces) associated with surface roughness length (L) and roughness length of uncovered surface (L_s). Where Eq. (5) shows that the f_{drag} is higher for larger L, and thus the threshold friction velocity (u_{thr}) according to Eq. (6) will be high. Thus, high values of u_{thr} results in decreased emission of dust particles into the atmosphere due to u_{thr}, which relates to a greater number of non-erodible obstacles such as rocks.

$$f_{drag} = 1 - \frac{\ln\frac{L}{L_s}}{\ln\left(0.35*\left(\frac{10}{L_s}\right)^{0.8}\right)} \qquad \text{Eq. (5)}$$

$$u_{thr} = \frac{u_{thrs}}{f_{drag}} \qquad \text{Eq. (6)}$$

Where, u_{thrs} is the threshold friction velocity over smooth surface. Furtherrmore authors such as Shao (2001), display the initial displacement of dust particles with X and Y axes by the saltation process for dust emitted into the atmosphere. Figure (1.7) shows the mechanism of dust uplift by saltation bombardment assuming spherical particles in shape. The symbol X_T shows the direction of particle distance as it moves under the influence of saltation, while the change in this distance horizontally and vertically is denoted by dX_T and Y_T, respectively. D is the diameter of a particle,

and α is the angle between surface and u wind. However, this may be not be a good explanation for dust emission, especially for non-spherical dust particles.

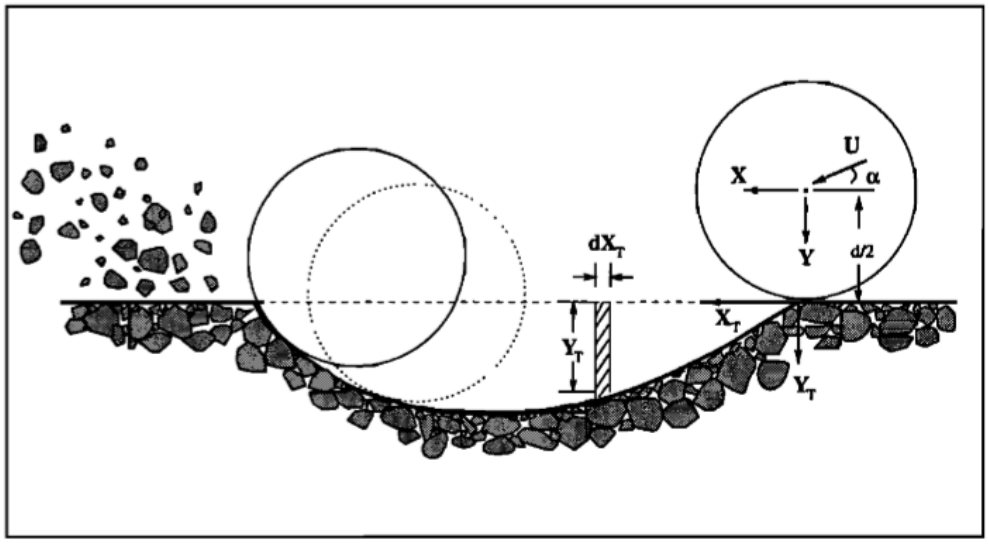

Figure 1. 7. A simplified mechanism of dust emissions by saltation bombardment. This mechanism assumes that particle with diameter (d) is spherical in shape and does not break while it moves along the (XT, YT) trajectory (Shao, 2001).

The key factors that control dust emission from land have been debated by many authors. These factors are used in models and compared to observations. For instance, Kim et al. (2015) used a global model to simulate dust emission from the Saharan Desert. Their results show that surface wind interacting with dust particles from Africa is the main factor for dust emission. They also show that dust emission is completely dominated by surface wind. Further work presented by Tsikerdekis et al. (2017), who used a regional climate model (RegCM4) for simulating dust emission over the desert, stated that the critical wind speed varies in value over the desert, depending on several parameters such as soil moisture, soil particle size distribution and surface roughness. In contrast, considering agricultural areas, Tegen et al. (2004) suggest that agricultural land does not influence dust emission and that the latter is controlled by future changes in climate and natural vegetation. To conclude, the possibility of dust emission from the land surface is controlled mainly by wind speed and, soil moisture; it relies on the characteristics of land surface, e.g. vegetation cover, surface roughness, precipitation and rocks (Marticorena and Bergametti, 1995). In addition, the possibility of high dust emission is linked to the Sahara Desert in north Africa, since it occupies about 8% of the global land area (135 x 10^6 km^2), with an area of about 11 x 10^6 km^2. Meanwhile, drylands contribute about 54 x 10^6 km^2 of global land area (White and Nackoney, 2003; Jickells et al., 2005; Feng and Fu, 2013).

1.3.2 Dust transportation

Several stages are involved as dust undergoes transport:

1. **Dust emission from land surface to the atmosphere.** This is the initial step of dust injection from land surface to the atmosphere. This step is the most complicated since dust emission is controlled by many factors which were outlined in the last section. For instance, it is characterised mainly by low-level wind speed and complicated processes at the surface that are difficult to represent fully in models. Generally, after the dust particles are eroded from dry land surfaces by winds, the dust can be lifted by turbulent convection created by high temperatures, especially during the summer season (Chouza et al., 2016). Therefore, wind and convection processes are mainly responsible for dust emission from African land to the atmosphere, although land erosion by wind can be affected by other factors, such as soil moisture and the nature of land soil.

2. **Dust transportation into the SABL.** The dust is usually lifted first into the surface layer, where wind speeds are affected by the drag of the surface and surface roughness. Dust events are characterised by strong convection taking place at the source region so dust will quickly be lifted into the well mixed boundary layer, named the Saharan atmospheric boundary layer (SABL). During dust events the SABL can extend up to 7 km or more in altitude. In these conditions, dust in the SABL can be transported mainly by the AEW, which was previously discussed in section 1.2.1.

3. **Dust transportation from land over the Atlantic.** As dust is transported from the source region to the African coastline and beyond, it will go from the SABL of the land to the marine environment and will experience the changes in environment discussed earlier in this Chapter. Transport will occur through the dust being advected within the SABL or detrained into the layer above the SABL and advected away. Rodríguez et al. (2011) found that dust transportation is generally different based on latitude, wind speed and direction. Although dust is transported by prevailing wind, dust can be transported in a different transportation system from north Africa since wind regime as well as dust source and transport change seasonally (Parker and Diop-Kane, 2017).

Previous studies that related to the simulation of dust transportation report that dust transported from north Africa occurs over many seasons. For example, Prospero and Carlson (1972) state that dust is transported from the tropical region of the central Sahara during the winter season within the trade winds (Prospero et al., 2002; Parker and Diop-Kane, 2017), but in the summer season, dust is transported above trade wind (roughly 5-7 km) by African Easterly Winds from west or northwest Africa over the Atlantic Ocean due to the large increases in sea-land temperatures in

the Sahara and Sahel (Van der Does et al., 2016). The westward direction of dust transported by AEW is reported by Chouzo et al. (2016), who looked at African dust transported toward the Atlantic by using flight observations implemented in north Africa. Their study revealed that the AEJ flow from the African coastline is due to the passage of the AEWs during their observations. These show that the mechanism of long-range dust transportation over the Atlantic occurs in different seasons and in different ways resulting in dust transport during the summer season often at higher altitudes than in the winter months.

In conclusion, the transport dust from the surface to the marine environment is challenging to a model as it involves complicated processes of sourcing of dust through erosion at the surface and many dependencies of the surface properties, through to complicated dynamics ranging over various lengths and timescales from turbulence operating over seconds or minutes through to synoptic or even global scales with variations over seasons.

1.3.3 General vertical dust profile background

One of the most crucial properties of atmospheric dust affecting the atmospheric heating rates and radiative effects is the vertical structure of the dust. In this section, I will show some examples of vertical profiles of dust from model simulation drawn from recent research. The full vertical analysis of dust profiles from observations, such as flight observations, will be provided in Chapters 2 and 3. The reason for showing these dust profiles from simple model results is to illustrate how dust profiles can change during transport over the Atlantic. The results are idealised but illustrate clearly how dust can evolve during transport over long distances, which is relevant for studying the radiative properties of dust.

The vertical distribution of atmospheric dust over land and ocean is generally located above the boundary layer and below some upper level height of background air (Ryder et al., 2015; Marsham et al., 2013). The larger dust particles will sediment into the layers below the SAL and will fall out relatively quickly. Dust over the land compared to dust over the ocean tends to have much higher loadings, and the vertical profiles of dust in these regions have different distributions because:

1. The atmospheric dust over land is located between the surface and up to about 7 km. This can be different over oceans, where Saharan dust is often more localised in layers between about 1.5 km and 7 km (Marsham et al., 2013).

2. The difference in dust profiles over land and ocean is that the height of the top of the dust layer over land can extend to higher heights with larger dust concentrations, well above 7 km in some cases, but the dust over the ocean (after about a day from dust transporting from the African coastline) in the Marine Boundary Layer (MBL) will contain greatly reduced dust (especially mass), aside from the small size and what is still sedimenting from the SAL. Also,

over the ocean there will no longer be a source of dust at the surface and often the dust can be significant in a layer and decrease above and below, depending on how far it is from the dust source. The higher altitude of dust concentrations over land compared to ocean is because of the very strong daytime heating, resulting in very strong convection, sometimes reaching high into the tropopause.

3. The particle sizes of dust over land tend to be characterised by large sizes of many tens of microns (e.g. Goudie and Middleton, 2001), but can frequently have sizes exceeding hundreds of microns (Mahowald et al., 2005). In contrast, particle sizes over the Atlantic Ocean are less well understood since few measurements are made over the oceans. Although particle sizes of dust over land and ocean have been evaluated by many authors, understanding the evolution of the dust sizes with transport for the marine environment is needed.

The vertical and horizontal distributions of dust, especially Saharan dust, at different distances away from the African coastline clearly vary significantly. This is evident in terms of visual plots of dust observed from satellites or ground (Fig 1.1). The dust particle size distributions vary strongly, which is evident from numerical modelling simulations, as shown in figure (1.8), which shows an idealised constant profile of two sizes that were entered into the model over the land and then advected out over an ocean. It is clear in the figure (1.8) that within 100 km, there are significant differences between the small and large sizes, with the small sizes generally spreading vertically above and below the initial profile as they are mixed up and down. However, the large particles are mostly seen to just sediment towards the surface. The larger sizes have a far greater magnitude below the initial SAL layer than the small sizes brought about by sedimentation out of the atmosphere.

Transport over the Atlantic ranging from 300-600 km shows that the large sizes tend towards a uniform profile at the lower altitudes, whereas the small sizes are still concentrated around the initial profile heights. By 1000 km, the large particles have mostly sedimented out of the atmosphere. The small sizes are largely unaffected by sedimentation, even by 5000 km.

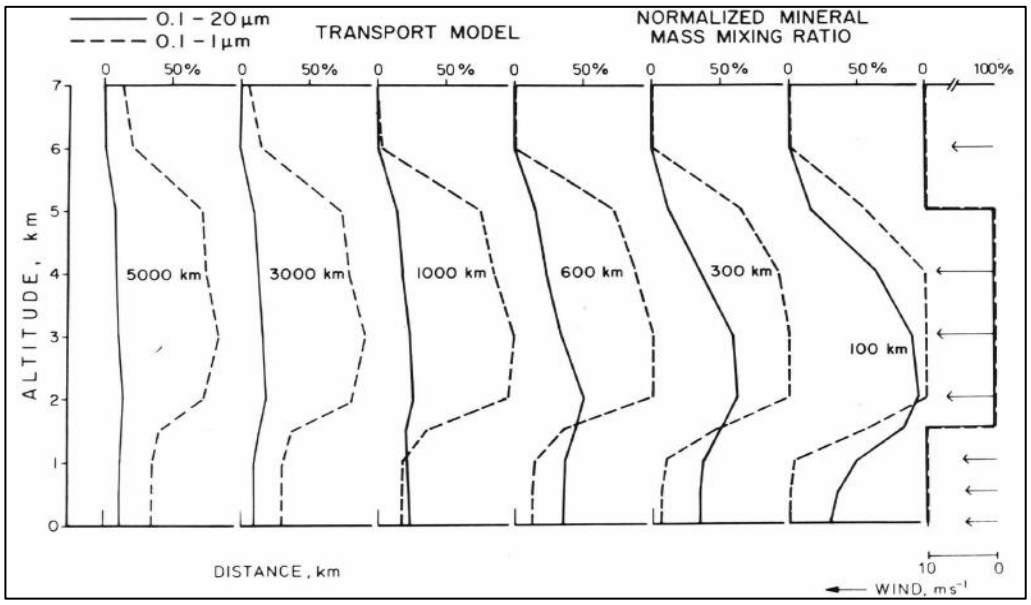

Figure 1. 8. Vertical distributions of mineral dust for selected transport distances from the African continent (dust source) toward the Atlantic. Vertical mixing ratios are plotted for the mass of mineral dust particles for two size ranges indicated in the plot and for the total mass normalized to the initial mixing ratio at the source (x = 0 km). This plot indicates the evolution of dust transported for about 5000 km across the Atlantic by using transport model. This figure is taken from Schutz et al. (1981).

It is useful to study the vertical variability of dust particle sizes using a numerical model, especially if you are seeking to estimate the dust size distributions away from observations. In the current work, a new model was developed to model the transport of size dependent dust over long distances and to estimate the dust altitudes on the other side of the Atlantic. I have radiosonde profiles in the Caribbean but I do not have dust mass concentrations. In order to make an estimate of whether representative amounts of dust would have an impact there, it is necessary to estimate the transport. This issue is addressed in Chapter 5.

1.3.4 Vertical profiles of Saharan dust over the Atlantic Ocean

Dust transportation and dust measurements have been presented in previous sections. In this section, I present much more detail about dust transportation associated with both African land and the Atlantic. Over land, the Saharan dust is lifted into the Saharan Atmospheric Boundary Layer (SABL). The injected dust particles in this layer are located between the surface and frequently extend up to 7 km; dust particles are frequently advected by winds away from the land in the SAL (Cuesta et al., 2008). To understand the transportation of dust over the Atlantic, it is important to distinguish between the SAL, the marine aerosol layer (MAL), the marine boundary layer (MBL) and the marine atmosphere (MA). The MAL extends from the surface up to the trade wind inversion, which is typically between 1.5 and 2.5km for our study region and

contains typically clear air containing aerosol which is often sea-salt in the pristine environment. The MBL is within the lower part of the MAL and is characterised by the turbulent dynamics due to surface fluxes from the ocean surface. The MA is the marine atmosphere extending from the surface up to the top of the troposphere in this work and can be either characterised as pristine or dust affected MA. The dusty marine atmosphere (MA) will have an intrusion of SAL at some height with dust aerosol sedimenting below into the MAL and MBL and may have higher values of water vapour as well.

The SAL is a layer of air that contains dust lifted up from the land surface, which in our case is then advected over the Atlantic Ocean, initially in a fairly well-defined layer called the SAL. The dust layer is often assumed to be dry since atmospheric dust often originates in dry, hot locations. Also, the dust is most easily lifted in dry conditions and the convection is strongest on very hot days with significant solar heating of the surface.

As the SAL layer advects away from the African coastline, the SAL layer rides up over the MBL or higher due to the typically warmer air temperatures. The MBL is the lowest layer of the marine atmosphere defined here, in which the air is usually well mixed and ranges from heights of 10 s of meters to a few km and contains high moisture levels due to the lower surface being the ocean (Rittmeister et al., 2017, ACP). The SAL mainly consists of dust from the African mainland whereas both the MAL and MBL can contain a range of aerosols including predominantly sea salt and sedimented dust particles.

The ATW can advect dust away from dust sources toward the marine environment. Once the dust reaches the boundary between the African coastline and the sea, dust will encounter vastly different surrounding conditions. The marine environment will typically be more stable (at least above the MBL) than the SABL over land; it would be expected that there would be much more moisture due to the ocean providing moisture into the marine environment. Radiation will also be dramatically changed, since the surface is much more absorbing over ocean than over land where it has a higher albedo, and the differences in water vapour molecule concentrations will also affect fluxes. As the Saharan dust is advected by the ATW over the Atlantic, the warm and dusty SAL from the land will typically ride up over the MBL due to higher θ. The SAL will be well-mixed over land, and it will stay that way at least at first as it advects over the ocean. Because the layer is well mixed, the intrusion will be distinct from the surrounding air and there will be a strong θ changes above and below the layer, creating inversions above and below. Below the SAL will frequently be a very deep stable layer, much more than usual for the pristine marine environment. Above the SAL will typically be a stable background marine environmental air. The boundary for the lower interface of the SAL is typically at about 1-2 km (Gross et al., 2015) whereas the upper boundary of the SAL is often at about 7 km (Prospero et al., 1996; and Birch et al., 2012).

To conclude, the SAL forms a distinct layer that transports into the ocean MA environment with dust contained in the SAL layer with the larger dust particles sedimenting through the MAL to

the ocean surface as the transport takes place. Over time, the SAL will evolve by interacting with the surrounding air at the boundaries which will act to stabilise the SAL layer as heat and energy are exchanged. In the next section, I will describe in more detail the dry and wet deposition that can take place during advection.

1.3.5 Dry and wet deposition of atmospheric dust

Once dust is lifted into the air and transported, dust removal from the atmosphere occurs through two processes: dry and wet deposition. Both mechanisms remove dust from the atmosphere to the surface and are important for the acidification and fertilization of the land soil and the oceans (Inomata et al, 2009).

The process of dry deposition in the atmosphere describes the sedimentation of dust particles onto the Earth's land or ocean in the absence of precipitation. The dry deposition of dust particles is controlled mainly by the size range of dust particles and the associated factors that influence on their sedimentation to the surface. For example, the size ranges of dust particles in the atmosphere can be categorized into three types: large, moderate and small dust particles. For the particle sizes between 10 μm and larger, dust is strongly affected by gravitational settling, while the sub-micrometre size range of dust particles is influenced by Brownian processes (Osada et al., 2014). The particles of sizes between these values are most affected by turbulent mixing and advection of air since they are too large for Brownian effects and not heavy enough to have appreciable sedimentation velocities.

In contrast, wet deposition is the removal process that occurs when dust particles either nucleate cloud droplets or collide with rain drops and are then removed from the atmosphere by precipitation of the resultant particle. Modelling studies such as Marticorena et al. (2017) illustrate that the variability in the modelling of dry and wet deposition is related to the ratio of wet-to-dry removal rather than other mechanisms such as dust emission and transport over the continent of Africa; however, in this study the wet deposition can be ignored since there is no precipitation.

As mentioned previously, dust deposition contributes to fertilizing soil and oceans by adding nutrients. For instance, Saharan dust fertilizes the land surface with minerals including Fe, Al, Mn, Mg, Ca, K, P, and Ti in the basin of Amazonian forest of south America (Bristow et al., 2010). Also, dust sediments and rains out (either by acting as a CCN or removed through collisions with sedimenting cloud particles) after being transported and this provides important minerals to the earth and ocean surfaces far away from the dust source region (Kienast et al., 2016). This provides nutrients to the oceans and replenishes the land of lost nutrients through farming and other activities, especially for the rainforest basin of south America (Bristow et al., 2010; Yu et al., 2015). Indeed, dust can play a key role in affecting the habitat of both the oceans and land (Jickells et al., 2005; Mahowald et al., 2005; Shi et al., 2011). Dust from Africa has a significant impact on the biological productivity of the ocean surface. Dust affects both the ocean

acidity as well as providing important minerals to ocean life such as phytoplankton. Mineral particles and dissolved iron can also play a role in carbon uptake by the sea causing a reduction in the atmospheric greenhouse gases, and thus influencing climate change (Wang et al., 2017).

Dry deposition is the removal process of dust particles that takes place in the absence and presence of clouds after dust is transported into the atmosphere by winds. As the focus of this work is on dust effects during non-cloudy conditions, the wet deposition process in this study is ignored. Recent work performed by Heinold et al. (2017) shows that the dry deposition of Saharan dust over the Atlantic Ocean is controlled by convective mixing in the tropical and subtropical regions. Although their simulations involved studying the impact of the MBL on dust deposition as well as the impact of radiative forcing on dust-cloud interactions, they did not focus on the quantification of dust radiative effects corresponding in the SAL.

1.3.6 Turbulent process influences on dust transportation

Dust transportation over land and ocean can be affected by turbulent mixing. This mixing can mix dust and varying concentrations or even mix dusty and non-dusty surrounding air. This process is addressed by Garcia et al. (2015) who state that dust within the SAL is extensively affected by the process of turbulent mixing within the SABL over Africa. When modelling, this effect can be determined by evaluating the degree of instability by assessing the gradient Richardson number, Ri_g, using the following criteria:

a) The atmosphere is not turbulent (i.e., laminar), where $Ri_g > 1$,

b) The atmosphere is unstable, where the value of $Ri_g < 0$,

c) The atmosphere is turbulent (due to shear effect), where $0 < Ri_g < 0.25$,

d) Transition from turbulent (laminar) to laminar (turbulent) flow $0.25 < Ri_g < 1$,

The last condition is a difficult one since the atmosphere is transitioning from or to a laminar state. Garcia et al. (2015) shows that the impact of shear at the top of the dust layer is a crucial factor in terms of inducing turbulence for the case (c). The equation of Ri_g can be written as below.

$$Ri_g = \frac{\frac{g}{T_V}\frac{\partial \theta_V}{\partial z}}{\left(\frac{\partial u}{\partial z}\right)^2 + \left(\frac{\partial v}{\partial z}\right)^2} \qquad \text{Eq. (7)}$$

This equation gives a measure of the strength of the shear to the stability of the atmosphere. If potential temperature increases strongly with height and the shear is weak then Ri_g will be large and no turbulence occurs, but if the vertical is well mixed such that the gradient of potential temperature with height is zero then any shear will easily create instability and turbulence. In this thesis, I focus on both the influences on potential temperature and wind shear. The changes in potential temperature come about from the dust radiative effects acting on the potential

temperature profile. I compare that with the background shear effects from the wind profiles. In addition to shear instability, turbulent mixing can be convectively driven by heat fluxes from the ground or ocean surface exchanging with the atmosphere. In the boundary layer, typically the convection dominates, and wind shear contributes to turbulence across the top of the mixing layer (Stull, 2012).

1.4 Literature review

The determination of spatial and temporal trends of atmospheric dust over land and ocean can be measured by satellite retrievals, in-situ aircraft observations, and ground-based measurements, including observations taken at the ground as well as remote sensing from the surface. This section presents the main ways to study dust from observations. From these various observations, it is possible to build an understanding of the characteristics of dust, such as the profile, size distributions, motions, etc. I must emphasise, however, that even with all these observations the coverage is limited, and modelling based on these observations should be considered as approximation rather than exact case studies. After the dust observations are presented, then radiation is presented along with its links to dust and how it can affect the atmospheric thermodynamic profiles.

1.4.1 Observing dust by satellite measurements

Satellite measurements have been used to provide data for large-scale assessments of dust, cloud cover and radiation budgets over both land and ocean. There are two common satellites, Terra and Aqua which were built by National Aeronautics and Space Administration (NASA) in 1999 and 2002, respectively. These satellites gather data from instruments such as the Moderate Resolution Imaging Spectra radiometer (MODIS) instrument. MODIS was designed to monitor the global and regional characterizations of the tropospheric dust aerosols (Alpert et al., 2001; Falke et al., 2001; Kaufman et al., 2005a). Figure (1.9) shows the observed dust transported using MODIS satellite observations during a dust outbreak in June 2012. The distance of dust transportation from its source is dictated mostly by the sizes of dust particles. As dust particles are injected into the atmosphere, large sizes of dust cannot usually be carried for long distances, as they will sediment out at the source region or close to the African continent, while small particles will have large residence times in the atmosphere, and can be advected for much greater distances and even globally. The transported dust particles over the Atlantic are usually mostly in a layer that intrudes into the marine environment (Prospero, 1981).

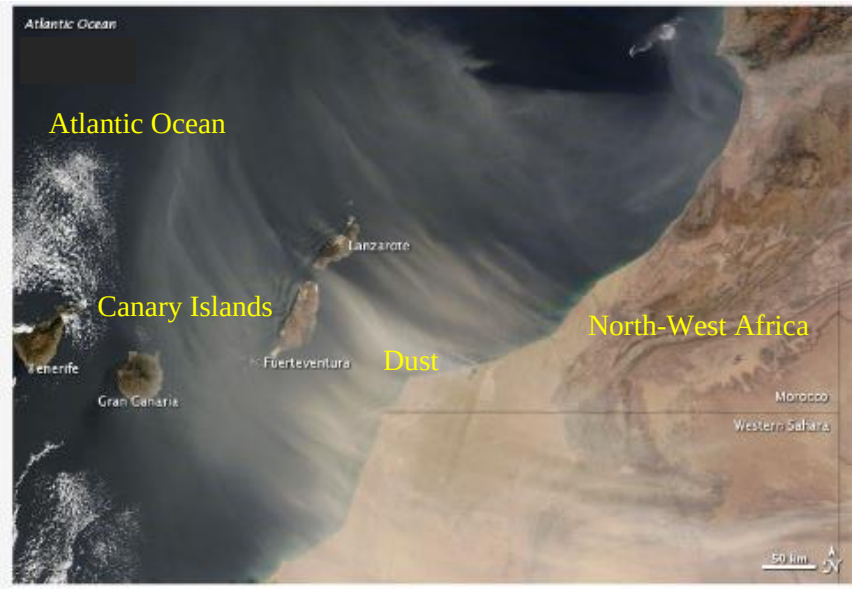

Figure 1. 9. The intensive Saharan dust over the Atlantic Ocean observed by MODIS-Terra satellite on 25 June 2012. This figure shows the highly dust advected from north Africa toward the Canary Islands.

In this current work, data from MODIS-Terra is used to investigate the movement of Saharan dust over the study region. The MODIS instrument measures data on a global scale in 36 spectral channels, ranging from 410 to 14400 nm in wavelength. These wavelengths are categorised in three spatial resolutions: 2 bands at 250 m, 5 bands at 500 m, and 29 bands at 1 km. Satellite images are utilized to retrieve dust aerosol from seven of these wavelengths (from 470 to 2130 nm). Over land, three wavelengths are used by MODIS to retrieve dust aerosol including 470 nm, 550 nm, and 660 nm, while over ocean, seven wavelengths are used: 470 nm, 550 nm, 660 nm, 870 nm, 1240 nm, 1639 nm, and 2130 nm (Remer et al., 2008). The observations of MODIS satellite provide hourly and monthly data of dust transportation for much of the globe. In addition, satellite observations are important for comparison with the results of dust transport model results and can be validated at point sources such as from AERONET measurements.

Although satellite observations are a good way to observe the large features of the atmospheric dust, the evaluation of dust radiative forcing by this technique for the globe is still very uncertain. For example, there is a contrast in the results of dust radiative forcing over global oceans. On the one hand, Remer et al. (2005) state that the uncertainty of satellite retrievals for dust-aerosol observations is at a minimum. They show that the dust radiative forcing in the globe for land is about ± 0.05 for AOD with standard deviation (SD) of about ± 0.15, while over oceans the radiative forcing is of roughly ± 0.03 and for SD of about ± 0.05. This difference in SD in ocean case is lower than land case, where the values of SD between land and oceans are quite significant. On the other hand, there is a significant difference in the direct radiative cooling of

dust over the oceans compared with over land. This is shown by Loeb and Smith (2005), where they overcome the limitation in dust radiative effects between MODIS satellites retrievals and complications of overlapping clouds. Their approach involved exploiting the synergy between these satellite observations due to restrictions in the coarse spatial resolution (where aerosol contributions at spatial scale for these satellites are smaller than the Earth's Radiant Energy System CERES footprints) of these satellite observations. Their results show that using MODIS satellite data for the clear sky over global oceans is 40% higher than over land. Also, their results reveal that for the regional scale the dust-aerosol radiative effects with high aerosol (i.e. desert land) in comparison to ocean environment are significantly different between MODIS and CERES observations. For example, the direct radiative effect of dust-aerosol for MODIS observation over Sahara Desert exceeds that from CERES by up to 10 W/m. This result implies that, although using satellite observations provides a good picture of dust observations on a global scale, considering MODIS observations in investigating the radiative forcing of dust over oceans may provide inaccurate results. In the current thesis, AOD from MODIS-Terra combined land and ocean satellite is mainly used. To ensure that MODIS observations were accurate, I looked at AOD data from AERONET observations for consistency.

1.4.2 AERONET measurements of dust

Another valuable source of measurements of the atmosphere and dust is by the AErosol RObotic NETwork (AERONET). It provides dust observations at point locations around the globe for long-term spectral AOD computed every quarter of an hour from direct sun measurements at 8 wavelengths of 340, 380, 440, 500, 670, 870, 940, and 1020 nm, except for a few locations in north Africa which have only the 440 nm wavelength available. AERONET measures AOD and categorises it into three data levels: level 1.0 data which is raw unscreened; level 1.5 which is cloud-screened; level 2.0 which is cloud-screened and quality-assured. This data is considered a worthy source of validation for satellite imagery such as TOMS-AOD (Torres et al., 2002). In addition, AERONET gives the microphysical and radiative properties for aerosol research and characterization and synergy with other databases. Here, an example will be presented for AOD from AERONET observations during July for 2001 and 2012. Figure (1.10) shows the daily averages of dust-aerosol at 500 nm in the study region during July for both years. The maximum amount of AOD roughly occurred after mid-July, with a peak value reaching up to 1 in 2012. However, the values of dust-aerosol during 2011 in general has more frequent outbreaks than during 2012. By comparison with satellite images, figure (1.10) does not show the same result because satellite images cover a large area over the Atlantic Ocean, measuring monthly averages of AODs, while AERONET data measures AOD in one location, i.e. Izana region and with high frequency measurements.

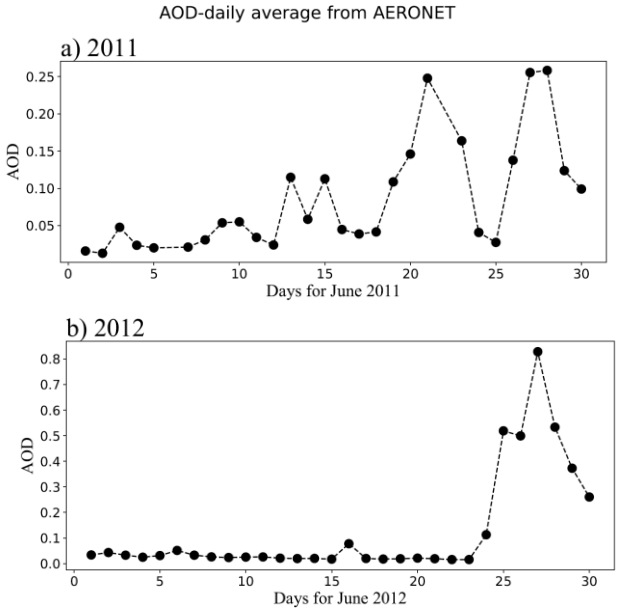

Figure 1. 10. The total column of AODs at 500 nm, level 2 data from AERONET observations at the Izana location during June in 2011, plot (a), and 2012, plot (b). The values of AOD for June 2011 are larger than the values during June 2012 while the latter has roughly a constant AOD values over most days of 2012.

1.4.3 Field campaigns focused on dust

Flight measurements provide important in-situ information about dust mass concentration and sizes, radiative observations and the vertical profiles of the atmospheric thermodynamic structure over the land and ocean environments, which can be supplemented with ground or ship measurements. Scientific campaigns have been operated using various aircrafts over both land and the Atlantic. For instance, the Facility for Airborne Atmospheric Measurements (FAAM) BAe-146 aircraft has been involved in many of these observations over Africa and the Atlantic. Many of the campaigns deployed aircraft over these environments including the African Monsoon Multidisciplinary Analysis, AMMA, project (Lebel et al., 2010; Formenti et al., 2011), NASA AMMA which is represented as a part of the AMMA project (Chen et al., 2011), SAharan Mineral dUst experiMent 2 (SAMUM-2) flights (Ansmann et al. 2011; Knippertz et al., 2011; Weinzierl et al., 2011), Dust Outflow Deposition to the Ocean, DODO (McConnell et al., 2008) experiment, Saharan Dust Experiment, SHADE (Formenti et al., 2003), FENNEC project (Marsham et al., 2013; Ryder et al., 2013a) and Saharan Aerosol Long-Range Transport and Aerosol–Cloud-Interaction Experiment SALTRACE campaign (Weinzierl et al., 2017). Some of these campaigns focused on understanding the West African Monsoon (WAM) system such as the AMMA project. Most scientific projects aim to understand the transportation and effects of African dust over the continent of Africa. However, most aircraft measurements including the Aerosol Characterization Experiment (ACE-Asia), Saharan Dust Experiment (SHADE), and Puerto Rico Dust Experiment

(PRIDE) were deployed over ocean areas (Osborne et al., 2008). For instance, previous works presented by Ryder et al. (2018), used data profiles from the AERosol Properties-Dust (AER-D) aircraft to focus on dust properties within and below the SAL west of Africa (e.g. Cape Verde Islands). Other airborne field campaigns were focused on dust profiles and dust optics far away from the sources of African dust such as the desert Puerto Rico Dust Experiment, PRIDE (Reid et al., 2003). Further campaigns include radiative atmospheric divergence using Atmospheric Radiation measurement (ARM) Mobile Facility.

A broad overview of what was involved in these campaigns will be presented. The specific details are contained in the campaign literature. These campaigns were generally equipped with multiple aircraft, satellite, and ground-based observations. The atmospheric profiles from these campaigns mainly consisted of vertical variables such as wind, temperature, dust-aerosol, humidity, and cloud particles. For instance, the AMMA project was used to understand the West African Monsoon (WAM) and to demonstrate the measurement of these variables over west Africa by using radiosonde instrument (Matsuki et al., 2010). As a part of AMMA, the NAMMA field campaign investigated Saharan dust properties, AEWs and tropical cyclogenesis over Cape Verde Island (west off the continent of Africa) during August and September 2006. Similarly, SHADE project aims to study Sharan dust at Sal Island of Cape Verde in September 2000 (Chen et al., 2010). Away from African coastline, several campaigns operated between June and July 2000 over Puerto Rico Island such as PRIDE experiment to study dust emission, dust transportation and dust deposition (Kleb et al., 2011; Colarco et al., 2003). Meanwhile, over oceans, AMMA focused on gathering data to the west of Africa (e.g. Cape Verde Islands) by National Aeronautics and Space Administration (NASA), and far away from the African coast (Barbados) by National Oceanic and Atmospheric Administration (NOAA) (Haywood et al., 2003; Parker et al., 2008; Zipser et al., 2009).

As this current work focuses on the dust radiative effects over the marine environments, the required data from flight observations can be sourced from the FENNEC flight measurements. These are recent observations and FENNEC deployed the aircraft to study dust over both Africa (in the dust sources over the remote Sahara, Ryder et al., 2013) and the Atlantic Ocean in the summer season (June) of 2011 and 2012. FENNEC also provides well characterised data profiles of Saharan dust and other scientific meteorological factors such as wind, temperature, etc. Furthermore, airborne observations for FENNEC were largely processed and ready for use.

FENNEC was an international project for measuring meteorological parameters and dust during flights often in early morning, noon and extended into afternoons (see table of FENNEC flight observation from Ryder et al., 2013) times and for selected geographical locations in the African continent and the Atlantic Ocean including Mauritania and Mali (Todd et al., 2013). The FENNEC is part of the common group of flights that took measurements (e.g. see Ryder et al.,

2013; Marsham et al., 2013; McQuaid et al., 2013; Allen et al., 2015) using the UK AE-146 aircraft, which is owned by the Natural Environment Research Council, NERC. FENNEC has been used by many previous studies to understand the structure of boundary layer and marine environment. The main aims of FENNEC are: (Allen et al., 2013; Todd et al., 2013)

1. To provide the observation of dust particles from the data sparse region of the central Sahara in north Africa.

2. To identify the mechanisms of dust emission and determine the contribution of dust emission to the total dust loaded from the African-Sahara Desert.

3. To understand the physical processes, such as convection, and controlling the Saharan climate system over the 2011 and 2012 period.

4. To characterise the Saharan dust effects and to evaluate the thermodynamic and dynamic properties of atmospheric dust over Sahel region, with a combination of operational numerical models.

Of particular interest in this work, the FENNEC flights routinely measured the size and concentration of dust particles in the atmosphere using an optical particle counters (OPCs) (Rosenberg et al., 2012). OPCs have been used to measure particle sizes on various observational platforms such as ground-based, balloon, and aircraft research measurements. The physical process involved in dust measurements by OPCs is to measure the dust particle's scattered radiation out of a beam of light (as an air sample passes through the illuminated region). The amount of scattered light analysed is based on optical properties of individual dust particles to extract the dust sizes. This approach assumes spherical particles and uses Mie theory and assumptions about refractive indices. The individual instruments of OPCs cover a size ranging from one or two orders of magnitude such as the PCASP, while OPCs were used to measure a wide range of particle sizes covering a range from about 0.06 μm to about 100 μm. The OPCs represented measured the dust particle size distribution providing real-time observations over a wide diameter during the flights. An overview of individual instruments for dust measurements is provided below.

1.4.3.1 PCASP 100-X measurements of accumulation mode particles

PCASP is a Passive Cavity Aerosol Spectrometer Particles (PCASP) probe used to measure dust particles with ranges from 0.1 to 3 μm diameter. PCASP is operated by the Facility for Airborne Atmospheric Measurements (FAAM) and used on the UK's BAE-146-301 Atmospheric Research

Aircraft. PCASP has been manufactured by two systems including (1) Particle Measurement System (PMS), and (2) Droplet Measurement Technologies (DMT).

The process to extract dust particle sizes and profiles from PCASP observations is explained by Rosenberg et al. (2012) and is briefly described below. The PCASP instrument uses a He-Ne laser directed across the air sample with a wavelength of 0.6328 μm. The air sample is directed into an optical chamber after sourcing clean air. The air sample has a flow rate that varies with flight height and is between 3 ($1/cm^3$ s) at the ground and 15 ($1/cm^3$ s) at the sheath. The sampling of particles as they proceed into the instrument and across the laser beam is controlled by a sheath. The goals of the sheath are to:

1. Focus and constrain the particles to the centre of the laser;
2. Accelerate the sample as it enters the chamber;
3. Spread particles in the passage of flow;
4. Minimise particle coincident impacts.

Direct air containing aerosol flows across the path of the laser and the scattering is recorded. The incident radiation within the optical chamber encounters three processes: firstly, the intensity of directed laser beam is measured by a photodetector by about 0.1 % of the radiation. Secondly, the remaining radiation of 99.9 % is reflected back along a reciprocal direction, and finally the scattered light is collected by a parabolic mirror at angles of 35-120^o relative to the forward direction of the laser beam and the reflected beam over an angular range of 45-60^o. Then the measured radiation from the photometer is treated by three parallel systems: a high, mid and low gain stage. As particles are registered within these stages, a pulse height ranging between 1 and 12,288 is chosen and gathered into one of thirty channels based on the received signal pulse height. The selected pulse height is dependent on the gain stage boundaries of the PCASP instrument, in which the selected pulse height is controlled by the saturation process in each gain stage (i.e. first, second and third stages). For example, as pulse saturates the first gain stage it is directed towards the second. When the second is saturated, it will pass to the third and if it saturates the third gain stage it is assigned as oversized. The full description of how pulse height is assigned based on size/saturation is found in Rosenberg et al. (2012). The received signal (i.e. pulse height) from three gain stages for every bin is shown as a histogram every 0.1, 1 or 10 s based on the pulse height recorded by the photodetector. The height of each pulse is represented by the scattering cross-section measurement (i.e. direct measurement of particle's cross-section) of particle corresponding to the optics of the OPC.

1.4.3.2 Cloud Droplet Probe (CDP) measurements of coarse mode particles

The Cloud Droplet Probe (CDP) is used for particle sizes ranging from 2 to 50 μm. CDP is different from PCASP in that it has an open path OPC, where it contains two arms separated by 111.1 mm. A diode laser with wavelength of 0.658 μm is directed between these arms and out of

a sapphire window and across an open sample area. Within the sample area, radiation scatters as the particles pass through the laser beam, while a second sapphire window is used to direct the rest of the radiation (i.e. the unscattered and subset scattered beam) into the detector arm and the intensity of non-scattered light will be measured by a spot monitor. Then 33 % of the light is scattered within a range of 4-12º is directed into the optical beam isolator called 'Sizer'. Similarly, 67% of scattered laser passes by another optical beam splitter named 'Qualifier'. A similar signal of the electronic pulse height to that of the PCASP is measured with 30 bins in a range from 1 to 4,096 every second. Figure (1.11) shows the parts of the CDP probe, while figure (1.12) illustrates where these components are located on the CDP.

In this current study, data collected and processed from the PCASP and CDP instruments for the FENNEC observations are used to create dust profiles. The CDP data measurements that were provided from Rosenberg et al. (2012) have been used with Mie calculations to get the diameter associated with each channel, which is required for extracting the dust sizes and hence profiles. The instrument calibration method (discrete method) was by Rosenberg et al. (2012) using suitable values of refracted index. Similarly, based on the calibration method applied for CDP, the PCASP data from flight observations was also calibrated. The calibration method was implemented for both PCASP and CDP for the June 2011 and 2012 observations using the calibration file provided by Rosenberg (based on his paper Rosenberg et al., 2012). This one calibration file was recommended to be used for all flight observations. I tested calibration file for flight cases from 2011and 2012 and the calibration results showed agreement. Although recalibration of the PCASP data is implemented in a similar way to that done by Ryder et al. (2013a), the results for the PCASP data in this thesis are performed with increased time resolution for generating scattering cross section to reduce uncertainty for large sizes of dust particles. The full explanation of calibration methods for PCASP and CDP is presented in Chapter 2, section 2.2.1.5.

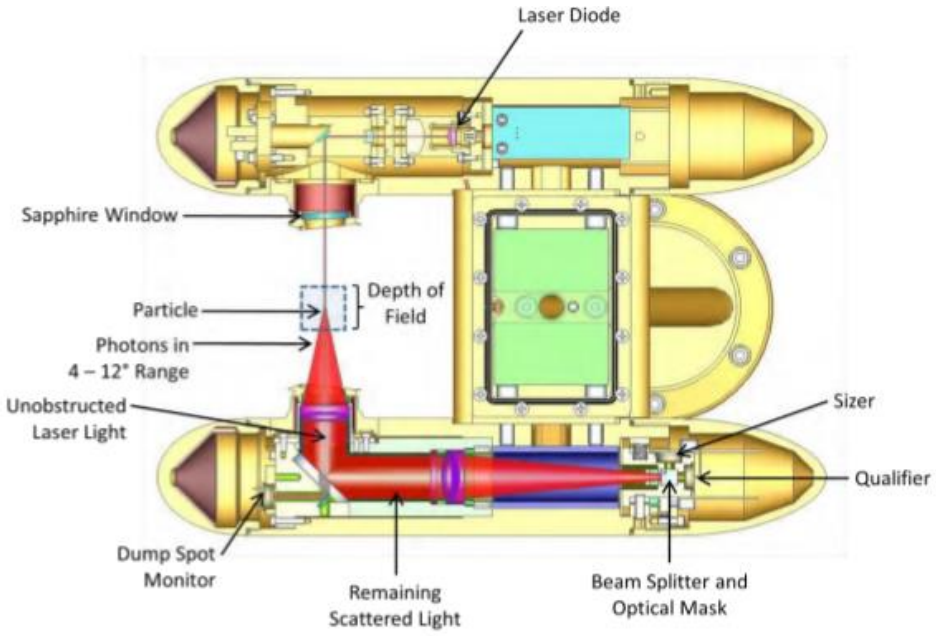

Figure 1. 11. CDP instrument with its physical components of FENNEC flight.

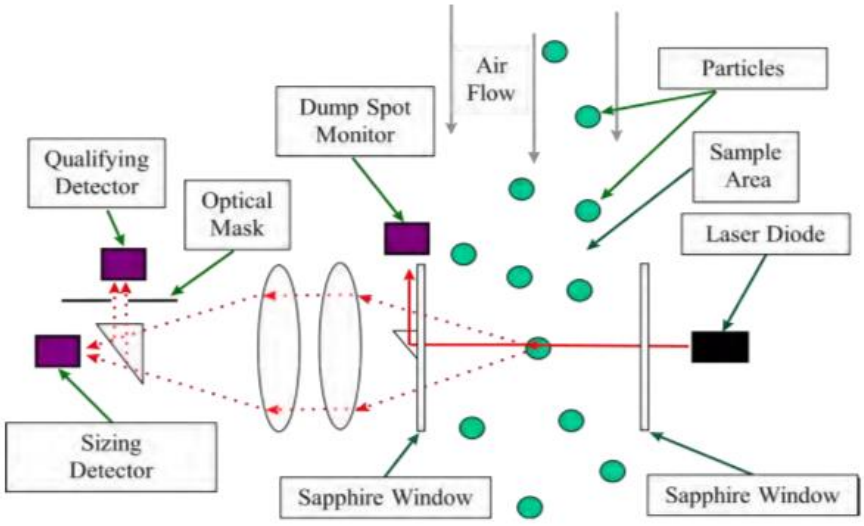

Figure 1. 12. Description of the location of components for CDP flight instrument.

1.4.3.3 CIP measurements of large particles

For giant aerosol sizes, the cloud imaging probe (CIP), which covers the size range from 15 to 930 μm, was used in this research. The CIP, in contrast to PCASP and CDP instruments, does not rely on physical process of light scattering, but depends on geometrical areas shaded by aerosol particles and so can only be used for particle sizes much larger than the wavelength of light which are able to create shadows. Therefore, CIP does not need to be calibrated for refractive index (RI) and scattering cross sections. All these instruments are mounted in suitable places on the wing of the research aircraft. PCASP, CDP and CIP instruments were placed on the wing in such a way as to prevent loss through the pipework of aircraft inlets. For example, for dust measurements that

use FAAM aircraft, it has been discussed that flight inlets for scattering and absorption measurements (these inlets were mounted behind Rosemount) allow only low particle size, less than 2 μm diameter (Ryder et al., 2013). This is a good way to derive dust size distributions using CIP data. On the one hand, considering large dust particles is suitable for measuring dust size distributions (Ryder et al., 2015); on the other hand, testing the overlap between coarse and giant particle sizes is important in quantifying the dust's radiative effects due to the contribution of large particles to absorption in the SW.

Ryder et al. (2015) mentions that there are uncertainties in the flight observations of the aerosol extinction coefficient using light detection and ranging (LIDAR). These problems occur when the signal of the LIDAR backscatter is converted to extinction coefficient, especially for observations below 2 km. They also mention that these uncertainties depend on the specific circumstances of the ambient aerosol in the atmosphere. Another uncertainty mentioned is due to streaking or electronic noise and image events; this had to be rejected under certain circumstances based on the aspect ratios of the particles (Ryder et al., 2018). In addition, Ryder et al. (2018) explained uncertainty arising in total number concentration, in which all size measurement uncertainties are propagated from 1Hz flight measurements. Their study states that the total number concentration measurements have random and systematic errors, where random error can be decreased by increasing the sample size, whereas systematic error often remains constant across the measurements. In this work, standard errors were shown in dust profiles (Chapter 3) for both dust number concentration and diameter.

1.4.4 Air mass trajectories of Saharan dust events

Air mass trajectories can be used to track the path of air parcels in dust outbreaks. Model results from the Hybrid Single-Particle Lagrangian Integrated Trajectory (HYSPLIT) can provide estimations on where the parcels of air come from and where they are going. By investigating the origin of air masses coinciding with the dust events from observations such as AERONET and satellites observations, an understanding can be gained about where the dust originated and how far it has travelled. The full information of HYSPLIT calculations will be described later in Chapter 2, section 2.2.3.

A sample of backward air mass trajectories are shown in figures (1.13) and (1.14) displaying the backward trajectories from NOAA-HYSPLIT model at three different altitudes including 1, 3 and 6 km, for a model run of 144 hours corresponding to various dust outbreak and non-dust events during June 2011 and 2012 ending at the Canary Islands at 2300 UTC. At high altitudes, air masses tended to originate from tropical and subtropical regions, while air mass trajectories with lower heights were from the northern hemisphere. These backward trajectories of air masses also showed that for non-dusty (see plots on top panel) and dusty days (bottom panel) the trend of air masses generally matches with these events with air masses for non-dust days from the non-

dusty east and north-east Atlantic, while the source of trajectories for dusty days were from the west and north Africa. The trade winds typically advected air from Africa and out over the Atlantic during dusty days. However, there are variations to this prevailing pattern. From looking at many back trajectories, occasionally air from Africa will not advect out over ocean even for a dust outbreak. Also, the air does not always originate from the east, some limited cases are seen where the air advects from the west over Africa, picking up dust, and back over the Atlantic. The trajectories can be complicated and involve significant changes in heights, both beginning from low levels and transporting up to higher heights, and vice versa but the general directions first outlined generally hold in most cases.

Analysis of air masses using backward trajectories is a good method to understand where and when air sources originate over time. Bergametti et al. (1989) showed that the time it takes for dust to arrive at the Canary Islands from north-west Africa is about 2 or 3 days, and it takes a week or more to travel across the Atlantic Ocean before reaching South America (Prospero, 1981). In this work, trajectories are used to understand where the dust is coming from, how it is mixing with other nearby air masses and how long it takes to reach at certain observation point.

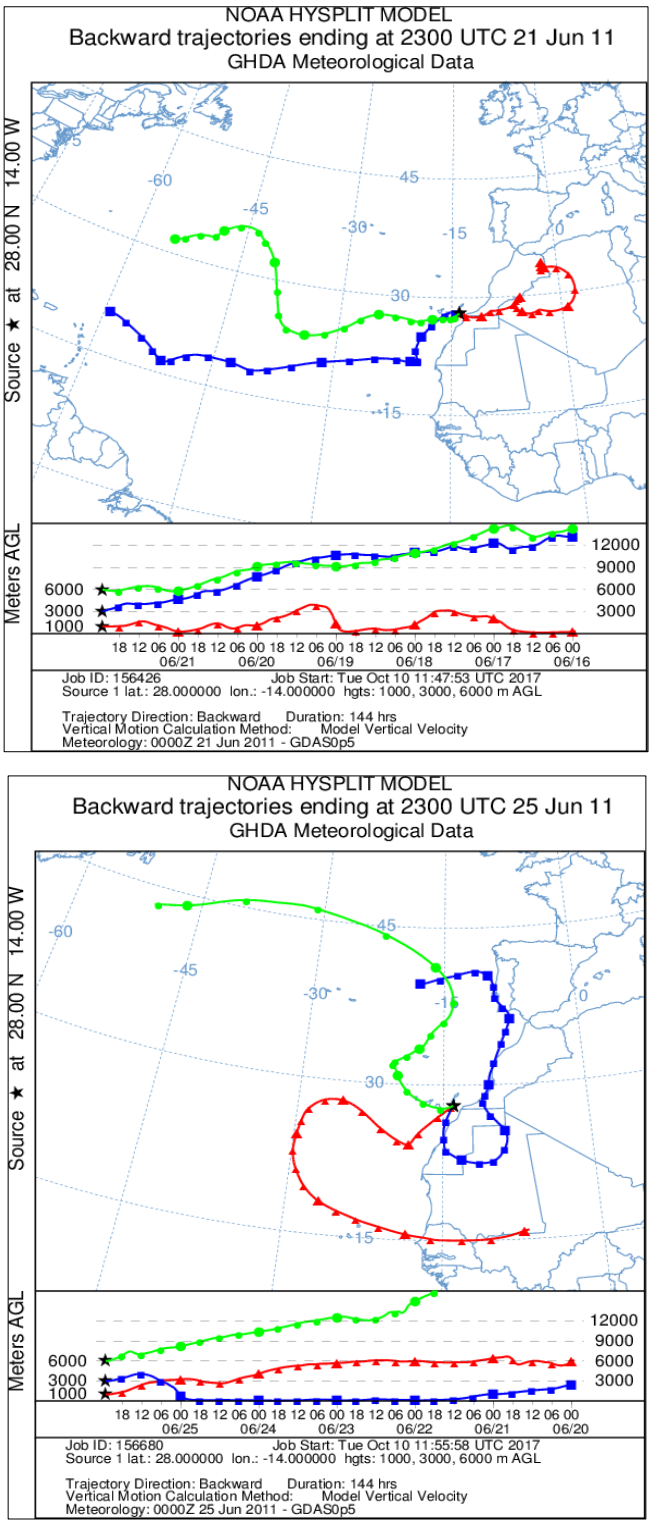

Figure 1. 13. Backward trajectories from NOAA-HYSPLIT model during 2011 with different heights (1, 3, and 6 km) above sea level and the duration time of model is 144 hours, ending at the Canary Islands at 23:00 UTC. Plot shows dusty days.

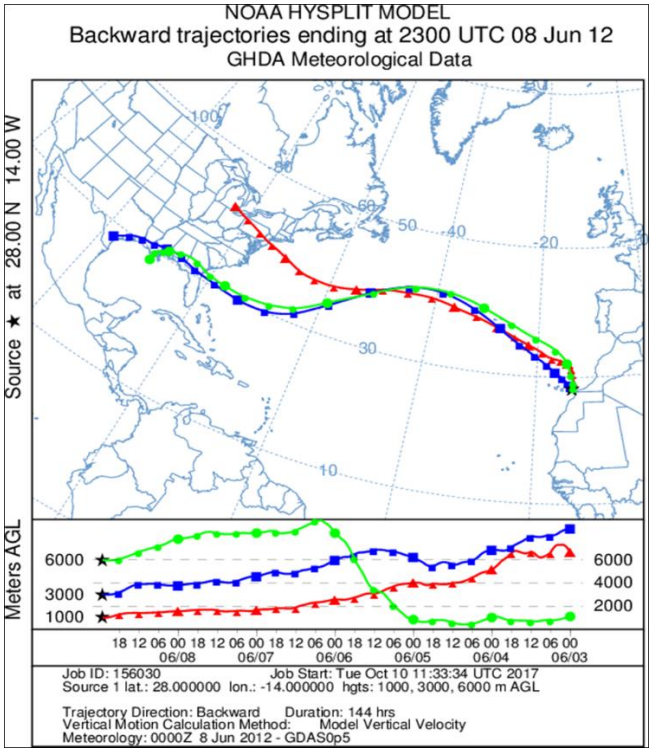

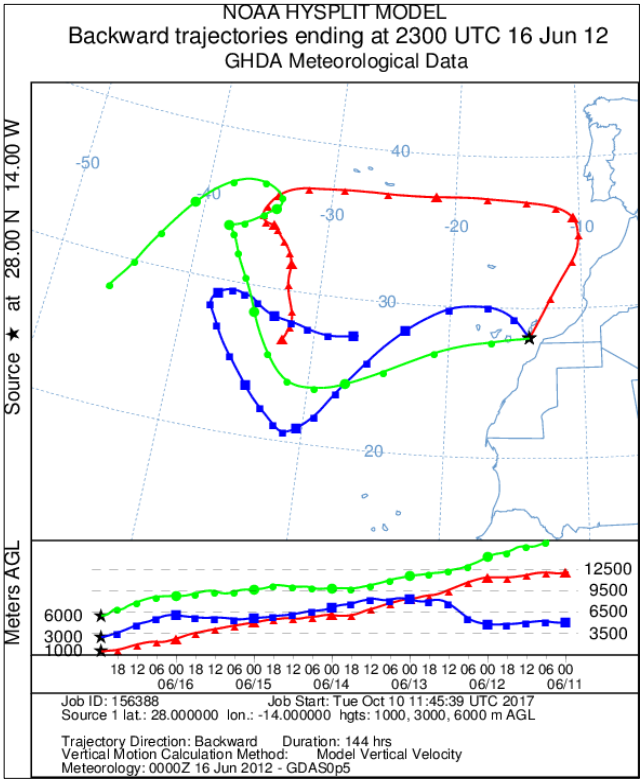

Figure 1. 14. As figure (1.13), but for trajectories associated with 2012.

1.4.5 Radiation concepts and interactions with the SAL

The SAL affects the marine environment in at least three ways: firstly, it brings from the land a well-mixed atmospheric thermodynamic structure into the marine environment. Where that layer is dusty and has different gaseous levels compared to MA. Secondly, dust particles sediment into lower layers as it transports affect those layers, and thirdly, the dust itself affects the radiation balance by scattering, absorbing and emitting radiation (Goudie and Middleton, 2001; and Mahowald et al., 2005) which can affect the dynamics of the atmosphere through direct heating by the dust and gases and by changes to the surface energy balance. In this section, the role of radiation will be introduced and the ways in which dust can interact with the SAL marine environment will be explained.

1.4.5.1 General radiative concepts relating to dust

One of the most important factors that is influenced by the SAL is the temperature of the atmosphere. The temperature couples with the radiation in a couple of ways. The solar and infrared radiation will be absorbed as the radiation propagates through the marine atmosphere containing the SAL. This will cause heating in the profile that will affect the structure of the marine atmosphere and could have important effects on the amount of dust retained in the SAL and marine layer overall, affecting turbulence as well as dynamics. The temperature will also affect the infrared radiation as it is strongly dependent on the temperature in terms of the amount of emission and absorption.

Near surface air temperature is considerably different over land and ocean environments and varies significantly with spatial scales (Ji et al., 2016). The results of Nicholson et al. (2013) indicate that the daily variation of temperature (difference between maximum and minimum) over north Africa in the summer season is about 50°C, whereas the variation is about 10 °C for the marine environment (Vittorio, 2010). This will have a significant effect on diurnal radiative fluxes emitted (and absorbed) at IR wavelengths by land and atmosphere, since emission in the IR is proportional to the fourth power of temperature, according to Kirchhoff's first law (Zhang et al., 1995). So, the fluxes over land will vary far more dramatically than over land diurnally. I will now begin to outline some general concepts of radiation useful for this study and how they relate to dust.

The incident radiation reaching the surface of Earth is characterised as electromagnetic radiation transferred as energy through unit area and time at a specific wavelength. This is called the monochromatic radiance, which is expressed in units of $W/m^2 sr$ μm (Wallace and John, 2006).

$$I = \int I_\lambda \, d\lambda \qquad \text{Eq. (8)}$$

Where, I is the intensity or radiance, I_λ is the monochromatic radiance, and λ is the wavelength ($\lambda = 1/$wave number (υ)). Transferred energy of radiation is encompassed by an ensemble of waves with a continuum of λ and υ. The energy emitted from the sun is predominantly at different wavelengths to the energy emitted by the Earth and the atmosphere. Therefore, it is useful to separate the two into categories called SW and LW radiation.

The reduction or increasing of radiation coming from the sun as SW or emitting from land or atmosphere as LW is affected by the dust, which has effects on radiative fluxes of the total Earth energy and when seeking to identify how much energy will be lost or retained from the Earth-atmosphere system. If I consider radiation passing through the atmosphere, its intensity will undergo scattering, absorption and emission by dust particles and gas molecules such as water vapour. The factors that deplete the incoming radiation from the initial beam are scattering and absorption which is collectively referred to as extinction. For the SW radiation,

$$dI_\lambda = -I_\lambda K_\lambda \rho \, ds \qquad \text{Eq. (9)}$$

Where, K_λ is the scattering/absorption efficiency, ds is the infinitesimal geometric path length that radiation is passing through and ρ is the density of the material. Thus, the transmitted radiation from path s to s+ds is changed based on dust and gases in the atmosphere. To determine what fraction of radiative energy is depleted and gained due to scattering or absorption from the top of atmosphere down to any height, integration of this equation, applying the integral equation of aerosol optical depth (τ_λ) and $ds = \sec\theta \, dz$ yields and defining

$$\tau_\lambda = \int_z^\infty k_\lambda \rho \, dz \qquad \text{Eq. (10)}$$

gives

$$T_\lambda = e^{-\tau_\lambda \sec\theta} \qquad \text{Eq. (11)}$$

Where, T_λ is the transmissivity of atmospheric layer, and θ is the solar zenith angle (SZA). This equation is a version of Beer's law for radiative transfer, in which the emitted energy is exponentially decreased as it passes along an aerosol optical path. So, the depleted radiation passing through the atmosphere from the top downwards is dependent on the depth of the dust and gases in the layer and the combined effects of scattering and absorption coefficients as well, i.e.

$$K_\lambda \text{ (extinction)} = K_{s\lambda} + K_{a\lambda} \qquad \text{Eq. (12)}$$

For the LW side, the emission of radiation at any given wavelength for a blackbody is given by the law of Planck, which is usually denoted as $B_\lambda(T)$.

$$dI_\lambda = \epsilon_\lambda B_\lambda(T) \, ds \qquad \text{Eq. (13)}$$

Where the ϵ_λ is the emissivity for a material describing how close the body is to a blackbody at the same temperature.

Because the LW and SW describe different spectrums with very little overlap, it is possible to solve the LW and SW radiative transfer separately. In general, the radiative transfer equation for both takes the form

$$\frac{dI_\lambda}{ds} = -I_\lambda \rho K_\lambda + J_\lambda \qquad \text{Eq. (14)}$$

But the source term, J_λ, is very specific to LW or SW with it being related to emission and absorption as a function of temperature for the LW and it represents the multiple scattering from and to a path for the SW (Liou, 2002).

This equation is called the general equation of transfer without any coordinate system imposed and it describes the change in transferred energy in the atmosphere as determined by the factors that deplete radiation and is due to the factors that add to the radiation. For the SW, extinction will diminish the radiation of the initial beam but scattered radiation from diffuse radiation can add to the beam. For SW, absorbed radiation will be entirely lost and converted into heat and then links with the LW through temperature. For the LW, all bodies including the land, ocean and atmosphere emit radiation based on the temperature and that radiation will propagate around the atmosphere. All bodies that emit also absorb and so the radiation in the LW will be absorbed and re-emitted along the paths in the atmosphere. These interactions will include the dust in the layer and gases such as water vapour. As a result, dust in the atmosphere will impact on the global energy budget through its influence on radiative fluxes by scattering and absorbing incoming solar radiation (the direct effect) and absorbing and re-emitting outgoing terrestrial radiation (Tegen et al., 1994; Prospero and Peter, 2003; Giménez, et al., 2010).

SW radiation is sensitive to solar zenith angle, surface albedo, and optical properties (extinction, scattering, etc.) of the particles in the air. LW is sensitive to emissivity, temperature and density. For example, figure (1.15) shows the global magnitude of net downward and upward radiations for the SW and LW radiation. For the SW, the highest value of net downward radiation is over oceans at locations with high humidity in the tropical and subtropical regions, while the lowest values of absorbed solar radiation is towards the poles where the solar energy reaching the surface is greatly reduced due to the angle of the surface to the sun.

It is important in this section to highlight the difference between radiative properties, radiative effects, radiative impacts and radiative forcing. Dust radiative properties are the radiances or fluxes that arise from measuring or modelling radiative quantities; the radiative effect is the effect radiation would have on a system such as the heating that resulted from SW radiation being absorbed by a dust layer, and radiative impacts are what comes about because of the radiative effects so changes to the dynamical systems are a result of the radiation. Radiative forcing is characterized by changes in dust radiative properties between the pre-industrial period and the present day (Heald et al., 2014). Radiative forcing is often also used to isolate the radiative change due to other changes in the system such as evaluating the radiative properties for dust and no dust atmospheres to isolate the radiative importance of dust for certain circumstances.

The net radiative forcing of dust is used in this work and is calculated as the SW and LW radiative differences between dusty and non-dusty skies for the net radiative fluxes at the top and bottom of atmosphere. Assuming $F_{(SW\ and\ LW)}\downarrow - F_{(SW\ and\ LW)}\uparrow$ are the net fluxes for the downward (↓) and upward (↑) SW and LW radiation, RF is the net radiative forcing. TOA defines the top of atmosphere, BOA denote the bottom of atmosphere, respectively (Zhang et al., 2013):

a) For the fluxes at the TOA,

$$\Delta F_{(dusty,TOA)} = F_{(SW\ and\ LW)}\downarrow - F_{(SW\ and\ LW)}\uparrow \quad \text{Eq. (15)}$$

$$\Delta F_{(clear,TOA)} = F_{(SW\ and\ LW)}\downarrow - F_{(SW\ and\ LW)}\uparrow \quad \text{Eq. (16)}$$

$$RF_{TOA} = \Delta F_{(dusty,TOA)} - \Delta F_{(clear,TOA)} \quad \text{Eq. (17)}$$

b) For the fluxes at the BOA,

$$\Delta F_{(dusty,BOA)} = F_{(SW\ and\ LW)}\downarrow - F_{(SW\ and\ LW)}\uparrow \quad \text{Eq. (18)}$$

$$\Delta F_{(clear,BOA)} = F_{(SW\ and\ LW)}\downarrow - F_{(SW\ and\ LW)}\uparrow \quad \text{Eq. (19)}$$

$$RF_{BOA} = \Delta F_{(dusty,BOA)} - \Delta F_{(clear,BOA)} \quad \text{Eq. (20)}$$

For the work in this study, I take the TOA to be the top of the model atmosphere. Generally, the dust will scatter more than absorb in the SW, so there will be more loss to space, resulting in a negative forcing and cooling by the SW. The dust will, however, in the LW trap more radiation so warm the planet. It is the balance between these two that determines the forcing. If the forcing is negative then it implies a cooling of the system and a positive indicates a warming.

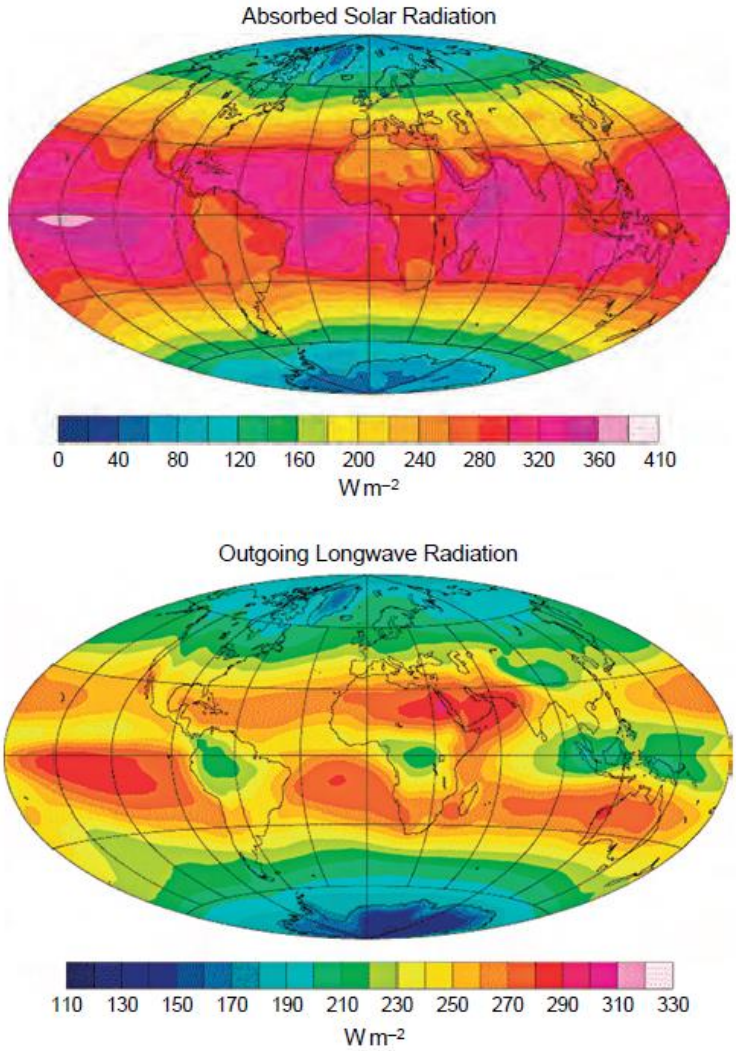

Figure 1. 15. Annual-mean radiation of downward SW and upwelling LW radiation at the top of the atmosphere (TOA) over the Earth environment. The magnitude of absorbed solar radiation in the tropical and subtropical regions is higher than that at poles due to different surface albedo and the elevation of sun. This figure is taken from Wallace and John (2006).

1.4.5.2 Factors influencing dust radiative forcing

Dust radiative forcing, as well as radiative properties, rely heavily on the optical properties which are the single scattering albedo (SSA), asymmetry parameter, mass specific extinction (K_{ext}), which all depend on the refractive index, particle size, shape and any orientation of particles. When radiation interacts with a dust particle, the SSA describes the fraction of radiation that scatters compared to scattering and absorption, so it is the fraction of total radiation that is scattered. The asymmetry gives a measure of the angular distribution in the scattering with all forward scattering if the value is 1 and isotropic if the value is 0. The extinction coefficient describes the amount of radiation that is interacting with the particle. So, these three parameters tell how much interacts, how much scatters to total interaction, and a measure of the angular scattering from the particle.

The radiative forcing further depends on other factors such as the amount and spatial distribution of dust, solar zenith angle, properties of the surface, and the presence of any gases or cloud and their distribution relative to the dust. The determination of these dust properties is approximated and is not that easy to capture accurately by routine observations. In the calculation of radiative forcing associated with dust properties, the particle size remains a major challenge (Ryder et al., 2018).

Generally, previous studies related to dust radiative effects have simulated dust in radiative transfer model with dust optical properties and size distribution. By modelling dust, microphysical properties are essential factors to control dust radiative effects for both the SW and LW radiations. For example, the essential parameters that dominate atmospheric absorption for the SW are AOD, SSA and surface albedo (Lacagnina et al., 2015). There is a large variety in SSA values used in the literature due to physical and chemical properties of dust that significantly vary (Takemura et al., 2002). However, recent work shows that dust optical properties (i.e. SSA) and dust size distributions have different dependencies between the African land and the Atlantic. Over the Atlantic, variations in dust are due mostly to composition rather than variations in size distribution in terms of what controls the variability of SSA, while over the African desert it is the dust size that is more important (Ryder et al., 2018).

SSA is highly sensitive to AOD, where it has lower uncertainty with high optical depth of dust (AOD of say 2) than low dust AOD where the uncertainty of roughly 0.02, while the uncertainty of SSA takes value of about 0.08 for low AOD (Bergstrom et al., 2003). The SSA indicates the ratio of scattering to combined scattering and absorption (attenuation); for dust there will be significant absorption and scattering by the dust layer. In contrast, other aerosols such as sea salt have negative impacts on radiation as sea salt can scatter solar radiation back to the space causing negative (cooling) impacts. Thus, it is important to obtain an appropriate value for SSA since even the sign of radiative effects for dust can depend on it and depending on surface albedo (Lacagnina et al., 2015). For example, Ryder et al. (2013a) showed that a reduction in atmospheric heating by about 26 % comes from increasing SSA from 0.92 to 0.95 between fresh dust to aged dust transported over the Atlantic. In contrast, Otto et al. (2007) showed increased absorption within the Saharan dust layers due to using an SSA value of 0.76. Therefore, SSA and AOD are crucial factors influencing the SW radiative effects of atmospheric dust. In contrast, for the LW, Haywood et al. (2005) show that in dust modelling of Outgoing Long-wave Radiation (OLR), neglecting dust composition (i.e. mineral dust) shows that monthly mean of OLR from model estimation is larger than that from satellite data, where the latter is lower than dust modelling by up to 50 W/m^2 in a comparison with satellite observations. Further studies by Wang et al. (2017) evaluate the downwelling long-wave radiation (DLR) at the surface for different land regions and different atmospheric conditions. Their results show that dust contributes to warming the atmosphere due to LW radiative effects. They state that dust radiative forcing for LW increased

with increasing AOD. In addition to the results of Wang et al. (2017), understanding the LW radiative forcing of dust associated with water vapour is essential for understanding the full impact on the atmosphere. Thus, in this research, I will consider the role of water vapour in influencing thermodynamic and dynamic characteristics over the marine structure, using Large-Eddy Model (LEM) to simulate the radiative impact of water vapour over the Canary Islands and far away from the continent of Africa, and then I will examine which factor (i.e. dust or water vapour) is the most influential on the marine atmospheric structure in both of SW and LW radiation.

The scattering and absorption properties of dust particles are a function of the size, shape and composition of dust particles based on the fundamental physics of light scattering processes (Ryder et al., 2013; Ryder et al., 2018). The refractive index of dust is very important for characterizing the optical properties, which can vary spatially and even depending on season, with winter values (i.e. refractive index for fine dust particles) significantly higher than summer values (Zhang et al., 2017). The real part of the RI relates to the scattering properties and the imaginary part relates to the amount of absorption as radiation propagates in that particle. Literature studies such as Ryder et al. (2013) and Rosenberg et al. (2012) explored using large values of the imaginary part of RI, which increases the absorption of SW radiation for dust particles, and thus causes warming of the atmosphere. However, further work done by Velasco-Merino et al. (2018) shows that the refractive index, SSA and asymmetry factor for long-range transport of Saharan dust (i.e. from western Africa to Caribbean) remain unchanged. Therefore, the dominant factor in determining the evolution of the dust's optical and radiative properties would be the amount and size of dust.

1.4.5.3 The role of thermodynamics in the dust radiative effect

Temperature is important for thermodynamics as well as for dust radiative effects and impact of other gases for the LW spectrum. Within an atmospheric model, the evolution of potential temperature can be described by the following equation (Roux, 1985):

$$\frac{D\theta}{Dt} = \frac{\partial\theta}{\partial t} + (v \bullet \nabla)\theta \qquad \text{Eq. (21)}$$

The first term on the right-hand of this equation shows the time rate of change due to sources and sinks of heat changing the potential temperature at that location (due to any substance, such as dust absorption of heat in the atmosphere), while the second term on the right-hand of thermodynamic equation gives the changes in potential temperature due to spatial variations and advection of heat into or out of the volume. The partial derivative of potential temperature with time is equated to vertical divergence of the turbulent heat flux ($\overline{w\theta}$) and the vertical gradient of the net infrared radiation (L) as shown in the potential temperature tendency equation below (Roux, 1985):

$$\frac{\partial \theta}{\partial t} = -\frac{\partial \overline{w\theta}}{\partial z} - \frac{1}{\rho_a C_P}\frac{\partial L}{\partial z} \qquad \text{Eq. (22)}$$

Where ρ_a, is the density of air and C_P is the specific heat of air. During daytime, the Earth's surface will be heated by the sun and the air above it will therefore be warmed through exchanges of heat by conduction, convection and radiation. During these conditions, the SABL height will grow. Primarily, turbulence and radiation will transfer heat to the atmosphere due to the temperature differences between the ground and the atmosphere. So, the heat flux that propagates upwards will be dissipated with altitude during time evolution. This implies that the potential temperature structure decreased with height (i.e. unstable condition, $\frac{\partial \theta}{\partial z} < 0$). Whereas, during the evening, cooling will begin at the surface of the Earth since the solar is no longer actively heating the ground and the LW will continue to escape to space. Thus, $\frac{\partial \theta}{\partial z}$ is positive and becomes large as the atmosphere becomes stable.

Previous authors such as Steeneveld et al. (2010) showed that the LW radiative flux divergence is very important for thermodynamic profiles as it can transfer heat upwards (downwards) from the surface (atmosphere) into the atmosphere (surface) during night-time (daytime). However, understanding the thermodynamic characteristics between land and ocean environments for the SW and LW with time is quite complicated. At the surface, the ocean absorbs large amounts of energy and stores it due to its high thermal heat capacity which results in not very large diurnal heat flux changes from the surface to the air. Over land it is very different since the land heats up during the day quickly and releases the heat to the air quickly. During night-time, the surface cools very quickly (compared to the ocean) and the fluxes escape to space. The dust acts to reduce the upward LW flux over land far more than over ocean by a factor of two or more.

For the SW, over ocean the outgoing fluxes are increased by the presence of the dust but it is difficult to compare to over land from satellite (Ackerman and Chung, 1992). Regarding earlier studies, Fouquart et al. (1987) discussed vertical radiative flux divergence due to Saharan dust influences between in situ observations and calculation using dust optics based on the Mie approach. Figure (1.16) shows IR profiles for downward fluxes with and without dust effects over the African land using values of AOD (0.08 and 0.09) based on Mie calculations. Although these AODs derived from Fouquart et al. (1987) are not really different, it indicates LW cooling is dominated at the top of the dust layers, whereas the SW heating takes place within the dust layer, which resulting in creating dynamics in the atmosphere. However, vertical flux divergence of dust within the SAL over the Atlantic can be different from that over land. The vertical structure of dust over land has been shown to be well-mixed (Marsham et al., 2013), i.e. it has a small variation in dust size distribution in the dust layer, and Fouquart et al. (1987) states that the IR cooling rate is mainly influenced by both the dust size distribution and the vertical structure of the dust layer. The size distribution of dust transported away from the continent of Africa is likely

to be different compared to over land due to convection, subsiding, turbulence and sedimentation changing the vertical structure and causing losses to the surface that are no longer replenished. Consequently, the dust layer may have a different thermodynamic structure between land and oceans that can modify the thermodynamic structure of marine structure compared to over land.

Further, studies performed by Alamirew et al. (2018) show similar results: LW has a strong impact on the radiative flux divergence over the SHL. Also, their results show that the diurnal cycle of the dust radiative effect is strongly dependent on SZA and surface albedo rather than only dust loading in the atmosphere. In conclusion, there are significant differences between dust over land and ocean due to differences in the distribution of dust in the vertical, the composition of the boundary layer, the surface albedo, and the sedimentation over time.

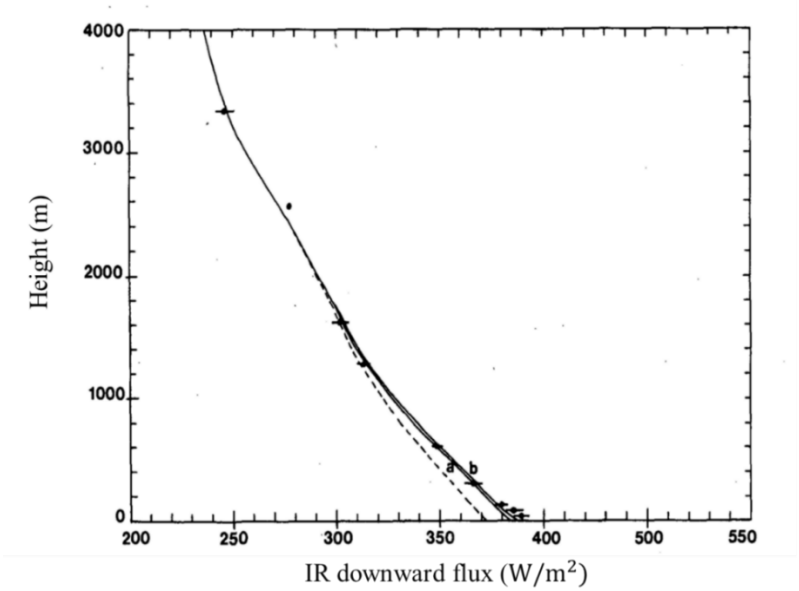

Figure 1. 16. Vertical profiles of IR downward flux for the Saharan dust over Africa (Sahelian dust layer). This plot shows, based on Fouquart et al. (1987), there is a similarity in Longwave downward flux between observations and Mie calculations. They used total AODs with (a) 0.08 and (b) 0.09 in Mie calculations. Dashed line is for calculation without dust and solid line is with dust.

1.4.5.4 Dust heating and cooling rates in the atmosphere

As mentioned previously, net radiative fluxes for solar and terrestrial radiation rely on how much energy interacts in the atmosphere by scattering and absorbing processes by dust particles and gases. The dust heating rate is defined by Quijano et al. (2000) as the rate of change of the temperature (T) in an atmospheric layer due to radiative heating/cooling and is mathematically described in the following way.

$$\frac{dT}{dt} = -\frac{g}{c_p}\frac{dF}{dP} \qquad \text{Eq. (23)}$$

Where, g is the acceleration due to gravity, and c_p is the specific heat capacity, F is the net radiative flux for SW and LW radiation, and P is pressure. Therefore, the rate of change of temperature with time is proportional to the vertical gradient of radiative flux. The negative sign ensures that a reduction of flux increases temperature. Land surfaces heat up quicker than oceans and they cool faster too. This phenomenon can be explained by the fact that the specific heat capacity (c_p) of water is larger than over land as water takes more heat to increase the temperature of 1 kg of water by one degree than land. Also, the depth of surface involved in being heated is larger over the ocean than land. The effects of heating rates for dust particles and gases such as water vapour will be discussed separately in this section.

Figure (1.17) shows a typical heating rate profile for SW (dashed lines), LW (dotted lines) and net radiation (solid lines) with the presence of atmospheric dust taken from Quijan et al. (2000). The lines with triangle symbols in the figure show Sahara dust heating rates, while lines with diamonds indicate dust heating rate profiles over the Afghan region. Heating rates without dust influences are indicated by lines with square symbols. There is a peak in the dust mass concentration around 2 to 2.5 km.

During daytime hours, SW will warm the atmosphere by absorbing radiation which will cause a decrease of flux as the radiation from the sun propagating down through the atmosphere, as mathematically shown in eq. (23). In addition, the dust layer will also cause scattering which some will propagate to lower levels and some will backscatter back out to space. Comparing the heating rates in the Figure (1.17) for SW with and without dust, I see that the non-dust heating rate decreases gradually with height which just relates to the decrease in density with height of the absorbing gases. Above the dust layer the SW for the dusty case has a similar profile but the increased absorption in the dust layer is clear. The peak in heating rates near the top of the layer likely indicates the bulk of the dust but also this is where the incident SW is largest and then as it propagates deeper into the dusty layer the SW flux is reduced so less and less absorption takes place until down towards the ground where the flux has been reduced and the dust is likely in lower amounts. The net result for the SW will be to the reduce radiation reaching the surface and increase the absorption in the atmosphere, with a warming of the dust layer. The SW can only increase the temperature of the atmosphere.

For the LW, the emission and absorption are related to the temperature of the atmosphere (according to the Stefan-Boltzmann equation). So, if radiation is emitted from a part of the atmosphere and that radiation is not returned in equal amounts from the atmosphere around it then this can remove energy from that part of the atmosphere, thus reducing temperature which is a cooling. The opposite can also be true, where a colder part of the atmosphere receives radiation from a warmer part, and this will cause a warming until the temperatures balance out.

From the figure (1.17), it is clear the absorption is much higher in the lower atmosphere in the SW by the dust. This will lead to higher temperatures and the dust will likely trap more

radiation also emitted from the surface leading to a higher surface temperature and higher temperature in the lower atmosphere. The effect of the higher temperatures in the lower atmosphere where the dust is located is to have higher emissions to the air above the dust. Above the dusty layer, the air will be cooler and so emission back to the dusty layer will be low in both the dusty and non-dusty cases. Since the fluxes for the dusty case are much higher the change in flux across the top of the dusty layer will be more dramatic leading to a more significant cooling rate in the dusty case.

The reason for focusing on dust heating rates is that the temperature profile in the absence of dust is mostly stabilised with height, i.e. potential temperature mostly increases with altitude, but when dust is present in the atmosphere there are well-mixed regions in the profile. It is possible that the well-mixed regions are caused by the dust; alternatively, they could be the result of the different air masses, compositional differences. The heating rates are the way in which the dust can impact the atmosphere temperature and so analysis of the atmosphere with these heating rates will be performed in later chapters to assess if they are strong enough to cause the well-mixed effects or not. It is also possible that the differences in the structure could be due to different composition of the air but the work in the later chapters will show if the dust heating rates are strong enough to cause the impact.

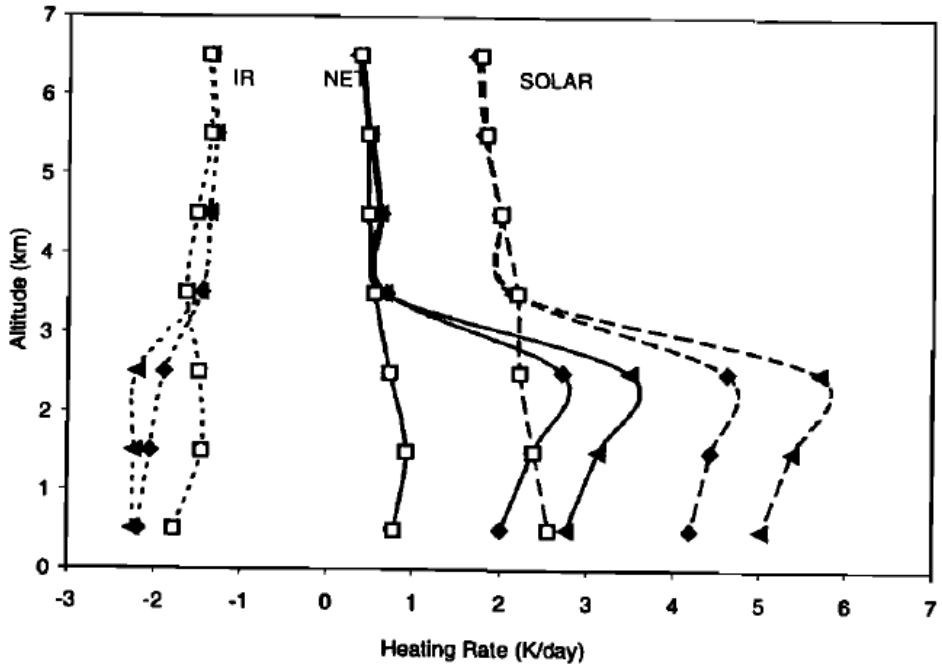

Figure 1. 17. Profiles of dust heating rates in units of K/day. These heating rates are caused by dust effects on solar, IR and NET radiation. Heating rate profiles with triangle symbol lines designate Sahara dust effects. Lines with diamonds are for dust heating rates over the Afghan region, while square symbols indicate the profiles without dust effects (clear sky). The highest heating rates are clearly shown for Saharan dust with peak values at a height of about 2.5 km. The figure is taken from Quijan et al. (2000).

1.4.5.5 Water vapour and other trace gases and the SAL

As mentioned in the last section, the differences in the atmospheric profile and explanation for the well-mixed potential temperature layers when a SAL is present could be due to differences in the composition of the air compared to background marine atmosphere without a dust outbreak. The air will have gases such as nitrogen, oxygen, carbon dioxide, methane, water vapour, etc., and the last three are important atmospheric components in affecting heating rates and radiative forcing in the Earth's radiative budget (Guichard and Miller, 1999). These gases influence the SW and LW radiation through having dipole moments which can interact with the radiation. Trace gas absorption takes place in both the SW and LW with water vapour and CO2 mostly affecting the SW in the near infrared wavelengths whereas these and other molecules interact throughout most of the LW aside from the windows. Thus, gases are likely to have a significant heating effect, which could be comparable with the dust aerosol effects. Therefore, it is important to consider them in evaluating the dusty day radiative effects.

The radiative impact of trace gases, especially water vapour has been debated in previous studies such as Dickinson and Cicerone (1986), who show that there is global warming due to IR being trapped by increased trace gases in the future (during the next 65 years). Water vapour is especially important since its concentrations in the atmosphere are highly variable. Lashof and Ahuja (1990) show that methane contributes about 4 times per mole to global warming compared to carbon dioxide so although the concentration can be low for methane it has significant potential but it tends to be well mixed in the atmosphere so it is not expected to have a role in this work.

The influence of water vapour in evaluating the atmospheric heating rates for the Saharan region has been discussed by Evan (2015) and Marsham et al. (2016). Evan stated that an increase of temperature for the SHL has an important role in atmospheric warming due to water vapour effects during the night. Marsham et al. (2016) quantified the corresponding total column water vapour (TCWV) with dust effects on daily variations in radiative heating during the summer over Africa. Their results show that TCWV strongly controls the daily-mean radiation at the TOA, while dust does not have much influence. The atmosphere is warmed by water vapour by +2.2 W/kg in terms of net radiation at the TOA. The boundary layer of the marine environment will have high water vapour naturally because the evaporation of water from the sea surface, and the water vapor content above the ocean is about two or three times greater than over the African land. Any motions near the surface will mix the water vapour up throughout the MBL and potentially detrain above the MBL. The higher the water vapor content the more significant is the reduction on the top of atmosphere outgoing long-wave (LW) fluxes (Weaver et al., 2002) and warming of the surface (Taylor, 1982).

These studies are focused on how water vapour can change the radiative heating of atmosphere over dry regions (i.e. the continent of Africa). As the current work focuses on the radiative effects of dust advected from north Africa over the east subtropical north Atlantic, it will

be important to understand the radiative importance of water vapour contained in the SAL on the marine atmospheric structure in a comparison to reference non-dusty water vapour environment. There is not full understanding of the importance of water vapour radiative effects on the structure of the background marine atmospheric profile. Thus, this current work will focus on extending previous work that has been done over land to the ocean environment where I will study the contribution of water vapour relative to dust effects in this marine environment, an environment with very different background values of atmospheric gases, different dynamics, surface properties, etc.

1.4.5.6 Effects of dust on atmospheric stability

Dust effects on atmospheric stability have been not received much attention from previous authors. For instance, Mallet et al. (2009) and Ji et al. (2018) conclude that the presence of dust within the atmospheric profile contributes to making the atmosphere more unstable. They suggest that this reduction in the convection over land (Sahara and Sahel) is likely to be the mechanism responsible for reduced precipitation compared to other regions such as oceans.

SAL effects on the atmospheric stability over the Atlantic have been reported by Sun et al. (2008). They used numerical simulations (e.g. WRF model) to study the role of Saharan dust on the stability of the marine atmospheric structure and focused on the impact of dust on the strength of hurricanes. Their findings show that dust increases the stability and vertical wind shear due to thermal structure of the SAL and in addition to dust influences, dust caused a temperature inversion at low level heights. They suggest that the direct impact of SAL on the stability of marine environment may have role in weakening the activity of tropical cyclones.

Atmospheric stability altered by dust can be linked to significant changes in the development of atmospheric circulation over oceans. Away from the continent of Africa in the Atlantic, dust loading can modify the development and intensification of hurricanes and tropical cyclones. Reproduced here is figure (1.18) from Sun et al. (2008) which shows the location of hurricane and tropical cyclones over three different sites including the Gulf of Mexico (GOM), Main Development Region (MDR, a region over the Atlantic located to the south of dust layer, the MDR is situated between the latitudes 10°-20° N, and longitudes 80°-20° W), and western north Atlantic (WNA) associated with dust outbreaks during summer time in 2005 and 2007. The results showed that strongest hurricanes, such as Katrina and Ritang, in 2005 were activated over the WNA and MDR regions, while tropical cyclones decreased in 2007. They pointed out that tropical cyclones are found to be frequently positioned to the west of African dust sources. Tropical cyclones developed at regions in which the AOD was greater than 0.3. 2007 was characterised as having dustier events than 2005. This point can be observed through the coloured circles below the dust plume over the Atlantic in the figure (1.18).

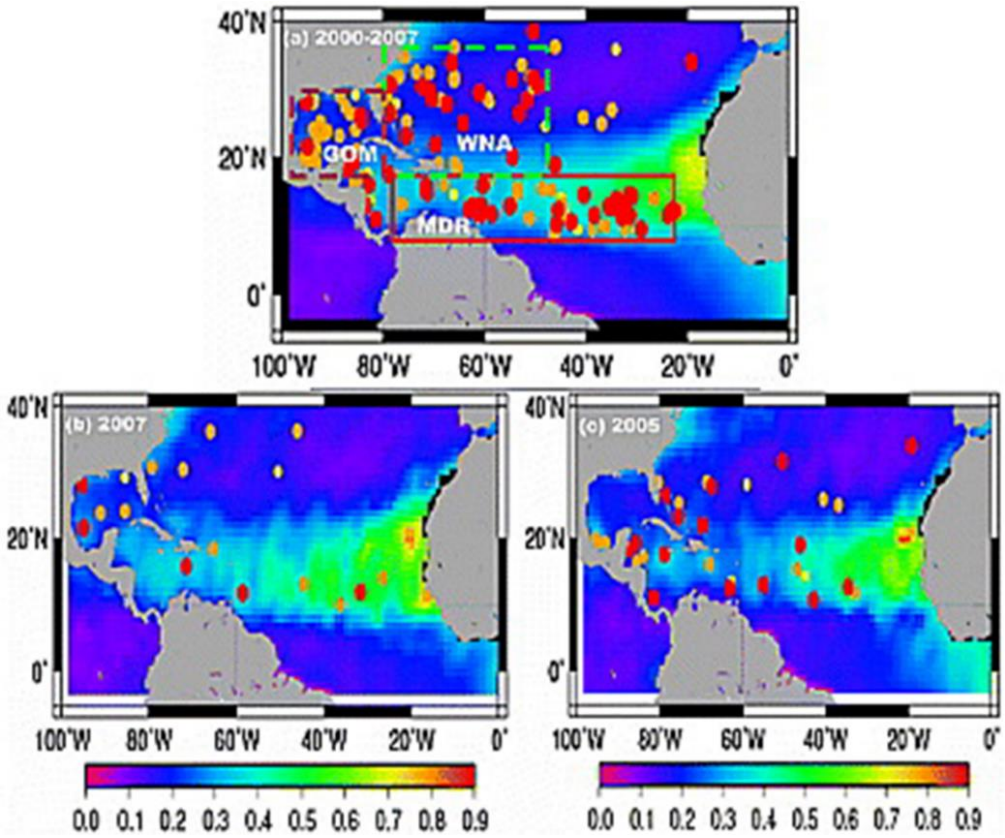

Figure 1. 18. Locations of tropical cyclone and hurricane over the Atlantic Ocean in June and July associated with dust transported across the Atlantic during 2005 and 2007 taken from MODIS data. Plots (a), (b), and (c) designate the mean of dust AOD from MODIS for the period from 2000 to 2007, 2007, and 2005, respectively. Yellow circles are for tropical depressions, while orange circles indicate to tropical storms, and hurricanes designated by red circles. Colorful bar is for AOD and is the same as in plot (a). This figure is taken from Sun et al. (2008).

However, the path of dust outbreaks over the Atlantic can shift to higher latitudes and away from the tropical region. This is shown in figure (1.19), where the strength of the transported SAL across the Atlantic is observed from the Geostationary Operational Environmental Satellite (GOES) imagery. This figure was obtained from Dunion and Veldon (2004) and shows that the interaction between SAL and north Atlantic tropical cyclone provides varied impacts in comparison with other oceans, such as the Pacific Ocean. This study reveals that it is better to consider meteorological observations from satellite retrievals rather than modelling results to understand the development of tropical cyclones in the presence of a SAL. Their results suggest that the spreading of dust over the Atlantic is potentially influencing the development and strength of tropical cyclones and hurricanes. In their work, they showed that dust advected by the dry SALs appear to provide evidence that it surprisingly contributes to diminishing the strength of hurricanes away from the continent of Africa. This explanation corresponds to that presented by Sun et al. (2008) who stated that tropical cyclones reduced in 2007, which had more intensive dusty events compared to 2005. Sun et al. (2008) also show that tracing the development of SAL

intrusions and their impact on the tropical cyclone and hurricanes do not provide a satisfactory understanding of SAL's thermodynamic properties.

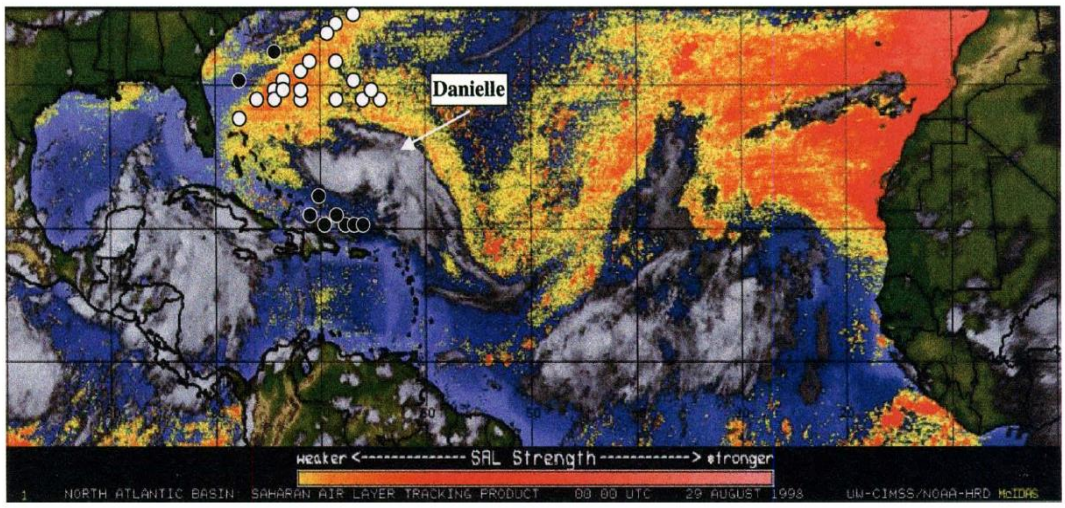

Figure 1. 19. SAL tracking by GOES satellite image with providing points of hurricane Danielle using GPS dropsonde on 0000 UTC 29 Aug 1998. High dust outbreaks are shown by yellow and red shaded colours on map. White and black circles indicate GPS sondes in and non-dust over tropical Atlantic. This figure is taken from Dunion and Veldon (2004).

To conclude, atmospheric Saharan dust plays an important role in interacting with both the solar and terrestrial radiation in the atmosphere. As dust exists in huge amounts during outbreaks it can have very important effects on the atmosphere and its circulations. Because dust is transported such large distances, dust can have an influence on the global scale, if not directly then through changes to circulations. Dust from north Africa (e.g. Sahara Desert) has significant effects on atmospheric conditions, including temperature, radiation, clouds (discussed below) as well as the fertilizing of land and ocean surfaces. In addition to dust impact, dust observations from satellite technique provide suitable way to understand the role of dust in the evolution of tropical hurricanes. Therefore, considering the way Saharan dust is transported and how it affects the marine environment during transport is of high importance and is the focus of this current research.

1.4.5.7 Dust impacts on clouds

Although dust effects on clouds are not the focus of this thesis, it is useful to mention the ways in which dust can influence clouds in order to understand the wider effects of dust impacts on the marine structure. The first way is if dust heating rates have an impact on the structure of the atmosphere then the dust may alter the potential for convection downwind where clouds would potentially form then Much more on this phenomenon will be address in later chapters. The second way that dust can affect clouds is by directly affecting the nucleation. Dust is believed

to play a significant role in affecting cloud formation by contributing as cloud condensation nuclei (CCN) and especially giant CCN contributions (Spracklen et al., 2005). Finally, dust causes warming of the layer and so if there is dust dispersed in the cloud (in or out of the droplets) then that warming can cause a semi-direct effect (Hill and Dobbie, 2008) by slightly warming the air and evaporating the smaller cloud droplets and so changing the cloud droplet distribution and radiative properties of the cloud. In this thesis, I avoid cases involving cloud so as to first make an assessment of the SAL effects on the background environment without clouds. Nevertheless, it is relevant to think about the impacts of changes in atmospheric structure brought about by the SAL, as they may influence the development of clouds. Clouds can be treated in future work once the effects are understood fully for the cloudless environment.

1.4.6 Overview of dust radiative effects from past studies

The radiative effects of atmospheric dust can be characterised in two ways: the net radiative forcing and the radiative effects in the atmosphere, as discussed earlier. For radiative forcing, the atmospheric radiative fluxes upward at the TOA with and without dust is evaluated and the difference is the forcing due to dust.

In much of this work, I use radiative forcing to evaluate the effect of a dusty day relative to a non-dusty day. The forcing is a measure widely used in assessments like the IPCC (Haywood et al., 2000) to relate to the effect a change in radiation would have on the global near surface temperature. The radiative forcing is controlled by dust optical properties, surface albedo and atmospheric conditions which can be quantified by either a warming (positive sign) or cooling (negative sign) or zero, which would typically be evaluated at the top and bottom of the atmosphere (Sokolik et al., 2001).

There are three different effects of dust characterised as radiative forcing: direct radiative effect (DRE), indirect radiative effect (IRE), and semi-direct radiative effect (SDRE). To understand the role of dust in terms of its radiative impact, the importance of dust in each one is discussed here. Firstly, DRE accounts for dust effects in the absence of cloud both at the top of dust layer and within it. In this case, the net radiative forcing is the difference between the upward TOA fluxes with and without the atmospheric dust. If it is positive (negative) then it is scattering less (more) radiation back to space and so retaining (losing) energy and thus is associated with a warming (cooling). The net radiative forcing of dust in both IRE and SDRE are more complicated to quantify compared to DRE. For the IRE, clouds are involved, and it is the way that dust can impact on radiation through its influence on the cloud that it addresses. The same calculation of the fluxes at the top of the atmosphere are performed but now the differences are indirectly due to how dust affects clouds, which may for example be by increasing cloud droplet number concentrations by providing more CCN, and thus the clouds become more reflective and increase the outgoing radiation (negative forcing) or perhaps the giant dust nucleate large cloud droplets

that scavenge efficiently and reduce cloud numbers cause a radiative forcing warming (Yoshioka et al., 2007). For the SDRE effect, the warming of the cloud layer by the dust causes greater evaporation of the smaller droplets thereby reducing the upwelling SW fluxes by the cloud thus causing a radiative forcing warming. The radiative forcing requires understanding of the way dust can influence clouds as well as the dust's and water's optical properties including particle size, shape, and refractive indices (Valenzuela et al., 2017). These effects can be highly dependent also on the shape of the dust profile in the vertical and the relative positioning and types of clouds involved.

Previous studies of dust radiative effects have been generally presented over land and ocean. For example, Bangalath and Stenchikov (2015), Solmon et al. (2012), Zhao et al. (2011), Lemaître et al. (2010), Mallet et al. (2009), and Heinold et al. (2008) simulated the radiative effect of dust on the atmospheric structure over land environment. Other studies have considered the radiative effects of dust over both land and oceans such as Carlson and Benjamin (1980), who determined the influences of Saharan dust (as additional heating rate effect of dust to other atmospheric components) over the eastern tropical Atlantic Ocean and the Sahara. Whereas dust effects purely over oceans have been investigated by Song et al. (2018), who studied dust's radiative effects on SW and LW radiation in the tropical north Atlantic between 2007 and 2010 during the summer season. Similarly, a much more extended study over different oceans has been presented by Zhu et al. (2007), who focused on determining the radiative effects of dust on three global oceans: the Pacific, the Indian, and the Atlantic. Their results pointed out that the net (SW+LW) radiative forcing of dust is significantly controlled by SW radiation for the Arabian Sea (AS). In addition, LW cooling has a significant effect within the SAL and this impact is reduced below this dust layer. In contrast, there is a peak warming effect for SW radiation in the SAL at about 4 km over AS with positive value of 0.5 K/day.

Most previous studies show that an evaluation of the dust-radiative forcing at the top of atmosphere and below is important for quantifying net radiative forcing. For instance, Lau et al. (2009) used General Circulation Model (GCM) to evaluate the dust radiative forcing over the African land and the Atlantic. Their results show that African dust causes a cooling impact over the African land surface and warming over the west Atlantic and Caribbean regions. They also reveal an opposite impact of dust particles between SW and LW radiation. For SW (LW), dust radiative forcing causes warming (cooling) in the atmosphere and cooling (warming) below it. They also state that the warming effect of dust over west Africa and the eastern Atlantic and sinking air over Caribbean, are driving large-scale overturning in the large-scale circulation. Their study did not consider the dust profile from observations, they derived data from the GODDARD model. Secondly, this paper did not provide evidence about factors that caused the well-mixed potential temperature, neither clarifying whether SW nor LW had the dominant impact on the marine potential temperature structures. In addition, although they did show that air rises over

west coast of African land and the air is sinking over Caribbean, they did not simulate what will happen in the well-mixed dust layer.

Global dust-radiative forcing has been discussed in many previous works. For instance, Zhang et al. (2013) show that global radiative forcing over Africa and Asia is increased from 0.2 to 0.25 W/m^2 for dust-SW radiation at the top of atmosphere. They also showed that dust-radiative forcing over the African land for LW decreased by about 0.2 W/m^2. Other results presented by the Intergovernmental Panel on Climate Change (2001) pointed out that the global annual mean dust radiative forcing ranges from -0.6 W/m^2 to +0.4 W/m^2 (Haywood et al., 2001), so there is a wide range in estimates and even signs of the overall effect. Furthermore, Péré et al. (2018) showed how the influence of large concentrations of dust particles on the radiative budget caused significant changes in net SW and LW radiative fluxes, both at the top and the bottom of atmosphere. They also stated that the value of surface air temperature in the simulation of dust radiative influences over Africa was an important factor.

Over the Atlantic, Li et al. (2004) evaluated the radiative fluxes of Saharan dust for the SW radiation during dusty and low-dust days. Their study showed that the difference in the diurnal mean forcing of Saharan dust at the top of atmosphere between dusty and low-dust days was roughly -10 W/m^2, and they also estimated that the upward radiative fluxes for these dust cases were about -35 W/m^2 (dusty) and -26 W/m^2 (low-dust), respectively. In the presence of cloud, dust-aerosol has a negative radiative effect at the top of atmosphere for the SW radiation and shallow cloud of about –11 W/m^2 over the Atlantic (Kaufman et al., 2005b, PNAS), and roughly -60 W/m^2 for the Saharan dust SW radiation off the west African coastline (Haywood et al., 2001). Their studies provide good insights into dust radiative fluxes over the ocean; however, nobody has examined at how radiative effects of dust can affect the stability of the atmosphere along with the role of other factors such as shear and water vapour, which is the focus of this work.

Dust transported from deserts plays multiple roles in influencing climate change by interacting with the SW and LW radiation budget of the planet (Harrison et al., 2001). Since the radiative properties of dust over land are different from that over oceans, it is necessary to understand the radiative properties for both to understand the radiative effects of dust on the global climate. For example, over land dust scatters the SW back to the space at the top of atmosphere and absorbs some of the SW within the SAL. Thus, dust causes cooling at the top of atmosphere and near the surface, with significant heating within the dust layer (Huang et al., 2009). In contrast, over the ocean, dust may have the same radiative impact on the top of the dusty marine atmosphere. However, the amount of SW radiation scattered by dust particles is controlled mainly by the height of dust layer and factors such as particle shape, dust distribution, the abundance of dust and refractive indexes (Myhre et al. (2003). In contrast, the dust effects for the infrared tends to increase the surface temperature, which results in retaining the terrestrial radiation emitted from the Earth's surface (Romano and Perrone, 2016). During the day and night, the net SW and LW

radiation will be altered by the dust. To present this more clearly, Zhao et al. (2010) showed the difference between dust effects on the atmosphere over African land for both SW, LW, and total (i.e. combination for the SW and LW) radiation. Figure (1.20) displays results from Zhao et al. (2010) for the radiative forcing of Saharan dust from the WRF model over Africa for the SW, LW and total radiation. From these plots, the dust radiative forcing for the SW within the SAL obviously has the greatest effects on the atmosphere, compared to the effect of LW radiation through heating the atmosphere by about 30 W/m^2 (see second row in figure (1.20)).

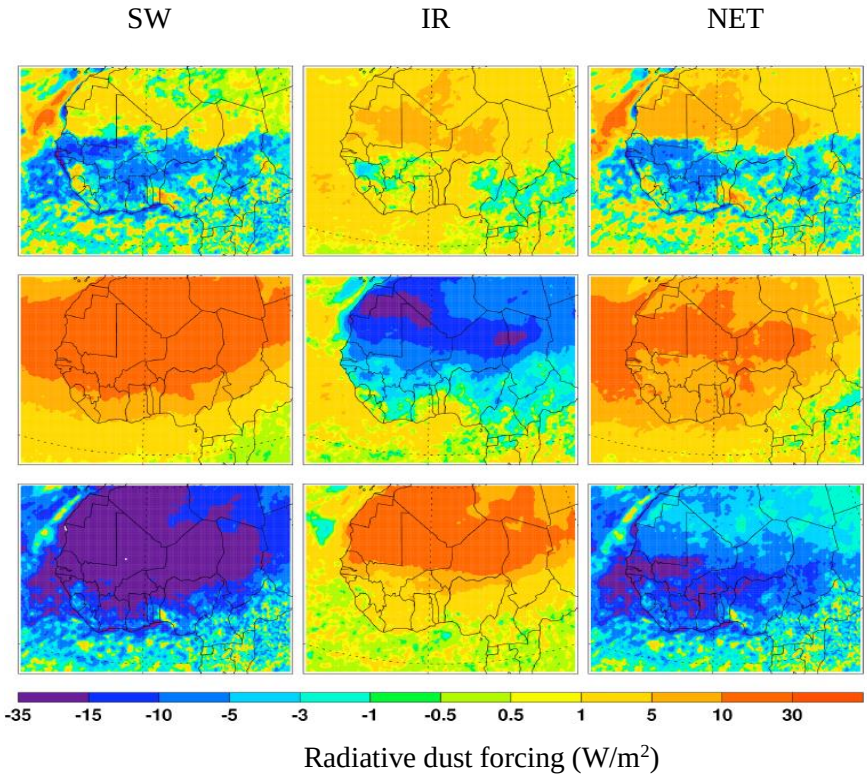

Figure 1. 20. Averaged-radiative forcing of Saharan dust for SW and LW radiations in W/m^2, from WRF-Chem model simulations over west African land. First row of plots indicates the downward radiative forcing of dust at the top of atmosphere for SW, LW and Net (SW+LW) radiation from left to right. The second row is the dust radiative forcing in the atmosphere, and third row at the bottom of atmosphere. The radiative forcing is represented as dust simulation results of averaged radiative forcing over 24 hours. This figure is taken from Zhao et al. (2010).

1.4.7 Simulation of dust radiative effects west of north Africa

Modelling studies of dust's radiative effects have been performed by Haywood et al. (2003), Myhre et al. (2003) and Haywood et al. (2001) near the western coast of Africa. As dust radiative effects are mainly dependent on dust profiles and dust optics, it is valuable to understand the role of dust particle sizes on radiation whilst also considering optical properties and dust profiles. It is important to assess factors such as dust size distributions and optics in evaluating dust's

radiative impact on the structure of well-mixed Saharan Air Layer over the Atlantic. This is quite a significant gap, particularly for understanding the importance of dust in the marine atmosphere. Over land, research work by Ryder et al. (2013) studied the optical properties of Saharan dust over African land based on FENNEC observations, while Ryder et al. (2013a) analysed the influence of African dust with its optical properties during transport between land and the eastern part of the Atlantic, using aircraft observations at different lifecycle stages of the dust outbreaks. Although these studies provide a satisfactory background to understand size distribution, optical properties, and time transport of Saharan dust over land and ocean, simulating the radiative influences of Saharan dust is also important beyond the Canary Islands at remote regions over the Atlantic and into the Caribbean. At this point, the structure of the SAL has been shown to be well-mixed over land and over ocean. However, the persistence of a well-mixed dust layer during dust transport for long distance has not been evaluated as to whether the SAL remains well-mixed during transport over significant distances nor the role of dust in creating and maintaining these layers. Furthermore, there is a lack of work on the way in which shear couples with the SAL and alters the structure of the MA with SAL intrusions.

1.4.8 Research gaps

As this thesis focuses on the radiative effects of Saharan dust over the Atlantic, the evolution of dust and associated outbreak levels of water vapour can be simulated by investigating the impact of gravitational sedimentation, long-term dust transport, microphysics of coagulation, and turbulent mixing processes (Lee, 1983) on the profile. The impact of the sedimentation process on the evolution of dust transported over the Atlantic within the SAL can be seen in the research of Lee (1983), who simulated the well-mixed SAL by investigating the influence of removal processes including, sedimentation, coagulation and turbulent mixing impacts on the evolution of dust particles between the African land and the Atlantic. In his simulation results, it was shown that dust particles within the SAL with a radius of 10 μm or less were not influenced by the processes mentioned above; these particles can be transported over the Atlantic for long distances. This finding may have a significant impact on the evaluation of dust's radiative effects for the SW and LW radiation, corresponding with the long transport time of dust particles on a local and global scale. Lee's study, however, did not address the importance of dust/water vapour on the structure of the atmosphere was not addressed as well as what will happen to the dynamic and thermodynamic structures of the SAL associated with the impact of these factors by processes such as a turbulent mixing as the dust advects across the Atlantic.

Further research performed by Chen et al. (2010) investigated the modification of transported well-mixed SALs and investigated the effects of dust layers and shear. Their study indicated that for the dust radiative effect the dominant factor is the SW heating in a compared to LW cooling within a dust layer between 750 hPa and 550 hPa. In addition, between these layers dust can

initiate a vertical zonal shear by increasing from 1 to about 2.5 m/s per km with height. Their study is an important work on the radiative effects of dust over the Atlantic Ocean since it is related to the current work. However, there are several gaps that are highlighted and need to be addressed in this work, which are listed here.

Firstly, Chen et al. (2010) simulated the evolution of the SAL over the Atlantic only for dusty case and they did not consider the impact of the dust altitude on the vertical thermodynamic structure. Secondly, their study was based on simulated temperature data taken from satellite observations rather than using directly observed data of mass profiles of the dust over the Atlantic. Thirdly, although Chen et al. (2010) explored vertical wind shear (shear is considered for intensive dusty cases only), which is increased from 1 m/s to 2.5 m/s per km between height levels roughly 750 hPa and 550 hPa, they did not investigate the impact of the wind shear on environmental stability. Finally, they investigated water vapour but it was focused on the impacts of dust on the water vapour rather than the water vapour itself and they found it to be a minor impact.

The most recent work in this area of the thesis shows that much more of a focus is required to understand the important factors driving and maintaining the thermodynamically well mixed SAL over the Atlantic, where most previous studies revealed that SAL was characterised by a well-mixed layer over land but there was no clear evidence about whether the structure of SAL sustains with the same dynamic and thermodynamic properties away from the African continent, nor is the relative role of water vapour and dust explored. In the current project, I will investigate the radiative effects of Saharan dust in terms of how SW, LW and total radiation influences the development of thermodynamic and dynamical properties of the SAL using LEM simulations to understand what causes the well-mixed regions, how long they take to form, how long they can persist and, together with an estimate of the bin resolved sedimentation and turbulent dust transport model, an assessment of whether dust is driving well-mixed SAL structures right across the Atlantic and into the Caribbean.

1.5 Thesis rationale

1.5.1 Aims of this project

The purpose of this current project is to fill a gap in knowledge about how SAL layers that intrude into the marine environment and will affect that environment. Specifically, I am interested in how the dust and water vapour in the SAL contribute to maintaining these characteristic well-mixed SAL layers. Tests will be performed to assess the radiative effects of dusty air and outbreak levels of water vapour compared with non-dusty air and non-outbreak water vapour levels. Which is more important, dust or water vapour? How long do the well-mixed layers take to form, how long do they take to decay and what is specifically responsible for forming and maintaining them in the marine environment? I will use a combination of different modelling techniques based on

observations of dust and meteorological variables from the FENNEC campaign. I am not aiming to reproduce exact cases but rather to use the flights to guide numerical modelling of the approximate values that would be appropriate for studying importance and sensitivities. Accordingly, the main aims of this study are to:

1. Understand the effects of dust on the thermodynamic and dynamic structure of the atmosphere in the dusty marine environment off the west coast of Africa.

2. Understand what is causing the vertically well-mixed potential temperature regions in the Atlantic dusty marine environment, as observed during atmospheric dust outbreak days.

3. Investigate the role of water vapour on radiative effects of the dusty marine atmosphere in a comparison with a non-dusty background water vapour environment.

4. Determine the relative importance of the solar and Infrared (IR) radiation for determining well-mixed regions during dusty events.

5. Assess whether the dust or water vapour are influencing well-mixed layers at significant distances from the African dust source region. The focus will be on the effects in the Caribbean approximately a week of transport from the source region.

1.5.2 Research hypotheses

Hypothesis 1: SAL dust and water vapour intrusions have a significant effect on the structure of the marine atmosphere by absorbing solar radiation and converting this energy into local increases in temperature. This process results in a dynamical overturning that sustains well-mixed regions in the dusty marine environment, which is important in terms of the dust transported long distances.

Hypothesis 2: It is expected that the dust will have the greater influence on creating well-mixed regions compared to the water vapour. This is expected since water vapour amounts are expected to be reduced for hot, dry dusty SAL air masses advecting into the marine environment.

1.5.3 Research questions

The project has one main research question:

1. What are the relative roles of dust and water vapour in maintaining thermodynamically well-mixed layers for dusty outbreaks over the Atlantic Ocean west of Africa?

1.6 Thesis outline

This chapter provided an introduction, motivation and literature review of dust aerosols from Africa and presented considerations of their transport over the dusty Atlantic marine environment. The final section of this chapter presented the research aims, research hypotheses and relevant research question. The contents of the next chapters will be as follows:

Chapter 2 presents the research tools that are used in this project, such as models, observations and other data sources. This chapter consists of two sections: firstly, complete details about the data used in this thesis, and secondly the simulations of dust radiative effects in the Canary Islands region. This will include dust optical properties and methods for calculating dust profiles and dust heating rates that will be simulated in the LEM. Tests are included for other factors, such as shear, in this section. Chapters 3, 4, and 5 are the main research chapters of the thesis. Chapter 3 describes FENNEC-dust observations including information about profiles of dust and winds from flight observations and data from model reanalysis sources. Presented in Chapter 4 are LEM results that predict the thermodynamic and dynamical responses of the modelled atmosphere driven by dust, water vapour, etc., through heating rates. In addition, the processes and the relative importance of dust and water vapour acting on the potential temperature profiles and stability are explored. These results are contrasted with effects due to wind shear. Estimates of dust profiles on the west side of the Atlantic Ocean are estimated using a simple new bin resolved sedimentation and turbulence model which is presented in Chapter 5 and compared to observations. Conclusions, limitations and future work are presented in Chapter 6. This addresses the overall structure of the thesis.

2 Chapter 2: Research data and tools

This chapter presents a range of data, tools, models and parameters needed to investigate the aims of this study. The objectives from the last chapter are related to the radiative effects of Saharan dust on the dynamic and thermodynamic characterisations of the dusty marine environment's vertical layers. So, to address the objectives, dust profiles and meteorological variables over the Atlantic are presented. To investigate the impact of dust this data is used in to derive heating rate profiles of Saharan dust using the Edwards-Slingo radiation model. The heating rates from the radiation model are then used with LEM simulations to predict the evolution of the atmosphere and quantify the effects of the dust. This chapter summarises data sources from FENNEC observations, ECMWF ERA-5 reanalysis, radiosondes, AERONET for use in models such as the LEM, the Edwards-Slingo radiation model, HYSPLIT as well as deriving some important parameters for the work including gradient Richardson number, CAPE and CIN, dust mass derivations, etc.

2.1 Research data

2.1.1 Data and Setup

This section gives an overview of the data sources used in this study. Dust observations are obtained from the FENNEC campaign using the following instruments: PCASP, CDP and CIP. The flight measurements for dust profiles were sourced from the British Atmospheric Data Centre (BADC). Dust profiles and meteorological variables including temperature, water vapour and wind observations were used mainly in the LEM simulations and radiation calculations to predict the dust effects on the atmosphere, while ECMWF ERA-5 and MODIS satellite data were used in the modelling of the dust transported over the Atlantic using a new bin resolved sedimentation and turbulent model, BRSedT, which includes advection, sedimentation, and turbulent effects. In addition, further data was used from radiosondes to supplement profiles where there was no flight data available. Radiosonde datasets sourced from the archive data of the British Atmosperic Data Center (BADC), The description of flight observations over the study area will be presented in the next section.

2.1.2 FENNEC flight observations

Aircraft flights from the FENNEC campaign provide dust and meteorological data observations covering the region of the Atlantic off the west coast of Africa. FENNEC flights started from Fuerteventura airport (Canary Islands) and flew to the African mainland during June in 2011 and 2012.

The BAE-146 research council aircraft (see figure (2.1)) was used for the FENNEC flights that flew between the Canary Islands and mainland Africa, including flying for long periods over the Atlantic. Various measurements of meteorological parameters were performed, such as

temperature, pressure, water vapour, and wind velocities and I am especially interested in the measurements of dust during ascending/descending flights over north west Africa and the Atlantic ocean, associated with time, altitude, latitude and longitude. These observations were important since they provided vertical profiles of the variables. In addition to FENNEC measurements, some other variables including solar zenith angle (SZA) and ozone, are useful for the radiation code as supplementary data to get an adequate dust heating rate profile. Table (2-1) shows the date and time of FENNEC flights used in this study; flights were typically undertaken during mornings and afternoons. Note that the times specified in table (2-1) show the selected time of profiles over the Atlantic Ocean, as FENNEC took off from Fuerteventura towards the coastline of north Africa. Therefore, this does not represent the complete flight path observations over the Atlantic and Africa. The time variation of a flight is determined by how long that flight takes over the ocean before it reaches African land.

Data profiles were acquired from by FENNEC flights from Fuerteventura airport, which is situated approximately 130 m above sea level (Alonso and Cabrera 2002), to west Africa and back to Fuerteventura over the Atlantic Ocean. Some flights were excluded including FB603, FB610, FB615, FB698, FB704, FB706, and FB707. There were excluded generally for three reasons: 1) relative humidity, which was calculated and presented in Chapter 3 indicated the presence of cloud that had formed in the marine boundary layer such as FB707 and FB610; (2) data profiles of water vapour and other meteorological features had errors/omissions over significant portions of the vertical profile of the flights, such as FB603, FB698 and FB706, and thus may influence the accuracy of the results; (3) some of the flights, such as FB615, were not relavent to the current study as this flight headed towards Portugal and flight measurments are implemented over regions different from study area between the Canary Islands and the west African coast. Figure (2.2) shows the time of observation of selected flight cases with the altitude on route between the Canary Islands and the African coastline during 2011 and 2012. The time and altitude in both plots of figure (2.2) are shown in x-axis and y-axis respectively.

Figure 2. 1. AE-146 FAAM aircraft that measures dust profiles and other profiles of meteorological variables over land and ocean environments.

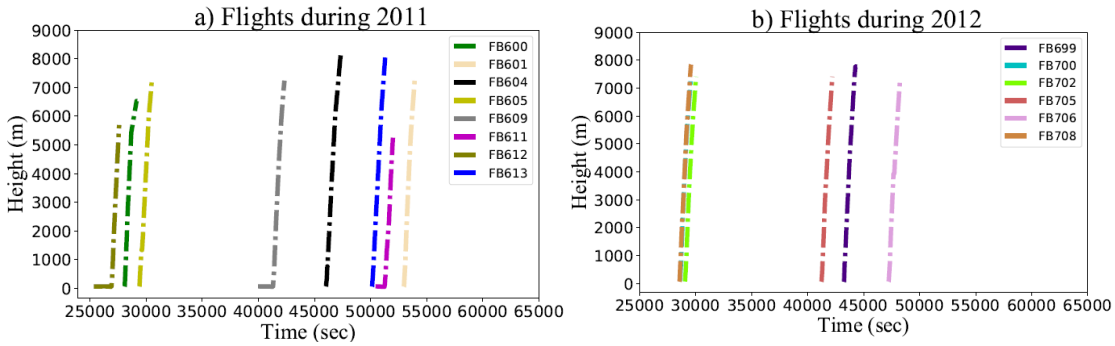

Figure 2. 2. Time of flight observations with altitude over the Atlantic Ocean during June 2011 and 2012. Plot a shows time measurement for flights on June 2011, while plot b is for flights during June 2012. Time variable in plot a and plot b is shown on x-axis, while height is presented in y-axis. Most flights have just one-time observation during the day such as flights FB604, FB609, FB700, FB705, FB706, and FB708. FB704 is not shown here due to error in the measurement of altitudes.

The Canary Islands are located 100 km from the African coastline, between 28°20'N and 14°1'W (Viana et al., 2002), as shown in figure (2.3), which shows the entire path of the FENNEC flights, where flight paths start from the Canary Islands and head off towards north Africa; they took off from Fuerteventura airport (ascending) over the Atlantic toward Africa (descending), and then returned from north Africa, passing over the Atlantic toward Fuerteventura. This study used only flight observations that had periods of time over the Atlantic, depending on flight paths from Fuerteventura airport until reaching the west African coastline, which is indicated by the dashed black line on the map. In a similar way to flights over land, the flight observations over the marine environment and these observations of dust profiles and meteorological variables during the flights will be used as initial dust profiles, for example, for the sedimentation process and turbulent mixing impact using BRSedT model, as presented in Chapter 5. Table (2-2) displays the number, date, and time of FENNEC observations over the north African land, where the height range of these flights were between about 0.1 km downwind from the African land and reaching about 8 km at the time of the African coastline.

Table 2- 1. The date and time of FENNEC flights. The selected times in this table indicate the flight times during which profiles were measured and used and so it is not the full time of flight of the aircraft.

N.	[1]Date (2011 & 2012)	Time for flight measurements (UTC)	Flight	[2]AOD	SZA degrees
1.	$17-06-2011\ (a)$	(0748 To 0806)	FB600	0.06	64
2.	$17-06-2011\ (b)$	(1442 To 1459)	FB601	0.06	21
3.	$20-06-2011\ (b)$	(1247 To 1309)	FB604	0.2	10
4.	$21-06-2011\ (a)$	(0809 To 0829)	FB605	0.5	63
5.	$24-06-2011\ (a)$	(1106 To 1145)	FB609	0.07	25
6.	$25-06-2011\ (b)$	(1400 To 1426)	FB611	0.06	14
7.	$26-06-2011\ (a)$	(0702 To 0739)	FB612	0.2	63
8.	$26-06-2011\ (b)$	(1355 To 1415)	FB613	0.2	13
9.	$06-06-2012\ (b)$	(1201 To 1234)	FB699	0.07	13
10.	$08-06-2012\ (a)$	(0752 To 0812)	FB700	0.02	66
11.	$10-06-2012\ (a)$	(0740 To 0820)	FB702	0.06	64
12.	$12-06-2012\ (a)$	(1113 To 1143)	FB705	0.06	20
13.	$14-06-2012\ (b)$	(1257 To 1322)	FB706	0.05	5.7
14.	$16-06-2012\ (a)$	(0756 To 0813)	FB708	0.04	69

[1] (a) and (b) refer to early morning and afternoon flight times.
[2] The values of AOD define the strength of dust events. AODs were taken from AERONET observations accounting for averaged-AOD in three different regions including Izana, La-Laguna, and Tenerife Islands.

The location of the Canary Islands is within the eastern subtropical Atlantic Ocean and in the advection track of the largest source of dust in the world (Menéndez et al., 2007 and Prospero et al., 2012) making these FENNEC observations very well suited for studying the effects of dust in the dusty marine environment. The vertical profiles of dust and meteorological variables including temperature, water vapour and wind components from the flights were interpolated (by using a computer program written in FORTRAN code) into 70 layers in agreement with the LEM and BRSedT modelling work, with vertical resolution of 120 m up to 8 km in height.

In this work, LEM simulations will be based on vertical data from the research flights where FENNEC flights provide profiles during ascending/descending over land and ocean. The observations are just a snapshot of the atmosphere at that time and location, and so the profiles are representative typically of the area and time during ascent/descent. Although the flights ascending or descending from Fuerteventura take measurements over the Atlantic, their observations are the lowest levels will be over land and so the lowest part of the marine boundary layer is only approximated by the flight observations. The initial (dust profiles over African land) and final (after dust transported over the Atlantic) data were also used in sedimentation and turbulent transfer model (Chapter 5) and in LEM simulations.

Table 2- 2. The date and time of FENNEC observations for the selected flight observations over north African land. The selected time in this table indicates the times during which profiles were observed in the flights, not the full time of each flight. The value of AODs is taken from daily averaged AOD from MODIS-Terra.

N.	**Date (2011 & 2012)**	**Time for flight measurements (UTC)**	**Flight**	**AOD**	**SZA Degrees**
1.	$20-06-2011\ (b)$	(1537 To 1732)	FB604	1.0	40
2.	$21-06-2011\ (a)$	(1017 To 1142)	FB605	1.0	32
3.	$25-06-2011\ (b)$	(1630 To 1857)	FB611	0.6	50
4.	$26-06-2011\ (a)$	(0928 To 1150)	FB612	0.8	44.7
5.	$06-06-2012\ (b)$	(1405 To 1632)	FB699	0.6	8.5

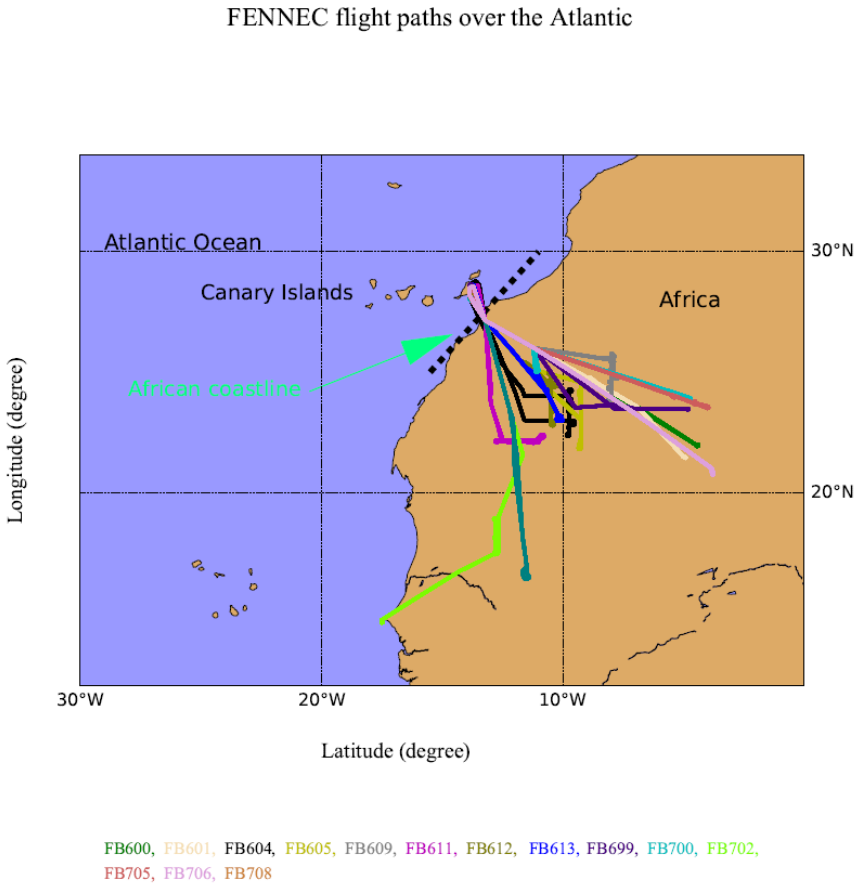

Figure 2. 3. All flight paths for FENNEC observations from Canary Islands toward northern-west Africa passing over the Atlantic Ocean. The selected flight paths used in this current study are indicated as crossing the west coast of African (see black dashed line) and towards the Canary Islands on the map. The data from these flight observations were taken depend on flight paths from Fuerteventura toward the coast of the African continent with height up to 8 km over the Atlantic Ocean. The coloured lines refer to different days of flight observations during June 2011 and 2012, which are shown by flight numbers (including FB600, FB601, FB604, FB605, FB609, FB611, FB612, FB613, FB699, FB700, FB702, FB705, FB706 and FB708) underneath this figure.

2.1.3 Wind data from ECMWF reanalysis and radiosonde observations

Wind velocities (u, v, and w) profiles were taken from ERA5-reanalysis data of the ECMWF forecast model for using in the LEM and dust BRSedT models in later chapters. Data from ECMWF is on a 1°x1° grid with 137 levels from the surface up to an altitude of about 80 km. Wind data from this reanalysis model is represented as hourly 4D-variables with latitude and longitude grids and with pressure heights each time steps. Vertical wind velocity from forecast models given in vertical pressure velocity (ω) units of Pa/s, which is converted to updraft speed in units of m/s with altitude levels. This can be calculated by using the simple formula (Holton and Hakim, 2012: Van der Does et al., 2018) as below:

$$w = -\omega * (1/\rho_a * g) \quad \text{Eq. (24)}$$

$$\rho_a = P/R * T \quad \text{Eq. (25)}$$

Where, w is the vertical velocity in units of m/s, ρ_a is the density of air (kg/m^3), g is the gravitational acceleration (m/s^2), ω is the rate of change of pressure with time dp/dt, P is pressure in units of mb, R the ideal gas constant for dry air (R_d = 287 J K/g K), and T is the temperature from the flight observations in Kelvin units. The selected height levels from ECMWF were from 1000 to 400 Pa, in order to fit with the vertical resolution of FENNEC observations, a polynomial fitting curve was applied to omega (ω) values with the geopotential heights from reanalysis data in order to obtain vertical profiles of wind corresponding with the height of flight observations. The wind profiles from FENNEC observations over the Canary Islands were used in model simulations, while the ECMWF hourly (every 3 hours) data of vertical wind velocity associated with latitude and longitude grids was used in sedimentation and turbulence model (BRSedT). Data of vertical profiles of temperature and pressure from radiosonde observations has been used in this study. These profiles are used along with data flight (at a given level) when modelling the dust over the Atlantic.

2.1.4 AOD observations

AODs were taken from AERONET and MODIS-Terra observations to categorise the intensity of dust events and to use AODs categories when running the BRSedT model. Classification of severity of dust outbreaks over Canary Islands were decided based AOD observations from both satellite and AERONET (see table (2-1)), while dust events over the African land and Caribbean were classified from MODIS-AOD satellite observations, see table (2-2). AOD values based on AERONET were taken at three different Canary Islands including Izana, La_Laguna, and Tenerife and an average of AODs was obtained to represent the region associated with each time of flight observations. In addition, AOD is calculated for BRSedT sedimentation and turbulent results by calculating AOD for initial and final profiles based on dust mass loading. The purpose of calculating the AOD is to compare the values those calculated from the evolved dust profiles from the BRSedT model to determine if the model has the correct order of magnitude.

The category (dusty, moderately dusty, non-dusty) of dust events for all flight cases were selected based on AOD from AERONET and satellite observations, where AOD ≥ 0.1 is specified as dusty cases, 0.05 ≤ AOD < 0.1 indicates the moderately dusty cases and AOD < 0.05 pertains to the non-dusty cases. The reliability of these categories is based on flight dust cases in the Canary Islands comparing to the intensification of dust events with AOD from satellite observations. The category of dusty cases is determined by whether the profile of dust mass is higher than non-dusty cases, while for moderate cases are specified to that dust profile is greater than non-dusty and less than dusty cases. The classification of dust events over the Canary Islands in some cases can differ with the classification that would be applied over land. The classification

I used is over the Canary Islands and this is consistent with the classifications transported across the Atlantic to the Caribbean.

To conclude, I have outlined the sources of data that will be used in the work including flight and satellite observations. In the next sections, I will outline the models that will use this data and I will introduce and discuss the modelling approaches.

2.2 Research tools and set-up

Presented in this section are the main research tools used in this work. There are various models and calculations used to address different parts of the study of how dust affects the marine environment. There are four key areas or calculations involved are:

1. Calculation of dust mass mixing ratios (DMMR) from FENNEC observations. Calculation of the dust size distributions was performed using the instrument data converting the scattering in each channel into sizes by using a Mie scattering code (Rosenberg et al., 2012).

2. Dust size distributions were used along with meteorological profiles in the Edwards-Slingo (ES) radiation code to do off-line radiative calculations with and without dust and at the same time with outbreak levels of water vapour and with using water vapour based on non-dusty background air. All simulations included dependence on gases, solar zenith angle and other properties such as surface albedo and emissivity. The aim of the calculations was to obtain fluxes and heating rates for use in assessing radiative importance (fluxes) or to account for dust or water vapour radiative effects in dynamics models such as the LEM.

3. Large Eddy Model (LEM) simulations using dust heating rates based on the FENNEC observations and ES model results from 2) and literature values (e.g. Zhu et al., 2007 and Otto et al., 2007) as well as the meteorological profiles from observations and large-scale subsidence from ECMWF data. Runs based on FENNEC observations were implemented by considering flight time observations and time-varying solar zenith angle. Outputs from the LEM are analysed to determine the impact on the thermodynamic and dynamical properties due to the dust and water vapour. Calculations were run to isolate the effects of dust and enhanced outbreak water vapour relative to a base run without dust and non-outbreak water vapour levels. A sensitivity test was included in the results of the thesis for enhanced dust outbreak levels of water vapour, with sensitivity of results explored by reducing the water vapour level.

4. The final model used was to estimate the amount of dust that would be transported across the Atlantic to the west side of the ocean. I have observations of meteorological values and observations of some well-mixed profiles of potential temperature during dust events at Caribbean (e.g. Puerto Rico and Guadeloupe regions) locations but do not have dust profiles locally. I have

developed an approximate size resolved dust advection, sedimentation and turbulence model, the BRSedT model, to estimate the order of magnitude of dust reaching the west Atlantic so that I can then assess the impact of dust on the environmental profiles and dynamics after a week of transport. The main question is that after the dust laden air has transported for a week, the locally observed profiles still suggest there is an almost well-mixed layer in the west Atlantic. What is the role of the dust on that side of the Atlantic? Is the dust or water vapour locally still driving this well-mixed layer? The BRSedT uses HYSPLIT and ECMWF results in estimating the transport and satellite observations are used to test integrated amounts to ensure they are of the right order of magnitude. All simulation runs for the LEM and radiation code were implemented with and without dust heating rates. In the next section, an overview of the LEM model is provided.

2.2.1 LEM simulations

Presented in this section is an overview of the descriptive information for the Large-Eddy Model (LEM) that is used in this study. The model, boundary conditions and dust used in the model are discussed in the following sections.

2.2.1.1 LEM description

In this current study, the Large-Eddy Model (LEM) V2.3 is used from the UK Met Office (UKMO), which is a three-dimensional high-resolution numerical model (Hill and Dobbie, 2008; Hill et al., 2008; Brown, 1999; and De Boer, 2010). The LEM has been used to simulate the atmosphere by performing the following two main procedures: integrating a Boussinesq-type equation set and including parameterizations for the sub-grid motion, cloud microphysics, and radiation (Pleavin, 2013). In past work, the LEM has been used to simulate the dry and moist atmosphere including various types of clouds, such as shallow and convective clouds. The LEM is distributed as a bulk cloud model; however, a bin version has been developed (Hill et al., 2008) to study the semi-direct effect (Hill and Dobbie, 2008). In this project, a 6.4 x 6.4 x 7.6 km domain (similar to BOMEX) is used with periodic lateral boundary conditions with 100 m resolution for the horizontal (x-axis) and approximately 120 m vertical resolution. The model was run for 8 hours of simulation time with large-scale subsidence used from ECMWF reanalysis. The LEM runs for this study were adapted from the BOMEX case study provided with the LEM but modified to agree with the conditions during the FENNEC observations. Almost everything was changed aside from the domain size. The large-scale subsidence for the case was taken from reanalysis of ECMWF ERA-5 data and dust, winds, and thermodynamic conditions were taken from FENNEC observations. Horizontal advective tendencies were set to zero since the LEM domain is considered to be advecting with the mean field of the marine environment.

I have selected cases from FENNEC for non-cloudy conditions so mixing ratios and number concentrations for rain, snow, ice cloud and graupel as well as graupel volume were switched off (parameters controlling microphysics). The clear sky (no cloud) in the selected flight cases over the Atlantic was tested by checking the relative humidity. When simulations were run using past heating rates, it was simple to implement since it just relied on integrating heating rates from Otto et al. (2007) and Zhu et al et al. (2007) into the model. Whereas, runs for dust heating rates driven from flight observations in the LEM were much more involved, including use of processing of observational data by Rosenberg et al. (2012) along with using optical properties from Ryder et al. (2013a). The vertical profiles used from FENNEC were pressure, density, water vapour mixing ratio, wind profiles, and potential temperature. These FENNEC profiles for various case days were used in all the LEM simulations.

The implementation of LEM simulation assumes that differences in horizontal density are sufficiently small and therefore, will be neglected from the momentum equation, except for when the gravity acceleration affects density differences. The Boussinesq-type equation set includes forces, momentum, thermodynamics, as well as microphysics terms as shown below:

$$\frac{Du_i}{Dt} = -\frac{\partial}{\partial x_i}\left(\frac{p'}{\rho_s}\right) + \delta_{i3}B' + \frac{1}{\rho_s}\frac{\partial \tau^s_{ij}}{\partial x_j} - 2\epsilon_{ijk}\Omega_j uk \qquad \text{Eq. (26)}$$

$$0 = \frac{\partial}{\partial x_i}(\rho_s u_i) \qquad \text{Eq. (27)}$$

$$\frac{D\theta}{Dt} = \frac{1}{\rho_s}\frac{\partial h_i^{\theta}}{\partial x_i} + \left(\frac{\partial \theta}{\partial t}\right)_{MPHYS} + \left(\frac{\partial \theta}{\partial t}\right)_{RAD} + \left(\frac{\partial \theta}{\partial t}\right)_{LS} \qquad \text{Eq. (28)}$$

$$\frac{Dq_n}{Dt} = \frac{1}{\rho_s}\frac{\partial h_i^{q_n}}{\partial x_i} + \left(\frac{\partial q_n}{\partial t}\right)_{MPHYS} + \left(\frac{\partial q_n}{\partial t}\right)_{LS} + \left(\frac{\partial q_n}{\partial t}\right)_{SED} \qquad \text{Eq. (29)}$$

Where, u is the resolved flow velocity, x is the three-dimensional position vector, P is the pressure, ρ_s is the density of air, P' is the perturbation from the reference state, h_i^{θ} is the subgrid scalar fluxes of potential temperature, $h_i^{q_n}$ is the sub-grid scalar fluxes of the resolved scalar variables including hydrometeors (all other resolved scalar variables are denoted as q_n where n indicates the different scalar variables), $\tau^s$is the sub-grid stress, ϵ_{ijk} is the alternating pseudo-tensor, Ω_j is the angular velocity of Earth, and $B'$is indicated to the buoyancy perturbation, g is the acceleration due to gravity, θ_v is the virtual potential temperature, the partial derivative terms $\left(\frac{\partial \theta}{\partial t}\right)_{MPHYS}$ and $\left(\frac{\partial q_n}{\partial t}\right)_{MPHYS}$ are the microphysical sources terms for the potential temperature and q_n, the terms $\left(\frac{\partial \theta}{\partial t}\right)_{RAD}$, $\left(\frac{\partial \theta}{\partial t}\right)_{LS}$, and $\left(\frac{\partial q_n}{\partial t}\right)_{LS}$ are the radiation and large-scale forcing sources and tendency due to sedimentation is $\left(\frac{\partial q_n}{\partial t}\right)_{SED}$. The buoyancy perturbation is represented by

$$B' = g\left(\frac{\theta'_v}{\theta_s}\right) \qquad \text{Eq. (30)}$$

Where, θ_s is the potential temperature reference state, while θ_v' is the perturbation from the mean potential temperature. A Bousinesq approximation is used by setting θ_s and density assumed to be constant with height. The main objective is to understand the radiative effects of Saharan dust and the LEM simulations provide a framework to understand the time-evolving profiles of potential temperature (θ) and other profiles.

2.2.1.2 LEM boundary conditions

LEM simulations are performed with periodic conditions in the horizontal, in which any propagation across a horizontal boundary is re-entered through the opposite side. The top and bottom boundary conditions are rigid lids, so no mass or momentum are transferred through these surfaces. Surface heat fluxes are prescribed (called as SHFLX_SEN in the LEM) over ocean to 5.4 W/m^2 (Pinker et al., 2014) and surface latent heat flux (SHFLX_LAT) to 100.0 W/m^2 (Edwards, 2007). These values are held fixed for the 8 hour LEM simulations used in this work. For the BRSedT model simulations presented in Chapter 5 which involves much longer times (7 days), the heat fluxes are varied over time. To prevent propagating gravity waves from reflecting back down at the top boundary, a Newtonian damping layer is applied. This is achieved by relaxing the prognostic variables back to their horizontal means through Newtonian damping. The properties of the surface can be defined by setting both the momentum (Z0) and scalar roughness length (Z0TH) to 0.0002 m. The 8-hour LEM runs were performed for a latitude of 28.39 degrees and longitude -14.0 degrees and with the incident solar flux set to 1365 W/m^2 (for overhead sun).

2.2.1.3 Dust profiles

To simulate the radiative influences of African dust, vertical profiles of dust over the study region (Canary Islands) are required. Dust profiles from the flight observations were obtained from the dataset of FENNEC flights for this region. The prepared dataset of dust requires physical processes to be suitable for use in the model simulations as well as in the sedimentation and turbulence model calculations. In the next sections, I will present how to get vertical data from data taken by the flight instruments, and I will show the full processes of calibration for the flight data.

2.2.1.4 Profiles from FENNEC flight observations

Dust profiles were obtained from three instruments on the BAE-146 aircraft used in the FENNEC observations, namely PCASP, CDP and CIP. The PCASP and CDP instruments measure scattering cross sections that are related to particle size based on assumptions about the RI and typically Mie theory for optics. The CIP instrument does not rely on refractive index nor on

scattering calculations since it evaluates directly by the shadow image generated by passing the light beam into the volume with the dust particles and noting changes in illumination on the diode array (Ryder et al., 2013; Ryder et al., 2015). Generating particle-dependence shadow image is captured by identifying the size of particle by quantifying the mean of the maximum size in the x and y directions along the axis of beam travel and across the diode array, respectively (Ryder et al., 2013). In the current study, CIP data was provided by Chris Reed, (FAAM instrument scientist) University of Manchester. The CIP instrument is suitable for observing large particles greater than 15 μm in diameter. Unfortunately, FENNEC flight observations for the CIP instrument were not recorded for many flights, only FB601, FB604, FB605, FB609, FB611, and FB613 (where CIP data for flight 2012 suffered from electric noise and so was ignored). Another challenge is that the first three bins of CIP for flight numbers FB604, FB605, and FB613 (dusty event cases) show very large number concentrations and discrepancy with the CDP. This can be caused by the electrical noise in the optical processing in of CIP. Since measuring giant particles from CIP depends on the shadow technique of dust particles, particle size can be quantified by determining the image of dust particles when particles pass across the beam of light in the sensing area of the probe and is directly imaged. Ryder et al. (2015) states 'Although the CIP15 is capable of measuring particles sizes of up to 930 μm, electrical noise only allowed measurements of up to 300 μm'. Figure (2.4) shows how the shadowing image is processed in the CIP instrument. This problematic issue in CIP measurements is also revealed by Ryder et al. (2013) as well as shown by Cotton et al. (2010). So, this is consistent with what I ignored for the data of CIP measurements from the FENNEC flights. Where I neglected three bins (i.e. bins of 15, 30 and 45 μm in diameter) in calculations due to the values being unreasonably large and inconsistent with the rest of the distribution. The complete results will be shown in Chapter 3, section 3.2.1.

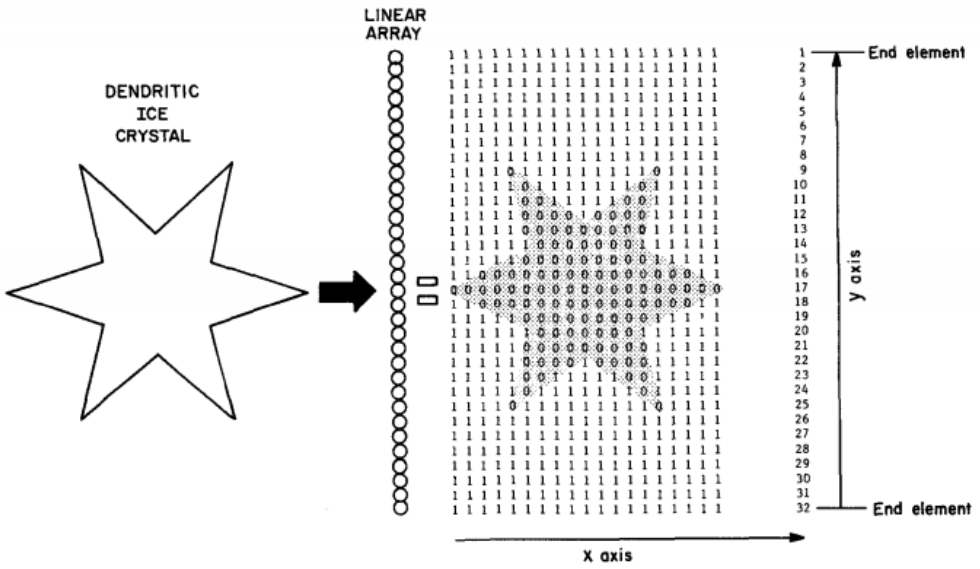

Figure 2. 4. Schematic diagram illustrating the CIP image processing.

As reported by Rosenberg et al. (2012), it is possible to improve the manufacturer calibration of the PCASP and CDP instruments. The CDP data that were obtained was already re-binned (re-calibrated) but the PCASP was not, so I proceeded to recalibrate the PCASP data to ensure the sizes determined were as accurate as possible. The calibration method used for both the CDP and PCASP data was performed by generating new channel widths and channel centres (diameters) for each bin (i.e. lower and upper boundaries). The benefit of using the calibration method of Rosenberg is that it provides significant improvement in the determination of the particle diameter from optical particle counters such as the PCASP and CDP. The improvements come about because the calibration method utilises calculations of the particles using Mie theory for the dust with RI and it is a probability based approach that takes account of the highly nonlinear relationship between the scattering and the particle diameter, especially for larger sizes. The newly re-binned PCASP results are about 30% different to the non-rebinned values and the improvement for the larger dust particles using the CDP can be orders of magnitude different from the manufacturer's calibration Rosenberg et al. (2012). The calibration process for deriving particle size, channel centre and channel width for these instruments is explained in the next paragraph.

2.2.1.5 Recalibration of Saharan dust profiles

The dust profiles are determined from the observations by the PCASP and CDP instruments. The physical process of generating dust profiles is based on these instrument's measurements of scattering cross-sections of particles. These instruments use light scattering optical particle counters (OPC) to measure dust particle sizes and dust concentrations by measuring scattering cross-section (pulse height) of particles from the light scattered by the dust in the air sampled by

the OPC. Therefore, calibrating the PCASP and CDP instruments is required to provide improved accuracy of dust profiles in this thesis. To address this problem, I calibrated the PCASP and CDP instruments by using discrete method explained by Rosenberg et al. (2012). This process resolves these measurement issues by defining a function, in which it is linked between scattering cross-section of particle to pulse height that is generated from the light scattered on the OPC's detector. Using the discrete process is an appropriate way to calibrate the dust measurements from these instruments. The PCASP and CDP use only linear amplifiers of particle scattering cross-section (Rosenberg et al., 2012). In this way, calibration for these instruments is done by using the PCASP data that was obtained from the core-FAAM datasets, while CDP data has been used from the data provided by Rosenberg et al. (2012). Both datasets, PCASP and CDP, were calibrated with a range of refractive indices, RI, including 1.43 and 1.53 for the real parts and 0.0001 to 0.005 for the imaginary parts. The scattering calculations were performed for the PCASP data using values for diameters ranging from 0.1 μm to 150 μm in steps of 0.01 μm and for CDP from 1 μm to 300 μm in 0.01 μm steps. To begin with the calibration, a Mie scattering conversion-table generator was created linking cross sections for light scattering particles to the particle size using Mie theory. This Mie scattering table is obtained by using Windows/FORTRAN code, which was written by Wiscombe (1980). MieConScat code was used to generate table of scattering cross sections with using:

1. **Min and max diameters:** For PCASP the min entered value in the MieConScat code was 0.1 μm and the max was 150 μm, while the min of 1 μm and max of 300 μm were used for the CDP.

2. **Real and imaginary parts of RI:** the values of 1.53 and 1.43 were used for the real parts and the imaginary were set to: 0.0001, 0.001, 0.003, and 0.005.

3. **Scattering angle ranges:** The PCASP collects light from a direct beam over the range 35-120 degrees, and from the reflected beam the light is collected over the range 60-145 degrees. Therefore, there are two angular ranges named primary and secondary. In contrast, the primary angular range of 4-12 degrees which is used for the CDP instrument with no secondary angular range.

4. **Wavelength of light used by the instrument:** Wavelength of 632.8 nm was used for PCASP instrument and 658 nm is used for the CDP.

Dust-derived sizes based on these input parameters mentioned in points 1 to 4 were obtained based on Mie theory with using software programs for PCASP and CDP flight instruments individually. To proceed, scattering cross sections of dust particle were generated by MieConScat software with using input parameters including the refractive index. Since cross sections are

characterised by non-linear and non-monochromatic function, cross sections need to be converted to diameter. In this case, CStoDConverter has been developed by Rosenberg et al. (2012) to solve this problem, where this program derives bin centres and widths from the measured cross section automatically. The CStoDConverter also allows this scattering data to provide their error uncertainties as well. After channel width and channel centre (diameter) are generated, there are omitted channels including 1, 6, and 16. Channel 1 is deleted due to it being in error, while both channels 6 and 16 are zero and these latter channels are determined by taking an average of the channels surrounding each channel, so channels 5 and 7, 15 and 17, respectively.

A range of different imaginary refractive indices were used (1.53+0.005i, 1.53+0.003i, 1.53+0.001i, 1.53+0.0001i) with results shown in Chapter 3. In addition, a couple of RI were used with changing real part, including 1.43+0.003 and 1.43+0.001 for both PCASP and CDP in order to investigate the sensitivity of the results for different real values as well. I used these values of refractive indexes based on Ryder et al. (2018), Ryder et al. (2013), Ryder et al. (2013b), and Rosenberg et al. (2012).

Corrected or re-binned dust size distribution profiles for the FENNEC observations were used to obtain offline heating and cooling profiles that are then used in the LEM. To obtain these, dust number concentration profiles were generated based on using RI values and then were converted to total dust mass profiles by multiplying the number concentration by the volume of particles and by an appropriate density of dust. This calculation for total mass profile was performed for PCASP and for the CDP data, but CIP was represented number concentrations provided from Chris Reed/FAAM. The number concentration of obtained CIP was in units of L^{-1}, and thus it needs to be divided by channel width of 15 μm and multiplied by 0.001. Total mass of dust particles derived from these instruments were converted to DMMR, since dust MMR profiles are required to be using in ES radiation model (Edwards and Slingo, 1996; Rap et al., 2013). DMMRs were calculated based on the conversion equation shown in the next section. The effect of the dust on the marine atmospheric structure was determined by implementing the dust heating rate profiles that correspond to the FENNEC dust loading and optical properties. Tracer transport of the dust was not undertaken in the LEM model.

2.2.1.6 Calculating dust mass and dust MMR

Dust mass profiles are significant not only in simulating thermodynamic and dynamic effects of Saharan dust on atmospheric structure of the dusty marine environment, but also in modelling dust of transport over the Atlantic (see Chapter 5). Dust profiles including dust mass loading and DMMR were calculated to generate heating rate profiles needed by the LEM runs with radiation switched on. Dust heating rates were calculated using the radiation code for flight observation cases, whereas literature-based heating rate profiles were also used and based on Otto et al. (2007) and Zhu et al. (2007) profiles and implemented in the LEM as well. In this section, I will present

the methods for calculating the dust profiles, while dust heating rates based on Otto et al. (2007) and Zhu et al. (2007) and flight observations will be explained later, separately. Therefore, the distribution of dust particle mass as a function to particle size based on FENNEC observations were calculated by integrating the number concentration of dust over all bins from the calibration methods (based on calibration processes of Rosenberg et al., 2012) for both PCASP and CDP data (provided by Rosenberg et al., 2012) and multiplied by the volume of dust particles in each bin to get mass loading of dust particles as shown below (Seinfeld and Pandis, 2016):

$$n_M(r_p) = (\rho_p)\frac{4\pi}{3} r_p^3 (dN/dD) \qquad \text{Eq. (31)}$$

Or in terms of diameter,

$$n_M(D_p) = (\rho_p)\left(\frac{\pi}{6}\right) D_p^3\ (dN/dD) \qquad \text{Eq. (32)}$$

Where, $n_M(D_p)$ is the distribution of dust particle mass which is as a function of diameter (D_p) of each bin in (g/cm^3 μm) unit. The term on the right hand of this equation indicates the total volume of dust-aerosols which is then multiplied by the density of particles (ρ_p) in units of g/cm^3. DN/dD refers to the size distributions of dust particles. Many previous studies, such as Maring et al. (2003), used the density of aerosol as an average value between 1.6 and 2.6 g/cm^3. However, the value of density for dust particles used in this mass calculation is 2 g/cm^3 (Jabonero et al., 2016). Two different values of ρ_p were used in sedimentation and turbulent code including 2 and 2.6 g/cm^3. The intensity of dust over land is likely to be greater than over the Canary Islands, and thus it will be good to investigate how these values can change the results of dust transport and sedimentation over the Atlantic.

Dust mass mixing ratio (DMMR) profiles are also needed in the radiation code to obtain heating rate profiles. However, as dust layers are transported over the Atlantic, dust will sediment, and dust also can be mixed with other particles such as sea salt concentrations, especially within the MBL. So, the sea salt concentration in the MBL may affect the result, and thus it is required to subtract out the sea salt effect. I applied a scale height for sea salt based on Gong and Barrie, (1997) and Gleeson et al. (2015) for estimating sea salt concentrations in order to calculate the net dust mass concentration (NC), i.e. removing the sea salt concentration. The full steps of calculating NC are described below as follows:

Step 1: Calculation of sea salt concentration at (10) m using ten metre winds near the surface (U_{10}), where the wind is taken from the ECMWF data. The sea salt concentration at 10 m wind is indicated by the symbol $C_{sea-salt}^{10}$, as expressed in Eq. (33).

Step 2: Calculation of sea salt concentration at the surface based on Step (1) and then calculating the sea salt with height based on a sea salt aerosol scaling-height (H). Sea salt concentration at the surface is indicated by the symbol $C_{sea-salt}^{sfc}$, as it is calculated in Eq. (34).

Step 3: Calculation of the sea salt concentration at FENNEC observation heights based on Step (2). The sea salt concentration at a height (z), i.e. FENNEC heights is indicated by the symbol $C^{z}_{sea-salt}$ in Eq. (35).

Step 4: Calculation of the NC of dust excluding the sea salt concentration is shown in Eq. (36). All these steps above are presented in the equations below.

$$C^{10}_{sea-salt} = b\, e^{a\, U_{10}} \qquad \text{Eq. (33)}$$

Where, a and b are constants over the Atlantic Ocean taken from Gong and Barrie, (1997) with values of 0.16 (s/m) and 4.26 (μg/m^3), respectively. The sea salt scale height, H, is the value of 500 m. The sea salt concentration at the surface in units of μg/m^3 can be calculated by:

$$C^{sfc}_{sea-salt} = C^{10}_{sea-salt}\ \ e^{\left(\frac{10}{H}\right)} \qquad \text{Eq. (34)}$$

So, the concentration at altitude for flight observations is calculated as the following equation:

$$C^{z}_{sea-salt} = \quad b\, e^{a\, U_{10}}\, e^{\left(-\frac{(z-10)}{H}\right)} \qquad \text{Eq. (35)}$$

Therefore, when given DTC for the total mass loading of dust (i.e. dust plus sea salt concentration) which is calculated based on size distribution, the NC of the dust can be obtained by using the following formula:

$$\mathrm{NC} = \mathrm{DTC} - \ C^{z}_{sea-salt}\ \mathrm{x}\ 10^{-6} \qquad \text{Eq. (36)}$$

Where the $10^{-6}$is to convert units to g/m^3. DMMR is calculated for dust size distribution based on the ECMWF conversion formula between DMMR that is calculated from size distributions from flight observations and the NC shown in Eq. (36). So, the DMMR required in the radiation code can be calculated from:

$$\mathrm{DMMR} = \frac{0.001\ \mathrm{NC\ R\ T}}{100\ \mathrm{P}} \qquad \text{Eq. (37)}$$

DMMR is in units of kg/kg, while NC in unit of g/m^3, T in units of K is temperature, P (hPa) is pressure, and R is the specific gas constant for dry air (287.058, J/kg K). The factor 0.001 is for conversion unit from g to kg, while the fraction 100 is for pressure unit conversation from mb to Pascal. The benefits of calculating the total mass loading of dust particles are: 1) To understand the vertical structure of dust profiles associated with dust size distributions over the Atlantic. 2) To understand the influence on the radiative impact of other potentially important factors such as water vapour on profiles over the Atlantic, and 3) To derive heating rate profiles that are required for the LEM simulations. The structure of dust profiles together with these points mentioned above will be shown in Chapter 3, which is the first step in terms of results for evaluating the dust radiative impact on the MA structure over the Atlantic.

The heating rates were implemented in the LEM by two approaches: Firstly, by updating with FENNEC meteorological profiles such as temperature, height, humidity, and wind speed components and with using dust heating rate profiles from Zhu et al. (2007) and Otto et al. (2007), and secondly by generating dust heating rates using the ES radiation model based on re-binned size resolved profiles of dust from FENNEC observations. In both simulations, the LEM was run

with updated subsidence from ECMWF reanalysis model data, as stated previously. As an initial method, I will present the modelling of the radiation-dust effects based on the literature heating rates first and then I'll present the results of the dust radiative effects based on the FENNEC observations.

2.2.1.7 Simulating dust radiative effects by LEM based on literature HRs

One of the crucial aspects of dust modelling is understanding the effect of the dust heating rates on the structure of dusty marine environment and the dust itself. Although previous studies cover a good range of dust-radiative effects over land, the dust-radiative effects downwind the Atlantic Ocean still requires more research. In addition to understanding the overall dust heating rates, it is also important to understand the relative importance of the SW and LW radiation separately.

In the first stages of simulating the radiative effects of dust, a representative fixed dust heating rate from literature was used that could be applied in the LEM. It was found that the profile of Zhu et al. (2007) had both LW and SW profiles that looked appropriate, but the peak magnitudes in SW and LW were not the largest seen in the literature and I was interested to test the extreme heating rates to evaluate if the heating rate effects were significant before proceeding to derive heating rates from radiative calculations. Therefore, the magnitude of the Zhu et al. (2007) was scaled to the largest value came across in the literature, which was Otto et al. (2007). Otto et al. (2007) wasn't used itself since the peaks in the heating rates were very sharp in the vertical and so were unlikely to represent the distributions in our observations. This fixed heating rate was obtained by using the peak values for SW and LW obtained from Otto et al. (2007) and applied to the profiles of dust heating rates of Zhu et al. (2007). The scaling method applied is shown by using the following formula which scales the heating rate, x_i at each height i, by the ratio of the peaks of Otto et al. (2007) to Zhu et al. (2007). The result is a profile that has the same shape as Zhu et al. (2007) but the magnitude is scaled to agree with the maximum values of Otto et al. (2007), PV, according to

$$\mathrm{HR} = \mathrm{x_i}\left(\frac{\mathrm{PV}}{\mathrm{X_p}}\right) \qquad \text{Eq. (38)}$$

Where HR is the actual heating rate used in the LEM simulation. The heating rate from Zhu et al. (2007) at each height, x_i, is scaled by the ratio of the peak heating rate of Otto et al (2007) given by PV divided by the peak value ($\mathrm{X_p}$) of Zhu et al. (2007) for both SW and LW. PV is 9 k/day for SW and 9.56 k/day for LW heating rate calculation. The simulated dust heating rates in the LEM based on the vertical heating rates of Zhu et al. (2007) and with their scaled to peak heating rate of Otto et al. (2007) are specifically related to over ocean including a surface albedo for the ocean with a value of 0.06, which is taken from NSIDC (2018). The LEM simulations were implemented using large-scale subsidence provided from ECMWF reanalysis data. All these data, including heating rate profiles, surface albedo, and large-scale subsidence were used in the LEM to be relevant for the dusty marine environment off the west coast of Africa.

In addition to the scaling described above, I wanted the profiles from literature to have peaks in the heating rates that aligned with the observed profiles of dust so the heating rate profiles of Zhu et al. (2007) which start at a height of 0.5 km and extend to a height of 6.5 km were scaled so the base was at 1.3 km and the top of dust layer was at 6 km. Also, below 1.3 km the heating rate profiles were assumed to be constant with that value at 0.5 km due to no values being available for these heights. It is noted that Otto et al. (2007) heating rates include not just dust but also other contributions from gases whereas Zhu et al. (2007) includes just dust heating rates. It is recognised that I scaling the values of Zhu et al. (2007) to heating rates that include more than just dust but this approach of using literature heating rates is only a first approach to estimate the most significant heating rate effects and so I accept there could be differences but that to test whether an effect is present or not it will suffice. If results indicate heating rates are important then more rigorous heating rates will be calculated using the observed dust and radiative transfer calculations.

The peak values of Otto et al. (2007) over ocean case for SW (orange line) and LW (red line) are 9 K/day and 9.74 K/day obtained from Otto et al. (2007), see figure (2.5). The SW and LW dust heating rates from Zhu et al. (2007) are shown in figure (2.6). In the figure (2.5), dust heating rate profiles are expressed in units of K/day for different locations for SW only in plot (a), LW only in (b) and total radiation in (c). The thesis uses dust heating rates for the SC (Saharan coast) case shown by dashed black lines in the figure (2.6). Figure (2.7) depicts the actual dust heating rates that are calculated based on Zhu et al. (2007) and Otto et al. (2007) which are used in LEM simulations. Orange and red lines show dust heating rate profile for SW and LW radiation described by SWHR and LWHR in the legend of figure (2.7), while TOTHR refers to total heating rate of dust effect.

The scaled heating rate profiles of Zhu et al. (2007) is only related to dust effect on Cape Verde location, while the largest (peak) value from Otto et al. (2007) contains heating rate for both dust and other atmospheric constituents influencing on the Canary Islands site. This may not have good comparison between these heating rates but it can be applicable process to use heating rate profiles from Zhu et al. (2007) with considering the peak heating rate of Otto et al. (2007

Zhu et al. (2007) work is appropriate for our work because:

1. The study of Zhu et al. focuses on the radiative effects of Saharan dust transported over the equatorial Atlantic (Cape Verde location) by using MODIS level-2 AOD data in the Monte Carlo Aerosol Cloud Radiation (MACR) transport model to evaluate the radiative effects and heating rate profiles of Saharan dust over the equatorial Atlantic. Their study also compared appropriate data of aerosol AODs from different satellite observations such as MODIS, TOMS, MISR, and Advanced Very High Resolution Radiometer (AVHRR). MODIS observations were also used to obtain the AOD over land and ocean for comparisons with the sedimentation model results to

check if the values had the right order of magnitude result. No vertical mass concentrations could be obtained from any of these satellite observations for the dates studied, where Zhu et al. (2007) derived dust heating rates based on AOD dataset from MODIS satellite observations.

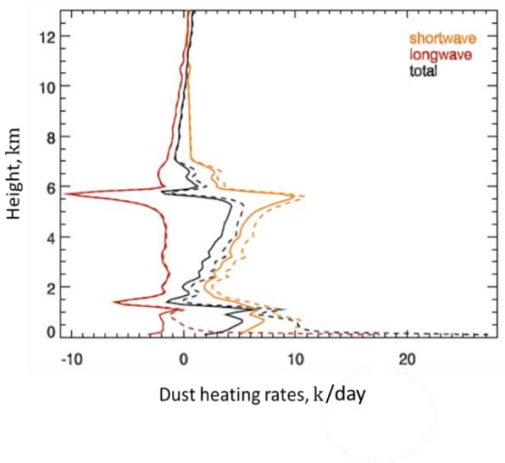

Figure 2. 5. Dust heating rates profiles over land (shown by dashed line) and the Atlantic Ocean (solid line) in K/day taken from Otto et al. (2007). Orange, red and black lines indicate dust heating rates for the SW, LW and total radiation, respectively. The peak values of dust heating rates from this figure are incorporated to the SW and LW heating rate profiles of Zhu et al. (2007) with scaling of heights (as mentioned before in the heating rates method), and then imposed in the simulation of LEM.

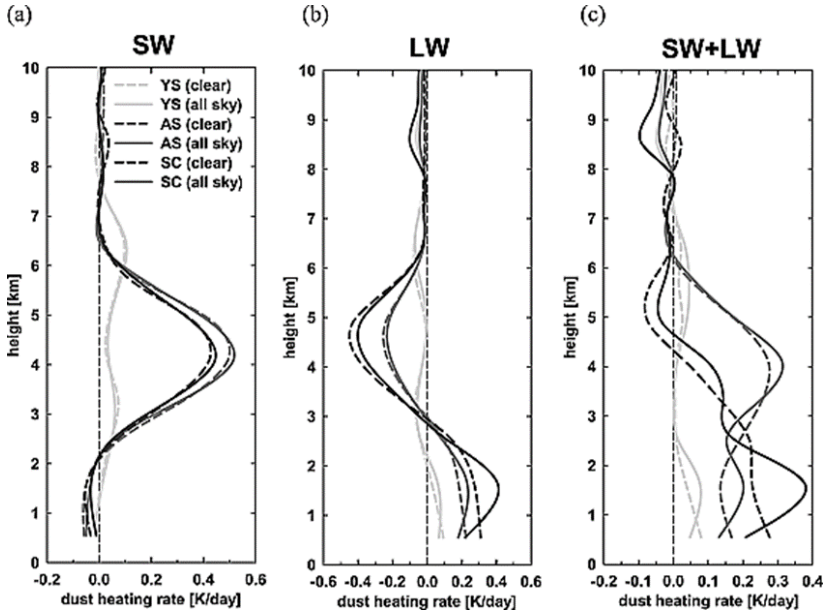

Figure 2. 6. Profiles of dust heating rates in three-different region studies from Zhu et al. (2007), which are: The Yellow Sea (YS), Arabian Sea (AS), and Saharan Coast (SC). (a) For the SW only and (b) for the LW only, and (c) total heating rate profiles. Where heating rates in SC is the literature-based profile (i.e. Zhu's case) in this thesis. See black dashed lines for clear sky. The rest of the cases are clear sky (dashed line) and all sky (solid line).

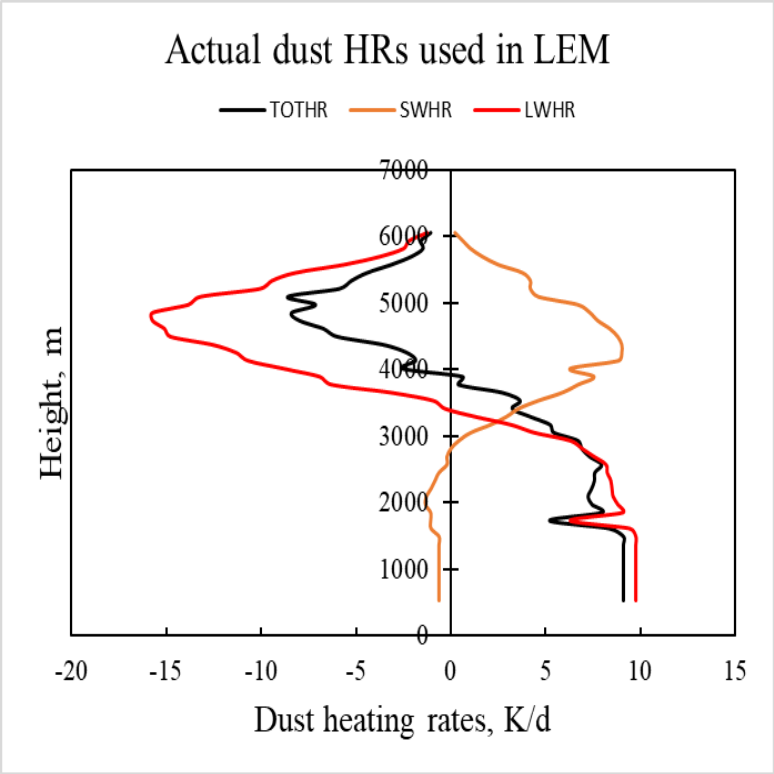

Figure 2. 7. Calculated dust heating rate profiles (expressed in units of K/d) based on vertical profile of Zhu et al. (2007) and peak heating rate from Otto et al. (2007). The profiles were used as a fixed heating rates in the LEM simulation for literature consideration. The calculated SW, LW and TOT heating rates indicated by symbols SWHR, LWHR and TOTHR in the legend of the figure, respectively. These heating rates were used in the simulation for all flight cases.

2. The Zhu et al. (2007) study involves both the SW and LW radiation, including scattering, absorption, and emission by dust and cloud. The Zhu et al. study also looked at water vapour from satellite observations to study the impact of dust on the water vapour budget and general circulation.

3. The direct radiative forcing is presented over the oceans of the globe with four main assumptions around the optical properties of dust, which are based on: spherical dust particles, single scattering albedo with a value of 0.94, asymmetry factor of 0.69, and Angstrom exponent with a value of 0.36. These parameters are important to account for the radiative effects of African dust transported across the Atlantic, and thus the results of simulated heating rates (heating rates based on literature) for flight cases can be compared to simulating dust heating rates based on FENNEC observations and also with other previous studies such as Ryder et al. (2013). The SSA of Zhu et al. (2007) has closer value to that shown by Ryder et al. (2013a) who stated that SSA for dust transported over the Canary Islands is 0.95. It seems not significant difference in SSAs between the Cape Verde and the study area in the current thesis. So, using heating rates based on

optical properties for Zhu et al. (2007) is good way to look at what high heating rates can change the atmosphere due to both destinations are located at closer distance from the African land.

4. Based on the optical properties of Saharan Coast (SC) mentioned above, Zhu et al.'s research shows that it is important to investigate uncertainty for the large mode dust in comparison to fine mode dust particles. Using the peak value approach of heating rates associated with Zhu et al.'s profiles may have limitation, including missing heating rate values at lower altitude (i.e. below 0.5 km) which can affect the results in the LEM. Scaled peak values of heating rates may also cause enhancement in the result of the LEM simulations for θ vertical structure as these values (i.e. SW and LW heating rates) represented peak values during noon-time. Finally, the water vapour impact is not accounted for in these profiles. Water vapour associated with SAL can contribute to changing the net radiative forcing by increasing/decreasing heating rate profiles, especially over oceans where water vapour is high at least near the surface. However, using these peak values can provide an idea about dust particle intrusion and its effect on the dusty marine atmospheric structure. This was the thesis starting point, to assess the dust effects in the LEM. The current preliminary study was performed with these scaled heating rates in the LEM. Once I determined if there were significant effects then I proceeded to use the more detailed observations from FENNEC to derive the heating rates. This next stage was far more involved as it included not only dust mass profiles but it also required significant work to derive re-binned dust size distributions.

2.2.1.8 LEM simulations of dust based on re-binned FENNEC observations

The version of the LEM available did not have interactive radiation and so I ran the radiative calculations off-line in the ES model and then applied the heating rates in the LEM. The radiation code was run with the dust profiles based on vertically re-binned size resolved data from the FENNEC flight observations. Dust simulations using the LEM were performed for flight cases using two approaches: Firstly, the LEM was run with FENNEC observations, ECMWF largescale subsidence, and with derived dust heating rates from ES over 8 hours of time simulations. In the current thesis, dust heating rates were derived based on two approaches; the first method was performed with using initially different solar values that depended on the start time of each flight case. The second way was by generating heating rates using time-varied SZA from early morning and afternoon times, where the initial solar elevation used in the ES is the same for all flight cases. The LEM is coupled with the derived heating rates based on these approaches to simulate dust effects over 8 hours of time simulations, where heating rates were based on FENNEC observations implemented for dusty cases and used to investigate the role of water vapour in the dusty atmosphere by contrasting the simulation results between dusty cases and non-dusty cases (with non-dusty background water vapour levels). The current research focuses on the first

method since dust and other meteorological profiles were used based on FENNEC flight start time for the observations. However, second approach (dust heating rate dependency for all runs at the same time of day for morning and afternoon start times) were also implemented to understand and analyse the thermodynamic and dynamic results using radiation and LEM simulations. The procedure for determining the heating rates based on time-varied SZA during the day will be explained in subsection 2.2.1.12. Simulations were performed for LW only, SW only and total radiation. Rather than attempting to perform exact case studies, I was looking to assess the leading effects of dust for daytime (total) and night-time (LW only) and then SW only helps to characterise the effects. Secondly, the LEM was run with heating rates varying with time accounting for the solar angle varying during the 8 hours of simulation. With the solar angle varying, it is less easy to attribute effects, but it provides for a more realistic simulation of the actual case. Obtaining dust heating rates from the ES radiation model involved several steps. In the next section, I outline the radiation Edwards and Slingo radiation code, then follow that with the dust optical properties used in the radiation code. These will be presented in the next sections.

2.2.1.9 Edwards-Slingo radiation code

To generate dust heating rates profiles for the LEM runs, the Edwards-Slingo (ES) model runs were performed using separate input files in NetCDF format for dust, temperature, pressure, and gases such as water vapour (Edwards and Slingo, 1996; Manners et al., 2015). These profiles were from FENNEC observations and standard atmospheric profiles to provide realistic profiles to then determine the heating rates from the ES model to then be used in the LEM. The ES model is a 1-D radiation scheme used to calculate the radiative fluxes and heating rate profiles of atmospheres including particles such as gases, aerosols and clouds. In this work, gases and dust heating rates were evaluated. In the model, the upward and downward total fluxes (diffuse plus direct) were calculated by summing the calculated results of band computations weighted by the solar spectrum. For the ES model, I used input spectral files describing the optical properties of the dust and gases with the following spectral bands; 6 wavelength bands for SW and 9 bands for LW radiation, as in Ryder et al. (2013a).

The ES radiation calculates 1D radiative transfer through the atmosphere divided up into levels (boundaries) and layers (mid-point) from the top of the modelled atmosphere to the surface for all input data. The calculations are done for a spectral wavelength band at a time. Data profiles have an input file each for of dust, pressure, specific humidity, ozone data profiles, etc. Except for the temperature profile which is characterized by two input profiles: temperature profiles for mid-level and every layer interface e.g., temperature values at mid points between z (i) and z (i+1) and temperature at every layer interface. The inputs were converted to the expected input units of the radiation code where the unit of mass mixing ratio (MMR) for all gases (kg/kg) was used.

These input files had to be formatted into NetCDF files or text CDL files to run correctly with the radiation code. For full information on the radiation code, refer to Edward and Slingo (1996) or Manners et al. (2015).

The fundamental optical properties for calculating the dust radiative fluxes in this work are: dust mass extinction coefficient, single scattering albedo and the asymmetry parameter. Given these optical properties and other general features of the atmosphere such as vertical extent of dust, surface radiative properties, and solar zenith angle, the radiative fluxes can be calculated with a two-stream equation code, where the optical properties of the layer (L) determine the total transmission and reflection coefficients. The total fluxes (TF) can be calculated by

$$TF = \sum_j F_{bi} \quad \text{Eq. (39)}$$

Where, F_{bi} is the partial fluxes in each of the bands. Then the F_{bi} is described as a band weighted sum of quasi- monochromatic fluxes, F_{mk}

$$F_{bi} = \sum_k wt_k \, F_{mk} \quad \text{Eq. (40)}$$

Where, wt_k is a weight for these number of band regions. Based on dividing the atmosphere into multiple layers (shown earlier), the fluxes as columns of homogeneous layers are determined by the following equations.

$$U_{i-1} = T_i U_i + R_i V_{i-1} + S_i^+ \quad \text{Eq. (41)}$$

$$V_i = T_i V_{i-1} + R_i U_i + S_i^- \quad \text{Eq. (42)}$$

$$Z_i = T_{0i} Z_{i-1} \quad \text{Eq. (43)}$$

Where U is upward flux and V is the total downward (diffuse plus direct) flux. T and R are the diffuse transmission and reflection coefficients and T_0 is the direct transmission coefficient. Z is direct solar flux and S is source term. The subscript (i) on U, V and Z fluxes refers to levels, while T, R, T_0 and S indicate values for the atmospheric layer. For monochromatic calculated fluxes, U, V and Z are the main fluxes used for solar, while upward and downward differential fluxes are used for infrared. The full information of the ES code can be found in Manners et al. (2015). From the ES model results, the heating rates are determined as well as the net fluxes (NF) which are the net upward flux minus downward fluxes at each layer and band. In terms of results, ES provides vertical heating rates and net fluxes for SW, LW and total radiation including the effects of dust, water vapour, and other gases.

2.2.1.10 Dust optical properties

Obtaining dust heating rates from the ES model relies on providing dust optical properties as outlined in the previous section. Dust optical properties and their sensitivity to RI affects the heating rates in two ways. The first is using dust optical properties (with a RI used to calculated these values) in the ES model to characterise the optical properties of the dust and the second is

to use dust RI and optical calculations to obtain the size distributions of the dust from the measurement instruments. Both the dust optics and the amounts of dust that were derived from dust optics will influence the heating rates determined from the ES radiation model. In this work, I use the optical properties of dust in the ES model over the ocean from Ryder et al. (2013a). based on Ryder's explanation for dust optical properties, dust optical properties can change between aged dust and SAL cause a reduction in instantaneous SW heating rates by about 17%. However, this percentage is lower than that between fresh and aged dust, which changes about 26%. It will be inaccurate to use optical properties for fresh or aged dust since I want to investigate the radiative effects of dust over the Canary Islands, which is located in the characteristic region of SAL. On the other hand, current study is not to study specific flight cases, but rather I take dust profiles from flight observations and look at the potential effect on the structure of air over the Atlantic. So, based on relative decreasing in the SW heating for SAL compared to over African land, I will consider these optical properties of SAL in the current research. In terms of obtaining the profiles of dust, these are calculated based on the recalibration method described in an earlier chapter (i.e. using the optics based method of Rosenberg et al., 2012) for both PCASP and CDP instrument data from flight observations, and so the heating rates are related to the observed dust profiles that were generated. The optical properties over the ocean are somewhat like over land if you take account of changes to the size distribution. With larger particles falling out during transport, the extinction per unit mass will increase because the larger particles have fallen out and the smaller particles that are more effective scattering particles are still present. With the loss of the larger particles, the absorption will decrease but the remaining particles are very effective at scattering per unit mass. Therefore, the single scattering albedo will increase (due to less absorption) and the asymmetry will also decrease (less forward scattering of the larger due to loss of large particles through sedimentation) for the ocean compared to the land. There is a range of values as seen in the figure (2.8) and reported in the literature. For example, Jabonero et al. (2016) used dust mass extinction of 0.32 m^2/g over Tenerife (Canary Islands), while Maring et al. (2000) used a value of 0.5 m^2/g at the same location. Figure (2.8) shows the optical properties from the calculations of Ryder et al. (2013a). The profiles of optical properties include dust mass extinction coefficient (K_{ext}), asymmetry parameter (g), and single scattering albedo (SSA). These optical properties were used in the radiation code with DMMR calculated from the FENNEC observations. All these optical properties are calculated in three different categories, which are: over Sahara for fresh (red lines) and aged (green lines) mode, and over the Atlantic for the SAL (blue lines). Dashed lines and shaded areas represent the 10th and 90th percentiles, while solid lines indicate means. In the current thesis, only optical properties over the Atlantic were used and are indicated by blue lines in figure (2.8).

To generate dust heating rates associated with dust optical properties, it is required to prepare spectral profiles for the radiation code. In this work, dust optical properties were provided from

Ryder et al. (2013a) for SAL. The reliability of different refractive indexes is uncertain and in Chapter 5 I investigate the sensitivity of the size distributions to the RI (since the observations are based on scattering). The sensitivity of optical properties derived from Mie scattering to RI for the dust is beyond the scope of the current work, but I do use the standard for this region and FENNEC observations (Ryder et al., 2013a). Spectral files for these atmospheric constituents are provided for the 6 wavelength bands for SW and 9 bands for LW radiation. The spectral files of dust optical properties used in ES are shown in tables (2-3) and (2-4) for the SW and LW radiation, respectively. As it is known that dust scatters and absorbs in the SW and absorbs and emits at LW wavelengths. The RI is defined as a dimensionless factor that describes the reduction in light speed and wavelength of radiation as it passes through a medium. RI is usually expressed as a complex refractive index (m), where m=a+ik consists of a real part (i.e. phase velocity), indicated by the letter a, and an imaginary part, indicated by the letter k, which relates to the absorption characteristics of the particle. The amounts of radiation propagating within the atmosphere and upwelling beyond the top of the model atmosphere are controlled mainly by the following parameters:

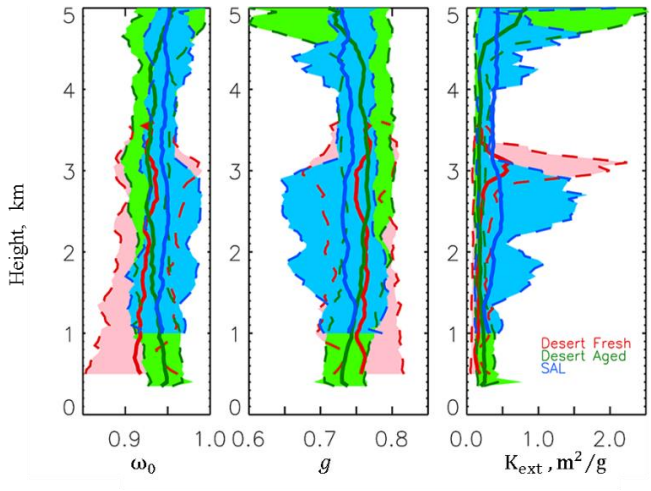

Figure 2. 8. Optical properties of SAL provided from Ryder et al. (2013a). (Left plot) single scattering albedo (ω_0, unitless), (middle plot) asymmetry parameter (g, unitless), and (right plot) mass extinction coefficient (K_{ext}, in units of m^2/g). The profiles of dust layer over the Atlantic were indicated by blue lines, while red and green lines show fresh and aged dust over the Sahara.

1. The magnitude of k (imaginary part of RI). For k > 0 there will be loss of energy due to light absorbed by the dust particles resulting in warming of the atmosphere. For k=0, the incident light on dust particle will not absorb, while using a value of k < 0, the light will be amplified which is not relevant for this work. In the current work, a value of k of 0.001 is used, which is the same value used by Ryder et al. (2013a). However, since there is uncertainty in the value, a range of k values were used including 0.0001, 0.001, 0.003 and 0.005. For the real part of the index of

refraction, a couple of values were used including 1.43 and 1.53 but there is little dependence on the real part for these applications.

2. The asymmetry parameter (g) for scattered radiation. This parameter characterises the difference in the scattered light between the forward and backward directions. The asymmetry is obtained by calculating the phase function weighted by the cosine of the scattered angle ($\emptyset$), where the magnitude of g ranges between -1 (all radiation scattered in the backward direction) and 1 (all radiation will be scattered toward the forward direction), and $g = 0$ represents isotropic scattering (i.e. the scattering is symmetric with respect to $\emptyset = 90°$). Since dust can scatter light in all directions, especially when dust particle size is much smaller than wavelength of radiation (i.e. Rayleigh scattering), specifying how much energy scattered by a particle of a given size is important for the radiative calculations.

3. The single scattering albedo (SSA) for measuring the attenuation of radiation, ranges between 1 for pure scattering of all radiation interacting with the particle to 0 which indicates all radiation interacting with the particle results in absorption.

I received spectral files for dust aerosols from Ryder, based on work published in Ryder et al. (2013a). These optical properties were derived assuming spherical shape so based on Mie scattering calculations. The optical properties include scattering and absorption of dust and gases (Rayleigh scattering for gases) and have all been weighted by the solar spectrum in each band for the radiative transfer calculations. In general, the ES model will linearly interpolate RI for wavelengths that are not covered but in this work the dust has a constant RI for all wavelengths. In the results of this thesis, although ranges of RI were tested, as explained in section (2.2.1.5), the most appropriate value of RI was taken to be that recommended by Ryder et al., (2013a) which is 1.52+0.001i which was over land. Since the typical dust events such as flight FB604 and FB605 show similarity in dust profiles between land and Canary Islands, I will take this RI value to be the most appropriate for the current study. Methods to calculate the optical properties for non-spherical dust particles would be beyond the scope of this work and would require detailed shape inputs as well.

Table 2- 3. Optical properties of dust for SW radiation for 6 spectral bands taken from Ryder et al. (2013a).

Band	Absorption (m^2/kg)	Scattering (m^2/kg)	Asymmetry Parameter	Wavelength (m) Lower limit	Upper limit	SSA	K_{ext} (m^2/g)
1.	6.242E+01	1.255E+02	8.419E-01	2.000E-07	3.200E-07	0.667	0.18815
2.	3.109E+01	1.556E+02	7.795E-01	3.200E-07	6.900E-07	0.833	0.18679
3.	3.109E+01	1.556E+02	7.795E-01	3.200E-07	6.900E-07	0.833	0.18679
4.	1.100E+01	1.750E+02	7.434E-01	6.900E-07	1.190E-06	0.940	0.18617
5.	8.033E+00	1.671E+02	7.806E-01	1.190E-06	2.380E-06	0.954	0.17515
6.	2.741E+01	1.102E+02	8.890E-01	2.380E-06	1.000E-05	0.800	0.13775

Table 2- 4. Optical properties of dust for LW radiation with 9 spectral bands. taken from Ryder et al. (2013a).

Band	Absorption (m^2/kg)	Scattering (m^2/kg)	Asymmetry parameter	Wavelength (m) Lower limit	Upper limit	SSA	K_{ext} (m^2/g)
1	1.081E+02	5.748E+01	4.241E-01	2.500E-05	1.000E-02	0.347	0.16564
2	1.071E+02	1.102E+02	5.850E-01	1.818E-05	2.500E-05	0.507	0.21735
3	8.211E+01	1.405E+02	6.700E-01	1.250E-05	1.818E-05	0.631	0.22266
4	8.129E+01	1.419E+02	6.690E-01	1.333E-05	1.694E-05	0.635	0.22346
5	1.240E+02	1.906E+02	6.892E-01	8.333E-06	1.250E-05	0.605	0.31504
6	1.555E+02	2.170E+02	6.726E-01	8.928E-06	1.010E-05	0.582	0.37285
7	7.573E+01	1.224E+02	8.150E-01	7.518E-06	8.333E-06	0.617	0.19837
8	7.573E+01	1.224E+02	8.150E-01	6.666E-06	7.518E-06	0.617	0.19837
9	5.814E+01	1.426E+02	8.755E-01	3.338E-06	6.667E-06	0.710	0.20084

2.2.1.11 Derived-dust heating rates from FENNEC observations.

Vertical profiles of dust in the dusty marine environment were derived from the FENNEC observations, so it was feasible to derive dust heating rates directly from these observations. Heating rate profiles for SW and LW in the radiation model were determined based on the vertical change in the flux for each band (Liou, 1992). The dust profiles from the FENNEC observations were measured by PCASP, CDP and CIP instruments mounted in place underneath the wings of the research aircraft. The dust size diameter ranges of these instruments have been reported by many studies such as Ryder et al. (2013) and Rosenberg et al. (2012), etc. The PCASP-100X covers the size range from 0.1 to 3.0 μm (using 30 size bins), which broadly represents the accumulation mode of dust particles, the CDP which measures from 2 to 50 μm and represents a portion of the coarse mode particles (using 30 size bins), and, lastly, the CIP instrument which measures the giant dust particles greater than 15 and up to about 300 μm by imaging the particle's shadow directly, recording data as two dimension images with 64 size bins. The PCASP data from the flight observations was calibrated based on the procedure of Rosenberg et al. (2012), while calibration method was also applied for the CDP data that was provided from Rosenberg et al. (2011). The total diameter covered by these three instruments is from 0.1 to 300 μm.

Dust heating rate profiles were generated from the CDP and PCASP data using the dust optics as a function of size as outlined in the previous section. So, to generate heating rate profiles from the radiation code, it was necessary to prepare files for the radiation code, as shown in previous section 2.2.1.9. As mentioned, these are profiles of dust mass mixing ratios, water vapour, ozone, pressure and temperature from FENNEC flights and Standard Atmosphere mixing ratios for gases (aside from water vapour and ozone). The spectral files contain the corresponding optical properties for the 6 bands for SW and 9 bands for LW in this case.

As mentioned previously in LEM simulation methods, dust heating rates in the current thesis were derived with using initially different solar values in each flight case and with using time-varied of SZA from early morning and afternoon times, where the initial solar elevation used in ES is the same for all flight cases. The procedure of deriving heating rates based on time-varied during day will explain in subsection 2.2.1.12. Clouds were turned off for the radiation calculations. The radiation code required mass mixing ratio of gases; therefore, water vapour and ozone profiles were taken from FENNEC observations, while other gases were taken from the literature and are presented in table (2-5). As current thesis involved in deriving heating and cooling rates with the absence of cloud formation, any input data that is related to cloud and water particle sizes was not used (set to zero) in the ES radiation code.

Table 2- 5. Mass mixing ratios of other gases over the Atlantic taken from literature.

Gas	Values	Reference
CH_4 (Methane, kg/kg)	**9.83e-07**	Corbett et al. (2017)
CO_2 (Carbon Dioxide, kg/kg)	**5.78e-04**	Machida et al. (2002)
N_2O (Nitrous Oxide, kg/kg)	**7.7e-06**	Imke Grefe, (2013)
O_2 (oxygyn, kg/kg)	**0.231**	Lenton and Watson, (2000)

2.2.1.12 Dust simulations and large-scale forcing

Dust can significantly influence the vertically heating rates of the dusty marine structure during the daytime. In the LEM, the large scale-forcing term is represented as a prescribed forcing acting on the temperature profile in the model for a prescribed 8 hours of time period. Use of prescribed large-scale forcing in the LEM can be performed by supplying an external data file, force.dat, which can be a time-varying data file and contain dust heating rates from ES output as input in LEM simulations. LEM Simulations were implemented over 8 hours in time for both SW, LW and total radiation with taking account of the variation in solar declination (change in SZA) initializing from morning until afternoon every 10 degrees. Table (2-6) shows the values of cosine of the sun angle to the zenith (SZA) and how it varies associated with the time evolution. Radiation runs were performed with dust, water vapour and other gases to understand the relative importance for each on SW, LW and Total heating rates.

Table 2- 6. Variation of SZA used in ES associated with time development.

SZA, degrees	**75**	**65**	**55**	**45**	**35**	**25**	**15**	**5**
Cos(SZA)	**0.25**	**0.42**	**0.57**	**0.70**	**0.81**	**0.90**	**0.96**	**0.99**
Time (local 24 hours)	**8.15**	**9.04**	**9.50**	**10.37**	**11.22**	**12.9**	**12.54**	**13.53**

2.2.2 Tools and background for assessing dust and other influences on atmospheric stability

Because dust absorbs radiation, it can alter the vertical atmospheric structure of temperature. This has the effect of potentially significantly altering the stability of the atmosphere. This study will investigate this in some detail in a later chapter. Another factor that would potentially compete with the heating rates to affect atmospheric stability in the free atmosphere would be shear induced instability. This will also be investigated in a later chapter and so I will outline the background material now for the later analysis.

2.2.2.1 Wind shear impact on atmospheric stability

As mentioned before, dust can be transported long distances by winds, even globally. The winds can vary significantly in the vertical and this variation with height is called wind shear. If wind shear is strong enough, it can cause overturning and mixing of air parcels, but it also depends on how stable the atmosphere is. Wind shear (WS) can be defined as a turning force which is created because a variation in wind speed/wind direction. Wind shear is described by either horizontal or vertical wind shear, which can be calculated by using the following equation (Tao and Zhang, 2015) for vertical wind shear:

$$\mathrm{WS} = \sqrt{\left(\frac{\partial \mathrm{u}}{\partial \mathrm{z}}\right)^2 + \left(\frac{\partial \mathrm{v}}{\partial \mathrm{z}}\right)^2} \qquad \text{Eq. (44)}$$

Where, u and v are zonal and meridional wind components, respectively. Z is atmospheric height. Figure (2.9) shows the magnitude of shear tendency in unit of KTS, while winds (wind speed and direction) at low level and mid and upper levels are shown in figure (2.10) and figure (2.11), respectively. These figures are derived from METEOSAT satellite images in the troposphere over the east Atlantic and African continent. Where METEOSAT provides large-scale meteorological observations such as wind shear and wind variations with altitudes (lower and upper troposphere) every 3 hours. The daytime wind and shear from the satellite images are consistent with FENNEC flight observations except for the following flight numbers: FB600, FB601, FB603 and FB702. Figures (2.9), (2.10) and (2.11) are for flight FB600. By looking at all these figures, the variation of wind shear tendency is related to vertical changes in wind speed, where at lower altitude (about between 800 hPa and 950 hPa) wind speed in troposphere is generally lower than at higher heights. Wind shear tendency can be seen to be concentrated between 10 and 60 latitude degrees with shear tendency relatively weak at roughly 40 latitude degree.

The variation of wind shear with altitude in the tropical Atlantic has a different dependency to other environments such as subtropical regions. For instance, at lower levels, vertical wind shear is up to 600 m above ocean surface depending on the wind profiles accounting for the oceanographic and meteorological conditions (Jones, 1953). In contrast, within the SAL the

variation of wind shear with height can be determined by the modification of easterly winds corresponding to dust effects (Chen et al., 2010). As a result, the significant factors influencing variability of wind shear can be summarised by the following points:

1. Vertical wind shear within the SAL is dependent significantly on the intensification of easterly winds due to dust effects on dusty outbreak days. This result is presented by Chen et al. (2010), who pointed out that the easterly winds are increased between pressure of 650 hPa and 500 hPa and decreased between the lower troposphere and 650 hPa. Their results show that vertical shear is increased between about 750 and 550 hPa from 1 to 2.5 m/s.km. However, they used intensive dust outbreak events over the Atlantic and did not focus on the variation of dust during transport over the Atlantic. Therefore, in the current work relative importance of shear compared to dust radiative heating rate influences on the structure of the dusty marine environment is important to assess.
2. The variation of wind shear with height at lower levels is directly dependent on meteorological factors such wind profiles rather than other factors such as dust.
3. The intensification of hurricanes in the tropical Atlantic may increase the shear. For instance, a decrease in the hurricanes over the Atlantic Ocean causes an increase in the vertical shear (Bogner et al., 2000).

AEWs are derived from the combination of tropical latitude (barotropic) and mid-latitude (baroclinic) instability of African Easterly Jet (AEJ) and propagate in the westward direction across the tropical and subtropical Atlantic. Therefore, AEWs may have impact on the variation of wind shear, as shown by Burpee (1974) who shows that the AEWs at upper air levels can vary when the meridional winds move in the opposite direction to the mean zonal shear. Further work presented by Jochum et al. (2004) evidenced that wave properties such as African Tropical Waves (ATWs) are not determined by meteorological forcings, but they are generated by an unstable flow field.

To investigate shear effects, several runs were done in the LEM with observed profiles of the atmosphere containing shear cases as well as idealised no-shear cases to compare with for all possible cases studied in June 2011 and 2012. The aim of running the LEM with constant and observed wind profiles is to test the highest shear to no shear to see if the atmospheric structure is significantly affected. LEM runs were not done for all cases since there was missing data from the FENNEC observations during ascending and descending flights over the Atlantic Ocean, due to calibration errors in the measurement of the flight instruments. In the present thesis, I considered flight cases during 2011 including FB600, FB601, FB604, FB605, FB609, FB611, FB612, FB613, FB699 and FB700.

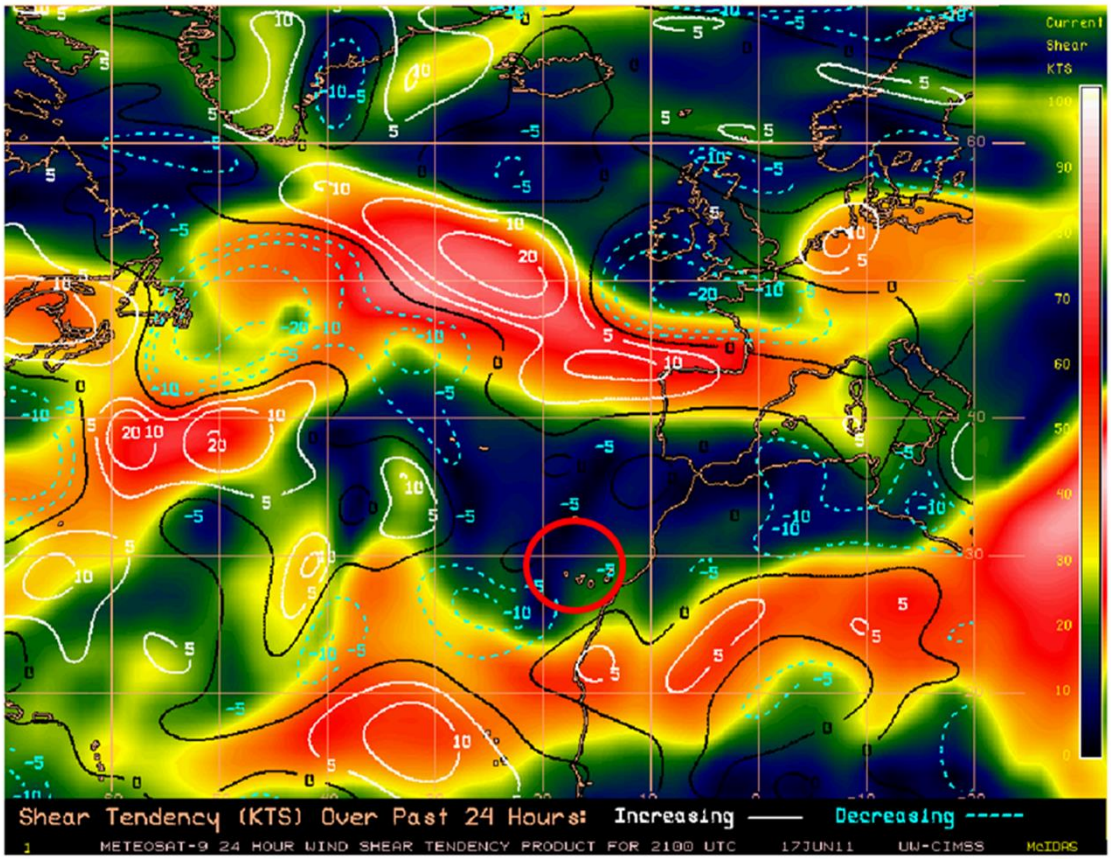

Figure 2. 9. Wind shear tendency in units of knots from the Cooperative Institute of Meteorological Satellite Studies (CIMSS) over the Eastern part of Atlantic and over Africa are presented. Shear tendency represents variation of shear during June 17, 2011 (flight FB600) at time 2100 UTC for a 24 hour period. The solid line on the map shows the increased wind shear tendency while decreased shear is indicated by dashed line. The red circle on this map shows the location of the Canary Island, west off the north African coast. This figure is taken from the University of Wisconsin-Madison (see link: http://tropic.ssec.wisc.edu/real-time/europe/winds/wm7shr.GIF), where it provides large-scale data for meteorological parameters such as winds of 3 hour time steps over land and ocean.

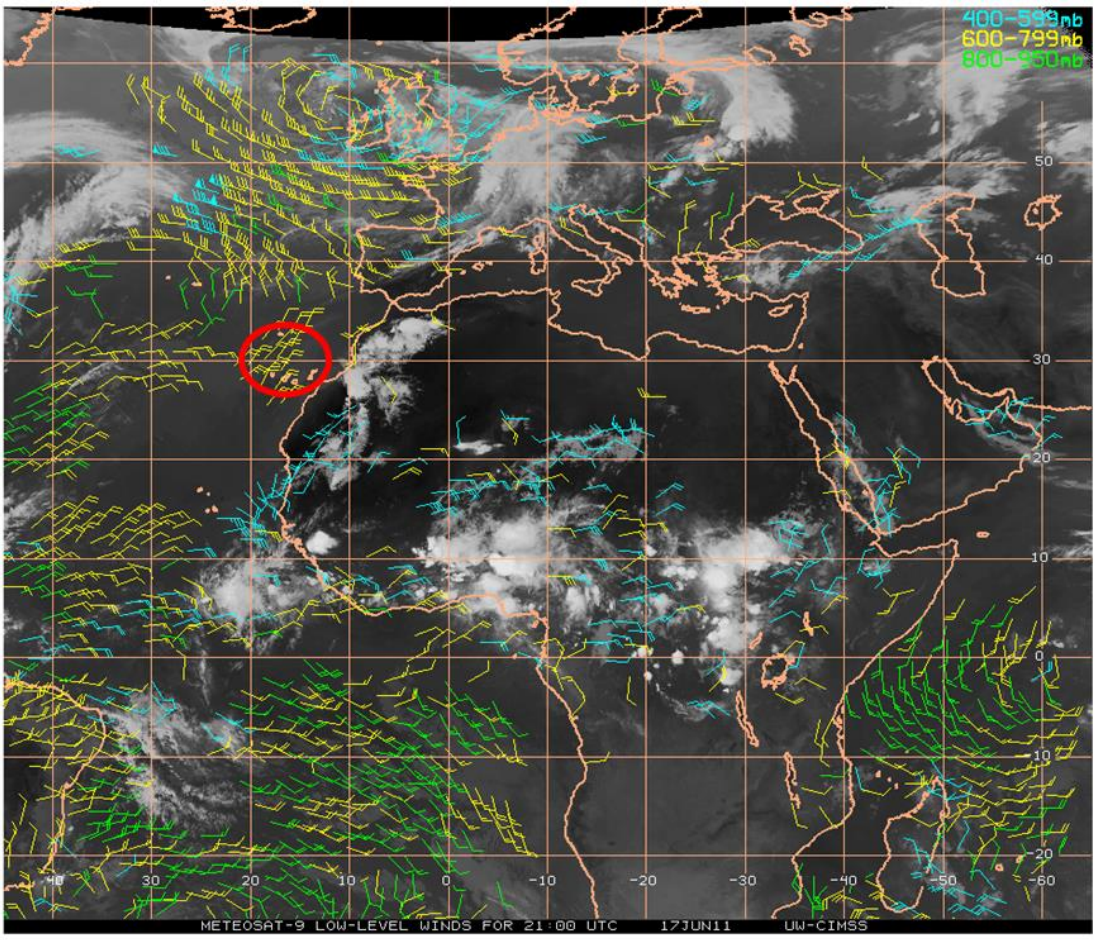

Figure 2. 10. Variation of winds which is represented from 950 hPa to 400 hPa (mid to low level winds). This data is taken from the same reference in figure (2.9). The red circle on this map shows the location of Canary Islands, west off the coast of north Africa.

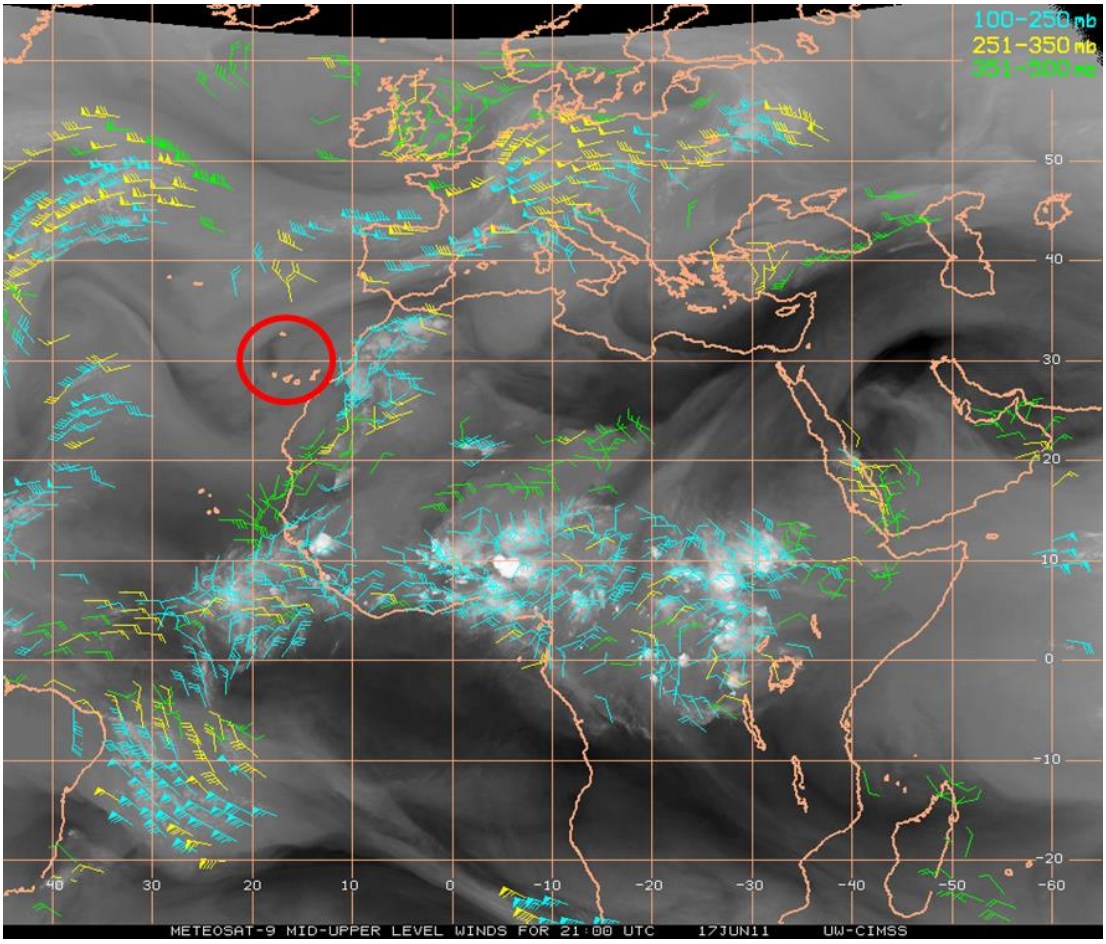

Figure 2. 11. Variation of winds for pressure heights 500 hPa to 100 hPa (mid and upper wind levels).

2.2.2.2 Assessing atmospheric buoyancy using CAPE & CIN

As dust can affect the temperature of the atmosphere by heating or cooling the air, this can affect the buoyancy. An estimation of how much potential energy can be converted into buoyancy for an air parcel rising through a layer is given by the convective available potential energy (CAPE). Similarly, negative buoyancy effects, or convective inhibition (CIN), can be calculated if a parcel loses energy as it rises through a layer. Since the dust is warming and cooling the marine atmospheric layers it can affect both the CAPE and CIN. The formulas to calculate CAPE and CIN are shown below (Monkam, 2002 and Blanchard, 1998):

$$\text{CAPE} = g \int_{ZLFC}^{ZLNB} \left(\frac{TV_p - TV_e}{TV_e}\right) dz \qquad \text{Eq. (45)}$$

$$\text{CIN} = -g \int_{ZSFC}^{ZLFC} \left(\frac{TV_p - TV_e}{TV_e}\right) dz \qquad \text{Eq. (46)}$$

Where, TV_p and TV_e are the virtual temperatures of the parcel and environment, g is the acceleration due to gravity, ZLFC is the level of free convection and ZLNB designates the level of neutral buoyancy. The unit of CAPE/CIN measured in J/kg due to the integral formula of

CAPE/CIN, it is represented as the work done by the buoyancy force minus the work done against gravity, and thus it is represented as an energy unit per unit of mass of air. Table (2-7) shows the typical magnitudes of CAPE for different atmospheric conditions. The CAPE and CIN are used in later chapters to assess the impact of dust radiative heating on the stability of the dusty marine environment.

CAPE and CIN were calculated numerically using a FORTRAN computer program developed to determine the contributions for the FENNEC observed and numerically simulated profiles. To confirm the accuracy of the results of these calculations, a thermodynamic based Stuve diagram was used to determine the areas of CAPE, CIN, lifted condensation level (ZLCL), level of free convection (ZLFC), and equilibrium level (EL). Furthermore, calculating CAPE and CIN parameters were evaluated in the presence and absence of water vapour in model simulations in order to investigate the impact of water vapour on the stability of the dusty marine structure. To do that, CAPE and CIN factors were computed based on temperature, virtual temperature and water vapour profiles from the LEM simulation results. This simulation will be shown later, in Chapter 4.

Table 2- 7. The strength of CAPE values for the convective potential energy of the atmosphere.

CAPE value (J/kg)	Convective potential
0	Stable
0−1000	Slightly unstable
1000−2500	Moderately unstable
2500−3500	Very unstable
>3500	Extremely unstable

2.2.3 HYSPLIT trajectory model

The HYSPLIT model is a computational model used widely to calculate air sample trajectories, dispersion, pollutant deposition, atmospheric transport and chemical transformation (Stein et al., 2015). HYSPLIT is a Lagrangian transport model that considers tracer transport by advection based on meteorological data (which are typically on a 3-D Eulerian grid). The approach of the HYSPLIT model is a hybrid between two scientific approaches, 1) a Lagrangian approach that uses a moving frame of reference for the advection and diffusion calculations as air parcels move from their initial location, and 2) The Eulerian methodology with a fixed 3-D grid as a frame of reference to compute pollutant air concentrations. Specifically, the Lagrangian model solves the total derivative trajectories for single point sources while the Eulerian is ideal for multiple sources

and solving local derivative air parcels. Schematic figure (2.12) shows the difference between Lagrangian and Eulerian methods for trajectory calculations.

In the current study, the HYSPLIT model is used from the online website version to compute trajectories. The model runs are initialised and run based on archived data from the global 3-D Gridded Meteorological Data (GDAS0p5) including pressure, temperature, relative humidity (RH), u, v and w components (Stein et al., 2015). In specifying the trajectories, I used an ensemble of trajectories and the HYPSPLIT model interpolates the data from the global meteorological model to the location of the starting trajectories. The ensembles trajectories are implemented with horizontal resolution of a 0.5 degree latitude-longitude datasets. The integration model timestep can vary during the simulation but it can be computed by requiring that the 3-D particle displacement should be less than 0.75 of the data grid spacing. Totally 27 ensemble trajectories were used in each 120 m with vertical height resolution for 67 layers. The interval time of HYSPLIT trajectory outputs is every 6 hours. Trajectories are stepped forward in time using the global model to determine the evolution.

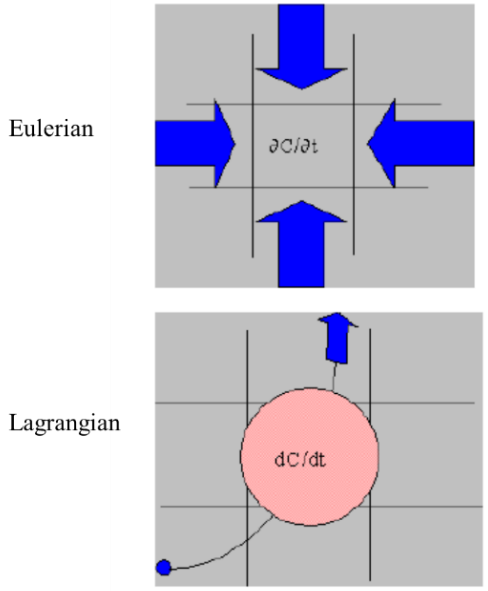

Figure 2. 12. Schematic figure shows integral Eulerian (top plot) and Lagrangian (bottom plot) methods of HYSPLIT model computations. The initial advected air parcels for single point sources are addressed by calculating the total derivative formula of Lagrangian method, which is solved along the trajectories with time evolving. The Eulerian approach is represented as an entire domain with multiple point sources for locally-solved derivatives. The derivative formula $\partial C/\partial t$ shows concentration changes of multiple source of trajectories at any location and time within the whole domain.

The computational basis of the HYPSPLIT model is shown by Stein et al. (2015). Assuming P_{mean} is a position vector of air parcels moving with the time t and V is the average of a 3-D

velocity vector started at its initialized position, the change in the location of an air parcel obtained by:

$$P_{mean}\,(t+dt) = P_{mean}\,(t) + 0.5\left[V\left(P_{mean}\,(t)\right) + V(P'_{mean}\,(t+dt))\right]dt \qquad \text{Eq. (47)}$$

$$P'_{mean}\,(t+dt) = P_{mean}(t) + V\left(P_{mean}(t)\right)dt \qquad \text{Eq. (48)}$$

The output of the HYSPLIT model provides single or multiple trajectories at each chosen location, which have been chosen to correspond to the location of the flight observations. Model runs were performed for both backward and forward trajectories from various locations including north African land, Canary Islands and the Caribbean. The complete method of trajectories for these locations will explain in Chapter 5 for the dust transport model BRSedT.

3 Chapter 3: FENNEC Study Area and Dust

This chapter focuses on characterising the site and observations used for the dust study and describes the recalibration of some of the dust observations from the FENNEC observations. The FENNEC observations are used to provide the observations basis of the modelling work. They form a reliable set of observations with profiles of dust measurements and thermodynamic profiles necessary for the modelling work in this thesis (Chapters 4 and 5). In this chapter, the observations are presented to characterise the non-dusty and dusty days including profiles of potential temperature, humidity, winds, etc. as well as identification of the condensation level, level of free convection, etc. Categorising of the dust days is performed using the profile of observations from the flights as well as information about the air masses from the previous days from HYSPLIT trajectories. To understand the potential effects of dust on convection within the marine atmospheric layers, the convective available potential energy (CAPE) and convective inhibition (CIN) are also evaluated.

3.1 The study region

As discussed in the previous chapter, the study focuses on dust transport in two main directions. The two directions were chosen based on evaluating the dust values primarily from the MODIS observations but also complemented from the FENNEC observations. The two directions are to the north-west off the coast of Africa and to the general westward direction across the Atlantic towards the Caribbean. The Canary Islands are in the area of latitude 28°20'N and longitude 14°1'W off the west coast of Africa and they are in the path of the north-west direction whereas the Caribbean is in the direction of the west. To begin with, the FENNEC observations at the Canary Islands are presented.

3.2 FENNEC observations at the Canary Islands

3.2.1 Dust size distributions from FENNEC flights

3.2.1.1 Recalibration of dust measuring instruments

As mentioned in Chapter 2, dust size distributions are calculated based on the measured scattering cross sections of dust aerosol particles from the PCASP and CDP instruments (except CIP which images shadows) by applying an improvement to the determination of the sizes derived from the instrument observations. This method is outlined in the calibration approach of Rosenberg et al. (2012) and Ryder et al. (2013b) for PCASP and CDP data, while CIP does not need to be calibrated in this way as this instrument is not dependent on scattering properties. The reason for using this method (I used discrete method in calibration) is that scattering cross sections of measured dust particles are not the same with those calibrated particles due to variations in the

refractive index and shape of particles. So new cross section bin boundaries needed to be determined to improve the conversion of diameter to size so that more accurate size distributions could be obtained. Converting scattering cross section to diameter is complicated because it depends on variable scattering cross sections and the relationship between them is non-linear and non-monotonic function. To address this, and as I indicated previously (Chapter 2), scattering cross section needed to be created with using an appropriate RI used in the MieConScatter code. The code generated the scattering cross sections accounting for the non-linearity and non-monotonic relationship with particle size. Therefore, to treat this a probability density functions can be used by using CStoDConverter Microsoft code which will let a particle with a particular diameter fall into a particular bin size (PCASP places each particle in one of 30 bins depending on the light scattered), and thus bin boundaries and size will be generated. Also calibration files for PCASP and CDP instruments were provided from Rosenberg et al. (2012) to be ready to use in the CStoDConverter tool. In this thesis, I used a calibration file developed for flights during 2011. In personal communication, Phil Rosenberg said it would be appropriate to use the 2011 calibration also for the 2012 based on his experience with the instruments. So, I considered the calibration file for flight 2011 to derive particle sizes and bin boundaries. A range of refractive indexes were used including the refractive indices from Ryder et al. (2018), Ryder et al. (2013), Ryder et al. (2013b) and Rosenberg et al. (2012). Although the method of calibration PCASP and CDP instrument is similar to that worked by Ryder et al. (2013a) and Rosenberg et al. (2012), however, few scenarios come from using this approach in the current thesis. Firstly, calibration method does not apply only for flight cases 2011 but also during flights 2012 which can provide a suitable comparison in the results of size distribution. Secondly, in this thesis, I used the same calibration file for flight cases 2011 to derive diameter and channel width and centre as for flights in 2012 (Personal Communication, Phil Rosenberg). Finally, the appropriate refractive index used in calculating the dust profiles was identified for the FENNEC period for the ocean environment to be that used by Ryder et al. (2013b) rather than using other different refractive indices. This was determined by obtaining good agreement in the curves of dust size distributions between CDP and CIP instruments, while these curves do not match well when the other refractive indexes were used. To perform these improvements, the updates require using the scattering observations from the instruments along with Mie calculations and appropriate refractive index to obtain the new recalibrated FENNEC flight dust observations.

3.2.1.2 Profiles of dust size distributions

In this research, dust profiles of size distributions were calculated based on FENNEC observations over the Canary Islands. The instruments used were the PCASP, CDP and CIP. In this section, I will show the size distribution of dust in all flight cases used in this project then I will present typically non dust (FB700 and FB708) and dusty (FB604 and FB605) day events in the section of dust profiles (subsection 3.2.1.4) over the Canary Islands. I present the results of observations from these three instruments (including PASP, CDP and CIP) showing dust number concentrations with diameter separated into categories of MBL, SAL and total number concentrations. Number concentration for dust within the MBL is represented as a mean size distribution of dN/dD with height between the near-surface and up to 2 km, while number concentration for the SAL are shown also as an average between the heights of 2 km and 5.5 km, where most intensive dust particles for dusty cases are located and the θ profiles indicate the SAL resides at relatively close distances to the African continent. The total refers to averaged value for the full profiles. The described dust size distribution in all of these panels is derived by generating channel widths, channel centres and sizes based on Mie scattering code and associated with using suitable RIs for each PCASP and CDP data, while CIP was derived by image shadowing process based on flight observations. Showing dust size distributions in these three categories provides a good understanding in each different atmospheric characterisation. Also, it will be good to compare between these specifications. Figure (3.1) shows the changes in the dust number size distributions for non-dust (FB700 and FB708) and low dust outbreaks (FB702 and FB705). Number of dust particles in the first, second and third columns represent the mean distribution in the MBL, SAL and the whole profiles, respectively. Where the size distribution for MBL is the mean between the surface and up to 2 km, the SAL value is the mean from 2 km up to 5.5 km, and the total represents averages throughout profile measured by the aircraft. All dust number distributions were calculated with using two refractive indexes, including 1.53+0.001i and 1.53+0.003i. The red and green symbols indicate PCASP and CDP for RI=1.53+0.001i, respectively; whereas, the black and blue show dust size distributions using RI=1.53+0.003i. All size distributions are shown here with error bars calculated from standard errors of each number concentration and particle size separately. The two RI values are commonly used and the most appropriate for the flights in this work will be determined.

The time of observation varies depending on the time of the FENNEC flights. For example, FB700 observations were taken from 0752 to 0800 UTC within the MBL, 0800 and 0807 UTC within the SAL, and 0752 to 0807 UTC for the total size distributions with altitude. Whereas for flight FB702, the times are 0804 to 0808 UTC for the MBL, 0808 to 0815 UTC for the SAL, and from 0804 to 0815 UTC for the total size distributions. However, the duration taken for observations in the MBL is generally shorter than the period in both the SAL and the total distributions just because the time spent at the lower levels is less.

The size distributions are obtained from the PCASP and CDP instruments by interpreting a scattering signal. The amount scattered in a given channel by the instrument is related to the amount of dust and the size range and also depends on assumption about optical properties. The optical properties in turn depend on refractive index. Results in figures (3.1) – (3.3) show low uncertainty in size distributions associated with diameters in all figures. Size distribution for dust particles shows no significant change for the PCASP data by using the two different RI values. In contrast, there is a significant change in number loading for CDP, where using a large imaginary part (i.e. high levels of extinction) for RI contributes to associated large sizes of dust particles and vice versa.

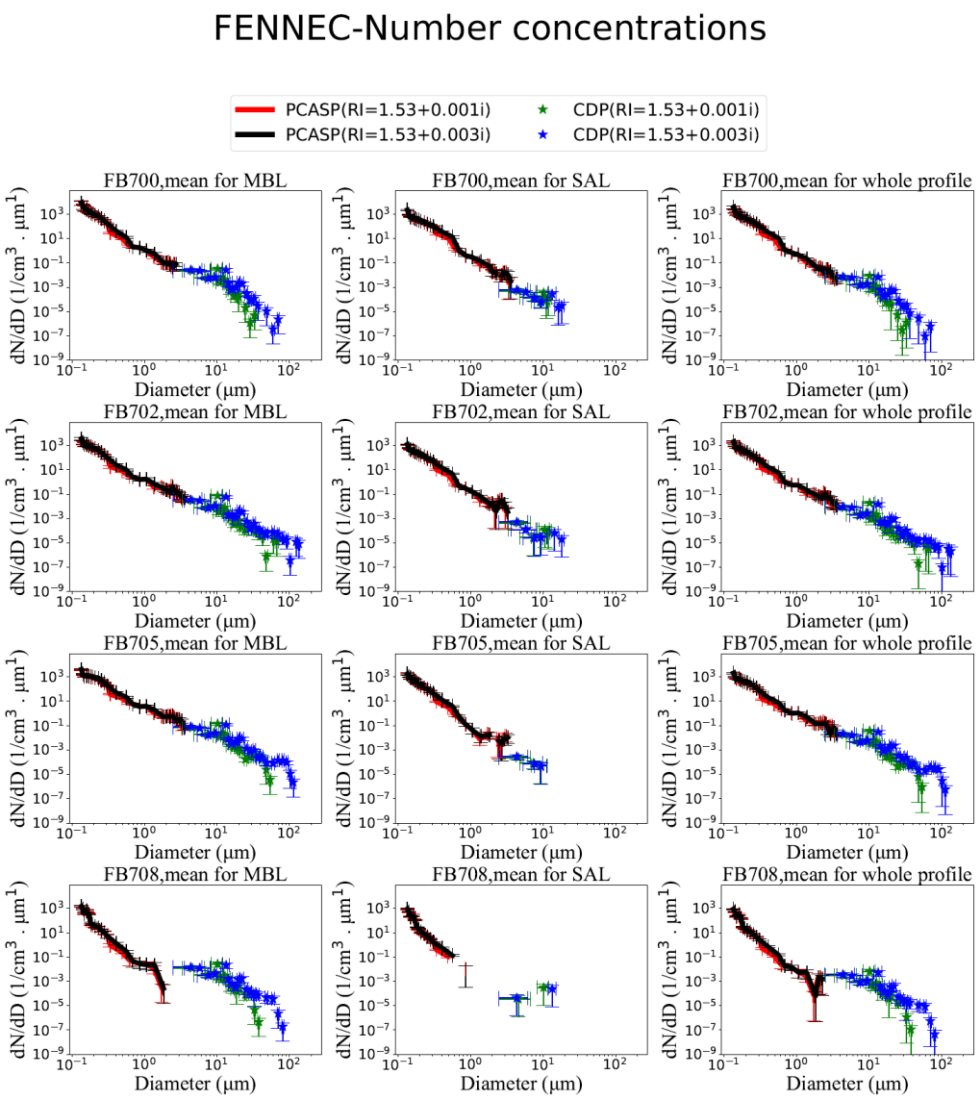

Figure 3. 1. Number size distribution (dN/dD) of FENNEC-dust profiles in units of (1/cm^3 µm) with diameters (µm) in non-dust (FB700 and FB708) and low dust events (FB702 and FB705) for PCASP and CDP instruments. Dust size distributions in all figures were represented as a vertical average profile in each category and bin size. Note for reader that CIP is not shown in these plots due to 2012 flights suffered from electric noise problems in the CIP instrument. Number loadings in first column (indicate mean number loading within the MBL from the surface and up to 2 km), second column (mean within SAL, between 2 km and 5.5 km) and third column (mean for whole profile with altitude up to 8 km) are calculated based on two different refractive indexes including: PCASP shows in red for RI =1.53+0.001i and black for RI =1.53+0.003i lines, and for the CDP green stars for RI=1.53+0.001i and blue stars are for RI=1.53+0.003i. Vertical bars show standard errors, which are calculated based on statistical formula of standard error (SD /$\sqrt{n}$), where n is the total number of data points with altitude and SD is standard deviation for each size. Horizontal bars indicate errors in the sizes, where horizontal error bars are calculated by taking the square root of the summation for both squared lower and upper cross section boundary errors.

For dusty days, such as FB604, FB605 and FB613, giant particle number distributions were measured by the CIP instrument during flights over the Atlantic. Figure (3.2) displays these observed giant particles (giant particles are also shown in figure (3.3) for FB611) number size.

Orange triangles indicate the number loadings of dust for mean MBL (first column), mean SAL (second column) and the total distribution (third column) with large sizes > 15 μm. The overlap region between the PCASP and CDP in all figures, i.e. figures (3.1) – (3.3) is matched for particle sizes. However, for the CIP distribution, in some cases there is large uncertainty in number loading between the last size bin of CDP and the first three bins of CIP data, where the overlap does not match well. This can be caused by, as mentioned in Chapter 2, electric noise in the optics of particle image with CIP measurements between about 15 and 300 μm (Ryder et al., 2015).

Size distributions in figures (3.1) – (3.3) show the re-binned dust size distributions with RI, following Ryder et al. (2013) and Rosenberg et al. (2012) using RI cases of $1.53 + 0.001\mathrm{i}$ and $1.53 + 0.003\mathrm{i}$, respectively. Ryder et al. states that there are uncertainties for using both these indexes in dust measurements. So, generating dust sizes using a range of RI provides reasonable approach to obtaining dust results. The profiles of dust mass loading were calculated including CIP data where data was available. Thus, the computed values of DMMR used in ES and dust mass profiles were presented with CIP data included.

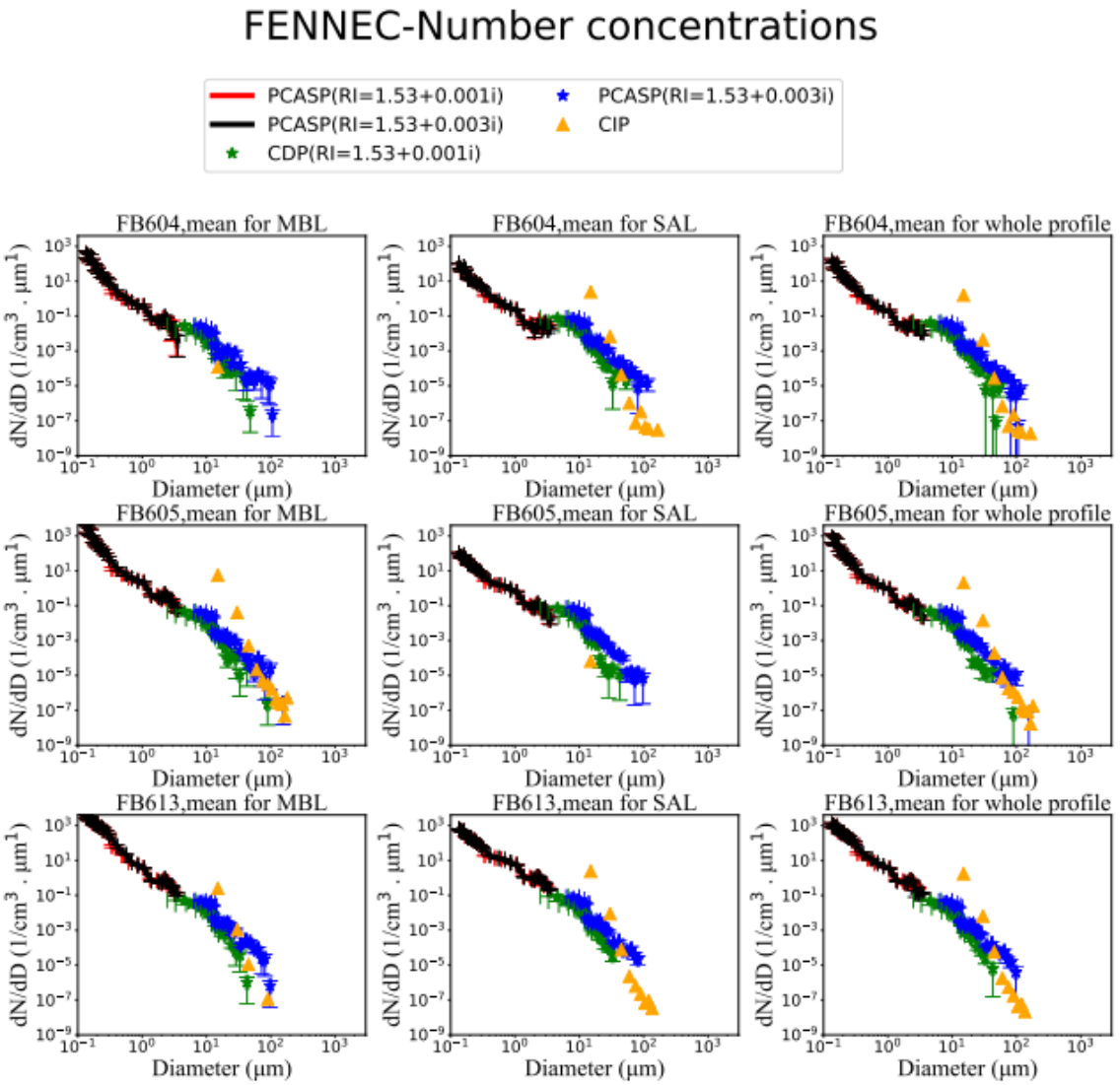

Figure 3. 2. Number size distribution (dN/dD) of FENNEC-dust profiles in units of (1/cm^3 µm) with diameters (µm) in dusty events (FB604, FB605 and FB613) for PCASP, CDP and CIP instruments. Number concentrations in the first column represent the calculated mean number loading within the MBL from the surface up to 2 km, middle column is the mean within the SAL, between 2 km and 5.5 km and third column is the mean for the whole profile with altitude up to 8 km. All of these panels indicate size distributions for PCASP, CDP and CIP within the boundary layer, SAL and between the surface and above the SAL (i.e. whole profile). All results are shown using two refractive indexes including: PCASP shown in red for RI =1.53+0.001i and black for RI =1.53+0.003i, whereas CDP is shown in green for RI=1.53+0.001i and blue for RI=1.53+0.003i. Orange triangles indicate results for CIP. CIP data matches well with CDP based of the value of RI=1.53+0.001i, except for the first three bins. Vertical bars show standard errors, which is calculated based on the formula of standard error (SD /√n), where n is the total number of data points with altitude and SD is the standard deviation for each size. Likewise, figure (3.1) horizontal error bars indicate here.

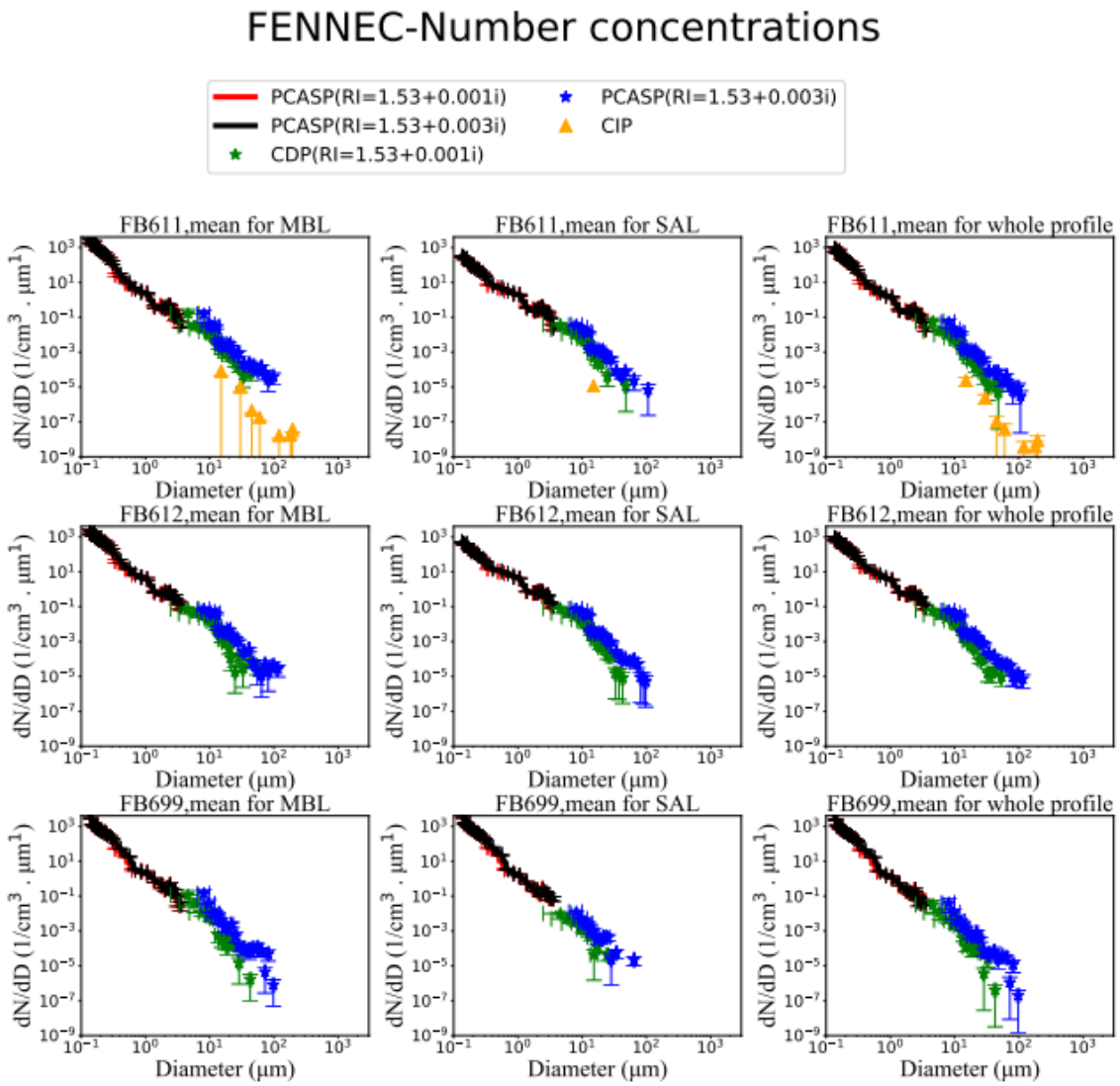

Figure 3. 3. As figure (3.2), but for more dusty events.

Here, I show dust size distributions which were derived from flight observation with a range of RI for sensitivity. Figure (3.4) shows the sensitivity of using different values of RI for the dusty case FB604. This figure shows the PCASP (left panel) and CDP (right panel) size distributions using different values of real and imaginary parts of RI. All figures are presented showing the size distributions with uncertainty in diameter and number concentrations included. The results show that the changes in the real and imaginary parts of RI have a slight impact on the sizes of accumulation mode particles (PCASP). Whereas coloured stars, indicating coarse sizes (CDP), display significant differences between using different values of imaginary part of RI. The differences in the size distribution for different RI used show that there are differences that arise for the complex part of the index of refraction. These show differences that are beyond the errors in the size distributions for sizes roughly larger than 10 µm. This is understandable since the complex part of the refractive index is related to the absorption and the larger particles have more

significant absorption. The differences in the size distributions for variations in the real component of the refractive index are not significant relative to the errors in the distributions.

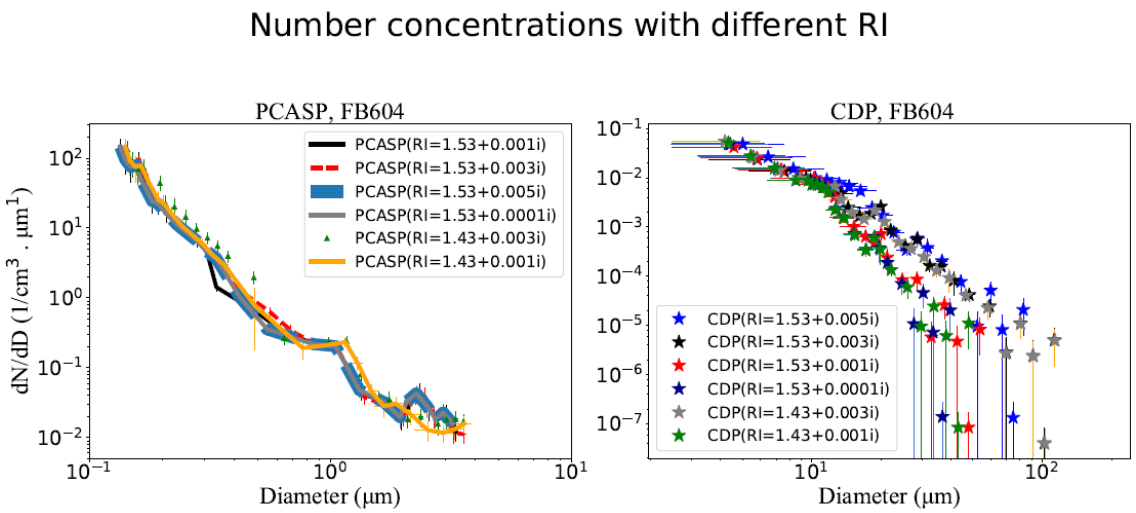

Figure 3. 4. Number loading for PCASP (left panel) and CDP (right panel) with using different refractive indexes (1.53+0.005i, 1.53+0.003i, 1.53+0.001i, 1.53+0.0001i, 1.43+0.001i, and 1.43+0.003i) for whole dust profiles. Different refractive indexes were used for typical dusty event (FB604) of FENNEC observations.

The imaginary value 0.003 is within the commonly used range of values, i.e. 0.001 - 0.006, in previous studies (McConnell et al., 2010), but the value of 0.001 is more appropriate of the dust observed in FENNEC (Ryder et al., 2013). The reasons for using a refractive index of 0.001 are: 1) FENNEC observations used in this thesis were the same time and spatial location as the observations used in Ryder et al (2013), see supporting information of flight tracks and times in this paper. 2) The dust size distributions are similar in profile to that calculated by Ryder et al. (2018), although number loadings for accumulation mode (PCASP) are slightly lower in MA. 3) There is good agreement between results from the CDP and CIP for RI=1.53+0.001i, see figure (3.2).

3.2.1.3 Dust size distributions with selected vertical heights

The RI value based on Ryder et al. (2013) is used to derive dust-size distributions, and thus dust mass loading. I presented in the previous section the size distributions of dust as mean values with altitude for the regions MBL, SAL and total concentrations, but it is also possible to view the size distributions as a function of height, in a similar way with Ryder et al. (2013a). This is shown in figure (3.5) including results from the PCASP and CDP observations. CIP data is not shown in this section as it was shown previously in figures (3.2) and (3.3), and CIP data did not involve in all flight heights. The results are separated into non-dusty and dusty days. The results are shown at selected heights including 500, 1500, 2500, 3500, 4500, 5500, and 6500 m. Since multiple

heights are shown on the same figure, the uncertainty is not shown but for reference it is shown in figures (3.1), (3.2) and (3.3).

Large numbers of dust in the size distributions appear at the smallest particle sizes and it decreases with increasing size. There is a jump increase in the number of dust particles in the MBL (at 500 m) compared to those at levels above it. Although the general trend of dust number decreases slightly with height for smaller diameters (D < 1.0 μm), the number of dust particles in some cases at low altitude (approximately up to 1.5 km) is smaller than dust number at high altitudes, see black symbol for FB600 and FB702 in figure (3.6). Thus, the PCASP results for dusty events show the trend in number loading of size distribution decreasing with height generally but has lower values in the MBL. Also, the number concentration of dust particles measured by the CDP at heights less than 1.5 km is less than at upper heights for particle sizes D > 10 μm. The dust heading over the Atlantic will typically be in a SAL that will ride over the marine boundary layer and particles will over time fall into the boundary layer and mix downward into the MBL and surface but the number will be lower in the MBL than in the SAL.

The figure (3.6) shows some interested points. Firstly, there is a kink in the curve of dust size distribution in moderate and dusty cases of CDP. This kink refers to the significant drop in dust number for the large size (D > 10 μm) of dust particles within the boundary layer. Secondly, in moderate cases there is a big difference in dust numbers from low to high heights in the CDP measurements, while the PCASP has a low difference. Dust particles within the MBL have low numbers and large sizes and the number of dust particles for CDP in moderate cases has a wider range of values than for the PCASP distributions within the vertical profiles of dusty marine environment. Large sizes and low numbers in the MBL are consistent with the large dust particles sedimenting from the SAL into the MBL.

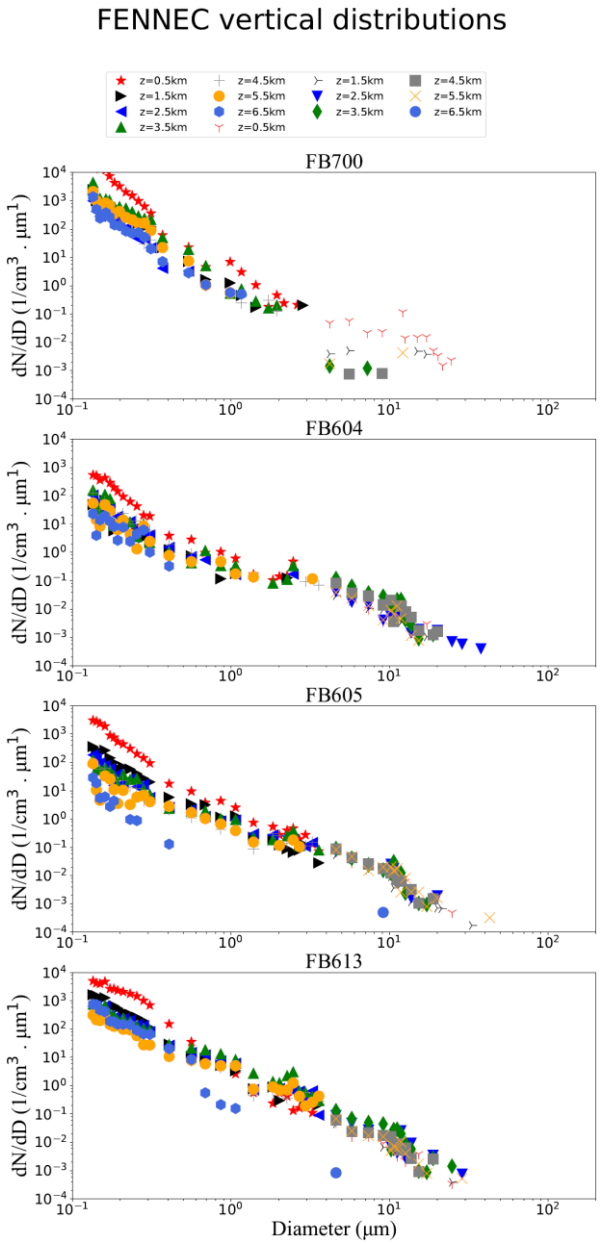

Figure 3. 5. Vertical size distributions of dust (dN/dD, 1/cm^3 µm) with diameter (µm) for selected heights for non-dusty (FB700), and dusty days (FB604, FB605 and FB613). The plots show PCASP and CDP size distributions at selected heights from 0.5 to 6.5 km for every 1 km based on flight observations. PCASP corresponds to the first symbols in the legend between 0.5 and 6.5 km followed by CDP profiles associated with the same height ranges. The different heights are indicated in the key at the top of the figure with an average of the dust at each height interval.

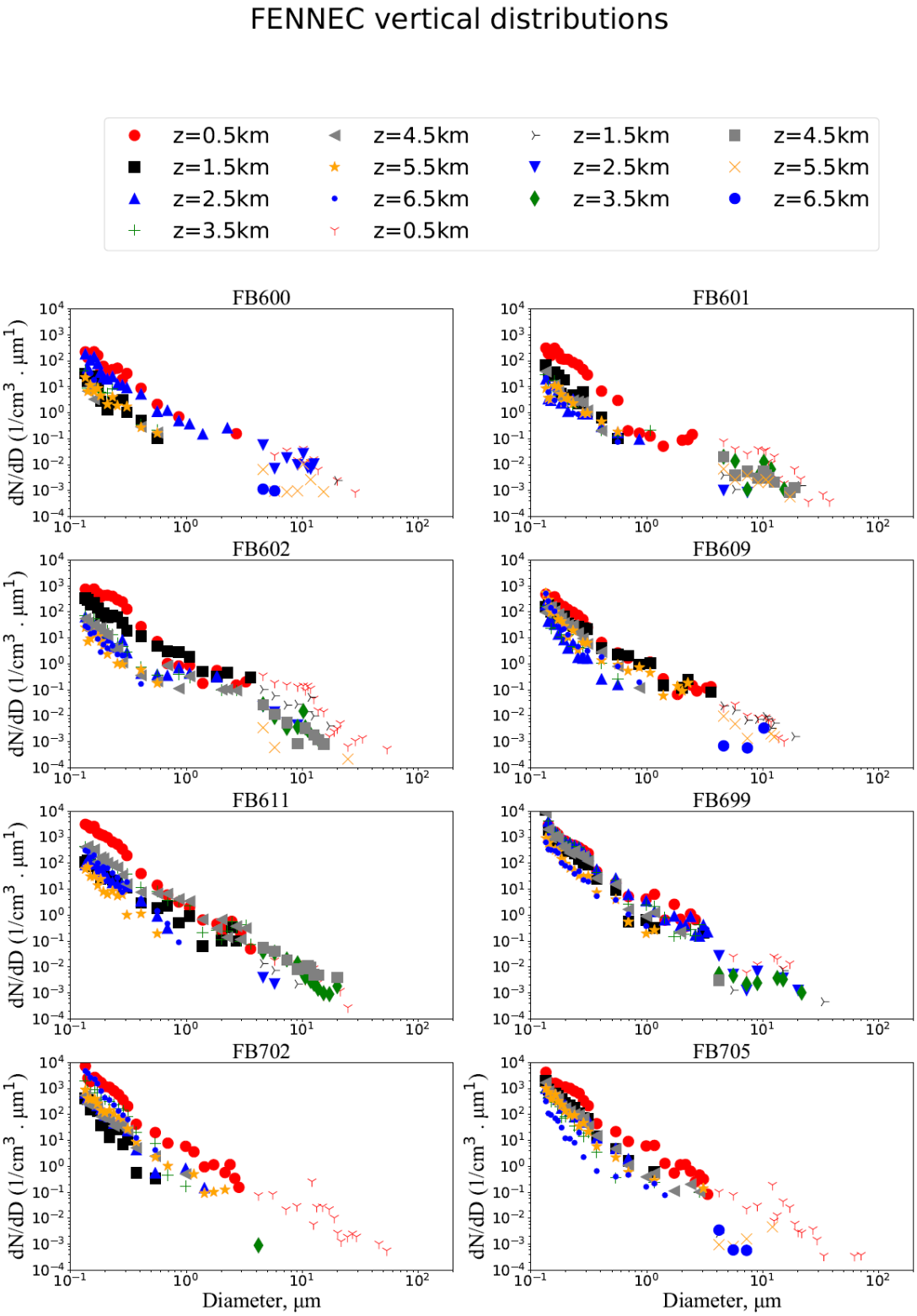

Figure 3. 6. As figure (3.5), but for more flight cases.

3.2.1.4 Dust profiles over the Canary Islands study region

The FENNEC flights used in this study take off and land from Fuerteventura Airport. They would almost exclusively fly towards mainland Africa, but at least one flight flew north towards Portugal. Measurements of the atmospheric profiles used in this study were taken during the aircraft ascending or descending during take-off or landing. The flights flew from land (Fuerteventura airport) with lowest layers about 60 m above sea level (briefly over land) and ascending gradually with height up to 8 km, while the lowest height of flights taking measurements for thesis cases passing over African land is 300 m. The presence of dust profiles over the Canary Islands can be determined by coarse mode (CDP), where the coarse mode is primarily due to dust (Rodriguez et al., 2011), when this dust particle concentration is larger than 10^{-1} cm^{-3}. While for size distributions over land, dust presence is determined when dust numbers are > 10 cm^{-3} (this was identified as the appropriate dusty conditions over African land as stated by Ryder et al. (2013a)), see figures (3.1) - (3.3) and also dust size distributions for the sedimentation model in Chapter 5.

The presence of sea salt loadings can affect the results and the assumed amount of dust and hence dust heating rates. Compositional analysis for the flights is not available and so I have had to estimate sea salt concentrations and subtract from the total aerosol number concentration in the MBL up to 1 km. This height was used because it has been shown that the top height of the MBL is typically located in the lower atmosphere between 900 and 800 hPa (between ~ 800 and 1000 m) over the Canary lslands (Carrillo et al., 2016). Therefore, I calculated the sea salt concentration at the sea surface and then I scaled the concentration with height up to 1 km. Then, the dust number concentration (NC) in the dusty marine boundary layer was determined to be equal to the total concentration minus the estimate of the sea salt.

The sea salt concentration, $C^{z}_{sea-salt}$, was obtained by assuming an aerosol scaling height (H), as it described in Chapter 2. I show here in figure (3.7) an example of the dust mass profile with and without sea salt for the non-dusty (top panel) and typical dusty flight (FB604). Blue lines show dust mass loading excluding sea salt up to 1 km, while black lines present total mass profile (i.e. combination of dust plus sea salt mass loading). Top and middle panels present mass profiles over the Canary Islands for these flights, while bottom panel show the sea salt after dust transporting from the African land over 7 days, i.e. Puerto Rico region. For clarity, I did not show the whole dust mass profile in this figure since I want to see the difference between total mass and sea salt mass loadings within MBL. Based on figure (3.7), percentage differences show that averaged sea salt was a lower percentage of the averaged dust loading within the MBL with a value of about 6.5 % over the Canary Islands and with value of about 15 % over Puerto Rico. Percentage difference in sea salt values between Canary Islands and Caribbean is assessed by You et al. (1985), who shows that sea salt concentrations have diurnal variations with time and with altitude of the lower atmosphere (roughly up to 500 m), where the highest loadings are located in

the lower heights. The results show that sea salt does not have a significant impact on the total mass profiles, but it is estimated that the percentage difference over the Caribbean is higher (double) than that over the Canary Islands because the dust is much lower after long transport. The sea salt concentration at the surface is slightly higher than PRIDE measurements (Colarco et al., 2003) where the typical measured values of sea salt concentration by PRIDE at Puerto Rico are between 10 and 20 $\mu g/m^3$, while the current thesis shows that sea salt at the surface is between 20 and 27 $\mu g/m^3$. However, sea salt has significant reduction with value reaches about 5 $\mu g/m^3$ at height 1 km.

Figure (3.8) shows the net total dust mass loading profiles (in units of $\mu g/m^3$) with the sea salt loading excluded from surface to 1 km for non-dusty (see black line for FB700) and dusty (see red and green lines for FB604 and FB605, respectively) cases. Figure (3.9) presents net total dust mass loading with more flight cases. In dusty cases (FB604 and FB605), the red and green lines show large loading of dust up to 6 km, and it drops significantly above this height. The NC for flights FB604 and FB605 is higher than the non-dusty case by a factor of about 10 to 100. The non-dusty cases (see solid and dashed black lines for ascending and descending flights) has roughly a constant value with vertical profile, except below about 1.5 km. This larger value below can be caused by FENNEC flight observations being taken over the African land and this having a dominant effect because of the coarse mode dust particles within about 1 km above the ground (Ryder et al., 2013). Flight observations implemented over the Fuerteventura airport, may be caused by the local dust which could cause a peak in the dust loading in the boundary layer, just like what is seen over Africa, possibly through convection being strong and mixing dust. I note that the low dust days for which flights were done often had dust events on the mainland so although the air was relatively low dust in the Canary Islands, often it was on the edge of an event. It is possible the higher concentrations were transported at the low levels first or experienced some sort of regional subsidence from the event transporting the dust on the surrounding areas at low levels.

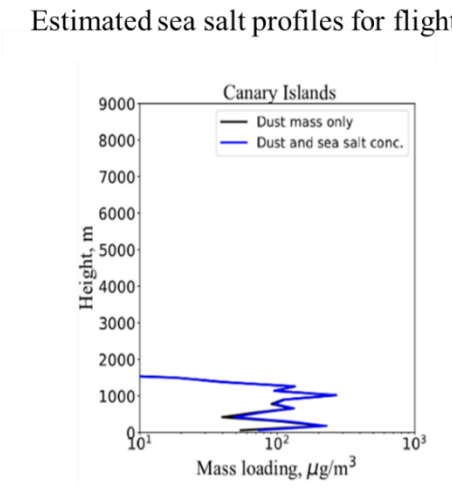

Figure 3. 7. (Top panel) extracting sea salt concentrations from the total mass (combination of dust and sea salt mass loading) over Canary Islands for non-dusty event (FB700). (Middle panel) for dusty case over the Canary Islands, and (bottom panel) over Puerto Rico. Blue and black lines show dust mass loading with and without sea salt concentration, respectively. X-axis is described in a log scale and ranged between 10 and 1000 for clarity.

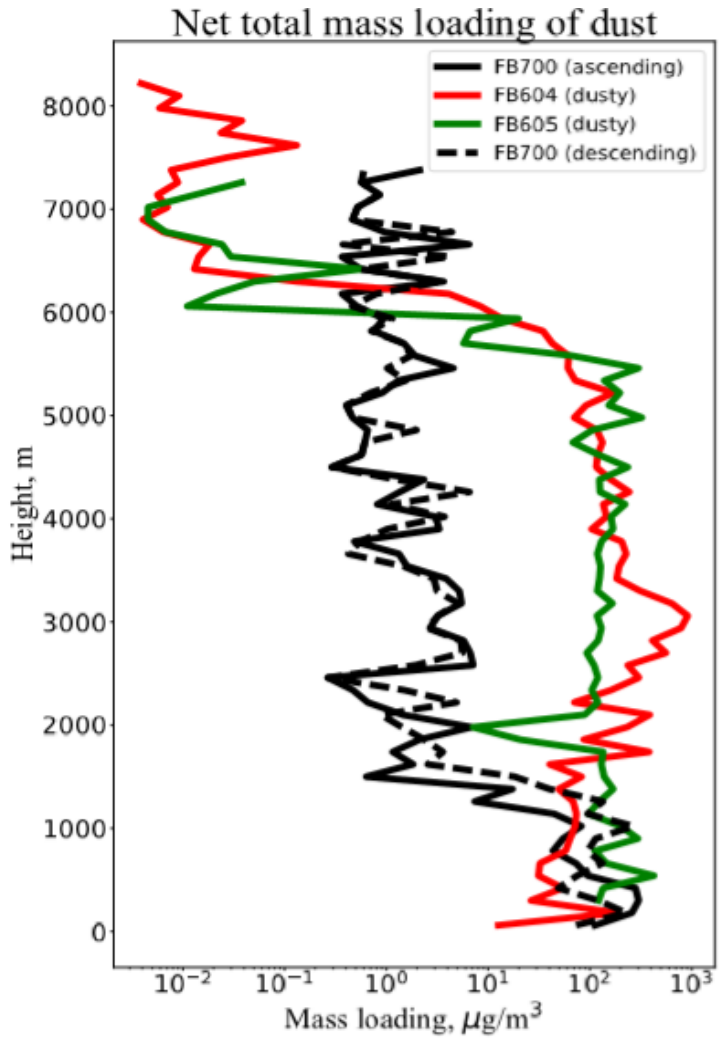

Figure 3. 8. Net total mass loading (i.e. summation of PCASP and CDP) in units of µg/m^3 calculated from the net of dust total mass loading for FENNEC size distribution with using refractive index of 1.53+0.001i. Ascending (black solid) and descending (black dashed) flights show dust mass loading for two non-dusty (ascending and descending flights for FB700) events over the Canary Islands, while red and green lines show flight numbers FB604 and FB605 for dusty outbreaks, respectively. Sea salt aerosol loading has been removed from the profiles in the MBL by using Eqs (33) – (36).

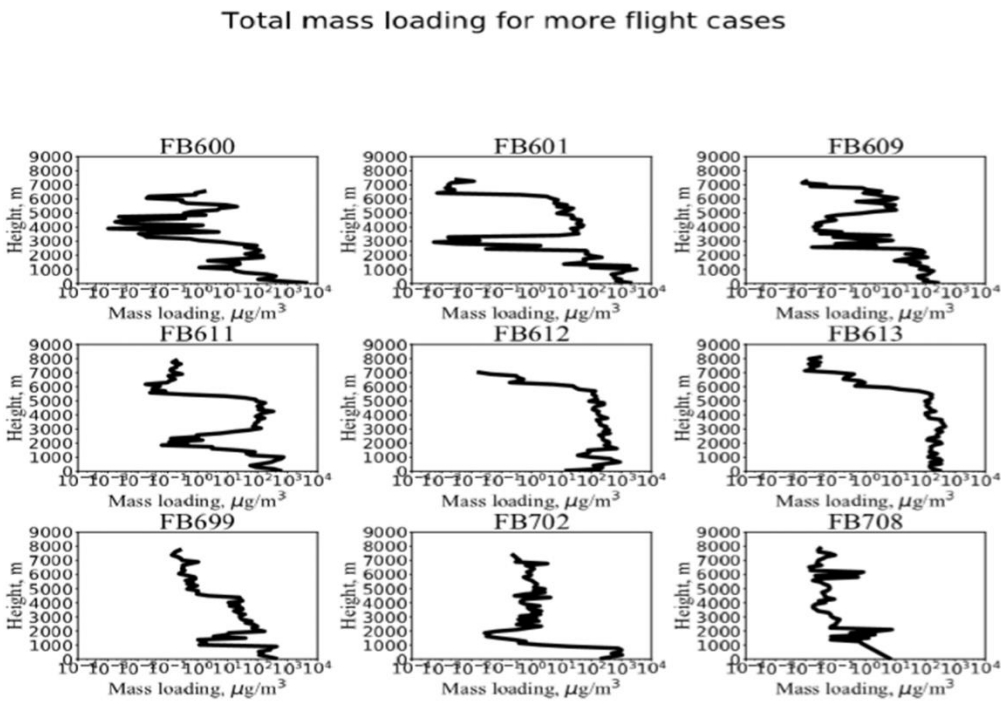

Figure 3. 9. Vertical mass loading of Saharan dust over the Canary Islands. Dust mass calculated based on flight observations and with using an appropriate RI from Ryder et al. (2013). The density of dust used to calculate mass loadings is taken from Jabonero et al. (2016) with value of 2.0 g/cm^3. Sea salt loading has been removed from the profiles in the MBL.

In figure (3.10), dust mass concentration profiles are shown for dusty events (see FB604 and FB605) over the African land (red line) and the Atlantic (blue line), which shows the distribution of total mass of dust over land and within the SAL over ocean tends to have different dust mass profiles with higher amounts typically over land as expected. A few factors are involved in this: firstly, although the duration of time of flight to measure a profile is nearly the same, over land surface fluxes will be vastly different giving rise to very different dynamics in the vertical. Secondly, during this transport the vertical wind/sedimentation will influence the levels of dust concentrations. This is shown by the profile of vertical wind (w) and fall velocity (v_t) in Chapter 5, causing the heavy particles to be depleted by the time it is advected over the ocean. Finally, the profile will also be affected by the SAL layer intruding on the background relatively pristine marine environment. All these factors will lead to different profiles. However, at some altitudes there is similarity in mass profiles between the African coastline and the Atlantic. For example, the peak value of total mass is at about 3 km over the dusty marine environment and is approximately the same with that value over the African land, see left panel of FB604. The impact of fall velocity and subsidence will be explained in detail in Chapter 5.

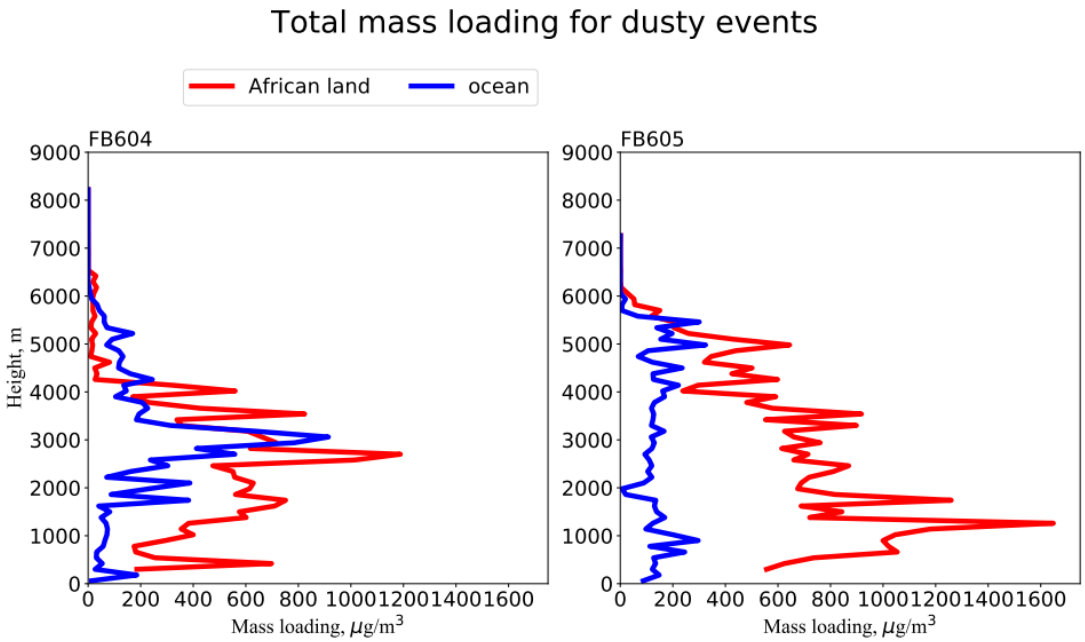

Figure 3. 10. Total mass loading of Saharan dust (in units of μg/m^3) calculated from the size distribution of FENNEC observations during June 2011 for flights FB604 and FB605 (dusty events). Red and blue lines display the total mass loading of dust over the African land and the Atlantic, respectively. Note, the total mass of dust over the Atlantic excludes sea salt aerosols in the profiles, i.e. blue line for FB604 and FB605 are the same profiles in previous figure (3.8). The values of dust mass loading at the (top) bottom on this figure show the flight being at (high) low levels during flight from Fuerteventura toward African land.

The results for total mass loading of dust were compared to literature. In this study, peak values of dust total loading over land and ocean were generally lower in value than presented by Ryder et al. (2019). The current study shows the maximum mass loading values (in typical flight cases, i.e. FB604 and FB605) of about 1600 μg/m^3 for land, and about 900 μg/m^3 for the ocean. Also, the typical dust mass loading over the Canary Islands was between approximately 30 and 250 μg/m^3, while results for Ryder et al. (2019), in figure (3.11), shows a maximum dust mass loading (orange and red lines indicate total mass loading of dust profiles at elevated and lower altitudes, respectively) during their cases of intensive dust events over the eastern Atlantic was about 4600 μg/m^3 and typically from 300 μg/m^3 (low dusty) to 1000 μg/m^3 (moderate dusty) over ocean. The lower value of the peak mass loadings can be caused different strengths of outbreak and by different locations of the source of dust as well as different paths of the winds from the source to the ocean and so different sedimentation. In some cases, dust mass profiles in a layer are likely to be the same between the African coastline and the Atlantic. For instance, in the previous figure (3.10), mass loading for the dusty event FB604 over the Canary Islands at an altitude of about 4 km is slightly less than over land, but at 3 km mass loading between African land and Canary Islands is approximately the same. It will depend on the amounts sedimenting from above and the concentrations of smaller particles in the layer that the larger particles are sedimenting into. It can also be affected by the advection.

Variations in dust mass profiles between land and ocean is related to the characterisation of convection and surface fluxes between them, which is quite different. Over land, dust uplifts to high heights by strong convective processes (Marsham et al., 2013). This results in high mass fluxes of dust over African land. So, in those regions dust mass loading is strongly affected by the source region and convection and results in well-mixed vertical profiles over land which can be different compared to over ocean (Ryder et al., 2015). In contrast, over ocean dust mass loading typically is in a different profile than over land since there is no dust source as well as convection is not strong over the Atlantic. In addition, air mass trajectories into the ocean can also make dust profiles different by mixing dusty air from the African land with other sources of air mass. Therefore, dust mass is quite different between land and ocean environment.

FENNEC flight observations during June 2011 and 2012 show variations in mass loading between land and ocean. These variations of mass loading can be controlled by dynamic meteorology for these environments. For example, Ryder et al. (2015) states that during June for 2011 and 2012, the dust loading over African land is mainly driven by significant easterlies and SHL movements (westward movement) over Algeria, while the Sahelian dust source is the most active region in producing African dust for 2012. But the intensification of dust loading over the Atlantic (Canary Islands) can be spread by winds and diluted or mixed with other air mass sources (as it is explained in previous paragraph) during dust advected toward the Atlantic. This can be seen in the FENNEC measurements over the Canary Islands, where the current thesis shows that the dust mass loading during June 2011 tends to be higher than dust loadings for observations in 2012, while over African land, Ryder et al. (2015) states that the high dust was for 2012.

The low dust profiles over the Canary Islands during 2012 can be observed by non-dusty day with corresponding to wind direction that is observed by flight measurements indicated in figure (3.16). The inconsistency of dust mass loading for flight 2012 between the explanation of Ryder et al. (2015) over the African land and thesis results over the Canary Islands can be caused by that the intensification of dust mas loading measured by flights 2011 and 2012 over land may receive different mass loading to that over the Canary Islands. This can be indicated by flight measurement sites over the African land in a comparison with Canary Islands. In previous figure (2.3), flight tracks are shown in coloured lines on the map, where most flights during 2011 are sited over western Sahara coast which is represented as main source of dust production, while most flights during 2012 are sited in areas toward northern-east from the western Sahara. For instance, flights FB604 (black line) for 2011, FB706 (light pink) and FB708 (red) for 2012, see figure (2.3). This can cause a variation in dust mass loading due to different flight locations during time observations over the African land corresponding with dust observed is over the Atlantic. Thus, the above shows that there is significant dependence on land/ocean differences as well as seasonally.

As such, using accurate inputs into the calculation of the dust from the instrument optics in calculating the dust size distributions is important. The mass specific extinction coefficient, K_{ext}, was used in this research in the converting dust column mass to AOD as it was described by Jabonero et al. (2018), see also explanation in chapter 5, section 5.4.2. Jabonero et al. (2016) used a mean value of 0.32 m^2/g over the Canary Islands. Where Jabonero et at. (2016) used K_{ext} over the Tenerife area, which is more distant from the African land in comparison with Fuerteventura.

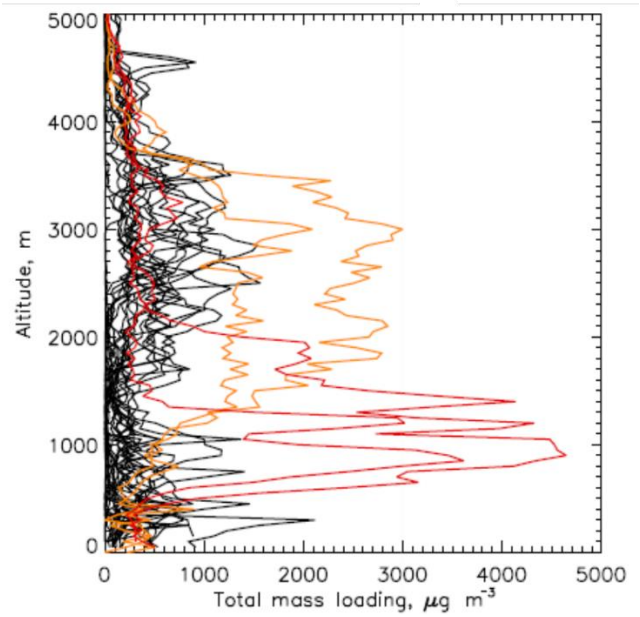

Figure 3. 11. Total mass loading of dust in unit of $\mu g/m^3$ over African continent and within SAL. The black lines show the comprehensive flight observations including moderate and high dust loading, while red and orange lines are referring to strong dusty events over land and ocean, respectively. Figure is taken from Ryder et al. (2019) using density of dust as a typical value for 2.6 g/cm^3

Other factors can also influence the optical properties and hence determination of the size distributions from the observations that are optically based. The optics are derived from the integral calculations (i.e. integration of Eq. (31) that is shown in the previous Chapter 2) over particle sizes and based on refractive index to determine size distribution by using a Mie scattering code. Uncertainty can come from the RI as well as assumptions such as the dust being spherical in shape and RI. These factors can all affect the size distributions of dust and hence mass loadings. There is a debate about the values of RI used in deriving dust profiles such as Ryder et al. (2013), especially regarding the complex part of the RI. It is the imaginary part of RI that relates to absorption, and thus uncertainty in that parameter can have an important influence on determining the amount of heating in the atmosphere, especially within the SAL. For instance, Müller et al. (2017) stated that deriving refractive index in the range of spectral wavelength by using Mie scattering calculations between total aerosol and dust mode is different with that mentioned in

previous studies. Regarding the spherical particle shape by using Mie calculations, Yi et al. (2011) stated that over ocean surfaces there is about 30% difference in the radiative transfer simulation of dust-like aerosol at the TOA due to non-dust particle shape. For clear sky, Wang et al. (2013) calculated dust optical properties of spherical and non-spherical particle shapes by using Mie theory with a combination between T-matrix and geometric optics approach. Their study reveals that the difference between spherical and non-spherical dust particle shape over the Sahara Desert does not have significant effect on the global annual mean instantaneous radiative forcing, although their work pointed out that non-spherical particle shape can decrease annual mean radiative forcing for three different locations, including the Sahara Desert, west Asia and northern China. This provides insight about non-spherical particle shape that it may not have a significant impact on global radiative evaluation but could have some regional influence over the deserts.

These uncertainties mentioned above would influence the evaluation of dust mass loading across the Atlantic when the SAL advects. The thesis results reveal that the dust size distribution for the PCASP does not match well with the CDP when using a large absorption term of 0.003 for the imaginary part of the refractive index. In addition, about 23% percentage difference in the net total dust mass profiles between using density of dust of a value 2.6 g/cm^3 and 2 g/cm^3 is presented. Further uncertainty such as fall velocity, particle shape, etc. will be shown in Chapter 5.

The profiles of total mass loadings of dust tend to be high within the MBL especially for the dusty cases over land. This is because particle sizes of dust in the coarse mode are large especially near the source regions over land. Over ocean, the very large mass contributions have sedimented and the profiles are now over the MBL so the concentrations for the dusty days tend to be larger above the MBL. Dust measurements have been taken for flights at different times, i.e. morning and midday/afternoon. During early morning, the concentration of large particles will be in low altitudes due to the strength of convection process is weak, while during daytime heating the land surface fluxes will cause convection and turbulence and allow dust to lift up to high heights. Another contribution to the profiles over ocean is the concentration of aerosol sea salt in the marine boundary layer. As the sea salt concentration was calculated by using a scale height approach, explained in the previous Chapter 2, sea salt is in addition to the dust profiles shown previously in figure (3.8) and would increase the aerosol profiles below about 1 km. As in You, et al. (1985) sea salt concentrations have a diurnal variation and with altitudes in the lower atmosphere (roughly up to 500 m), where the highest concentrations are in the lower heights. This can influence the radiative effects of the atmosphere and in the SAL by causing increased reflectance below the SAL by the sea salt. (Prospero, 1979).

The results of current thesis show that the dust near the Canary Islands is typically distributed in substantial amounts during outbreaks in the vertical between 2 and 6 km (SAL) and dust mass mixing ratio (DMMR) is between and $7.5 * 10^{-8}$ g/g and $5.5 * 10^{-6}$ g/g. This is consistent

with other general measurements. For instance, Kaly et al. (2015) shows that the mean value of DMMR over the Sahel region is about 1.6 $*10^{-7}$ g/g. There is a wide range of DMMR values spatially, as indicated by the results of McConnell et al. (2008) for the Cape Verde region.

3.2.2 Dust mass variability and uncertainty

The profiles of dust-mass loading over the Canary Islands show that all dusty cases have a roughly constant profile from the surface up to 6 km and are larger in magnitude than other low dusty cases, as expected and as shown in figures (3.8) – (3.9). The mass loading of dust in low dust events dropped significantly between heights of 1 km and above. The difference in mass loading between dusty and low dusty cases within the SAL is about two orders of magnitude. In addition, low dust outbreaks have more variability in dust mass profiles than dusty cases. The variability in dust mass loading is likely to be linked to the duration and direction of transport between the African land and the Canary Islands during these dust outbreaks. In these lower dust cases, the dust events in Africa were sometimes intense but depended on the direction of the advection, the Canary Islands were sometimes on the border of a dusty outbreak and so the variability is likely due to some dust at certain levels being advected over the Canary Islands but not at other levels.

This variability leads to uncertainty in classifying low dust case events over the Canary Islands using AOD. For instance, there is uncertainty in specifying the dust profile categories by AOD observations from AERONET. This uncertainty is found in days that have less dust outbreaks such as FB600 and FB699, since the data of AOD over the Canary Islands is calculated as an averaged AOD from three regions, including Izana, La-Laguna and Tenerife. This may not necessarily agree with Carlson et al. (2017) who show that AOD is proportional to dust depth AODs in some flights (i.e. FB600) is represented as averaged data in two regions due to no data being available in the other region. Therefore, it will be hard to precisely classify dust outbreaks into multiple dust events such; low, moderate and dusty events, based on observations so this should be taken into consideration when results are analysed. Since the flights were categorised based on their dust loading over the Canary Islands, some of the lower dust events could have high dust loadings further away. So, some lower dust loading cases had similar dust mass loading over Africa to the dusty cases, but it is just over the Canary Islands it was less.

3.2.3 Dust profiles associated with meteorology

3.2.3.1 Potential temperature, θ, profiles

Dust profiles can be obtained from the meteorological profiles from the flight observations, as in figure (3.12) which shows the vertical profile of potential temperature (θ) and virtual potential temperature (θ_v) associated with dust mass profiles for the non-dusty case FB700 and dusty case FB604 in the region of the Canary Islands see blue dot line for θ and red for θ_v with dust profiles

indicates in orange solid lines. Within these θ profiles in figure (3.12), the vertical structure of the marine environment in the presence and absence of dust are presented. For the clear sky FB700 case (left panel), the atmospheric profile is clearly stable according to the θ profile. In contrast, with the presence of dust in the atmosphere (right panel), the structure of the profile is very different from clear sky/non-dusty cases. Here, categorising the atmospheric structure into four main layers can be done. These layers are: 1) a well-mixed potential temperature layer extending from the sea surface and a few hundred meters (up to 1000 m in some cases), 2) a very stable (inversion) layer from the top of boundary layer to the base of SAL, 3) the SAL which is the deepest layer so far that extends from the top of the inversion layer up to approximately 6 km, and 4) the stable layer above the SAL. The profile of potential temperature shows that the dust layer intrudes into the marine environment introducing a nearly constant potential temperature layer with stably stratified air above and below (see potential temperature structures and dust mass profiles within the SAL in figure 3.12). The dusty and non-dusty profiles of potential temperature are very different because of this well-mixed SAL layer. For example, dust mass profiles over the Canary Islands for flight numbers FB604 and FB605 in figure (3.12) and figure (3.13), respectively, agree with potential temperature profiles between heights of about 1.8 to 6 km, where the mass loading increases/decreases with potential temperature layer is increased/slightly increased. In contrast, the non-dusty profile (i.e. FB700) is stratified throughout the vertical. The transport of dust mass concentration downwind over the Atlantic will be shown in Chapter 5.

The depth of the well-mixed boundary layer varies depends on the sea surface fluxes of moisture and heat. However, figures (3.12) – (3.13) show that the θ profiles within the MBL during dust events (e. g. flights FB604, FB605, and FB611) is slightly unusual in that it is not completely well-mixed. See potential temperature and virtual potential temperature with dust mass loading profiles for more flight cases in Appendix A4. The dynamics of this layer relies on the nature of the ocean surface including surface wind speed, temperature and roughness, but does not necessarily depend on the dust mass layer. However, over Africa the existence of dust in the boundary layer depends on many more factors that affect its uplift such as friability, vegetation cover, soil humidity, and grain size (Carlson, 2016). This difference in the profiles of potential temperature is a key point for understanding the presence of dust within the boundary layer. Well mixed potential temperature in the MBL indicates surface fluxes are driving turbulent mixing with the MBL, whereas a stratified potential temperature will indicate that the atmosphere is not being driven primarily by these fluxes and is stabilising through radiative processes.

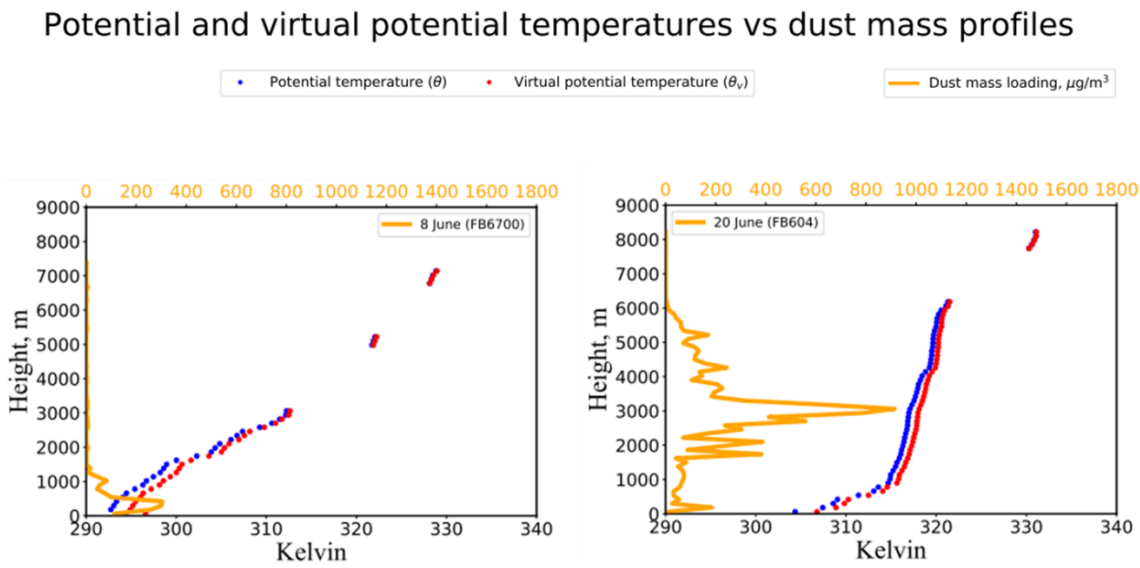

Figure 3. 12. Profile of potential (θ) and virtual potential (θ_v) temperatures vs dust mass loading from FENNEC observations for non-dust case FB700 and dusty case FB604 over the Canary Islands. Blue and red dotted lines refer to θ and θ_v in units of Kelvin, while orange line shows dust mass loading in units of μg/m^3. Virtual potential temperature in all cases are slightly higher than potential temperature up to 1 km due to large moisture, and thus it will be considered in stability calculations for CAPE and CIN factors. In some cases, slightly larger amounts of water present within the dusty marine environment SAL. This is surprising since dusty layers are often considered to be dry. The role of this water vapour increase will be assessed in this work. The heavy dusty cases that determined based on AERONET-AOD observations are: FB604 and FB605, while non-dust event is indicated by flight FB700. The gap in the profiles of potential temperature was interpolated linearly to be ready as input data in the model simulation.

The steepness of the stabilising inversion layer (IL) between the top of MBL and the base of SAL is dependent on the properties of the SAL as it intrudes into the MA. Since the large heating of SAL to the radiation describes steep gradient in IL, thus the stability of the SAL structure is controlled by dust optical properties due to dust size distribution, particle shape and potentially absorption by trace gases, etc. Therefore, it is possible that potential temperature profiles can be influenced by the dust particle sizes impacting on radiation, where at the TOA the scattering process is more influential since the absorption by large particles is weaker due to sedimentation. SALs nearer the coast can be more influenced by the absorption since many of the larger particles are still present.

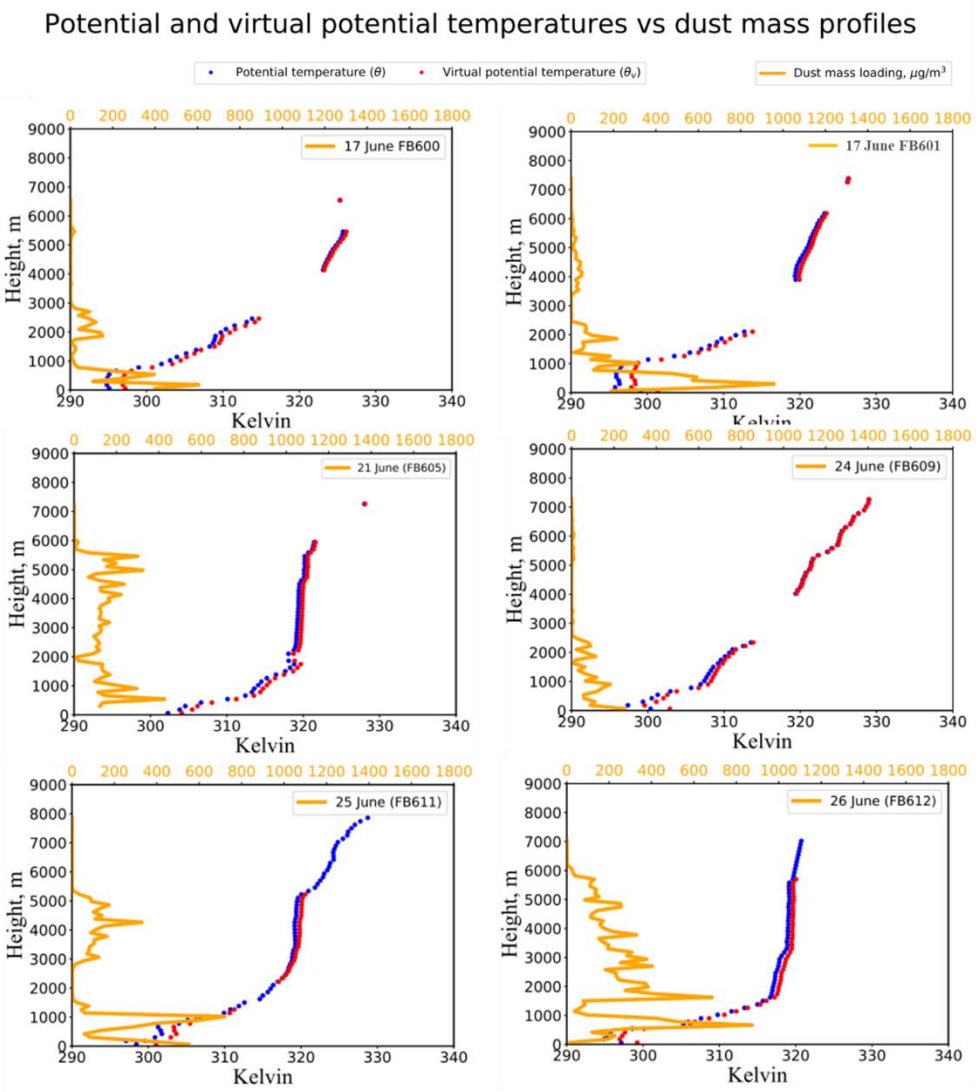

Figure 3. 13. As figure (3.12), but for more cases over the Canary Islands.

3.2.3.2 Humidity profiles

The largest values of the water vapour mass mixing ratio are in the MBL, near the sea surface with averaged value of about 12 g/kg, and it decreases significantly with height, see figures (3.14) – (3.15). It is interesting to note that in the SAL dust-carrying layers, the water vapour mass mixing ratio is elevated for dusty events. This contrasts with the conventional opinion that the SALs are dry and dusty (Prospero and Carlson, 1972 and Karyampudi, 1999). The relative humidity ($RH = \left(\frac{wv}{ws}\right)$ x 100) will be high when water vapour (wv) is large compared to the saturated water vapour (ws). This explains why the virtual potential temperature (θ_v) below 1 km is higher than θ due to $\theta_v \cong \theta(1 + 0.62wv)$, see the θ_v profiles in figures (3.14) – (3.15) as well as see Appendix A4 for more cases. The interesting point comes when considering the effect of the water vapour in comparison to the dust impact on absorption/scattering and hence the radiative

properties including SW, LW and total radiation and ability of water vapour to influence the structure of the MA. Potential temperature is a good parameter to use to investigate the changes in the atmospheric profiles since it depends on the temperature and atmospheric pressure and can inform whether the stability is changed. As dust particles absorb radiation, the temperature of the atmosphere will increase, but the dust can also cause scattering and so decrease the amount of warming in the layer and layers below. Solar radiation is likely to stabilise layers because of this since warming at the upper levels and partial shielding of layers below (if the dust is optically significant). In addition to this, water vapour will complicate the effects since it can absorb radiation in the SW and LW as well as cause some Rayleigh scattering in the SW and emission in the LW. If the SAL layers have elevated water vapour, then it will likely cause more warming of the layer and increased cooling at the top of the layer. Therefore, in the region of heating the potential temperature will be increased and where there is cooling it could destablise the atmosphere and cause overturning.

Water vapour profiles are shown in figures (3.14), (3.15) and figure (A4.2) in Appendix A4.2 are characterised by values less than 20 g/kg within the MBL. Above this, it drops significantly until about 1-3 km. Above 3 km for the non-dusty case (e.g. FB700), the water vapour has a low value and is almost constant above that height. Water vapour is a key factor in determining CAPE and CIN values, where the height of saturated water vapour is calculated based on surface value of temperature and water vapour when air parcel lifted adiabatically until it reaches saturation, thus the lifted condensation level (LCL) which indicates the height that cloud would form if the parcel of air from the ground could be lifted within the background air profile. The CAPE/CIN can be affected by optically thick dust layers that affect the near surface temperature and the stability of the atmosphere.

As mentioned, one of the most interesting factors in this research is that although the SAL is generally characterised by dry and hot dust layer over the Atlantic (Prospero and Carlson, 1972; Karyampudi et al., 1999), I find in this work that the water vapour is elevated in the SAL. Looking at figures (3.14), (3.15) at FB604, FB605 and FB612, water vapour in dusty events within SAL is significantly higher and has a well-defined maximum in the SAL which is completely different to the non-dusty cases (e.g. FB700 and FB708). This research will focus on this water vapour peak as well as the dust influences on the radiation and characterisation of the atmosphere. This finding over the Atlantic has been not studied in term of what the dynamic and thermodynamic role of water vapour on radiative effects in the dusty marine environment, although over land, few previous authors have investigated the relative importance of water vapour and dust in the radiative simulations, including Alamirew et al. (2018), Marsham et al. (2016) and Evan (2015), and over the marine environment, the water vapour/dust interaction with the SAL and well mixed profile has not fully assessed. In the current thesis, the realistic way to investigate the importance of water vapour is to contrast the radiative results of dusty cases from

a non-dusty water vapour reference case, where it is inappropriate way to consider non water vapour (wv=0) profile in the consideration of radiative simulation since the standard atmospheric environment does not characterise by zero water vapour.

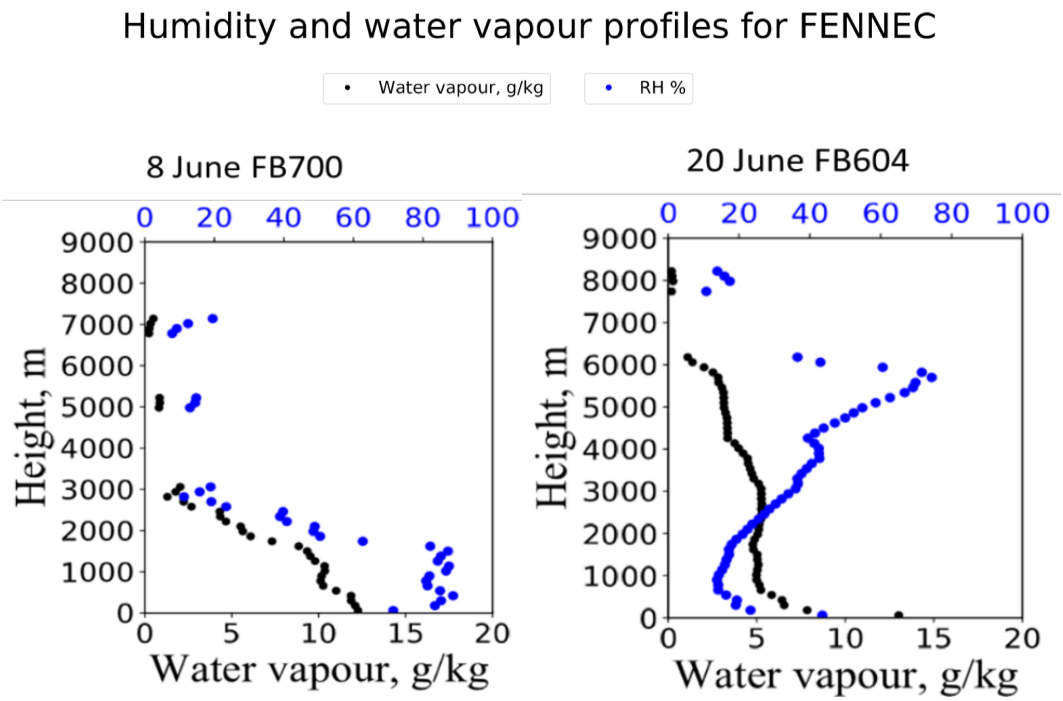

Figure 3. 14. Profiles of water vapour mass mixing ratio in units of g/kg and relative humidity (RH %) calculated from FENNEC observations for flight cases FB700 (left panel) and FB604 (right panel) over the Canary Islands. Large amount of water vapour was observed within the transported Sahara dust. Evan (2015) and Marsham et al. (2016) state that water vapour over the Sahara has a larger impact on the radiative effects than the dust layer, and therefore, quantification dust outbreaks must include both the dust and the elevated water vapour. Categories of dust events are coincident with these profiles of potential temperatures. The gap in the profiles of water vapour was interpolated linearly to be ready as input data in the model simulation.

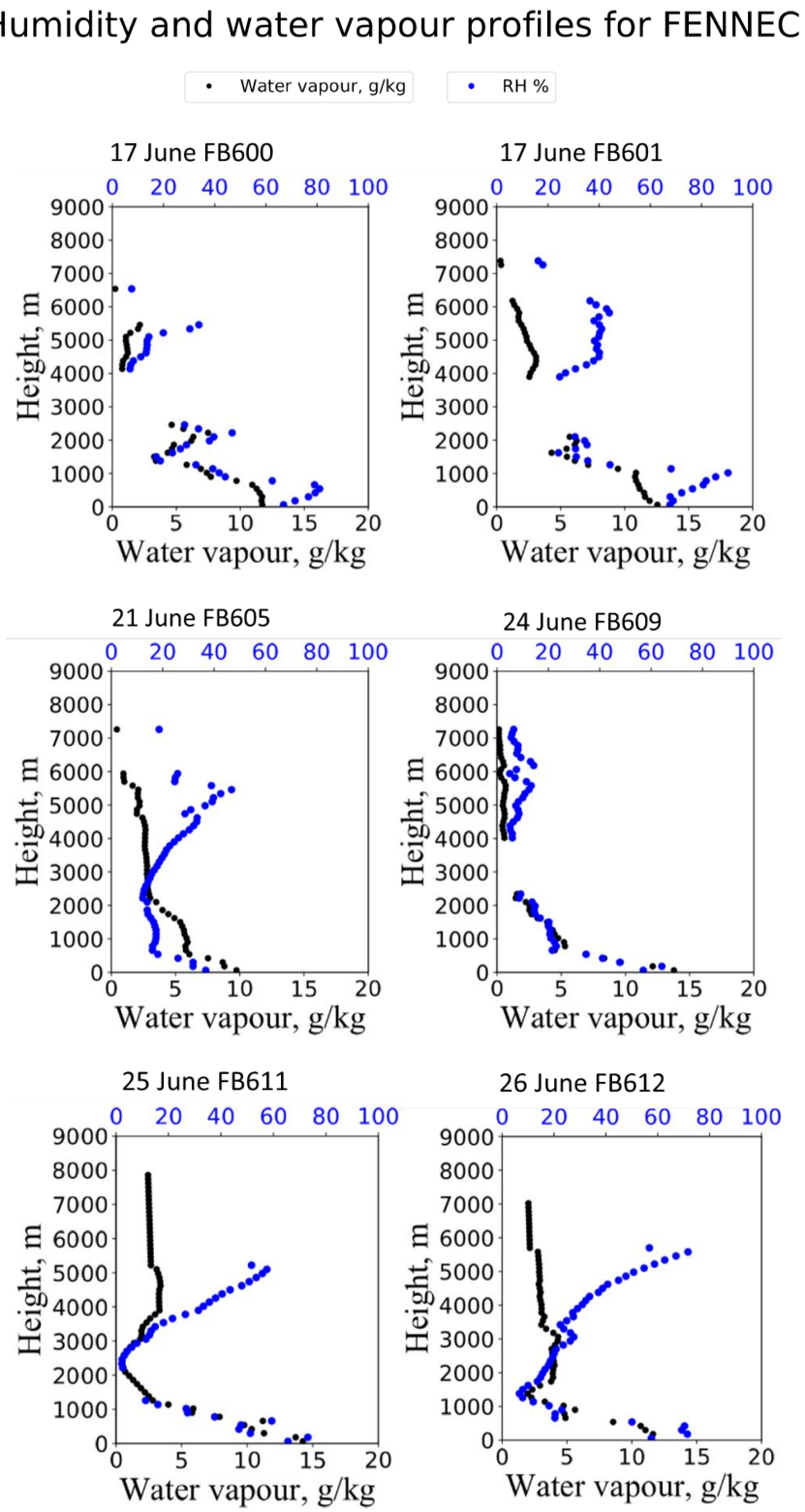

Figure 3. 15. As figure (3.14), but for more cases.

The influence of the dust and water vapour on the profiles of potential temperature, stability (CAPE and CIN) and heating rates will be strongly dependent on the time of day, and thus the strength of the SW and LW effects. During daytime, dust absorbs significant SW radiation especially near mid-day compared to earlier or later in the day. This radiative heating causes

temperature to increase within the SAL atmospheric layer, but this depends on the amount of dust mass loading and water vapour levels over the Atlantic. In contrast, during night, dust absorbs and re-emits LW radiation down to the surface causes warming and is characterised by a cooling at the top of the dust and water vapour layers where there is a net loss of LW to space and little returning. These concepts are important for quantifying the radiative effects of dust/wv. The contribution of dust and water vapour to the stability over ocean is different from that over land, since land and ocean are described by different surface albedos. Over land, and in the absence of dust, the ratio between solar radiative flux (irradiance) that is received by the surface and reflected fluxes from land is high due to land surface being a good reflector to the solar radiative energy coming from the sun, while dark surfaces such as ocean are weak reflectors due to ocean surface allowing radiation to penetrate it into the ocean surface where it is absorbed. Also over the marine environment the SAL will be in a layer within the MA. So, this means that the characteristics of surface fluxes over land are significantly different from ocean.

3.3 Wind profiles over the eastern sub-tropical Atlantic Ocean

This research uses the wind profiles from FENNEC flight observations and ECMWF reanalysis output. Winds from flight data were used in LEM simulations over the Atlantic Ocean, while large-scale ECMWF wind profiles were used in the sedimentation and turbulence model (shown in Chapter 5) for dust advection over the Atlantic since flights are very limited in terms of spatial coverage. In addition, the HYSPLIT trajectory model makes use of wind data from the meteorological data to derive air mass trajectories over the Atlantic. The data used from flights were profiles of horizontal (u and v component) and vertical (w) winds with height observed during ascending/descending flight between Canary Islands and north west Africa. The ECMWF data downloaded was for wind (u, v and w wind component) values with pressure levels which were converted into heights. Both sets of data were extracted for latitude and longitude.

Figure (3.16) shows the profiles of wind speed and direction from the FENNEC observations (see first column) for non-dusty (FB700) and dusty (FB604 and FB605) events observed over the Canary Islands. Wind profiles for all dust cases have variability in the direction and magnitude from the surface to the top of the atmosphere. In terms of direction, generally wind profiles at low levels tended to be in the east and south-easterly direction. But wind can also blow toward north-west direction, i.e. toward the Canary Islands (Menéndez et al., 2014). Where the current study shows agreement in general with wind directions of Menéndez et al. (2014), who provide evidence for wind-transferring dust from north Africa toward Canary Islands.

Wind profiles from flight observations and ECMWF dataset show a remarkable variation in wind trend in the vertical. For example, Molina et al. (2018) shows that above the inversion layer the wind speed is increased, but below this inversion layer between land and Canary Islands it is decreased. Current research shows that wind at altitude about 4 km tends to be altered in the

direction toward the Canary Islands (i.e. south-easterly to north-westerly) and sometimes toward the easterly direction, especially at higher altitudes (Maring et al., 2000). This variability may provide evidence for the intensification of dust outbreaks over the Atlantic; however, wind direction above the inversion layer from ECMWF does not match that well with FENNEC observations. This can be caused by the very different spatial and temporal scales involved. The ECMWF wind speed and direction in figure (3.16) based on (-10, -13 W) degrees, and thus wind may vary significantly in reality within these westerly degrees. Another possibility is that FENNEC measures each level for a very short time duration, where FENNEC flight measurements take place at vertical velocities of 5 m/s and horizontal velocity of about 110 m/s, which provides sloping vertical velocity covering horizontal area of 170 km (Ryder et al., 2013), while ECMWF operates analysis at 1 degree grid boxes with a typical time step between a few minutes to 0.5 hour.

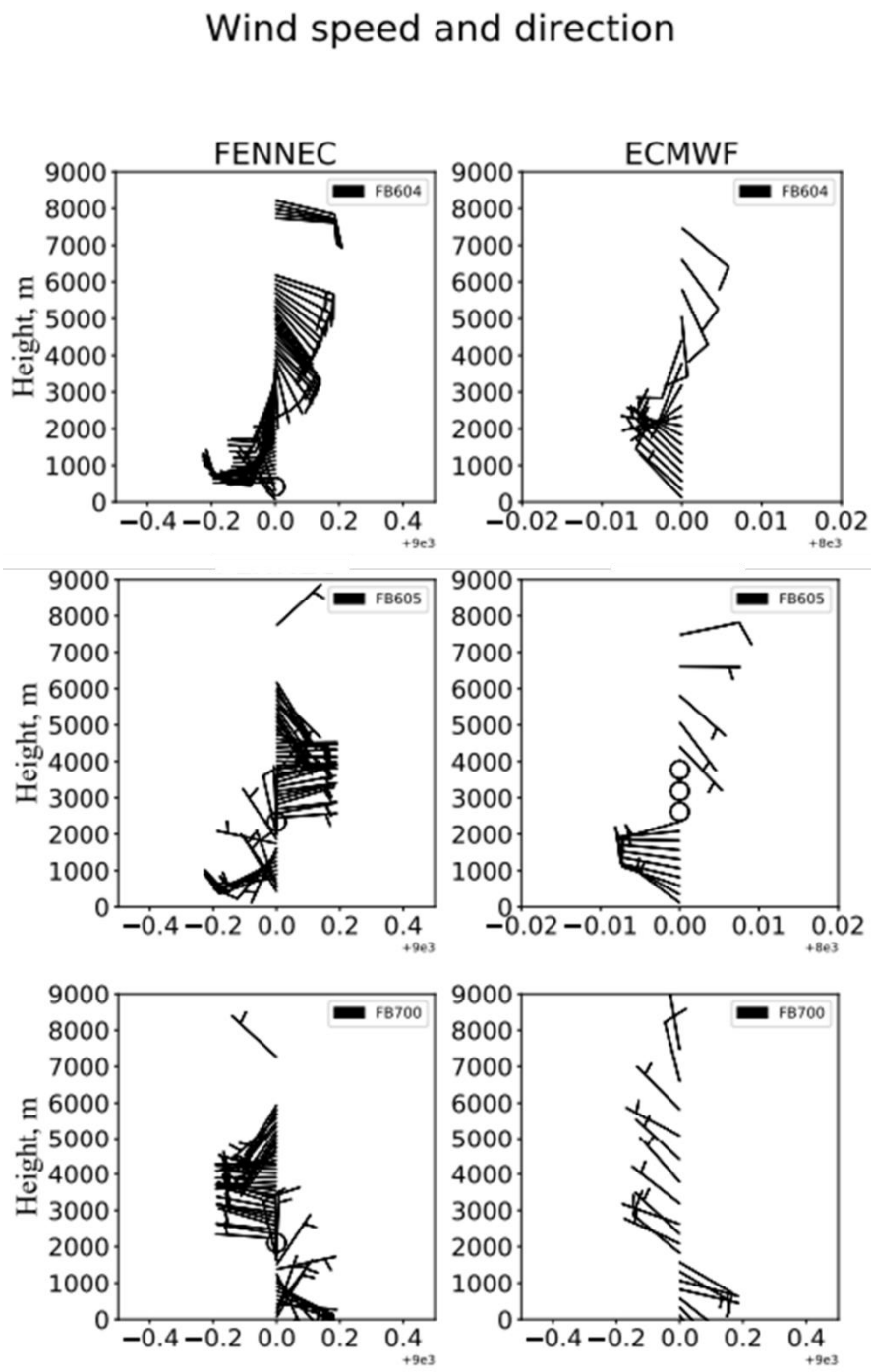

Figure 3. 16. Wind speed (m/s) and direction taken from FENNEC observations (left column) and ECMWF reanalysis (right column) data over the eastern sub-tropical Atlantic Ocean. Data profiles shown here are for dusty (flights FB604 and FB605) and non-dusty (FB700) days. The x-axis represents the sign of wind direction and the tails of the lines represent the magnitude, in agreement with standard meteorological notation. ECMWF wind data is taken for selected altitudes and not for all heights for comparison with FENNEC observations. Interpolations were not performed.

The wind speed and direction profiles during ascent and descent over the Canary Islands and the African coastline can be compared to get an understanding of the changes in these profiles going

from land to ocean. In figure (3.17), wind speed and direction are plotted for the African coastline and the Atlantic Ocean/Canary Islands. During dusty events, the general direction of wind over the African land is towards the west, especially above boundary layer, see left column in figure (3.17). Whereas wind is oppositely directed at higher levels. Over the Canary Islands, wind profiles within the MBL are mostly oriented towards the east and south-easterly reaching a maximum value of 12 m/s, but above the MBL the winds are easterly and south-easterly directions. Beyond the African continent the winds are potentially controlled mainly by prevailing wind (ATW), as described in Chapter 1 (Prospero and Carlson, 1972, Prospero and Nees, 1986, Schepanski et al., 2017). Superimposed on this prevailing wind, there is some degree of variability as evidenced by the HYSPLIT trajectories performed in this work. Individual trajectories can have significant variability but the transport of dust etc. can be understood from using ensembles of trajectories (Stein et al., 2015).

To conclude, wind data from the ECMWF model is appropriate for considering dust transported in the large-scale over the Atlantic and it is not easy to match with wind direction from the flight measurements due to variability in wind profiles over different spatial and temporal scales. The predominant wind at least during dust outbreaks is easterly and south-easterly direction from the land, and this is evidenced by satellite observations of dust transport. In contrast, wind direction within the MBL over the Canary Islands is likely to be the same orientation to that over land, but it can be shifted from west to north westerly direction at about 3 km in height. In addition, the magnitude of wind profiles within the boundary layer over land is less than this value over the Atlantic, since friction between wind and surface is large. Furthermore, wind not only changes in direction, but also varied in its magnitude with height. For dust transportation, vertical winds from observations and model data will be used in Chapter 5 to provide an estimate of the dust transported over the Atlantic by using a developed sedimentation and turbulence code since the HYSPLIT model does not do bin resolved dust transport trajectories.

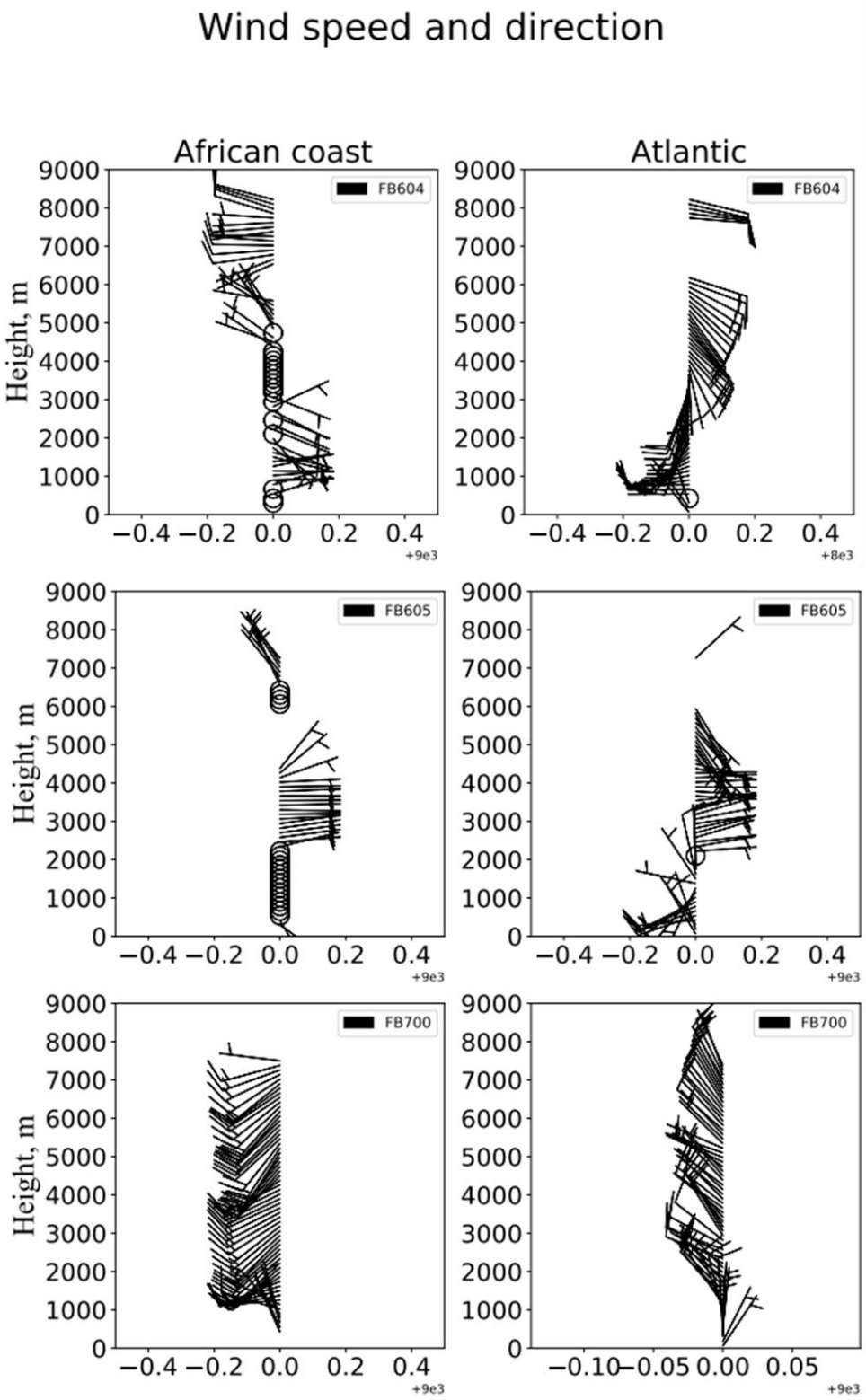

Figure 3. 17. Wind speed in unit of m/s and directions taken from FENNEC observations taken during ascent and descent at the African coastline (left panel) and the Canary Islands/Atlantic Ocean (right panel). Data profiles for dusty events shown in the first and second rows, while third row is for non-dusty observations. Negative and positive values in x-axis show the direction of wind toward the west or east, respectively.

3.4 Role of dust profiles on CAPE and CIN

In this section, the atmosphere is assessed in terms of the ability for a buoyant air parcel to undergo convection. This is investigated in terms of the CAPE and convective inhibition is assessed in terms of CIN. The cases studied do not have clouds so the buoyancy of air parcels in the MBL are not enough to break through the inversion at the top of the MBL but the CAPE and CIN offer a way of characterising the atmospheric profile and to be able to look at differences in this for dusty and non-dusty days.

CAPE is evaluated in the atmosphere by considering an air parcel that is lifted adiabatically from the surface along a dry adiabat and then when saturation is reached the ascent is then along the moist adiabat. Non-dusty days will be saturated at lower altitude compared to dusty days due to the increased temperature of environment by the presence of the dust. Therefore, the height that an air parcel would have to ascend to be saturated will be higher for dusty air parcels than non-dusty days because the lifted air will likely be dry and hot dusty air that is likely far from saturation (Wong and Dessler, 2005). This can provide understanding about dust impacts on the convection process within dusty marine atmosphere. Although thesis cases do not have cloud, downwind from the study region there will eventually be cloud in the air, it is useful to understand the potential impacts. To calculate the CAPE and CIN, mathematical calculations were performed to evaluate their values.

The CAPE and CIN are most easily understood from figure (3.18) in which the thermodynamic profiles are represented in a Stuve diagram. This diagram can be used to identify the height an air parcel needs to reach to attain saturation (lifted condensation level, ZLCL) corresponding to RH of 100 %. Table (3-1) shows the ZLCL for non-dusty and dusty days calculated from the FENNEC observations, where RH = 100 %. It is clearly shown that ZLCL increases with the presence of significant dustiness. The value of ZLCL for the non-dusty category was 701 m, while for the dusty category (i.e. FB604) it was 1491 m, as well as 823 m for low dust event such as FB601. The dust layers absorb radiation in the well-mixed SAL altitudes resulting in increased temperature, and so ascending air parcels remain sub-saturated until higher heights where ZLCL is reached.

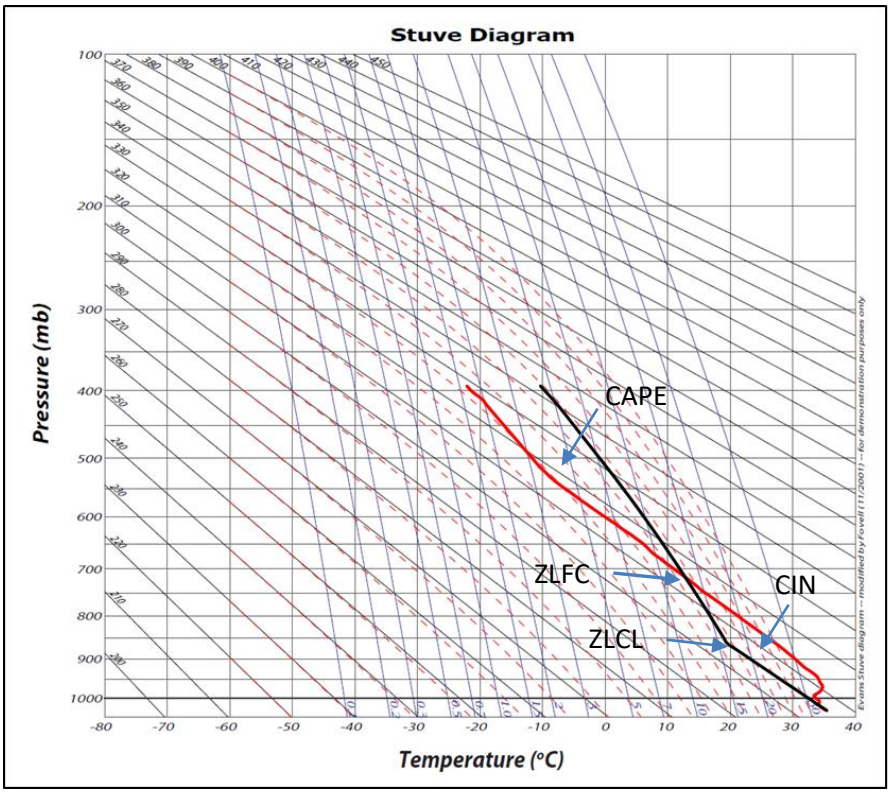

Figure 3. 18. CAPE and CIN areas shown on a Stuve diagram for a dusty case. The solid red and black lines indicate the temperature of the environment and parcel, respectively. The grey slanted line indicates the dry adiabat in which the temperature decreases at the dry adiabatic lapse rate (DALR) of about 9.8℃/km. Whereas, the red dashed line shows the saturated adiabat, in which the temperature decreases at a varying saturated adiabatic lapse rate (SALR) between about 4 and 6 C/km. Blue slanted lines refer to the mixing ratios of water vapor. Horizontal and vertical lines indicate the isobars and isotherm, respectively.

By determining these height levels from the Stuve diagrams, it becomes easy to calculate the contributions of both CAPE and CIN which are then used as a measure to understand the impact of changes to the structure of the atmosphere and understand the potential for convection which could be very important, especially downwind over the Atlantic from the study areas. Here, CAPE and CIN are calculated in an automated way by developing a FORTRAN code to obtain the values from the profiles and these were compared to the results seen in the Stuve diagrams. The heights in the Stuve diagram were difficult to get accurately which is why the calculations were done numerically and checked graphically to ensure the results were sensible. The results of CAPE and CIN calculations for the FENNEC profiles are shown in figure (3.19). These CAPE and CIN

results are layer contributions defined as differential CAPE and CIN. Therefore, they are the layer contribution as a parcel ascends.

Table 3- 1. Lifted condensation level (ZLCL) of non-dusty and dusty days for the cases of FENNEC observations during 2011 and 2012.

Flight cases	ZLCL (m)	Time of flight obs. (UTC)	AERONET-AOD (Listed from low to high values)
FB700 (Non-dust)	**701**	**0752 To 0812**	**0.02**
FB708	**793**	**0756 To 0813**	**0.04**
FB600	**815**	**0748 To 0806**	**0.06**
FB601	**823**	**1442 To 1459**	**0.06**
FB611	**872**	**1400 To 1426**	**0.06**
FB702	**850**	**0740 To 0820**	**0.06**
FB705	**1183**	**1113 To 1143**	**0.06**
FB609	**1104**	**1106 To 1145**	**0.07**
FB699	**1061**	**1355 To 1415**	**0.07**
FB604 (very dusty)	**1491**	**1247 To 1309**	**0.2**
FB612 (dusty)	**1064**	**0702 To 0739**	**0.2**
FB613 (dusty)	**936**	**1355 To 1415**	**0.2**
FB605 (very dusty)	**1644**	**0809 To 0829**	**0.5**

For dusty cases, the values of CAPE are larger than for non-dusty days and the CIN values are much larger for the dusty days. The effect of the dust on the thermodynamics can inhibit the convection process significantly at the top of the MBL, indicated by the negative values of CIN calculation where the stronger inversion is established by the intrusion and warming of the dust

layer. The results in figure (3.19) show that dusty days have significant CIN at the lower levels and if a parcel does break through this, then there is not much CAPE to encourage convection. For CIN, there is an increased magnitude just below the SAL where the potential temperature increases significantly from 20 J/kg in FB700 to about 60 J/kg in FB605, to match with the SAL, but if an air parcel breaks through the CIN then it benefits from CAPE for the dusty cases where there is easy passage of air parcels through the well-mixed dusty layers. In thesis calculations, the ZLCL is determined from the temperature profile and the water vapour content at the surface, lifted vertically, within an environmental profile. Since the profiles are taken from the aircraft flights, the lowest layers will be over the Fuerteventura Island at about 60 m which isn't representative of the near ocean surface where water vapour will tend to equilibrium with the ocean surface. Therefore, I replace the water vapour in this lowest level with its saturation value to approximate the air being over the ocean. The significance of African dust in the dusty marine atmosphere is that the dust layer can contribute to inhibiting convective underneath the base of the SAL. Thus, dust can inhibit the convection process that is responsible for cloud production across the Atlantic. However, the effect of SAL on CAPE results may not attributed to dust alone

only, since the amount of water vapour from flight observations is observed to have significant values within the SAL. This will clarify further in Chapter 4.

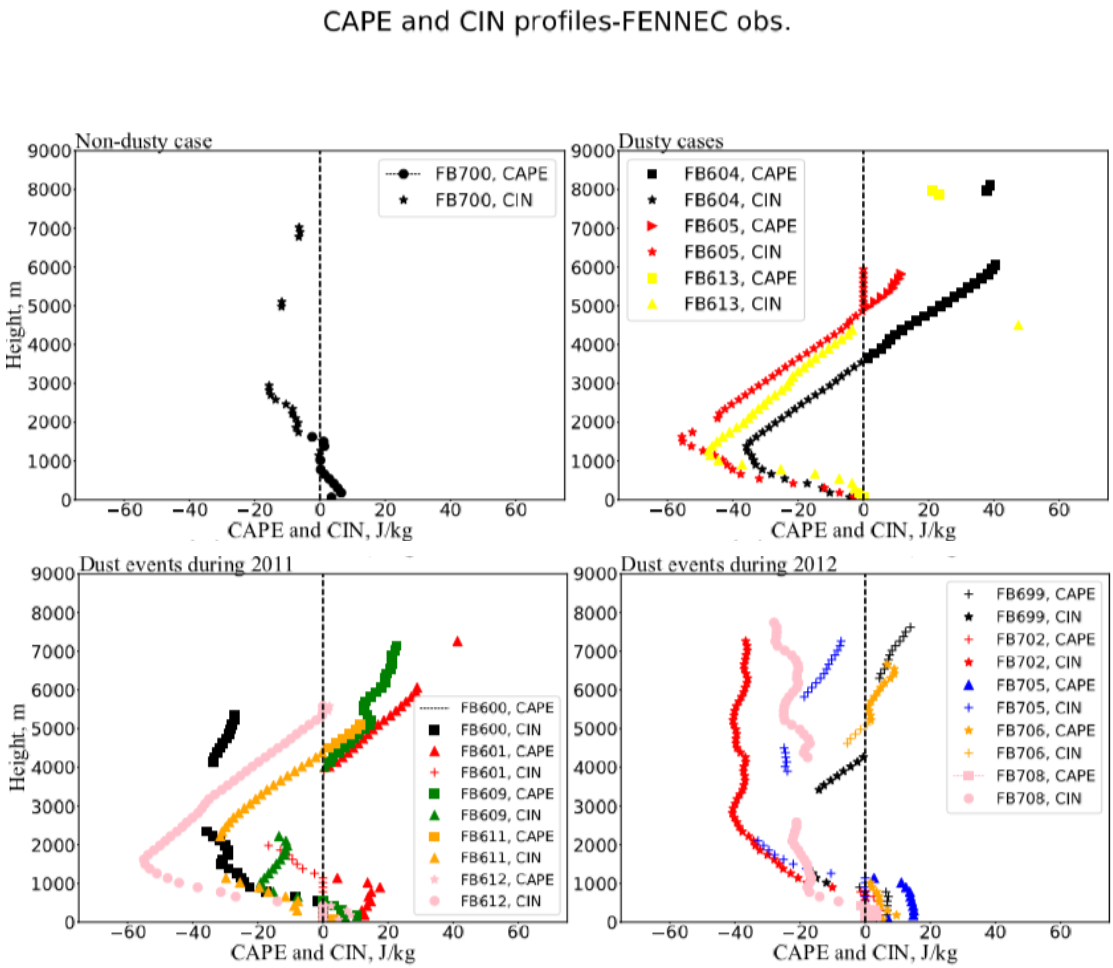

Figure 3. 19. Vertical contributions of CAPE and CIN in units of J/kg calculated from FENNEC observations over the study region. The top left panel is a non-dust event FB700 and the top right panel are dusty cases. The left panel in the bottom are CAPE and CIN profiles for all dust-event cases during June 2011, and the right panel at the bottom is the same for 2012. The CAPE values are represented as positive magnitudes while CIN are negative values in all plots. The flight cases are from FENNEC measurements shown previously, which are include flight observations during June 2011 and June 2012. Except flight number FB704, which is ignored in this calculation due to large multiple gaps in the data of water vapour. It is obvious that during dusty days there are increased values of convective inhibition (compared to non-dusty days) from about 20 to 60 J/kg (increased by more than double value). Although the maximum values of CAPE/CIN are not huge in general, but there are significant differences in the CAPE and CIN calculations between non-dusty and dust cases.

3.5 Evaluating air sources using HYSPLIT trajectories

Using HYSPLIT trajectories is a standard technique for determining air mass sources and can be used for the thesis cases to determine the recent history of air masses and whether they are advecting over sources of dust. There are limitations in the assessment of dust-carrying air layers with altitudes when comparing to satellite imagery observations. HYSPLIT uncertainties can be related to these trajectory models being unable to provide information about land surface conditions such as surface wind and soil properties. For example, Ryder et al. (2018) and Trzeciak

et al. (2017) show there is inconsistency between backward trajectories and satellite images such as SEVIRI satellite observation, in which the back trajectories of air masses does not provide an adequate background of dust outflows and dust transportation at lower heights over the Sahara. They suggest that it is not an accurate approach using tracer transport trajectories to determine the dust air mass sources. However, calculating air mass trajectories at specific points away from the dust sources may have better information, especially over the Atlantic, where backward trajectories across the Atlantic (e.g. Caribbean region) indicate that more than half number of total mass trajectories of dust event days originate from the African dust during the year in the period 1996 - 2014. This is shown by Merino et al. (2018) who estimated 167 days (daily averages) over these years (i.e. for 19 year) to track backward trajectories at the Caribbean back to the origin of dust over the African land. They state that there is air mass consistency between African dust and dust-carrying air layers. Using trajectories can determine the dust layer at mid and high altitude, about 3.5 km and upwards, during the summer season from the period May to September across the Atlantic, but during winter this occurs in the opposite direction, in which dust layers tend to be in the lower altitude over the Atlantic.

Over the Canary Islands, African air masses show a low fraction of dusty air for air mass sources as using backward trajectories over Tenerife station. Alonso-Pérez et al. (2007) identified about 54 dust intrusions, on average, into the marine environment per year with total of 322 dust outbreak air masses advecting over the Canary Islands over five years from 1998 to 2003. They used back trajectories to objectively identify the air sources by calculating trajectories at three low heights of 0.2, 1.5 and 2.4 km to identify what was originating from north Africa. The low contribution of dusty air in comparison with non-dusty air advecting towards the Canary Islands can be explained by the role of prevailing wind, which blows from east to west and south-easterly to north-westerly directions, where the wind in this area is characterised by a complicated interaction of African Easterly Jet (AEJ) and African Trade Wind (ATW) caused by pressure-temperature gradients between the marine environment and African continent.

Other possible causes of the low source for dusty air masses may be diluting of the air by other air masses from different sources. Wind advection provides the transportation of dust from the African land towards the west or other directions including the Canary Islands. But it can be difficult to determine just from wind the vector plots the paths of air that combine to arrive at a location. Therefore, HYSPLIT backward trajectories are used to investigate the sources of air masses that are involved in determining the dust contributions and the diluting effects of dusty and non-dusty air for this region. Figure (3.20) and figure (3.21) present results from investigating the sources of air masses over the Canary Islands by using HYSPLIT backward trajectories associated with dusty and non-dust events in marine atmospheric layers, respectively. The model was run over 48 hours in time and based on GDAS0P5 meteorology in the region of the Canary Islands. I show here in these figures the trajectories within SAL, i.e. focused on the air mass

trajectories within the depth height of the SAL for typical dusty and non-dust events: non-dusty (FB700) and dusty case (FB604) events. The ensemble air mass trajectories were used to show the sources of dust-carrying layers at various heights including 2220 m, 3060 m, 4020 m, and 5100 m (I show here trajectories at one selected height (4020 m) for FB604 and FB700, while the other heights will be shown in Appendix A1 and A2). HYPSPLIT was run as an ensemble with a total number of 27 trajectories from individual meteorological field to assess the air masses. The figure (3.20) shows that most of the air masses come from the east and south-easterly regions and sometimes from north-easterly regions of the African land for dusty days. In contrast, figure (3.21) displays air mass trajectories for the non-dusty FB700 case generated from the eastern sub-subtropical north Atlantic at high altitude (about 8 km) which can be characterised by cool and non-dusty air sources.

The backward trajectories show similar trends to previous studies in showing the source locations and transport times of dust in the south-easterly part of the African continent, but sometimes the time of dust transport is less than as determined by Ryder et al. (2013a). Their results stated that the SAL is arrived at Canary Islands after approximately 18 hours of advection. The backward trajectories shown in figure (3.20) indicate that in the thesis cases the advection took about 13 hours to arrive at Fuerteventura, and of course depends strongly on the strength of winds for each case. Also, note that some air contributing to the observations originated from the ocean regions and gathered dust from the western Saharan coastal line and then returned to the Canary Islands. It is possible that the observed peaks in water vapour in the SAL may be contributed because of this transport over ocean before picking up dust. In addition, the backward trajectories over the Canary Islands point to the air masses originating from the African coastline at high levels (up to 8 km) at least by the end of the model simulation.

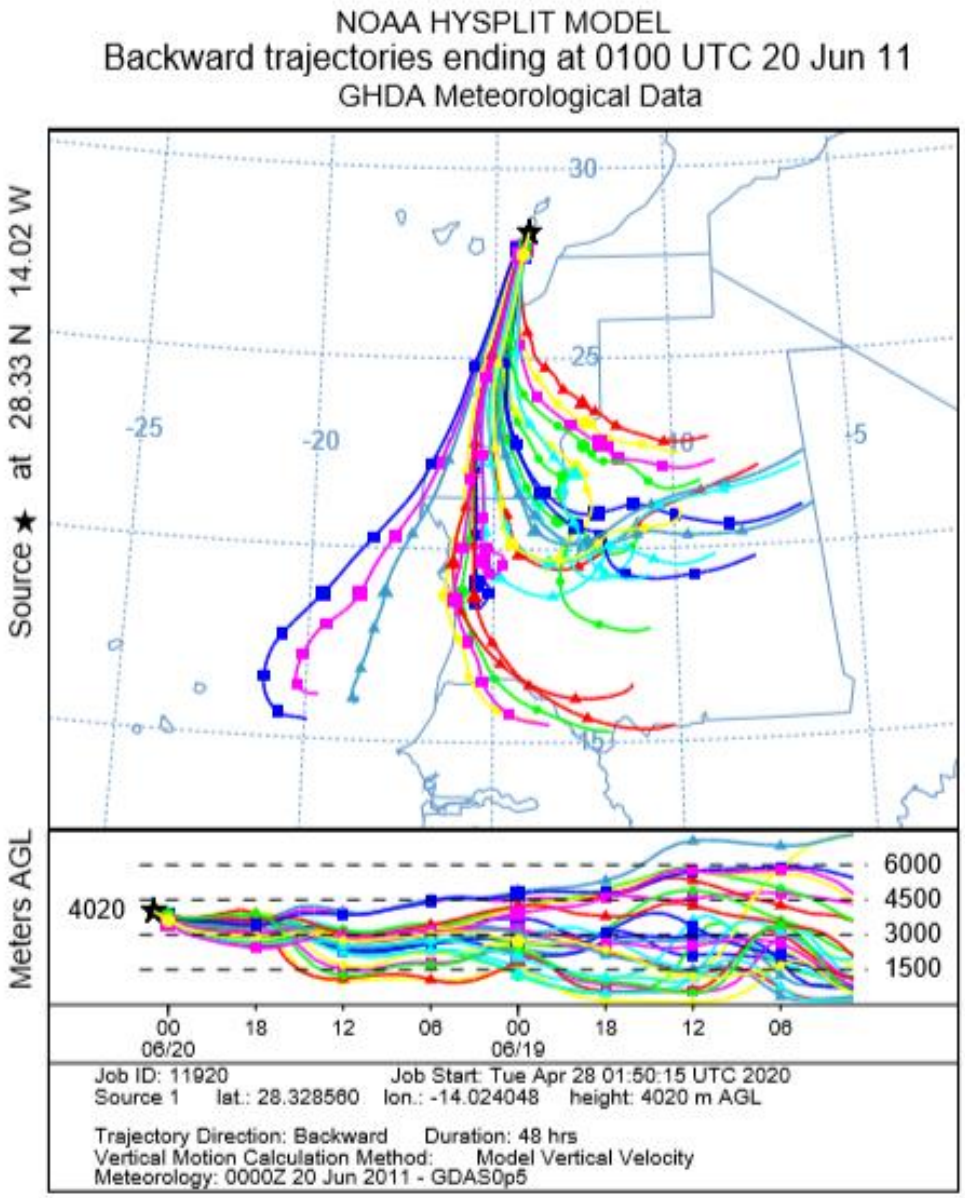

Figure 3. 20. Backward trajectories from NOAA HYSPLIT model during June 2011 with height 4020 m. The ensemble trajectories are obtained by running the HYSPLIT model at 0.5 degree and the model results here show trajectory intervals (time does not represent how long time takes for the model) every 6 hour on the map over 48 hours over Fuerteventura (Canary Islands). The model was started at 28.2 latitude and -14.02 longitude at the Canary Islands. Runs show backward air mass sources of the dust event for flight number FB604.

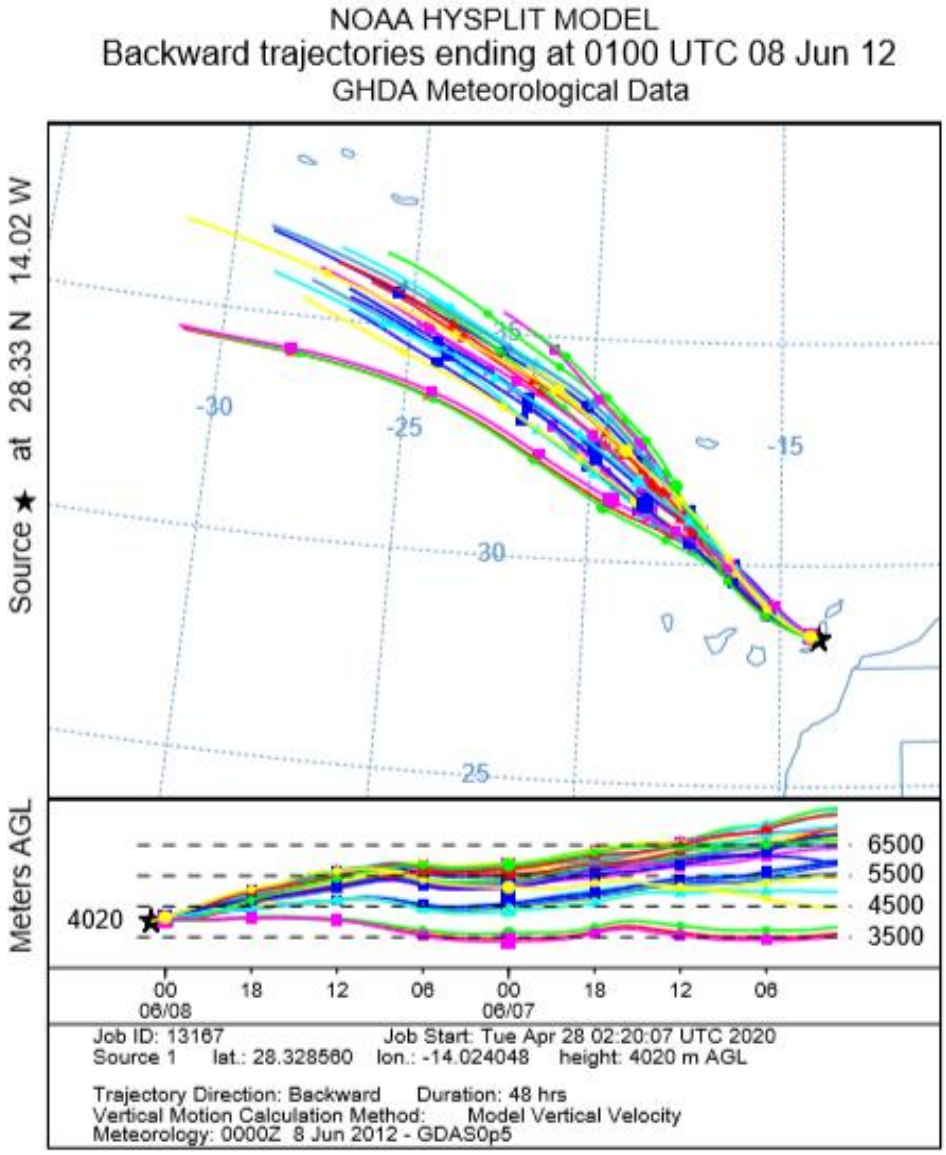

Figure 3. 21. As figure (3.20), but for non-dust case (FB700).

Forward trajectories show that air masses from north Africa have complicated paths even though the mass loading from satellites shows quite a simple trend of dust being transported mostly over the Atlantic towards the west and some mass observed being transported to the north. However, from figures (3.22) – (3.23), forward air mass trajectories from north Africa are not necessarily matched with these overall movements when looking at individual trajectories. This can be caused by the difference in the trajectory dispersion between the forward and backward results, where the forward trajectory is quite constrained, but the backward air mass trajectory is so dispersed. One of the main reasons for using a back trajectory approach is that I know the observing location I am interested in and to determine where the air comes from that reaches this point then using the forward trajectory approach would mean starting countless forward trajectories from all around the site including all of Africa and all of the ocean nearby to determine

which small fraction of trajectories went through the study region, which is impractical. Using an ensemble of back trajectories from the location allows an assessment of the main origins of the air and the proportion from dusty and non-dusty sources. Trajectories are useful in this research, however, for starting trajectories where the dust is located to evaluate how much from a source region is likely to advect in a direction towards the study region and back trajectories to see where dust is coming from (not just a chosen start location). Therefore, a combination of approaches is most useful as both have benefits and shortfalls with both forward and backward linking the sources of dust from north Africa and the study region in order to determine the air mass sources and time evolution of dust transported over the Atlantic.

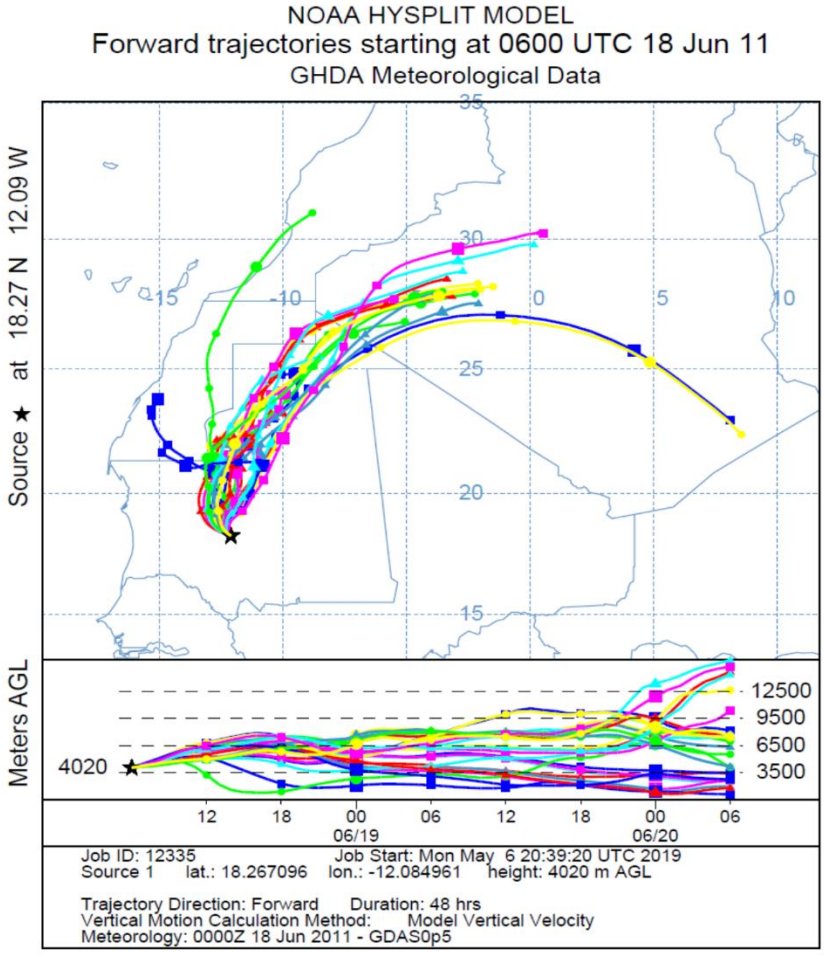

Figure 3. 22. Forward trajectories from NOAA HYSPLIT model during June 2011 with 4020m. The ensemble trajectories are obtained by running the HYSPLIT model at 0.5 degree and they are shown with symbols every 6 hours of simulated time and with time duration of 48 hours over Fuerteventura (Canary Islands). The model runs start at 18.2 latitude and -12.08 longitude at western Saharan. Runs show forward air mass sources of the dust event for flight number FB604.

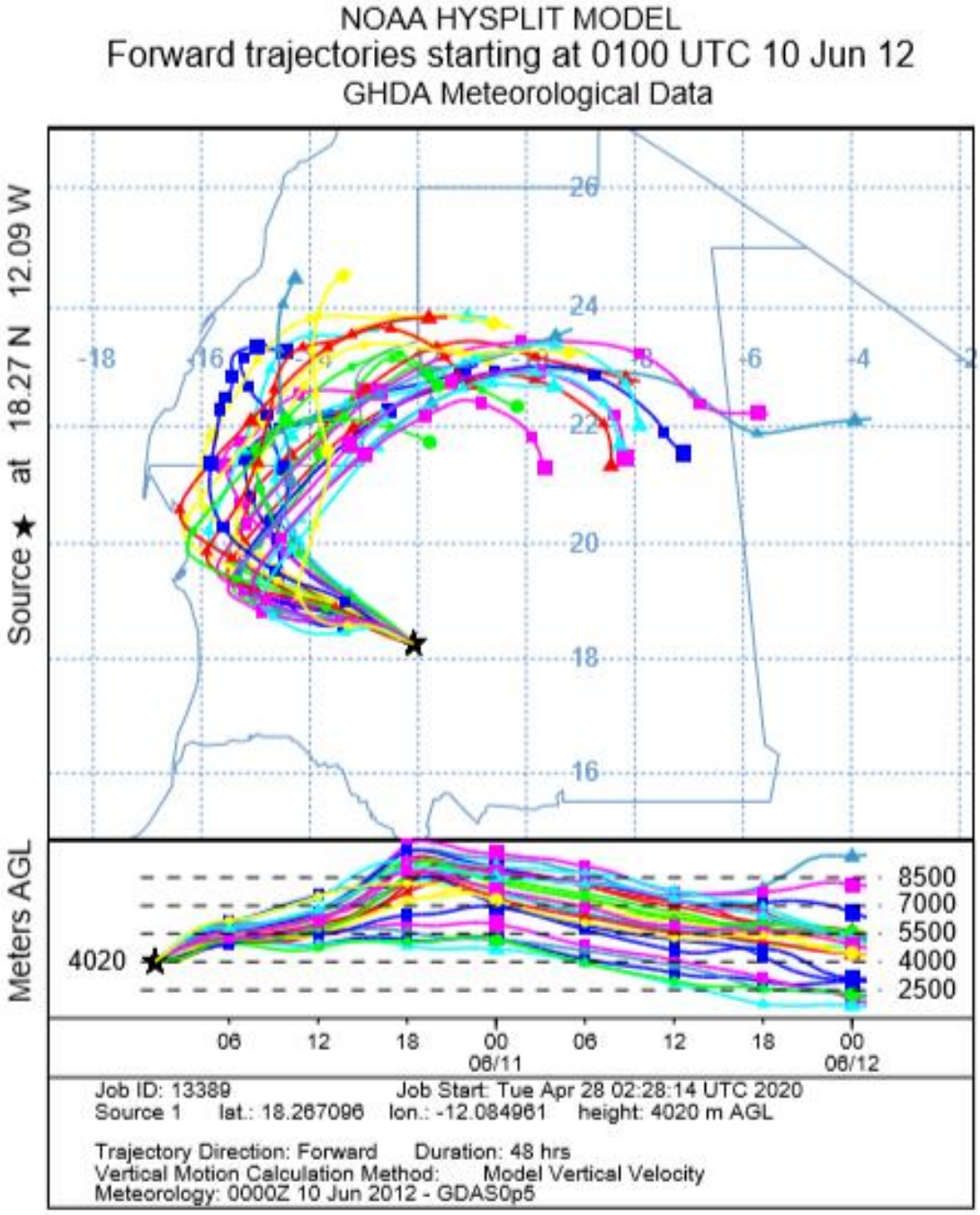

Figure 3. 23. As figure (3.22), but for non-dust event, FB700.

3.6 Summary

In this chapter, dust profiles and atmospheric conditions were presented for the study region. First, the study region was defined as being the area of the Canary Islands approximately 100 km northern west from the west African coastline in the eastern part of the Atlantic Ocean. The purpose of selecting this region was that the Canary Islands is susceptible to frequent outbreaks of advected African dust, especially during summer season from the northern part of Africa. Based on this, determining vertical profiles of dust layers is important to investigate the radiative influences of these dust outbreaks in the vertical structure of the marine atmospheric environment. FENNEC flight observations were considered to quantify dust profiles, in which size distributions of the MBL, SAL and total were evaluated and presented. Calculating vertical profiles of dust were performed using plausible dust optical properties provided from Ryder et al. (2013a). In this work, a recalibration (i.e. generating particle diameters and channel widths) was performed based on the discrete method of Rosenberg et al. (2012) for the PCASP data from FENNEC observations due to the more accurate procedure developed by Rosenberg et al. (2012) in deriving sizes from the scattering observations of the instrument. The calibration method was also applied for CDP data that was provided by Rosenberg et al. (2012) based on both a Microsoft-generated scattering cross section and Mie scattering. Although the calibration method is similar to that worked by Ryder et al. (2013a and b), deriving particle size and channel width was based on using a combination of RIs from Ryder et al. (2018), Ryder et al. (2013), Ryder et al. (2013b) and Rosenberg et al. (2012) for flight cases not only during 2011 but also for more flights during 2012.

The calibration method was tested for two different calibration files in these flight observations and calibration results show no significant changes between flights 2011 and 2012. In addition, the dust profiles based on this calibration method were used not only over the Canary Islands but also away from the African land. Moreover, Observations were derived from both these instruments using plausible refractive indexes for Saharan dust. Lastly, the dust size distributions for all the flights were then developed using these re-binned and updated refractive indexes and presented. These will be used in Chapter 4 to obtain dust heating rates for the LEM simulations and in Chapter 5 to perform sedimentation/turbulence model runs.

The results from the FENNEC flights were then categorised based on MODIS-Terra and AERONET observations for AOD to determine low/non, moderate and high dust cases. The potential existence of dust profiles was identified between about 2 and up to 6 km with the removing of the sea salt concentration from within the MBL. Comparison of the dust mass loading between observations over the Atlantic with literature showed that maximum dust profiles in this research are in a lower magnitude category compared with Ryder et al. (2019) for the Atlantic. In addition, uncertainty in dust profiles over land (i.e. high dust concentrations up to 2 km) from the FENNEC observations is probably caused by the convection process rather than sea salt concentrations.

In this research, thermodynamic and wind profiles were discussed and presented, illustrating a well-mixed potential temperature region where the SAL resides with the differential CAPE increased in the layer and the differential CIN increased below this layer in comparison to the other categories. Dust contributes to increasing the height of the lifted condensation level (ZLCL) to more than double the height compared to non-dusty days due to the high temperature caused by dust and gaseous effects absorbing radiation requiring air parcels to need to ascend to higher heights if they are to reach saturation. The warm dusty air intruding into the marine background air brought with it the well-mixed region along with the strengthening of the inversion above the MBL. This then inhibits convection as it makes air potentially ascending to higher heights more challenging. Thus, quantification of dust radiative effects is mainly dependent on the amount of dust and water vapour in the vertical and their associated optics.

Air mass trajectories corresponding to dust outbreaks provide good insight in determining the origin of air masses over the Canary Islands. There is good agreement between dusty events and the air mass back trajectories coming from sources of dust (i.e. African land). Whereas, forward trajectories were shown to have strengths in determining what fraction of dusty air makes it to the Canary Islands from a source region.

Overall, this chapter presents the study region, shows the results for the dust profiles, provides the results for the re-binning of the dust, categorises the dusty/non-dusty days, assesses the CAPE/CIN to characterise the dusty and non-dusty days, and provides information from trajectories as to where the air masses originated before advecting to the study area of the Canary Islands.

4 Chapter 4: Dust radiative effects on the structure of the dusty marine environment

4.1 Overview

Previous Chapters 2 and 3 have presented a wide range of material covering the study area focused on, the research tools and data used, the work undertaken to rebin the dust size distributions, and information and characterising the dust and non-dust events. This chapter now builds on this to investigate the effects of atmospheric Saharan dust on the evolution of the structure of the marine atmosphere using the UK Met Office LEM model with flight observations from the FENNEC campaign. The following questions were addressed:

1. What are the general changes to the atmospheric structure of the marine environment brought about by the presence of a SAL as it transports over the Atlantic Ocean to the Canary Islands?
2. When a SAL enters a non-dusty marine environment, will the stratified layer turn well-mixed and how long will that process take?
3. What is the strength of the water vapour radiative effects and does it play a role in affecting the structure of the atmosphere with a SAL for this study region?
4. What happens to a well-mixed SAL if the dust falls out and the layer begins to revert to a non-dusty marine environment? Will the layer stratify and over what timescale?
5. How does the atmospheric dust affect the stability of the atmosphere, and is it likely to affect convection downwind?

In this study, the simulation of dust heating rates is performed by two methods, which are 1) by using dust heating rates used from previous studies in the literature (i.e. based on Otto et al., 2007 and Zhu et al., 2007 cases), and 2) dust heating rates calculated directly from observations using the FENNEC observations, optical properties spectral files and radiative calculations by the Edwards-Slingo radiation model (ES). The LEM was run using the thermodynamic and wind profiles from flight data including θ, wind speed components, specific humidity and the radiative heating rates from both methods stated above. Large-scale subsidence was taken from ECMWF reanalysis results. Further information on the heating rates is provided in the next sections.

This chapter addresses the change in the net fluxes as a function of height, which is considered as part of dust-direct radiative forcing evaluated at the top of atmosphere (Zhao et al., 2010; Bellouin et al., 2005; Li et al., 2004; Weaver et al., 2002). The net fluxes can be calculated based on Eqs (15) – (20) in Chapter 1. Differences in net fluxes between dust presence and dust absence for

both SW and LW radiation (and individually) will be presented in this chapter in the section on radiative fluxes.

4.2 Heating rates based on Otto et al. (2007) and Zhu et al. (2007)

In this first method, I use dust heating rates based on previous studies by others where simulated heating rates used in the LEM pertain to dust effects only, without gases impact. As explained previously, I use a large value from the literature to estimate what the effects of the heating rates could be for the more extreme cases. The heating rate profiles are based on dust-only Zhu et al. (2007), and Otto et al. (2007) is used only to adjust the magnitude to be representative of large peak values. It is approximate and if results are significant then more rigorous calculations will be performed (and used in any publications to follow from this work). It is also a simple approach to estimate the possible effects before undertaking detailed analysis involving processing dust size distributions from the FENNEC observations. So although using dust heating rates based on Zhu et al. (2007) and with incorporated a peak heating rate value from Otto et al. (2007) may cause a large effect because they are some of the largest heating rates for this area, this approach allows to perform a quick estimate of what is the potential impact of a dust layer on changing the thermodynamic and dynamic characterization of the dusty marine environment. In addition, comparison between dust heating rates based on maximum value from these studies and generated value from flight observations provides supporting to understand dust radiative effects on study region.

This method uses the peak value of dust heating rates from Otto et al. (2007) of 9 K/day and 9.56 K/day for SW and LW radiation, respectively. These peak values of heating rates were included in the vertical heating rates of Zhu et al. (2007) to get actual profiles of dust heating rates for the SW, LW and total that used in the LEM. In this section, the discussion of heating rate profiles is only related to dust effect and without other gaseous component impacts.

Figure (4.1) shows the LEM simulation of dust heating rates only over 8 hours that are calculated based on the scaled vertical profiles from Zhu et al. (2007) to the peak values of Otto et al. (2007). The heating rate profiles were used in simulations for the effect of dust with short-wave (red line) effects only, for dust interacting with the long-wave (green line) radiation only, and total radiative effects of combined short-wave and long-wave effects on (blue line), where DSW, DLW and DT indicate dust SW, dust LW and dust Total radiation. The black lines in the figure shows observed profiles from the FENNEC data. The figure presents the profiles of potential temperature from the LEM simulation over an 8 hour time simulation over the Atlantic Ocean (surface albedo and large scale subsidence taken to be over the Atlantic Ocean as the dust transports over water) for cases of non-dusty (FB708) and dusty (FB604 and FB605) cases, where the peak heating rates were used for only dust effect in all flight cases. I investigate the radiative effects for the non-

dusty case FB708 to evaluate what would occur if dust only was to become present in an otherwise background non-dusty layer.

There are generally three effects taking place in these plots. There is shortwave warming of the dust layer which is warming the profile of θ in all figures at heights roughly between 3 and 5.5 km. Then there are two effects taking place from the longwave. There is loss of LW from the top of the dusty layer to space and there is trapping of LW radiation upwelling from the surface within and below the dust layer. The first cools the profile of θ at the top and above the dust layer and the second warms the dust layer and the atmosphere both within and below the layer.

In terms of the dust influencing the structure of the atmosphere, it can be seen from the figure (4.1) that the LW is more influential on the evolution of the structure of atmosphere. It causes a well-mixed layer during the early morning and day times.

So, the strong values taken from Zhu et al. (2007) and Otto et al. (2007) indicate that the radiation due to dust effect only can have important effects on the structure, therefore, the next step was to consider dust profiles and heating rates more relevant to the case by using the dust profiles from the FENNEC flight observations. To fulfil this, optical properties from the FENNEC observations were provided from Ryder et al. (2013a) and the dust profiles were prepared according to the previous chapter and used to determine the heating and cooling rates by using the ES radiation model. These heating rate profiles are then applied in the LEM for 8-hour simulations to determine the effects on the structure.

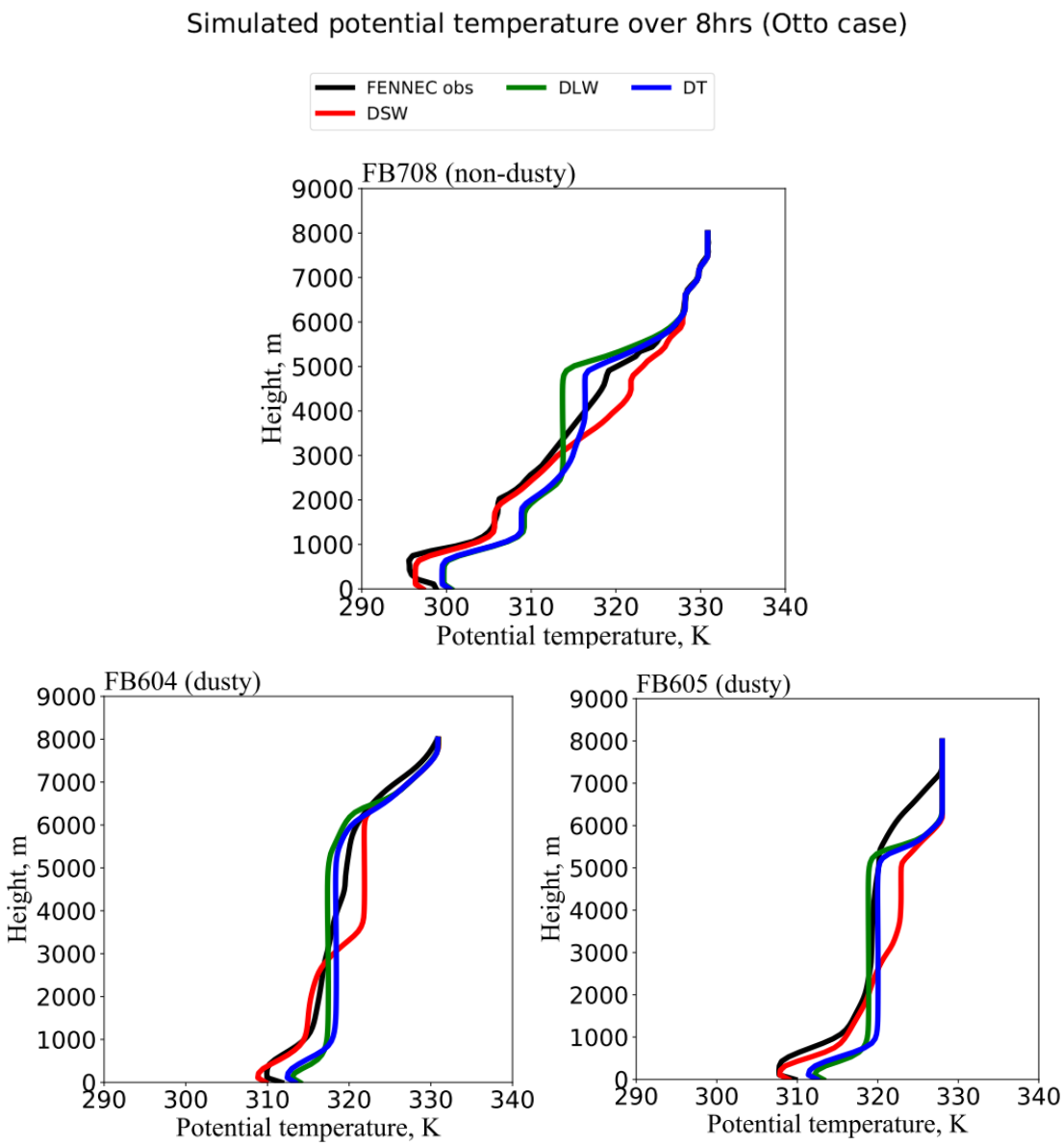

Figure 4. 1. Potential temperature profiles (in unit of Kelvin) from LEM simulations obtained by using observed profiles from FENNEC observations and included dust heating rates from Otto et al. (2007) in the vertical profiles of Zhu et al. (2007) cases during 8-hour time simulations over the Canary Islands. The top panel is for non-dust (FB708), while left below panel and right below panel are for dusty cases FB604 and FB605. Profile of flight observations is indicated by black lines in all cases; whereas red, green and blue lines show the results of potential temperature from LEM runs including dust SW (DSW) only (long wave is off), dust LW (DLW) (solar is off) and dust Total (DT) radiation (in which both LW and SW are on), respectively. Simulation runs by using only dust heating rate profiles of SW and LW heating rates (heating rates were taken from Zhu et al., 2007) that are scaled to the peak values of Otto et al. (2007).

4.3 FENNEC dust heating rates

Dust heating rates were generated based on flight observations using the profiles from FENNEC-PCASP and CDP instrument measurements. In this, I used the observed giant particles in the dust profiles measured by the CIP instrument. Input meteorological data, including temperature, water vapour, atmospheric pressure (taken from FENNEC measurements) and other gases taken from

previous studies (shown in the previous Chapter 3) were used in the ES radiation model with the correction applied for missing data in the vertical, particularly the water vapour profile, which was corrected by interpolating the data linearly across each vertical gap. Deriving dust heating rates for these instruments is implemented using the ES radiation model. In this thesis, heating rates were derived by using different solar times based on FENNEC observations (section 4.3.1) and I derived heating rates associated with solar time elevations from early morning to afternoon (section 4.4). For the first process (i.e. derived heating rates based on flight time observations), heating rates were generated by using data profiles from flight observations, where the initial time of observation (and associated SZA) is different in each flight case. The second approach (i.e. derived heating rates based on time-varied started from morning to afternoon), comprises generating heating rates based on the elevation of sun from morning to afternoon times. The derived heating rates based on these approaches were then used in the setup file of the LEM separately for the SW, LW and total radiation. The purpose of considering these methods is to understand the importance of solar changes on the heating rates and thus radiative effects of dust and water vapour factors will be accounted. Dust heating rates will be explained in the next subsections.

4.3.1 Dust heating rate profiles using data from PCASP and CDP measurements

The atmospheric structure over the Atlantic is shown for a non-dusty outbreak case in figure (4.2) (blue line). Figure (4.2) shows the vertical structure of potential temperature calculated by FENNEC observations for the Fuerteventura region. The θ profile is representative of non-dusty conditions, in which the atmosphere is mostly stratified for the whole potential temperature profile. When dust advects from north Africa into the marine environment, the layer of Saharan dust (as mentioned in Chapter 1) will intrude into the atmospheric layers over the Atlantic. The SAL is generally believed to be dry and warm and its temperature will be higher than the air of a similar altitude over the Atlantic, so it will rise up and over the MBL until the equilibrium is found where the potential temperatures matches the environment. It is interesting to note that in many cases the observations indicate that the dust layer is characterised by containing significant amounts of moisture present within dust layer, see humidity profiles in flight cases FB604, FB605 and FB708, Chapter 3.

In this environment, the radiative effects over the Atlantic will be controlled by the evolution of dust during transport as well as the amount and vertical distribution of water vapour. The impact of enhanced water vapour in the SAL is evaluated by comparing elevated water vapour profiles from dusty cases to a background water vapour profile that is representative of the non-dusty background marine environment. For example, I would derive heating rates of dust and water vapour for a dusty case such as FB604 and compare to a similar case using the same FB604 dust profile but with a non-dust outbreak background water vapour profile such as FB708. Note,

FB700 and FB708 are considered non-dusty background marine profiles of water vapour for our purposes.

This represents a good way to investigate the radiative effect of enhanced water vapour compared with dust effect. I initially used a used a zero water vapour data approach but it was unrealistic. In addition to the water vapour comparison, two other runs will also be performed: the first run is with the absence of dust (i.e. dust =0) and using the observed FB604 water vapour and second run is with using water vapour from FB708 but with dust set to zero. By these run tests, the contribution of dust and enhanced water vapour can be investigated in the SAL.

To set up data for radiation and hence LEM simulation, meteorology, and dust profiles from FENNEC observations over the Canary Islands in the LEM are utilized to simulate the effects of the dust/water vapour on the atmosphere for 8 hours near the Canary Islands and dust radiative effects are related to the evolution of dust profiles the background marine environment.

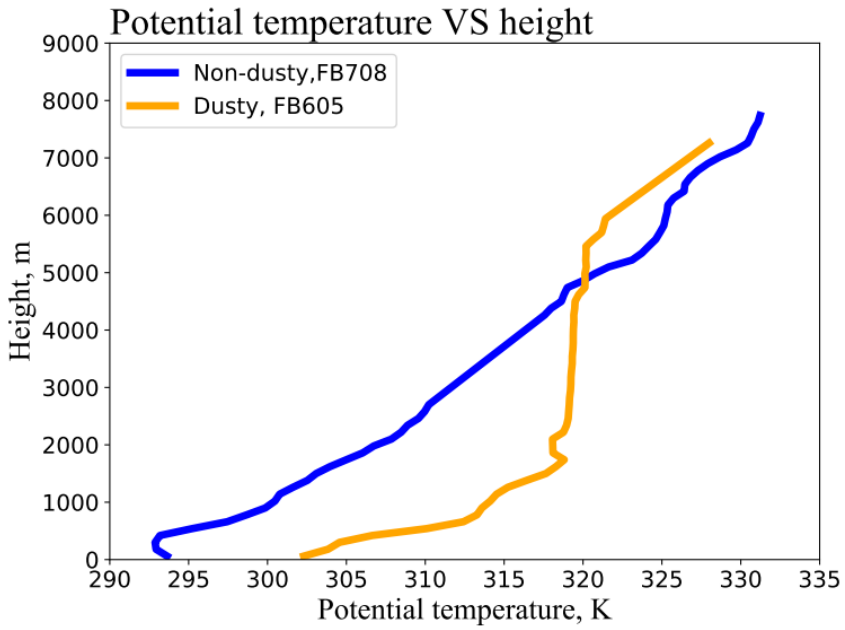

Figure 4. 2. The profiles of potential temperature (K) for non-dusty (blue line) and dusty (orange line) days from FENNEC observations over the study region. This plot shows the θ profiles from flight observations for FB708 (non-dusty) and FB605 (dusty) cases. The structure of the marine environment during non-dusty clear sky is characterized by stratified profiles above the MBL, where the atmosphere is generally well-mixed up to 0.5 km but can be higher during the day for some periods. In contrast, the orange line in this figure shows that the θ profile is shifted to the right within the region of the dust layer from roughly 1.5 km up to 6 km. This means that dust layer changes the structure of θ from a stable layer to a neutrally unstable layer with significant depth of about 4.5 km in height. This large depth of dust can potentially change the radiative structure of atmosphere. Note these lines (i.e. blue and orange) are referring to different times of FENNEC observations, they are just representative of the characteristic non-dusty and dusty profiles, respectively.

Figure (4.3) shows derived dust heating rates for non-dusty flight FB708 (top left panel) and dusty flight FB604 (bottom left panel) cases under using SZA of value 66 degree. Top right and

bottom right panels show dust mass loading expressed in units of μg/m^3 over the Atlantic for FB708 and FB604, respectively. The first column shows dust heating rate profiles in units of K/day with using dust profiles and all gases (i.e. water vapour and other gases) for DSW (red line), DLW (green line) and DT (blue line). SW, LW and total dust heating rates are related to model results with using dust, water vapour and other gases. Other cases are shown in Appendix A3.

Presented are results using dust heating rates with water vapour effects for dusty cases and compared to heating rates with using non-dusty water vapour case based on flight FB708. In the current work, I used FB708 water vapour to be a representative non-dusty case and water vapour profile is taken to be represent the background non-dusty profile. Initially I tested cases with zero background water vapour but that was not representative of the background. This is because the realistic global atmosphere does not characteristic by zero amount of moisture and thus using zero wv profile in radiation consideration is an unrealistic method to be proceed. Dust heating rates in figure (4.3) were derived from the ES based on using PCASP and CDP data from FENNEC observations with setting solar zenith angle to 66 degrees where based on flight time measurements. Henceforth, dust mass profiles in all figures were used with sea salt concentrations removed, as detailed in Chapter 2. There are variations in dust heating rates during the early morning and afternoon measurements. During early morning (between 5 and 9 am), there is a slight warming in both MBL and dust layer in comparison to the afternoon time, while there is significant cooling by dust-LW effects at the top of atmosphere, see figures (A3.1) – (A3.2) in Appendix A3 for flights FB600, FB601, FB612, and FB613. During the non-dusty case FB708, heating rates have peak profiles with SW heating rate of less than 2 K/day, but there is a cooling (green line) of about -4 K/day at the top of the SAL. In the figure (4.3), LW cooling by dust effect is higher than LW cooling by other gas impacts (black dotted line). There are clearly significant radiative effects associated with the intensive dust loadings. For example, FB604 has SW heating rates with peak of about 3 K/day within SAL, but this value can reach with peak of 5.5 K/day during noon time, where SW heating rates reached about 5.5 K/day as SZA has a value of 10 degrees. In some cases, there is more than one peak of dust heating rates within SAL. This can be noticed at a height about 3 and 5.5 km with maximum SW heating rate value of roughly 3 K/day. The peak heating rate at 3 km matches well with the dust profile and the SW heating at 5.5 km is caused by radiation entering the top of the dust layer at this altitude for FB604. It will be interesting to investigate what is cause this cause of this unexpected peak in the profile. It is noted that the increase of heating rate with the increasing values of SZA allows an investigation of the heating rate dependency during the time evolution in the LEM simulation. This will be presented later in subsection 4.4.

Results in the current work show that the maximum value of dust heating rates during midday are lower than peak value from previous works outlined earlier, where for the current results, SW

and LW heating rates have peak value of about 5.5 K/day and -8 K/day, while peak value for Zhu et al. (2007) was 8 K/day and -9.46 K/day, respectively. In addition, the peak value of dust heating rates for solar radiation is likely to be greater than dust and other gases heating rate which stated by Carlson and Benjamin (1980) who show that heating rates of dust effect were added to heating rates caused by other atmospheric gases. Indeed, water vapour and other gases impact in a comparison with dust effect are needed to be investigate since flight observations in the current thesis indicate that SAL is characterised by enhanced water vapour. As results to thesis discussion, in figure (4.3) tests for considering dust and gases individually are required to understand what is the most important factor in influencing the heating rate structure?.

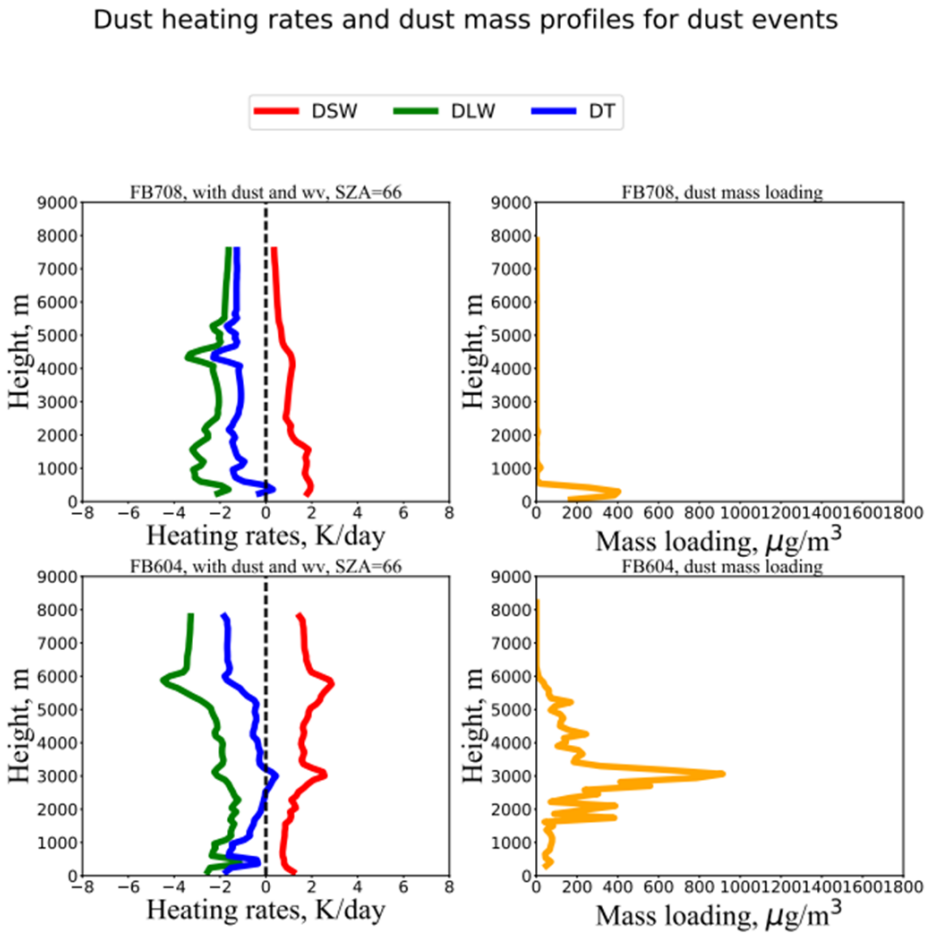

Figure 4. 3. Dust heating rates derived for non-dusty FB708 (top panel) against dusty FB604 (middle panel) in units of K/day associated with dust mass profiles expressed in units of μg/m^3 over the Atlantic. Panel below shows the heating rates derived for a typical dusty FB604 case and with using a realistic non-dusty water vapour profile. All profiles were derived with using RI=1.53+0.001i (value based on Ryder et al., 2013). Runs for FB604 and FB708 were performed with using SZA of 66 degrees. Red, green and blue lines display dust heating rates for SW, LW and total radiation, respectively. Vertical dashed line is plotted for distinguishing between positive and negative values of heating rates with vertical. In the figure, the label wv refers to water vapor.

4.3.2 Dust heating rates involving giant particles

Previous works such as Ryder et al. (2018) state that giant dust particles may have role in changing dust radiative effects due to high absorption by dust particles by the SW radiation. Therefore, to investigate the sensitivity to this, figure (4.4) displays the dust heating rate profiles in the presence of giant particles from FENNEC observations for the dusty case FB605. Other flight cases including FB601, FB605, FB609, FB611 and FB613 recorded giant particles but did not have significant impact on the heating rates, and so are not shown.

The heating rate profiles shown in figure (4.4) are represented as a typical dusty case (i.e. FB605), in which the SAL may carry large particles right across the Atlantic. But these giant aerosols have very large fall velocity and so will likely sediment out into the ocean. In this figure, heating rates were driven from using dust mass mixing ratio in the ES model with and without giant dust particles included. The size of CIP data used in deriving heating rates was greater than 45 μm. The solid coloured lines indicate heating profiles without giant particle while coloured stars refer to heating profiles with considering giant particles from the CIP data in the radiation results. Radiation results for dust heating rates from flight case FB605 shows peak values under 2 km, but other cases did not show these large values. One possibility can be explained about this, is the dynamics of the winds between African land and Canary Islands associated with the short distance between these regions. In other words, uplift wind from the African coastline toward the Canary Islands may contribute to sustaining large particles in the lower atmosphere at least at very near distances to dust sources (region between Canary Islands and African land). Another possibility is the impact of turbulent process on the development of dust transported over the Atlantic. So, the large dust particles that sediment due to their high sediment velocity can be trapped by turbulent mixing associated with dust transported into the marine environment, particularly within MBL. These probably explain why there is a peak in dust heating rates below 2 km with an increase in SW heating rates of about 1 K/day at this height. Turbulent process may keep these particles as they transport in the atmosphere off west Africa, but at far distances these giant particles will be likely fall to the surface. To conclude, giant particles of dust may influence heating rates, and thus have an impact on the dust radiative effects, but this needs to be investigated in the LEM simulation for a much more accurate assessment. In this chapter, simulating dust heating rates for giant dust particles will be investigated in the LEM by taking the dusty case (I will consider here flight case FB605) and seeing if the radiative impact of the dust for SW and LW will cause a significant change on the atmosphere.

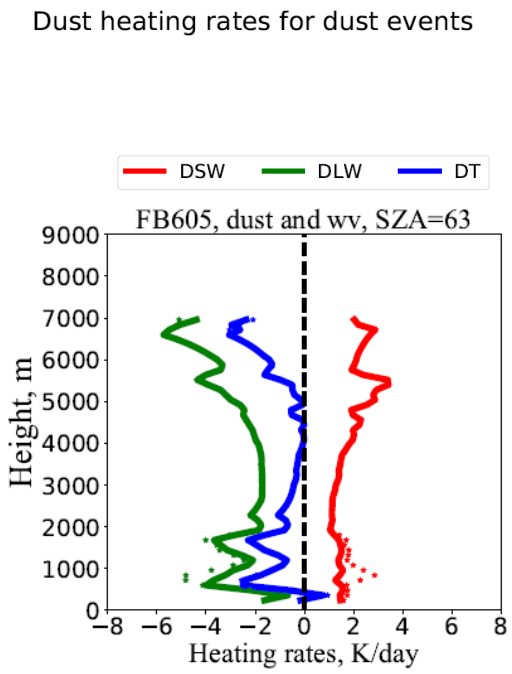

Figure 4. 4. Vertical dust heating rates in units of K/day from radiation results for FB605 with SZA=63. Red lines show SW heating rates, while blue and green lines indicate to heating rates for LW and total radiation, respectively. Stars show heating rates involving giant dust particles (i.e. CIP data) in the mass mixing ratio of dust particles with size of > 45 µm. Giant particles that captured by flight observations for other cases (i.e. FB601, FB604, FB609, FB611 and FB613) did not show significant change in heating rate profiles and therefore, these cases are not presented here.

4.4 Dust heating rates associated with water vapour

Dust and water vapour heating rates based on flight observations are presented in previous section 4.3. As mentioned in Chapter 2, the dust layer shows significant values of humidity over the Atlantic and these high values of water vapour in the SAL can influence the heating rates profiles. So, in this section I will evaluate the impact of dust, water vapour and other gases in the thermodynamic structure of MA, especially in the SAL. Figure (4.5) displays the vertical heating rates generated from ES using four tests (i.e. FB604, FB605 and FB613) isolating different factors including: 1) First column: run includes all the factors including dust, water vapour and other gaseous profiles. 2) Second column: run uses dust profile for each dusty case and with using water vapour from non-dusty case (FB708) with all the other factors included. 3) Third column: this run has dust set to zero with all other factors included. 4) Fourth column: run has dust set to zero and

with using water vapour profile from FB708 so it is run with gaseous effects included. The SZA in each plot was taken from the initial value of FENNEC time observations, where the derived heating rates are not the same in each flight case since each flight has different time observations. Therefore, heating rates will be derived also by considering the variation in solar time between early morning and afternoon time with using the same SZA in the radiation model for all flight cases. This will be explained in next section 4.4.

The results in figure (4.5) show clearly that water vapour is the most important factor in these numerical tests in all these cases by contributing most significantly to the heating and cooling rates, see second and third columns for run experiments 2 and 3. Where the fourth column shows that other gases (i.e. in the absence of dust and with water vapour based on a background amount of FB708 and with other gaseous contributions included) have a cooling effect within and above the SAL but far less than dust and water vapour effects. I note that during intensive dust events (e.g. FB604), water vapour has a very significant impact on heating rates especially within the SAL.

It is noted that in general the SW heating rate for the dusty case FB605 (see second row), is lower than for other dusty cases of flights FB604 and FB613. This is because FB605 initialises with a larger value of SZA (non-peak of solar heating during daytime), where it has a value of 63 degrees as compared to 10 degrees for solar zenith angle for flight FB604 and 13 degrees for flight FB613. So, based on these heating rates for dust and water vapour, the most important finding here is that water vapour is elevated within the SAL and this indicates that water vapour plays the most important role in determining the thermodynamic structure of the dusty marine atmospheric, especially above 3 km. The key point in simulating elevated water vapour in the SAL is to contrast it to the non-dusty wv case. I have studied the elevated wv effects of dusty outbreaks compared to both no wv and to background wv typical of low or non-dusty days. It is clear from these heating rates that the contribution of elevated water vapour is just as important if not more important than the dust when considering what is controlling the structure of the MA during dusty outbreaks. The effects on the structure accounting for the dynamical links to the heating rates is included in later work using the LEM. The simulation results will be presented in section 4.10.

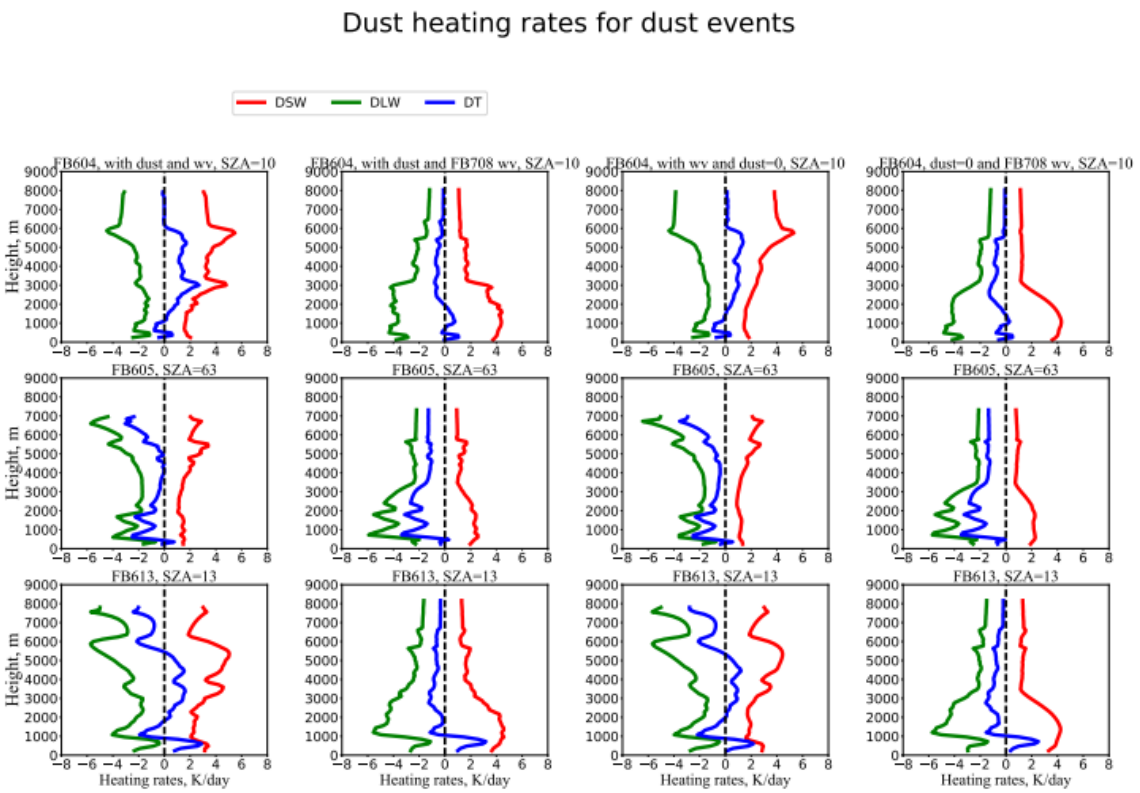

Figure 4. 5. Heating rates profiles (K/day) contrasting the effects of dust and water vapour (wv) for 8-hour simulations over the Canary Islands. The heating rate profiles with both dust and wv included (first column), heating rates using dust but with using wv profile from FB708 (second column), heating rates with using water vapour and other gases but with dust set to zero (third column), and (fourth column) heating rates with gasses impact only, i.e. with using wv for FB708 and with set dust to zero. Red lines present SW heating rates, green lines show LW heating rates and blue lines are for total (SW+LW) heating rates. The first, second and third rows show three dusty outbreaks cases as indicated by their respective flight numbers and SZAs based on time observations.

To compare thesis results with literature, Gutleben et al. (2019) studied the impact of enhanced water vapour on radiative heating in the SAL over the western north Atlantic. Their work used a water vapour profile based on the tropical standard atmosphere (reference case as annual averaged wv profile) to contrast with the heating rates generated from the outbreak days. Dust heating rates in the current thesis show higher values of SW and LW heating rates than these shown by Gutleben et al. (2019). The reason of less heating rates by Gutleben et al. (2019) is possibly related to deriving heating rates as daily averages during August, while thesis results show heating profiles under dust and water vapour effects during summer based on the time measurement of flight observations. So, the elevated water vapour seasonally may be diminished since it is averaged with less elevated days for the SAL and thus less radiative magnitude. Whereas the thesis results present, by comparison, high time resolution and so higher peak SW heating rates for dust and water vapour of about 5.5 K/day at altitude 5.5 km, while Gutleben et al. (2019) stated value of about 2.2 K/day at height 4 km. So, the peak SW heating rate takes

place at lower height than in this thesis but that just depends on how the outbreak enters the marine environment. Other simulation runs in the thesis have peaks at lower heights such as heights of 3 km, see heating rates for flights FB604 and FB613 in figure (4.5).

In addition to heating rate comparisons, Alamirew et al. (2018) derived heating rate profiles under dry and moist conditions, see heating rates profiles in figure (4.6). Although the comparison methods between the current thesis and Alamirew et al. (2018) is different, there is significant heating with a peak of about 5.5 K/day at altitude 5.5 km under dust and water vapour impact, while at near surface peak value of heating rates is about 2 K/day. For the LW, the cooling effects at the top of atmosphere due to water vapour is dominant in comparison to the surface with a value of about -5.5 K/day at 5.5 km in height. In the lower altitude of SAL, both water vapour and dust particles contribute to the atmospheric heating rates. For instance, at a height about 3 km, the peak value of SW heating rates is observed in the presence of dust and water vapour impact, while this peak is reduced in the absence of dust but with humidity impact, see red lines for flight number FB604 in the previous figure (4.5).

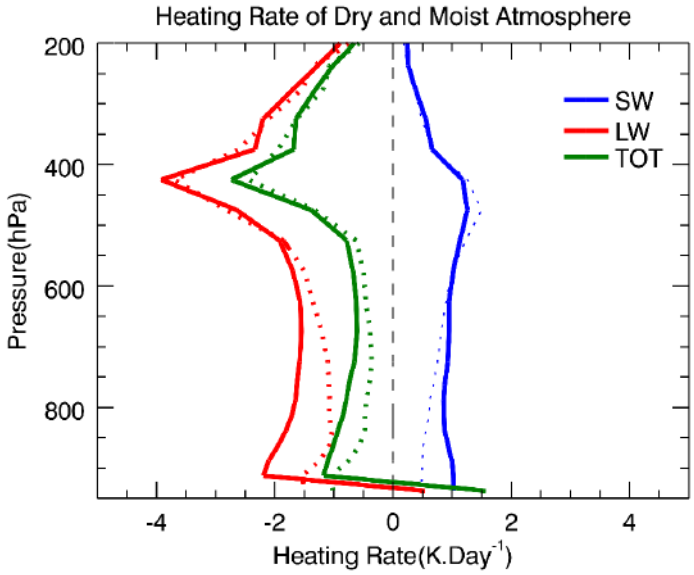

Figure 4. 6. Vertical profiles of dust heating rates over Sahara taken from Alamirew et al. (2018) results. The heating rates were chosen for three separate times. Dashed lines indicate dry periods during June 11, 12, and 16, and solid lines indicate humid days, June 18, 19, and 25. Blue, red, and green lines show SW, LW, and total radiation.

Is there a link between the level of dust and water vapour in the air? This can be tested by investigating the relationship between dust and water vapour. In this work, I present the profiles of water vapour and I illustrate that high water vapour accompanies dust with higher values than similar levels for non-dusty flights. The results shown in figure (4.7) are for dusty and non-dusty

flight cases including, FB604, FB605, FB611, FB612 (dusty days), FB700, FB702, FB705 and FB708 (non-dusty) cases. From the figure (4.7), I show four structural atmospheric layers, as shown in the vertical dashed lines. The first layer starts from near ocean surface and extends up to the lower base of the inversion layer, which is indicated by BL in the figure. The second layer is the inversion layer (IL) which is located between the BL layer and the SAL. The third layer is the SAL which is usually situated above the inversion layer and below the fourth layer, i.e. free atmosphere (FA).

The depth of these layers can vary during the day and night; however, in this figure I focus on the role of water vapour and dust factors on heating rates in the atmosphere. It is evident that the water vapour in figure (4.7) has elevated water vapour in the SAL compared to the non-dusty flights. For instance, within SAL in flight case FB604 the blue line shows high values of water vapour with a mean of 4.14 and a standard deviation (SD) of 0.97, while for non-dusty case (often containing small amounts of dust as defined previously) it has mean of about 2.45 and SD of 2.31, see statistical results shown in Appendix A4, table (A4-1). In addition, water vapour in the IL is decreased significantly, particularly in the clear atmosphere. It can be also seen that there is a decrease in the mass of water vapour in the free atmosphere. Higher levels of water vapour are found for higher dust outbreaks. Similarly, the statistical results show that high values of water vapour mixing ratios in dusty flights are comparable with other dusty cases, see table (A4-1) in Appendix A4.

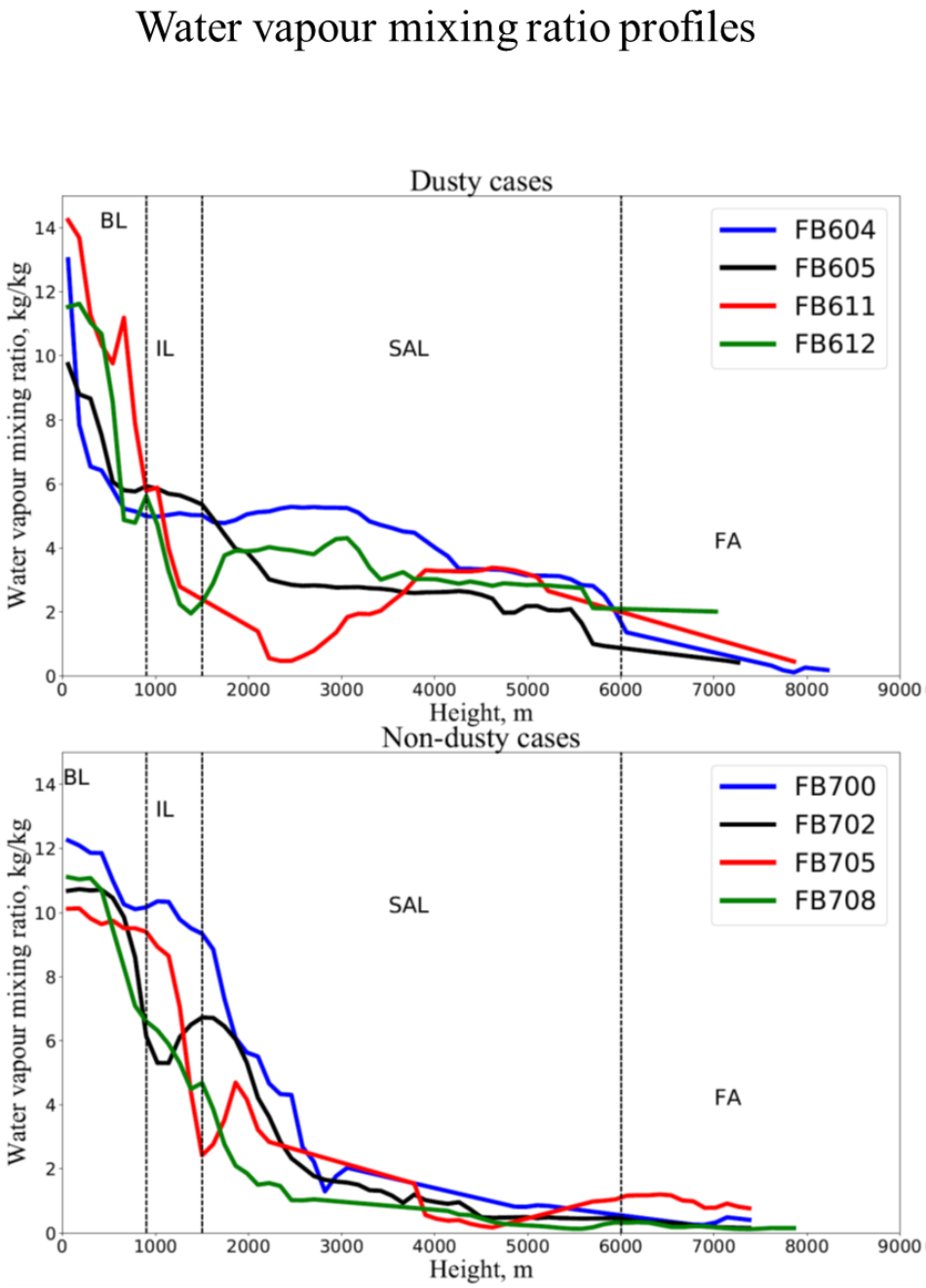

Figure 4. 7. Water vapour mixing ratio in units of kg/kg with height. Top panel indicates dusty cases (including FB604, FB605, FB611 and FB612) in the legend, while non-dusty cases shown in bottom panel. The layers BL, IL, SAL and FA present boundary, inversion, Saharan air and free atmospheric layers.

4.5 Sensitivity tests for dust and enhanced water vapour

Sensitivity tests were implemented for deriving heating rates associates with decreasing the dust and water vapour profiles individually by 10 %, 20 %, 40 %, 60 % and 80 % to investigate the SW and LW heating rates sensitivities to dust and water vapour for the dusty flight case FB604 in a comparison to the background heating rates of the non-dusty flight case FB708. So, I reduced dust and wv profiles for all these percentage decreases in the ES radiation code to see the effects that allow dust or water vapour to reach to the background non-dusty environment levels. Figure (4.8) depicts heating rates derived from the ES radiation code using dust and water vapour and with other gases included based on the dusty flight case FB604. Solid thin lines (green and orange) indicate SW and LW heating rates for FB708 (background non-dusty environment), while solid red and blue lines show SW and LW heating rates of FB604 with using dust and water vapour profiles. The dotted lines show the heating rates with reducing dusty water vapour profiles by these percentages, but with keep dust profiles in each run unchanged. Similarly, figure (4.9) presents heating rates for dusty wv profiles but with reducing the dust mass mixing ratios in each run by these percentage reductions and keeping the wv unchanged.

In figure (4.8), it is clearly seen that SW heating rates at about 5.5 km dropped significantly from about 5 K/day to 2.5 K/day under 80% reduction from the observed dusty water vapour level. In contrast, there is a minor reduction in SW heating rates (from about 4 K/day to 3 K/day) corresponding with 80% reduction in dust profiles associated whilst holding the dusty water vapour unchanged. At lower levels of the SAL (approximately 3 km) reducing the dust profile shows reduction in SW heating rates but still lower heating rates than wv percentage reductions. Additionally, reduced wv of amounts by 10 %, 20 % and 40 % only slightly decreased SW heating rates compared with significant decreases in heating rates noted for 60 % and 80 % wv reductions. For LW, figures (4.8) and (4.9) show minor decreases in heating rates associated with reducing the dust profile, while there are relatively large decreases in the LW heating rates above 6 km corresponding with reducing water vapour. It is seen here that changes in SW heating rates at the top of SAL are far more sensitive under wv reductions than dust reductions. Also, sensitivity tests for wv and dust are more at the upper levels of the SAL compared to smaller changes at the lower levels of the SAL, where at about 3 km the SW heating rates with decreased dust levels are seen to be a little more sensitive than wv percentage reductions at that one level.

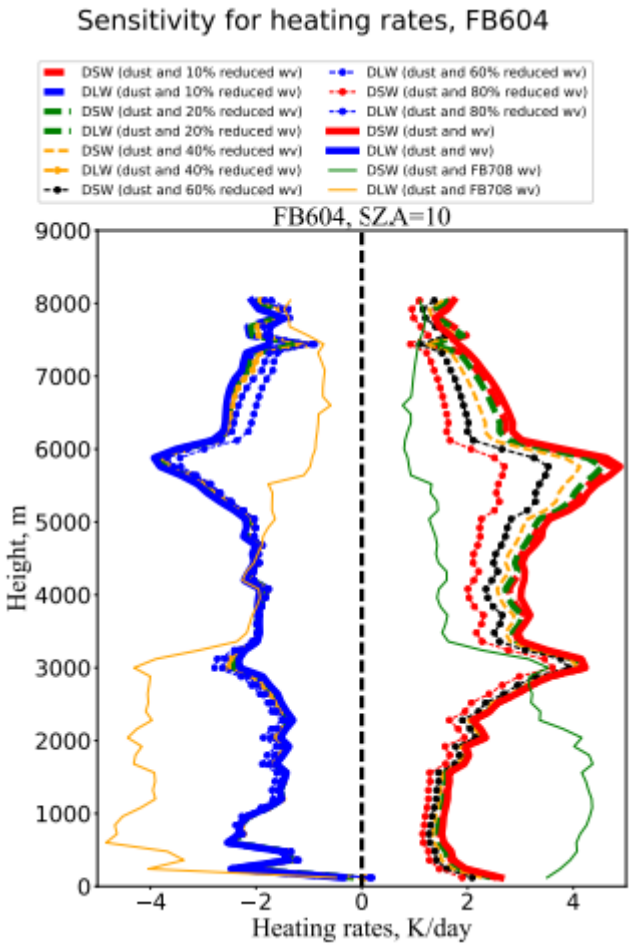

Figure 4. 8. Heating rate profiles from the ES model corresponding to the wv profiles with reductions in percentages from the original enhanced water vapour profiles for the typical dusty flight FB604. The percentage reductions are 10%, 20%, 40%, 60% and 80% which were applied to the observed original profile of water vapour with keeping the dust profile the same in each run. The solid red and blue lines present SW and LW heating rates for dust and with dusty wv, while coloured dashed lines indicate heating rates corresponding with reducing water vapour profiles by these percentages listed above. The thin green and orange lines show SW and LW heating rates for the non-dusty flight FB708. All runs were performed using a SZA of 10 degrees.

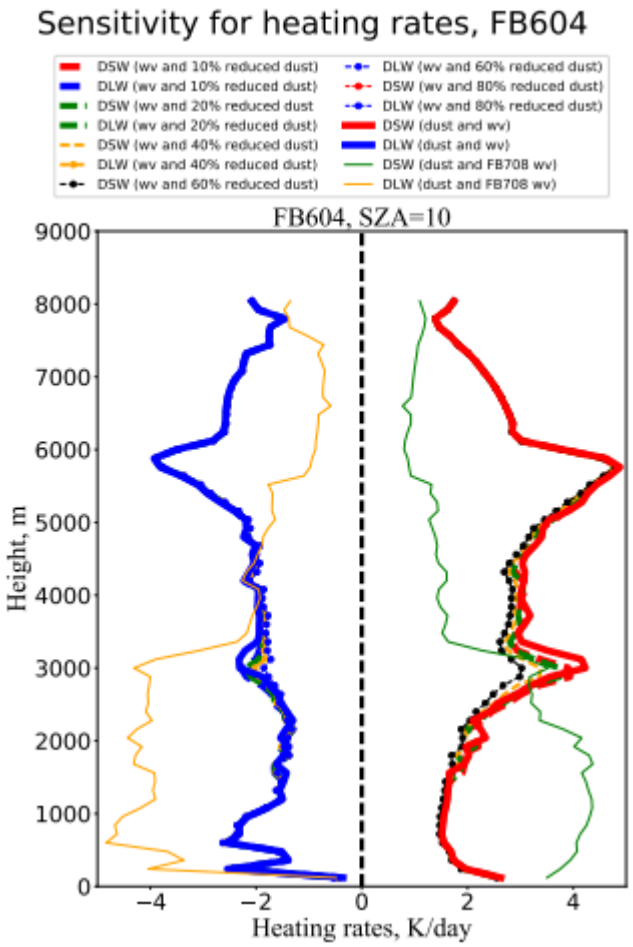

Figure 4. 9. As same figure (4.8), but with reduced dust profiles used in the ES radiation.

4.6 Heating rates as a function of solar zenith angle

The focus of this section is to illustrate the importance of the contributions of water vapour and dust to the heating rates as a function of solar zenith angle. I will begin with taking the various dusty cases based on the flights B604, B605, B699, etc to investigate the effect of SZA on the heating rates due to both wv and dust. Once the SZA effect on the heating rate is understood, then I will show the relative contributions to the heating rates from dust and water vapour separately. This is an important assessment to illustrate the relative importance of these two factors in the radiation.

In all the assessments so far, I have taken the flight observation time and used the SZA from that time based on FENNEC observations and varied the SZA during the simulation but now I will consider each of these cases with SZA ranging from a low sun angle through to an overhead sun (the values of SZA between low and overhead sun time were taken from an online sun calculation website:https://www.suncalc.org/#/40.1789,-3.5156,3/2020.08.31/15:58/1/3). I

provide plots for 8 angles ranging from 75 degrees (low sun) through to 5 degrees (near overhead) to look at the dependence across the full range. The results are shown in figures (4.10) and figure (A4.3) in Appendix A4. In figure (4.10) the dust heating rate profiles are shown for FB604, FB605 and FB613. SW, LW and total heating rates are indicated by red, green and blue lines, respectively. The SZA is listed on each plot (i.e. from the top to the bottom) and shows the radiation varying corresponding with times from morning until afternoon for each flight, with the time variation as presented in previous tables (2-6).

At morning time (SZA=75 degrees), dust heating rates cause net cooling within most of the dusty marine atmosphere for all dusty cases with only very minor heating in some limited range of altitudes. However, as the sun rises and tends towards the overhead, the heating rates have a different net effect with significant vertical regions of warming. In these regions, there is net heating effects within the dust layers, but cooling is dominated below and above the SAL over time. From early morning to afternoon, the maximum SW heating rates due to dust absorbing/scattering are between about 2.5 and 5.5 K/day when the solar angle is overhead (i.e. SZA=5 degrees), except for FB601 (where large heating rates are at about 1 km and are likely caused by sedimentation of large dust particles from dust layer).

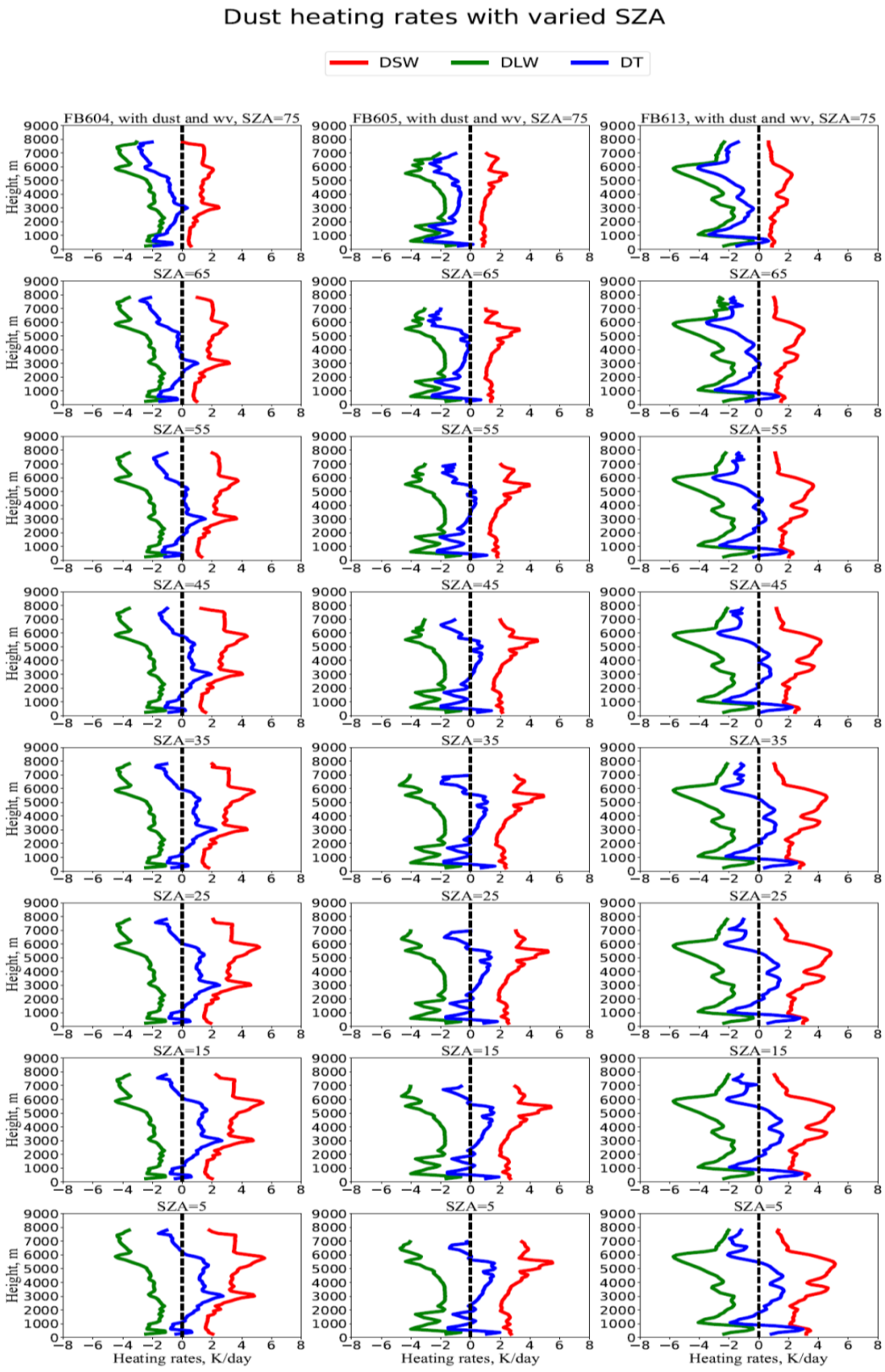

Figure 4. 10. Dust heating rates with using a variation in solar zenith angles (SZA) for dusty days (FB604, FB605 and FB613). Heating rate profiles were simulated for SW (red line), LW (green line) and total (blue lines) radiation based on values of SZA initializing from morning until afternoon time, see table (2-6). Runs indicate heating rates with dust, water vapour and other gases.

I now investigate the relative importance of water vapour compared to dust in terms of the contribution to the heating rates, which is shown in figure (4.11). In column one, the dusty air including dust and elevated wv are present for FB605. In column two, the wv is no longer the same as for FB605 as it is changed to the background marine air of FB708. The difference between columns one and two indicate the effect of enhanced wv during the SAL outbreak. In the right column (third), again other gases are included but no dust and non-dusty wv FB708, and it shows that it is somewhat like column two with mostly LW effects with a small peak due to solar arising as the sun is progressing towards overhead. The difference between column 2 and 3 is the presence of dust so this illustrates that the effect of dust is minor. In terms of the effects of SZA variations, figure (4.11) shows that the main shape of heating rate profile remains similar with variations of SZA, with larger heating rates for overhead that diminish somewhat with increasing SZA.

The most interesting point in the figure (4.11) is the relative contribution of dust and water vapour (wv). I see from comparing columns one and two that the wv has the far larger effect on the heating rates compared to dust for the SW and LW but when combined to produce the total heating rate a lot of cancellation occurs. The total is similar for dust and wv contributions lower in the modelled atmosphere, but the wv dominates the total heating rate near the top of the atmosphere with cooling off the top of the wv layer.

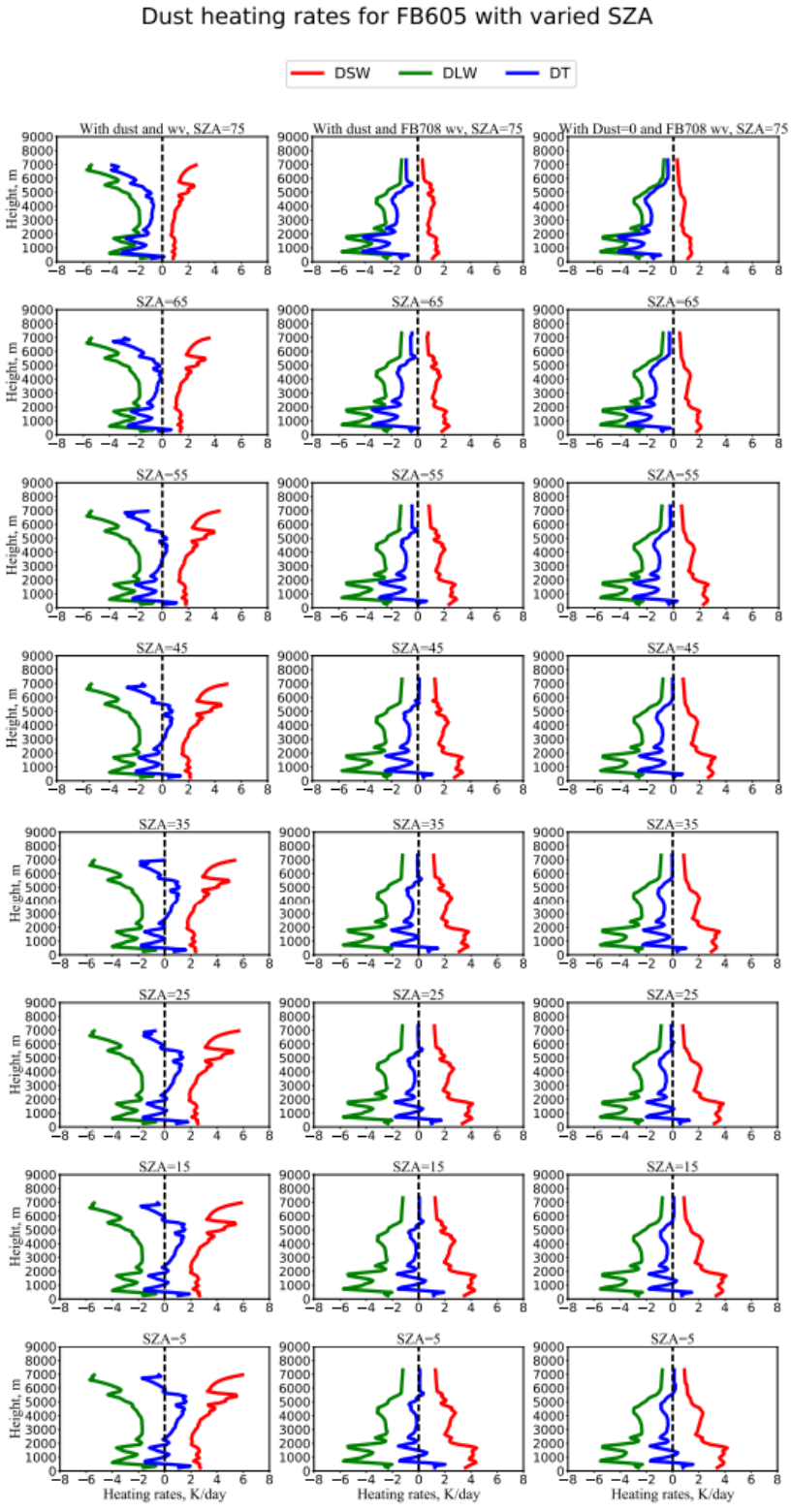

Figure 4. 11. Dust heating rates with using a variation in SZA for dusty day (FB605) associated with water vapor (wv) impact and other gases. Heating rate profiles were simulated for SW (red line), LW (green line) and Total (blue lines) radiation based on values of SZA initializing from morning until afternoon time, see previous table (2-6) in Chapter 2. First column indicates heating rates with all factor impacts, second column shows heating rate profiles with using dust from FB605 and with using FB708 water vapour, while third column is for other gases impact (without dust and with using water vapour of FB708), respectively.

4.7 General features of the environmental profile over the Atlantic

Aside from the FENNEC flights, there is very little in the way of observations over the Atlantic to evaluate the effects of the dusty intrusion into the marine environment. I can, though, look at the profiles of θ at some key locations and comment about the changes that take place as the air transports from land over the Atlantic Ocean. In this, I have used the θ profile at three locations, over land near the Atlantic Ocean from FENNEC flights, over the Canary Islands, also from FENNEC flights, and on the other side of the Atlantic from radiosonde data taken in Puerto Rico. The benefit of the measurements taken near the islands is that they will contain information about the way the dust from the land has evolved in the marine environment.

So, figure (4.12) displays the vertical structure of potential temperature in the three different locations at the time of the dusty event FB605. The curve for the African land is shown in black, the Canary Islands in blue, and the radiosonde observations at Puerto Rico in red line. The profiles in Puerto Rico are presented to agree with the arrival time for the dust transported across the Atlantic. The outbreaks would not usually travel towards the Canary Island and then on to Puerto Rico so it is not a time series of the transport, but it is usual to note at the Canary Islands as to how the dust may modify the θ profile after a couple of days of travel across the marine environment and then on to Puerto Rico after several more days. FENNEC observations indicated that the dusty environments are characterised by high amounts of water vapour in which water vapour is elevated in the SAL during outbreaks of dust transported over the Atlantic and these elevated water vapours can impact on the structure of the atmosphere. This is important to be considered in thermodynamic and dynamic evaluations of outbreak conditions during simulations. So, water vapour is potentially considered as a competitive factor with dust effects on the structure of well-mixed SAL.

In figure 4.12, the θ profile over land (black line) illustrates a characteristic well-mixed layer up to about 5.5 km from the surface, and it exhibits very different results from the dusty marine air results, especially in the MBL. The land profile (black) would be consistent with an environment where dust is being lofted dynamically through convection up to the levels of 5.5 km. The profile is well mixed and so the surface and the levels up to 5.5 km are likely to be dynamically connected.

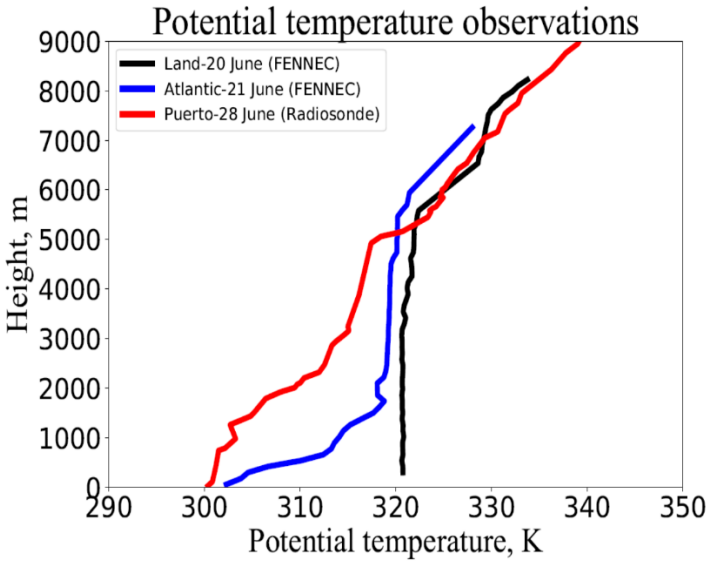

Figure 4. 12. Potential temperature profiles from flight and radiosonde observations over three different regions. Black line shows profile over African land, while blue and red lines show θ structure over Canary Islands and Puerto-Rico regions, respectively. The profiles of potential temperature over Canary Islands and Puerto-Rico regions, respectively. The profiles of potential temperature over Canary Islands are relative to flight time measurements on 21 June 2011, i.e. flight number FB605.

Once the dusty air has advected into the marine environment, the warm dusty air is expected to advect over the cooler marine boundary layer environment. It is important to note that this dusty air is not only dust but also contains elevated wv levels as well. The much warmer well-mixed dusty layer will then be above the dynamically active MBL and the differences in temperature will create a strong inversion just underneath the SAL involving the air that extends down to a few hundred meters from the ocean surface. The peak in the dust in the well mixed dusty region, seen previously in figure (4.5) supports this conclusion about the well-mixed warmer air riding over the MBL as well as basic thermodynamic arguments based on potential temperature of two air masses.

One other interesting point here is that the well-mixed potential temperature over the Canary Islands is extended slightly upwards. This is agreed with what was reported by Carlson (2016) for the depth of SAL. The well-mixed region can be extended upwards through a couple of ways including large-scale lift which was common on the transport towards the Canary Islands from the ECMWF reanalysis or through turbulent processes breaking down the inversion above (by shear or radiatively driven).

Well away from the African continent, at Puerto Rico, the θ profile is significantly more aged and looks like it is somewhat similar to the stable background marine environment that is seen in figure (4.2), but with the leftover of a well-mixed region between about 2.5 (or possibly 3.2 km) and 5 km. This less stable region is obviously the dust layer remnant that may be slowly stabilising over time.

There appears to be a well-mixed MBL up to about 800 m and then stratified until the remnant of the dust layer. It is unclear whether the dust layer containing dust aerosol and elover Puerto Rico has enough dust to maintain this characteristic well-mixed structure or not. This is the focus of the next chapter is to provide a rough estimate of the bin resolved dust that may be advected that distance and to then evaluate whether it is enough to make the layer dynamically active.

It is very clear from these limited plots that the dusty layer that is evident over land is evident as a layer at altitude as the air intrudes into the marine environment and over a very long transport time the structure is still evident. Also clear, is that the marine boundary layer is not dominated by the dusty intrusion. As noted earlier, the warmer air from the land is likely to ride up over the lower levels of the cooler marine environment leaving the MBL in-tact. The link between the MBL and the SAL is a strongly stratified layer that is very stable and will inhibit all but very strong convection reaching the SAL. In contrast, over the Atlantic and underneath the SAL, θ is significantly less than the value over land, but it decreases slightly away from the African coastline. It is clearly seen from the figure (4.12) that surface potential temperature over land is much higher than values at these locations (Canary Islands and Puerto) with different magnitude of about 2 K, while the difference in surface potential temperature between the African land and Canary Islands / Puerto is extremely more than 2 K. The marine environment will have far lower heat fluxes from the ocean surface compared to the intensive heating that will take place over the African land during the day when the dust is lofting into the atmosphere.

4.8 Dust entering a non-dusty marine layer

In previous section, I looked at the structure of θ over the African coastal line and the Atlantic. That provides the key to study the importance of intrusive Saharan dust entering into the marine air over the Atlantic Ocean. What will now be tested is if a background marine atmosphere that is stably stratified has an intrusion of dusty air enter in a SAL then what will happen to the stably stratified background MA profile over time? I am interested to understand the timescale for a stable MA layer to become well mixed by dust at the levels observed in our dusty days. This is an approximation for investigating what happens when an intrusion of dusty air enters a stable MA layer. An LEM simulation was established with a stable low-dust profile from FENNEC observations and radiative heating rates based on Otto et al. (2007) and Zhu et al. (2007) for a dusty outbreak are imposed.

The UK Met Office LEM version V2.3 is used in this current study. The model was presented in Chapter 2 and so a reminder of only some of the setup details is provided here. The LEM model was run in 3-dimensions with a domain of 6.4 km with x and y axes and 7.6 km in the vertical height. The resolution is 100 m in the x and y directions and 120 m in the vertical. The LEM was run with and without dust heating rates over 8 hours of simulation time, approximating air transporting from Africa to the Canary Islands. The main aim of using the LEM for simulating

the dust layers is to evaluate the thermodynamic and dynamic impacts of Saharan dust and to understand the radiative effects of the dust layer corresponding with meteorological parameters such as water vapour and other atmospheric gases on the structure of atmosphere over the Atlantic Ocean.

The LEM model was run for 8 hours and the effect on the potential temperature is shown in figure (4.13). The black line shows the observed data from flight observations for the non-dust case (FB700). Potential temperature profiles for the SW and LW indicate the red and green lines, while blue line shows potential temperature vertical layers for total radiation.

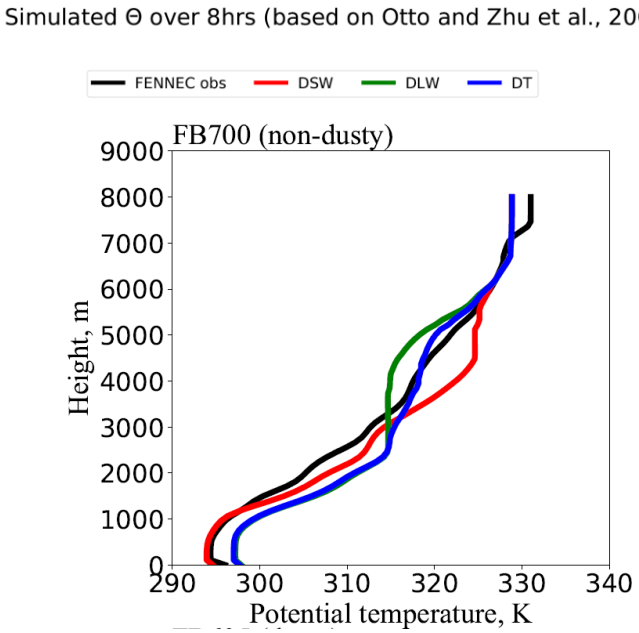

Figure 4. 13. Potential temperature (θ) from the LEM for an 8-hour simulation beginning with a non-dusty day. The figure is representing vertical profiles of potential temperature (K) with potential temperature on the x-axis and height on the z-axis. The simulated dust heating rates are based on the profiles from Otto et al. (2007) and Zhu et al. (2007), where the black line is from the flight observations. The red line shows dust heating rates for the SW radiation, while green and blue lines are for LW and the combination of SW+LW radiation, respectively. It is noted that the radiation does not vary with SZA in these runs since the literature profiles are fixed.

From figure (4.13), the introduction of dust (hence heating rates) into the stable marine atmosphere causes a well-mixed potential temperature layer to establish on the timescale of 8 hours. This shows that dust heating rates will clearly modify the layer above the MBL to have a well-mixed potential temperature profile where the SAL was simulated. The LW radiation is most important in causing the well-mixed layers and establishes efficiently overnight whereas during daytime (when SW+LW) the SW and LW effects tend to compete and have a far reduced effect. This well-mixed layer is generated from simulating heating rates based on Zhu et al. (2007) peak values without investigating gaseous effects, and thus the presence of gases such as water vapour may influence the result as well, but it is not possible to test with Zhu et al. (2007) heating rates.

4.9 LEM assessment of the decay of a well-mixed SAL without dust radiative effects

In the last section, a numerical experiment was performed evaluating how long it would take for a dust layer intruding into the background MA to form a well-mixed potential temperature profile. Next to be evaluated is how long a well-mixed layer that was formed from a SAL would persist if the dust was no longer in the layer. The SAL over land will often be well-mixed before it intrudes into the marine environment (Marsham et al., 2013). If the dust is depleted over time through sedimentation, how long will the thermodynamic structure last?

To investigate this, I ran the LEM with a dusty profile from flight FB605 observations and switched off the radiation to see how much time it would take for the potential temperature layer to return to a stratified layer. Figure (4.14) displays the results of the LEM simulations with a final profile (runs including both dust and water vapour (top panel), with dust profile and with non-dusty water vapour profile (middle panel) and without dust and with non-dusty water vapour profiles (bottom panel)) after 8 hours of simulation time. First column is for SW radiation, while second column shows results for LW radiation. The heating rates profiles used in the LEM simulations are performed here associated with using an initial SZA from flight observations, where different flight have different times of measurements. The results of potential temperature were simulated based on dust heating rates determined from ES model calculations. After 8 hours, the profiles for SW and LW do not return to be a stabilized layer. In fact, there is very little stabilising of the layers in the lowest figure with dust switched off. There is some reduction in the depth of the well-mixed region to be noticed.

To conclude, if a vertical temperature structure is well-mixed coming from the continent and entering the Atlantic environment (as a SAL) then the well-mixed structure will remain like that for long distances, even if the dust has sedimented out. The time it will take to revert to a stable layer will depend on the strength of factors such as turbulence and shear to break down the well-mixed layer, but it will take significant time based on these runs using the LEM simulations based on the observations from FENNEC.

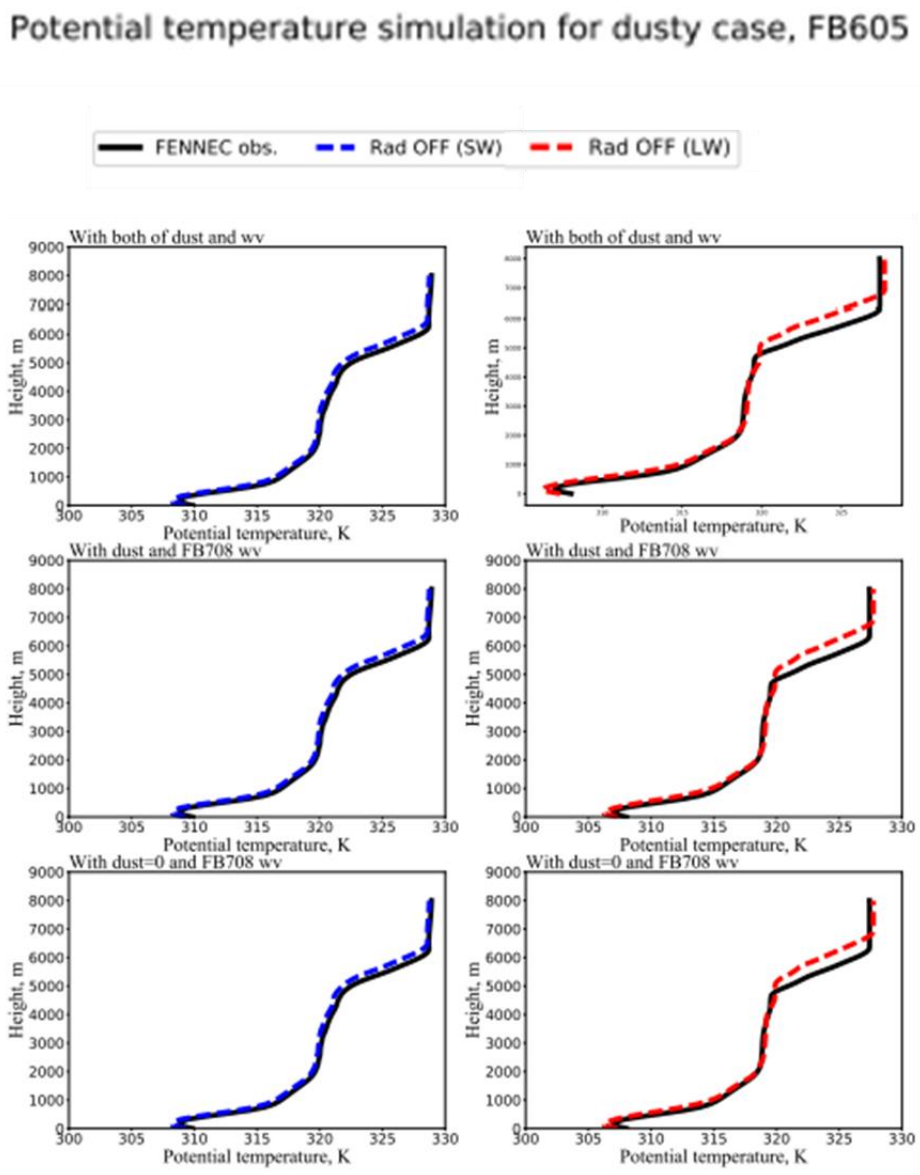

Figure 4. 14. LEM simulated profiles of potential temperature (in units of K) after 8-hour simulations for dusty case FB605. The observed FENNEC profile is shown in solid black line which is the initial dust profile for the LEM runs. Shown in blue dashed lines are LEM runs are performed for dust SW only radiation runs using observed initial potential temperature from FENNEC observations (shown in black). The red lines are LEM results the same as the blue lines except for LW only. Plot in the top shows results testing radiation for dust, water vapor and other gases included, while the plot in the middle displays potential temperature profiles in the present of dust, but with non-dusty water vapour based on FB708. The lowest plot shows results using dust sets to zero and with non-wv water vapor, and with other gases active.

As noticed from the bottom panel of figure (4.14), there is a relative cooling effect by gases only (i.e. non-dusty wv and with other gaseous effect) compared with other factors; however, there is little stabilisation from 8 hours. It will be interesting to understand what will happen for a longer time period of 7 days if the radiation is turned off with gases (non-dusty wv included) impacting only. To investigate this, a simple program was developed to approximate the evolution of potential temperature across the Atlantic to approximate a longer LEM run. This is performed

by considering a dusty case from the FENNEC observations and imposing only a radiative effect due to gases but with non-dusty wv and with no dust radiative effects. The code simulated 7 days into the future for the evolution of potential temperature with different initialised time (i.e. varied SZA) over the Atlantic Ocean. This ignores dust as well as dynamical effects and so is very approximate, it is just taking the non-dusty and other gaseous profile of heating rates and applying it for longer periods of time. Figure (4.15) displays the potential temperature profiles with the initial observed profile in black and in red after the 7-day simulated profile with non-dusty wv and with other gaseous cooling applied. Seven days is typical time of air being transported over the Atlantic so is a useful time to consider. In blue is a typical stratified non-dusty day which can be considered to represent the background dust-free air profile. The potential temperature profile tends to cool back towards the stratified layer, but the fact the blue and red lines overlap is not important. What is important is the slope of the red line which is becoming more stable and tending towards the slope of the stratified layer in blue. It is still quite different from the stability of the stratified layer and so it shows that under gaseous cooling but with non-dusty water vapour impact it would take many more days to become fully stratified, but some degree of stabilisation has taken place.

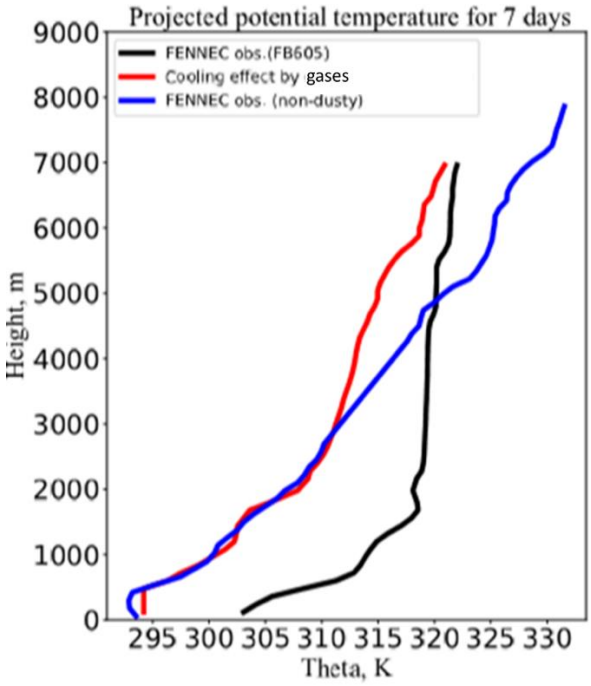

Figure 4. 15. This figure shows the decay of a dusty profile observed near Africa after seven days of projected decay. The initial profile is shown in black and represents a dusty day profile of FB605. This is then projected forward seven days and is shown in red. The red curve only has heating rate effects from gases but not elevated wv nor dust. The wv for the red curve is taken from FB708. This can be compared to the blue curve which represents a typical non dusty day FB708 to show the decaying profile FB605 towards an FB708 non outbreak profile over time.

In this section, I investigate the development of a well-mixed potential temperature decaying without dust effects. Next is to understand the significance of dust radiative effects by using the

LEM corresponding with other meteorological factors in the marine structure. Dust, water vapour and atmospheric gas profiles may all have a contribution in changing the radiative properties of atmospheric structure. This is fully presented in the following section.

4.10 LEM simulations of the dusty marine atmosphere

The main part of current thesis is to investigate the impact of dust and water vapour in the SAL by using updating FENNEC flight observations in the LEM to simulate the thermodynamic and dynamic characteristics of MA over the Canary Islands under the radiative effect of these factors. Since flight cases have different time observations, LEM simulations are performed by, firstly, using dust heating rate profiles (heating rates generated from the ES radiation code) in the LEM based on Otto et al. (2007) and Zhu et al. (2007) and run the model over 8 hours of time simulations. Secondly, LEM runs with using derived heating rates and with using meteorological variables and wind datasets based on flight time observations. The simulation is implemented with using initially different time in each case of flight observations and run LEM with using initially the same time of solar in all flight cases. The latter approach uses time-varied started from early morning until afternoon. I will investigate whether the simulation results between using initially different and the same time observations are different or not. Before this, I will show in the next section the simulation results based on literature.

4.10.1 Simulation with the combined Otto-Zhu dust heating rates

As part of the simulation of dust intruding into the marine environment, more results are shown here for a range of flight observations to understand the influences of peak value dust heating rates by using the LEM model. As I showed in the previous section (4.2) for the LEM simulations of thermodynamic and dynamic influences on the potential temperature structure by the presence of a dust mass layer. It will be of interest to base the LEM simulations on more flight observation cases in order to assess how varying levels of dust profiles can evolve during transport over the Atlantic. Figure (4.16) shows the potential temperature layers from the LEM output for dust heating rates based on the profiles of Zhu et al. (2007) scaled to the peak heating rate from Otto et al. (2007) with projected dust arrival at Canary Islands after 8 hours of time simulation. The figure (4.16) shows results for the selected moderate (FB600, FB601 and FB609) and dusty (FB604, FB605, FB612, FB611 and FB613) cases. As expected, the impact of dust heating rates is large on the structure of potential temperature due to using the peak value of heating rates. But there are two noticeable influences: the first is the dust warms (cools) the structure of the atmosphere for the SW (LW) radiation; warming for the SW/LW occurs within SAL/MBL, while cooling is characteristic for the LW above about 3 km. And thus, the net impact of dust radiative effects will be warming below and within the SAL. The second influence is related to the role of

dust in figure (4.16) illustrating that it is keeping the SAL well-mixed, which is mostly controlled by the LW radiation rather than the SW. I note these cases all have different SZA and that will also impact the strength of SW effects and is consistent with expected as seen in figure (4.5).

The dominant role of LW radiative effects of the dust is seen as an interesting finding of this thesis. This is consistent with Meloni et al. (2014) who stated that dust heating rates in the Mediterranean area (i.e. Lampedusa Islands) for the LW radiation when compared with SW are large. Also, their results show the large impact of LW radiation causing a net cooling at these levels. However, the nature of the marine atmospheric environment is different from the environment over land. Dusty air that advects from African land toward ocean is usually considered dry in terms of moisture, whereas the FENNEC observations are indicating that there is appreciable water vapour in the dusty marine environment mixed in with the dust layer, and this may contribute to change the radiative impacts. So, simulating dust heating rates related to the optimal dust profiles from the flight observations with considering these issues will provide good estimation whether the LW dust radiative effect is dominant or not, and this will be studied in the next section.

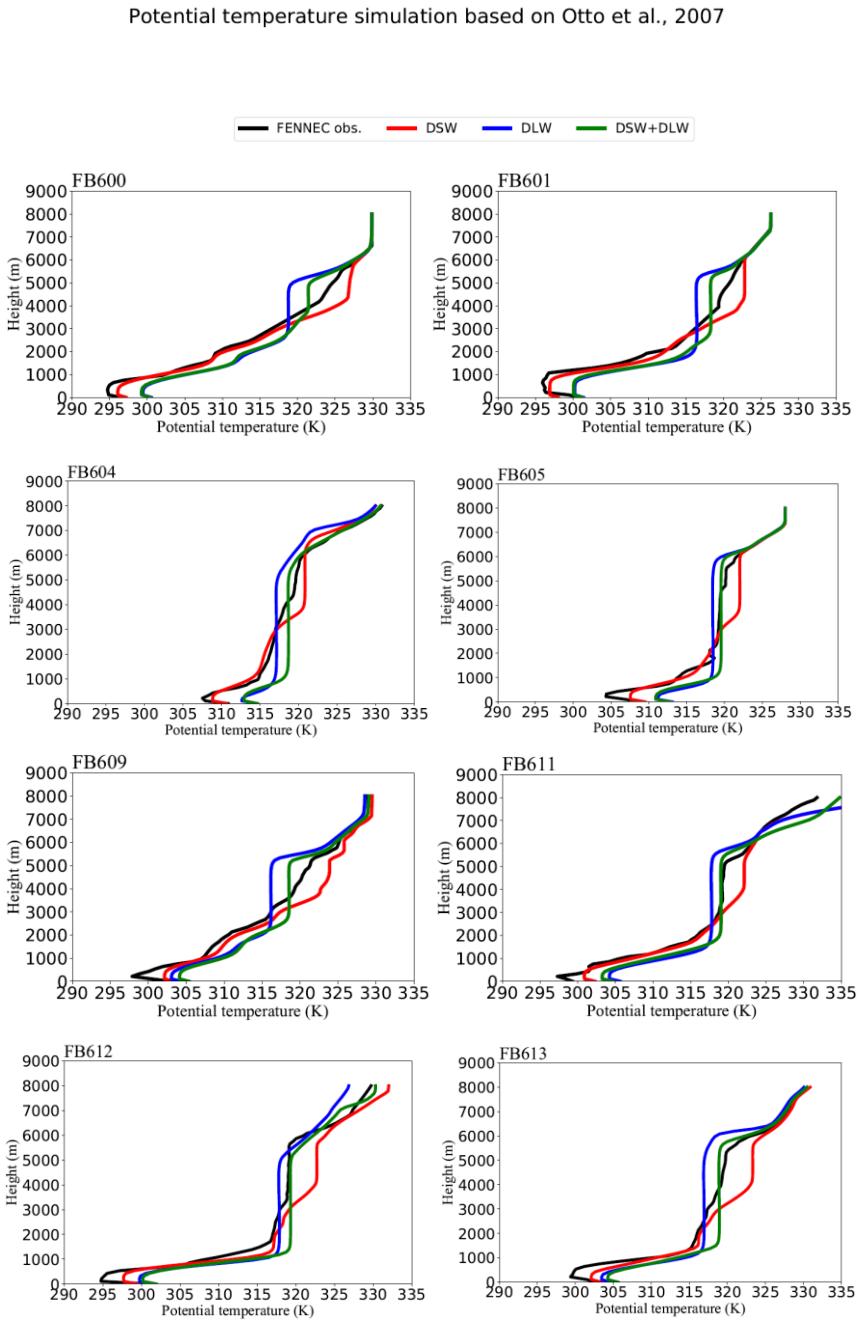

Figure 4. 16. The simulation of potential temperature for 8 hours by the LEM over the Atlantic Ocean. Black line shows the FENNEC observational profile, while red, blue and green lines represent SW, LW and the combination of SW and LW radiation switched on in the LEM simulations. The simulations were based on the maximum values of SW and LW heating rates taken from Otto et al. (2007) that are scaled to the profile of heating rates from Zhu et al. (2007). SZA is not varying in these simulations as the heating rates are fixed to the literature values.

4.10.2 LEM simulations using dust, water vapour and other gases for FENNEC heating rates

In this section, I will investigate the radiative effects of dust, water vapour and other gases on the evolution of the dusty marine environment during dust outbreaks using re-binned FENNEC observations.

4.10.2.1 LEM results comparing dusty and non-dusty outbreaks on structure.

In past chapters, I have assessed the background stratified non-dusty layers over the Atlantic responding to dust intruding into the environment and assessing the time it would take for a stratified MA profile to have a well-mixed layer because of the SAL. I have also examined the ability of the marine structure to recover a stratified layer once the dust had gone from the profile. I am now in a position to perform the most realistic simulations that can be considered for the current study, in which I consider LEM simulations of the dusty atmospheres based on the flight case observations and assessing what the impact will be on the time evolution of the potential temperature profile. For this, I use the various FENNEC observed profiles for the different flights and utilise the re-binned dust observed size distributions and heating rates for the cases and run the simulations for 8 hours. These are the most realistic of the runs and approximates the evolution of the atmosphere as the dust is transported from Africa and advecting over the Atlantic Ocean towards the Canary Islands. It is acknowledged that I am not modelling specific case studies, but rather taking representative profiles of dust and evaluating the potential effects on the profiles of air in the direction of the Canary Islands.

The LEM simulations are based on the thermodynamic profiles of the atmosphere such as pressure, temperature, water vapour, etc. as well as winds based on the FENNEC aircraft observations combined with large-scale influences of subsidence or uplift based on the ECMWF reanalysis. I did not assess any advective heat and moistures tendencies since I wanted to isolate what the impact of the dust on the atmosphere. For all of these simulations, radiation calculations are derived starting with different SZAs that corresponds to the time of the observations and evolved with time. The SZAs are indicated in the figure captions.

I begin with showing the result of the simulation for the non-dusty case FB708 (a low dust case) which is presented in the left top panel of figure (4.17). The potential temperature structure shown in the figure (4.17) is related to the simulated dust heating rates using dust profiles (if any) and gases over the 8-hour period. The LEM results in this section as well as in section 4.10.2.2 explain LEM runs with using different SZAs based on each flight observation and evolve with time (i.e. over 8 hours). Where dust heating rates used in set up file of LEM were derived from the ES radiation code based on different SZA of each flight. In contrast, in later section 4.11 the LEM runs are performed with using a constant SZA for each flight, where the initial time is the same for all flight cases started at 8.15am (low sun elevation) and the SZA varies over 8 hours until 4.15pm (overhead sun). The heating rates in section 4.11 were derived corresponding to low sun until overhead sun elevation from 8.15am to 4.15pm. This will present in more details in section 4.11. This provides good understanding about what the changes in thermodynamics under changes in heating rates corresponding with sun elevation during time evolving. The underneath panel of figure (4.17) shows a dusty case FB604 which has a very different structure. Together

with profiles both of dust mass loading in unit of $\mu g/m^3$ and water vapour mass mixing ratio in g/kg are shown in this figure (i.e. figure 4.17) in the second and third columns for each flight case, respectively. The LEM simulation results show that the vertical structure of potential temperature for non-dusty days (top left panel in figure 4.17) is characterised by slightly warming (cooling) effects for SW (LW) radiation but the structure generally remains stratified throughout the vertical. In contrast, underneath this plot, the dusty case (FB604) shows that dust warms the atmosphere between about 3 km and 6 km, while there is LW cooling from about 4 km to 6 km. Although that SW heating rate at about 5 km is likely larger than the LW cooling, the figures shows that the blue curve between 4 and 6 km has become well-mixed and this would be due to the LW cooling effects. Given the profiles of wv and dust in the same figure, this well-mixed structure is likely caused by the wv effects. Dust outbreak day radiative effects are related to the presence of dust and water vapour profiles. During non-dusty days, dust total mass dropped significantly above about 2 km, while for dusty days it is characterised by a high value in comparison with non-dusty day. For non-dusty days, the low effect of dust for SW and LW radiation corresponds with the low amount of both dust and water vapour. In contrast, changes in the results of LEM simulations (i.e. potential temperature layers) are related to high dust and water vapour present. This suggests that dust and water vapour contribute to affecting the atmospheric structure radiatively over the Canary Islands in typical flight cases.

For more understanding, figures (4.18) – (4.19) shows more results from the LEM based on other FENNEC flight cases. Flights FB600 and FB601 represent moderate dust event since they have low values of AOD (AOD = 0.06). There is slightly higher warming in FB601 for SW from surface up to 1 km than FB600 due to the relatively higher concentration of dust mass and moisture in FB601. Within the inversion layer, no significant impact for SW and LW is detected in these profiles. These flights (FB600 and FB601), together with other moderate dust events such as FB609, FB611 and FB699, are characterised by high variability of mass and humidity in the vertical, but some of these flights are characterised by large values of these factors than other cases. For instance, FB601 tends to have more dust and moisture amounts within the atmospheric layers, in which between 3.5 km and 6 km there is a dominant LW cooling impact for both FB600 and FB601, which is caused by the presence of water vapour and dust profiles in the SAL. The impact of water vapour in these flights is less than that in flight FB604 and flight FB605. So, as dust and water vapour are high in the atmosphere, these factors have a radiative effect on the structure of atmosphere, except at the top of SAL where water vapour is the main factor in a creating cooling impact rather than dust effect, which is presented in an earlier section of this chapter. This explanation can be applied for other flight cases as well that have lower dust mass loading, including flight numbers FB702 and FB708.

It is also noticed in all figures that the strength of radiative effects is dependent on the vertical gradient of dust/water vapour in the atmosphere. As the vertical change in one/both these

parameters is significant warming/cooling impact is noted compared to profiles that are more constant with height. For instance, in flight case FB605 the dust mass concentration and water vapour between 2.5 and 4 km in height, are approximately constant, while these factors are varied above this level. This causes that radiative response to be lower in magnitude within those atmospheric layers than in the layers with different structure. The heating rates were shown in a previous chapter to depend on the variation of the flux with height so if the profiles are approximately constant then the heating rate will not be significant. It is also noted that the SZA will also impact the results in terms of the strength of the SW effects with more significant effects for overhead then grazing angles, as previously noted in figure 4.4.

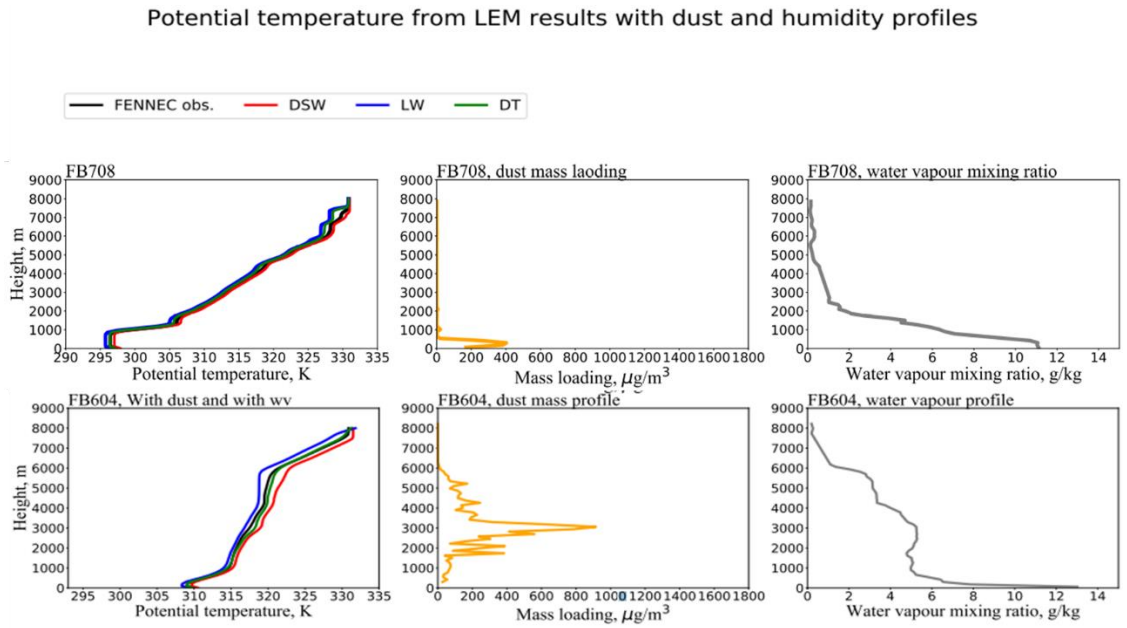

Figure 4. 17. Potential temperature profiles from the LEM simulations over 8 hours associated with mass loading and water vapour mixing ratio profiles for non-dust day FB708 and a dusty case FB604. Both were simulated by using heating rates that were obtained from the ES model with using all profiles, i.e. using dust, water vapor and other gaseous profiles. Top left and bottom left panels show modelled and observed profiles for the FB708 and FB604 flight cases, respectively. Red, blue and green lines refer to LEM runs and the black curve is the initial observed FENNEC profile. The results include SW, LW and total dust heating rates, which are indicated by DSW, DLW and total (DT) in the legend, respectively. The orange and grey lines in second and third columns show dust mass loading and water vapour mixing ratio profiles. The LEM implemented with using heating rate profiles corresponding to different SZA (SZA for FB604 is at 5 degrees, while it has a value of 66 degrees for FB708 based on each flight time observation) and run over 8 hours of time simulation. The results of potential temperature in this figure are shown without including giant dust particles, since when deriving the dust heating rates for flight FB604 these giant particles do not have significant impact on heating rate profiles, and there was no data captured for FB708. Water vapour is indicated by wv in this plot and dust profiles were calculated with excluding sea salt concentration in the MBL.

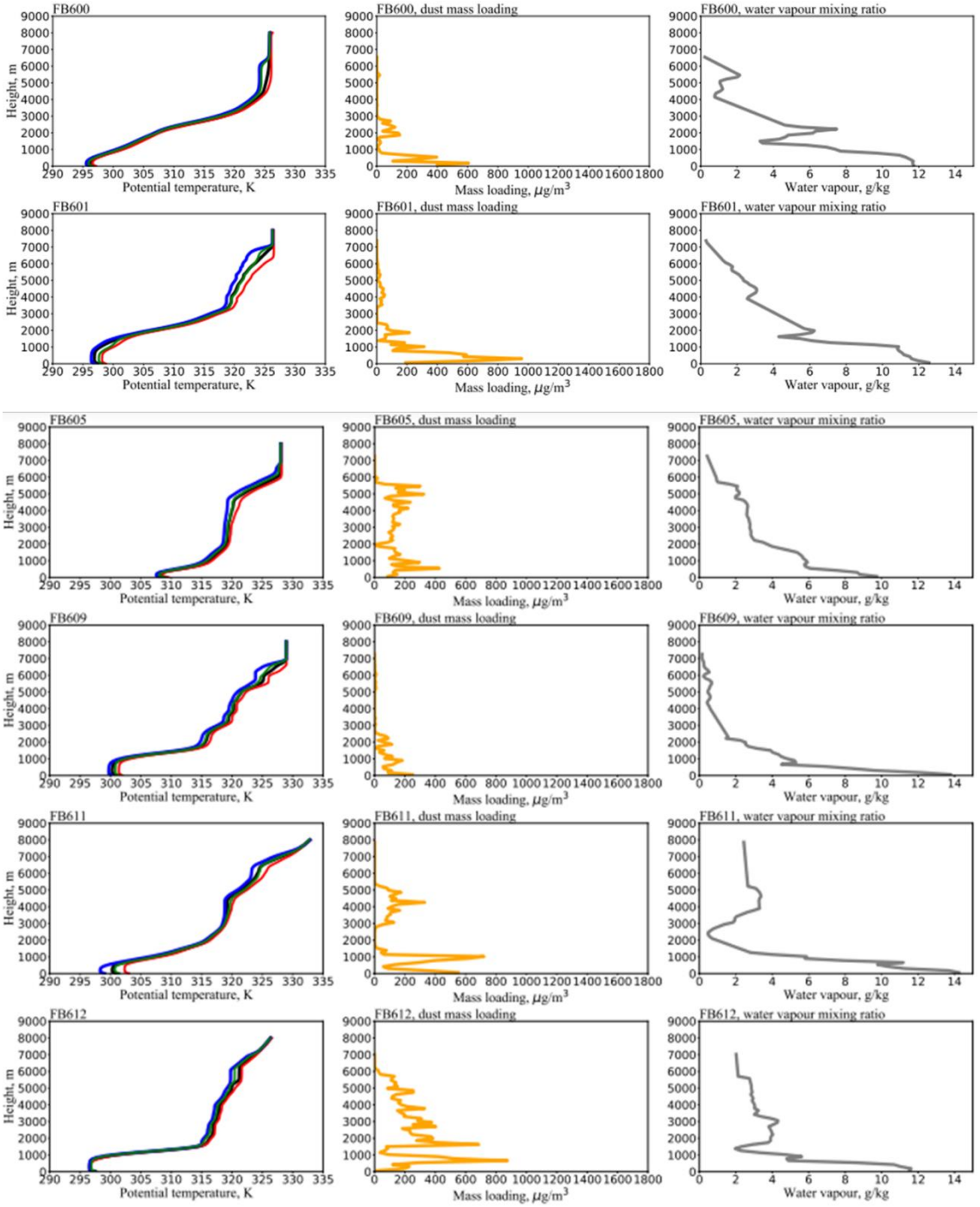

Figure 4. 18. Same as figure (4.17), but for more flight cases with dust and other gases included. The potential temperature results of LEM runs with SZA varying from an initial SZA for runs FB600, 601, 605, 609, 611, and 612 given by SZA of 64 degrees, 21, 63, 25, 14, and 63, respectively.

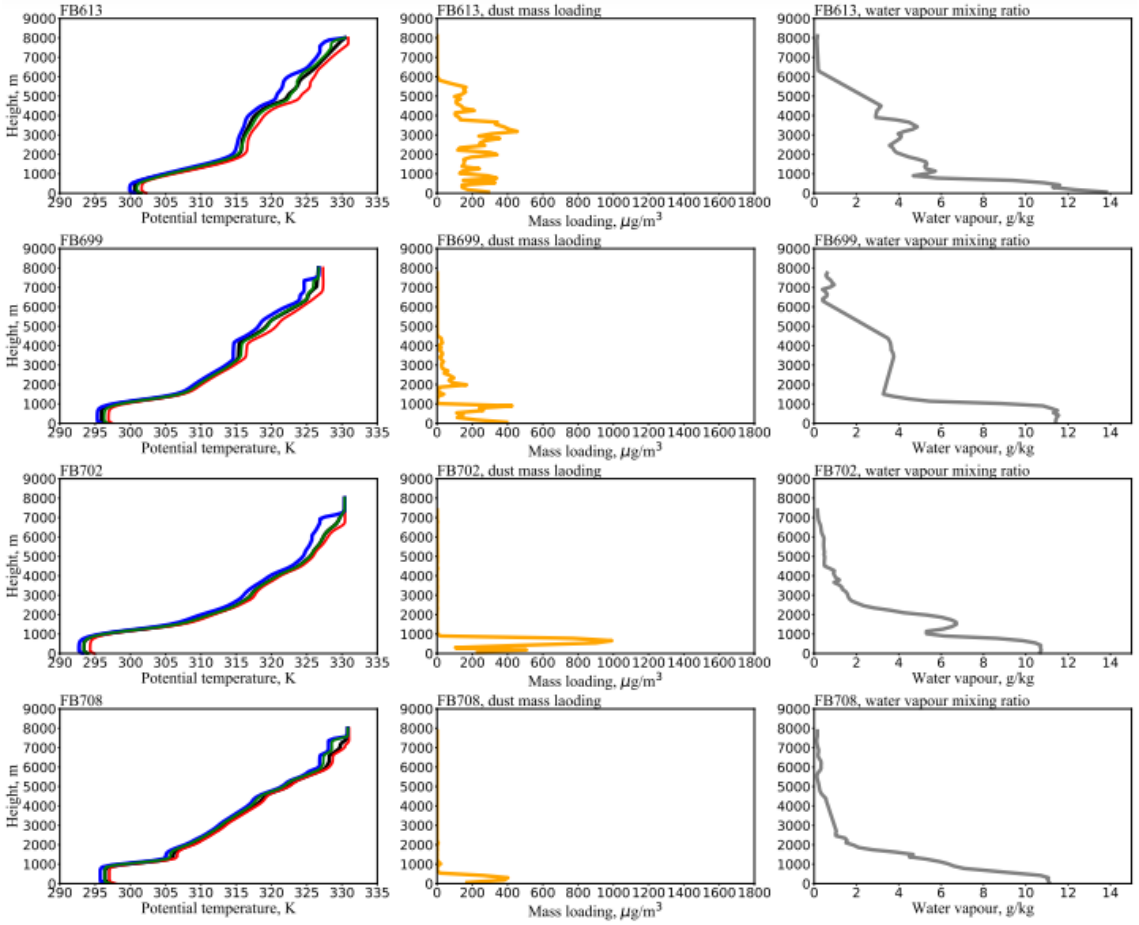

Figure 4. 19. As figure (4.18), but for more flight cases with dust and other gases included. Same as figure 4.16 and SZAs for FB613, 699, 702, and 708 are given by SZAs of 13 degrees, 13, 64, and 69, respectively.

The warming impact (red dashed line) of dust based on dust absorbing in the SW radiation, while cooling impact (blue dashed line) is caused by dust LW radiation being lost back to the space. The potential temperature profiles for the LW dust effects are again shown in these figures to have the largest effects. Also, the SW warming often offsets the LW and so this means that the dust radiative properties in the night have the strongest dynamic and thermodynamic effects on the dusty marine structure and far more than when the SW is active during the daytime.

It is possible to separately simulate dust heating rates associated with the trace gases. Firstly, dust radiative effects using water vapour profiles are implemented in the ES model. The FENNEC flight observations reveal that the SAL is characterised by high water vapour mixing ratios. Secondly, in the next section, I will test the effect of the other non-water vapour trace gases compared with dust and water vapour impacts on the structure of the dusty marine environment.

4.10.2.2 Importance of dust, water vapour and other gases on the atmospheric potential temperature structure using LEM simulations

I now focus on assessing the relative influence of dust verses water vapour and other gases in terms of what is creating the characteristic potential temperature profile with the well-mixed region in the SAL. I note that previous sections indicate that there is significant water vapour present in the SAL air along with the dust. This section will assess the role it plays in dictating the structure of the atmosphere and compare it to the effects of the dust.

LEM simulations were performed in this section for four test cases shown in figure (4.20) including (as explained previously in section 4.4) a) with dust and water vapour both representative of a dusty day (FB604) in terms of contributing to the heating rates used in the LEM, b) with dust on and water vapour changed to a marine background non-dusty amount from FB708, c) with water vapour again set to FB604 (dusty) and dust off, and d) with dust off and water vapour set to non-dusty marine background (FB708). In all simulations, the other gases (aside from water vapour) are included in the heating rates. The figure isolates the different circumstances where dust and water vapour are representative of dusty conditions then each is individually set to background marine conditions (wv set to non-enhanced levels of the background and dust set to zero) and then lastly purely non-dusty conditions.

What is most clear in the results in figure (4.20) is that the blue lines (longwave only) in the plots a) and c) show a very well-mixed layer between heights of about 4 and 6 km. The potential temperature is far more vertical than in the other cases. By comparing a) and c) which differ only by the presence of the dust, I see that it is water vapour that is causing the well mixed region since it is present whether dust is there or not. The dust-only (plus non-dusty wv and with other gases) in plot b) shows that dust is not having any significant effect on establishing or maintaining well-mixed θ profiles. So, water vapour is driving the well-mixed regions of the SAL at least for the cases studied. I see also that during the daytime when SW is active then the SW and LW will nearly cancel and the wv will have a similar effect as the dust, but during the night time the LW will only be active, and this is key to creating or strengthening the well-mixed regions in the SAL. The LW is expected to have this effect for SAL layers over the ocean if there are elevated wv levels in the SAL. Cooling at the top of the layer will cause downdrafts and circulations within the layer directly below the cooling and if the layer is already well-mixed it will sustain it. This is likely unique to over oceans since over land daytime heating of the surface will drive strong convection that can mix to high heights. Over oceans, there is a parallel between the well-mixed SAL cooled at the top by wv driving the dynamics with that of stratocumulus clouds in the boundary layer where they have significant cooling at cloud top driving the dynamics and maintaining well-mixed layers below cloud. During the daytime, the SW acts to compete and diminish the impact of the LW and thus the dynamics and weakens the cloud (Hill et al., 2008). Dust layers over oceans appear to have some similarities.

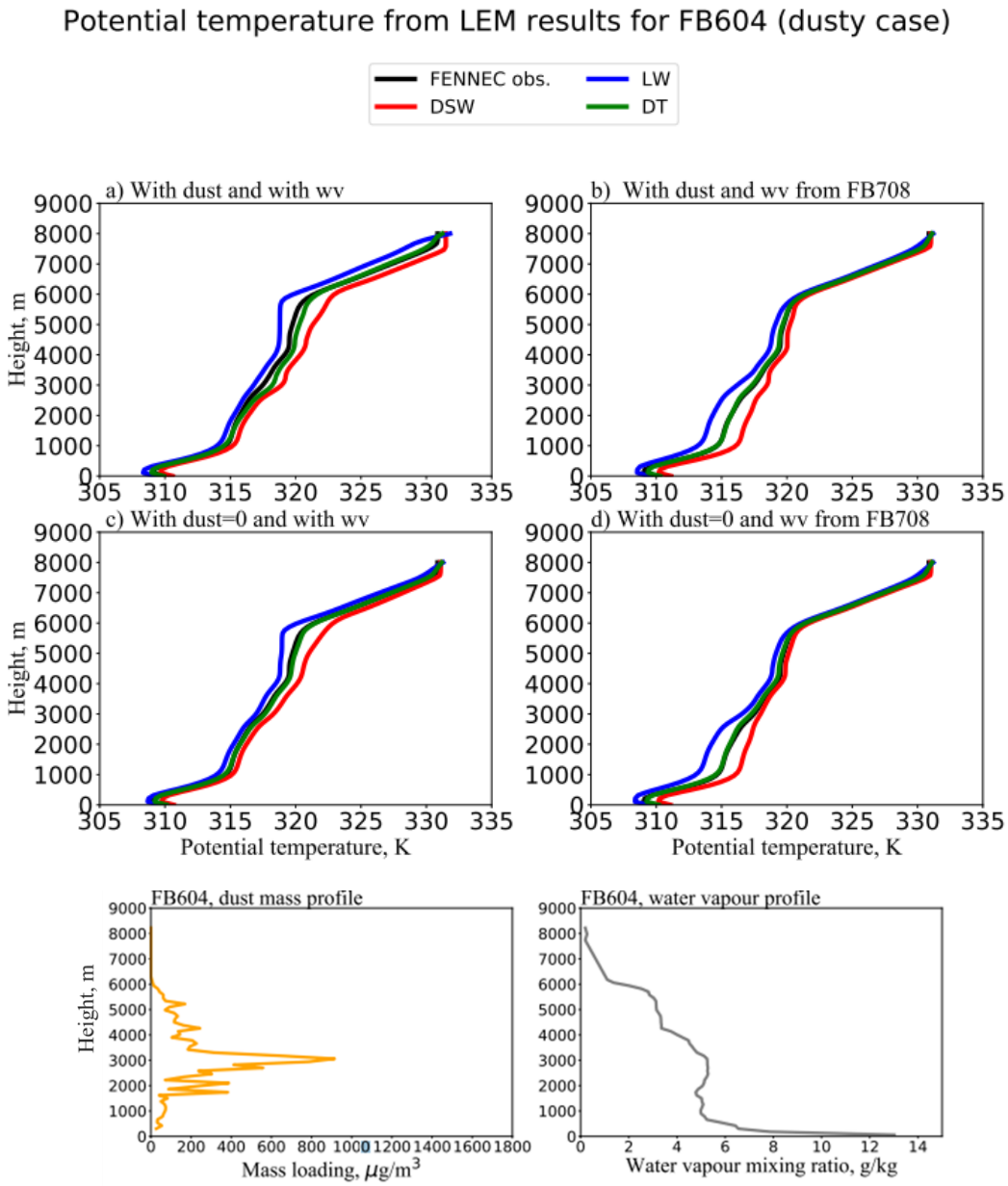

Figure 4. 20. (a-d) Potential temperature profiles from LEM simulations over 8 hours for dusty day FB604. Simulation results are based on runs using offline Edward-Slingo radiation results in the LEM with using the re-processed FENNEC observations and with using a time varied SZA based on each flight time observation over the dusty marine environment. The initial SZA for this run was 10 degrees. Black lines show the vertical structure of potential temperature from FENNEC observations and are used as the initial conditions for the LEM runs. The red, blue and green lines show the LEM results after 8 hours simulation time for DSW, DLW and Total (DT), respectively. (a) Potential temperature profiles from the LEM simulations with dust and water vapor. (b) With dust profile and with non-dusty water vapor. (c) Without dust and with water vapor. (d) With sets dust to zero and with non-dusty water vapor profiles with other gases included. Together with vertical profiles of dust mass loading (plot in left below), and water vapour mixing ratio (plot in right below) are shown underneath the results of LEM simulations.

Lastly, in figure (4.20) plot d) the results are shown for LEM runs using non-dusty wv (other gases included, as usual) and no dust. It shows that there is almost no effect due to other gases on the structure. The water vapour and the dust are significantly larger in terms of effects and much greater during night-time. The mass profile of dust and water vapour displays high levels within the SAL and reaches maximum values a little less than 1000 $\mu g/m^3$ for mass loading and about 5 g/kg for moisture at about 3 km.

In Chapter 3, I presented the dust profiles with giant particles in flight case FB605. Figure (4.21) displays the simulation of Saharan dust over 8-hours with involving giant particles in the distribution. The figure shows the results of simulations with dust but without the giant mode (solid lines) and with dust including the giant particles (dashed lines) for SW (red), LW (blue) and total (green) radiation over the Atlantic. Heating rate profiles presented in Chapter 3 show a peak at about 2 km, particularly for flight FB605. It is suggested here that the dashed line for the LW profile has a very small difference compared to the solid line and the LEM simulation results do not show any significant change in the potential temperature structure in the presence of giant dust particles.

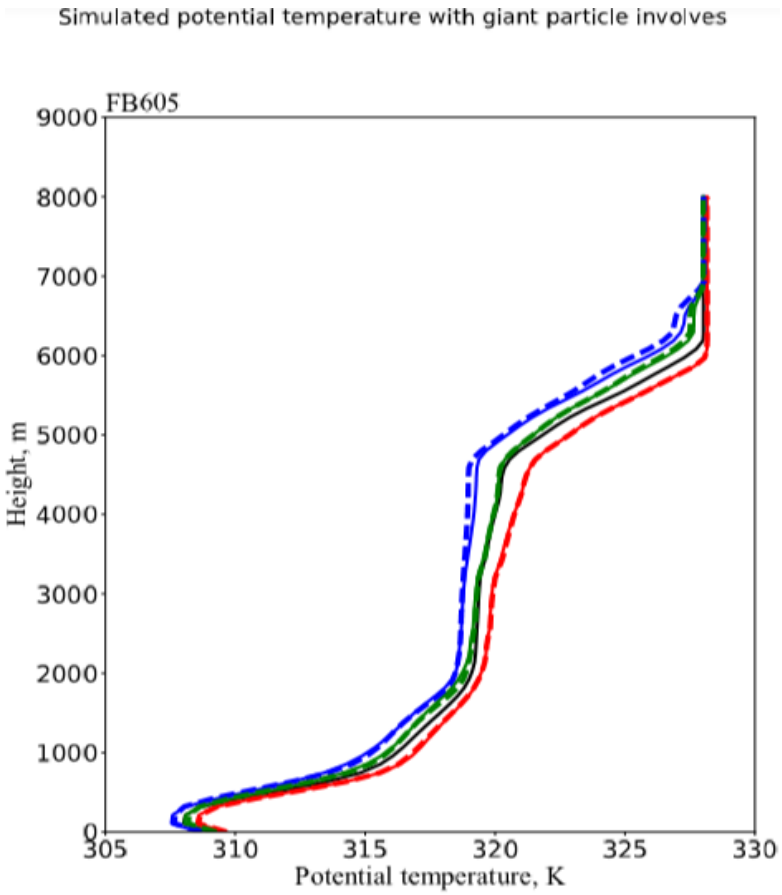

Figure 4. 21. Potential temperature structure from LEM simulations with and without giant particle impact for typical dusty day, i.e flight number FB605. Black line indicates flight observation. Red solid line shows potential temperature for SW in the presence of giant mode, with particle size greater than 30 μm, while red dashed line presents results without giant particle involved. Similarly, LW (blue) and total (green) results are shown on this figure. This run is implemeneted over 8-hours with considering all factors (dust, water vapour and other gases).

4.11 Solar zenith angle influence on evolution of structure.

The LEM runs in past sections have all been for 8 hours starting with at different SZAs that corresponds to the time of the observations and evolved with time. In this section, I investigate idealised scenarios in which all the runs are begun at the same starting SZA corresponding to a time of 8.15am and the SZA varies over 8 hrs until 4.15pm. This gives an opportunity to see a number of profiles based on observations responding to the same SW influence over time and SZA varies over this period in the same way. LEM runs were performed simulating the evolution of the potential temperature profiles using these initial SZAs in figures (4.22) – (4.23).

Top panel in figure (4.22) shows the θ profile evolution at various times from the LEM corresponding to the strength of the solar heating for the dusty case FB604. The figure presents time-varied radiative effect of dust and water vapour for SW radiation only. The solid line indicates the flight observation, while dashed lines show evolution of potential temperature from simulation output over different selected times, with 5 and 8 hours shown in the plots. Plots below

display dust mass loading and water vapour mixing ratio profiles from the FENNEC observations. θ profiles from LEM for dusty flight cases shows that the strength of radiative effect increases slightly for SW associated with 5 hours of time evolution, but this strength is significantly increased over last 3 hours (i.e. between 5 and 8 hours), see dashed lines in flight case FB604. This implies that the characteristics of dust radiative dependency for solar radiation do not develop gradually during the daytime. The dust radiative peaks around mid day with some effects in the first stage from about 8 am to 1 pm but then increases in effects for the afternoon from 1 to 4 pm. The earlier stages have a low sun angle and so contribute very little to the change in θ whereas it is likely that most of the effects are when the SZA is near or at overhead.

The runs in figures (4.22) and (4.23) are implemented by considering dust and water vapour heating rates with other gases included for the SW radiation. So, the runs are all begun at 8.15 am and the SZA is evolved with time. It is noticed from these figures that potential temperature changes corresponding with the time of day and hence the associated elevation of sun, especially at the top of dust layer. The plots show that the SW absorption leads to warming over time and that shows in the potential temperature plots. For example, flight FB611 shows significant change in θ compared with weak change in the structure for very dusty cases such as FB604. This possibly is caused by the high amount of wv shown in the bottom right panel of this figure (4.22), in which the value of wv above about 4 km is high and remains large even above 6 km, while it dropped gradually from 6 km and above this height, for this typical dusty case FB604. This high value of wv will add heating at the top of the dust layer, which is shown by increased potential temperature. Therefore, the response of the potential temperature is shown to be most affected in the areas where the water vapour is significant and less effects at the dust levels. Thus the results are highly affected by the wv.

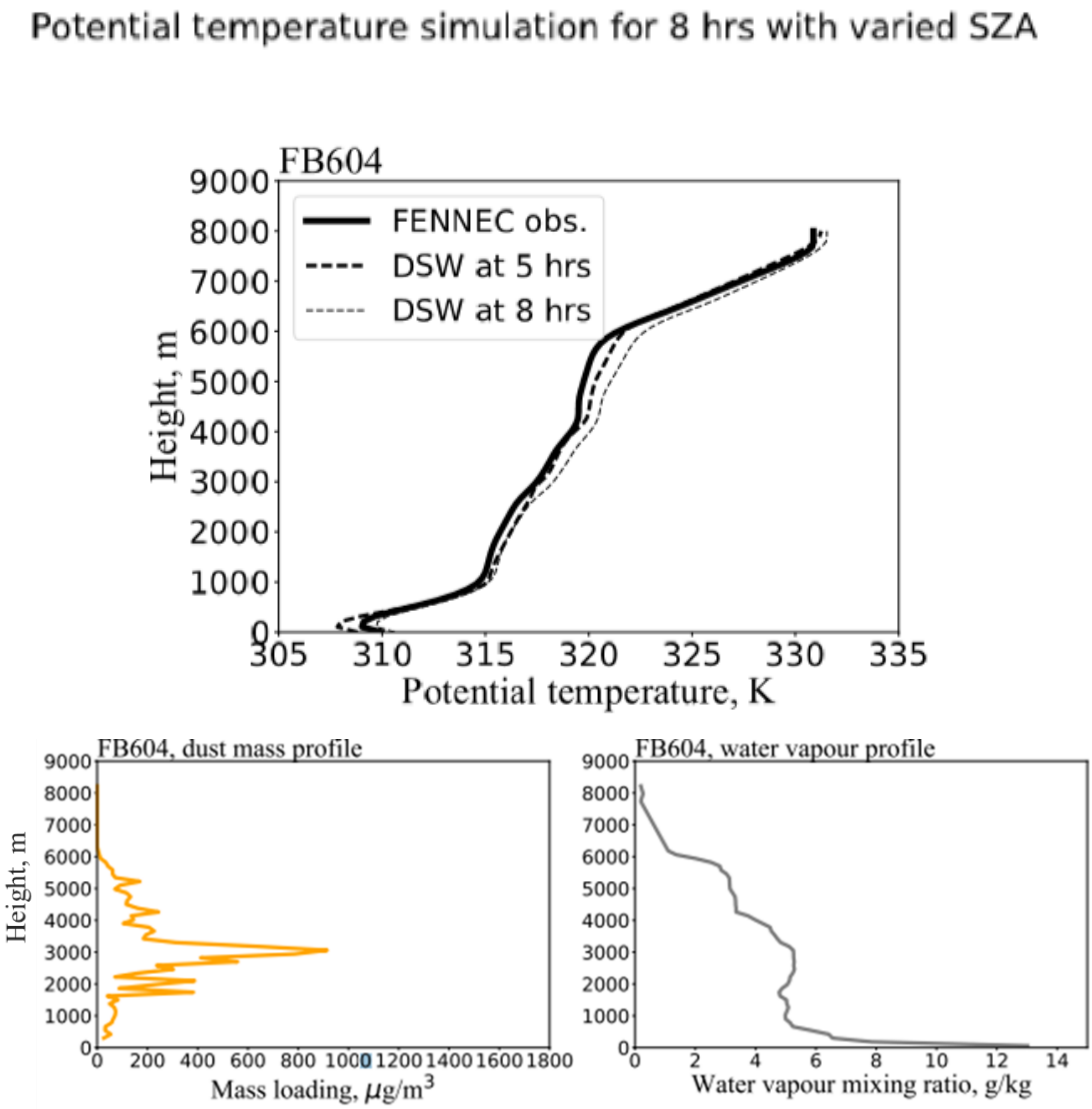

Figure 4. 22. (Top panel) LEM Simulated potential temperature over 8-hour time simulation of LEM with radiation using different values of SZA initialising from time starting at 8.15 am in the morning to 4 pm for a typical dusty case FB604. LEM runs associated with solar inclination (i.e. variation in the values of SZA) every 10 degrees for the SW are calculated. I did not show results for LW. The black lines show the potential temperature from the FENNEC observations initial profile for the LEM runs. The dashed black lines show the potential temperature after different time evolving (i.e. 5 and 8 hours) of simulation time. The bottom left panel shows the dust mass loading in units of μg/m^3. The bottom right panel shows the water vapour mixing ratios in units of g/kg.

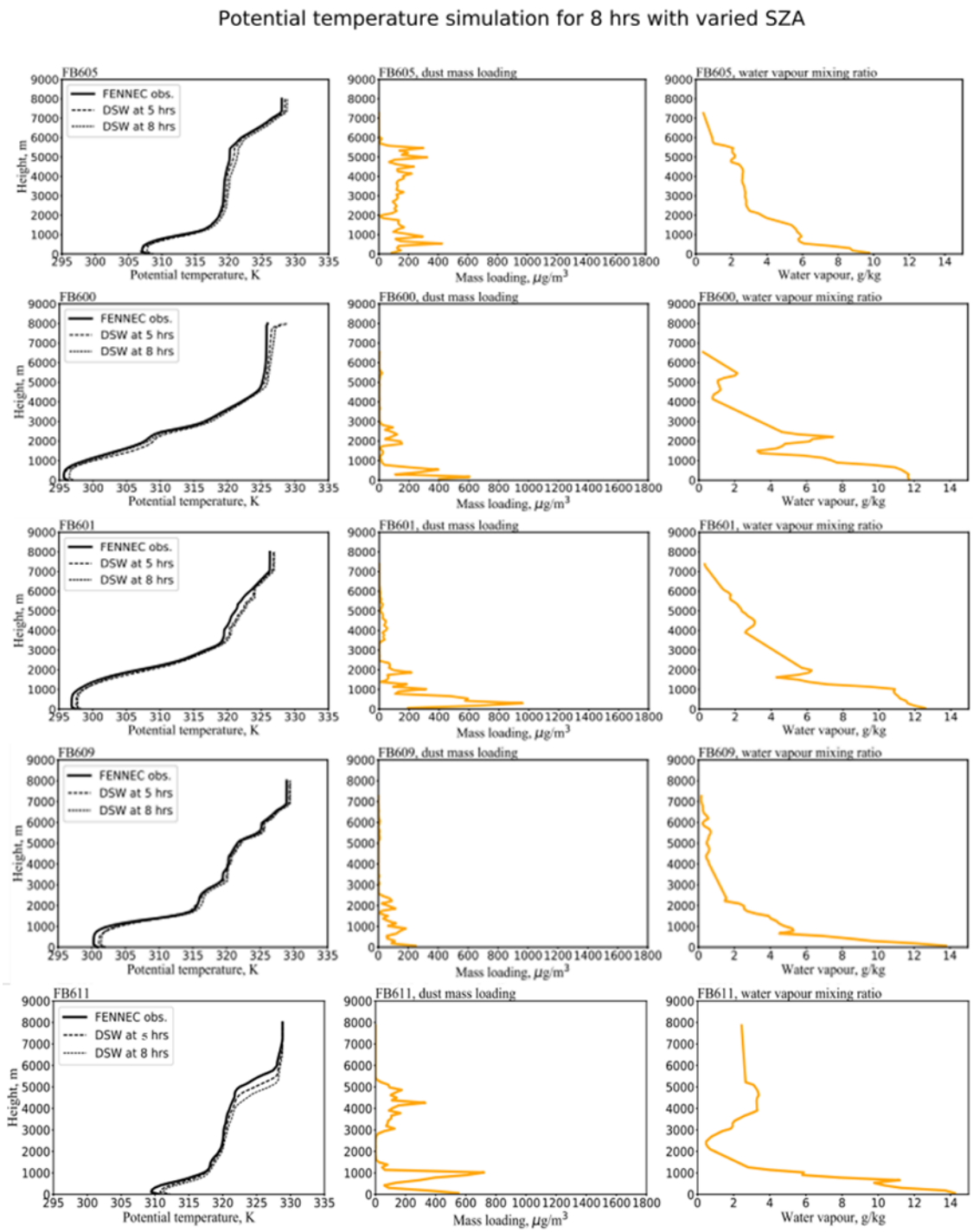

Figure 4. 23. As figure (4.22), but for more cases, all initializing at the same time of 8:15 am.

Most previous studies such as Mallet et al. (2009) focused on the radiative budget of dust, in terms of the role of dust in warming/cooling the atmosphere. In the current thesis, the focus is to understand what the significance of the SW/LW due to dust/water vapour impact is on the dusty marine environment vertical structure. The literature studies such as Alamirew et al. (2018)

pointed out that the dynamical impact of the African dust on the Sahel heat low (SHL) is lower than water vapour. ECMWF ERA-I and Modern-Era Retrospective analysis for Research and Application (MERRA) reanalysis modelling to include the dynamical effect are not suitable due to the model not being able to capture the variability of this impact on the large-scale, the dynamical role of whatever radiative influences on the structure of MBL has been focused on far less.

For the current thesis, dust can contribute to the vertical motion because of SW and LW radiation at any location where there is a change in the flux in the vertical resulting in a heating rate. For very dusty cases such as FB604, shown in previous figure (4.5), there is heating in the layers of atmosphere as dust particles absorbing in the SW spectrum of radiation at about 3 km. Above this altitude and for LW radiation, there is cooling due to scattering by dust at the top region of the profile resulting in a net warming within the SAL and cooling at the top of atmosphere (above SAL). This radiative effect on the temperature of the marine atmospheric structure in the vertical can influence the dynamics in the atmosphere. The cooling at the upper levels will cause descending motion until the particles find a new equilibrium level. The warming can cause overturning or stabilisation depending on the background θ profile. For example, if the θ profile is stable then the heating will likely further stabilise the layer especially below the heating but if the profile is initially neutrally stable then the heating can cause destabilisation and overturning with air above the region being heated. This overturning in the atmospheric layer can make the SAL is persistently well-mixed state.

Thesis results show that the dust layer is not dry during dusty events, where dust layer characterised by large levels of moisture, more than present typically in the MA. Referring to figure (4.5), the vapour can locally cause a cooling over extended heights from 4 km and above to 8km and within this a peak also due to water vapour can occur due to local heating at 6 km. Depending on the initial θ profile, this could cause destabilisation especially above the heating at 6 km and some stratification potentially below this height due to the warming. Also seen in that figure is that dust can also likely cause similar effects at the lower height on 3 km. It depends on the specific θ profile that this dust is heating but generally above the heating there can be destabilisation and stratification below.

In this section, I investigated the heating rate dependency on time with variations based on SZA, but after this I will show results based on the SZA at the start of the flights and evolved with time since the following research focuses on observations of flight cases at these times in the study region.

4.12 Modelling dust and gaseous radiative fluxes and forcings

Investigated in this section are the radiative fluxes. I present the net downward fluxes including the presence or absence of dust and elevated or non-elevated water vapour for SW and LW. Figure

(4.24) shows the net downward flux for SW (right side of plot for values greater than zero) for dust and water vapour impacts for non-dusty (FB708) and dusty (FB604 and FB605) cases, while on the left-hand side values indicate results for LW fluxes. Note that non-dusty cases (FB708 and FB700) displayed here are for net downward fluxes with and without dust and associated with water vapour impacts only, while moderate and dusty flight cases are shown with using four test runs as explained previously in sections (4.3) and (4.4). In the figures (4.24) and (4.25) the flights FB604, FB605, FB612 and FB613 are dusty cases, FB601, FB602, and FB702 are moderate dusty cases and FB700 and FB708 are non-dusty cases. In all cases, non-dusty use a background water vapour for non-dusty outbreak conditions (but is not wv=0). What is first evident from the figures is that the NetSWF at the top of the model atmosphere is, as expected, dependent on the SZA. The cases for SZA that are low (nearer overhead) show NetSWFs that are near the value of the incident solar flux (taking account of the SZA). In all cases, the NetSWF decreases as the flux propagates through the atmosphere to the surface where most of the flux is absorbed by the ocean. As the flux propagates downwards through the atmosphere, it decreases by absorption and scattering processes. The absorption directly decreases the flux whereas the scattering will either continue downwards unchanging the flux downwards or scatter upwards which will decrease the net flux downwards. The difference between the blue solid line and the blue triangles is the dust effect in the NetSWF. It shows that the effect of dust is minor and acts to diminish the flux since it acts to absorb and scatter some of the radiation.

For the LW, all the fluxes are similar in magnitude at the surface since the fluxes depend on the temperature of the surface. At heights of the SAL the largest differences occur due to the differences in the water vapour levels there. By comparing the various fluxes, I can assess the importance of the dust and water vapour. The difference between the red solid line and the blue triangles (which both have dust=0) is the effect of elevated water vapour since the red is for dusty outbreak elevated water vapour and the blue triangles is for non-dusty background marine water vapour. The results clearly show that the outbreak water vapour effects are more significant than the dust effects. Similar effects are shown in the NetLWF. Comparing the blue dots to the solid green line isolates the water vapour effects. When this is compared to the difference between the green line and black dots, which isolates the effects just due to dust, then it is again clear that the most significant effect is due to the differences in water vapour rather than dust for the LW as well.

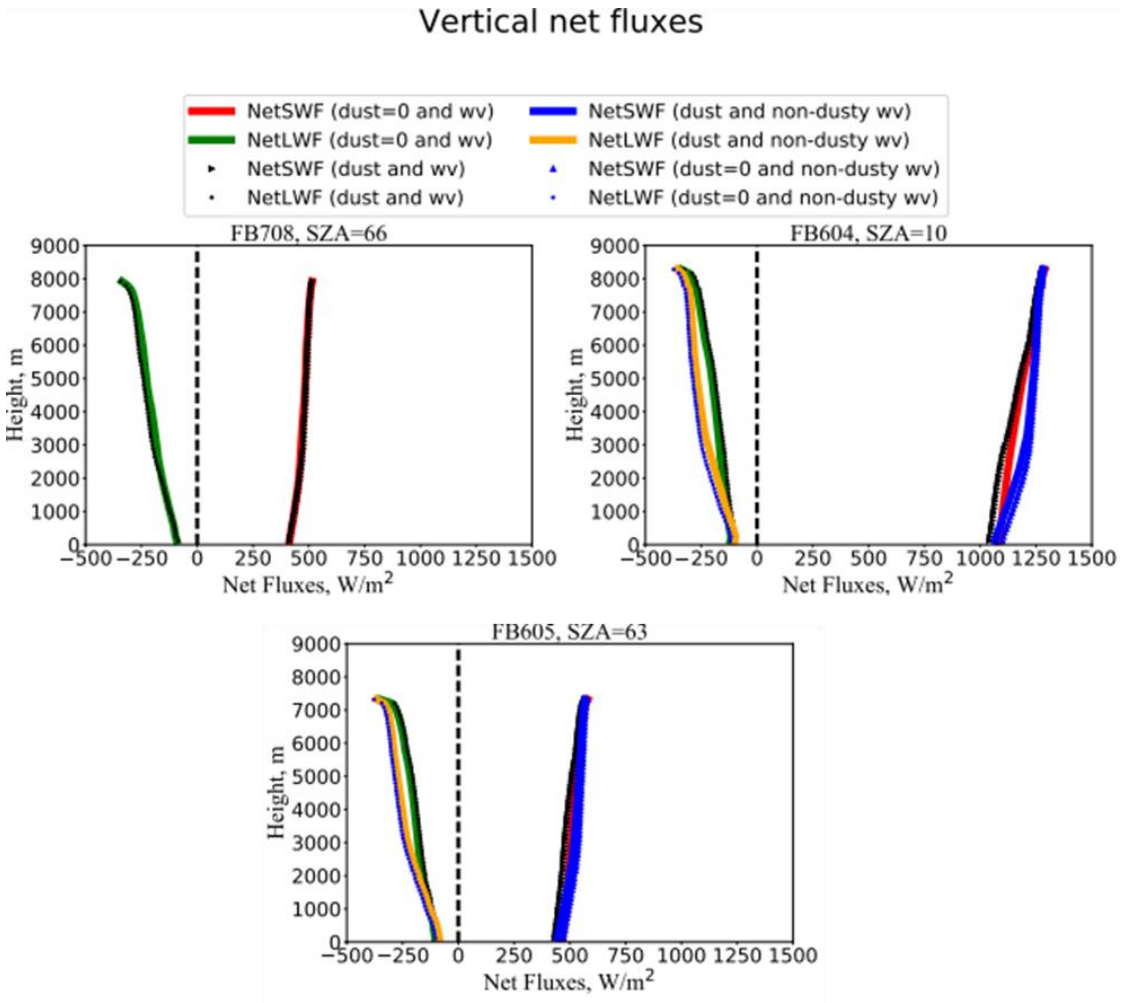

Figure 4. 24. Vertical profiles of change in fluxes for the SW and LW in non-dusty (top left plot) and dusty (top right and bottom plots) cases with presence and with using realistic non-dusty wv based on FB708. Change in fluxes/net fluxes are calculated as (shortwave downward flux, SWDF-upward shortwave flux, SWUF) and in the same way for the LW and for water vapour instead of dust. SW and LW Net fluxes in this plot indicate NetSWF and NetLWF which are calculated based on run LEM results with different cases over 8 hours of time simulation. The profile of fluxes is associated with the initial time of flight observations in which LEM runs with using different SZA based on flight observations in each flight case. The SZA is indicated in each sub plot which relates to the time of day of the start of the simulation and the time of the flux calculation.

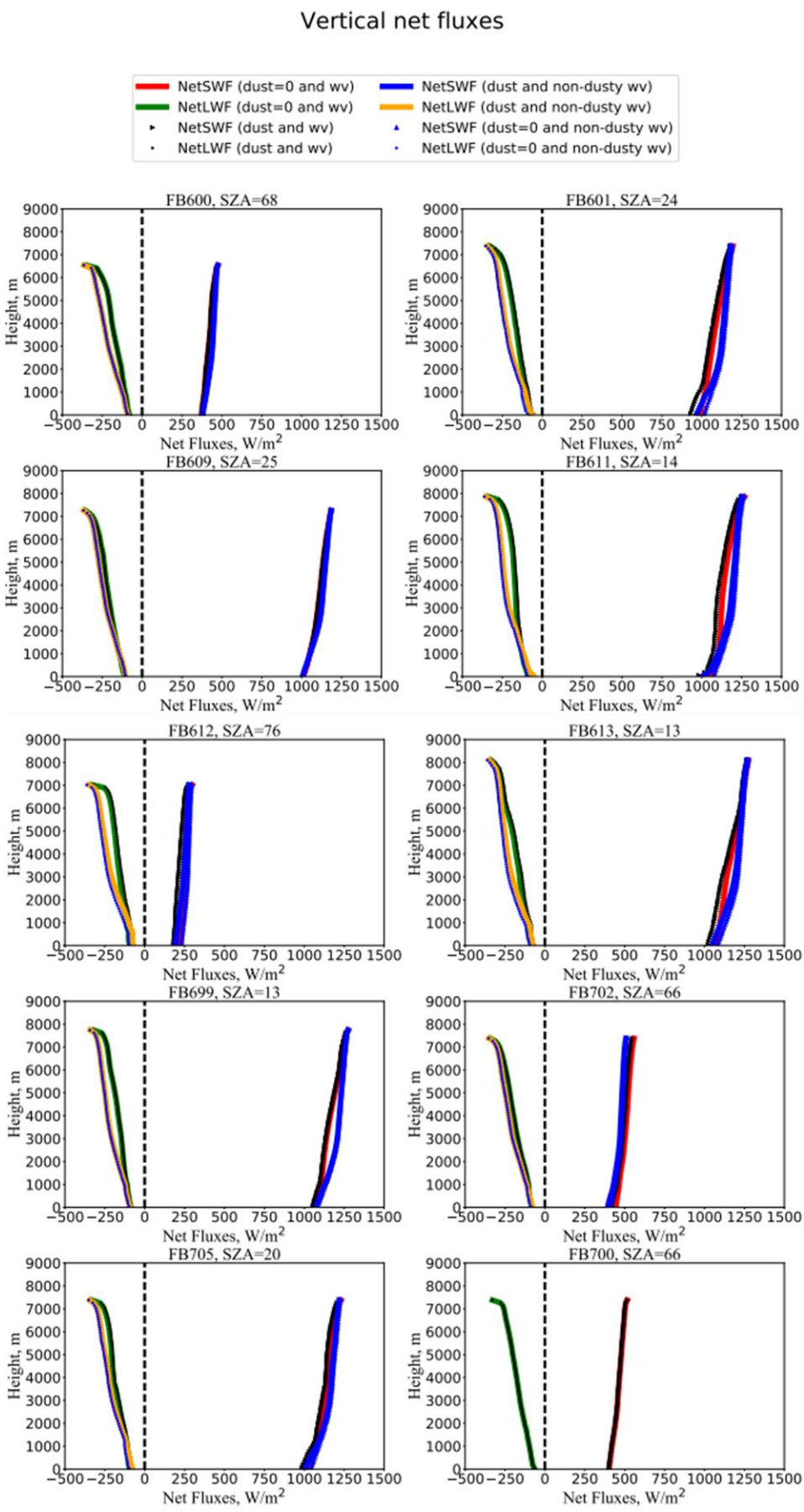

Figure 4. 25. As figure (4.24), but for more flight cases.

4.13 Vertical atmospheric motions within the dusty marine environment

In this section, I investigate the ability of vertical velocity effects on the SAL and the radiative heating rates to generate dynamics. Data was obtained from various sources for the cases in terms of vertical velocities, both large and small scale. These included FENNEC observations, ECMWF large-scale data (profiles in Chapter 5), and updrafts/downdrafts from the LEM simulations, denoted by symbol w_{LEM}. Vertical winds from the ECMWF model were obtained for hourly data profiles at each grid as the dust transports into the marine environment. The ECMWF data was downloaded based on grid boxes in terms of latitude and longitude in two directions, to the north-west (towards Canary Islands) and to the west (towards the Americas) from the African continent. The grids, both in space and time, used were estimated from the mean horizontal wind field for each case for the air motion either towards the Canary Islands or westward towards the Americas. These large-scale vertical air motions were then used in the next chapter for the transport calculations.

Compared to the large-scale vertical air motions just discussed, FENNEC observations provided high resolution local vertical winds corresponding with time and location of the flight over the Atlantic. The FENNEC flight observations offer estimates for local vertical wind profiles for dusty air outbreaks for the region off the west coast of north Africa. However, there are differences between the vertical velocity of flight observations and modelling data. This variability is shown in figure (4.26) for non-dust event FB708. The black line shows the vertical velocity from the FENNEC observations, while w_{LEM} is shown in coloured lines, where red, blue and green lines show vertical up-draughts for SW, LW, and total radiation, respectively. The panel underneath the vertical velocities shows the dust mass loading (left plot) associated with water vapour (right plot) profiles.

A couple of things are evident from the figures. The observations have a larger average magnitude and more variability than the modelling. This has been observed in other LEM simulations for other cloud types (Marsham et al., 2006). The large-scale results of ECMWF can underestimate due to the scale of the grid box and/or averaging times.

FENNEC vertical velocities show most variability from the surface up to about 2 or 3 km and then stable conditions above the MBL. The large values of vertical velocity from flight measurements agree with Lenschow et al. (2012), where there is a consistency in the variation of vertical velocity, in which it is significantly decreased above altitude about 1.5 km.

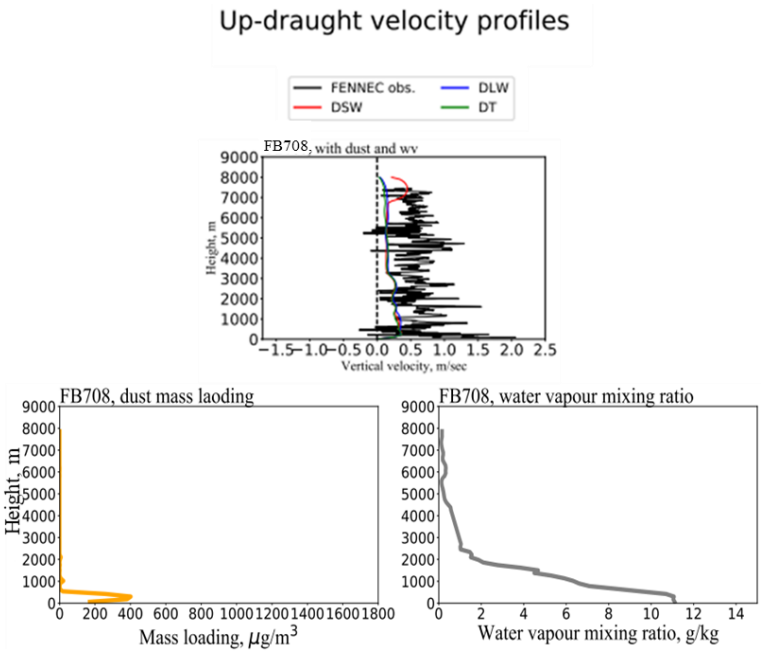

Figure 4. 26. The top panel are updraught velocities from the LEM simulations (w_{LEM}) for 8 hours based on heating and cooling rates from re-processed FENNEC observations for a non-dusty case (FB708). The black line refers to the flight observations. Red, blue and green lines refer to vertical velocities from the LEM for the SW, LW and total radiation, respectively. The bottom panel shows dust mass loading (left plot) and water vapour mixing ratio profiles (right plots). Vertical velocity from LEM simulation identifies the results of simulations with dust and gases including water vapour influences.

Looking at figure (4.27), illustrated is the w_{LEM} for four runs, including the top left plot with both dust and water vapour for the dusty FB604 flight, top right with dust and with non-dusty water vapour (from flight FB708), middle left without dust and with outbreak water vapour (from FB604), and middle right without dust and with using non-dusty water vapour. The lower panel shows the dust mass loading associated with water vapour mixing ratio profiles, right plot. I see that the water vapour (lower panel on the left side of this figure) only appears to affect the upper levels in the model runs where there are potentially higher values of wv. This can be observed in the profiles of water vapour mixing ratio between flight cases FB604 and FB708 present in the figures (4.27) – (4.28), where high values of moisture above about 3 km exist for the non-dusty case (FB708) whereas values are about 2 g/kg or less in the layers above that. In contrast, for a typical dusty case number FB604, water vapour reaches large magnitudes of about 5 g/kg at a height of about 3 km and drops to 3 g/kg at the top of dust layer. These values for dusty events are higher than non-dusty cases, particularly within SAL. The results of vertical velocity show that flight FB604 has peaks in the blue and red lines (evident to some degree in both) at the upper levels that disappear when the water vapour is switched off. Again, this shows that the water vapour is more important than the dust, in this case driving the local atmospheric circulations. It

is also clear that there are other processes at work generating the dynamics such as shear and heat fluxes from the surface.

Using high resolution in modelling may provide much better agreement between model results and aircraft observations for vertical velocity (Guo et al., 2008). However, vertical velocity from LEM results may not agree well with aircraft observations. This is discussed by Guo et al. (2008) who studied the spatial-temporal variations of vertical velocity between high-resolution LEM results with using different resolution of the model and aircraft in situ measurements. Their study reveals that good agreement between model outputs and observations takes place in much higher model resolution than coarser resolution. Also, they state that vertical velocity from LEM results is characterised by lower magnitude than observations due to modelling vertical velocity underestimates the variation in vertical motion at various scales, especially within the marine boundary layer at small-scale. So, differences in vertical velocity between model and FENNEC observations can be observed in figure (4.27), in which vertical velocity profiles from LEM simulation are lower than the FENNEC observations.

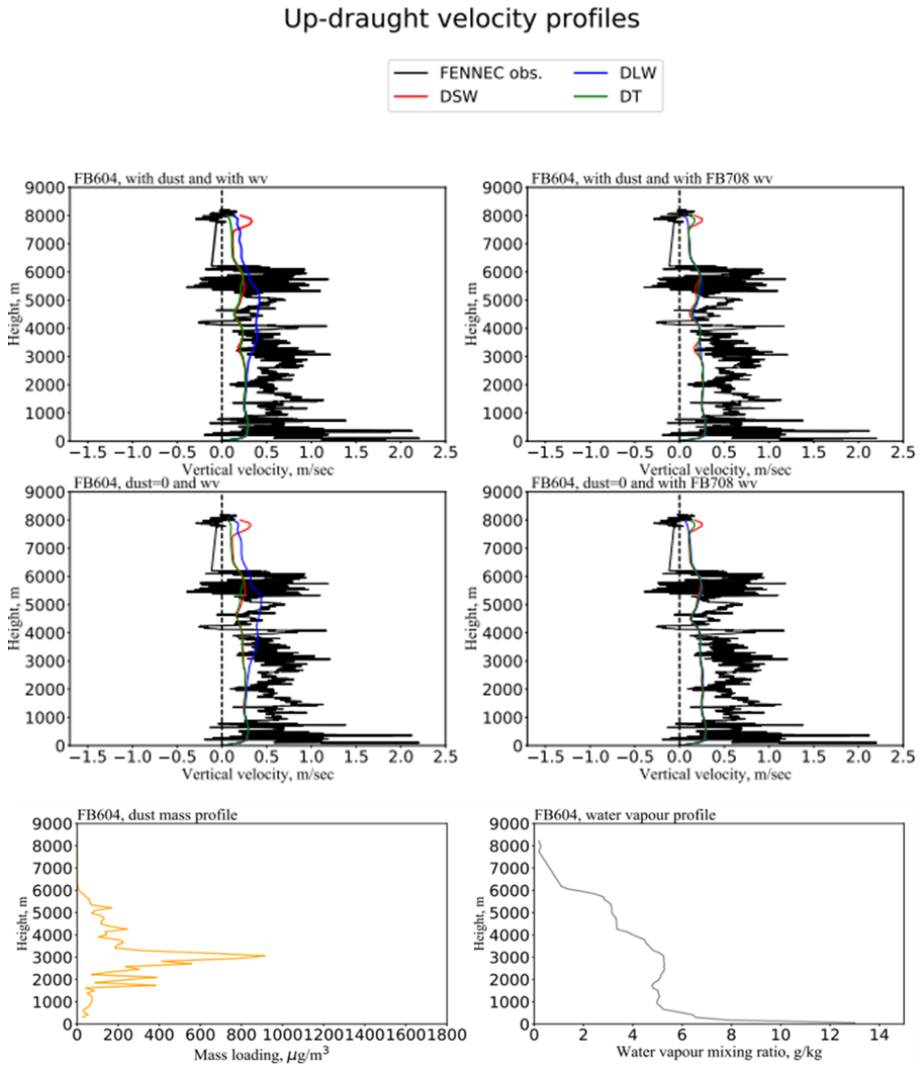

Figure 4. 27. First and second rows show w_{LEM} for 8 hours simulations based on heating and cooling rates using pre-processed FENNEC observations and with using SZA based on aircraft observations starting with the SZA representative of the start of the flight and evolved with time for dusty cases (i.e. FB604). All figures show the values at the end of the 8 hour simulations. The black line refers to the vertical velocity of flight observations. Red, blue and green lines indicate the vertical velocities from the LEM for the SW, LW and total radiation, respectively. The top left panel shows vertical velocities in the presence of dust, water vapour and gases included. The top right panel shows profiles of vertical motion in the absence of dust and with using water vapour heating rates. The middle left panel shows vertical velocity profiles in the presence of both dust and humidity and plot next to it is related to vertical velocity with dust heating rates and with using water vapour of non-dusty flight, i.e. FB708. The last panel shows dust mass loading (left plot) and water vapour mixing ratio (right plot) profiles for flights FB604.

Another reason that explains the modelling-observation differences is related to spatial-temporal variations in vertical velocity between aircraft observations and modelling results, in which Guo et al. (2008) shows that the variation of vertical velocity from aircraft observations with horizontal distance is larger in magnitude than that for model results. They addressed this by computing the statistical structure function (statistical function describes the absolute change in vertical velocity with horizontal distance denoted by Monin and Yaglom (1975)). Based on this, vertical velocity

from flight observations were found to be generally larger than that for the LEM results, and it has strong variability, particularly within the MBL since there is strong inversion layer that causes significant sensitivity with using different model resolution.

For aircraft observations, limitations in the variation of vertical velocity from flight observations can also occur. For example, uncertainly in vertical motion observations due to incomplete measurement records and restrictions in instrumental measurements. I suggest here that variation in vertical wind profiles in small and local scales contributes to difficulty in comparing between high-resolution atmospheric models such as LEM and flight observations, but for large-scale consideration, vertical winds can be appropriately used from other modelling results such as ECMWF datasets.

4.14 Dust effects on CAPE and CIN indexes

CAPE and CIN calculations provide an assessment of an atmosphere's convective potential or potential inhibition, depending on the exact profiles. LEM profiles were used to calculate CAPE and CIN based on vertical distributions of temperature, pressure, and water mass mixing ratio for the various runs including SW only, LW only and total radiation. This section shows the results of these parameters, where CAPE and CIN have been calculated from LEM simulations using heating rates based Otto et al. (2007) and Zhu et al. (2007) and FENNEC observations.

4.14.1 CAPE and CIN for runs based on Otto et al. (2007) and Zhu et al. (2007) heating rates

Figures (4.28) and (4.29) show the distributions of CAPE and CIN for the simulated flight cases based on dust heating rates profiles from Otto et al. (2007) and Zhu et al. (2007). The figure (4.28) shows imposed dust heating rates in the LEM for two selected flight cases: non-dust event (FB700) in the first row and dusty events (FB604 and FB605) in the second and third rows. CAPE and CIN profiles for the SW, LW and total heating rates due to dust effects were calculated from the simulation of dust HRs for different days of FENNEC observations. LEM results show that the dust impact on convective potential energy and the convection process will differ depending on whether heating rates are derived from flight observation or based on literature heating rates, as previously shown for CAPE and CIN in Chapter 3, figure (3.19). The initial state of the LEM runs will agree with FENNEC observations, but the CAPE and CIN may vary from the observations during the evolution of the LEM simulations. The determination of height at which an air parcel is saturated from an adiabatic ascent shows significant difference between flight cases. This is shown in table (4-1), in which it contains four columns. The first column shows the calculated values of ZLCL heights in the absence of dust heating rates, while second, third and fourth columns show heights of air parcels in the presence of SW, LW and total dust heating rates, respectively. The height at which air is saturated is computed by ZLCL= $(20 + T_e – (273.16/15))$ $(100 - RH)$, where T_e is temperature of environment and RH is relative humidity. The difference

in results between flights can be seen in this table (table 4-1). For instance, ZLCL for dusty case (FB604) is higher than FB700 with total values of 1776 J/kg and 1033 J /kg, respectively. The main result is that the ZLCL value is clearly increased during intensive dust events for the SW radiation. This implies that the presence of dust in the atmosphere makes parcels of air that might convect upwards saturated at higher altitudes than in low or no dust clear sky conditions.

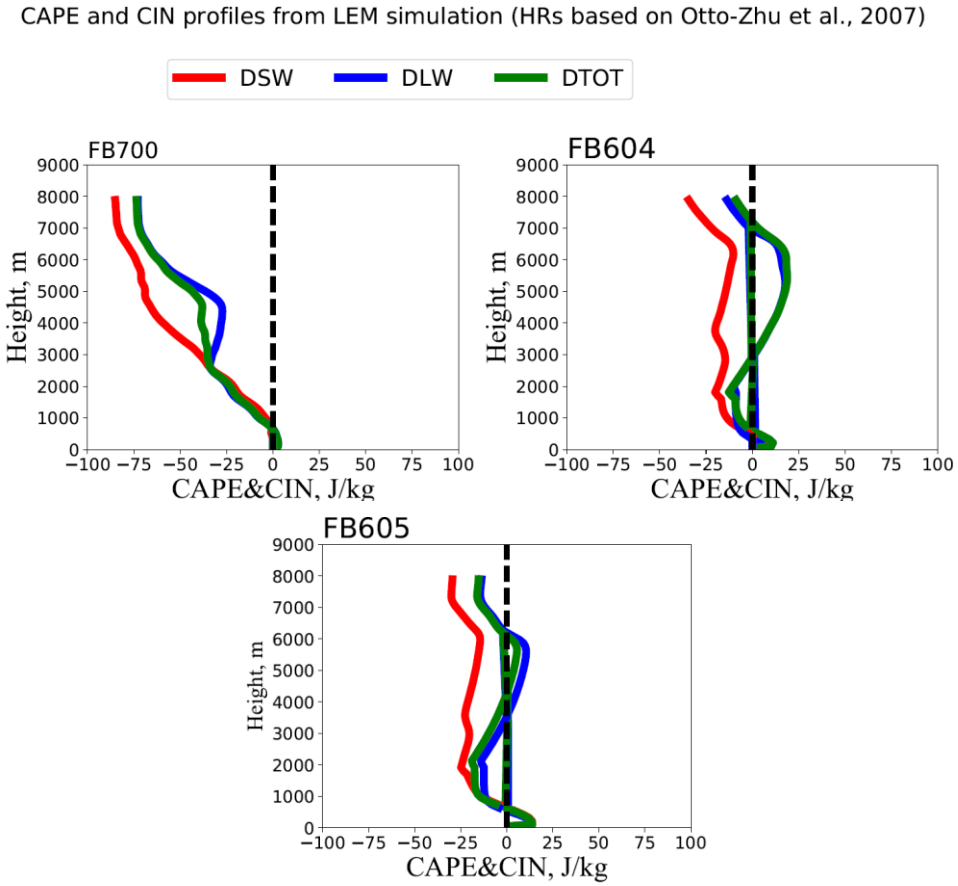

Figure 4. 28. CAPE and CIN profiles in units of J/kg from the LEM simulations after 8 hours for non (top left) dust, and dusty (top right and below) cases. CAPE and CIN profiles in black, red and green lines show the LEM results for SW, LW and total heating rates based scaled peak values from Otto et al. (2007) applied to the profile of Zhu et al. (2007).

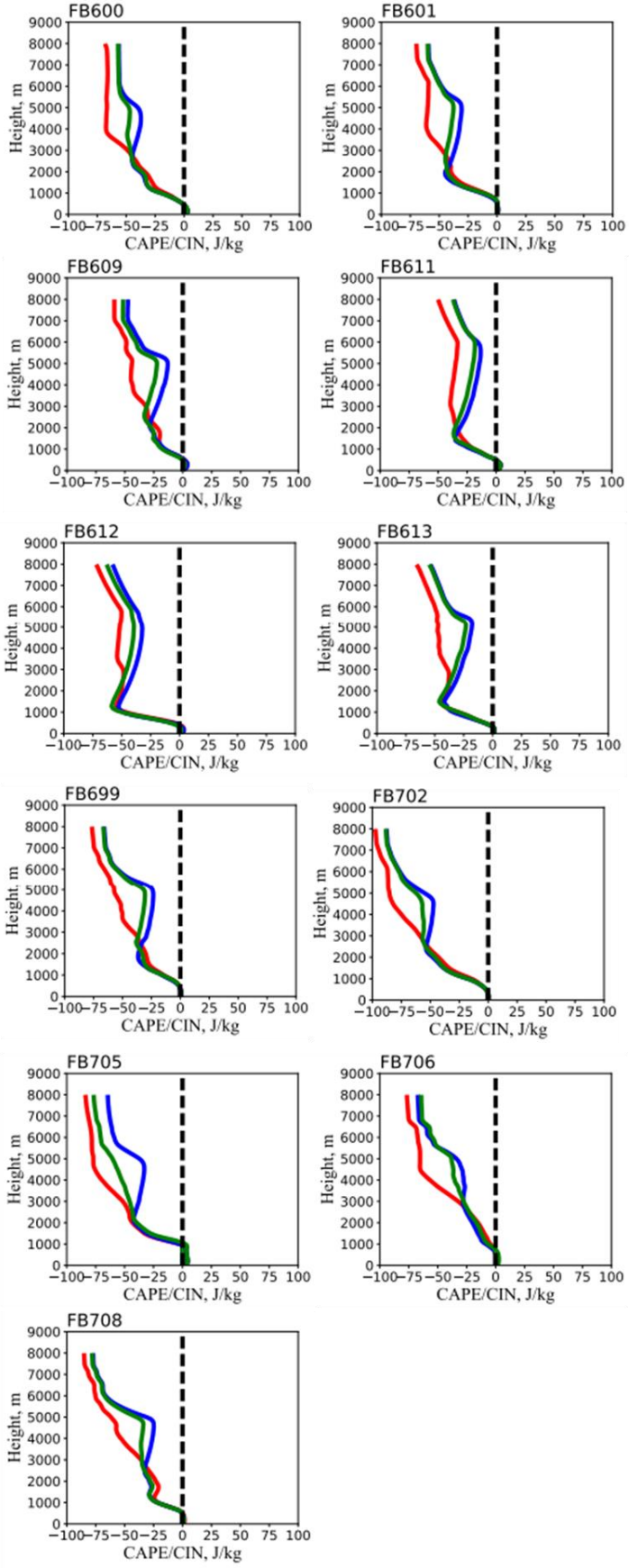

Figure 4. 29. As same figure (4.28), except for more flight cases.

Table 4- 1. The ZLCL of air parcel for the SW, LW, Total radiations. The results are based on simulating dust heating rates with using peak heating rates from Otto et al. (2007) and Zhu et al. (2007).

Flight N.	ZLCL, m			
	Non-dust HRs	With dust HRs		
		SW	LW	TOT
FB700 (Non-dusty)	853	700	1052	1033
FB708 (non-dusty)	556	987	1402	1386
FB705 (dusty)	681	724	769	716
FB600 (moderate)	696	792	1132	1114
FB601 (moderate)	1031	929	1248	1230
FB611 (moderate)	1177	1075	1379	1361
FB702 (moderate)	966	815	1147	1129
FB609 (moderate)	1293	1207	1487	1473
FB699 (moderate)	1133	935	1252	1234
FB604 (very dusty)	1957	1810	1927	1776
FB612 (dusty)	650	882	1234	1206
FB613 (dusty)	1316	1183	1473	1454
FB605 (dusty)	2043	1951	2145	2130

4.14.2 CAPE and CIN results based on LEM simulations using FENNEC data

Dust and water vapour radiative heating rates in the LEM simulations give rise to well-mixed potential temperature layers in the SAL and this is likely to increase the CAPE; however, the base of the well-mixed region is at a significantly increased potential temperature and this creates a more stable layer below the SAL which will have a large CIN. So, the result is likely that the presence of the SAL will inhibit convection breaking into the SAL from below, but if it does it will rise to significantly through the SAL without much resistance.

In figure (4.30), the vertical profiles relating to CAPE and CIN parameters are presented for the FENNEC based LEM simulations of 8 hours over the ocean. The top left and top right panels show the vertical distributions of CAPE and CIN for the very low dust cases including FB700 and FB708 and the dusty day event FB604, while the left bottom and right bottom plots show the results with more flight cases during 2011 and 2012, respectively. Calculations using dust and water vapour are shown in coloured stars for CAPE and triangles for CIN profiles. All figures are based on the re-binned sizes of dust mass loading that were generated from flight observations. It can be seen that the convective potential energy is determined by dust and water vapour impact, however, as mentioned, dynamics below the SAL will be prevented from reaching the SAL by the strong CIN layer which is larger at the low levels (near surface up to 2 km) for the dusty compared to non-dusty cases. This is shown by triangles for the moderate and dusty cases compared with non-dusty cases (e.g. FB700 and FB708).

In terms of the level of condensation (ZLCL), table (4-2) shows again that dust and wv contributes to increasing the altitude at which saturation will take place. Table (4-2) also illustrates the value of the ZLCL in the presence of dust and water vapour for SW, LW and total radiation. Together with surface water vapour relating to the previous figure (4.7), ZLCL for total radiation is high in the case of dust and water vapour. For instance, flight case FB604 has value of 1790 m with dust and moisture active, which indicates that lifted air has higher altitude to become saturated.

Another important point is that the CIN values below the SAL that arise for the dusty cases will inhibit convection, but this effect is likely to diminish as you progress further and further away from the African coast.

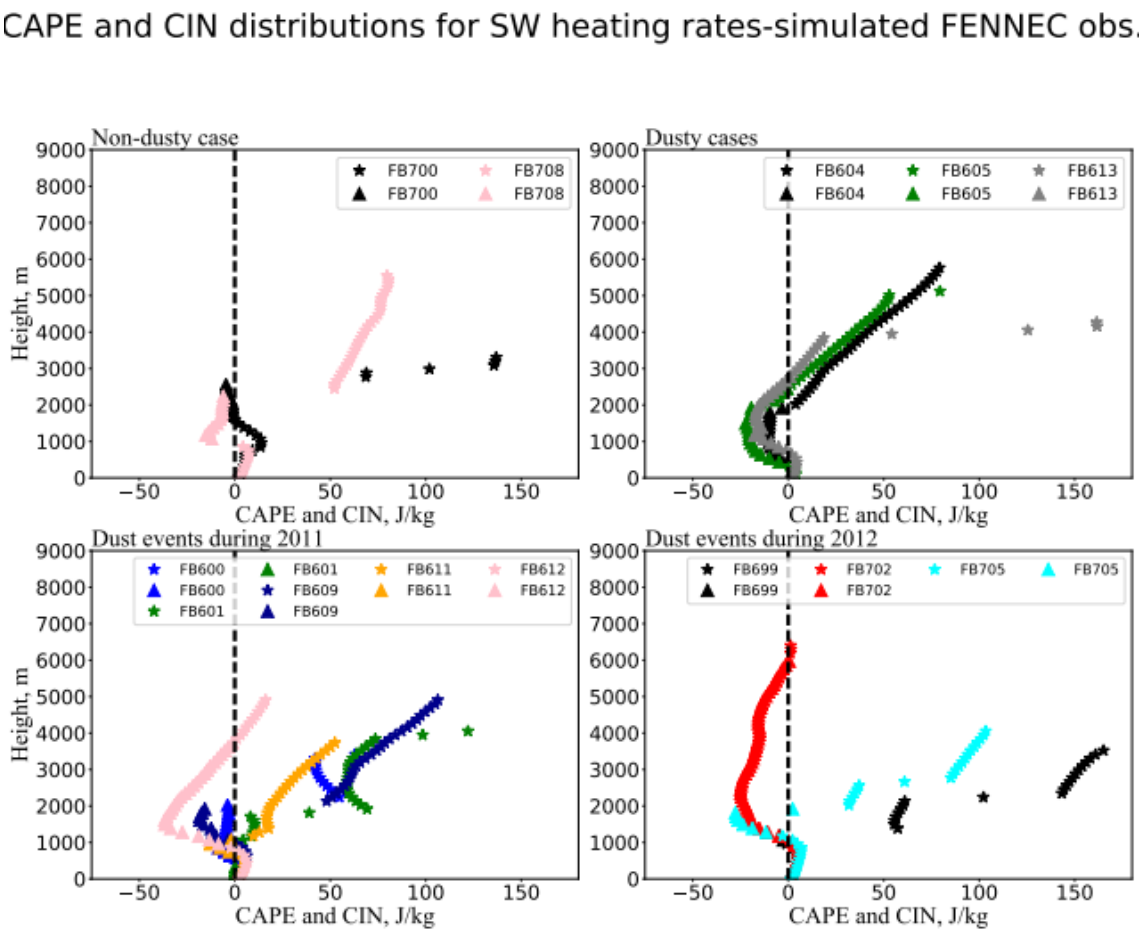

Figure 4. 30. Vertical distribution of CAPE and CIN parameters from LEM simulations after 8 hours for: non-dusty event (top left), dusty event (top right), dust events during 2011 (bottom left) and dust events during 2012 (bottom right). The calculations are related to simulated re-binned dust mass concentrations from FENNEC observations for the SW radiation. Stars show CAPE values, while triangles show CIN profiles. Coloured stars and triangles indicate different flight profiles. All panels show vertical profiles with both dust and WV. Results are expressed in units of J/kg.

Table 4- 2. ZLCL for non-dust, moderate and dusty days from the LEM simulations for 8 hours.

Flight N.	ZLCL, m		
	With dust and wv HRs		
	SW	LW	TOT
FB700 (non-dust)	687	592	634
FB708 (non-dust)	1123	1006	1063
FB705 (moderate)	1038	840	988
FB600 (moderate)	937	833	874
FB601 (moderate)	1008	830	957
FB611 (moderate)	1220	838	1077
FB702 (moderate)	880	716	806
FB609 (moderate)	1163	1009	1110
FB699 (moderate)	1009	853	951
FB604 (very dusty)	1832	1750	1790
FB612 (dusty)	1021	1000	1027
FB613 (dusty)	1188	1034	1128
FB605 (dusty)	1985	1935	1960

In the previous sections, the role of Sahara dust in determining the atmospheric structure of the dusty marine environment was presented by showing the heating rate profiles from the radiation model, in which dust and water vapour radiatively heats and cools the layers and that this

contributes to vertical motions. The calculation of CAPE and CIN parameters are mostly dependent on temperature of both environment and air parcel. These calculations are represented as a theoretical calculation to quantify the changes in the energy available if ascent took place. However, whether ascent is present for the CAPE and CIN to act on is another question. In the thesis cases, flight cases were used that were clear air profiles, without cloud. Although the dust and water vapour were shown to have key roles in determining the structure of the dusty outbreak air profiles, it is possible that other factors could compete. For example, shear effects can also have a role in determining the structure of atmospheric profiles. Since the magnitude of wind shear over the Atlantic, as is shown in Chapter 2, is often higher than over land, see previous figure (2.8) then it is important to evaluate the relative importance of shear effects compared to dust/water vapour, and this is addressed in the next section.

4.15 The role of wind shear on the well-mixed SAL and dusty marine atmosphere

Although dust and water vapour can form and sustain the well-mixed marine structure and maintain it far away from Africa, other factors such as wind shear may be involved in influencing the air layer. Therefore, wind shear (WS, equation (43) section 2.2.2.1) effects were investigated for the atmospheric layers by using the LEM simulations along with the FENNEC observations of winds. Simulations with and without shear were run to determine if shear could cause the structure changes noted (well mixed layers with strong below-SAL inversion) earlier. Wind shear was calculated based on the equation of Tao and Zhang (2015) as it was shown in Chapter 2. Figure (4.31) shows the potential temperature with observed profiles (red line) and with a constant eastern wind component (black line) from the LEM simulations. A couple of runs were performed in the LEM with constant winds and with original wind profiles for both eastward (u) and northward (v) wind components to assess the effects of shear from no shear. Figure (4.31) shows examples of LEM results for runs with no-shear in the eastern wind component for the moderate dusty case FB609 and the dusty case FB612. Runs for all flight cases were implemented by taking one wind component as observed and the other as constant and comparing to a run with both components constant with height, no shear, in the LEM simulations, where the results of the northern simulations are not shown here because there is no change in results for both simulations of wind components. Although there is a slight effect of wind shear on the atmospheric structure within boundary layer, however, the results show that the WS does not have a significant effect on the dusty marine environment for any of the dust outbreak cases studied. Where LEM simulations show a low percentage change of about 1 % between with and without wind shear profiles.

Turbulent flow can be generated by wind shear effects, and thus it is worthwhile to assess the dynamic stability in comparison to dust/wv effects. Dynamic stability can be expressed by the

gradient Richardson number (Ri_g), which is defined as presented previously in Chapter 1 Calculations for Ri_g from FENNEC observed potential temperature with wind shear factors provide a good way to the evaluating of dynamic stability in the presence of shear, since Ri_g is dependent on the changes of potential temperature (i.e. $\Delta\theta/\Delta z$) and water vapour with height (Feltz et al., 2003). Therefore, Ri_g was calculated based on the observed profiles of θ etc. to obtain an assessment of dynamic stability of atmosphere.

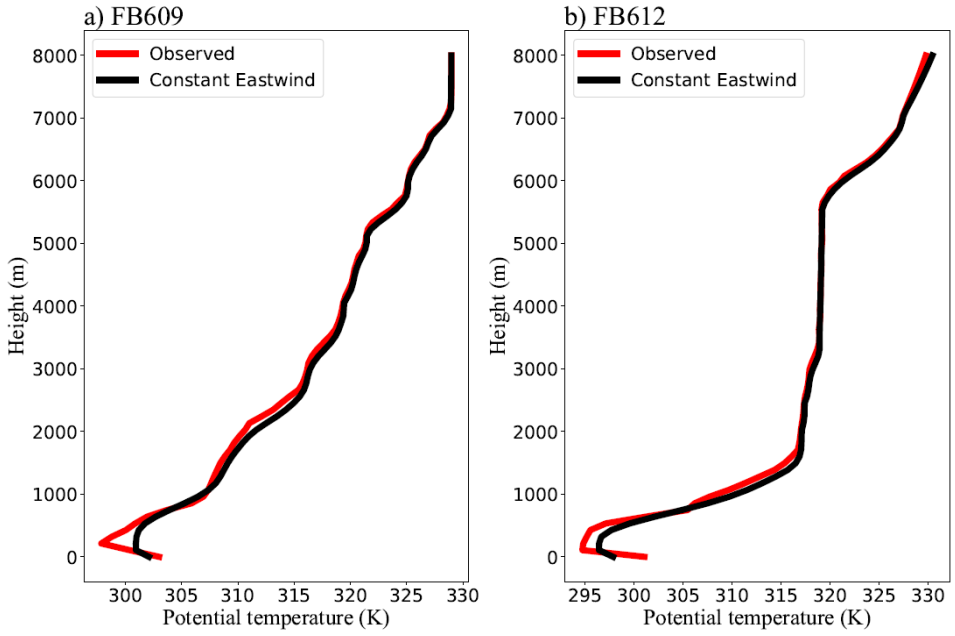

Figure 4. 31. Wind shear effects on the potential temperature profiles from LEM simulations. (a) Moderate case and (b) a dusty case. Red and black lines indicate the observed profiles from FENNEC with constant no-shear east wind profiles.

Based on the dynamic stability, dust and water vapour can cause turbulent flow in the atmospheric layers, and thus calculating the dynamic parameters provides a good way of evaluating the dust influences associated with shear. It appears from the figures (4.32) – (4.33) that the magnitude of WS (red line) is high within the MBL and starts to decrease slightly above it and upward with altitude. There is a relation between the Ri_g (blue line) calculation and the WS profile, in which results show the high values of Ri_g is largely associated with low WS, the atmospheric structure is characterised by a dynamically stable state, i.e. Ri_g is greater or equal to 0.25. In contrast, turbulent flow occurs when the magnitude of WS is large and the changes in the θ profile with height are small, since the shear will overcome the stratification and cause instability for periods of time, where $Ri_g < 0.25$. For instance, at altitude below 4.5 km for the flight number FB604, where the atmosphere is dynamically stable as the potential temperature is increasing with height with low WS. This can be noticed as well as for FB605 at a height of 5 km.

Based on all profiles, there is a variation in the magnitude of calculated Ri_g with height, but results show that the average of Ri_g in dusty profiles ranges between about 0.1 and 0.5, while for other cases Ri_g is greater than this range. This indicates that very dusty events result in a marine vertical structure that is more unstable than moderate or non-dusty events.

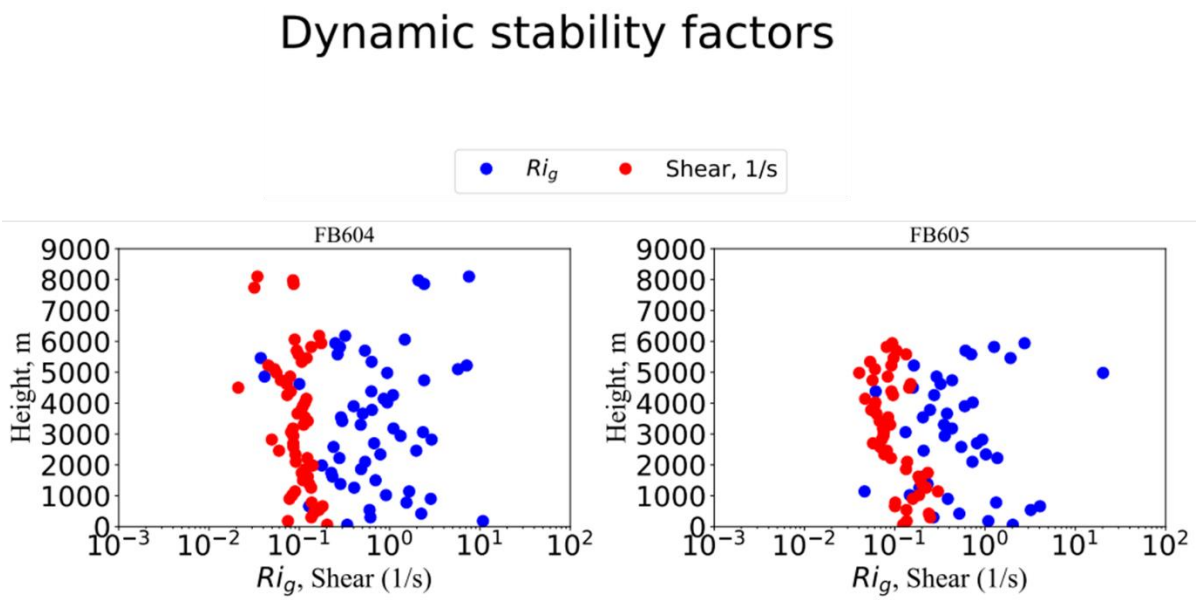

Figure 4. 32. Vertical values of the Ri and shear (1/s) calculated based on FENNEC observations for the dusty outbreak flight cases of FB604 and FB605.

Away from the African coast, the same conclusions are drawn when considering the case of shear and no shear effects for profiles of a dusty case over the Atlantic in Puerto Rico, as shown in figure (4.34). The shear estimation can be performed from this figure and combined with using the projected potential temperature data at Puerto Rico based on the FB605 flight case (dusty case) using a cooling impact by other gases without dust and with non-elevated water vapour cases. It is likely that the turbulent flow due to the dust and wv influences can sustain well-mixed potential temperature structure profiles right across the Atlantic to the Puerto-Rico region (see Chapter 5) For example, with the dusty day, FB604, which θ is approximately constant and the term of $\Delta\theta/\Delta z$ is almost zero, which means it is conditionally unstable. The tendency of shear shown in the previous figure (2.8) in Chapter 2 near the coastline of the African land, e.g. over the Canary Island, is larger than away from the African continent, west across the Atlantic Ocean. This suggests that shear does not have significant impact on instability away from the dust source (e.g. Sahara Desert), although horizontal winds can modify the distribution of the dust profile (Chen et al., 2010). In addition, shear may have influence tropical cyclones over the Atlantic (Chen et al., 2010), but this is not within the focus of this work.

The main finding here is that the simulation of WS has a minor impact on the SAL compared to dust and wv radiative effects, and thus it has not a significant effect on the atmospheric stability studied in this work. In addition, calculations for Ri_g show that dust and wv within the SAL contribute to continuing turbulent flow in the dusty marine environment even after dust is transported away from the north Africa coast, but the magnitude of Ri_g tends to increase (more stable condition) as the potential temperature changes in height increase over the Caribbean, increased in a comparison with the Canary Islands.

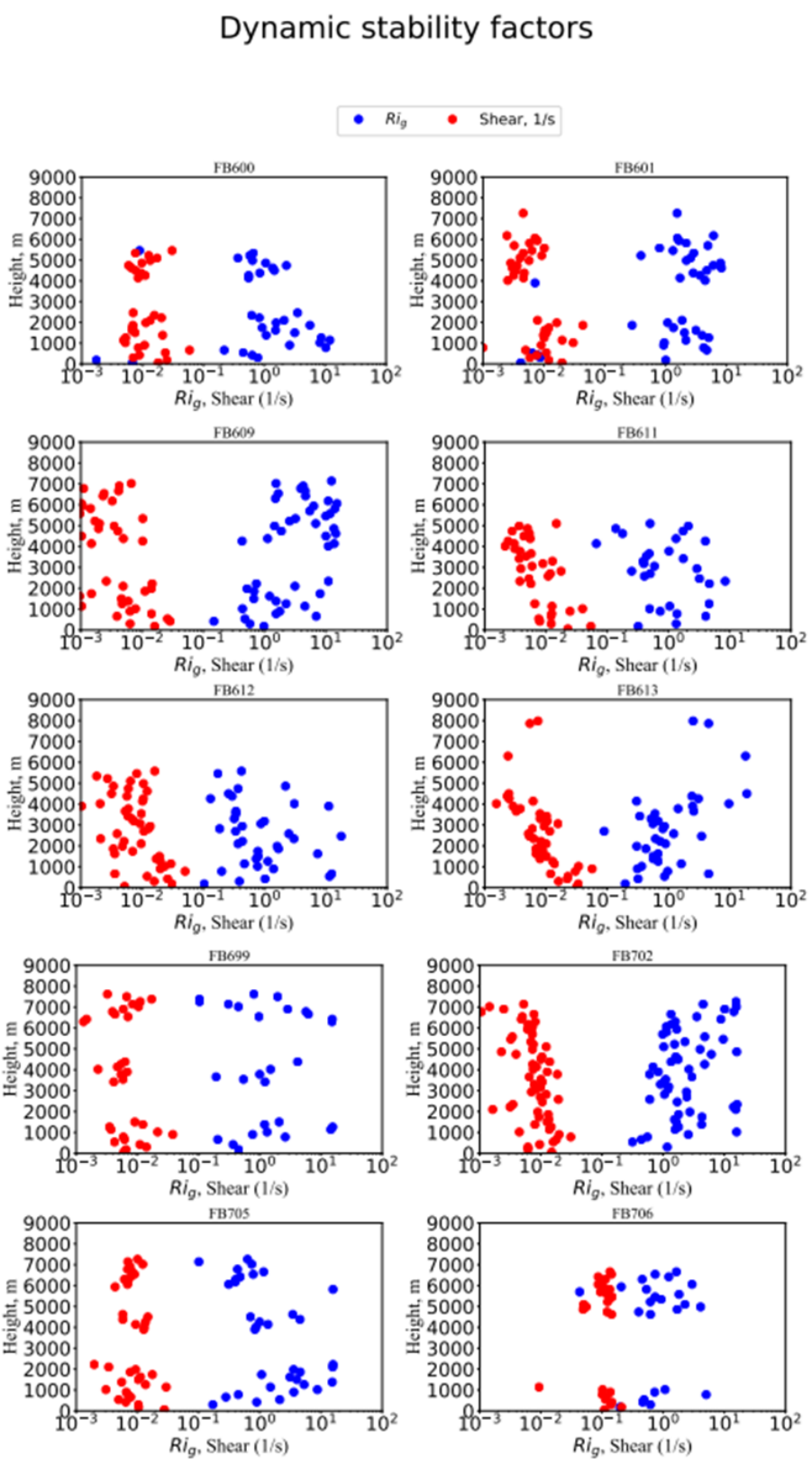

Figure 4. 33. As previous figure (4.32), but for more cases.

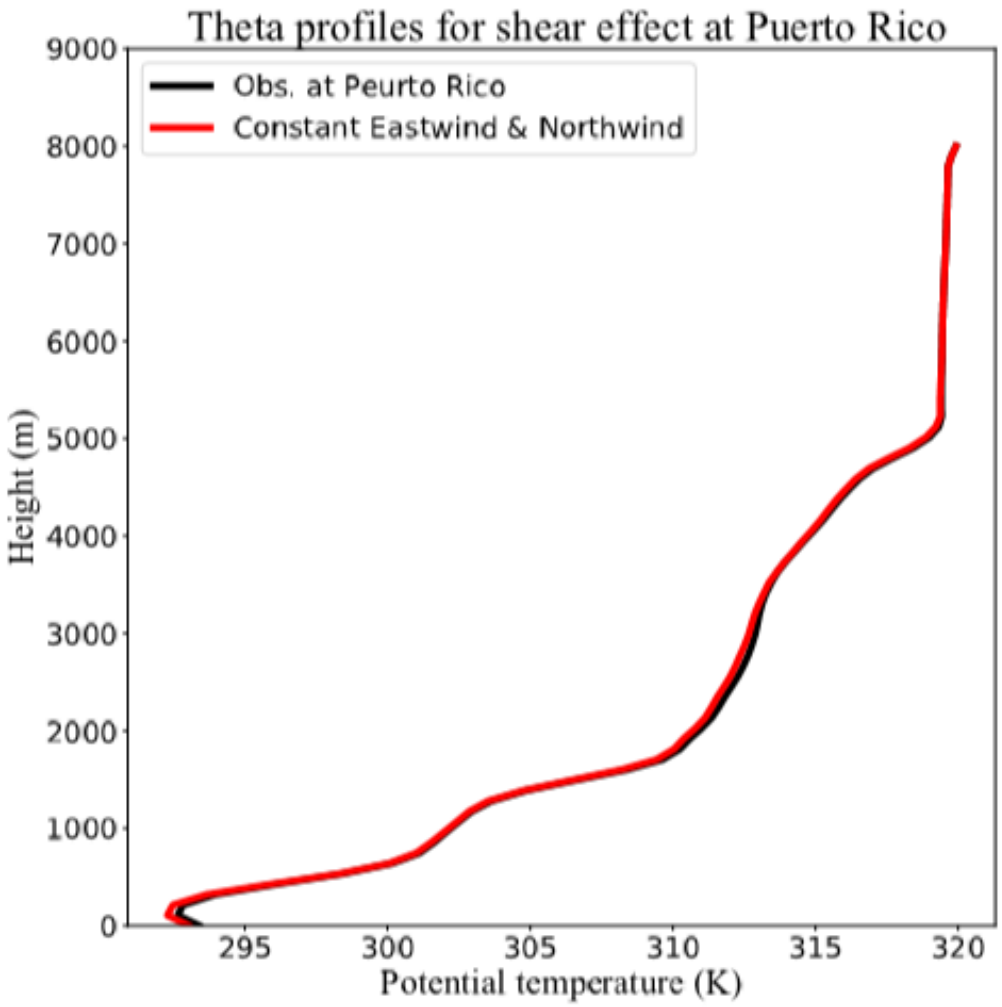

Figure 4. 34. Potential temperature profiles for the simulation of wind shear effects for the Puerto Rico region in the presence of cooling effects by other gases only (i.e. without dust and with non-elevated water vapour heating rates). The black line refers to the observed profiles in the presence of the cooling effect by other gases (without dust and moisture impacts). LEM runs with set both eastward and northward winds to constant value within whole profile. Vertical profiles of potential temperature were taken from the output file (considering flight FB605 with initialized SZA=63 degrees) from the projected θ by a mathematical code under cooling impact by other gases over 7 projected days. The difference in top height values of simulated potential temperature from observed one is the top value of observed potential temperature is at about 7 km, while in LEM is at 8 km.

4.16 Summary

Various tests were performed in this chapter to analyse the effects of dust outbreaks on the atmospheric structure over the Atlantic Ocean. Some idealised assessments were performed in the earlier sections including assessing how long it would take for a background non-dusty air profile to be affected if dust and water vapour associated with a dusty outbreak entered into background marine profile. It was shown that if dust enters a stable layer, either by intruding into it or dust sediments into it from above, then the dust/wv radiative heating rates causes that layer to become well mixed on the timescales of about eight hours based on the dust altitudes

observed in the FENNEC cases studied. Potential temperature profiles from the observations (including flight and radiosonde observations) show an agreement between the SAL and θ structures over land and the Atlantic for much of the profile, but below the SAL and especially the MBL there are large differences. The potential temperature of the lower layers is far lower than for over land. This comes about due to the warmer land-based dust advecting over the cooler ocean and riding over the MBL.

In the next idealised test, I addressed what would happen when a well-mixed SAL lost its dust. How long would it take for the well-mixed region to become stratified? Eight-hour LEM simulations showed that there was very little change in structure over that timescale. By running a simple code extending the timescale to 7 days using a well-mixed dusty profile with the dust switched off, but allowing the clear air gaseous radiative effects with different initialized times, I found that the layer was more stable but the layer does not completely stabilise. So, from these tests I conclude that elevated water vapour and dust can establish well-mixed layers quickly and they will last well beyond when the dust has gone and potentially right across the Atlantic with somewhat well-mixed layers.

It is usual that dust outbreaks will be in warm dry air, but the observed dusty outbreak air in these cases studied contained usually higher levels of water vapour compared to the background marine environment and so more than expected for dusty cases. To account for water vapour radiative effects in comparison with dust effects, it is unrealistic to use non-wv (i.e., wv=0) profiles in the radiative simulations, thus I use a wv profile based on a non-dusty environment background that is considered as a realistic background profile typical of non-dusty air. I use the reference non-dusty background marine wv input data for FB708 to determine radiative heating profiles and then in the LEM simulations. The non-dusty background wv approach of using FB708 was used for both the Canary Islands and the Caribbean region (e.g. Puerto Rico site). The SW and LW heating rates for dusty cases are associated with high amount of water vapour and are significantly higher than those for non-dusty wv environment, where the SAL water vapour had the most important effect on the radiative heating rates. The water vapour was much more significant than the dust in creating and maintaining well mixed potential temperature layers in the dusty marine environment. LW cooling at the top of the elevated water vapour profiles destabilised air causing mixing below and maintained or established well-mixed SALs. Sensitivity test explored that derived SW heating rates are more sensitive with decreasing dusty wv by about 80% reduction than reducing dust profile, but dust reduction associated with fixed water vapour can change heating rates at low level of SAL under this percentage reduction.

These well mixed layers have the potential for convecting air to rise right up through them, however, the stability below these layers is greatly increased, compared to non-dusty days, with large CIN values that will inhibit convection reaching the well-mixed layer. The ZLCL is higher for higher levels of dust in the atmosphere. This is likely due to the higher temperature of the SAL

base of the mixed-layer in the SAL, which would contribute to reducing the relative humidity and raising the ZLCL. So, these well-mixed layers that form will inhibit convection downwind.

Other factors that could have established the well-mixed layer could have been shear. But the results of this study show that shear in the flight cases was not strong enough from the observations in FENNEC to do this, and so the shear takes a negligible role in establishing the structure compared to the dust and wv radiative effects. Dust causes warming from SW radiation within the dust layer by absorption, but water vapour has the largest contribution through its increasing of LW cooling at the TOA.

The evaluation of dusty outbreak radiative effects led to the understanding that water vapour is radiatively the most important. Although the method in the current thesis for investigating the radiative effects of dusty/water vapour air may not be the same approach as Alamirew et al. (2018) and Marsham et al. (2016), but the evaluation of dust and wv effects can be compared with these works since thesis results are based on contrasting the thermodynamic and dynamic effects of dust/water vapour for dusty cases to a reference background of non-dusty wv environment. I found that water vapour contributes significantly to changes in the LW net fluxes at the top of SAL which by comparison was much larger than the weak dust effect. However, within the SAL and underneath it, dust remained an active factor in changing the radiative fluxes but just to a less amount than water vapour. In the LW, the dust will trap LW radiation emitted by the surface and it will be partly re-emitted back toward the surface, thus causing warming of both the dust layer and the air below the dust. It was also found that warming effects below the SAL can be caused by large dust particles, but generally giant particles that are captured in several flight observations do not have a significant impact on the radiative effects for the whole marine structure due to low number concentrations.

5.Chapter 5: Effects of SAL downwind across the Atlantic

5.1 Overview

In Chapter 4, the radiative effects of Saharan dust and water vapour heating rates were studied using an LEM model to assess the radiative and dynamical characteristics of dust laden profiles. The modelling was based on eight-hour simulations based on FENNEC observation profiles taken during aircraft ascent/descent over the Canary Islands to measure the dusty marine environment. Since significant dust outbreaks involve dusty air being transported long distances across the Atlantic, I wanted to know if the dusty air was important for the atmospheric structure on the other side of the Atlantic. Much of the dust will sediment out of the advected air before arriving there but radiosonde profiles from Puerto Rico show that there is a signature of the SAL in the observed potential temperature profile. So how important is the dust and water vapour in the air on the west Atlantic for these FENNEC dust cases? To address this, I needed to estimate how much dust at each level and each bin would make it that far. To do this, I developed a simple model to estimate the amount of dust that could be expected to transport across the Atlantic during the FENNEC cases studied in this work. The model is called the bin resolved sedimentation and turbulence model (BRSedT) and includes advection, large-scale subsidence, dust particle sedimentation and turbulence processes. I recognise that for a week-long transport, the amounts of dust that will be transported will be difficult to predict and so I accept that the estimate will be approximate, but I have made some comparisons of predictions to dust optical depths from satellite and vertical profiles from FENNEC aircraft observations of dust arriving at the Canary Islands to illustrate that the model provides acceptable estimates.

So, the focus is on transport in two directions (based on HYPSPLIT observations presented in a previous chapter): from the African land towards the north-west, passing over the Canary Islands and then towards the north east; and 2) directly west, towards the Caribbean. For the first direction, I refer to it from now on as towards the north-west since comparisons to observations in this chapter took place once it arrived at the Canary Islands. The modelling of the dust was performed with the BRSedT model. It is initialised with dust profiles from FENNEC flight observations over the African land. The transport in the BRSedT model is predicted from a hybrid treatment of ECMWF winds and HYSPLIT trajectories.

The main aim for this chapter is to assess if dust and water vapour transported long distances away from Africa will still be able to radiatively influence the structure of the atmosphere. To do this I developed simple transport model that can be used to estimate the size and layer resolved dust mass concentrations when compared to observations.

The BRSedT model is validated by comparing profile results with aircraft profile observations that were measured during ascent over Africa and compared to what was measured from flights in the Canary Islands the next day. As part of the validation, I also test sensitivity to such factors as fall velocity, turbulence and dust density. In addition to comparing flights ascents to descents, dust results from sedimentation runs were also compared with MODIS-Terra satellite observations, since Kaufman et al. (2005a) showed that using MODIS satellite observations can be an accurate way to quantify dust measurements over the ocean where there are very few observations.

5.1.1 Dust sedimentation and trajectories over the Atlantic

Many previous works used HYSPLIT trajectories for dust transport models to investigate the evolution of dust including advection, sedimentation and turbulent diffusion over long distances over oceans, such as Schutz et al. (1981), Gasteiger et al. (2017), etc. The methods used will frequently transport dust in a western direction from the African desert source, but satellite observations as well as modelling results such as the MERRA model indicate that dust transportation is split into two directions (as mentioned before). Therefore, I will take a novel approach of scaling the dust mass loading originating from the land source by the fraction of trajectories that proceed towards the north west and west directions. This approach is based on the following steps:

1. Determination of the origin of the air mass sources by using HYSPLIT back trajectories. This method is based on running the HYSPLIT model online with each flight height as the starting altitude for 60-70 trajectories and this is done at every 120 m altitudes starting from two locations: The Canary Islands at latitude 28.2˚N, longitude 14.0˚W, and over the Atlantic Ocean at latitude 18.20˚N, longitude 66.6˚W (Puerto Rico).

2. The starting locations were chosen based on MODIS observations of where the dust was being transported. Outbreaks would generally get advected in a corridor towards the west and another path that deviated towards the north-west direction from the African land (i.e. towards the Canary Islands). Backward trajectories were started from both the west corridor of dust as well as from the Canary Islands to determine the fraction of the trajectories coming from the dusty sources (trajectories observed to go over land hence picking up dust) as opposed to staying over more pristine ocean.

3. Dust factors were calculated by dividing the number of trajectories that crossed over the continent (picking up dust) compared to the total number of trajectories started. Dust factors

were calculated for both directions separately and implemented in the BRSedT model. A simple formula for calculating dust scaling factor (SF) is written as follows:

$$SF = \frac{N}{TN} \qquad \text{Eq. (49)}$$

Where N, the number of air trajectories that came from dust sources (i.e. African land) for each height level, whereas TN is the total number of trajectories started with that height level. So, the final profile of dust mass loading or dust size distribution used in the BRSedT model is multiplied by the scaling factor (SF) in order to account for the amount of dust going in the direction of interest, either the Canary islands or over the Atlantic. This will account for diluting of dusty air masses by air from non-dusty air sources whilst capturing the amount of dust from land sources. The main approximation in this is using the dust profile over land observed during the flight ascent to be appropriate for all trajectories originating over land. Forward trajectories could also be used to estimate the dust arriving at the two locations, but it was deemed too involved since trajectories would need to be started at too many locations including right around the end locations to determine the fraction originating from the dusty sources. It was deemed that back trajectories were far more computationally efficient and would give the same result if the forward trajectories were set up carefully to cover the whole region.

Estimating the trajectories far across the Atlantic by using the SF approach may be perceived to have less and less accuracy as the distance from Africa increases (i.e. Puerto Rico), but the accuracy of trajectories are still expected to be reliable because the wind profiles are dominated by large-scale easterly winds, and the checking of the origin of air mass sources at several locations at various distances from Africa indicate a good agreement with this direction of transport.

5.2 BRSedT Model description

In this section, the BRSedT model is described including the model structure, the sedimentation, the largescale subsidence, advection, turbulence scheme and trajectory scaling factor (introduced above).

5.2.1 Overview of the BRSedT model and structure

As huge amount of Saharan dust transported across the Atlantic far away from the African land, dust particles play significant role in influencing radiative energy balance in the globe. So, determining dust size distribution and dust profiles were needed to model the development of dust profiles during dust transportation which is important to understand the radiative effects of African dust on the structure of marine environment. According to dust simulations by large-scale transport models, the evolution of dust removal over the Atlantic is controlled by many factors such as sedimentation, turbulent mixing and large-scale processes. So, I will discuss dust

modelling approaches performed by past previous works and then provide an evaluation for these studies. After that, I will present the structure of a new model (i.e. transport and turbulent model) in this thesis. Most previous works used dust profiles over African land and simulated the development of dust within SAL associated with factors impacts on dust advection across the Atlantic. For example, Gasteiger et al. (2017) focused on the vertical mixing process in the upper 1 km of the SAL over the Atlantic Ocean. They stated that gravitational settling is the crucial factor affecting dust transport across the Atlantic. Within the development of dust profiles over the Atlantic, Gasteiger et al. (2017) stated that only this process (i.e. gravitational settling impact) can maintain very small sizes of particles to remain above MBL away from the African land. However, their study may have a gap in evaluating the evolution of dust size distribution profiles with transport within MBL and in free atmosphere. This can be explained by their theoretical consideration for modelling the SAL top with assuming irregular particle shape over the Atlantic. Focusing on the upper 1km of SAL is not a good approach to apply for quantifying dust removal between African land and tropical Atlantic as this can ignore the changes of dust size distribution below and above SAL during time, and so underestimating the profile of dust size distribution in the whole atmosphere over the Atlantic. In addition to simulating the SAL top, selecting particle shape mode is an important factor in affecting how far particles can remain aloft from the dust source (African land) during dust transportation. Their study revealed that gravitational settling velocity maintains super-micron particle sizes in the marine environment. This means that using irregular particle shape in a transport model may contribute to retention of these small sizes in the atmosphere for long distances across the Atlantic rather than settling velocity impact.

Other factors such as turbulent mixing process and coagulation can also influence the development of dust size distribution over the Atlantic. This can be seen from Lee (1983), who simulated the dynamic and microphysics processes for dust removal in three atmospheric locations, including the MBL, SAL and above the SAL. On one hand, Lee gave a good explanation as to what size distributions of dust particles can be affected by different factors (including turbulent mixing and coagulation), where he shows throughout the full size distribution of dust particles that dust particles > 3 μm in diameter were reduced by sedimentation impact during time, which is in agreement with similar points for particles greater than 3.6 μm stated by Gasteiger et al. (2017). On the other hand, the removal process discussed by Lee (1983) varied the dust altitude between these three atmospheric layers (MBL, SAL and above the SAL) which is indicated by a ratio 2:1 in dust concentration between marine boundary layer and dust layer, and with no impact of sedimentation in the free atmosphere. Although results in determining the particle sizes under dust removal process for Lee (1983) and Gasteiger et al. (2017) are quite the same, dust modelling performed by Lee (1983) provides better understanding in the development of dust size distribution than Gasteiger et al. (2017). However, findings for both Lee (1983) and Gasteiger et al. (2017) show that dust particles (> 3 μm) that influenced by removal processes are

characterised by smaller sizes from these stated by Maring et al. (2003), who studied the changes in dust size distributions between the Canary Islands (e.g. Izana, Tenerife) and Puerto Rico by calculating the fraction of dust lost during dust transportation between these locations. Their findings revealed that particles greater than 7.3 μm in diameter are preferentially removed corresponding to Stokes settling velocity effects in the marine atmospheric environment. Maring et al. (2003) used a model to examine the changes in dust size distribution by assuming that the vertical velocity of dust particles is equal to the difference between Stokes settling and upward velocity (assigned for value of 0.0033 m/s). According to the discussion above, there is a variation in the results of dust simulation for particle sizes that are affected by these factors along dust transported between Africa and Caribbean sites. This variation can be created by the impact of dynamical factors such as large-scale winds as well as the characteristics of the SAL. To tackle how much dust is removed from the atmosphere during transport, it is important to set an appropriate approach for simulating dust transport including sedimentation, turbulent mixing and large-scale winds. This is both challenging and interesting to focus on. Flight observations for potential temperature shows a well-mixed SAL over land and the Canary islands, and therefore, based on these factors (sedimentation, turbulence, etc) it will be interesting to explore how the well-mixed dust layer evolves with these processes and see the time evolution effect on the dusty marine atmospheric layer. It would then be possible to estimate whether the SAL is playing a role in affecting the marine atmospheric structure at large distances from the source region.

In this work, a new model, BRSedT, is developed to project forward the amount of dust from the initial profiles (based on dust profiles from FENNEC observations) as a function of each layer (i) and bin (b), over time accounting for large-scale vertical motion (w) and sedimentation of dust particles with a terminal velocity (v_t) and turbulent mixing. In the BRSedT model, a sub-grid turbulence scheme was implemented acting on the dust vertical transport and is estimated by implementing a first order turbulent diffusion scheme based on the local diffusion scheme by Holtslag and Boville (1993) and Jeričević et al. (2009) in order to study the changes in dust profiles due to the turbulent diffusion process over the Atlantic. The description of the turbulent diffusion scheme in the model will be explained in section 5.4.

Dust simulations by BRSedT is performed for 7 days across the Atlantic Ocean (typical timescale to reach the Caribbean) and 4 days towards the north-west direction (projecting past the Canary Islands and eastward) from the continent of Africa in both cases. The BRSedT is a Fortran code (see Appendix B2) with inputs for potential temperature (θ), expressed in units of K), fall velocity (v_t, m/s) for each size bin, turbulent diffusion coefficients (k_z, m^2/s) with height, dust scaling factor (SF, unitless), and the number concentrations of dust (dN/dD, $1/cm^3$ μm) for each bin and layer. The bin diameter used in the BRSedT ranges between 0.134 μm and 106.39 μm. The input data of vertical velocity (w) was taken from ECMWF reanalysis dataset and interpolated to fit with the heights of FENNEC observations which are used by the model as well.

Fall velocity for each diameter is calculated for spherical and non-spherical particles by using the equations from Zhiyao et al. (2008) and Gasteiger et al. (2017), respectively. The equation sets for calculating v_t will be presented in section 5.2.3.

The flow diagram of BRSedT is given in figure (5.1), which presents the entire simulation process of the dust sedimentation transport over the Atlantic. It is a 1-D model in which each bin at each level is tracked in the vertical over time with the sedimentation acting depending on particle size, turbulence acting throughout the profile and large-scale subsidence prescribed to model the variation over time as the air advects. The model is a hybrid Lagrangian-Eulerian model. The parcels at each height containing a bin size of dust are tracked individually and allowed to evolve under sedimentation and large-scale subsidence to any subsequent level. The model is 1-D in that parcels cannot advect at different rates. The mean advection (determined from HYPSPLIT trajectories) determines the location of the 1-D grid and the relevant subsidence at each height from ECMWF is applied. Therefore, the model is a 1-D model that is advecting with the mean flow of the large-scale winds and in the vertical, there is Lagrangian tracking of all bins. Turbulent diffusion is applied at each timestep between the equivalent Lagrangian bins sizes in the vertical. Bins that reach or go below the surface are counted as being deposited on the ocean surface. This can only occur through sedimentation, subsidence or turbulence. At the end of the simulation, the dust bins with height are scaled by SF to account for dust profiles that went in that direction. The evolution of dust over the Atlantic with time in the BRSedT model is represented by the following:

I begin with the dust profile measured over the African land and the dust of each size i and bin size b is tracked in height by the variable z(i,b) and dust number nr(i,b). At each timestep, Δt, the height of the dust of bin size b is updated by,

$$\Delta z(i, b) = nw * \Delta t \qquad \text{Eq. (50)}$$

Where, nw is the net velocities influencing the dust location, which is represented by the subsidence w(ilay) and fall velocity $v_t(b)$ expressed by,

$$nw = w(ilay) - v_t(b) \qquad \text{Eq. (51)}$$

These two parameters in Eq. (51) control where the final level of dust particles will be located for each bin after each timestep. Note, the ilay will differ from i after the particle has fallen out of the initial layer that it started at. From then on, z is used to track the particles and can take on any values, not just layer values, and i allows knowledge of the initial starting height to be retained. The value of z is then determined to be within a specific layer, identified as ilay. So ilay is the layer of the specified particle after it has sedimented a given time step. The ilay is used to determine which layer the particles are in order for the subsidence to be applied. Similarly, the turbulent mixing impact is simulated at the height ilay of dust particle at each time step. I calibrated the model for each of these velocities on the final profiles of dust mass loading

separately by validating the BRSedT and checking that the dust responded correctly. This is shown in a later section 5.3.

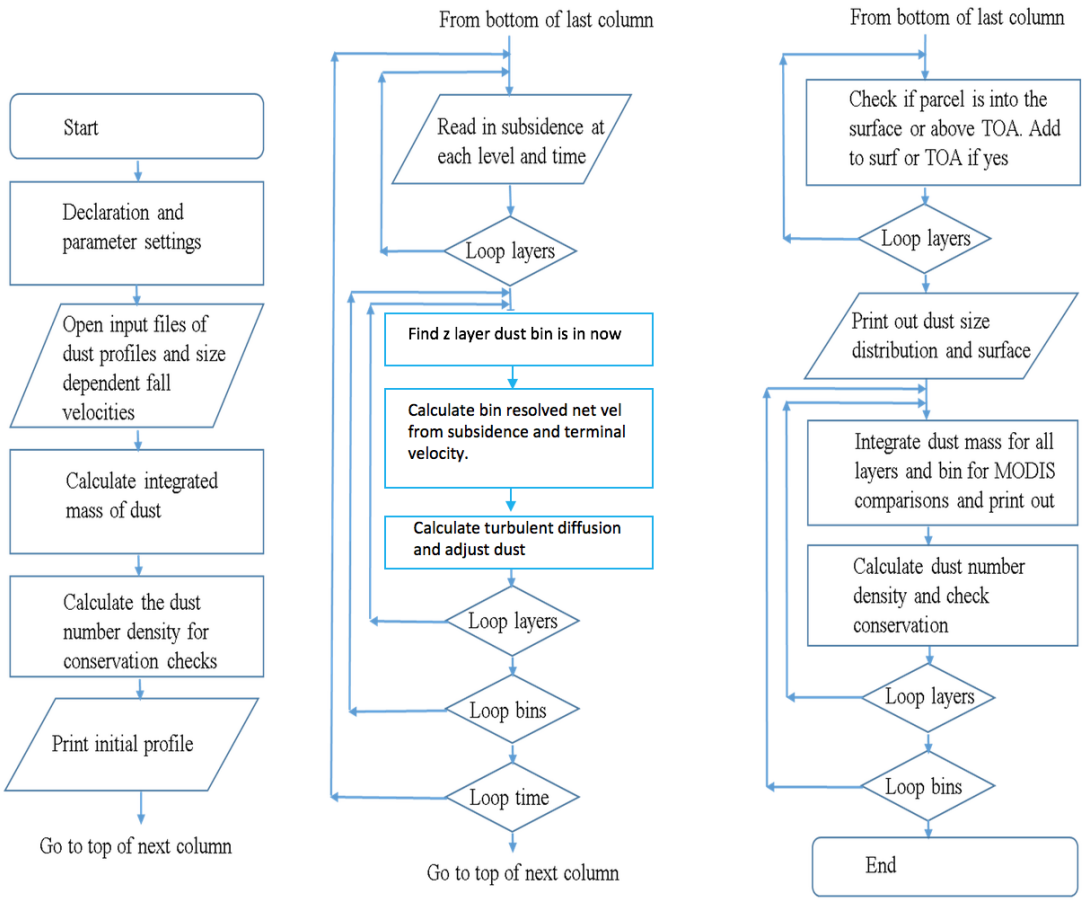

Figure 5. 1. Flow diagram describing the BRSedT model.

5.2.2 Turbulent diffusion scheme in BRSedT: k_z-diffusion scheme

Turbulence plays a significant role in atmospheric dynamics, especially in the boundary layer by causing mixing of heat, momentum, moisture, particles and gases. To account for turbulent mixing of the dust, I have installed in the BRSedT model with a 1st order turbulence closure k_z-diffusion scheme (Holtslag and Boville, 1993; Jeričević et al., 2009). In the current thesis, investigating turbulent diffusion is implemented based on k_z-diffusive scheme explained by Holtslag and Boville (1993) and Jeričević et al. (2009). I updated the BRSedT model with a turbulent diffusion parameterisation that acts on the vertical dust profiles as the parcels advect across the Atlantic and toward the Canary Islands or west coast of the Atlantic Ocean. Four different flights were used, including FB604, FB605, FB612 and FB699. The turbulent diffusion of dust scheme required a number of variables including wind profiles and surface fluxes, etc., which were taken from the ECMWF reanalysis datasets.

The determination of the turbulent fluxes is based on stability and shear effects in the free atmosphere by local wind gradients and potential temperature profiles. In the boundary layer, the turbulent effects were more dependent on the surface heat flux. The turbulent mixing of a quantity x given by $\overline{w'x'}$ is equal to the vertical gradient of x multiplied by eddy-diffusivity coefficient (k_z, m^2/s), where x describes one of the potential temperature (θ), and u or v wind components in the atmosphere. Therefore, the vertical flux in sub-grid turbulent scale can be expressed by the following formula (Holtslag and Boville, 1993),

$$\overline{w'x'} = -k_z\left(\frac{\partial x}{\partial z}\right) \qquad \text{Eq. (52)}$$

The term between the brackets is the vertical gradient of any quantity x. In the case of current work, the quantity x will be the concentration of dust. To solve Eq. (52), one challenge is to determine the turbulent diffusivity coefficient (k_z, m^2/s). As turbulent diffusivity can impact on the vertical profile of dust, k_z needs to be calculated throughout the atmospheric-structure layers and consistent with dust transport west or towards the north-west directions from the African land.

To solve for k_z, the first step is to categorize the atmosphere into three layers for consideration by the turbulence scheme. The first is the shallow surface layer just above ground level, which is approximately 200 m in depth (Jeričević et al., 2009), the second is atmospheric boundary layer (ABL), and the third is the free atmosphere.

I follow the scheme of Jeričević et al. (2009) for the surface and boundary layer and I follow Holtslag and Boville (1993) for the free atmosphere. Jeričević et al. (2009) has a better treatment of the surface layer using Monin-Obukhov similarity theory and links to surfaces fluxes whereas the Holtslag and Boville have a better treatment of the free atmosphere shear.

So, from above, the concentration of dust C is written for the free atmosphere above the BL as

$$\overline{w'C'} = -k_c\left(\frac{\partial C}{\partial z}\right) \qquad \text{Eq. (53)}$$

Where k_c is the turbulent diffusion coefficient for dust (Holtslag and Boville, 1993). k_c is represented as a function of the length scale, shear and gradients in potential temperature.

$$k_c = l_c^2\, S\, F_c(Ri) \qquad \text{Eq. (54)}$$

Where S is the shear, and F_c is the stability function defined below. The shear is given by

$$S = \left|\frac{\partial V}{\partial z}\right| \qquad \text{Eq. (55)}$$

The l_c is given by

$$\frac{1}{l_c} = \frac{1}{kz} + \frac{1}{\lambda_c} \qquad \text{Eq. (56)}$$

Where k is the von Kármán constant (k=0.4), Ri is defined below, and λ_c is the asymptotic length scale. For this simplistic approach, the λ_c was taken to be 300 m for 1 km or below and above it is specified by (Holtslag and Boville, 1993),

$$\lambda_c = 30 + 270\exp\left(1 - \frac{z}{1000}\right) \qquad \text{Eq. (57)}$$

The stability function for unstable conditions (Ri < 0) is given by

$$F_c(Ri) = (1 - 18Ri)^{1/2} \qquad \text{Eq. (58)}$$

Where the Richardson number is given by

$$Ri = \frac{g}{\theta_v}\frac{\partial \theta_v / \partial z}{S^2} \qquad \text{Eq. (59)}$$

And for the stable condition where Ri is replaced in Eq. (59) by the Bulk Richardson number. All the above equations came from Holtslag and Boville (1993).

Next the surface layer is considered. The surface layer is between the surface and a few hundred meters from the surface, the exchange in heat fluxes are assumed constant and the turbulent diffusion is specified by Monin-Obukhov similarity theory (Stull, 1988).
In the surface boundary layer, the turbulent diffusivity coefficient (k_s) is calculated by

$$k_s = \frac{U_* \, k \, h_s}{\Phi\left(\frac{z}{L}\right)} \qquad \text{Eq. (60)}$$

Where U_* is the friction velocity (m/s), k is von Kármán constant, h_s is the height of the surface layer, and the function in the denominator is the universal function depends on z/L where L is the Monin-Obukhov length (L) scale. The function is expressed for stable and unstable conditions by

$$\Phi\left(\frac{z}{L}\right) = 1 + 5\left(\frac{z}{L}\right) \ , \qquad \text{(stable conditions)} \qquad \text{Eq. (61)}$$

$$\Phi\left(\frac{z}{L}\right) = \left(1 - 16\left(\frac{z}{L}\right)\right)^{-1/2}, \qquad \text{(unstable conditions)} \qquad \text{Eq. (62)}$$

Where the Monin-Obukhov length (m) is given by

$$\mathrm{L} = -\frac{\theta_s \, U_*^3 \, \rho_a C_p}{k \, g \, Q_h} \qquad \text{Eq. (63)}$$

Where, Q_h is the surface sensible heat flux (W/m^2), θ_s is the surface potential temperature (K), and ρ_a is the density of air (kg/m^3) calculated from surface pressure and temperature, g is the acceleration due to gravity (9.8, m/s), C_p is a specific heat capacity of dry air at a constant pressure expressed in 1005 J/kg K. The friction velocity in both Eq. (60) and Eq. (63) is given

$$U_* = \sqrt{\frac{f_s}{\rho_a}} \qquad \text{Eq. (64)}$$

Where f_s, is the surface turbulent momentum flux (N/m2) and ρ_a is the density of air (kg/m3). At the top of the atmospheric boundary layer, the characterization of the atmosphere is stable within a thin layer, while the gradient variation of shear is significantly dominated above this stable layer.

Lastly, above the surface layer and below the free atmosphere, Jericervic et al. (2010) use the O'Brien scheme for the unstable ABL

$$k_z = k_h + \left(\frac{(z-h)^2}{(h-h_s)^2}\right)\left(k_s - k_h + (z - h_s)\right) * \left(\frac{\partial k_s}{\partial z} + 2\left(\frac{(k_s - k_h)}{(h-h_s)}\right)\right) \qquad \text{Eq. (65)}$$

where, k_h is diffusivity at the top of BL, k_s is diffusivity calculated at the surface layer, z is the height above the ground (m), h is the height at the top of BL (m), and h_s is surface layer height.

The other challenging factor in calculating the turbulent mixing is the determination of the top of the atmospheric boundary layer (h). Previous works such as Jeričević et al. (2009) assume that the height of atmospheric boundary layer is determined whenever the bulk Richardson number reaches the critical bulk Richardson number which is equal to 0.25. In this work, the value of h is obtained from ECMWF reanalysis along with the profiles that were used across the Atlantic and towards the Canary Islands.

Although the friction velocity equation is provided by Eq. (64), I used the friction velocity also from the ECMWF reanalysis. I also calculated U_* based on the above equation and compared it with values obtained from ECMWF reanalysis and there was good agreement.

In this project, I will estimate how changes of kz profiles with time during advection over the Atlantic can impact on dust mass loading during transport in the marine environment. The vertical profiles of turbulent diffusivity coefficient are calculated based on these groups of equations mentioned above. The data sets of wind profiles, virtual potential temperature, and atmospheric boundary layer height were taken from ECMWF reanalysis data every 3 hours stepping across the Atlantic for 7 days in the west direction and 4 days toward the north-west direction passing over the Canary Islands. From these profiles and equations, the turbulent diffusion coefficients were obtained for use in the BRSedT simulations.

5.2.3 Terminal velocity of dust particles

Terminal velocity factor is another significant parameter influencing on the dust size distribution during transportation. Therefore, fall velocity in dust transport modelling requires a suitable value to be calculated. In this work, I calculate the fall velocity for spherical and non-spherical particles using a range of values to also account for uncertainty. Spherical shaped dust particles are assumed in this work, where the formula that is applied for sedimentation velocity in this code is shown below (Zhiyao et al., 2008):

$$v_t = \frac{4}{3A}\frac{\Delta g D^2}{\nu} \qquad \text{Eq. (66)}$$

$$\Delta = \rho_p / \rho_a - 1 \qquad \text{Eq. (67)}$$

Where $\rho_p$is the density of dust particles and ρ_a is the density of the air, D is the diameter of the dust particle, ν is fluid kinematic viscosity, g is the gravitational acceleration and A represents the calibration coefficient of particle shape, which is a dimensionless taken to be a value of 50 based on the averaged values between 34.1 and 66 that are reported by Camenen (2007) and Zhang (1989). The value of ρ_p is taken to be 2.0 g/cm^3, while density of air is calculated based on Eq. (25), and the value of 0.000015 m^2/s was used for ν. Note, fluid kinematic viscosity is expressed as a ratio between dynamic viscosity (μ, Pa. s) and air density (kg/m^3), where the ν value is obtained from the standard atmosphere (Montgomery, 1947).

The uncertainty of v_t in the calculations of BRSedT is tested in terms of varying the density of dust and ν. Therefore, ranges in the values of density for dust particles and kinematic viscosity

were used in the formula of fall velocity (fall velocity for spherical particle case) to test the variation in the results. I used ρ_p values of 1.5, 2, and 2.5 g/cm^3, and the used values of ν from the International Standard Atmosphere Properties (ISAP) of 0.000015, 0.00002, and 0.000025 m^2/s.

The effect of these variations on the fall velocity is shown in figure (5.2) for flight FB605. The results clearly show that the most uncertainty is for the larger particles. It is estimated that the largest values of fall velocity for the large sizes are as much as 6 times larger than the smallest values. The sensitivity to fall velocity becomes very clear when, for instance, assuming two dust particles at a height level 6 km (i.e. SAL), one with fall velocity of 0.05 and the other 0.3 m/s as shown in figure (5.2). So, over 6 days the first one, with the lower value (i.e. v_t = 0.05 m/s), will reach the boundary layer at a height of about 1.6 km, while the second particle with fall velocity of 0.3 m/s will be entirely sedimented out into the ocean.

In this work, the value of ν is taken to be the average within the depth of the SAL and is approximately equal to 1.5 x 10^{-5} m^2/s, and the dust density of 2 g/cm^3 was used as it is a typical value used in dust calculations (Maring et al., 2003). In figure (5.2), it is shown that as viscosity increases, fall velocity will decrease, whereas increasing dust density causes increased fall velocity with sizes of about greater than 10 μm in diameter, so they have opposite effects for increasing values, but is consistent with expectations. So, it is expected that particles will decrease in fall velocity with higher viscosity. Whereas increasing dust density for a fixed size particle will result in a heavier particle which will experience a greater gravitational force with less air resistance, and so will fall faster. V_t is more affected by density changes of dust than kinematic viscosity for the ranges considered here.

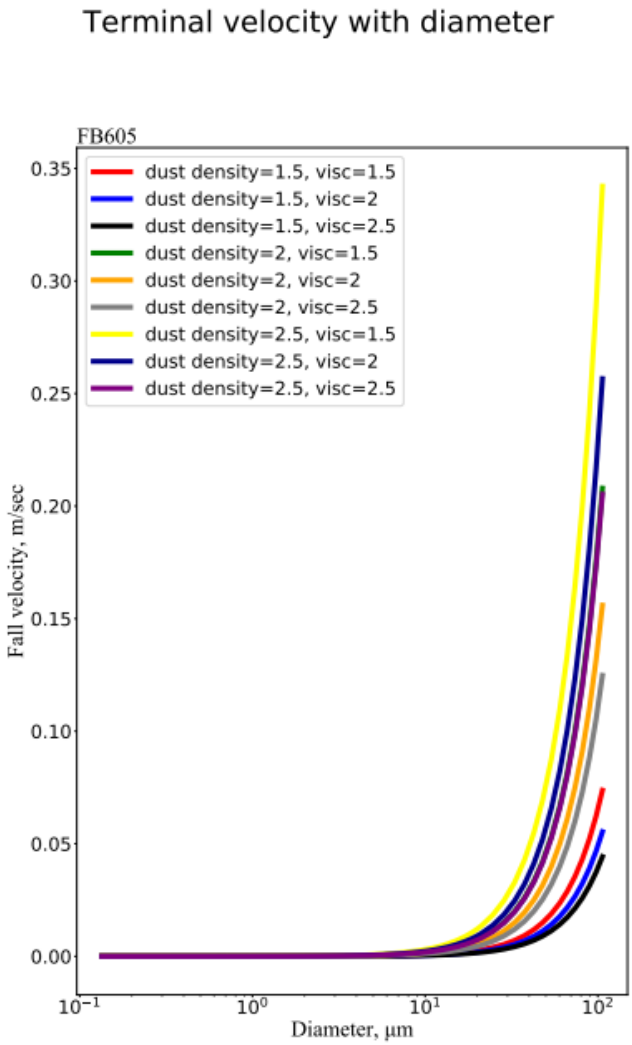

Figure 5. 2. Fall velocities for spherical particles in units of m/s calculated with different densities of dust and kinematic dynamic viscosities (ν, which is indicated by visc in the legend) with diameter (in units of μm) for flight number FB605. The fall velocity that used in sedimentation calculations was based on calculations with dust density of 2 g/cm^3, and 0.000015 m^2/s for the value of ν. Note that the value of ν is multiplied by 10^{-5}.

For non-spherical particles, I calculated the fall velocity based on Stokes settling theory (fall velocity is determined by equalizing the forces between gravity and drag impacts) from Gasteiger et al. (2011, 2017). The formula of terminal velocity for non-spherical particle shapes can be represented by,

$$v_t = \left(\frac{2\,g}{9\,\eta}\right) r_c^2\, \xi^3 \qquad \text{Eq. (68)}$$

Where, η = 17 is the dynamic viscosity of air expressed in units of μPa s, taken from Gasteiger et al. (2017). The squared r_c in Eq. (68) represents the cross-section equivalent radius of the dust particle and ξ is the conversion factor for the dust particle shape derived from Stokes theory in which $\xi = \frac{r_v}{r_c}$, where r_v is the volume equivalent radius of the particle. There is complexity in assigning the radius of the particle for calculating the fall velocity of non-spherical shaped

particles, so the aspect ratio (ξ) is defined by the ratio between longest and shortest axis of spheroids and can be applied to calculate fall velocities for non-spherical particle shapes (Koepke et al., 2015). This consideration follows the assumption of Gasteiger et al. (2011), who stated that for spherical particle, ξ is typically equal to one, while for non-spherical particle, $\xi < 1$, and six values of ξ including, 0.955, 0.932, 0.911, 0.871, 0.925 and 0.866 were used. Gasteiger et al. (2011) also assumed that r equals to r_c in the Eq. (68), where r is defined as the size of the non-spherical dust particle shape and it is expressed in units of μm. The key issue of using this approach is that modelling of dust optical properties based on size distributions and refractive indexes in a comparison with other ways such as Mie theory may provide inconsistent results for non-spherical particles (Koepke et al., 2015). I calculated the fall velocity for non-spherical dust particle based on this assumption; however, I will not consider the role of other shape on deriving the sizes from instruments (such as PCASP) since using this assumption (i.e. based on both Gasteiger et al., 2017 and Gasteiger et al., 2011) is dependent on particle shape. In addition to this approach, to determine fall velocities for non-spherical particles typical size-dependent aspect ratio distribution of spheroids need to be specified, which would be taken from aircraft observations (Koepke et al., 2015).

In figure (5.3), fall velocities (m/s) are shown associated with different ξ values (listed in the legend) and with diameter. The coloured lines show the calculated sedimentation velocities with different models of non-spherical dust particles based on Eq. (68) with dust density used of 2 g/cm^3, see the panel below in the figure (5.3). In the current thesis, results of non-spherical fall velocities agreed with the result of Li and Osada (2007), who show that non-spherical dust particles fall slower than spherical particle shape and they also stated that assuming spherical particle shape for dust transported long distances in sedimentation and radiation studies is quite appropriate since the large particles which have the biggest differences in fall velocities will have fallen out, so I generally proceed with assuming spherical and test sensitivity to non-spherical shapes. Note to the reader, I listed the same results of fall velocity for spherical particle shape, that are shown in the previous figure (5.2), on the top panel of figure (5.3) to compare fall velocities between these two particle shape modes (i.e. spherical and non-spherical particle shapes). Where the values of v_t for spherical particle shapes shown in the top plot are related to using different values of dust density (including 1.5, 2 and 2.5 g/cm^3) resulting in a large difference in fall velocities compared with these values of non-spherical particle that used in the five particle modes. This will provide fall velocities for spherical particle calculation with orders of magnitude larger values than that for non-spherical particle shapes.

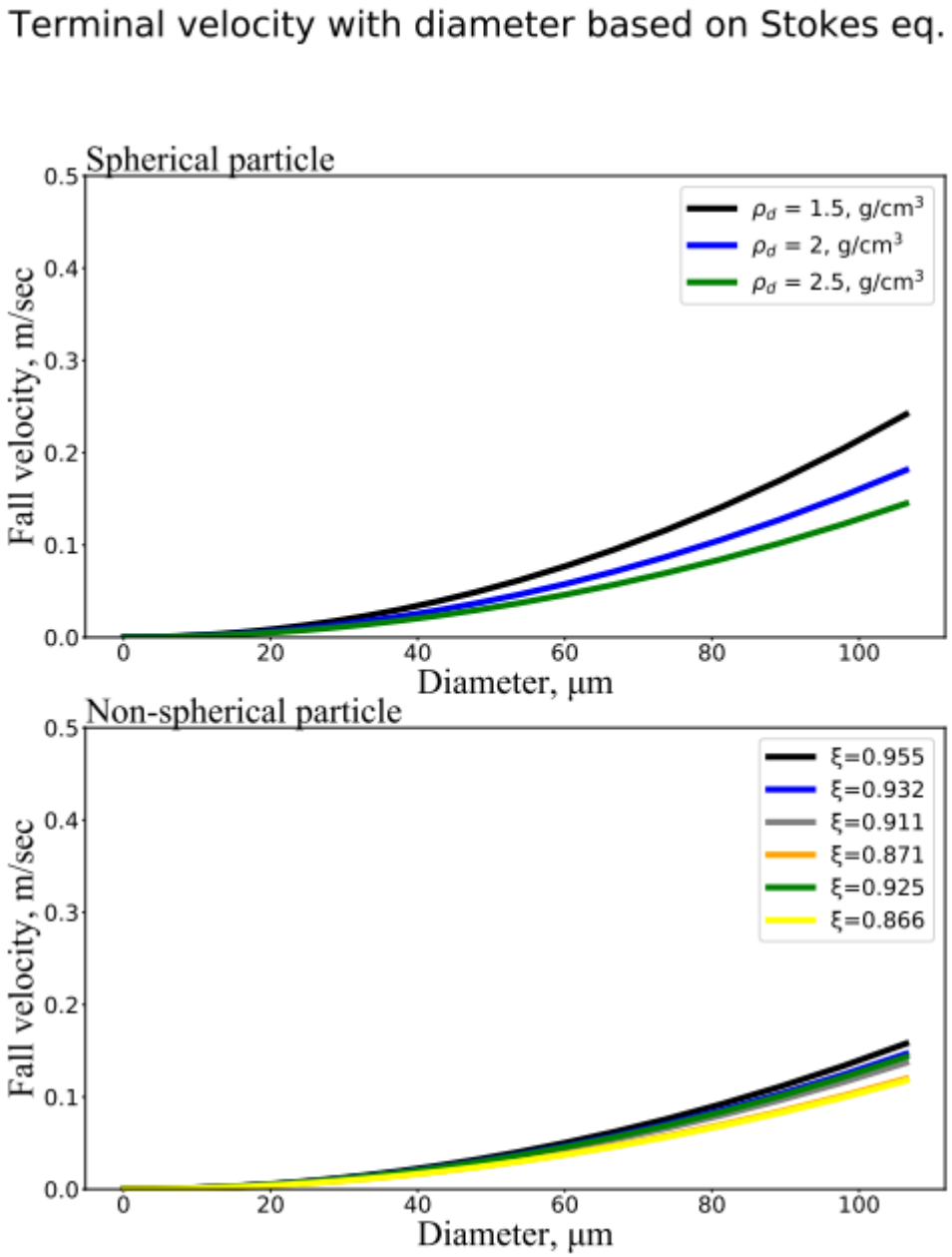

Figure 5. 3. Fall velocity expressed in unit of m/s based on Stokes theory. The top panel shows the fall velocities calculated with diameter for spherical dust particle shape. The bottom panel is for the non-spherical particle shapes calculated with different models of non-spherical shapes with diameter (in units of μm) for flight number FB605. Six non-spherical-model particle shapes were used based on Gasteiger et al. (2017), including ξ equal to 0.955, 0.932, 0.911, 0.871, 0.925, and 0.866. Fall velocity for spherical particle shape (top panel) is calculated based on Eqs (66)-(67), while for non-spherical particle shape mode fall velocity is computed based on Eq. (68). Panel below shows results with using dust particle density of 2 g/cm^3.

5.2.4 Impact of dust-particle shape on v_t

In the BRSedT model, initial dust profiles were used from FENNEC observations over the north African coast and it is recognised that shape of particles may influence the sedimentation of dust with non-spherical particles creating more drag and slowing the terminal velocity compared to a spherical shape (Ginoux, 2003). Further works by Colarco et al. (2003) show that there is big difference in fall velocity between spherical and flat disk particles, where a disk shape is assumed

to approximate the non-spherical shape of dust particle (Arimoto et al., 1985). The shape of dust particles does not only influence the sedimentation results, but also can impact on evaluating the radiative properties, where a spherical dust shape is characterised by more absorption for solar radiation than non-spherical or even just spheroidal particles (Song et al., 2018).

In the current study, spherical and non-spherical shaped dust particles are considered in the BRSedT, as explained in section 5.4.4.1. There are several considerations for using spherical shaped particles compared to non-spherical, which are:

1. Statistical analysis presented by Ginoux (2003) indicates that differences between spherical and non-spherical dust particles on dust modelling at dust sources over north Africa are quite low. Figure (5.4) shows the global mass loading of dust column (top panel) and the difference between spherical and ellipsoid shapes (bottom panel). His study presented that the spherical shape of Saharan dust has a slight impact on transport model calculations except for elongated dust particles.

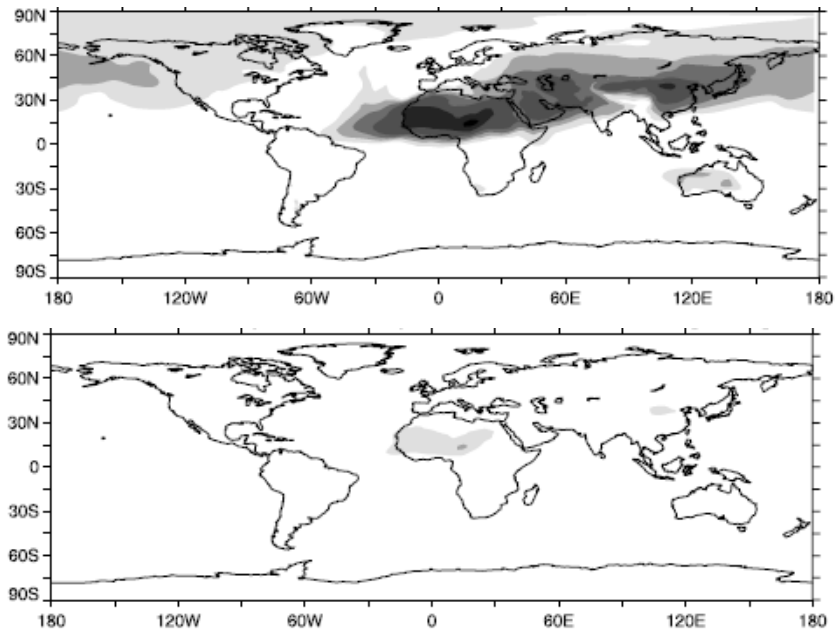

Figure 5. 4. (Top panel) global mass column in the units of g/m^2 taken from GOCART transport model using spherically shaped dust. Bottom panel shows the difference in mass column between spherical and ellipsoid shape of global dust. This figure is taken from Ginoux (2003).

1. Literature studies including Rocha-Lima et al. (2018), van der Does et al. (2018), and Ginoux (2003) state that Sahara dust particles are characterised by spherical or well-rounded shapes.
2. Li and Osada (2007) show that away from the dust sources, it is appropriate to consider spherical dust particles in the sedimentation process as well as in the dust radiative model (mentioned before in section 5.4.4.1).

3. Sensitivity studies between particle shape and fall velocity for dust profiles between dust sources and the Atlantic show relatively good agreement in their results. For example, Saxby et al. (2018), show that the effect of particle shape on dust sedimentation is consistent for both spherical and non-spherical particle shapes after about a day and a half of transport. Where dust reaches the Canary Islands after about 1-2 days being advected from north African land, while away from dust sources Li and Osada (2007) pointed out that the characteristics of dust particle shape acceptable to be assumed spherical.
4. As the current work includes investigating the impact of giant dust particles > 15 µm, figure (5.5) displays that dust particles are characterised by well-rounded giant shapes within the SAL at 3500 km from the north African coast. Thus, giant particles are observed over the African land and after advection, some large dust will make it over the Atlantic, as it shown in the size distribution of dust particles in Chapter 3.

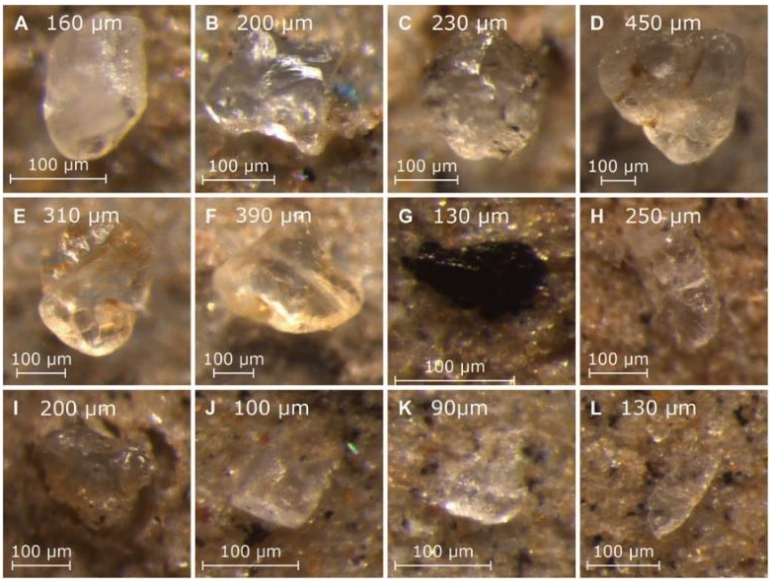

Figure 5. 5. Giant Saharan dust aerosol particles sampled at about 3500 km away from the African continent over the Atlantic. This picture is taken from van der Does et al. (2018).

Lastly, the non-spherical dust optical properties can differ from spherical, but this is beyond the scope of this work (Song et al., 2018) and is a topic for future studies.

5.2.5 Subsidence and advection

The third important factor determining how the dust evolves during transport in the BRSedT model is the subsidence (w). The large-scale vertical velocities were taken from the ECMWF reanalysis associated with specific grids in the direction towards the Canary Islands and towards the Caribbean. The ECMWF grids that were selected were chosen based on the mean advection speed of the air in the two directions of interest as determined from HYSPLIT ensemble simulations. The grid locations are given in a plot of the Atlantic along with a satellite picture

underlaid at one instance of the dust transported for flight FB604, see figure (5.6). The mean wind speeds in the grids are provided in the table (5-1) along with latitudes and longitudes. For example, first grid (A) in table (5-1) and table (5-2) shows the latitude and longitude grids associated with dust transported within 24 hours from dust source toward Canary Islands and easterly from the African coast, respectively. These tables (5-1) and (5-2) correspond to the flight FB604 shown in figure (5.6). The wider the grid the faster the wind speed since each grid represents one day so a faster speed of transport will make it farther in one day. The expected dust arrival within each grid is estimated by using the mean advection speed of HYSPLIT air mass trajectories for forward trajectories over 7 days and 4 days initialised from the first grid (A, a) of each case. This will be shown later for forward trajectories initialised with latitude and longitude locations from the African land for each direction of flight number FB604.

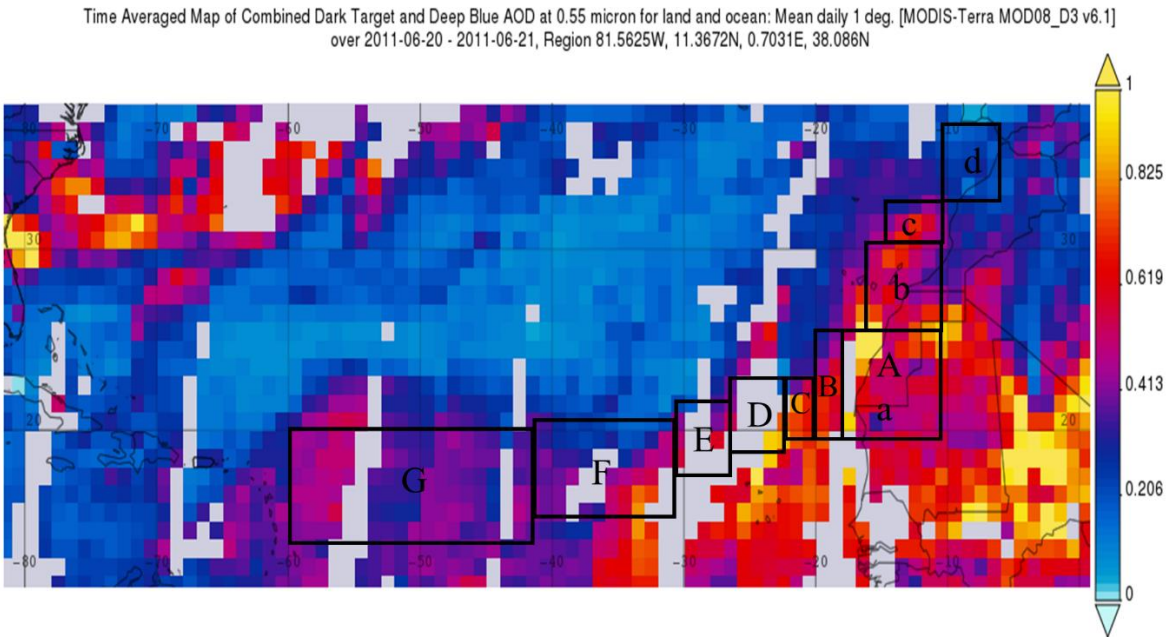

Figure 5. 6. Shows the grids used for flight FB604. The grids were obtained from HYSPLIT simulations indicating the mean speed and direction. Black boxes show latitude and longitude grids over the African land and over the Atlantic labelled by A, B, C, D, E, F, and G indicate from land across the Atlantic toward the Caribbean and a, b, c, and d indicate from land toward the Canary Islands. Grids are plotted on MODIS-Terra satellite observations associated with time averaged AOD over African land, Canary Islands and across the Atlantic. Date of MODIS-AOD is presented as daily averaged data between 20-06-2011 and 21-06-2011.

Table 5- 1. The grid points of latitudes and longitudes across the Atlantic. The table corresponds with figure (5.6).

Number of grids	Lat1 (°N)	Lat2 (°N)	Long1 (°W)	Long2 (°W)	Wind speed (m/s)	Wind direction	Date
A	19.0	25.0	-10.0	-18.0	4.6	NW	21-06-2011
B	19.0	25.0	-18.0	-20.0	6.8	NE	22-06-2011
C	19.0	23.0	-20.0	-23.0	6.1	NW	23-06-2011
D	18.0	23.0	-23.0	-26.0	3.7	NW	24-06-2011
E	23.0	17.0	-26.0	-30.0	5.7	SE	25-06-2011
F	15.0	21.0	-30.0	-42.0	8.4	SW	26-06-2011
G	14.0	20.0	-42.0	-59.0	9.1	NW	27-06-2011

Table 5- 2. The grid points of latitudes and longitudes toward north-west Atlantic. The table corresponds with figure (5.6).

Number of grids	Lat1 (°N)	Lat2 (°N)	Long1 (°W)	Long2 (°W)	Wind speed (m/s)	Wind direction	Date
a	19.0	25.0	-10.0	-18.0	4.6	NW	21-06-2011
b	25.0	30.0	-10.0	-15.0	2.88	NW	22-06-2011
c	30.0	32.0	-10.0	-12.0	7.1	NE	23-06-2011
d	32.0	36.0	-7.0	-10.0	4.8	NE	24-06-2011

Winds over west Africa are characterised by various time and space scales. For example, Parker et al. (2005) state that mesoscale convective systems (MCSs) induce significant meridional winds and MCSs controlling on synoptic variability (Liu et al., 2018) of the African Easterly Jet (AEJ). Based on the BRSedT model applied for Saharan dust, initialised with FENNEC observations, beyond the fall velocities, the initial profiles of dust and vertical velocity are the key variables factors to be considered. As this study focuses on dust effects during the summer period, dust is frequently transported within the SAL over the Atlantic by prevailing trade winds (TW). As dust is uplifted from the African land, the main process that influences the dust uplift into the atmosphere (annual cycle of dust uplift) is related to the increased convergence at dust sources, which is mainly responsible for generating small-scale high winds and vertical velocity. This is presented by Engelstaedter and Washington (2007) who pointed out that mean surface wind does not have a significant impact on the dust uplift, but ECMWF vertical velocity and gusty

winds at the small-scale are the main factors affecting the dust uplift into the SABL. I can avoid having to model the uplift since I take the aircraft profiles of the dust that has been observed to be lifted into the atmosphere so there is no need to model the dust uplift from the surface. The large-scale wind profiles in this work show that there is subsiding air over 3 or 4 days for the air passing over the Canary Islands which is much stronger than the air crossing the Atlantic toward Caribbean. This can be seen in figure (5.7), which shows daily-averaged profiles of vertical velocity in non-dusty (FB700) and dusty (FB604) days, where the first row is the profile over 7 days as it crosses the Atlantic, while the plots in the second row show the vertical velocity profiles over 4 days towards the north-west direction. Coloured lines show profiles of vertical velocity for each day. The other figures, figures (5.8) and (5.9), show the vertical wind across the Atlantic toward the Canary Islands for all flights, respectively. This finding of strong subsidence generally occurs in the subtropical region, which is characterised by the cool air being subsiding due to Hadley cell circulation and is persistent in most tropical regions off the west coast of continents. Results in the current thesis for air subsidence over the Canary Islands are in a good agreement with the results of Carrillo et al. (2016). Therefore, using the vertical velocity from ECMWF data which agrees with others suggests it is adequate to use in the BRSedT model. I will selectively use four dust cases including, FB604, FB605, FB612, and FB699. I chose these cases since I want to investigate the role of the turbulent diffusion process for the most intensive dusty cases (i.e. FB604, FB605, and FB612) and for one moderate dusty case (FB699) for two directions (towards Caribbean and Canary Islands).

The magnitude of subsidence cannot be obtained from the flight observations since the slow large-scale subsidence is not obtainable from the turbulent vertical wind measurements reliably from a single aircraft. Single aircraft observations cannot reliable provide wind data covering large-scale areas across the Atlantic. Thus, it can be hard to compare vertical winds from flight measurements with these values for up-draught velocity profiles from ECMWF data unless there are several aircraft that can measuring the large-scale winds converging or diverging for a region.

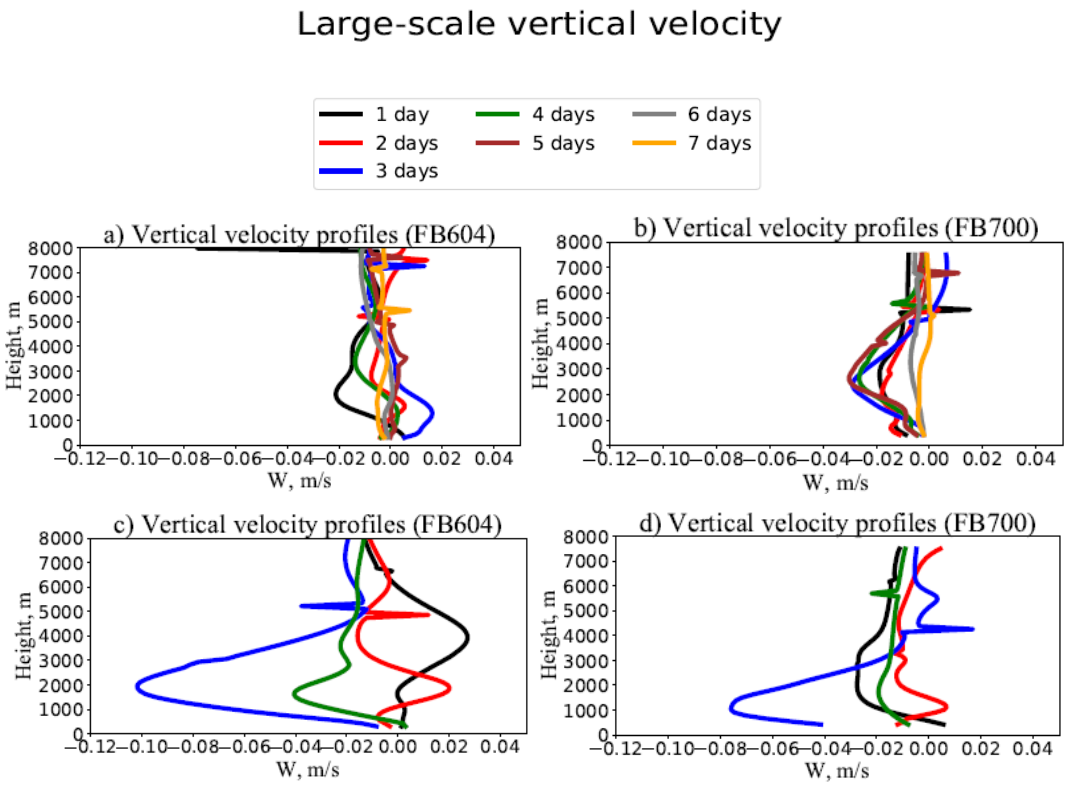

Figure 5. 7. Subsidence profiles in units of m/s from ECMWF reanalysis for non and dusty cases. The first row (plots a and b) indicates vertical velocities across the Atlantic, and the second row (plots c and d) shows vertical velocities (w) towards the Canary Islands. The first column is for dusty cases while second column is for non-dusty case cases. The vertical velocity in all figures shows the daily averages of largescale w from north Africa along 7 days (across the Atlantic) and 4 days (towards the Canary Islands). The large-scale velocity for non-dusty cases is shown here to understand the general trend of vertical velocity in different flight cases over time, where only moderate and dusty cases are shown.

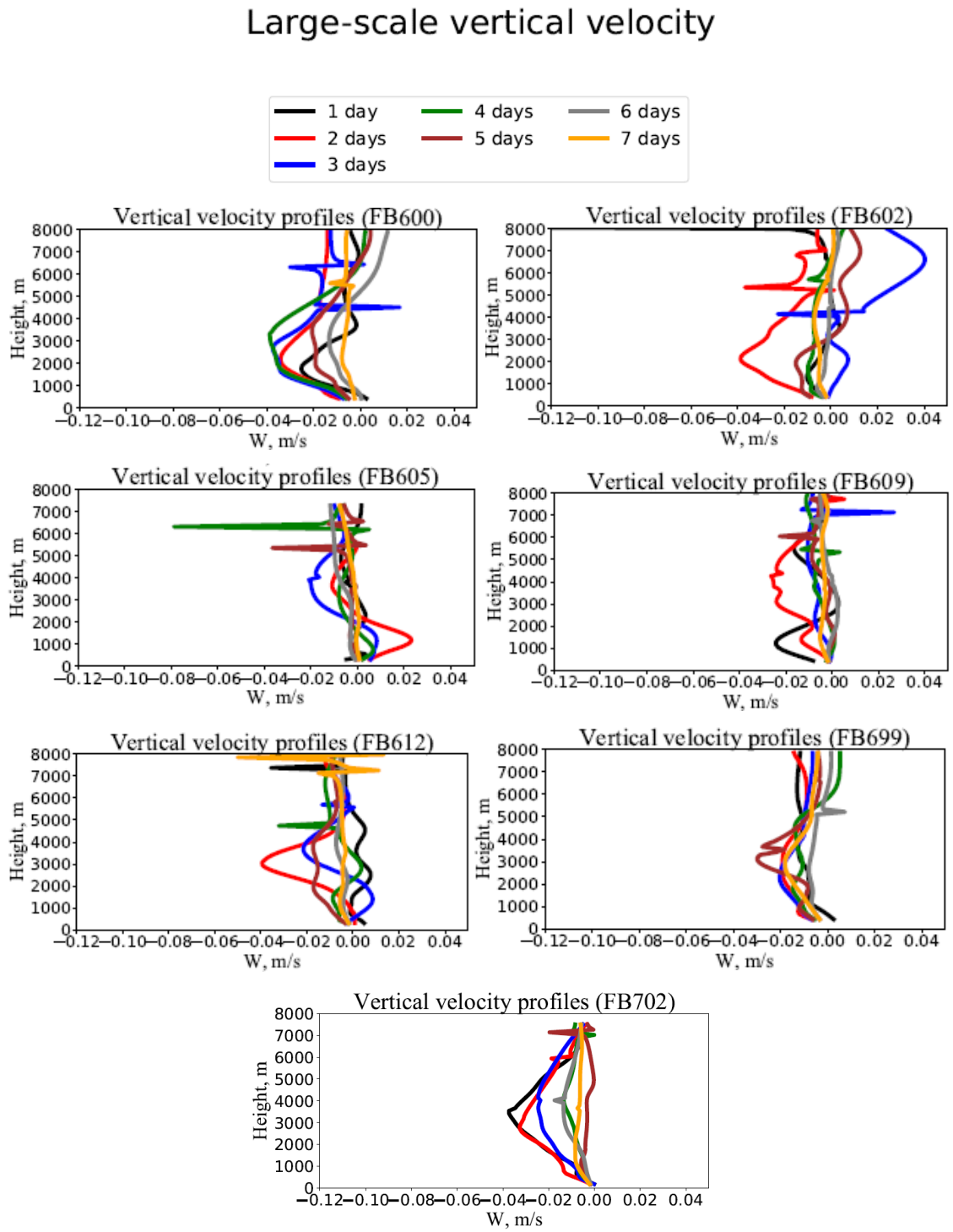

Figure 5. 8. Subsidence profiles in units of m/s from ECMWF reanalysis for low dust (FB702) and dusty (FB605 and FB612) cases across the Atlantic (over 7 days). Other cases refer to moderately dusty cases. Vertical velocity in all figures show daily averaged values of large-scale w with each specific grid.

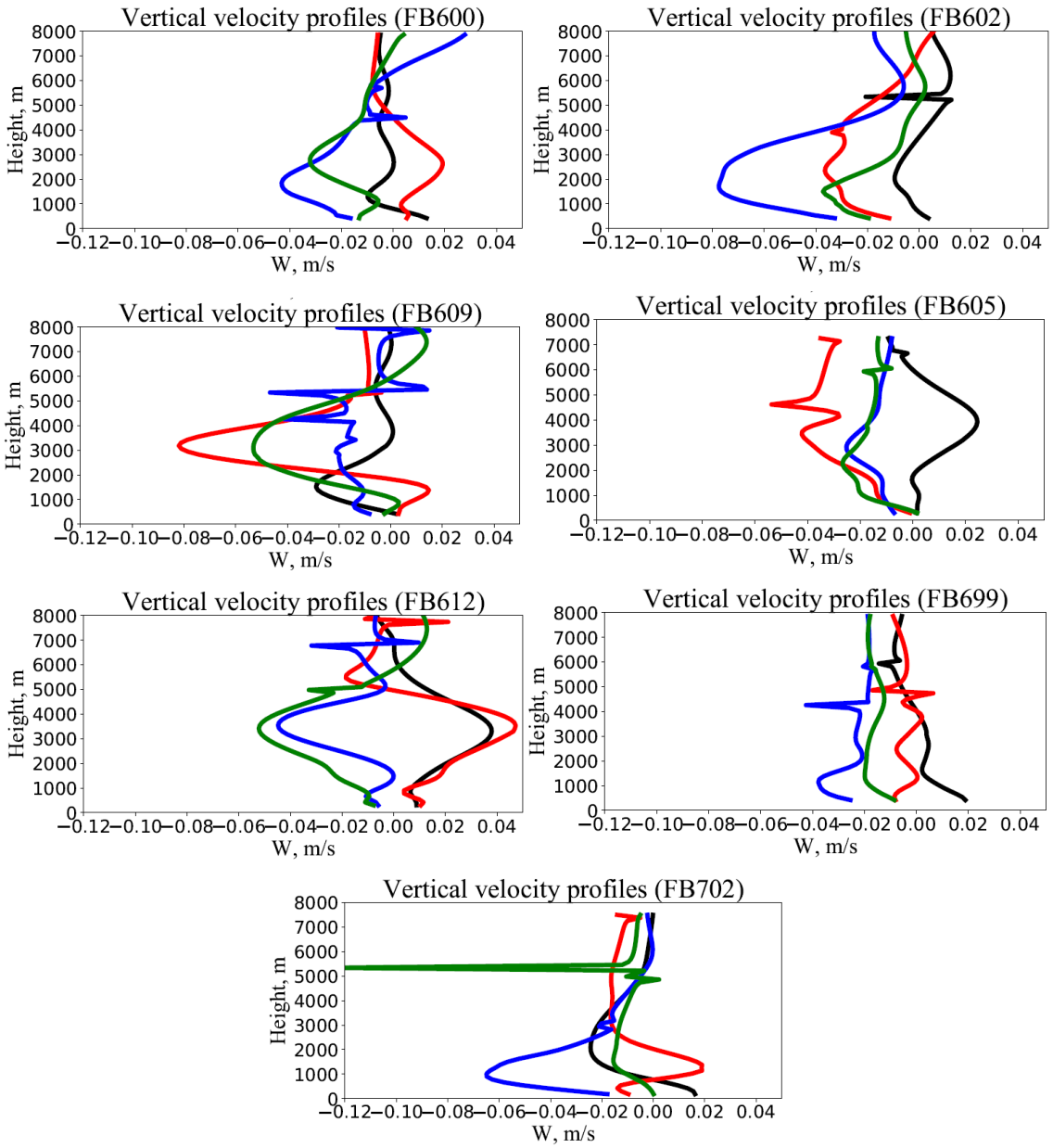

Figure 5. 9. As figure (5.8), but towards the Canary Islands (4 days).

In general, there is noticeable large-scale subsidence shown in the value of vertical velocity across the Atlantic and over the Canary Islands at a height of about 3 km, see figure (5.9). This is expected as there is typically subsidence (Rodríguez et al., 2004) in this region historically, and the results show that this is still the case during dust outbreaks. There is variability in the subsidence, and this gives rise to effects seen in the profiles of dust over time.

The weaker large-scale subsidence in the direction of the Caribbean causes a lower loss of dust particles, since the weaker subsidence will cause less particles making it into the boundary layer and loss to the surface. Figure (5.10) shows that for dusty cases (FB604, FB605 and FB612), the values of averaged w within the height of SAL have less change over the 7 days across the

Atlantic Ocean (plot on the left) than these values over 4 days toward the Canary Islands. In addition, averaged vertical velocities toward the Canary Islands (plots on the right) show greater subsidence, up to about -0.05 m/s after about 3 days of dust transportation. This contrasts with the low-dusty case, in which there is strong subsidence in the eastern Atlantic.

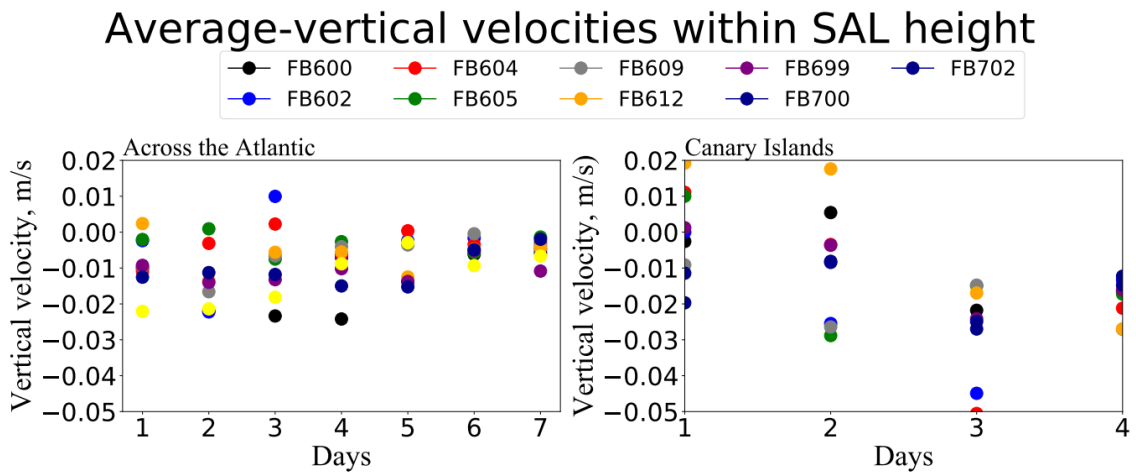

Figure 5. 10. Average vertical velocity profiles in unit of m/s calculated with the height averages (averaged heights between the surface and 5.5 km) within SAL and days for non (FB700), moderate (FB600, FB602, FB609, FB699 and FB702) and dusty (FB604, FB605 and FB612) cases. Left panel is for across the Atlantic over 7 days, while the right panel is for the Canary Islands over 4 days.

The large-scale vertical velocities over the Canary Islands for case FB612 are weak in magnitude (comparing right column to left), see figure (5.10). However, it is a different when looking at the daily values which show the first two and last two days have strong velocities but opposite in sign.

5.2.6 Dust transport from large-scale velocities and observations

Dust event cases over the Canary Islands and across the Atlantic are selected based on AOD from MODIS-Terra satellite data. The calculation of the AOD is performed at the African land both for the initial profiles of dust from the FENNEC data and the final output profiles from the BRSedT code. Comparisons between observed and calculated values are compared for consistency. For the radiative simulations using the ES model for the Canary Islands, a selection of dust events is categorized as non-dusty, moderate and dusty cases.

To simulate the transport of dust in the BRSedT model, horizontal wind vectors are needed to determine the time of the dust profile within a specific Atlantic region. These horizontal winds are taken from ECMWF reanalysis. Figures (5.11) - (5.12) show an example of wind vectors from ECMWF data which are taken at pressure heights 500 and 700 mb (in the SAL) during times 1500 UTC and 2100 UTC for FB604, and these wind vectors agreed well to the source of the dust from the coastline of the continent of African, shown by backward trajectories from HYSPLIT

over the Canary Islands and over Puerto Rico regions, see figures (5.13 and 5.14) and also figures A4.4 and A4.11, shown in Appendix A4. The general trend of wind vectors from north Africa is toward west direction over the Atlantic. However, above ~20 °N degree a portion of wind within the SAL is south-westerly. The way forward is to apply an appropriate method to quantify how much dust leaves from the African land in the directions of interest.

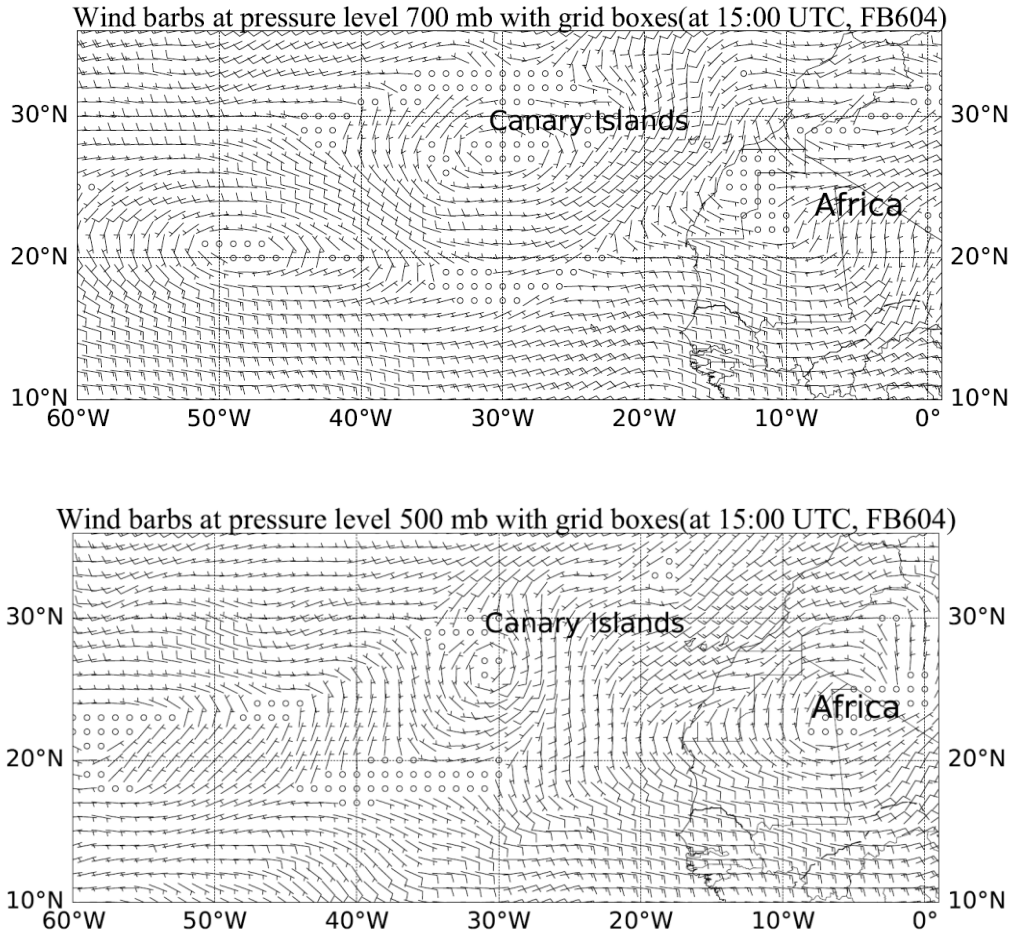

Figure 5. 11. Wind vector over the Atlantic Ocean during time 15:00 UTC, 20 June 2011. The top panel is wind speed and direction for pressure level 700 mb, whereas in the bottom panel is wind at pressure level 500 mb.

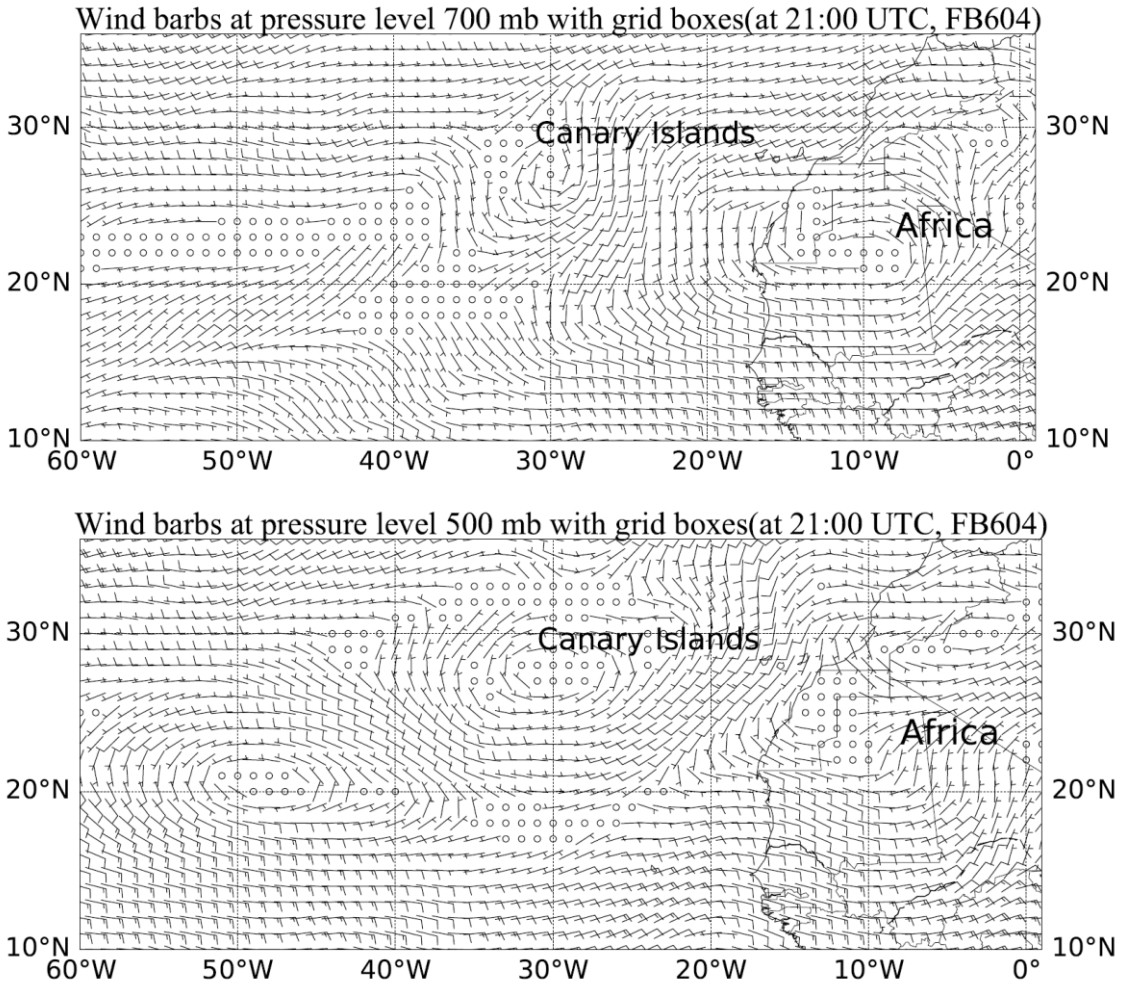

Figure 5. 12. As figure (5.11), but for time 2100 UTC.

5.2.7 Trajectory scaling factor

The BRSedT is used to specify the transport of the dust accounting for the terminal velocities of the dust, the large-scale vertical velocities, the turbulent diffusion, and the advection by horizontal winds over time. The mass concentration of dust that is advected in a given direction can be obtained by back (and forward) trajectories from HYSPLIT and used in the BRSedT, see previous section 5.1.1. Unfortunately, I cannot use the HYSPLIT to model the dust as it does not account for the bin resolved dust transport mentioned above, thus the need for the BRSedT model. The benefit of using the HYPSPLIT trajectories is to determine the proportion of the winds that are coming from dust source regions with dusty air from Africa out over the Atlantic in the directions of interest toward the west (towards the Caribbean) and north-west directions (towards the Canary Islands) (as seen in MODIS observations).

I have observations of dust from FENNEC over land but the air passing through this region can take the air in several directions. By performing back trajectories from the chosen end point (either west Atlantic or Canary Islands), I can identify the fraction of air that originates over dusty

land masses compared to originating from non-dusty oceanic regions. Forward trajectories from the dusty source are far more difficult and computationally expensive to implement for this since trajectories would have to be established all the way around the location of interest to identify which locations advected over the location of interest.

It is important to quantify the number of trajectories between the dust sources and the Atlantic Ocean by a scaling factor (i.e. the dust scaling factor), SF, that is explained previously in section 5.1.1 as the number of trajectories that arrive at the Canary Islands/far west over ocean compared to the total number of trajectories that originates over the African land. For example, if 50 % of the trajectories that arrive at the Canary Islands cross over Africa and 50 % are from oceanic sources then a weighting of the BRSedT result by 50 % is applied to account for mixing of dusty and non-dusty air parcels. Backward trajectories were started at 28.2˚N, -14.0˚W (Fuerteventura location), and 18.20˚N, -66.6˚W (Puerto Rico) over 2 and 7 days, respectively,

Typically, 60-70 back trajectories were used for each case (e.g. FB604) to determine weighting factors. Where flight cases FB604, FB605, FB612 and FB699 were selected for this experiment. Figures (5.13) and (5.14) show ensemble backward trajectories for flight case FB604 from the Canary Islands and Puerto Rico locations with duration times of 48 and 168 hours, respectively. I show in all the figures one height (i.e. 4020 m) ensemble trajectories while other trajectory heights (including 1020, 3180, 6060 and 5100 m) will be shown in the Appendix A4. The arrival time of dust transported between the dust source and these destinations (i.e. Canary Islands and Puerto Rico) can be estimated based on the mean wind (u and v wind components) profiles and the distance between the western Saharan sector and these locations (about 475 km, 5571 km between Fuerteventura, Puerto Rico and African coastal line, respectively). Dust can reach the Canary Islands after about 1 day or 2 days and reach far across the Atlantic typically in about 6-7 days corresponding to the mean value of wind with 5 m/s and 10 m/s, respectively.

It is clearly seen that the origins of air masses using backward trajectories at the Canary Islands are in very good agreement with dust outbreaks, but for the Puerto Rico region the source of air masses at about 5.1 km is generated from different locations (see figure A4.11). Figure (5.14) depicts the origin of air sources at Puerto Rico by using trajectory model over 7 days of time simulation. In addition, the backward trajectories at low altitudes (1 km) in Puerto Rico show that most air masses are generated from high atmospheric heights at the African coastline, see other figures in Appendix A4, e.g. figures (A4.11, A4.12, A4.13, and A4.15). This suggests that the air masses have descended significantly far away from the continent of Africa. In contrast, back-trajectories from Canary Islands show that air masses are descended following it backwards toward the African coastline, which is reasonable since the top layer of well-mixed potential temperature over land is at a lower altitude compared with that over the Canary Islands and there is subsidence acting during this path.

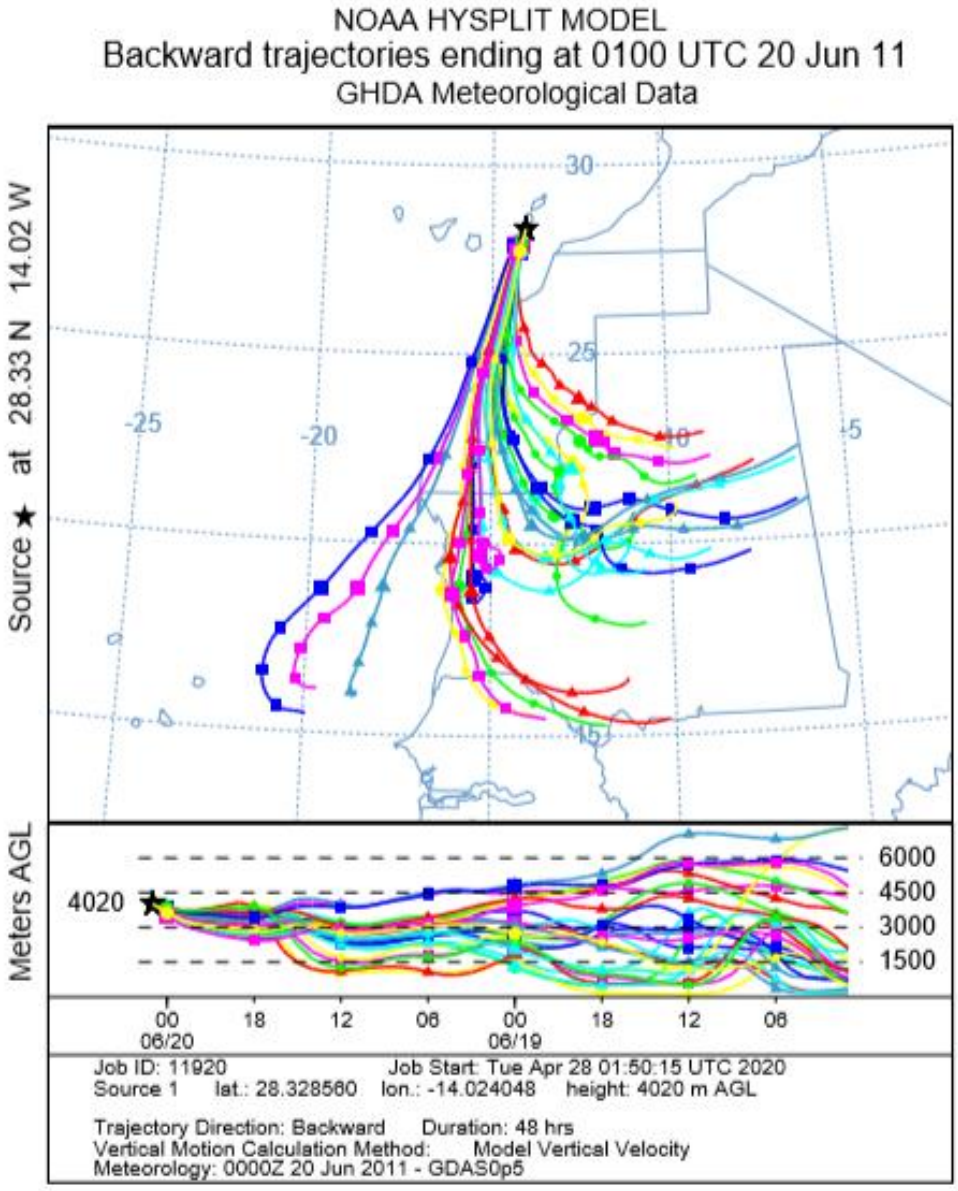

Figure 5. 13. Ensemble of backward trajectories from the HYSPLIT model starting at a distance from the Canary Islands coincident with 2 days dust arrival toward north-eastern direction. Model runs for 48 hours for height 4020 m. Figure refers to the flight FB604 where the backward simulation starts on 20 June 2011.

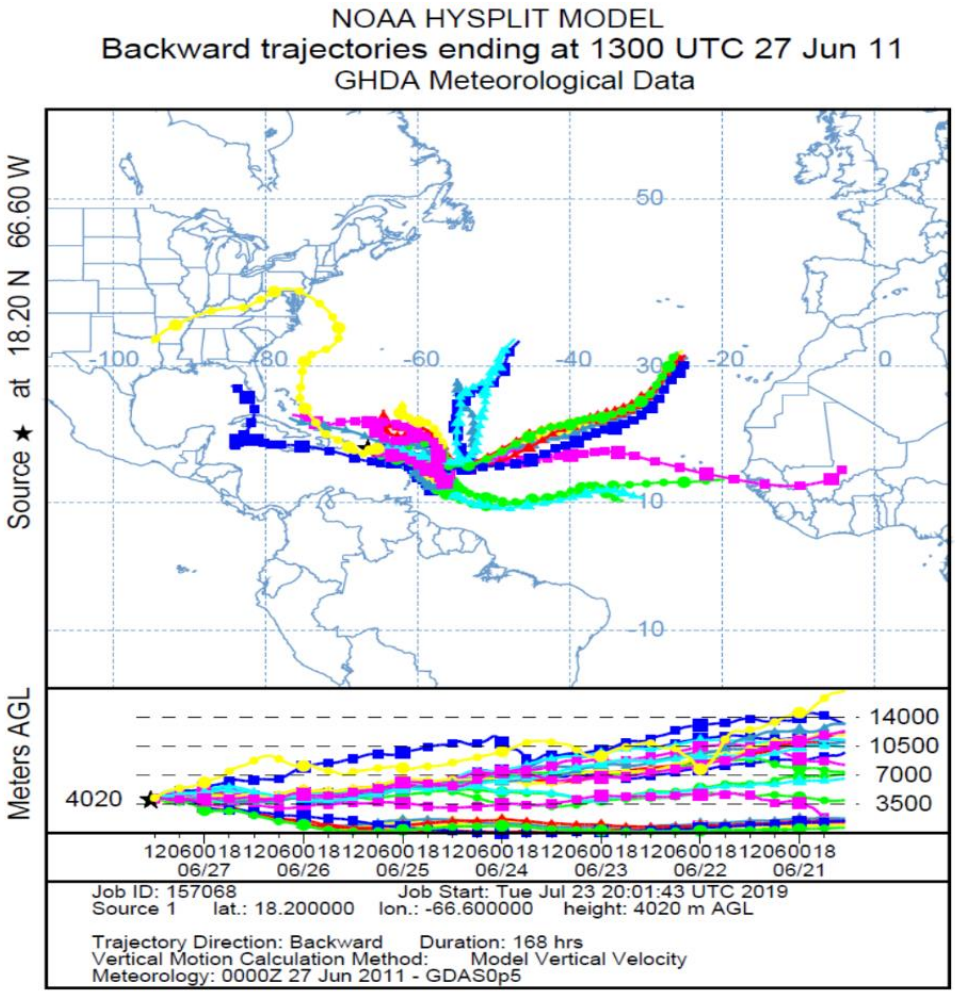

Figure 5. 14. Ensemble of backward trajectories from the HYSPLIT model starting from the Puerto Rico region. Model runs are for 168 hours for height 4020 m. Figure refers to the flight FB604 where the backward simulation starts on 27 June 2011.

Forward trajectories from the dust source region are useful for understanding the direction of dust transport from the source and so plots are shown below in figure (5.15) but they are not used for determining the dust scaling factor (SF) because, as explained, there would need to be far more forward trajectories from non-dusty ocean sources to determine the diluting of the dusty air mass. Only if all the air passes over the source and destination sites will the forward and backward trajectories be comparable and agree with a simple comparison.

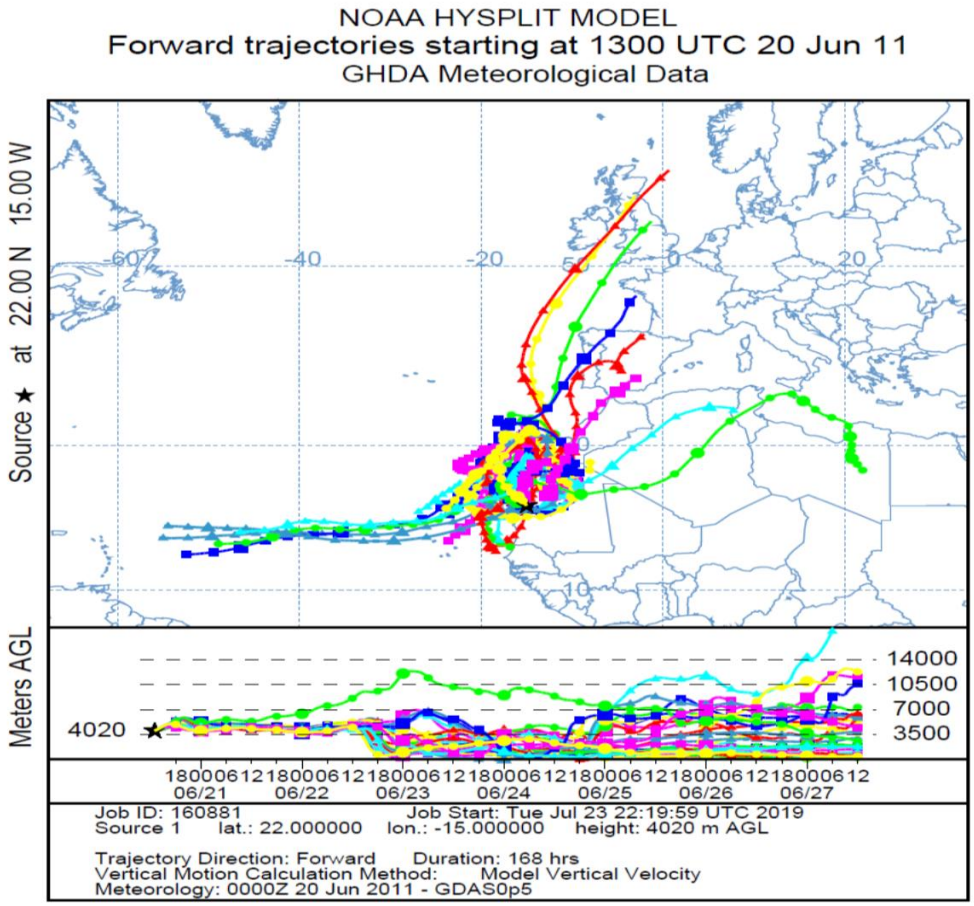

Figure 5. 15. Ensemble forward trajectories from HYSPLIT model starting at the African coastline (22.00 N, 15.00 W degrees) and simulated for 7 days from the location of the dust observations forward in time. Model runs for 168 hours with trajectories for height 4020 m.

Tables (5-3) and (5-4) show the scaling factors for the four flight cases studied including FB604, FB605, FB612, and FB699. The BRSedT runs are aligned with flights so that initial dust profiles input into BRSedT for the relevant cases. In the case of the Canary Islands, dust profiles are observed as an additional checking of the dust transport model since I have flights from both the Islands and from the mainland, and so this is a way of checking the BRSedT.

Table 5- 3. Dust scaling factors (SF) based on backward trajectories for selected four flights towards the Canary Islands.

Flight cases	Weighting factor	Starting time of trajectory
FB604	0.50	20 June 2011
FB605	0.60	21 June 2011
FB612	0.80	26 June 2011
FB699	0.15	6 June 2012

Table 5- 4. Dust scaling factors (SF) based on backward trajectories for selected four flights over the Atlantic Ocean towards Puerto Rico.

Flight cases	Weighting factor	Starting time of trajectory
FB604	0.40	27 June 2011
FB605	0.64	28 June 2011
FB612	0.70	03 July 2011
FB699	0.20	13 June 2012

In conclusion, prediction of how much dust is advected over two different destinations is estimated by applying dust scaling factors (SF) using backward HYSPLIT model simulations for the destinations of Canary Islands and Puerto Rico. The final-weighted profiles were used in the BRSedT to investigate the changes in dust profiles due to sedimentation, subsidence, and turbulent diffusion after 7 and 4 days of the model runs in the direction of the Canary Islands and the west side of the Atlantic Ocean, respectively.

5.2.8 Summary of assumptions in the BRSedT model

The assumptions in the BRSedT model are described in the model development section and many sensitivities are explored but I thought it would be good to include a short summary of the main assumptions in one location. The following are the assumptions: the model is a 1D quasi-Lagrangian model and so the 1D profile advects with the mean advection speed and thus does not treat the full 3D dynamics, the dynamics are offline and so do not interact with the atmosphere and dust, and turbulence in the model is parameterised. Direct radiative coupling with the model is not treated. The model ignores dust microphysics (collection/coalescence) but includes sedimentation. Dust particles are modelled as bins rather than continuously varying as in reality but I used the same bin sizes as in the FENNEC instrument observations, so it is relatively high resolution. The aging of the dust was treated for the long-range transport to the Caribbean but was parameterised and so is approximate. Surface parameters such as fluxes are obtained from a large-scale model and not directly modelled interactively. Assumptions had to be made regarding a range of input variables including dust fall velocities, assumptions about kinematic viscosity, dust densities assumed uniform with size, particles mostly assumed spherical and although the non-spherical particles are studied in this chapter, they are still idealised compared to what occur in reality and testing of these on the results take place in section 1.4.3.

5.3 Testing of BRSedT processes

This section is the first step in evaluating the model. In the first section, the sedimentation and subsidence effects on dust are shown to work for individual parcels for individual model

timesteps. The sedimentation and subsidence, shown in 5.3.1 are easier to treat than the turbulence which involves exchanges of dust between parcels. The turbulence process in the model is shown to be valid in the second sub-section 5.3.2.

5.3.1 Testing of BRSedT for sedimentation and subsidence

As part of the validation, I tested individual processes operating in the BRSedT model, such as sedimentation or large-scale velocity effects on the dust parcels. To do this validation, I took a flight case and shut off all processes acting on the dust aside from one, either subsidence or sedimentation. I then compared the results in time to offline calculations to confirm that the model was correctly simulating that process. I tested all the three main processes of fall velocity, large-scale subsidence, and turbulent diffusion. The sedimentation (fall velocity) and large-scale subsidence were tested in a similar way since they acted on parcels by altering the parcel height. I used the initial mass value of dust from the flight case FB604 going west across the Atlantic. A specific layer (at 4020 m) was chosen and the following was applied:

1. Subsidence was set to zero and used only fall velocity data in the BRSedT and ran the model for 24 hours in order to test if dust particle falls the correct amount by comparing to offline calculations.
2. Set fall velocities to zero and used only subsidence (w) acting on the dust at 4020 m over 24 hours and then checked if dust particle at that height is correct as verified by offline calculations.

For the first validation test, figure (5.16) shows the initial height of a particle for bin 32 (black star) with size of 10.60 μm and the final height (blue star) after one day of simulation run. I used a single layer or parcel of dust mass data in this test for simplicity and clarity, where the effects of turbulence on this layer are also shut off.

It is clearly noticeable that the dust particle that started at the height 4020 m descended due to its fall velocity over 24 hours from 4020 m to 3841 m, where the final height of particle is well matched with the vertical distance (Δz) calculation based on fall velocity equals to 0.00206479 m/s and time changes (Δt), where $\Delta z = v_t \, \Delta t$. So, the calculated distance that the dust particle falls by fall velocity alone is about 178.40 m For the large diameters, these particles will sediment and (i.e. 4020 m) will hit ocean surface.

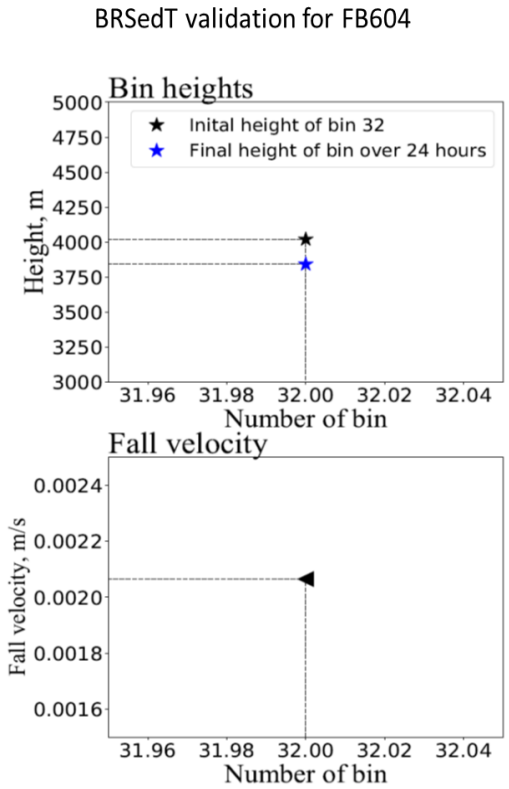

Figure 5. 16. BRSedT process validation for the initial height of bin 32, case flight FB604. The top panel shows the initial (black star) and final (blue star) heights of dust for bin 32. The bottom panel shows the fall velocity (m/s) that is influencing on the particle's sedimentation for bin 32. BRSedT was run without vertical velocity impact nor turbulence for one day simulation across the Atlantic.

The second test is shown in figure (5.17), where the dust particle has the initial height of 4020 m and experiences a subsidence (w). Now the fall velocity is switched off and the turbulent diffusion is also off again. In the bottom panel, the value of w is negative of about -0.0045 m/s at height 4020 m, and so the dust particle after 1 day will be affected by the subsidence causing a falling to the height of about 3100 m. Subtraction between the latter value of height (i.e. 3100 m) and the initial height (i.e. 4020 m) will give very close to the value that is computed by the subsidence. This shows that the BRSedT model provides correct vertical movement for dust by sedimentation and large-scale subsidence. Both processes have also been switched on (not shown) and the correct value for the vertical motion was obtained when both were operating.

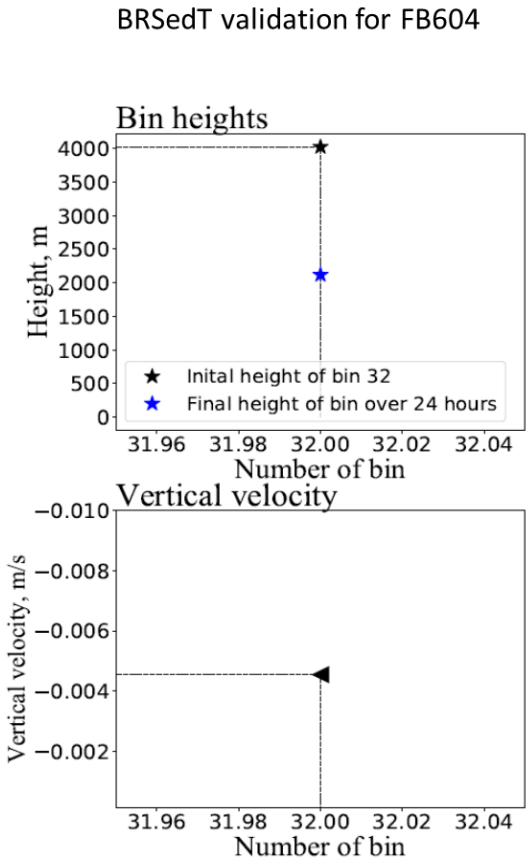

Figure 5. 17. As figure (5.16), but for subsidence effects.

5.3.2 Testing of BRSedT for turbulent diffusion

The testing of turbulent diffusion is very different to fall velocity and large-scale subsidence because instead of parcels of dust just falling to a new vertical location, for turbulent diffusion the dust is redistributed to neighbouring parcels depending on the strength of the turbulence.

Therefore, in this test, I begin with amounts of dust at two heights, as shown in figure (5.18). The BRSedT model is then run using these initial values and I have set both sedimentation and large-scale subsidence to zero. The dust is at heights of 4980 m (red solid symbol) and 5100 m (blue symbol), shown in the figure (5.18). Over one timestep of model run, the layer with the larger dust (i.e. red symbol at layer 4980 m) is expected to be reduced through turbulent diffusion, while the layer above it (5100 m) should increase since it starts out with a lower amount. This turbulent diffusion is related to the effect of the diffusion coefficient, where I use a value of 10 m^2/s at layer 4980 m for this test.

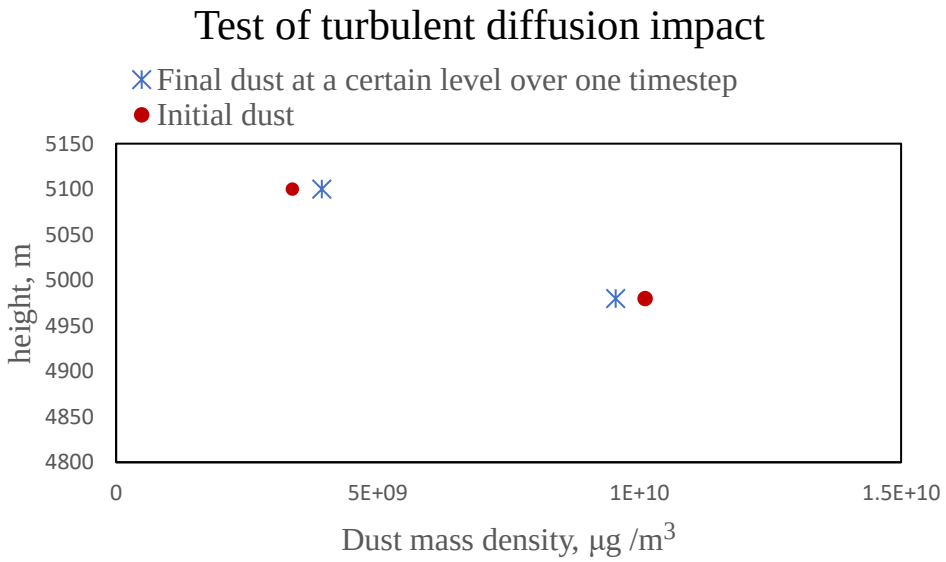

Figure 5. 18. Validation test of turbulent diffusion using dust mass profiles from aircraft observations as input values in the BRSedT model without using both the sedimentation process and large-scale velocity process. The test runs over one timestep at two layers including 4980 and 5100 m. The initial dust mass is indicated by the red solid symbol, while the final value is shown by the blue symbol.

Over time, I would expect the dust to be mixed so that the layer with the higher value decreases and the neighbouring parcel value increases until they equalise in time. The flux of dust from the height with the higher amount of dust to the neighbour, which are separated by 120 m, is 375 x 10^5 μg/ m^2. s over a time of second. This offline calculation is confirmed in the BRSedT model where I show the redistribution of dust over a single timestep. As predicted from the flux calculations, the mass concentration of dust leaving the peak through turbulent diffusion is 9.8 x 10^5 μg/m^3. This is confirmed in the model results by looking at figure (5.18) where final values are stars.

The next test is to investigate the model validation at two different levels, including below and above 300 m. From the observations, the 300 m and above is where the initial dust values are specified from observations, so I test both above and below 300 m to ensure it handles this vertical properly. In test A I start with dust all below 300 m and let it spread above and below through turbulent diffusion. In test B, I start with dust that is above and below 300 m and let it spread through turbulent diffusion. In both cases, I have another layer with 0 dust which is at 340 m in test A and 440 m in test B. So, in figure (5.19), the top panel (i.e. test A) shows initial (left box) and final (right box) amounts of dust. The amounts of dust are just relative dust values of 0, 100 or 200 for the purpose of testing and don't represent observed values. The bottom panel (test B) shows model results for dust with values initially above and below 300 m. The BRSedT model is used to step the profiles forward in time one step (multiple steps were also tested but are more involved to show results for) through turbulent diffusion and the results in the figure (5.19) shows that the higher dust altitude are appropriately spread to the lower and zero dust layers

around it. By showing test A and B results are the same, it shows that the treatment above and below the initial observations is treated consistently. These test runs were both implemented assuming turbulent diffusion coefficient is 100 m^2/s and with the absence both of sedimentation and subsidence impacts. The results show that the initial dust of 200 units at height 100 (test A) or 200 m (test B) will spread (reduce) to the heights 220 and 340 m for test A and 320 and 440 m for test B. The initial 200 units at a3 and b3 are shown to reduce by 8.33 units which is received at a2 and b2. At the same time the values of a2 and b2 also lose dust through turbulent diffusion to the heights a1 and b2 (which initially have 0 units) in the same amount of 8.33 and so this shows that the final values for both tests are 8.33 at a1' and b1', 100 units at a2' and b2' and 191.66 units at a3' and b3', as expected. I have tested the turbulence for a variety of initial dust profiles and it performs as expected, moving dust down the gradient in the expected amounts by basic turbulent diffusion calculations.

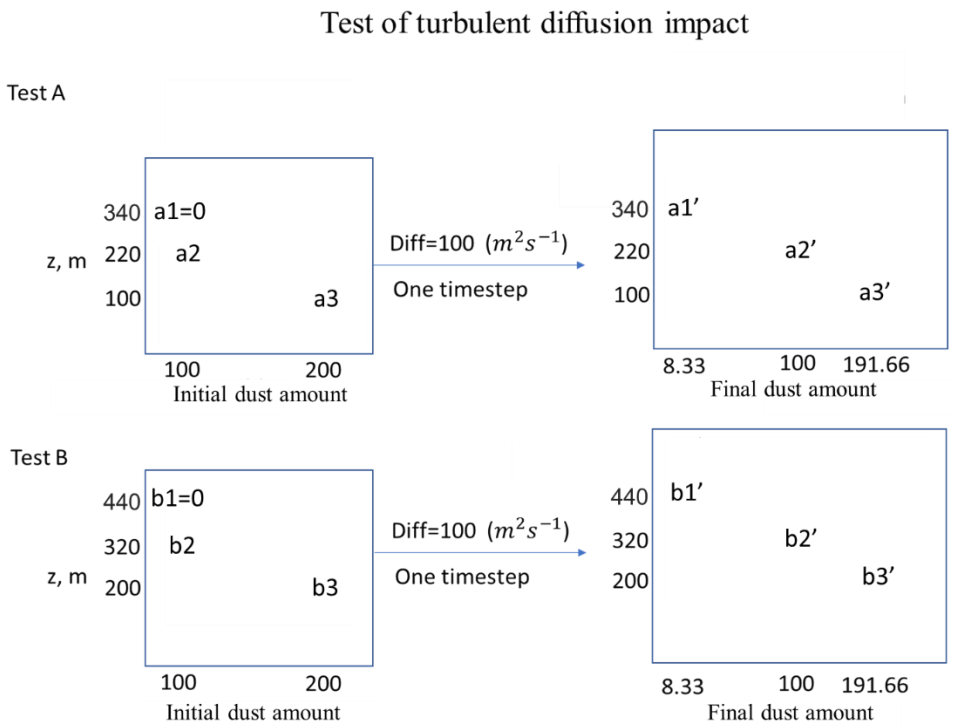

Figure 5. 19. Validation of BRSedT model with using turbulent diffusion impact with dust values over one step of time. Top panel, Test A, shows results with using a layer below 300 m. The bottom panel, Test B, shows results with using layers above and below 300 m. Both runs use a diffusion coefficient of 100 m^2/s.

5.4 Validation of BRSedT model results with observations

In the previous sections, I show that the BRSedT model correctly predicts the movement of dust through the three processes acting in the model (sedimentation, large-scale subsidence, and turbulent diffusion). There is one further comparison that can be performed to test the model performed appropriately and that is by comparing with observations.

5.4.1 Validation of transported dust mass concentrations with FENNEC results

In this, I show that the predictions of dust transported give sensible results by comparing the BRSedT model output to FENNEC observations for dusty air from the African land advecting over the Canary Islands. The flights from the African mainland to the Canary Island are far quicker than the typical advection time of the dust laden air on this same journey so I will compare the vertical profile from flights on two different days which is a more appropriate test for comparing the profiles considering the dust advection speed. The timings of a couple of flights works out well in terms of timings within roughly one hour for a roughly one day transport time. In addition, further comparisons are made with AOD using satellite observations but those are column integrated comparisons. It is only the flights involve vertically resolved profiles.

Two flights were used to check the dust mass loading and optical depths between the final profile from the BRSedT (i.e. final profile for flight FB604 and FB611) and dust profiles from the FENNEC flight observations (i.e. flight FB605 and FB612). The take-offs/landings and ascending/descending were used to obtain the profiles and integrated column mass loading. I compared the final dust profiles for flight FB604 and FB611 simulated by the BRSedT model with the flight observation for FB605 and FB612 over the Canary Islands, respectively. Both the initial and final profiles were considered, in which the time of transport of dust to arrive at the Canary Islands is estimated to be consistent with observations. Comparison between these flights is the best possible way to make use of the FENNEC observations to provide a sense check and further validate the BRSedT model. The large-scale wind speed and direction at 700 mb and time of 15:00 UTC for FB604 shown in previous figure (5.11) indicates that the dust arrival over the Canary Islands is roughly consistent with flight FB604. Averaged wind speed is about 3.5 m/s within the SAL (roughly 3 km) and the distance between the western Sahara (I determined the location of the African land here based on the flight track shown previously in the figure (2.3) of Chapter 2) and Fuerteventura is about 412 km. Thus, dust arrives at Canary Islands after about more than 1 day. The observation time of flight at African land for FB604 (i.e. initial dust profile) was between 1537 and 1732 UTC. Whereas, over the Canary Islands, the observation time for flight FB605 was from 1107 to 1206 UTC. Note, the time of FB605 indicates the time of the return flight to the Canary Islands, in order to be coincident with the time of dust arrival (i.e. more than 1 day). Therefore, dust reaches there after one day which agrees with the time duration between FB604 and FB605 flights.

Figure (5.20) displays the consistency between simulated dust mass loading ($\mu g/m^3$) for one day of transport for the dust mass loading from flight observations over the Canary Islands. The solid lines indicate the final mass profile from the BRSedT model, while dashed lines show the dust profiles from the FENNEC observations. Runs were performed using spherical particle mode for calculating fall velocity with using kinematic fluid viscosity for value of 0.000015 m^2/s and

with density of aerosol of 2 g/cm^3. In the left panel, agreement is reasonable between the final profile for FB604 and observed profile of FB605. However, within the lowest height (i.e. below 1 km) the profiles do not match well. This is understandable near the coast of the mainland since the BRSedT model does not explicitly model the transition of the mainland boundary layer air out over the marine boundary layer. As discussed earlier, it is likely that the mainland air will rise over the marine boundary layer, and thus the dust may be retained at lower levels for a little longer than in the model because of this ascent during transport. I see this in both plots in figure (5.20). Also, observations taken at Canary Island at the lowest levels are close to the island and so may be affected by the land. So, the differences at the lowest levels are not a cause for concern, especially since they do not influence the well-mixed SAL layer profiles that is the main focus. Within the SAL, it is noticed that left panel depicts reasonably good agreement in dust mass profiles in a comparison to right panel. For instance, between about 2 km and 3 km the profiles are match well between flight FB605 and simulated dust (initial) mass for flight FB604 in BRSedT. Similarly, between about 4 km and 5 km the agreement in the results is reasonable. In contrast, left panel does not show good agreement in the whole profiles, where discrepancy is sometimes high (factor of more than 2) but reasonable agreement can be seen at heights about 2 km, 3 km, 4 km and 5 km. It seems that less discrepancy is associated with dusty cases (i.e. FB604 and FB605) and increased with moderately dusty cases such as FB611. In addition to the modelling considerations, the observations had differences at the lowest levels in terms of flight measurements with height, where the lowest altitude of observation over land was 300 m, while over the Canary Islands it was 60 m. Although this section uses different heights in flight observations, height extrapolation from 300 m to the surface was applied in the BRSedT model. Outside of the boundary layer and in the SAL, the results show reasonably good agreement, both modelled and observed profiles of dust concentrations are matched well.

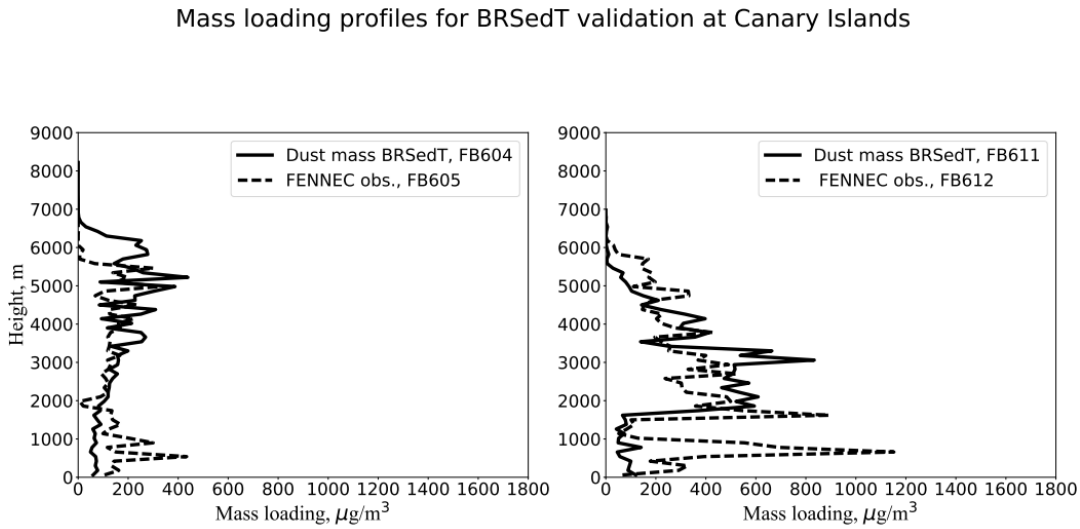

Figure 5. 20. Dust mass loading profiles determined by BRSedT using the profile from FB604 (left) and FB611 (right) as the initial profiles and then simulated in BRSedT for a day transport. Also in the plots are the profiles at the Canary Islands taken during the time the dust from the BRSedT simulations is expected to arrive at the Canary Islands. So the FENNEC observations for FB605 (left) and FB612 (right) are the observed profiles comparable with the BRSedT results shown in flight FB604 and FB612, respectively. Dashed lines indicate dust profiles from the FENNEC observations at Fuerteventura, while solid lines indicate BRSedT predictions of dust over 1 day of dust transport time calculated from the BRSedT model. The dust mass profiles (in unit of μg/m^3) are both evaluated over the Canary Islands. The BRSedT code was run with assuming spherical particle shape for fall velocity under using Kinematic fluid viscosity for value of 0.000015 m^2/s and with density of aerosol of 2 g/cm^3.

5.4.2 Validation of BRSedT results with AOD and uncertainty analysis

The validation of the model BRSedT is now used to compare AODs from the model with satellite observations from MODIS-Terra satellite. The calculation of AOD is implemented based on the column integral of dust extinction (σ) with altitude (Jabonero et al. 2018), where $\sigma = k_{ext} *$ dust mass profile. k_{ext} is assumed to be 1.0 m^2/g and 0.75 m^2/g (Jabonero et al., 2016) over land/Canary Islands and Caribbean, respectively. In addition, statistical calculations (percentage differences) are applied for the results of total mass profiles using two values of density of dust including 2 and 2.6 g/cm^3. Table (5-5) shows the total modelled profile of dust mass from the BRSedT model associated with total mass over the Canary Islands. The calculated values of AOD for dust transported for 24 hours are in a good agreement between the total mass of dust modelled (AOD=0.6, 0.3) and that observed by MODIS-Terra (AOD=0.56, 0.2-0.4), where the values of AOD here are obtained from MODIS observations. Based on table (5-5), using different values of dust density results in reasonable percentage differences; using alternative dust density values of 2.6 g/cm^3 (first line) and 2 g/cm^3 (second line) for a typical case (i.e. FB604) results in differences of about 26 % and 35 % for Canary Islands and Caribbean orientations, respectively. Also, the difference in the total mass of dust loading between final mass (BRSedT results) and

FENNEC observations for flight FB604 and FB605 is about 4 % and 5 %, while percentages of about 18 % and 11 % are related to the flights FB611 and FB612, respectively.

Table 5- 5. Comparison of column mass loading and AOD of dust predicted by BRSedT after 1day transport from the African coastline and FENNEC observations taken at the Canary Islands. There are two values in each entry. The top and bottom values for each flight column indicate integrated dust column mass for the whole atmosphere with dust densities of 2.6 g/cm^3 and 2 g/cm^3, respectively.

Final dust column mass from BRSedT, (μg/m^2)	FENNEC obs. at Canary Islands. (μg/m^2)	Percentage Diff. (%)	AOD at Canary Islands
FB604: **5835** **4489**	FB605: **6134** **4719**	**5** **4**	MODIS/BRSedT: **0.56 / 0.6**
FB611: **6212** **4780**	FB612: **7434** **5351**	**18** **11**	MODIS/BRSedT: **(0.2-0.4) / 0.3**

5.4.3 Various other sensitivities and testing

The accuracy of the BRSedT model is tested in the previous section 5.4.1 for the flight observations and model results. Now in this section, I will simulate the impact of input parameters on the BRSedT model. The goal here is to explore some sensitivities to different parameters that go into calculating the dust, especially fall velocities. I include BRSedT runs for flights FB604, FB605, FB612, and FB699 including changes to the following:

1. Runs using BRSedT using a suitable fall velocity (fall velocity was used in BRSedT based on Eq. 5.66 with using kinematic viscosity of 0.000015 m^2/s and with density of dust of 2 g/cm^3 considered for spherical particle shape, I will name it as base fall velocity). This was compared to BRSedT runs with density of dust altered to a value of 2.6 g/cm^3. The effect of the different densities was assessed.
2. Inserting minimum and maximum values of v_t in the BRSedT model based on figure (5.2) and figure (5.3) for a range of dust density.
3. Using different RIs for flights over the African land and Canary Islands.
4. Investigate spherical and non-spherical particle shapes effects on v_t.

The results are presented in the next two sections split according to spherical and non-spherical assumptions with using turbulent diffusion coefficient in the BRSedT model.

5.4.3.1 Sensitivity to non-spherical particle shape assumption

In this section, the sensitivity of transport to the shape of dust, e.g. sphericity/non-sphericity assumption, is considered in the BRSedT calculations. This is explored by calculating the percentage difference in the final total mass loading of dust sedimented between using spherical and non-spherical particle shapes in the BRSedT model for simulations towards the Canary Islands (i.e. after 4 days) and across the Atlantic (after 7 days) for each flight number including the most dusty cases FB604, FB605, FB612 and moderately dusty case FB699. The total mass of dust sedimented (i.e. final total mass) was computed using terminal velocity (base fall velocity) and subsidence in the BRSedT for the respective spherical particle shape. The total mass transported is predicted using terminal velocity for non-spherical particle assumptions performed using minimum and maximum fall velocities (i.e. with shape factors ξ =0.866 and 0.955) based on equation (68) from Gasteiger et al. (2017) and Gasteiger et al. (2011). The terminal velocities in BRSedT are shown previously in figure (5.3), subsection 5.2.3. All total mass results were implemented with turbulent diffusion and subsidence on during the evolution of dust transport to these destinations. The BRSedT model results are shown for initial and final mass sedimentation for ξ =0.866 for each flight case and it is noted that the different non-spherical values produced small variations compared to spherical and non-spherical.

Tables (5-6) and (5-7) presents the final total mass loading (expressed in units of μg/m^2) of dust calculations from BRSedT using non-spherical particle shape (first column) and spherical shape (second column) modes. Note, scaling factor (SF) is applied to the total mass loading of the dust in these tables. These tables contain two lines where the first and second lines show the total mass loading using density of dust with values of 2.6 g/cm^3 and 2 g/cm^3, respectively. Percentage differences between spherical and non-spherical mass results are also shown in the last column of these tables. The thesis results show that the difference in final total mass column of dust between non-spherical (second column) and spherical particle (third column) shapes is significantly large. The non-spherical dust has a lower fall velocity and this explains that the magnitude of dust profile in the atmosphere based on non-spherical dust particle shape is greater than that for spherical shape since more is retained in the atmosphere for non-spherical shape.

The impact of fall velocity on the final total mass of dust profiles for non-spherical particle shapes are presented in tables (5-6) and (5-7) for dust transported towards the Canary Islands and towards the west off Africa, respectively. Fall velocity is calculated with using kinematic fluid viscosity, with a value of 0.000015 m^2/s, and with the density of dust aerosol of 2 g/cm^3 and a spherical particle shape. Percentage differences in the total mass between spherical and non-spherical particle shapes under fall velocity, turbulence and subsidence effects and with using ρ_p of 2 g/cm^3 are: 18.09%, 60.49%, 3.8% and 7.4% after 4 days over the Canary Islands, while

percentage differences (including 60.05%, 83.77%, 26.1% and 95.93%) are huge across the Atlantic for FB604, FB605, FB612 and FB699, respectively. Although BRSedT simulations have different input parameters and different timescales between dust towards the Canary Islands and dust towards west of the African land, the dust transported across the Atlantic is for much longer duration, but there is generally more loss of dust towards the Canary Islands which is likely due to the largescale subsidence being much stronger on that path for these cases. In addition to this comparison, large percentages for spherical and non-spherical particle shapes for dust transported across the Atlantic are reasonable since final total mass loading relies on the effects of fall velocity, subsidence and turbulence over the Atlantic.

Based on tables (5-6) and (5-7), it shows that fall velocity for a spherical particle assumption compared to non-spherical shape affects the total mass column of dust in BRSedT, where it shows significant differences over fall velocity based on non-spherical particle shape over the Canary Islands as well away from the African coastland. For instance, for FB604 the final total mass of dust after 4 days transport towards the Canary Islands assuming a spherical and with a density of dust of 2 g/cm^3 has value of 3626 $\mu g/m^2$, while using a non-spherical assumption it has value of 4587 $\mu g/m^2$. These numbers are larger than for dust transported over 7 days across the Atlantic, see results for total mass in table (5-7). The high (low) number of column integrated mass indicates dust can remain in the atmosphere with large (less) mass profiles over the Atlantic. However, the main finding is the percentage difference in total mass calculated based on BRSedT between spherical and non-spherical particle shapes shown in table (5-7) for these flight cases, as it shows it is larger than for results of table (5-6), which are related to the Canary Islands. This reflects the case that shape assumption influencing fall velocity for dust transported long distances over the Atlantic is an important factor in results from BRSedT.

Table 5- 6. Total mass of transported dust towards the north-west over Canary Islands during 4 days of transport from the African coastal line assuming non-spherical shapes.

Flight	BRSedT final total mass loading, (μg/m^2)		Dust density, (g/cm^3)	Percentage diff. $\frac{\lvert(col2-col3)\rvert}{\frac{(col2+col3)}{2}} x100\%$
	Non-spherical particle mode (with v_t and w, ξ =0.866)	Spherical mode (with base v_t and w)		
FB604	**5817** **4587**	**4714** **3826**	**2.6** **2**	**20.94** **18.09**
FB605	**8005** **6158**	**4010** **3298**	**2.6** **2**	**66.5** **60.49**
FB612	**2177** **1621**	**1961** **1560**	**2.6** **2**	**10.43** **3.8**
FB699	**8** **7**	**7** **6.5**	**2.6** **2**	**13.3** **7.4**

Table 5- 7. Total mass of dust sedimented over Caribbean (Puerto Rico) during 6-7 days of transport from the African coastline assuming non-spherical shape.

Flight	BRSedT final total mass loading, (μg/m^2)		Dust density, (g/cm^3)	Percentage diff. $\frac{\lvert(col2-col3)\rvert}{\frac{(col2+col3)}{2}} x100^{\circ}$
	Non-spherical particle mode (with v_t and w, ξ =0.866)	Spherical particle mode (with base v_t and w)		
FB604	**4707** **3603**	**2415** **1939**	**2.6** **2**	**64.3** **60.05**
FB605	**10159** **8565**	**3985** **3508**	**2.6** **2**	**87.3** **83.77**
FB612	**5600** **5019**	**4159** **3859**	**2.6** **2**	**29.53** **26.1**
FB699	**101** **91**	**35** **32**	**2.6** **2**	**97** **95.93**

Further sensitivities relating to fall velocity and density are shown in figure (5.21) and illustrates their effect on the vertical profile of the dust mass concentration.

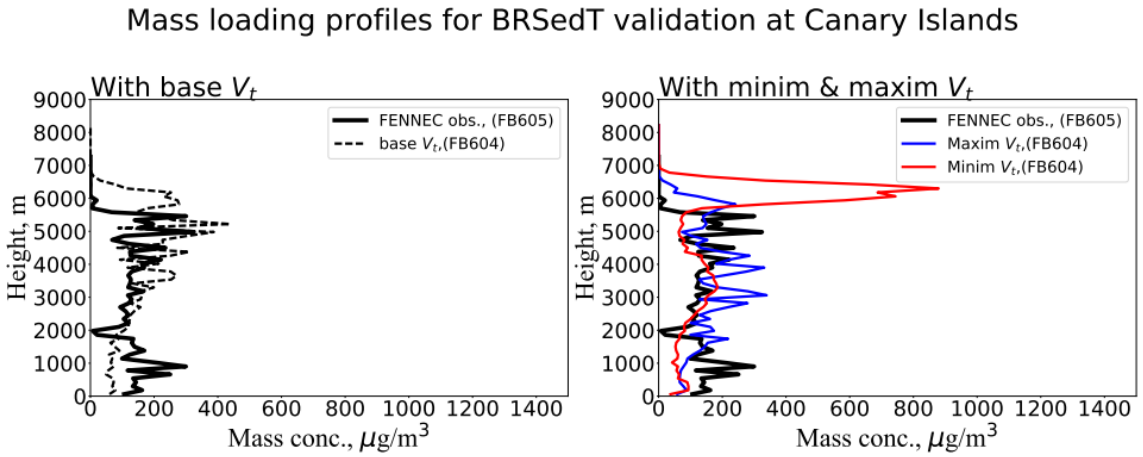

Figure 5. 21. Mass loading profiles (µg/m^3) of dust are shown with variations in fall velocity, density of dust (ρ_d) and kinematic fluid viscosity (ν). The left panel shows sedimented (dashed black) dust profiles after about one day based on predictions by the BRSedT model from the African land toward the Canary Islands. Sedimented dust mass profiles in the left panel are related to flight FB604, which is calculated using the base fall velocity, based on Eq. (66) assuming spherical particle shape, using ρ_d= 2 (g/cm^3) and with ν = 0.000015 (m^2/s). The right panel shows a minimum fall velocity used shown by a red solid line, as calculated using ρ_d= 1.5 (g/cm^3) and ν = 0.000025 (m^2/s), while max fall velocity (blue line) is calculated by setting ρ_d=2.5 (g/cm^3) and ν = 0.000015 (m^2/s). Black solid lines in both panels indicate initial mass profiles of dust over the African land based on FB605 flight observations. Base, min and max fall velocities are presented in table (5-8). Note, the top height of FB604 and FB605 is not the same so this can create large difference in dust mass profile between observed and sedimented profiles over the Canary Islands, where the top height of flight FB604 over African land is 8220m, whereas for FB605 over the Canary Islands it is about 7260 m. Sensitivity tests in all panels are performed using the spherical dust particle shape. All runs were performed using RI=1.53+0.001i.

In figure (5.21), sensitivity test in dust mass profiles between flight observations and BRSedT results over the Canary Islands is considered depending on fall velocity (Eq. (66)) associated with density of dust and viscosity impacts. Where I use BRSedT with dust mass profile initializes over the African land for dusty flight FB604 and run it over 1 day towards the Canary Islands with using turbulent diffusion, large-sale subsidence and base fall velocity associated with using density of dust of 2 g/cm^3 and with ν = 0.000015 (m^2/s), see black dashed line in the left panel of the figure (5.21). In contrast, right panel displays the results with using two different fall velocity inputs, which are: red line presents dust sedimented under these factors (turbulent diffusion and large-scale subsidence) and with calculating min fall velocity, and blue line indicates mass profile

of dust with using these factors but with using max fall velocity. Minimum fall velocity was computed with using ρ_d= 1.5 (g/cm^3) and ν = 0.000025 (m^2/s), while max fall velocity (blue line) was calculated with sets ρ_d to 2.5 (g/cm^3) and ν = 0.000015 (m^2/s). The results of these fall velocities are stated in table (5-8). In the figure (5.21), black solid lines in both panels present observed mass profiles over the Canary Islands based on flight FB605. Spherical particle shape is assumed in the calculations of BRSedT for these panels based on Eq. (66). I will not show the impact of viscosity on the results since it is tested in earlier section (section 5.2.3), so I will show here the impact of different fall velocities associated with density of dust and comparing them with that base fall velocity used in the BRSedT for dust transported towards the Canary Islands. For the base fall velocity (left panel), it shows that the sedimented profile of dust shown in dashed line based on the BRSedT (run with initial dust for FB604) is agreed with that presented by flight (FB605) observation over the Canary Islands. However, at higher levels (i.e., above about 5.5 km), the results are not well matched. This can be explained by two possibilities, firstly is that top height levels of flights FB64 and FB605 are different, where the top height of FB604 over land is 8220m, while for flight FB605 is about 7260m. So, there is about 1 km height difference between what the BRSedT predicted and with that shown by flight observations. Secondly, the BRSedT results show profile at 1 day of dust transport from the African land but dust mass takes about more than one day to arrive to Canary Islands, see section 5.2.5 for dust advection under mean wind effect. So, what I mean here that the BRSedT may not agree well with flight observation for inconsistency top heights due to the transport model used input data over the African land and simulated them over the Atlantic. Within SAL, there is good agreement in dust mass profiles between the results of BRSedT and FENNEC observations with using density of dust with value of 2 g/cm^3 in the calculation of fall velocity, while using density of 1.5 g/cm^3 for min fall velocity and using 2.5 g/cm^3 for max fall velocity does not have good agreement in the results since high density used in fall velocity calculation results in much more dust sedimented than low density, see red and blue dashed lines in the right panel of figure (5.21). Below the SAL (i.e. below 2km), using density of dust with value of 2.5 g/cm^3 instead of 2 g/cm^3 is likely to make the dust profile (shown in blue line) much close to the observed profile (black line) for flight FB605 over the Canary Islands. In contrast, above 5.5 km, using ρ_d = 2.5 g/cm^3 for max fall velocity calculation in the BRSedT still show relative high dust mass compared with the flight observations.

The density of dust and kinematic fluid viscosity are important factors in fall velocity calculation, where it can be seen that for the large dust mass shown in red line associated with calculating min fall velocity with using ρ_d = 1.5 g/cm^3 and with ν = 0.000025 (m^2/s), sedimented dust profile in a comparison with observed profile is very large at the top height and it is not significantly changed within the SAL. The reason for high mass profile can be related to the high value of viscosity for this value of 1.5 g/cm^3 of density of dust, while for no big change in the sedimented dust associated with this low density of dust (i.e. 1.5 g/cm^3), it is represented as low

value compared to that density used with the value of 2 g/cm^3 for calculating observed dust mass profile based on FB605 over the Canary Islands. To conclude, using fall velocity in BRSedT with using density of 2 g/cm^3 and with viscosity of 0.000015 (m^2/s) provides good agreement with flight observation in the SAL, while there is significant sensitivity in using different viscosities at the top of SAL with less sensitivity for viscosity below SAL due to the top height of flight cases FB604 and FB605 are not the same. It is not suitable to use min/max fall velocity in predicting dust mass profiles by BRSedT over the Canary Islands. In addition, viscosity may affect the result below and above SAL where viscosity is ranged (based on international standard atmosphere) between about 1.5, 2 and 3 m^2/s in the BL, SAL and above the SAL.

5.4.3.2 Sensitivity to refractive index

Previous works used various refractive indices for dust size distributions when they accounted for dust profiles in transport modelling. In this study, two plausible values of refractive index (RI) are used and the thesis results show that the sensitivity is large. As a reminder, I use the RI to extract the size distribution information from the dust measuring instruments that are scattering based (PCASP/CDP). The often-used value of the imaginary part of RI is 0.003 but this has been shown to give large column mass densities, as shown in figure (5.22), for two dusty events over the African land and Canary Islands. All profiles in figure (5.22) indicate the calculated values of dust profiles from the FENNEC observations over the African land (see first row and first plot in second row) and the Canary Islands (second and third plots in second row), where black (green) lines come from RI = 1.53+0.003i compared with the red (blue) lines which come from assuming RI = 1.53+0.001i and indicate the mass loading of dust over land (ocean), respectively. Two different flights (including FB604 and FB605) shown in the top panel of figure (5.22), where they measured dust profiles during flights descending over the African land. In addition, I would also to show here flight FB604 (left panel underneath top plots) during ascending flight over western Sahara to understand the measured dust profiles from different flights and to provide evidence about dust observations from FENNEC flights can be considered for both ascending and descending flights. By looking at these dust profiles in each individual flight, they can give similar order magnitude between profiles with using these refractive indexes. The reason for this is that dust altitudes over land are quite similar for the same flights (e.g. FB604) for both to and from Fuerteventura airport. Secondly, it offers a way to look at how the dust profiles vary over time. Results show that the 0.003 value of Ri has led to much larger column masses of dust because of the larger sizes that are required to satisfy the levels of absorption. Given that the validation used of 0.001 agrees with observations, this shows that using larger absorption will lead to very different results that do not agree with observations, at least for these cases. For CIP data mentioned in Chapter 3, it is estimated that using CIP with diameter of greater than 45 μm can

remove from about 42 to 63 % of the uncertainty between using these values of RI in the calculations, see previous figures (3.2) – (3.3). This uncertainty agrees with Ryder et al. (2019), where she stated that about 40 % uncertainty is due to removing giant dust particles from dust mass loading of Saharan dust over the African land, while this uncertainty is not high but should not be neglected for the SAL. Although thesis results do not show significantly radiative cooling impact due to giant particles over the Atlantic, however, radiative cooling by the presence of giant particle sizes can be involved (Ryder et al., 2019).

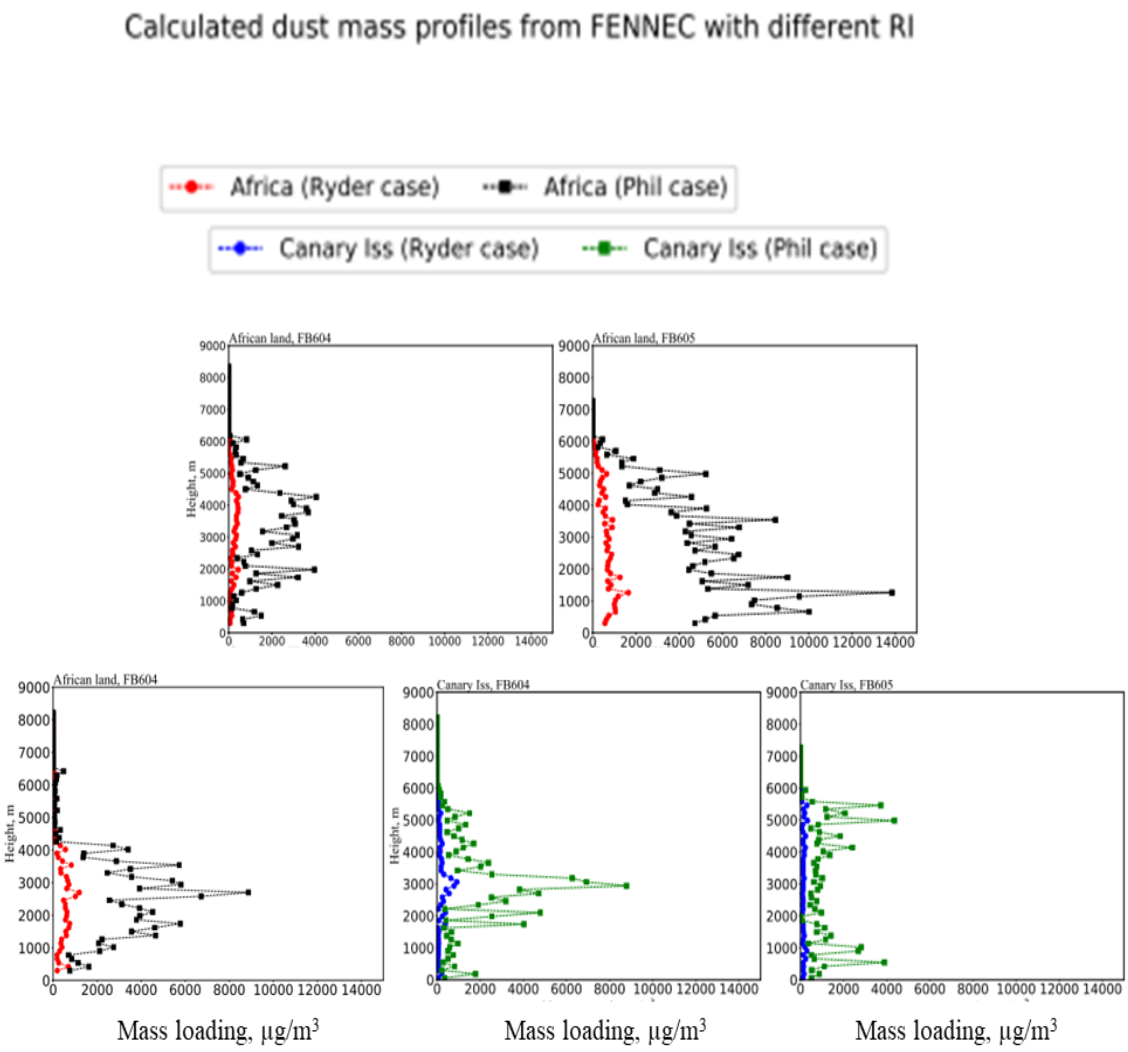

Figure 5. 22. Top panel, mass loading profiles (µg/m^3) of dust calculated by using different refractive indices; for RI =1.53+0.001i (red and blue lines) and 1.53+0.003i (black and green lines) for two dusty cases over the African land. Lower panel, dust mass results for ascending flights over the African land, for flight FB604 shown in first plot, while second and third plots show mass profiles for using these two different RIs over the Canary Islands. All profiles represent calculated mass loading based on the FENNEC flight observations, where flight FB604 and FB605 are labeled on each plot. Profiles for African land in the first row shows results during a descending flight towards Africa, while the second row shows profiles for the ascending flight FB604 over the African land (first plot) and Canary Islands (second and third plots) for FB604 and FB605. Key, Canary Iss refers to Canary Island location.

Although sensitivity tests for different RIs, and their effect on the dust profiles over the Atlantic, were not included in the BRSedT, I presented in figure (5.23) sedimented dust profiles for typical dusty case (FB604) after 7 days across the Atlantic with using different RIs, including 1.53+0.001i (i.e., RI based on Ryder) and 1.53+0.003i (based on Rosenberg). The results are calculated in the BRSedT model considering the impact of spherical fall velocity, large-scale subsidence, turbulent

diffusion and using density of dust with a value of 2 g/cm^3. The solid black line indicates an initial dust profile from the African land used in the BRSedT, while the dashed black and dashed blue lines show the final dust mass profiles after 7 days dust transport across the Atlantic. The figure shows significant differences in the final dust mass between using these RIs with percentage difference of about 62%. This percentage is large but it is related to long transport of dust for 7 days across the Atlantic and thus using BRSedT with considering RI of 1.53+0.003i can provide more sensitivity in dust sedimentation than using low imaginary part of RI, e.g. value of 0.001i. It is also noticed that below 800 hPa (below the SAL) there are significant differences in the final mass of dust between using these two cases, which indicates that using different RIs has a significant impact on the change of dust profile for the Caribbean site. The reason for less mass of final dust with using high imaginary part of RI is due to the large amounts of dust sedimented more than low dust mass concentrations for transport across the Atlantic.

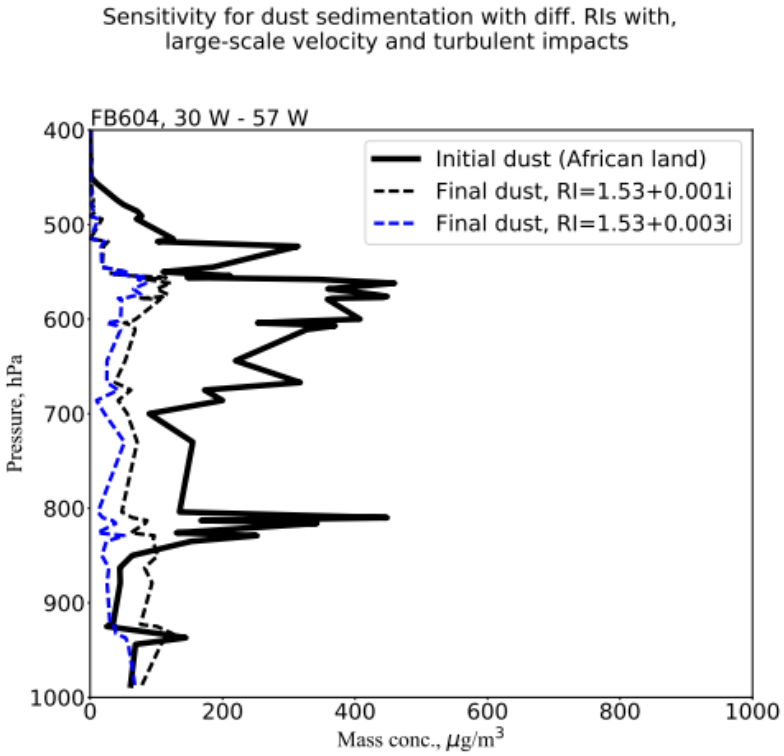

Figure 5. 23. Vertical mass concentration of dust sedimented after 7 days transport across the Atlantic. The final profiles of dust mass were calculated based on BRSedT under impact of large-scale vertical velocity, turbulent diffusion and density of dust with value of 2 g/cm^3. Solid black line shows initial dust profile from African land used in the BRSedT model. Dashed black and dashed blue lines present final mass profiles with using RI=1.53+0.001i and RI=1.53+0.003i, respectively. Spherical particle shape is applied in the simulation

5.4.4 Establishing longer duration BRSedT simulations over 4 and 7 days including sensitivities

The BRSedT simulation of dust transportation towards Canary Islands and Caribbean destinations is explained here with considering some sensitivities to different parameters that go into calculating the dust, such as density of dust and fall velocities. The BRSedT used initial dust profiles based on rebined dust size distribution from FENNEC observations over the African land. the simulation is performed with using dust profiles, large-scale subsidence, fall velocity and density of dust. The input profiles of the initial dust are scaled by SF based on air mass trajectories under fall velocity impact with considering spherical shape of dust particles based on Eq. (5.66). The fall velocity used is related to values taken from figure (5.2), where it is calculated with using density of dust ρ_d= 2 g/cm^3 and kinematic fluid viscosity ν = 0.000015 m^2/s (see second column in table (5-8)). The BRSedT runs with large-scale subsidence based on ECMWF dataset given dust sediment profiles every 3 hours for 4 and 7 days. The purpose of using these factors as input data in the BRSedT is to simulate the evolution of dust transported over the Atlantic. These runs were extended to use different values of these parameters, where in this thesis I include BRSedT runs for flights FB604, FB605, FB612, and FB699 including changes to the following:

1. Runs of BRSedT with using density of dust of 2 and 2.6 g/cm^3 and calculating different initial dust mass loading.
2. Inserting minimum and maximum values of v_t in the BRSedT model based on figure (5.2) and figure (5.3) for a range of dust density.

As the dust mass profiles are derived by integrating number concentration over all bins and multiplying by the density of dust based on values shown in point 1, the mass profiles will have two different mass vertical values depending on density. The reason for running the BRSedT model with these variations in points 1 and 2 is to understand what the changes in dust profiles between the initial and final total mass will be for variations in density and high/low fall velocities, see columns 4 and 5 in table (5-8), respectively. The low fall velocity for spherical particle is computed based on Eq. (5.66) with using ρ_d= 1.5 (g/cm^3) and ν = 0.000025 (m^2/s), while high velocity is calculated with using ρ_d= 2.5 (g/cm^3) and ν = 0.000015 (m^2/s). So the minimum and maximum values of fall velocities used in the BRSedT are changed associated with using different values of density of dust and viscosity, while the base value calculated in the BRSedT for these flight cases is calculated using the base fall velocity with density of dust of 2 (g/cm^3) and kinematic fluid viscosity of 0.000015 (m^2/s). Note that the initial and final total mass of dust density is calculated by integrating dust number concentration over all bins and with

multiplying by density values of dust of 2.6 g/cm^3 and 2 g/cm^3 separately in the BRSedT, where the initial and final values of total mass are shown in the first and second lines of tables (5-9) and (5-10). One of the key approaches taken with the modelling using BRSedT was to use it for the easiest of conditions to model. For instance, if the majority of the dust is going in one direction then the model is more likely to capture the relevant transport. I want to avoid cases where the dust is being transported in all different directions and only a small amount is transported in the direction of interest. This approach has been mathematically checked by using the scaling factor, SF, introduced earlier. I selected the scaling factors to be as large a possible which indicates that most of the dust was heading in that direction of interest towards the Caribbean. This is the case for flights FB604, FB605 and FB612 which have scaling factors of 0.5, 0.6 and 0.8, see previous table (5-3) and table (5-4).

Table (5-9) shows BRSedT simulation results for these runs including initial and final total mass (μg/m^2) for 4 days of transport towards the Canary Islands. Values of total mass in the first and second lines in all tables for each flight case shows results using dust densities of 2.6 g/cm^3 and 2 g/cm^3. In contrast, table (5-10) reveals that during dust transport across the Atlantic for 7 days, fall velocity is dominant for determining the dust altitudes in that direction, far distances from the African coastal line. This is because the subsidence after three or four days of transport is weaker than near the coast, as can be seen in figure (5.8). Dust mass loading for flight number FB699 shows a low value in comparison to other cases, since a low fraction of dust profile is determined by SF as well as the classification of dust indicates a moderate dust event over the African land. The density of dust aerosol shows again influence on the results of total mass profiles, where the value is increased with increasing dust density.

The removal of dust over the Atlantic is the key issue for understanding the dust size distribution evolution from the initial profile of dust over the African land. Dust removal over the Atlantic is very sensitive to the initial size distribution of dust over land and dependent in the model on particle sizes, density of dust-aerosol, fall velocity and large-scale subsidence. This can be seen from figure (5.2), where large particles with size > 20 μm fall faster than smaller sized spherical particles, and thus large particles will be preferentially removed from the atmosphere.

Table 5- 8. Calculated fall velocities (v_t, m/s) for spherical, non-spherical, minimum spherical and maximum spherical particle shapes used in BRSedT. First column shows diameter of bins.

Diameter, µm	v_t, m/s			
	spherical particle	non-spherical	Min spherical	Max spherical
0.134	3.316E-07	1.88E-07	7.060E-08	5.460E-07
0.140	3.649E-07	2.07E-07	7.770E-08	6.000E-07
0.148	4.052E-07	2.29E-07	8.629E-08	6.669E-07
0.160	4.733E-07	2.68E-07	1.009E-07	7.790E-07
0.168	5.192E-07	2.94E-07	1.109E-07	8.540E-07
0.182	6.097E-07	3.45E-07	1.300E-07	9.999E-07
0.192	6.805E-07	3.85E-07	1.450E-07	1.119E-06
0.208	7.984E-07	4.52E-07	1.700E-07	1.310E-06
0.230	9.773E-07	5.53E-07	2.080E-07	1.610E-06
0.254	1.189E-06	6.73E-07	2.529E-07	1.959E-06
0.280	1.441E-06	8.16E-07	3.069E-07	2.369E-06
0.306	1.730E-06	9.80E-07	3.680E-07	2.850E-06
0.336	2.079E-06	1.18E-06	4.430E-07	3.419E-06
0.489	4.397E-06	2.49E-06	9.359E-07	7.239E-06
0.618	7.026E-06	3.98E-06	1.500E-06	1.160E-05
0.851	1.331E-05	7.54E-06	2.830E-06	2.189E-05
1.054	2.044E-05	1.16E-05	4.349E-06	3.360E-05
1.344	3.319E-05	1.88E-05	7.069E-06	5.460E-05
1.717	5.419E-05	3.07E-05	1.150E-05	8.920E-05
1.979	7.197E-05	4.07E-05	1.530E-05	1.180E-04
2.140	8.417E-05	4.77E-05	1.789E-05	1.380E-04
2.361	1.024E-04	5.80E-05	2.180E-05	1.679E-04
2.574	1.217E-04	6.89E-05	2.590E-05	1.999E-04
2.809	1.449E-04	8.21E-05	3.089E-05	2.390E-04
3.034	1.691E-04	9.58E-05	3.600E-05	2.779E-04
3.327	2.033E-04	1.15E-04	4.329E-05	3.349E-04
4.585	3.861E-04	2.19E-04	8.220E-05	6.350E-04
5.764	6.104E-04	3.46E-04	1.300E-04	1.000E-03
7.352	9.930E-04	5.62E-04	2.110E-04	1.629E-03
9.098	1.520E-03	8.61E-04	3.239E-04	2.499E-03
10.197	1.910E-03	1.08E-03	4.070E-04	3.139E-03
10.601	2.064E-03	1.17E-03	4.400E-04	3.400E-03
11.140	2.280E-03	1.29E-03	4.849E-04	3.749E-03
11.785	2.551E-03	1.44E-03	5.430E-04	4.199E-03
12.558	2.897E-03	1.64E-03	6.169E-04	4.770E-03
13.656	3.426E-03	1.94E-03	7.290E-04	5.640E-03
15.245	4.269E-03	2.42E-03	9.089E-04	7.019E-03
17.121	5.385E-03	3.05E-03	1.150E-03	8.860E-03
18.762	6.466E-03	3.66E-03	1.380E-03	1.059E-02
19.985	7.337E-03	4.15E-03	1.560E-03	1.209E-02

*21.211	8.265E-03	4.68E-03	1.760E-03	1.360E-02
24.698	1.120E-02	6.34E-03	2.390E-03	1.840E-02
28.598	1.502E-02	8.51E-03	3.199E-03	2.470E-02
32.984	1.998E-02	1.13E-02	4.259E-03	3.290E-02
37.608	2.598E-02	1.47E-02	5.530E-03	4.270E-02
42.711	3.351E-02	1.90E-02	7.129E-03	5.510E-02
47.882	4.211E-02	2.38E-02	8.969E-03	6.930E-02
53.764	5.310E-02	3.01E-02	1.130E-02	8.739E-02
60.226	6.663E-02	3.77E-02	1.420E-02	0.1099
66.657	8.162E-02	4.62E-02	1.740E-02	0.1340
73.784	0.1000	5.66E-02	2.129E-02	0.1650
81.350	0.1215	6.88E-02	2.590E-02	0.2000
89.269	0.1463	8.29E-02	3.119E-02	0.2408
97.754	0.1755	9.94E-02	3.739E-02	0.2888
106.392	0.2079	0.117721	4.430E-02	0.3420

*Complementary to table (5-8).

Percentage changes (PC) between initial and final mass profiles for base fall velocity show that for flight cases including FB604, FB605, FB612, and FB699, the dust is removed in high percentages for both dust transport towards the Canary Islands and across the Atlantic. PC are also calculated between initial and final mass under using minimum and maximum fall velocities, where ‘M1 and M2’ in these tables indicate the total mass of dust initial and final results. Where under based base fall velocity, mass profile percentages have values of 79.71 %, 83.93 %, 72 %, and 98 % between African land and Canary Islands, while over Puerto Rico, percentages are 89.75 %, 82.91 %, 30.96 %, and 93.4 %, respectively. These high percentage changes are expected since the final total mass column of dust across the Atlantic such as dusty FB604 is scaled by 0.5 based on SF, and thus total mass will be reduced significantly under this scaling factor. Although dust transporting time is much longer towards the Caribbean, the proportion of mass that survives the transport is similar since half the values are higher and lower for the two regions despite the Canary Island transport being much shorter. It shows that the losses are higher towards the Canary Islands and likely due to the larger subsidence.

Table 5- 9. Total mass of dust transported toward the north-west direction over Canary Islands during 4 days from the African coastline (spherical shape). The first row, for each flight number, is for a density of dust (ρ_d, 2.6 g/cm^3) and the second row is for ρ_d= 2.0 (g/cm^3). All values of final total mass include the scaling factor applied, relevant to each flight. Letter 'M' in this table refers to final total mass.

Flights	Initial total mass loading, (µg/m^2)	BRSedT final total mass, (µg/m^2)			ρ_d, (g/cm^3)	Percentage Changes %, $PC = \left(\frac{(M2 - M1)}{\lvert M1 \rvert}\right) x\ 100$		
		with w and with base v_t	with low v_t based on calc. from figure (5.2)	with large v_t based on calc. from figure (5.2)		col2 & col3	col 2 & col4	col 2 & col5
FB604	24616 18935	4714 3826	5638 4450	1120 961	2.6 2	80.8 79.8	77.0 76.5	95.5 94.9
FB605	26686 20528	4010 3298	4115 3365	2510 2104	2.6 2	85.0 83.9	84.6 83.6	90.6 89.8
FB612	7268 5590	1961 1560	2534 2139	836 743	2.6 2	73 72	65.1 61.7	88.5 86.7
FB699	631 485	7 6	8.6 7	3 1.1	2.6 2	98.8 98.7	98.6 98.5	99.7 99.7

Table 5- 10.Total mass of dust transported to Puerto Rico in the Caribbean during 6-7 days from the African coastline (spherical shape regime). Same densities as in the previous table. All values of final total mass include the scaling factor applied, relevant to each flight. Letter 'M' in this table refers to final total mass.

Flights	Initial total mass loading, (μg/m^2)	BRSedT final total mass, (μg/m^2)			ρ_d, (g/cm^3)	Percentage Changes %, $PC = \left(\frac{(M2 - M1)}{\lvert M1 \rvert}\right) x\ 100$		
		with w and with base v_t	with low v_t based on calc. from figure (5.2)	with large v_t based on calc. from figure (5.2)		col2 & col3	col2 & col4	col2 & col5
FB604	24616 18935	2415 1939	3667 2856	238 190	2.6 2	90.2 89.8	85.1 84.9	99.0 98.9
FB605	26686 20528	3985 3508	5183 4148	1492 1309	2.6 2	85.1 82.9	80.6 79.8	94.4 93.6
FB612	7268 5590	4159 3859	4366 3639	485 398	2.6 2	42.8 31.0	39.9 34.9	93.3 92.9
FB699	631 485	35 32	30 30	30.4 30	2.6 2	94.5 93.4	95.2 93.8	95.2 93.8

5.5 Estimating the transport of dust outbreaks to the Caribbean using BRSedT

In this section, the evolution of dust profiles over the dusty marine environment using BRSedT including sedimentation, large-scale subsidence, advection and turbulent mixing are presented. The focus is now on modelling the dust altitudes in the Caribbean so all simulations will be for the 7day period now and using the inputs into the BRSedT relevant for the transport west across the Atlantic.

5.5.1 Setting up the vertical turbulent diffusion for transport to the Caribbean

To establish the simulations, dust number concentrations from the FENNEC observations over the African land were used as initial data profiles in the BRSedT model. The procedure of simulating dust mass with turbulent diffusion impacts included was used for four flights,

including FB604, FB605, FB612, and FB699. For simulating sub-grid turbulent mixing impact on the results, the most challenging issue that controls the vertical extent of turbulent mixing is the depth of BL height in the atmosphere from the surface over land and ocean (Jeričević et al., 2009). In addition, the sensible heat flux (W/m^2) and surface turbulent momentum flux (W/m^2) are also needed to be specified in the simulation. It is known that the depth of the BL height (H) varies with time. Therefore, it will be necessary to determine H with time to provide a good evaluation of turbulent diffusion impacts on the evolution of dust transport over the Atlantic. In the BRSedT model, the values of BL height, surface heat and turbulent momentum fluxes and wind profiles were obtained from ECMWF data reanalysis. Based on these, the vertical profiles of turbulent diffusion coefficient were computed every 3 hours of time as the air advected for 4 and 7 days associated with specified grid boxes shown in figure (5.6), shown earlier. Changes in size distributions of dust profiles under turbulent mixing influence together with vertical values of k_z will be presented in the next section.

5.5.2 Estimating dust vertical size distributions transported to the Caribbean

The vertical changes of dust size distributions during transport across the Atlantic for flight FB604 and FB605 are shown in figures (5.24) and (5.25). The figure presents the size distribution (in unit of $1/\mu m\ cm^3$) of dust with changes in diameter (μm) over 7 days as the dust crosses the Atlantic. Seven height levels are selected in these plots, including 0.5, 1.5, 2.5, 3.5, 4.5, 5.5, and 6.5 km.

The figures (5.24) and (5.25), I note that the size distributions shape is similar at most levels but decreased in magnitude. Only at the 6.5 km height and above does the size distribution significantly change shape with size and it especially affects the larger sizes. This is due to the lack of particles of larger sizes falling into the layer since it is at the highest level. For the other layers, generally the shape is preserved.

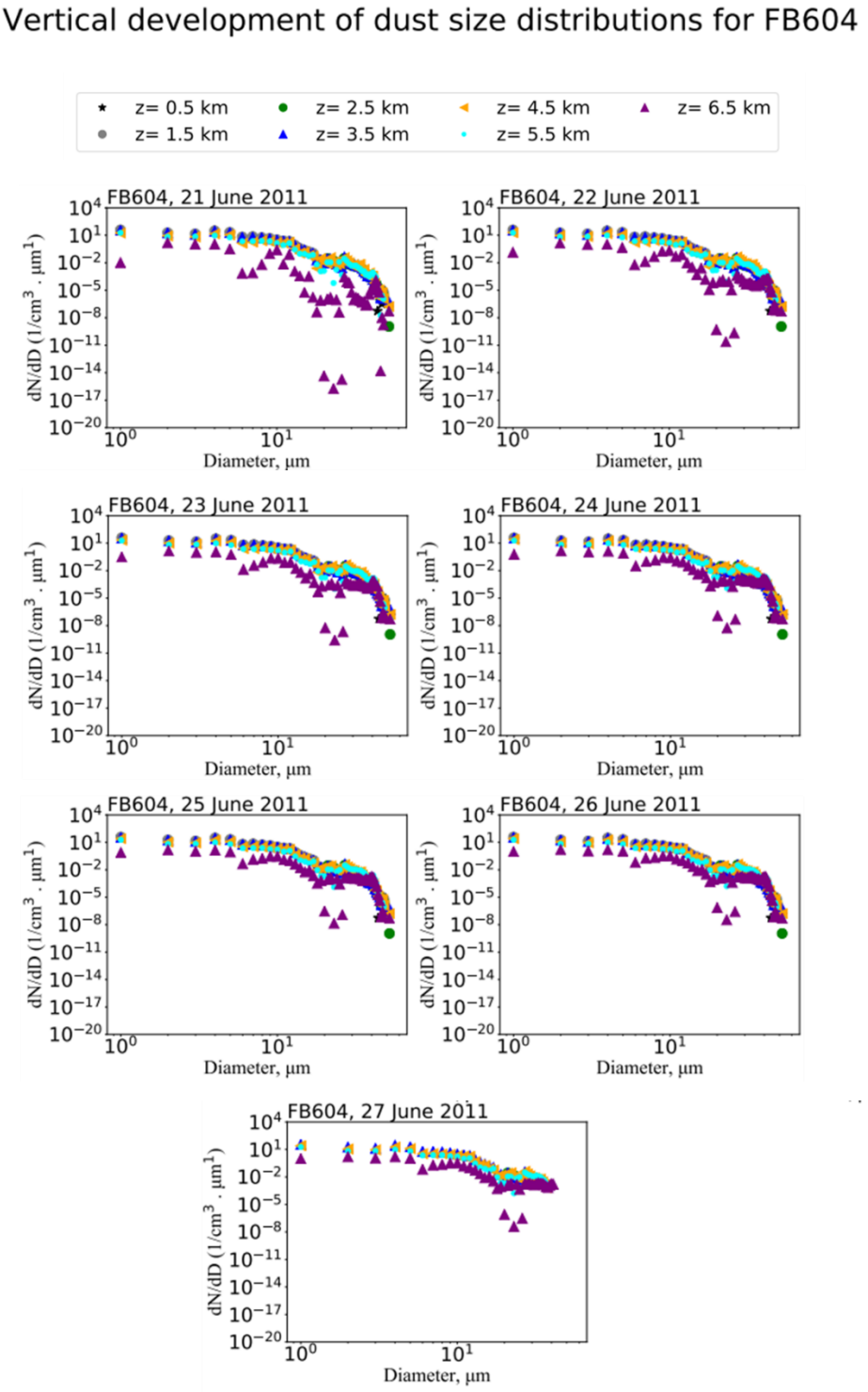

Figure 5. 24. Vertical number distribution (1/cm^3 µm) of dust particles simulated by BRSedT with selected heights of 0.5, 1.5, 2.5, 3.5, 4.5, 5.5, and 6.5 km. Dust number distributions indicate the full vertical profiles for flight FB604, showing after 7 days transport across the Atlantic. The x-axis indicates the diameter of dust particles in units of µm.

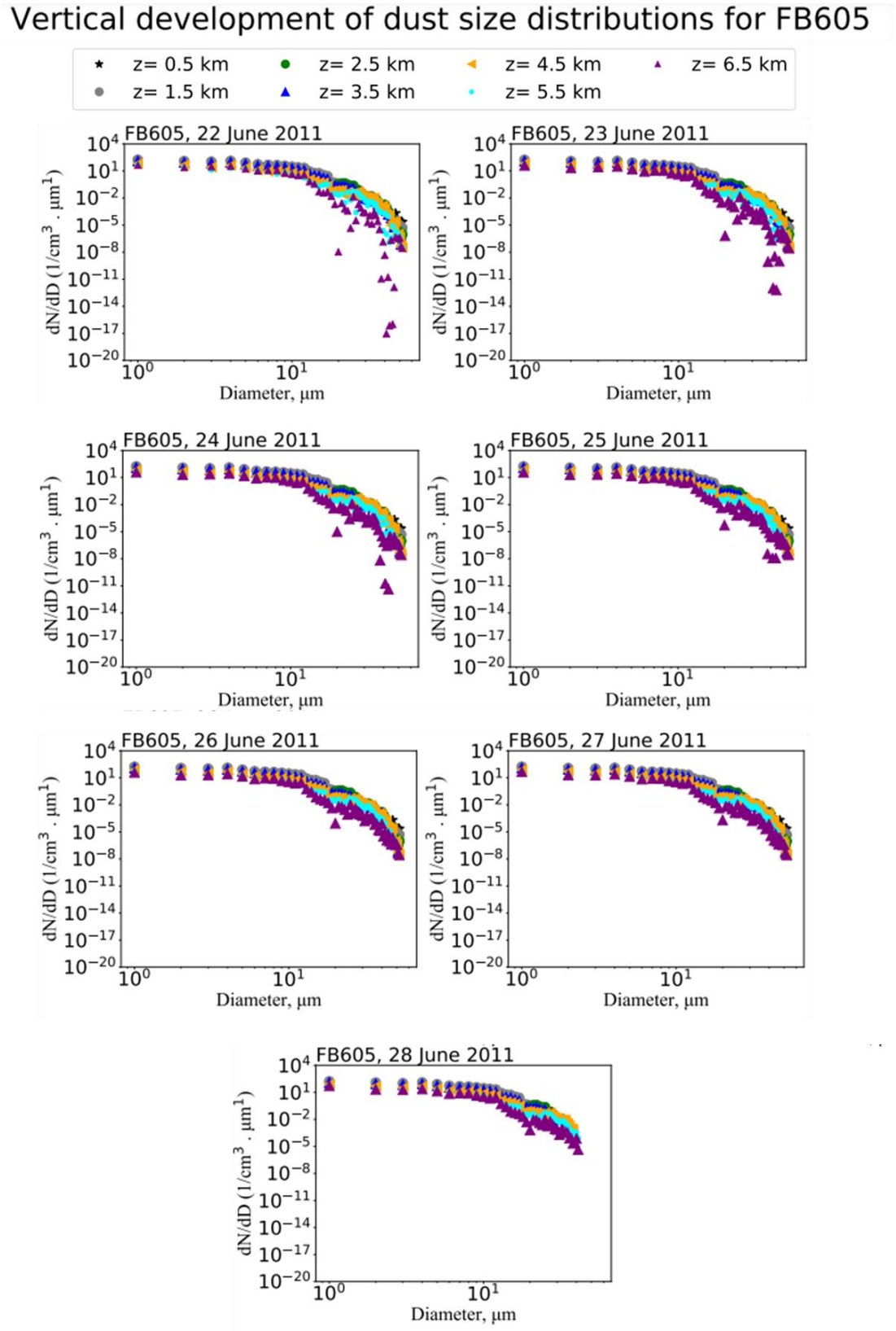

Figure 5. 25. As figure (5.24), but for flight FB605. The vertical number distributions of FB605 are simulated by BRSedT.

5.5.3 Estimating the dust mass profile changes during transport to the Caribbean

The purpose of this section is to evaluate the impact of the sedimentation process, large-scale velocity (subsidence) and turbulent mixing on the vertical mass changes of dust as the dusty air transports into the marine environment. So, I did two runs using the BRSedT model, firstly, with using all these processes (i.e. sedimentation, large-scale and turbulent mixing impacts) and secondly, with turbulent mixing effect, but without including other factors such as the sedimentation and large-scale subsidence influences. Beginning with flight FB604, implemented over the African land, figure (5.26) presents the vertical profiles of calculated diffusion coefficient, k_z, based on the local-scheme turbulent diffusion over 7 days across the Atlantic. Note, the scale on the x-axis in the first two plots (top left panels) in the figure (5.26) is different due to high values of k_z. The diffusion coefficient profiles are calculated every 3 hours to provide a good background of profile changes over the transport period. For simplicity, I will show diffusion coefficient profiles at three selected times, but the values of turbulent diffusion at other times have similar profiles to the presented profile shown here, and thus I will not show profiles of all times in the figures. It is clearly seen that k_z is characterised by a maximum magnitude at about 1 km in height during daytime with a value of about 100 m^2/s. Then during the night-time, high, k_z are present with an altitude up to 3 km, but the depth of turbulent diffusion is noticeably smaller over the ocean than land. Turbulence in general will mix layers and the strength of the mixing will depend on the k_z value. If dust is high at one level and low at another then the turbulent mixing will cause the dust from the high region to exchange with the lower dust altitude region. This mechanism will cause an equalising of dust at altitudes in neighbouring layers if the mixing is strong enough or left long enough. Near the surface and below the pressure height of 950 mb, dust mass increases, since the diffusion is large at this location from above but very weak near the surface.

The vertical variability of dust mass loading can be investigated by considering the impact of turbulent diffusion, sedimentation and large-scale velocity individually in the BRSedT model. Figure (5.27) shows the dust mass profiles in unit of $\mu g/m^3$ for the case FB604 with the presence of both turbulent mixing effect and other factors such as fall velocity and subsidence, while figure (5.28) shows the dust profiles in the presence of turbulent mixing impact only. The solid lines show the initial mass profiles based on the observations, while the dashed lines show the results of the BRSedT simulations of dust mass profiles over 7 days of transport.

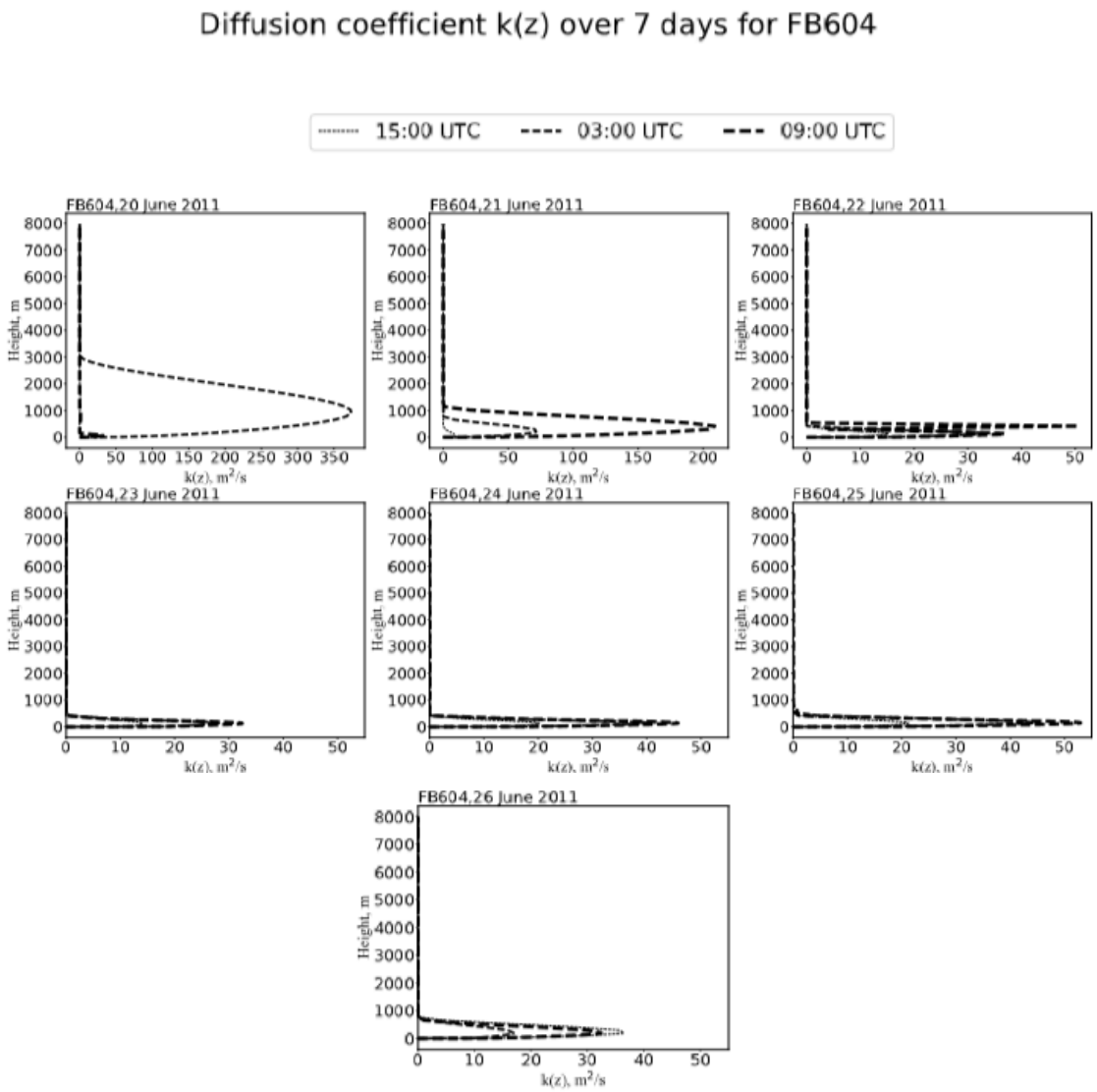

Figure 5. 26. Calculated vertical turbulent diffusion coefficient profiles (kz, m^2/s) at three different selected times; 1500, 0300 and 0900 UTC over 7 days across the Atlantic. Turbulent diffusion coefficients are calculated based on local-diffusive scheme from Holtslag and Boville, (1993) and Jeričević et al. (2009).

In the presence of all factors, dust mass profiles are influenced by competing factors between fall velocity, turbulence and large-scale velocity. For instance, based on the net effect of subsidence (i.e. Eq. 52) on the dust transport, see figure (5.26), the dust mass increases at the height of about 6 km as dust arrives across the Atlantic after 3 days. This is caused by the net effect of the large-scale ascending atmosphere, since small particles have low fall velocity at this height. Therefore, the sign of the vertical velocity is dependent on the value of w, which is positive in magnitude, see previous figure (5.7). Below this height, the importance of sedimentation and large-scale velocity is significant. Where the negative impact of net subsidence provides a

downward impact on the mass of dust loading down to level 800 hPa (about 2 km) along the dust transportation over the 7 days. In contrast, the turbulent diffusion impact can be observed by comparing the two panels in this figure. Turbulent diffusion contributes to reducing the dust profiles at the lower atmosphere, where dust particles at or below 400 m are lost to the ocean surface. In the figures that follow, including figures (5.26) through to (5.39) there are plots showing the dust mass concentrations with sedimentation, subsidence and turbulence effects as well as just turbulence effects. By evaluating the initial and final dust mass concentrations, it can be seen that the sedimentation and subsidence take a lead role in determining the main amounts of dust in the atmosphere throughout most of the vertical except for near the surface where the turbulent diffusion coefficient is largest and the losses to the surface are increased. The significant finding here is that both turbulence, sedimentation and subsidence contribute to determining the mass profile of dust over the Atlantic, but the atmosphere is vertically structure is most impacted by the sedimentation processes and subsidence effects.

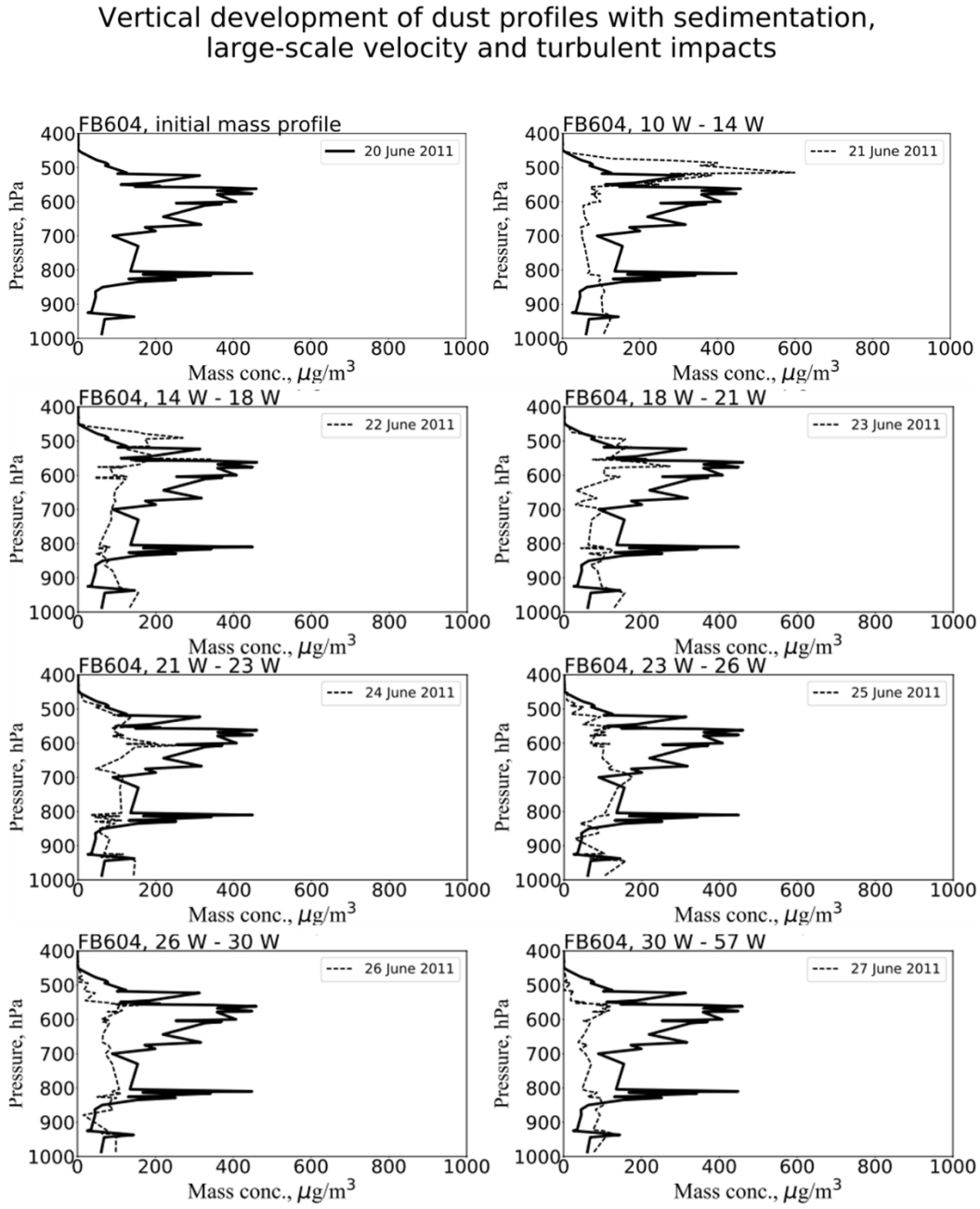

Figure 5. 27. Dust mass concentrations (μg/m^3) calculated from the BRSedT model over 7 days across the Atlantic for case FB604. Solid lines indicate the initial profiles of dust mass over the African land, whereas dashed lines show the evolution of the mass in the model associated with sedimentation, large-scale process and turbulent diffusion impact. All panels indicate results with including all processes active. The plots from top left to bottom right specify the results from the African land to Caribbean.

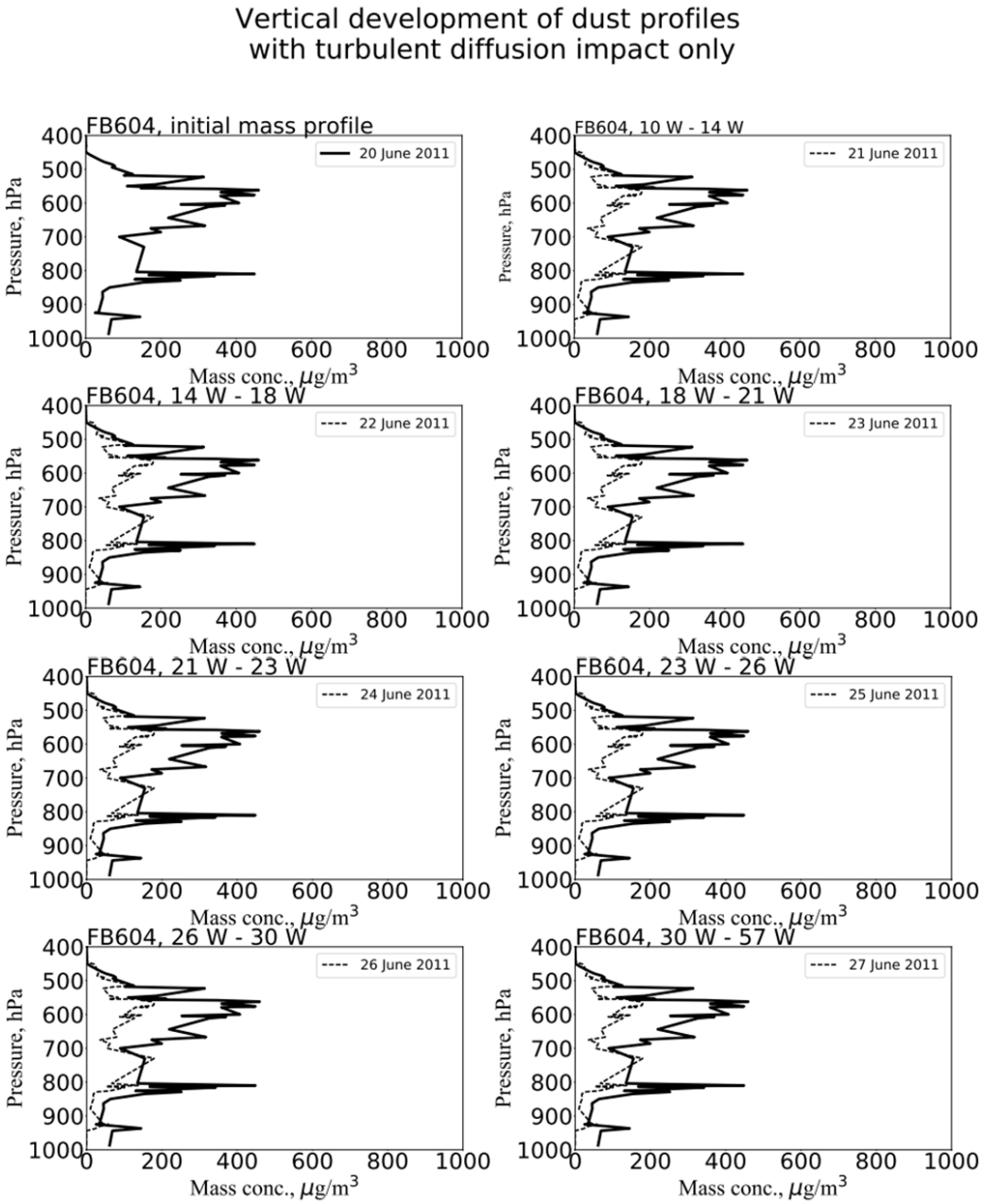

Figure 5. 28. As figure (5.27), but for turbulent diffusion effects only.

Similarly, figure (5.29) shows the diffusion coefficients for flight case FB605, while figures (5.30) and (5.31) present the development of the dust mass profiles across the Atlantic. In the flight case FB605, the impact of turbulent mixing is likely to be less than the results for flight FB604. The reason for this is probably related to the vertical structure of dust mass loading. The vertical flux depends on the vertical gradients of dust mass and the magnitude of the turbulent diffusion coefficient, see Eq. 52. So, if the change in dust mass between two different levels and turbulent diffusion coefficient are large then the vertical flux is increased. For instance, the dust profile has more multiple peaks (i.e. significant change in the dust with height) within the structure

of flight FB605 compared to FB604, where the FB605 tends to have less peaks in the vertical, except for level 900 hPa. Correspondingly, the turbulent diffusion will make the mass profile diffuse from the level that has high mass to level with less mass. In contrast, the diffusion will be less significant for FB605 where the vertical gradients are less. However, dust mass profiles again can be kept at the top of dust layer by diffusion effects, while sedimentation and large-scale subsidence can make the mass profiles more uniform in the vertical for long distances over the Atlantic.

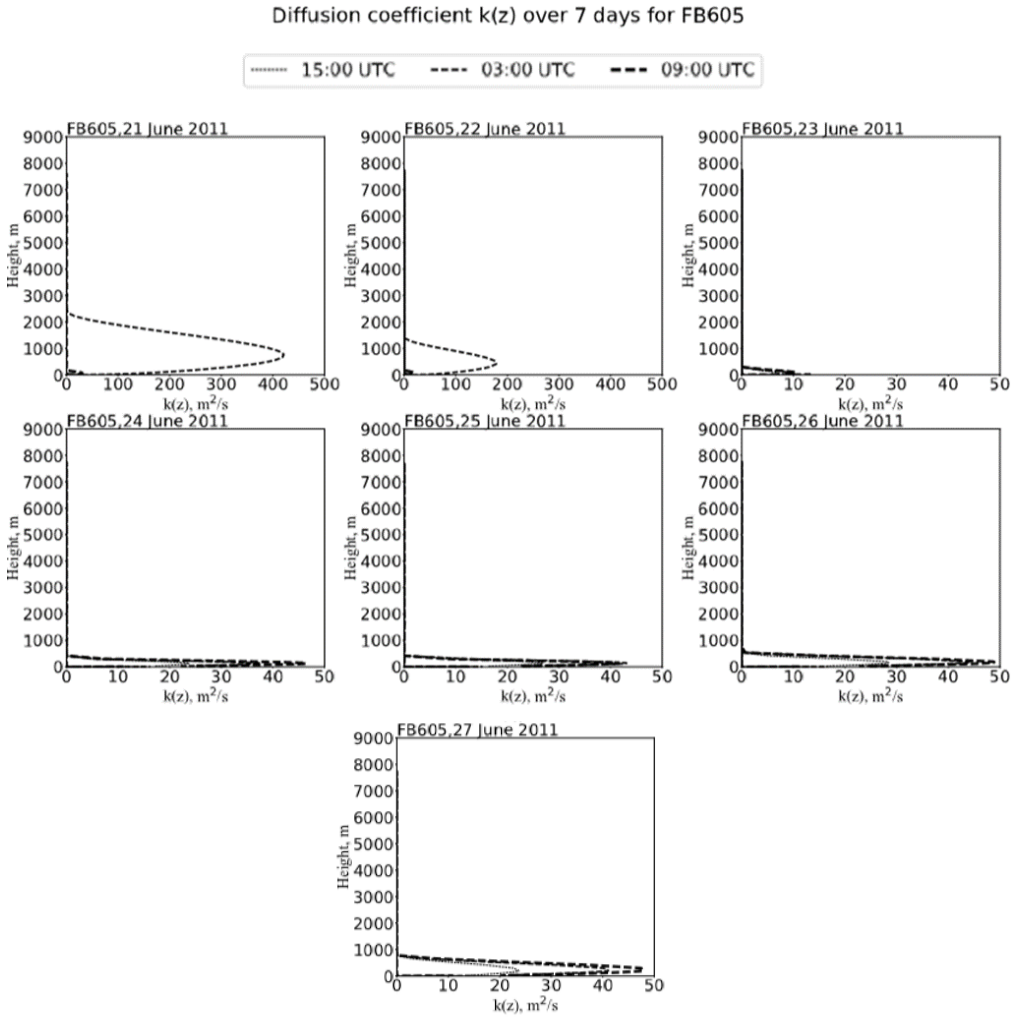

Figure 5. 29. As figure (5.26), but for flight FB605.

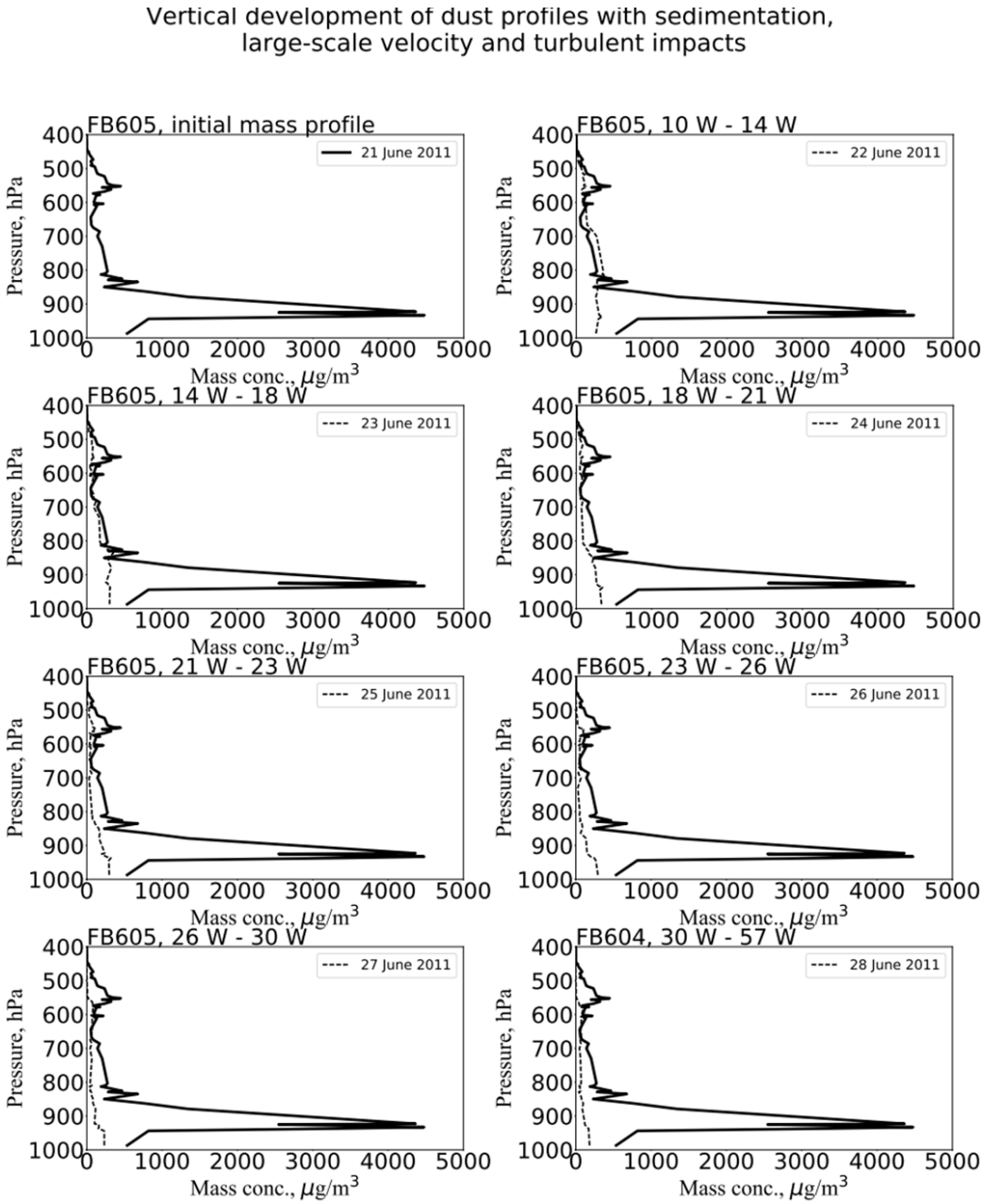

Figure 5. 30. As figure (5.27), but for flight FB605.

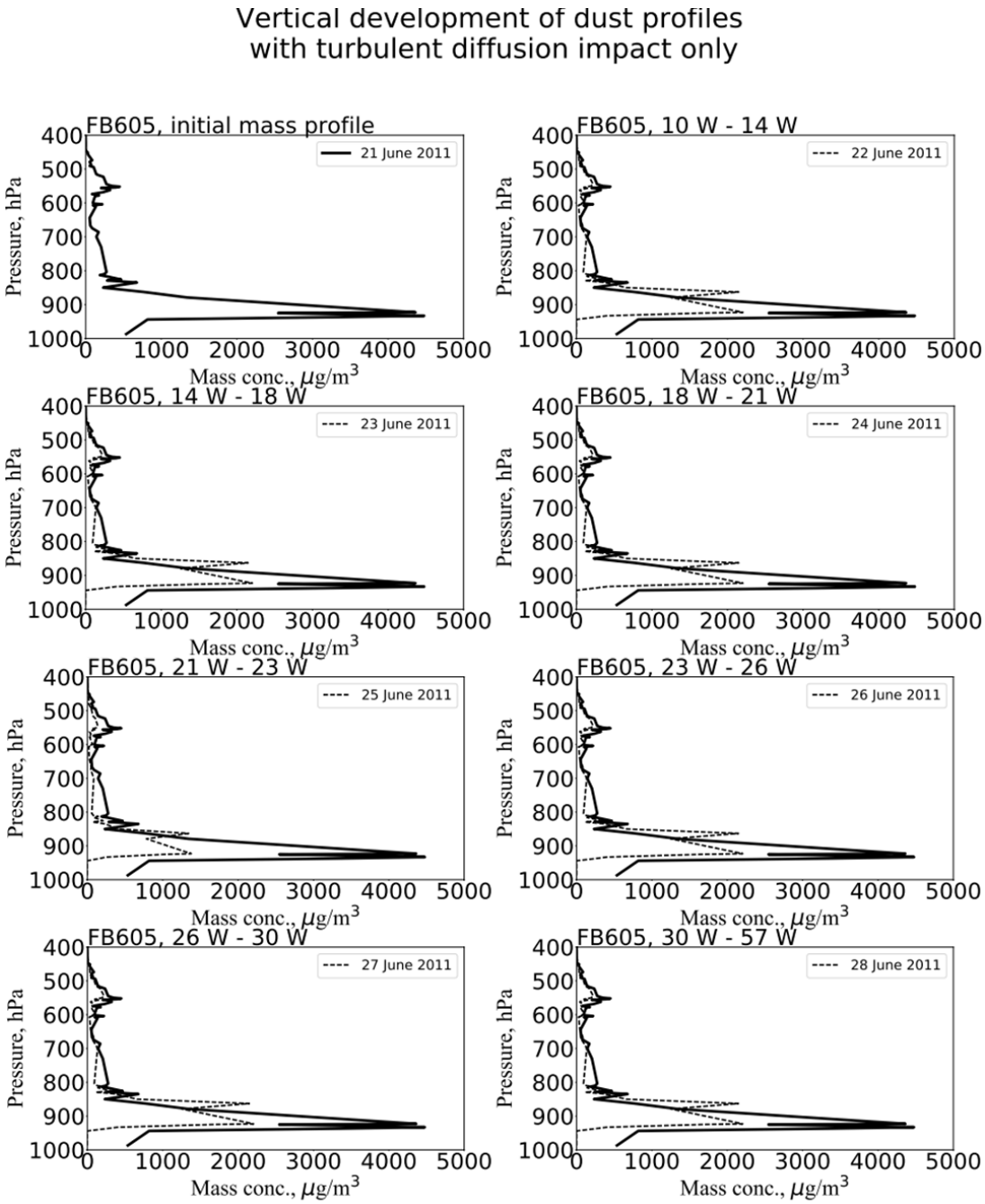

Figure 5. 31. As figure (5.28), but for flight FB605.

For flight FB612, results are presented in figure (5.32) of the profile of diffusion coefficients across the Atlantic. The interesting point here is that the mass loading of dust profile significantly decreases after the third day of dust transport across the Atlantic, while at distances near the African coastline the mass profile is slightly reduced. The results of dust loading across the Atlantic are shown in figures (5.33) and (5.34). The high/low reduction in mass loading is generated by the high magnitude of subsidence in flight FB612 in comparison with flights FB604 and FB605, as shown in the previous figure (5.8).

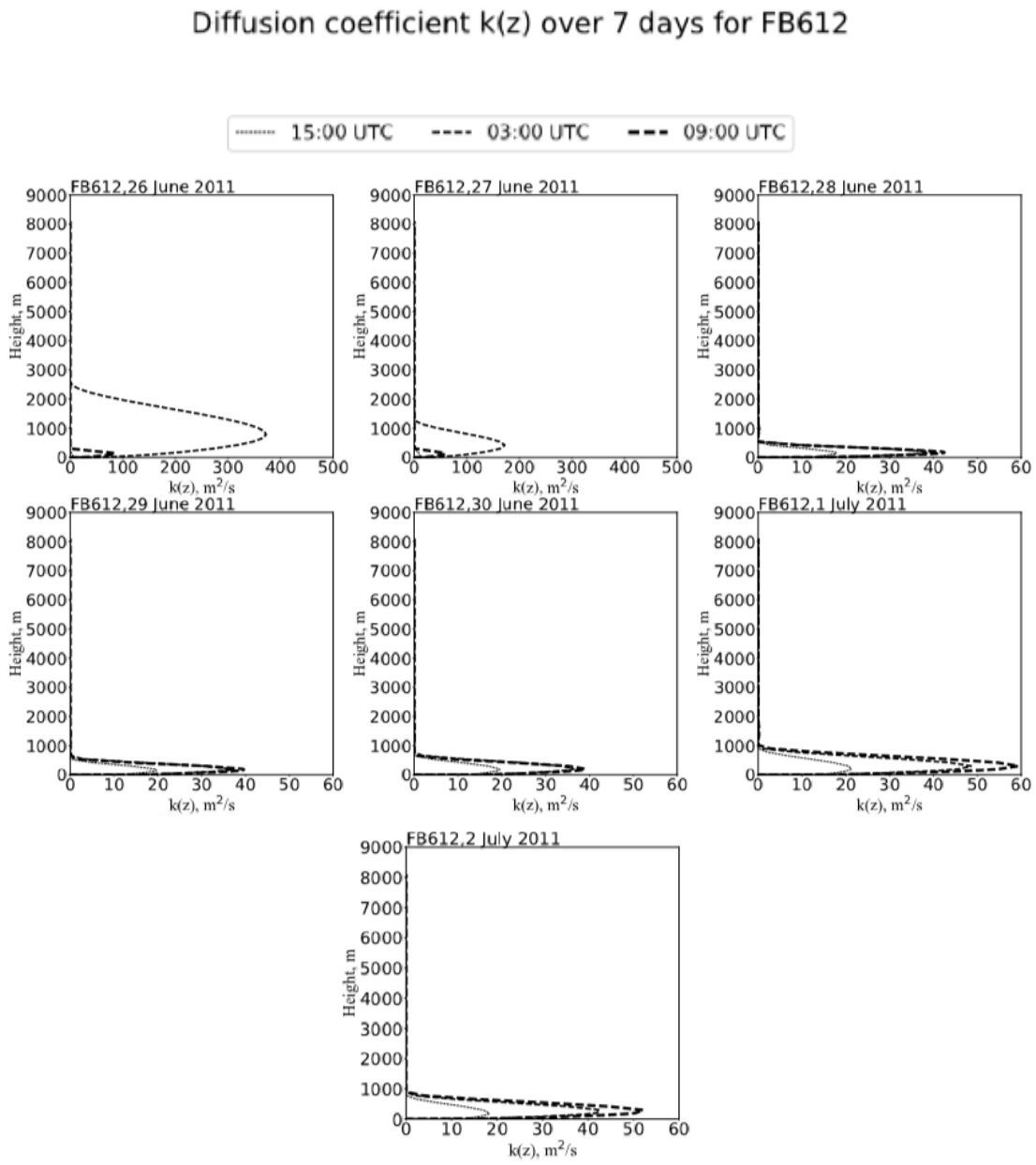

Figure 5. 32. As figure (5.29), but for flight FB612.

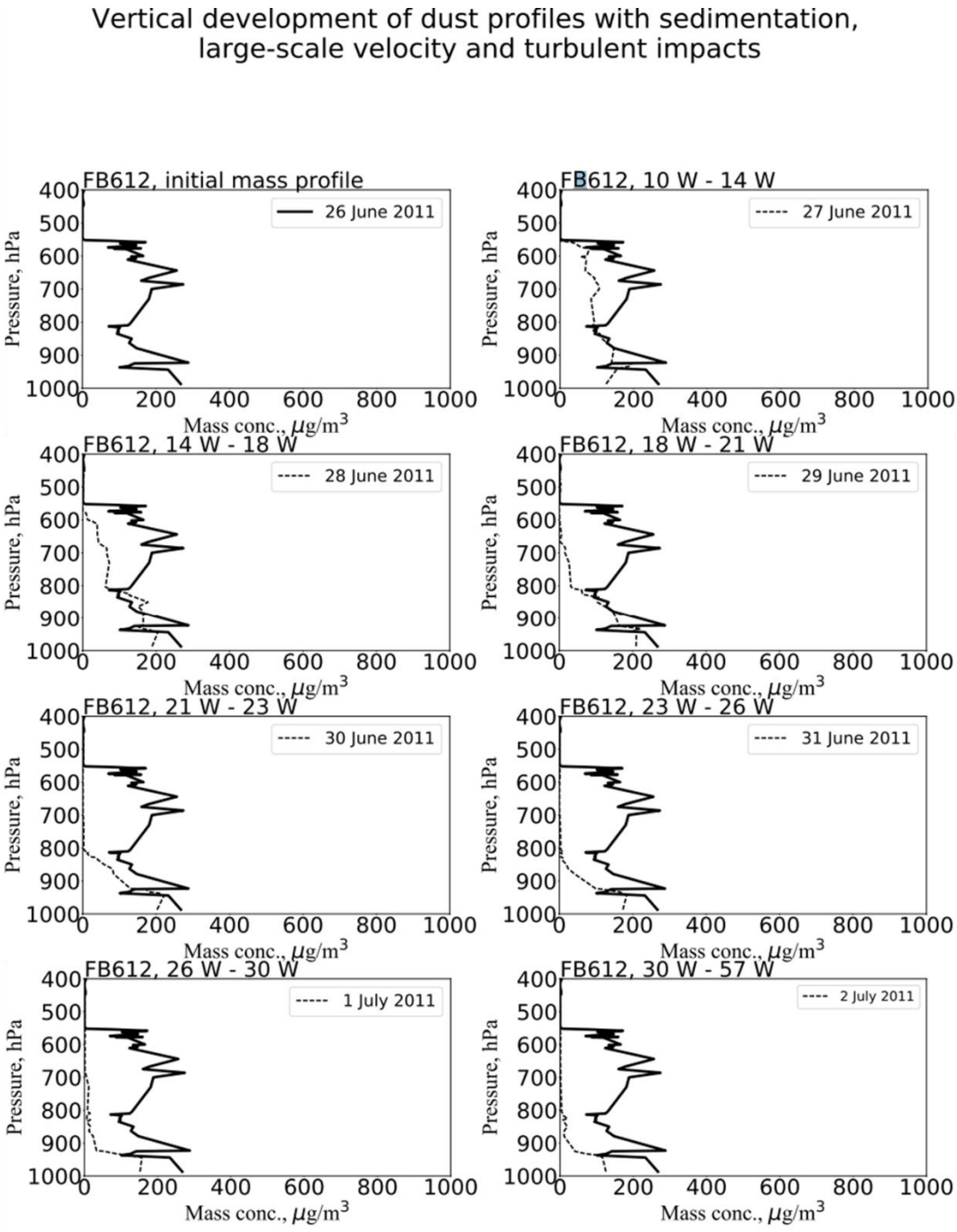

Figure 5. 33. As figure (5.30), but for flight FB612.

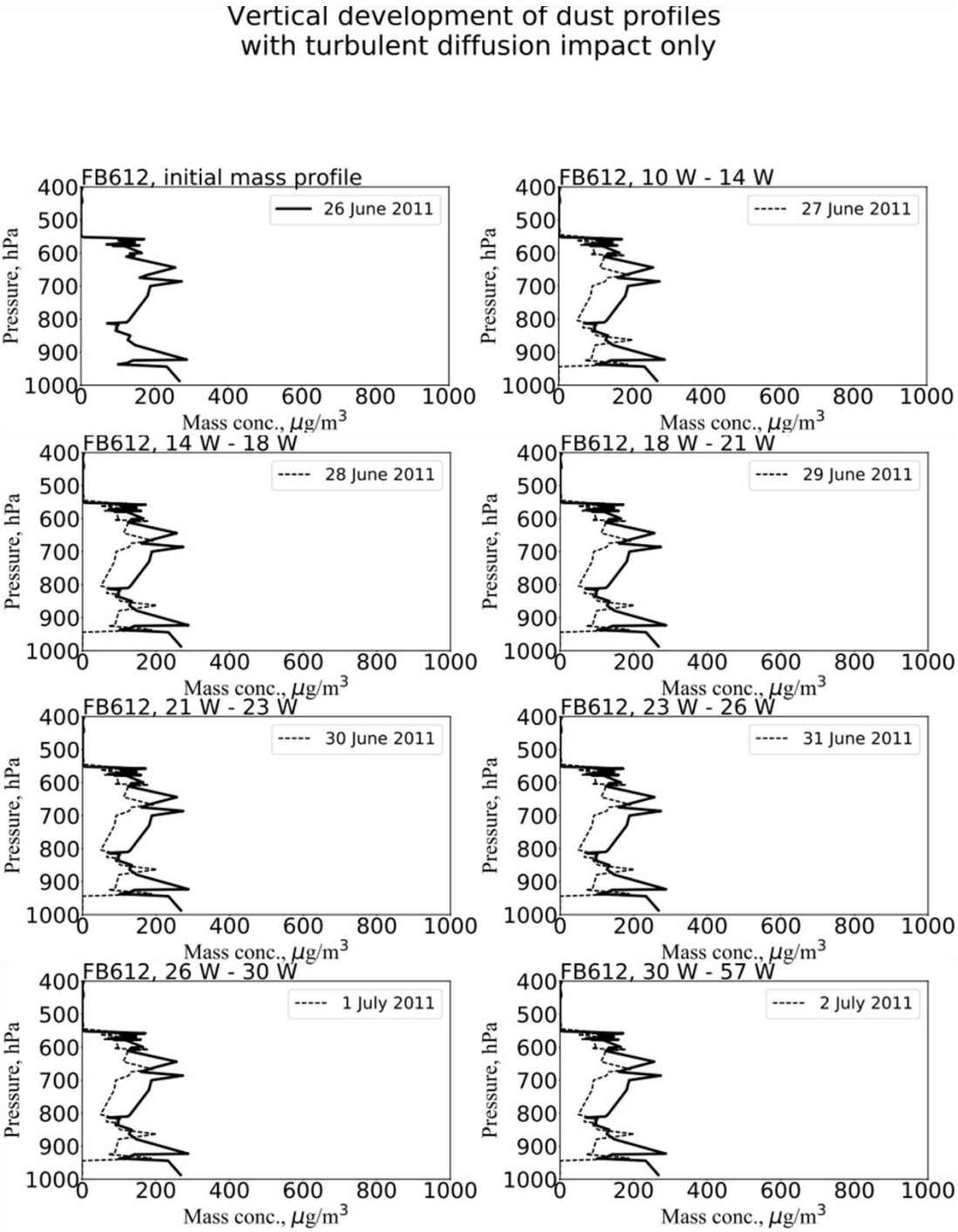

Figure 5. 34. As figure (5.31), but for flight FB612.

By contrast, in the low dust case FB699, the turbulent diffusion shown in figure (5.35) is likely to have a significant impact on the vertical structure of dust mass loading in both BRSedT model runs since the turbulent diffusion has less of a vertical extent but it still shows similar behaviour near the surface. At the top of the dusty layer, the net effect between large-scale vertical velocity and calculated fall velocity based on the previous Eq. (51) is a key factor on determining the change of dust profiles across the Atlantic. This can be seen between figure (5.36) and previous

figure (5.27) for flight case FB604, where the dust profile over 5 days transport for FB699 between about 600 hPa and 500 hPa is much less than that for flight FB604 due to the large-scale vertical velocity associated with flight FB699 being lower than that for FB604, as seen in the large-scale subsidence previously shown in figures (5.7) and (5.8). The figures reveal that the turbulent diffusion effect can be important in influencing the structure of the dust mass profiles with/without other factors. Although the magnitude of turbulent diffusion is low within the SAL, however, the turbulent diffusion may contribute to redistributing the mass profile. Vertical gradients are also important for the turbulence to take effect and strong gradients exist near the SAL.

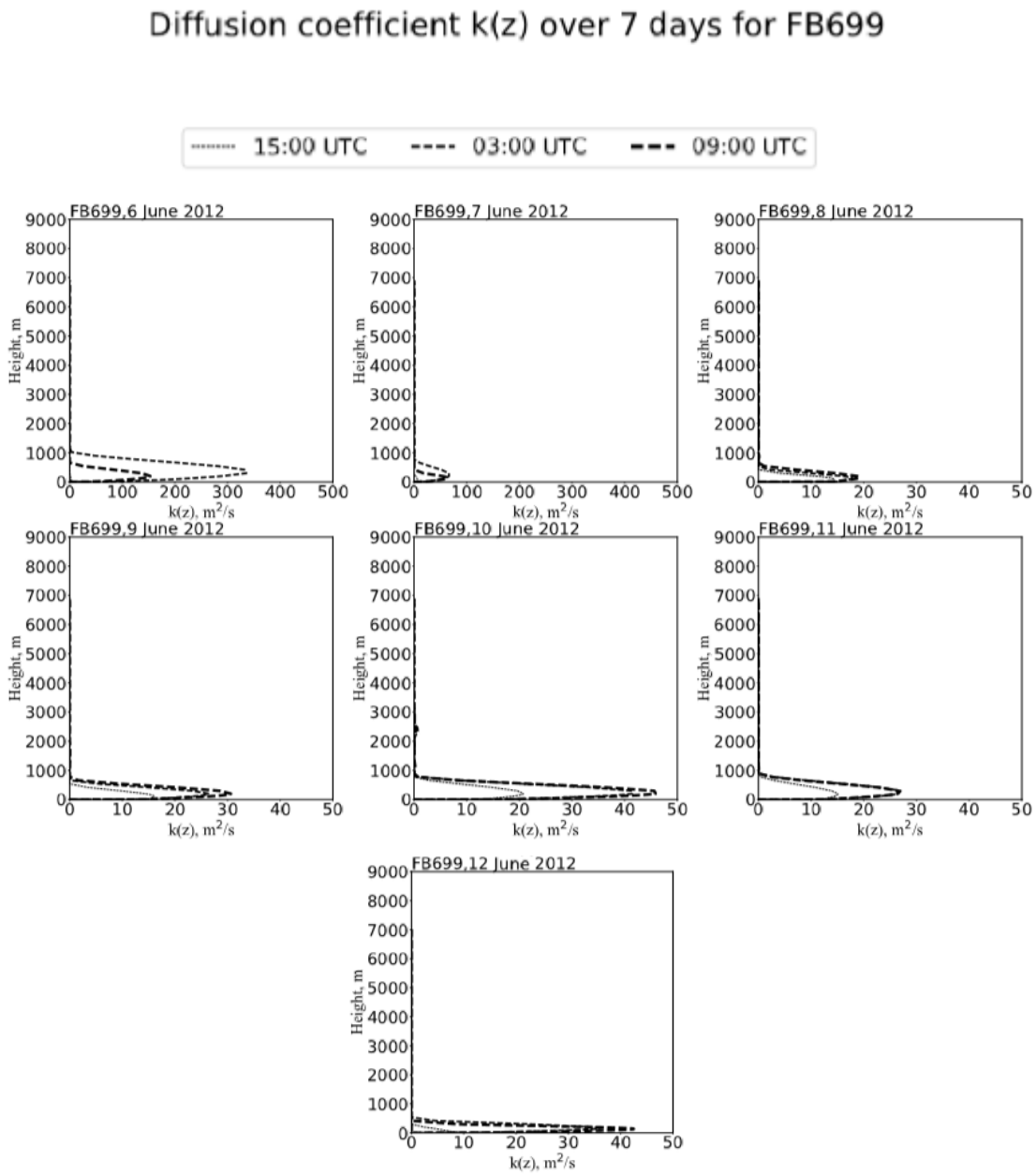

Figure 5. 35. As figure (5.32), but for flight FB699.

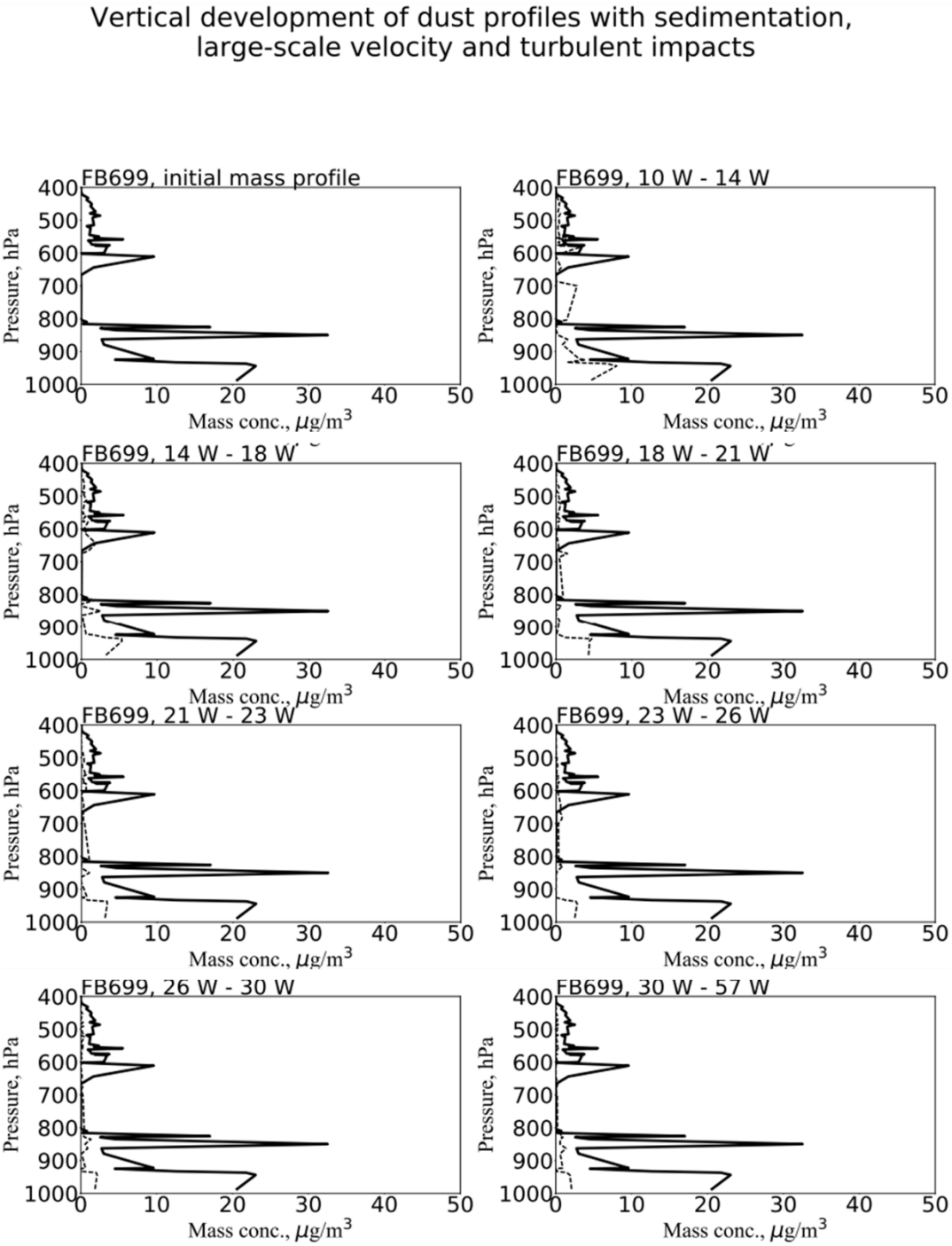

Figure 5. 36. As figure (5.33), but for flight FB699.

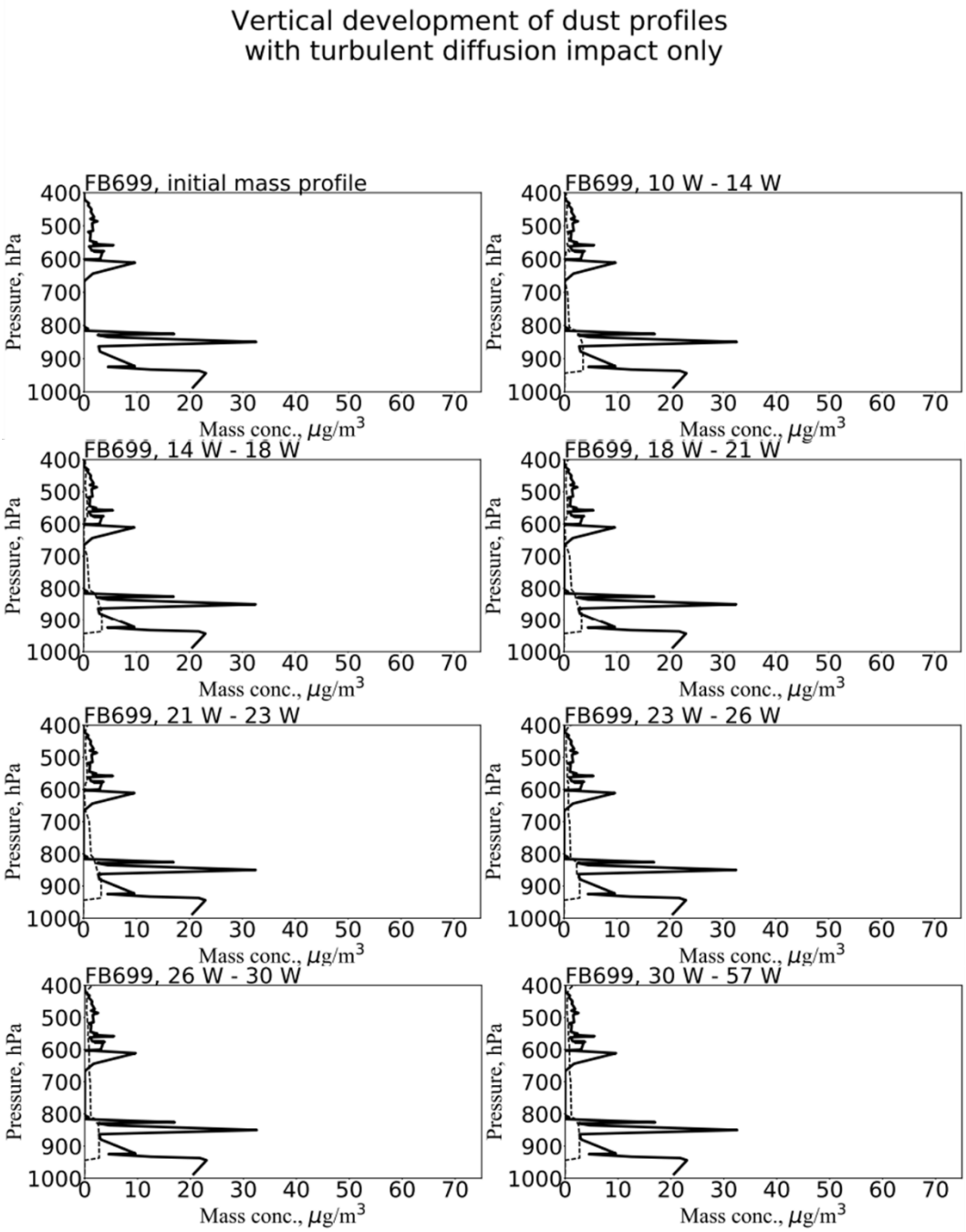

Figure 5. 37. As figure (5.34), but for FB699.

The second general direction of dust transport studied is towards the north-west passing over the Canary Islands (and then heading east afterwards). It is shown in a previous table (5-3) that significant portions of the dust that left from the north African land went toward the Canary Islands with values of 0.5, 0.6, 0.8, and 0.15 for SF in flight cases FB604, FB605, FB612, and FB699, respectively. I will show here the turbulent diffusion coefficient values and vertical development of dust mass over 4 days (toward Canary Islands) for flight cases FB604, FB605, and FB612; however, I will ignore flight case FB699 since the dust transported towards the north-

west direction in this flight and takes less than 4 days of transport time. In the main text here, I will show results for the standard dusty flight case FB604, while other cases including FB605 and FB612 are shown in the Appendix B2.

Turbulence results for the eastern subtropical Atlantic region is likely to be lower in magnitude than across the Atlantic (near tropical region). Figure (5.38) shows the vertical profile of turbulent diffusion coefficient calculated based on equations (53) - (65), while figures (5.39) and (5.40) depict the development of the dust vertical mass loading between the African land and the Canary Islands, respectively. I note that at the upper levels the high dust loadings tend to be driven by the large-scale vertical velocity which can be seen by the largest large scale updraft values of the cases for day 1 for FB604 in figure (5.7c).

The interesting finding here is that the dust mass profile toward the Canary Islands is significantly reduced over the few days of transport compared with long transport of dust profiles across the Atlantic, i.e. transport toward Puerto Rico. The reduction of dust mass profiles is affected by the strong subsidence in this region. In addition to the thesis findings, I find here (by looking at all the figures of dust development across and towards the north-west of the Atlantic) that the profiles of dust mass loading are significantly decreased in the presence of sedimentation and subsidence effects, while turbulent mixing effects contributes to increase dust mass loading over the Atlantic, especially within SAL, and at the top of it. This is consistent with other works, such as Rittmeister et al. (2017), who states that the strength of dust falling between west Africa and the Caribbean regions is reduced in the SAL, while vertical mixing and vertical movement between the base and the top of dust layer are increased.

The results of the current thesis based on the BRSedT shows good agreement with modelling results of Schutz et al. (1981), in which for typical flight case FB604 and at about 1000 km from the coast, large particles are lost from the atmosphere over the Atlantic in the presence of sedimentation and large-scale subsidence, see previous figure (5.27). Whereas small dust particles are affected by turbulent diffusion during dust transporting air towards the Caribbean region. However, in the other cases (i.e. FB605, FB612 and FB699), dust removal in the atmosphere occurs between 2000 and 3000 km, but how long it takes for dust particles to be removed from the atmosphere is mainly dependent on the net velocity between the fall velocity and the subsidence.

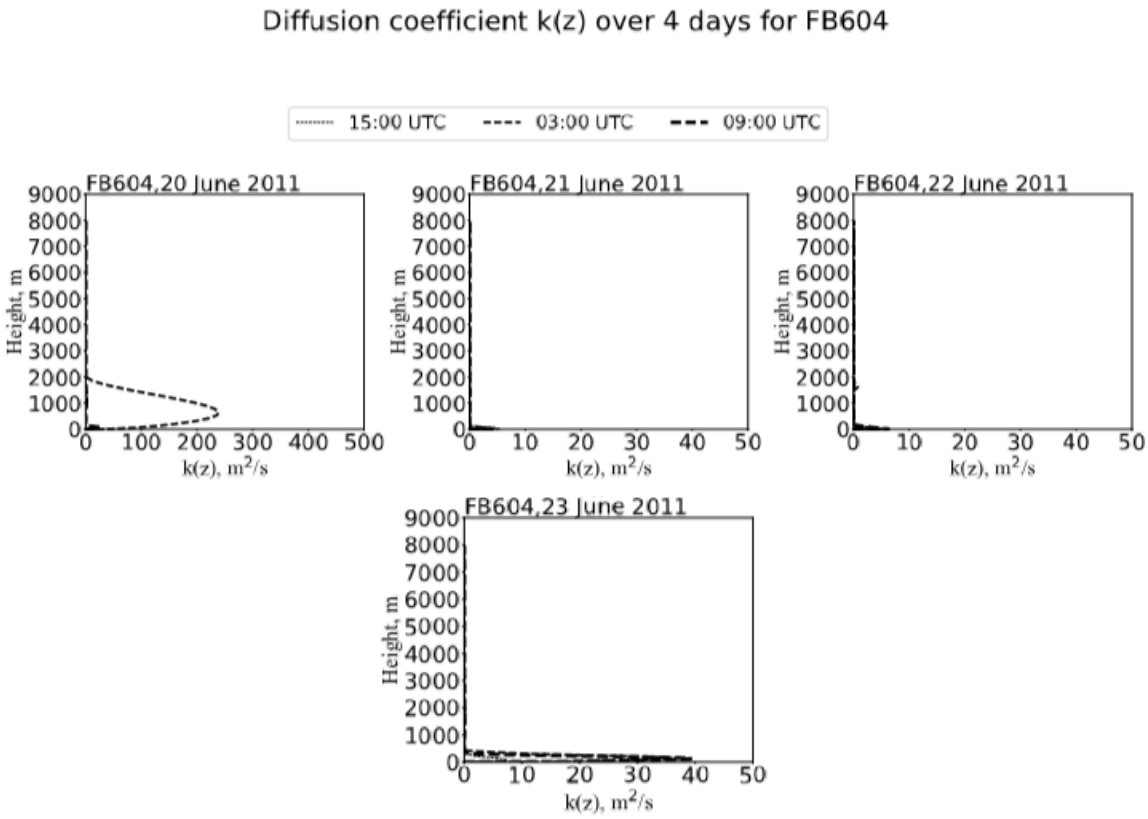

Figure 5. 38. Diffusion coefficient profiles for dust transports over 4 days toward north-west direction and for flight FB604.

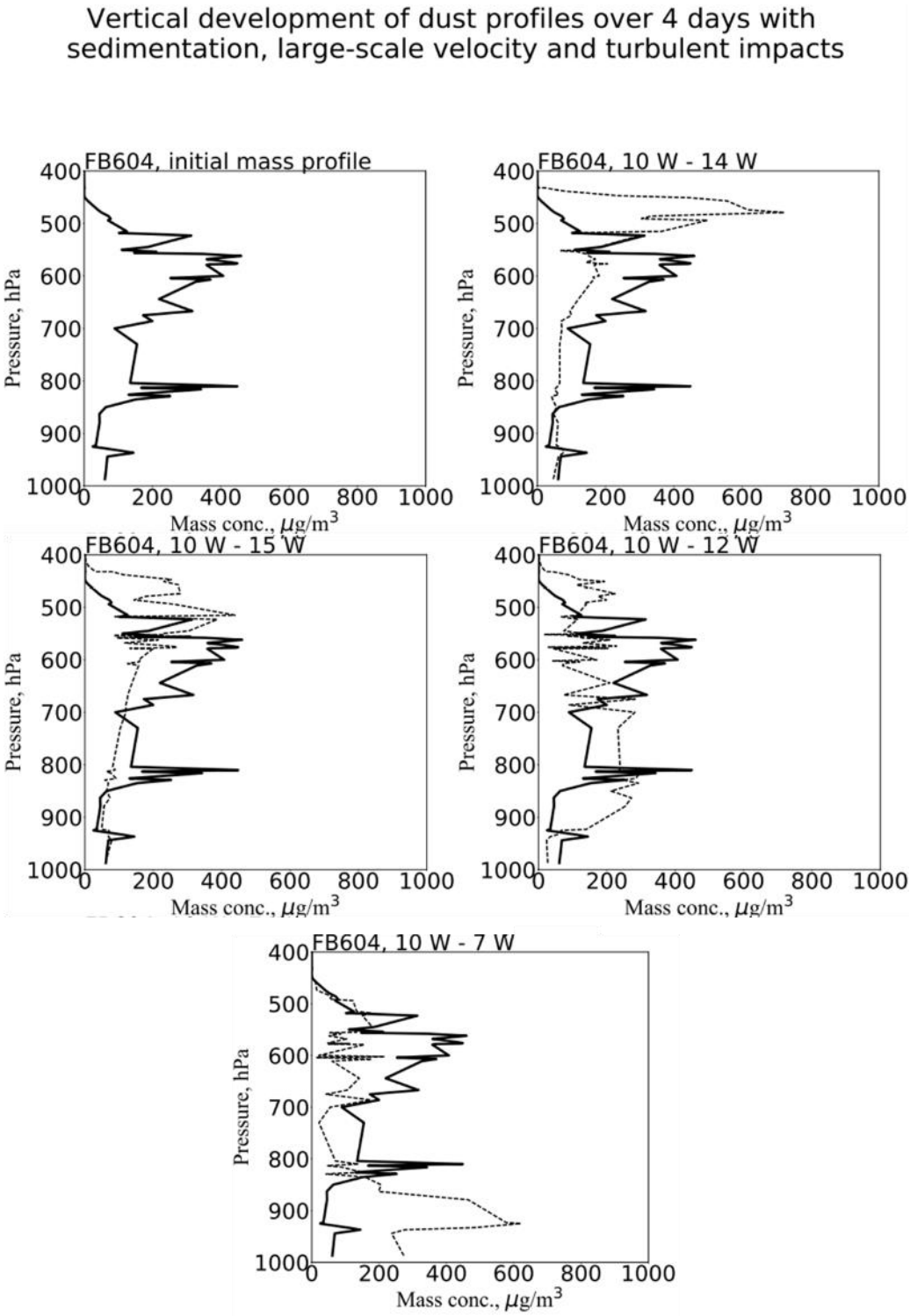

Figure 5. 39. Dust mass concentrations (μg/m^3) calculated from the BRSedT model over 4 days towards north-west direction and for case FB604. Solid lines indicate the initial profiles of dust mass over the African land, whereas dashed lines show the evolution of the mass in the model associated with sedimentation, large-scale process and turbulent diffusion impact. The plots indicate results with including all processes active. The panels from top left to bottom right specify the results from the African land to north-west region (i.e. Canary Islands).

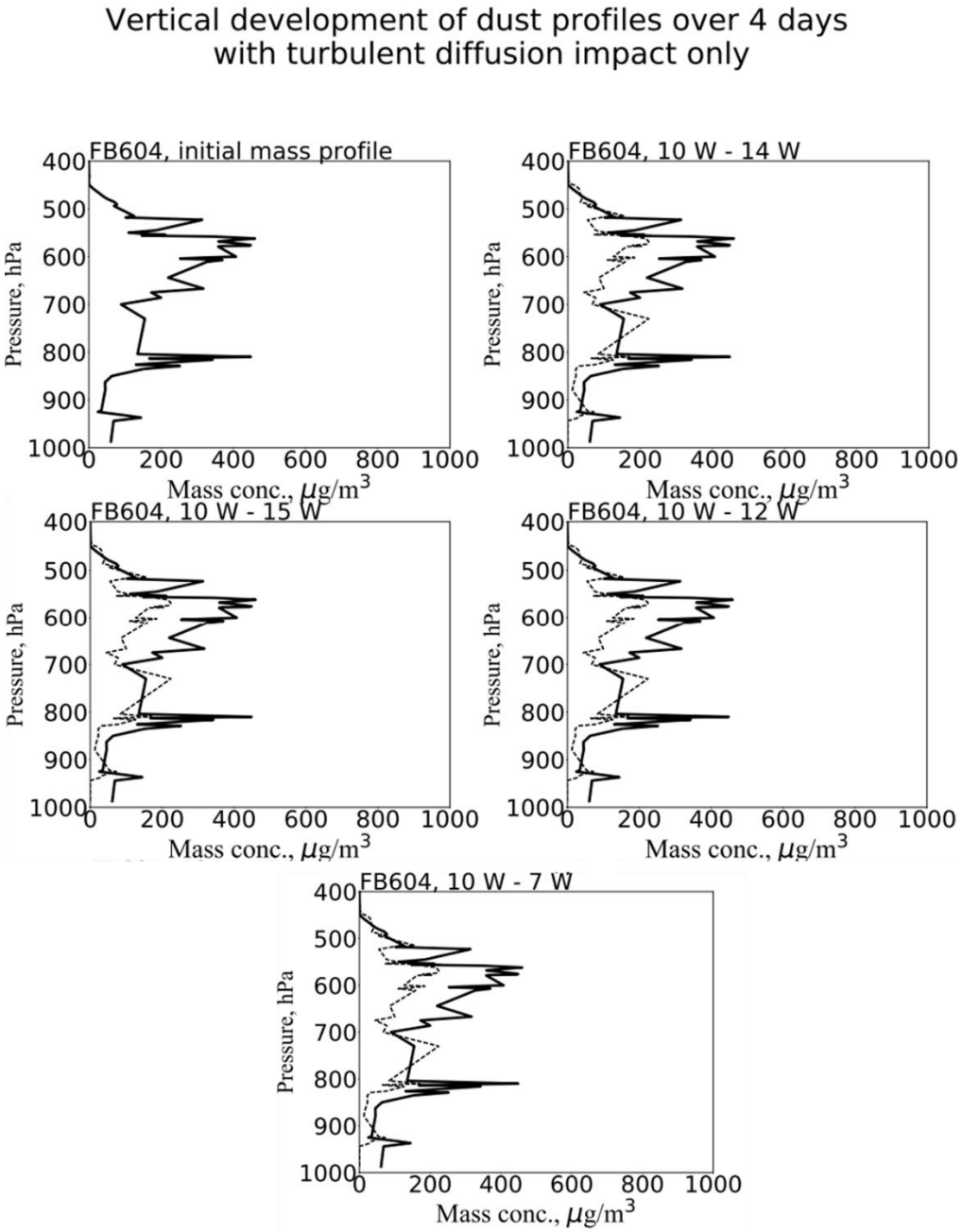

Figure 5. 40. As figure (5.39), but for diffusion turbulent effect only.

From the plots, it is evident that the turbulence performs a very different role compared to the subsidence and sedimentation. The turbulence effects on dust tends to be limited to within regions where the stability is not to stable and there is little mixing across stable layers as expected. The sedimentation tends to move dust across these stable regions so the different processes all have their roles. In some cases, there are high values above the observed in height and this appears to the result of large-scale vertical velocities that may not perfectly align with the observed as they are derived from large scale models and will have uncertainty.

5.5.4 Aged optical properties: estimating dust optical property changes for SSA, K_{ext} and g

As dust transports over the Atlantic over long distances, the optical properties of dust particles, such as single scattering albedo (ω_0) can change. The optical properties were used in the radiation model provided from Ryder et al. (2013a) to obtain vertical heating rates of dust profiles ready to be used in the LEM. It will be interesting to estimate whether the optical properties of Saharan dust are changed or remain unchanged during Atlantic transport. This can be investigated between the Canary Islands and Caribbean by obtaining the dust heating rates from the ES radiation model with using two different optical properties, i.e. using dust optical properties for the SAL and aged dust separately. The aged state is defined by Ryder et al. (2013a) as being at least 12 hrs old but less than 70 hrs and over African land. The SAL were defined as further aged in which the dust has been transported over the Atlantic to the Canary Islands and is 18 hrs old or older. Ryder et al. (2013a) notes at 500 nm that the ω_0 increases from aged to SAL from 0.94 to 0.95 so more scattering as the larger particles' sediment out of the atmosphere (60-90 % of particles greater than 30 μm for aged and 100% for SAL). The asymmetry is decreased going from aged to SAL from 0.75 to 0.74 (less forward scatter because particles are smaller) and the specific extinction increases from 0.23 to 0.39 m^2/g (since per mass, smaller particle extract more radiation from the incident beam). I note that the evolution of the dust, modelled by the BRSedT model, was not used to evolve the optical properties during transport and the small change SSA of 0.01 is unlikely to properly represent the significance of the changes during transport across the Atlantic. These dust optical properties were provided from Ryder et al. (2013a), in which these optics are related to SW and LW radiation. For the SW, six wavelength bands and 9 bands for LW radiation. The spectral files of dust optical properties used in ES are shown in previous tables (2-3) and (2-4). The set-up of the ES radiation with this spectral file is a hybrid 6 bands as there are six band calculations but bands 2 and 3 are not independent bands and must be combined to represent that wavelength band (Manners, 2015).

Figure (5.41) shows the dust SW heating rates from the radiation results implemented with using FENNEC-dust observations and with using all gases including water vapour (water vapour profiles were taken from the ECMWF) over the Canary Islands (top plot), while dust final profiles from the BRSedT model were used in the radiation model with all gases for the Guadeloupe (bottom plot) region. Black lines show dust heating rates for the aged dust mode, while orange lines indicate the results for SAL optical properties. This figure shows that after dust is transported over the Atlantic, the difference in dust heating rates over the Canary Islands between SAL and aged dust optical properties can be significant at certain levels like 3 km where the difference in heating rate is 10 to 15% more for SAL and due in large part to the dust (for the same profile of

dust particles are used for the Canary Islands) but for the majority of heights it is very similar. Over the Caribbean, the dust altitudes are too low to have an impact or difference and the main profiles of heating rates are due to changes in water vapour or other gases. It seems that dust optical properties do not change too much going from aged over land to SAL aside from the extinction. Even so, the heating rates were typically 10-15% at most since much of the heating rates were due to the water vapour. So in general, as the dust particles age, they will scatter more in proportion to the amount of radiation that interacts with a particle, they will scatter less in the forward direction and they will interact with more of the incident radiation per unit mass of dust particle, but the SAL will lose more particles from the size distribution since it is transported for longer so this will counteract the increased extinction.

To compare with satellite observation, I collect daily-averaged data of $\omega_\circ$ and AOD from OMI/Aura Multi-wavelength satellite data for seven days across the Atlantic. The OMI/Aura produces multi-wavelength algorithms, where its pixel level products are binned into 0.25 x 0.25 degrees grids and provides observations associated with time between 00:00:00 and 23:59:59.9999 UTC each day. Table (5-11) shows $\omega_\circ$ and AOD for flights FB604, FB605, FB612, and FB699 taken from OMI/Aura observations associated with the transport time over the Atlantic for 7 days in the dust plume. Columns from 2 to 8 in the table present the values of these optical properties for grids from 1 to 7, respectively. Although the values of SSA from Ryder et al. (2013a) are not quite the same to these observed in table (5-11), however, it is a comparable way to be considered here, since SSA from satellite observation for some flight cases, such as FB605 and FB612 are similar to that used in the radiation model, where these flights are represented as dusty cases. Table (5-11) shows that $\omega_\circ$ is slightly increased during transport days associated with the flight numbers FB604 and FB605, which are represented as intensive dusty days, and it is slightly changed over the days of transport. These changes in $\omega_\circ$ are understandable in which scattering processes become more significant as the larger particles fall out of the air mass over time, and thus the ratio of scattering to the total of scattering (i.e. scattering and absorption) is slightly increased. So, in this regime, the optical properties of dust transported over time are likely to have change slightly.

Neither the calculations nor the observations for $\omega_\circ$ are in perfect agreement. There are a several possible reasons including that the $\omega_\circ$ from OMI/Aura observations indicates average values for multi-wavelengths compare to the spectrally derived values of $\omega_\circ$ input into the radiation model. The values of SSA from OMI observations are significantly lower than values used from flight observations. This provides lower scattering in a comparison with SSA based on aircraft observations, and thus the OMI SSA would result in a higher fraction of absorption to scattering during dust transported across the Atlantic. In addition, away from the African coastline, sea salt aerosol may contribute to increase $\omega_\circ$ in the satellite observations due to reflection process by sea salt particles as the dust above it becomes less optically significant.

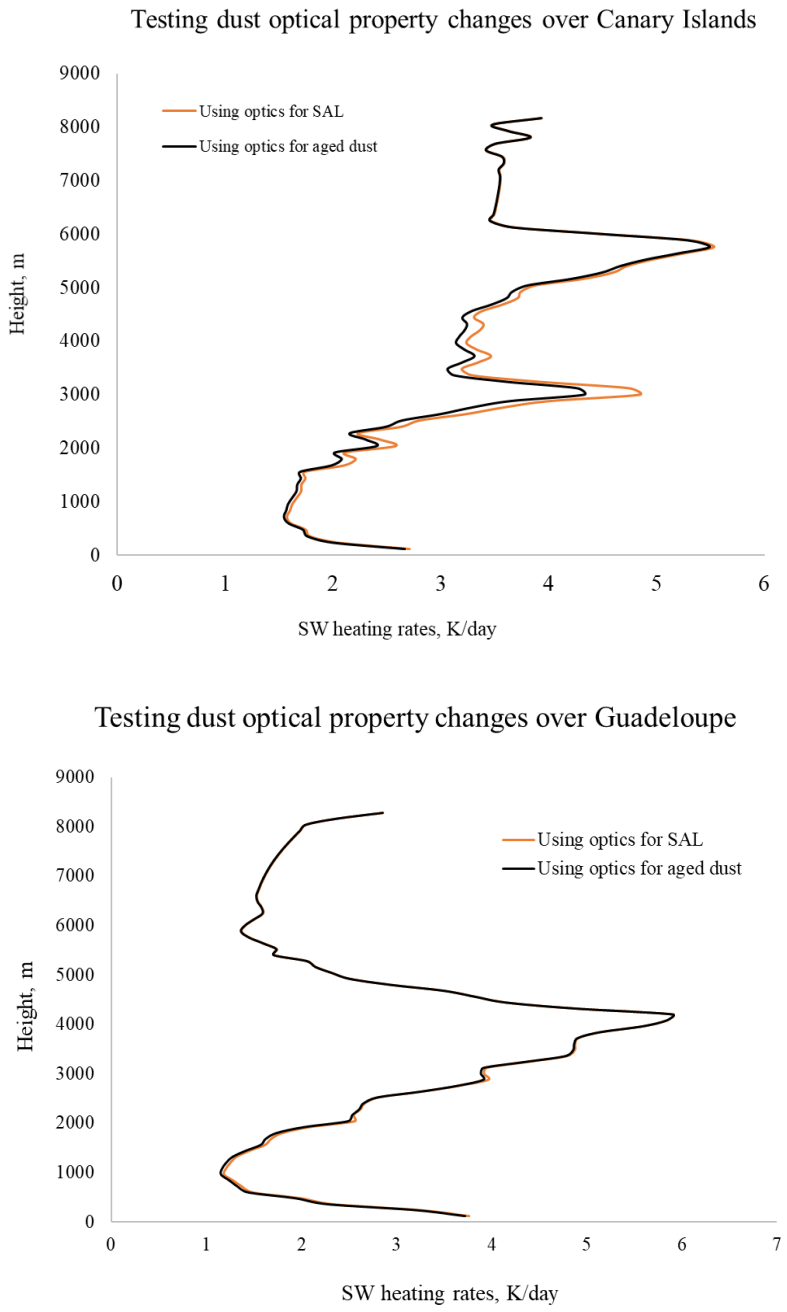

Figure 5. 41. The top panel shows the dust heating rates from ES radiation runs with using dust profiles from the BRSedT model and with using all gases (including water vapour and other gases) over the Canary Islands and (bottom panel) over Guadeloupe. Orange line shows SW heating rate from the radiation model with using dust optical properties for SAL, while black line shows results with using optical properties for aged dust over the Atlantic. Top panel shows profiles for flight case FB604, while bottom panel indicate SW heating rates associates with dust sedimentation for flight FB604. Dust optical properties used in the ES were taken from Ryder et al. (2013a).

In the above, it is assumed that the dust are not chemically altered. It is possible for the dust particles to take up soluble components on the surface and then take up water. This modified dust is not treated in this work where the optical properties are related to high relative humidities. Where the changes in extinction specific mass efficiency (k_{ext}) are associated with relative humidity (RH) in the dusty marine atmospheric layers. For instance, Denjean et al. (2015) noted that k_{ext} was reduced from 1.9 to 0.85 m^2/g, but $\omega_\circ$ was only slightly changed. They noted that this reduction takes place as RH increased from 75 % to 94 % and this process agrees with the deliquescence point of the sulphate soluble elements and NaCl. It has been suggested that the NaCl may aggregate with the dust at high relative humidity resulting in reduced k_{ext}. Figures (5.42) – (5.43) show the evolution of RH over 7 days across the Atlantic for the typical dust outbreak flight FB604 and the humidities in the SAL can reach high levels.

Table 5- 11. Daily averaged single scattering albedo ($\omega_\circ$) and AOD for each flight across the Atlantic from OMI/Aura satellite data and based on BRSedT-AOD calculations. The OMI measurements cover a spectral wavelength region at over 331 nm and 500 nm. The observed optical properties in this table can be compared with that provided by Ryder et a. (2013) in the earlier Chapter 2.

$\omega_\circ$ and AOD	**Day 1**	**Day 2**	**Day 3**	**Day 4**	**Day 5**	**Day 6**	**Day 7**
FB604							
$\omega_\circ$	0.860	0.902	0.915	0.900	0.918	0.920	0.935
AOD	1.3	1.1	1.0	1.1	1.2	0.9	0.5
AOD (BRSedT)	1.0	0.9	0.9	0.9	0.9	0.8	0.3
FB605							
$\omega_\circ$	0.894	0.910	0.907	0.917	0.922	0.971	0.952
AOD	1.75	0.85	0.74	0.55	1.1	0.79	0.79
AOD (BRSedT)	1.0	0.9	0.8	0.7	0.6	0.5	0.23
FB612							
$\omega_\circ$	0.941	0.878	0.909	0.966	0.96	0.97	0.94
AOD	1.7	1.19	2.5	0.94	0.22	0.99	0.98
AOD (BRSedT)	0.8	0.8	0.8	0.7	0.5	0.4	0.23
FB699							
$\omega_\circ$	0.861	0.923	0.930	0.921	0.930	0.939	0.959
AOD	1.0	0.50	0.80	1.4	1.2	1.3	0.67
AOD (BRSedT)	0.07	0.06	0.06	0.05	0.04	0.03	0.04

RH profiles in these figures show the RH (%) every 3 hours of time to provide a good background to the variation each day. The time is represented by UTC, where each two rows of plots indicate data over one day. The data of RH is taken from ECMWF reanalysis data.

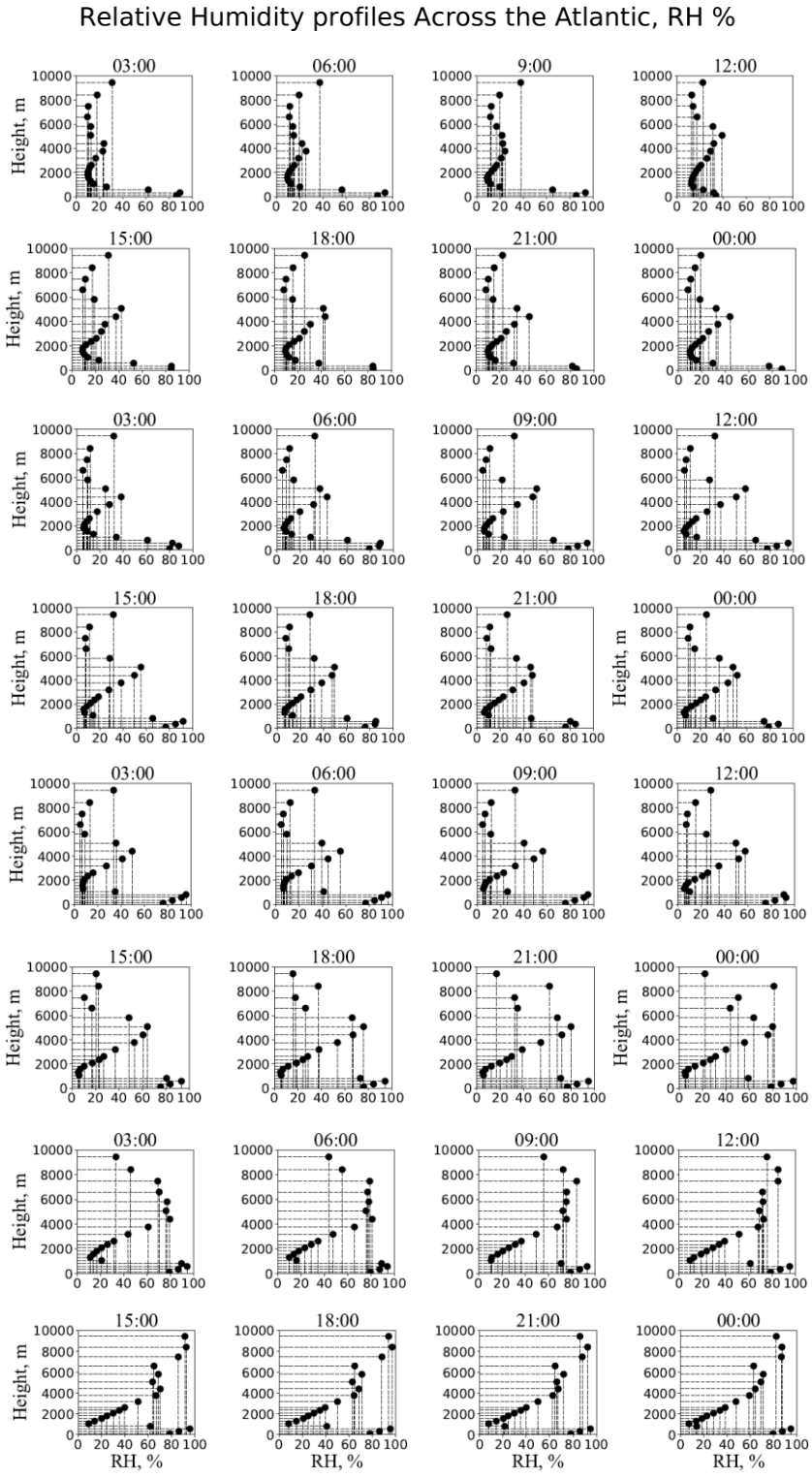

Figure 5. 42. Relative humidity (RH %) profiles across the Atlantic Ocean for flight FB604. The profiles represent the values during advection across the Atlantic with every 3-hour time-steps from left to right, respectively. Where the first two rows show RH for entire one day and the second is for next day, etc. RH profiles were taken from ECMWF data: https://www.ecmwf.int/en/forecasts/datasets .

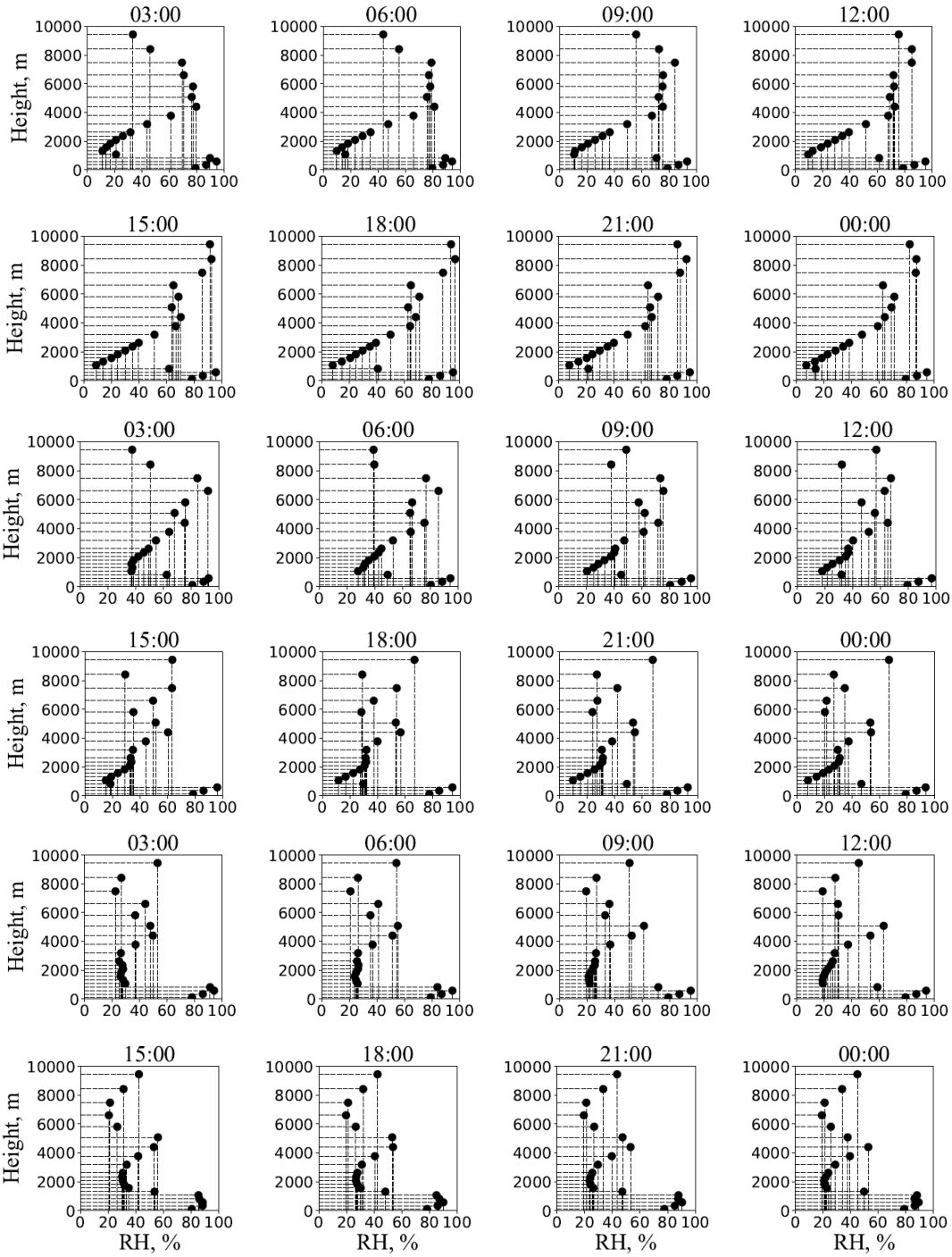

Figure 5. 43. A continuation of figure (5.42).

From the ECMWF results, the following are noted from the data, the first point is related to the significant increase of RH from about 20% within the SAL (at about 4 km) after 5 days to 80 % for dust ladened air transported away from the continent of Africa and then from 80 % it reduces to 50 % by the end of 7 days transportation. Corresponding with the development of large dust particles during dust transportation across the Atlantic, FENNEC flight observations capture giant

dust particles over the Canary Islands, and this suggests that $\omega_\circ$ is decreased since large particles contribute to absorbing more than scattering. Together with RH from ECMWF data, figures (5.42) and (5.43) show that RH above 2 km increased over about 5 days and then generally decreased after 5 days across the Atlantic, where each two panels in the figure refer to humidity profiles over 24 hours, see times on the top of each plot. These increased values of RH can be associated with the decreased k_{ext} over these days due to this change as discussed by Denjean et al. (2015). In contrast, large particles will no longer be in the atmosphere after long distances so after several days of dust transport across the Atlantic (over 3 days), $\omega_\circ$ will be increased. This can be noted for $\omega_\circ$ observations from satellite in table (5-11) where $\omega_\circ$ is generally increasing over the days across the Atlantic. This reflects that k_{ext} is likely to have a reduced contribution from absorption since the large particles will mostly sediment from the atmosphere during transport between the African land and Caribbean.

The relative humidity from the ECMWF data has high values in the SAL and these values agree with FENNEC observations for large humidity out over the Canary Islands for dusty cases. This provides a very interesting point that the water vapour is high for the dust within the SAL as compared with low moisture cases found in the literature studies such as Prospero and Carlson (1972) and Karyampudi (1999). Results of dust heating rates in Chapter 4 reveals that water vapour over the Canary Islands plays a dominant factor in sustaining the well-mixed SAL and contributes to high cooling at the top of dust layer, and this is likely to be again important and will be investigated in the section 5.6.

Dust aging and dust coated with gases (mainly sulphate) after long dust transportation may affect the optical properties such as AOD, and thus dust radiative effects. This is highlighted by Abdelkader et al. (2016) who analysed the difference in dust effects between fresh dust and aged dust on AOD over west Africa and Caribbean regions. Their study stated that over west Africa (at near distances to the coastline of African land), aged dust is characterised by large particles over the Atlantic. The large aged dust sizes have an influence on the optical properties, in which dust aged contributes to increasing AOD by about 0.15, but this amount is a monthly average. Their study also explains that aged dust in the Caribbean region does not have significant impact on AOD; dust increases AOD by about 0.05. This is plausible since most large dust particles will sediment before reaching the Caribbean. However, there is still debate on this topic since Desboeufs and Cautenet (2005) revealed that dust coated with sulphate are observed not only over the north-eastern Atlantic Ocean but also in the remote regions such as the Barbados in mass concentrations of approximately 1 $\mu g/m^3$. It is possible that the dust aging process is involved in highly increasing the AOD over the Caribbean due to water vapour uptake on specific components of the dust such as calcium salt (Abdelkader et al., 2016). The suggestion is that although dust-sulphate interaction (aerosol-gas uptake) processes can affect the AOD, the large particles of dust are potentially reduced after long distance transport across the Atlantic, and thus dust radiative

effects (dust particle scattering to the SW radiation) will not be significantly changed by dust particles since that dust (aerosol sea salt) is characterised by low (high) contributions over the Caribbean region. On the other hand, dust particle sources from the African land have a wide variety in mineral compositions and some compositions make it easier for uptake to occur (Liu et al., 2008). Therefore, to accurately investigate whether dust optical properties change over the Caribbean, it is useful to look at dust composition associated with the dust being lifted into the atmosphere at the source. This can be taken forward in future work.

5.5.5 Comparison of transported dust and AOD to MODIS observations in Caribbean

The predictions in the last section give some further checks by comparing the BRSedT model results and MODIS-Terra satellite observations to illustrate integrated mass and AOD values agree well. AOD can be calculated as presented in the earlier sub-section (5.4.2). The comparison is performed in section 5.4.2 for dust transported toward the Canary Islands between flight observations and BRSedT calculations. In this section, further comparisons between the AOD results based on BRSedT and satellite observations at African land, Caribbean and Canary Islands are presented to evaluate the AOD consistency.

Figure (5.44) depicts the initial and final values of AOD from MODIS-Terra satellite observations over the African land (top panel), the Canary Islands (middle panel), and the Caribbean regions (bottom panel). The images show daily averaged data for AODs at 0.55 μm during 20, 23, and 26 June 2011, which are consistent with the time measurements of flight case FB604 (dusty case). These dates (including 20, 23 and 26 June 2011) correspond to the cases of total mass loading for the African land, north-west from Africa and Caribbean locations, respectively. The calculated AODs from the BRSedT model associated with these dates, are 1, 0.2, and 0.3. These values of AOD for initial and final profiles are in good agreement with MODIS-AOD observations, as shown in the top, middle and bottom panels of figure (5.44), respectively. Black squares are shown in each plot to indicate the area covered in the AOD calculation based on BRSedT results. Where the observed AOD values over African land is ranged between about 0.5 and 1, and between 0.1 and 0.3 during 4 days transport towards the Canary Islands and between roughly 0.2 and 0.6 at the Caribbean sites. However, the observed and calculated values of AOD between BRSedT calculations and satellite observations do have differences in the way they are obtained so I cannot expect perfect agreement. AOD from MODIS observations is retrieved from a single satellite as it passes over the region of interest whereas BRSedT calculations compute AOD based on a specific SF and the calculated AOD depends on mass extinction coefficient used to convert the dust mass concentration to AOD. So, the values of AOD from BRSedT provide many factors that can contribute to the values. MODIS satellite retrievals can also be affected from many sources of error (Anderson et al., 2013) so I must accept that the comparisons are approximate.

Spatial-temporal variations of AOD with grid boxes observed by satellite may provide significant differences in the results when comparing to higher resolution point measurements, especially for FB699. It can be the case that part of the grid may have significant dust and other parts very little, especially over land. It is possible that this difference come from the variability of AOD during daytime over the Atlantic, see AOD in table (5-11) based on the BRSedT results across the Atlantic. In addition, it may due to the uncertainty in the measurements of satellite observations, and thus the averaged value of AOD from OMI/Aura observations may be different from that calculated by BRSedT model results or it may be due also to uncertainties arising from the model. Finally, as dust transports far distances from the African coastline, some of dust mass loading can be reduced or shifted to the northern or southern subtropical regions before reaching Caribbean region, and this may influence on the final profiles of dust prediction across the Atlantic, but I have attempted to limit this effect by applying a scaling factor (i.e. SF) in the BRSedT model, since the calculation of SF is based on backward trajectories initialised at Puerto Rico.

The main aim of the BRSedT model is to provide an approximation of the right order of magnitude of dust altitudes in the Puerto Rico region so that the dust may be used in the LEM to determine if the dust is enough to influence the structure in the Caribbean, long distances away from the source. The tests of the BRSedT and comparisons with observations such as these gives confidence that the dust loadings are appropriate for such an estimate of effects. Further comparisons are provided below.

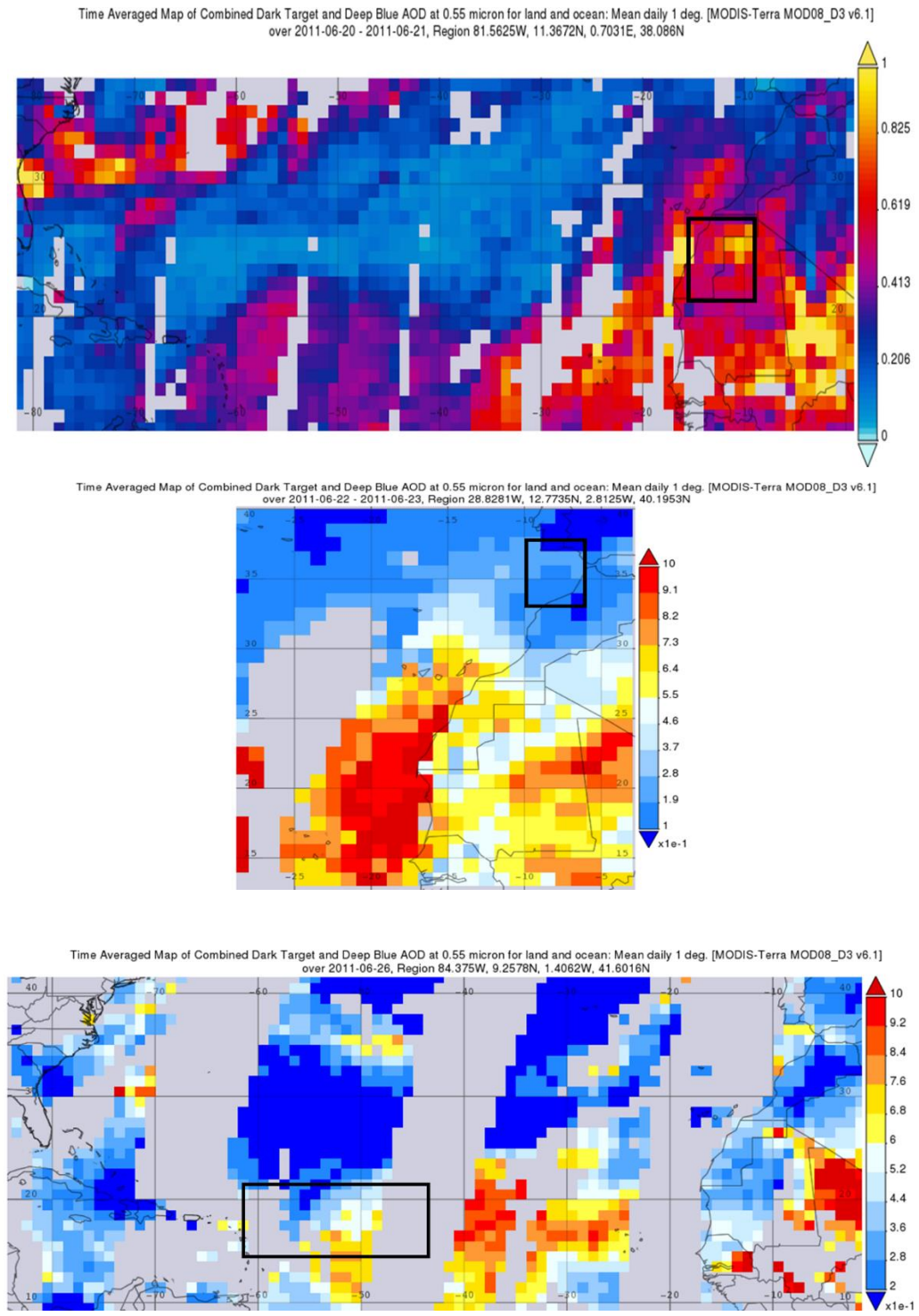

Figure 5. 44. AOD from MODIS-Terra satellite observations associated with flight case FB604. The top panel shows AOD values corresponding with the initial profile of flight observations at the African coastline. The middle panel shows AOD values for dust transported toward the north west then east over 4 days, and the bottom panel shows values of AOD for dust transported over 6-7 days from the dust sources. The black boxes in each panel present the area covered AOD over the African land (top panel), Canary Islands (middle panel) and Caribbean (bottom panel) sites.

Flight FB605 shows similar intensity to the values of AOD for flight FB604. In both flight cases (FB604 and FB605), MODIS observations show that dust remains fairly strong even after transportation away from the African land but the dust at remote regions is affected by sedimentation, and thus dust will have lower mass loading after long transport. This is shown by the red plume of AOD in the bottom panel of figure (5.44) and figure (5.45) for these flights. Also, the simulation can be performed with studying the role of moisture and other gases. I will address this issue in the last section of this chapter.

In contrast, AOD for FB612 is characterised as a dusty case, but not intensively dusty as it is for FB604 and FB605 flights, see figure (5.46). The calculations of AOD from the BRSedT model are in a good agreement with MODIS-AOD observations, where the calculated AOD from the model takes values of 1, 0.16, and 0.23 (African land, Canary Islands, and Caribbean, respectively) for flight FB605 and values of 0.8, 0.155, and 0.23 for the flight FB612 for the African land, toward the Canary Islands and Caribbean, respectively. The comparisons in AODs between the calculated BRSedT-AOD (table 5-11) and with the observed AODs from MODIS observations shown in figures (5.44) – (5.46), are in reasonable agreement.

The intensity of aerosol optical depth over the African land is quite varied during low and moderate cases. For example, during flight FB699 in figure (5.47), the calculated AOD over the continent of Africa from the BRSedT shows value of 0.07, while the daily-averaged values from the MODIS observations shows a wide range covering at least an order of magnitude from about 0.01 to 0.4. This variability is indicated by black box in the top panel of figure (5.47) where blue to red colourful area on the map explains the intensity of AOD from low to high magnitude, in which these locations are associated with the path of flight FB699 over African land. This will impact on the results of AOD on the other side of Atlantic, where the calculated AOD over the Caribbean based on the BRSedT model will be probably be lower than measured by satellite, since the final profile of weighted dust mass is linked to the FENNEC flight observations. Furthermore, at mid distances between Puerto Rico and the African land, AOD shows large variability in comparison to the relatively constant AOD for intensive dust events along transportation across the Atlantic. This may reflect why the calculated values of AOD from the BRSedT model in comparison to satellite observations is sometimes different especially for these cases.

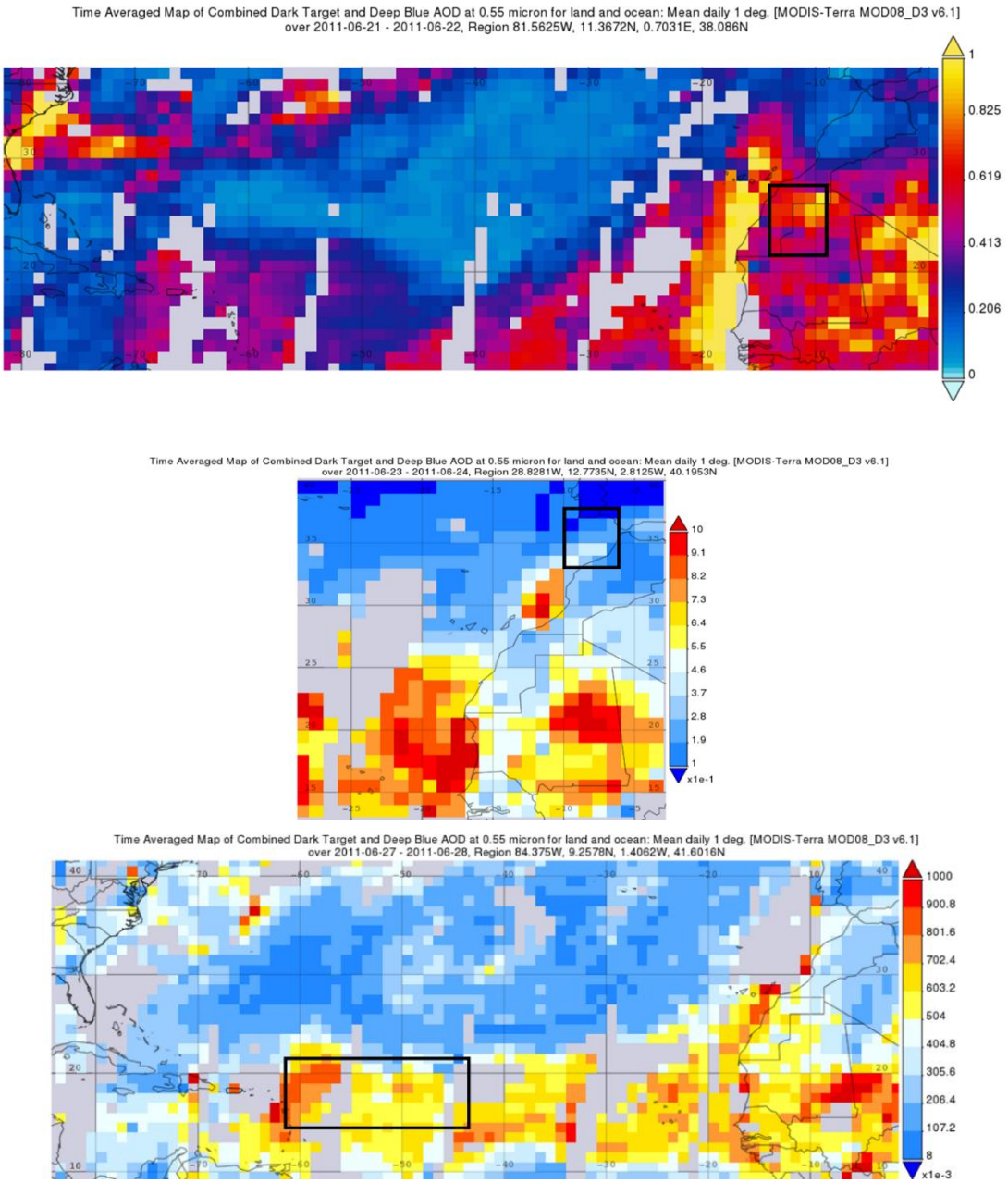

Figure 5. 45. As figure (5.44), but for flight FB605.

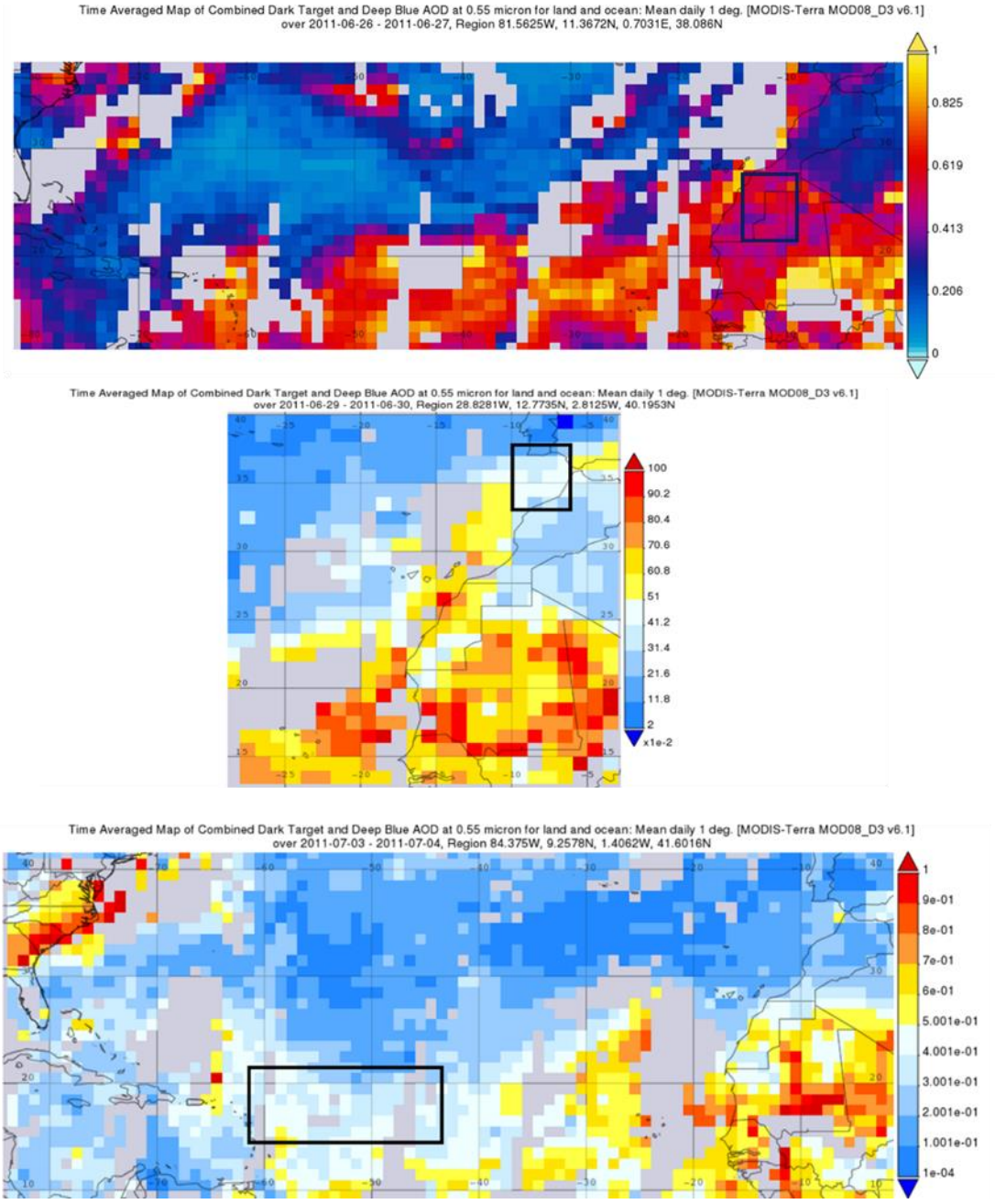

Figure 5. 46. As figure (5.45), but for flight FB612.

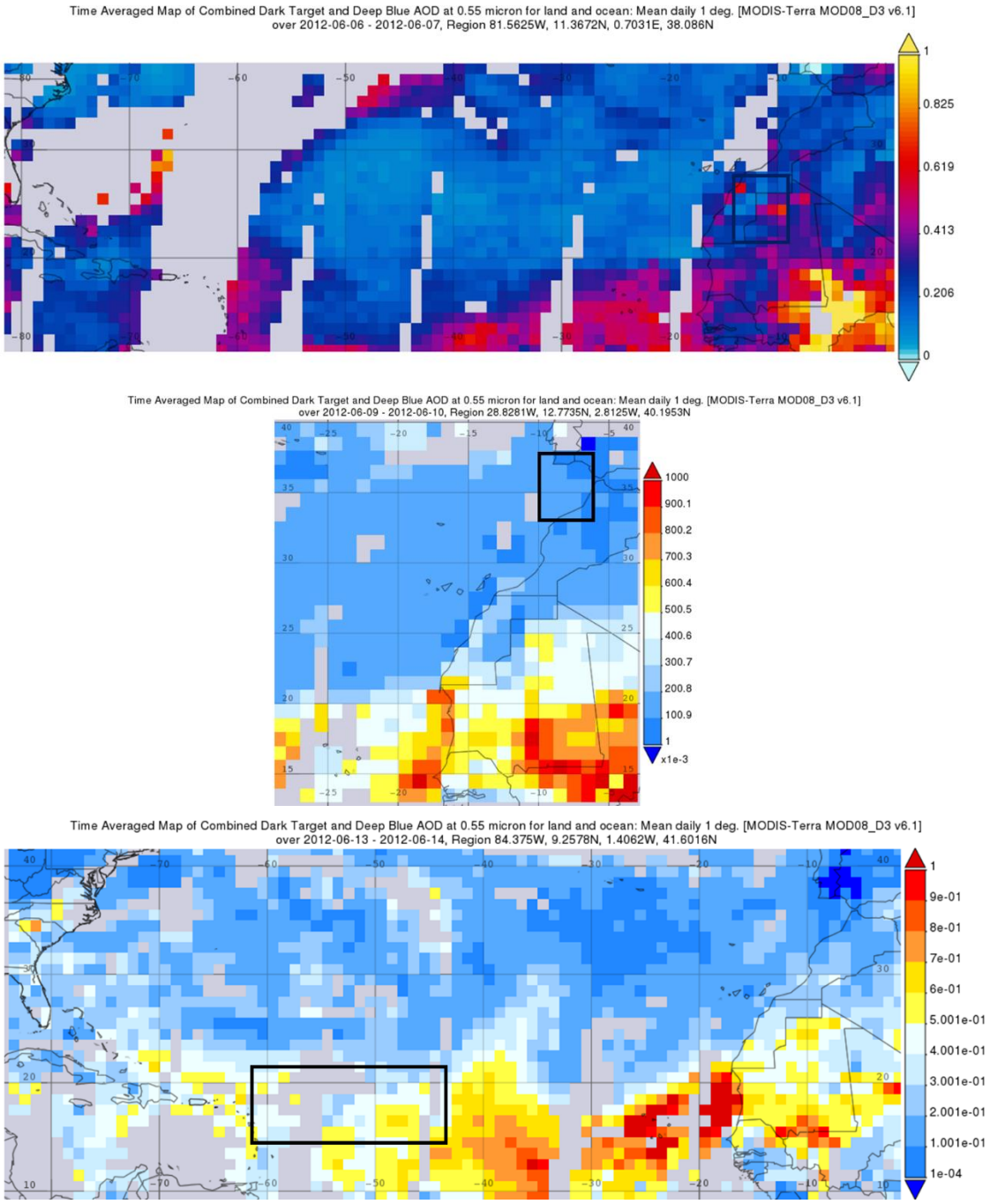

Figure 5. 47. As figure (5.46), but for FB699.

Water vapour in a comparison with dust vertical changes has the dominant role in influencing atmospheric heating rates, as shown in Chapter 4, and thus plays the important role in the radiative effect of the dusty marine environment near the African coast. On the other side of the Atlantic, I will investigate if water vapour and or dust influences the dusty marine structure in this much depleted layer far away from the African land. The simulation of dust, water vapour and other gases will be presented in the next section, section 5.6.

5.6 LEM simulations of dust outbreak impacts in the Caribbean

This is the section that all the previous sections in this chapter have been building up to. In this section, the LEM simulations are used to evaluate if the dust or other gases such as water vapour in the Caribbean are significant enough to maintain a well-mixed thermodynamic structures far away from the African mainland and dust sources, or whether the appearance of the well-mixed structure in the radiosondes in the Caribbean are a left-over structures from processes that took place near Africa and advected over the Caribbean. Using a realistic water vapour test in radiation and LEM simulation as similar as to chapter 4 (explained in section 4.4). This includes a non-dusty water vapour based on flight case FB708 as a reference non-dusty wv instead of using zero profile of water vapour, where set wv to zero is incorrect approach to be considered as it explained in chapter 4.

To do this, meteorological profiles including potential temperatures were obtained for various locations in or close to the Caribbean. Five locations on the west side of the Atlantic were selected, including Puerto Rico, Guadeloupe, Miami, Bahamas and Cayman Islands. The potential temperature profiles for these locations are shown in figure (5.48). The time of dust transport from FENNEC observations for dusty cases FB604 and FB605 is consistent with the time of potential temperature profiles observations that were measured by radiosonde at Guadeloupe, Puerto Rico and the Bahamas. From these plots shown in figure (5.48), some locations seem to be affected by the advected dusty outbreak as they exhibit nearly well-mixed potential temperature layers, such as for Guadeloupe and Puerto Rico. The θ profiles at these locations have near neutrally stable or unstable regions in the vertical whereas for Miami, Bahamas and the Cayman Islands do not.

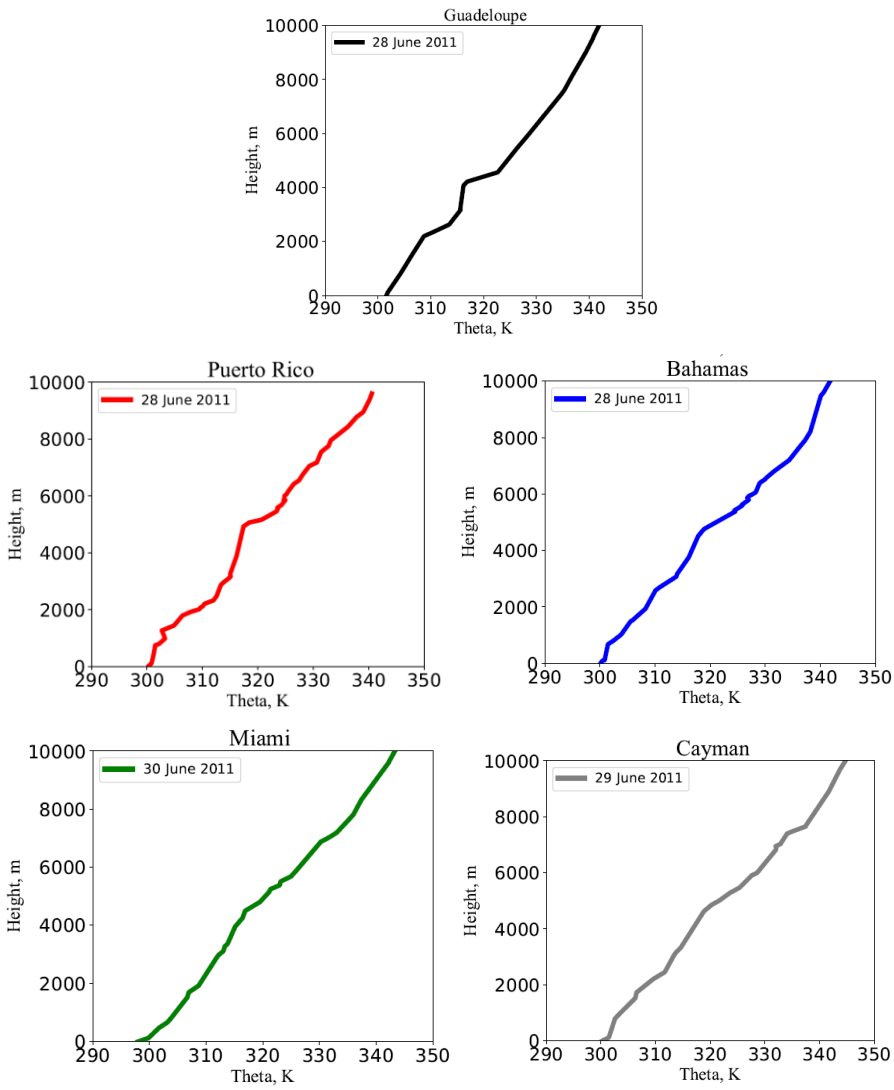

Figure 5. 48. The potential temperature profiles are shown for five locations in the Caribbean, across the other side of the Atlantic from the African coastline and the dust sources. These profiles are taken from radiosonde observations at Guadeloupe (black line), Puerto Rico (red line), Bahamas (blue line), Miami (green line) and Cayman Islands (grey line) at the time of 11:00 am on June 2011. Accounting for advection, the dust observed from the observation number FB604 (flight time observations was on 20th June 2011) corresponds with the Miami and Guadeloupe observations. The θ profiles from radiosonde observations at the Bahamas and Puerto Rico were approximately coincident with flight number FB605 (time observation for this flight was on 21st June 2011), taking account of advection of the dust. The observation date of radiosondes for each location is shown in the legend of each plot.

Dust coverage shown by satellite observations over these other three locations (Miami, Cayman Islands, and Bahamas) shows they were unlikely to be largely affected by the dusty outbreak. So,

from the radiosonde profiles, the cases affected by dust have an appearance of a well-mixed potential temperature in the vertical structure at heights where the SAL would be located and locations not affected by the dust do not have this structure or it is very weakly visible.

The BRSedT model was used to predict the dust profiles in the Caribbean (see figures (5.49) and (5.50)). The dust was then used to calculate the radiative heating rates which were then used in the LEM to perform simulations of the Caribbean region at the time of this dust event (also in figures (5.49) and (5.50)). The LEM is used to evaluate the influence of the dust and water vapour on the potential temperature profile for an 8 hours simulation period to determine the radiative impact of dust and water vapour on the observed structure. Focus was on two locations, Guadeloupe and Puerto Rico, since satellite observations showed the dust was advected right over those sites, as compared with the lower dusty levels over Miami and other locations, as observed by CALIPSO satellite observations. This is evidenced in figure (5.51) which explains the high vertical values of dust and water vapour profiles over the Guadeloupe, while figure (5.52) shows the low dust profile over Miami region. The vertical dashed lines in these figures are shown to specify the latitude/longitude grid associated with dusty (i.e. FB604) day event. The water and dust profiles are shown in blue and yellow shadow areas in the figures (5.51) and (5.52) from the top to bottom panels, respectively. Radiosonde observations were obtained from the archived British atmospheric data centre (BADC) for Guadeloupe and Puerto Rico and radiation simulations were performed with these observations input into the ES radiation model along with dust concentrations from the BRSedT model after a simulated week of advection across the Atlantic was performed. The heating rates were generated from the ES radiation model for four modelled cases (consistent with that done in Chapter 4). The four cases are:

1. Including the dust mass mixing ratio profiles, water vapour and other trace gases,
2. Including the dust profile and other gases, but with using a reference non-dusty water vapour,
3. Including the water vapour and other gases, but without the dust profiles,
4. Including other trace gases and non-dusty water vapour, but without dust profile.

Using these four cases for heating rates in the LEM allows testing of which factors are having effects on the structure in the Caribbean, if any. For flight case FB604, figure (5.49) shows the results of heating rate profiles for Guadeloupe (Caribbean region). Similarly, figure (5.50) shows the results of heating rates over Puerto Rico associated with flight FB605. Red, green and blue lines show heating rates for SW, LW and total radiation, where the top left panel presents results including dust and all gases including water vapour. The top right panel depicts heating rate profiles including dust and all gases including using the water vapour profile based on non-dusty flight case FB708, which was considered as a suitable reference non-dusty wv rather than using zero values. I used the non-dusty water vapour profile of FB708 to generate heating rates and for use in LEM simulations to assess dynamical and thermodynamical evolutions during transport

and to compare with water vapour effects from dusty days. Underneath the top panels, results are shown excluding dust but including water vapour and other gases, as shown in the left panel, and in the lower right panel are results exclude dust profile but with using non-dusty wv and other gases are included. Plots below the heating/cooling rate results indicate the final mass profile of dust from the BRSedT model (left panel), and specific humidity from the ECMWF data over the Guadeloupe and Puerto Rico shown in the right panel of the figures (5.49) and (5.50), respectively. Where black solid and dashed lines show moisture profiles for dusty (FB604) and non-dusty (FB708) days.

The results of the heating rates indicate that SW heating over Guadeloupe is higher than that at Puerto Rico due to a higher total mass loading of dust in the atmosphere. This is reasonable because Guadeloupe is situated closer to the dust sources (African land) than Puerto Rico as well as it is in the intensive dust region over the Atlantic. For Guadeloupe, as water vapour dropped off significantly above a height of about 2 km corresponding to relatively high dust profile at this height, so the high SW and LW heating rates below the SAL (i.e. below 2.5 km) can be caused by not only by high amounts of water vapour but also dust may have a contribution since dust is sedimented to lower altitudes over time during transport over the Atlantic. However, above this height and within the SAL, there is a peak in SW heating rates at about 4 km over Guadeloupe and Puerto Rico , which is caused by the amount of water vapour but it is doubtful that dust is significant to cause much of an effect, as see figure (5.49) and figure (5.50). Heating rate profiles in both Guadeloupe and Puerto Rico regions show that water vapour has the main impact on the atmosphere, while dust and other gases have secondary contribution. This can be clearly shown in the figures (5.49) and (5.50). The figures on the left have the strong contributions in the heating rates whereas the dust and other gases have little impact by comparison. From the plots on the left in these figures, there is almost no difference between top left and bottom left so dust is not having any significant effect. The dust altitudes at these distances are not strong enough to impact the structure. The figures show that LW cooling due to water vapour is the dominant factor in the heating rate profiles. For Guadeloupe, the LW is dominant but the SW has a significant warming effect that shows through even in the total heating rate at about 5.5 km. There is a strong cooling at 4.3 km dominated by the LW. For Guadeloupe, the net heating rate is mostly controlled by the LW and at night when SW is off the effects will be increased mostly. For Puerto Rico, again there is an offsetting of the LW and SW heating effects but the net is only cooling and this will again be enhanced at night when SW is off. For Puerto Rico the cooling is most important at about 3.5 to 4.5 km, with a far less sharp cooling peak than Guadeloupe. From both figures, the all gases (with non-dusty wv included) are noted to have a similar impact to the dust in terms of contribution to the heating rates.

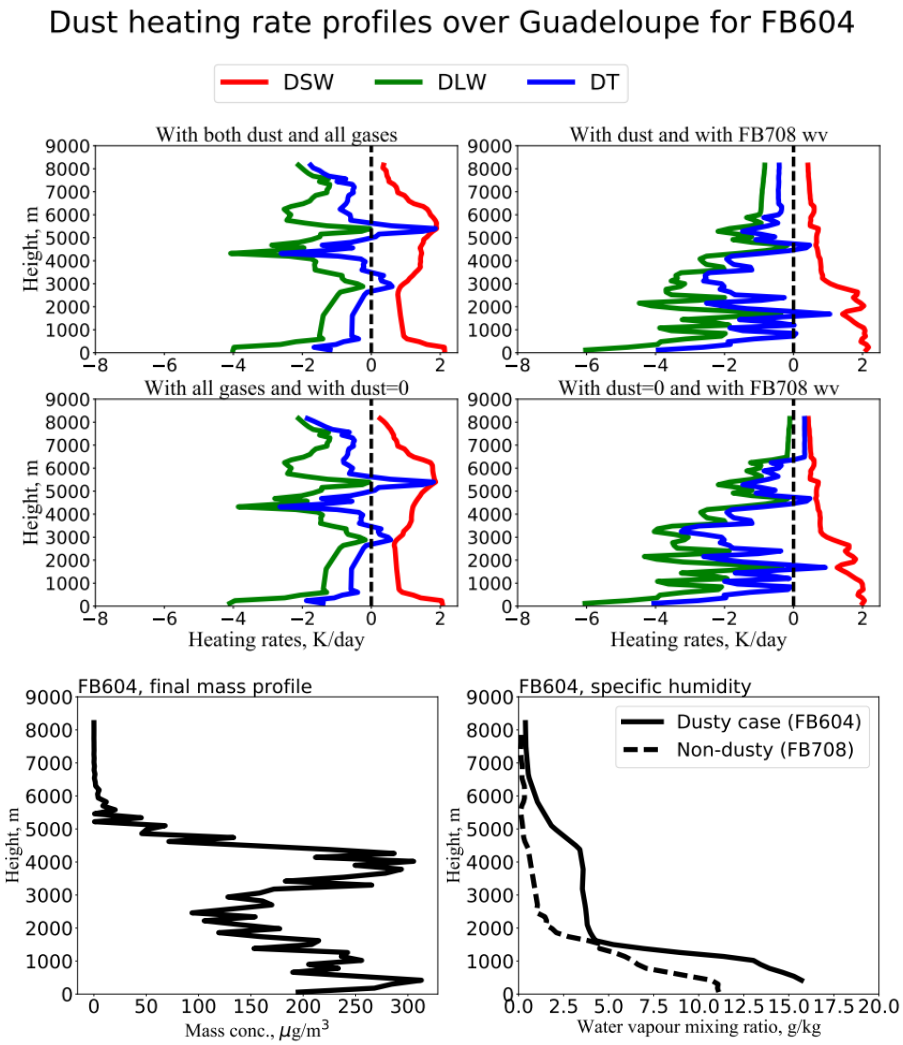

Figure 5. 49. The top and middle panels show the heating rate profiles in units of K/day calculated from the ES radiation model using dust from the results of BRSedT model after being transported 7 days across the Atlantic to the Caribbean and all other profiles from local radiosonde observations. The ES calculated heating rates are based on dust profiles at Guadeloupe for flight FB604. The top left plot shows the heating rate profiles in the presence of dust, water vapour and other gases impacts. The top right shows heating rates with dust and other gases, but with using non dusty water vapour based on FB708. The bottom left plot shows heating rates in the absence of dust profiles, but in the presence of water vapour and other gases, and bottom right plot shows results with other gases impact (without dust but with non-dusty water vapour included). The BRSedT model uses the FENNEC observations and then predicts the dust profiles at these locations after approximately seven days. Red, green and blue lines show the dust heating rates for the SW, LW and total radiation for these regions, respectively. Heating rate profiles associate with using initial SZA of 63 degree in the ES code and correspond with the time of 28 June 2011. The calculated AOD based on BRSedT is about 0.3 over Guadeloupe site. The bottom panel shows the dust mass profile after 7 days in units of $\mu g/m^3$ and water vapour in units of g/kg shown from left to right. Dashed black shows the water vapour for the non-dusty day FB708 as reference and the solid line shows the dusty day FB604. WV data is taken from ECMWF source data.

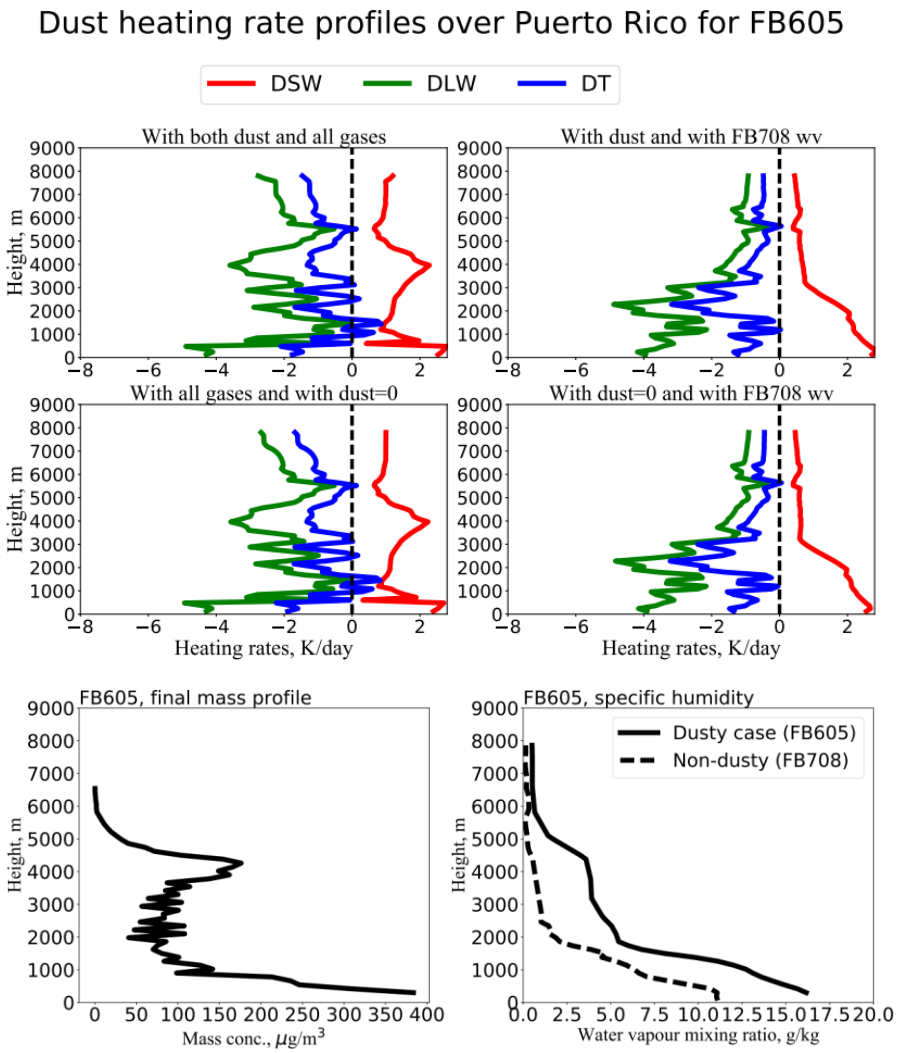

Figure 5. 50. The top and middle panels show the heating rate profiles in units of K/day calculated from the ES radiation model using dust from the results of the BRSedT model after being transported 7 days across the Atlantic to the Caribbean. The ES calculated heating rates are based on dust profiles at Puerto Rico for flight FB605. The top left shows the heating rate profiles in the presence of dust, water vapour and other gases impacts. The top right shows the heating rates with dust and other gases, but with using a reference non-dusty water vapour based on FB708. The bottom left shows the heating rates in the absence of dust profiles, but in the presence of water vapour and other gases, and the bottom right shows the results with other gases effects only (with using non-dusty water vapour). The BRSedT model uses the FENNEC observations and then predicts the dust profiles at Puerto Rico after approximately seven days. Red, green and blue lines show dust heating rates for the SW, LW and total radiation for these regions, respectively. Heating rate profiles associate with using initial SZA of 63 degree in the ES code and correspond with the time of 28 June 2011. The calculated AOD based on BRSedT is about 0.1 over Puerto Rico site. Bottom panel shows dust mass profile after 7 days in units of μg/m^3 and water vapour in units of g/kg shown from left to right. Dashed black shows the water vapour for the non-dusty day FB708 as reference and the solid line shows the dusty day FB605. There is no value of integrated dust mass above about 6.5 km since dust particles sedimented during transport time across the Atlantic.

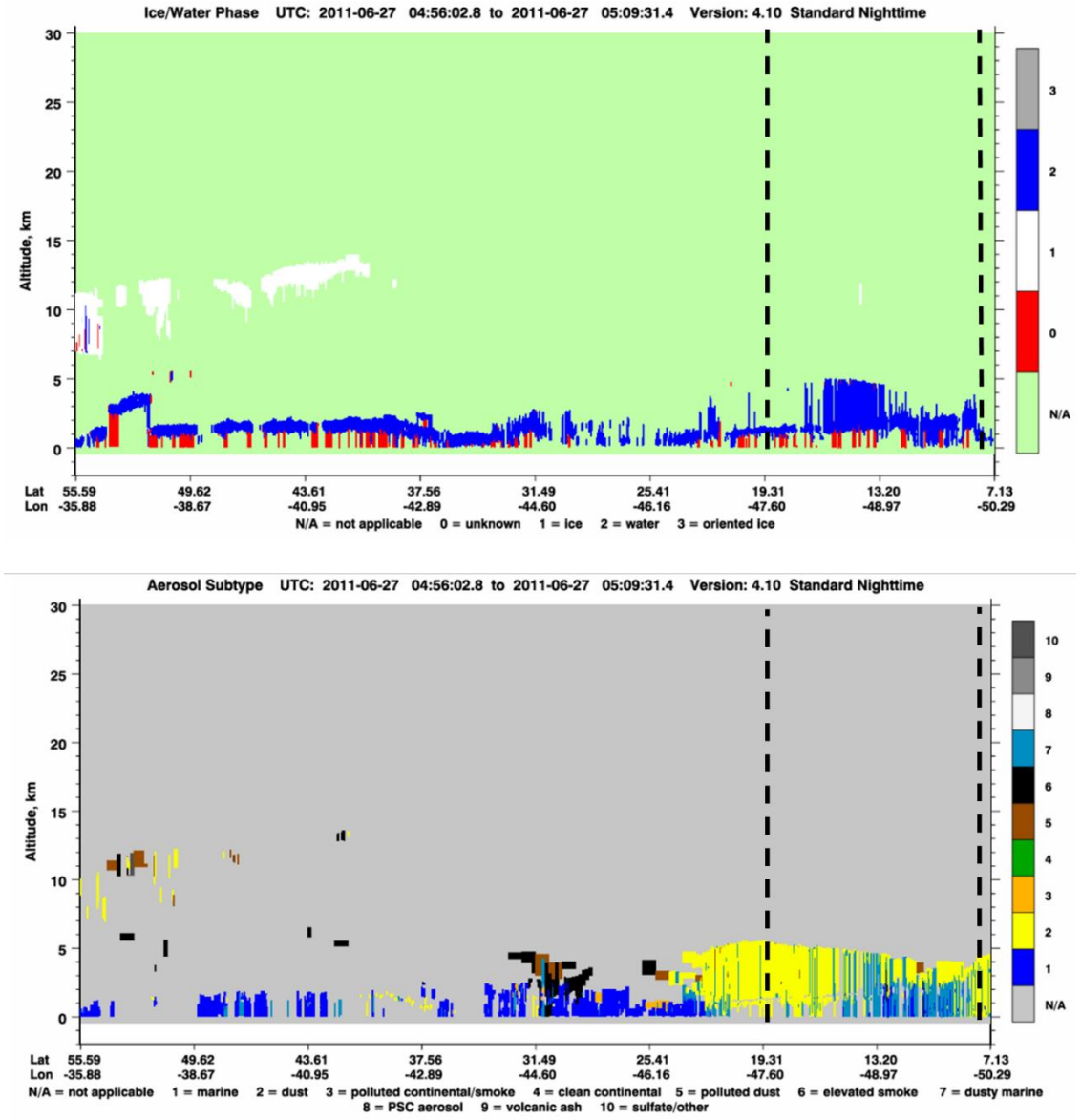

Figure 5. 51. Vertical profiles of water and dust taken from CALIPSO satellite observations over Guadeloupe during the dusty day outbreak on June 27th, 2011. Dashed black lines in top and bottom panels indicate the specified altitude/longitude (x-axis) grid regions in the Caribbean. Blue shaded region on the top panel shows water profile, while yellow colour in the bottom represents the dust vertical data with height (y-axis).

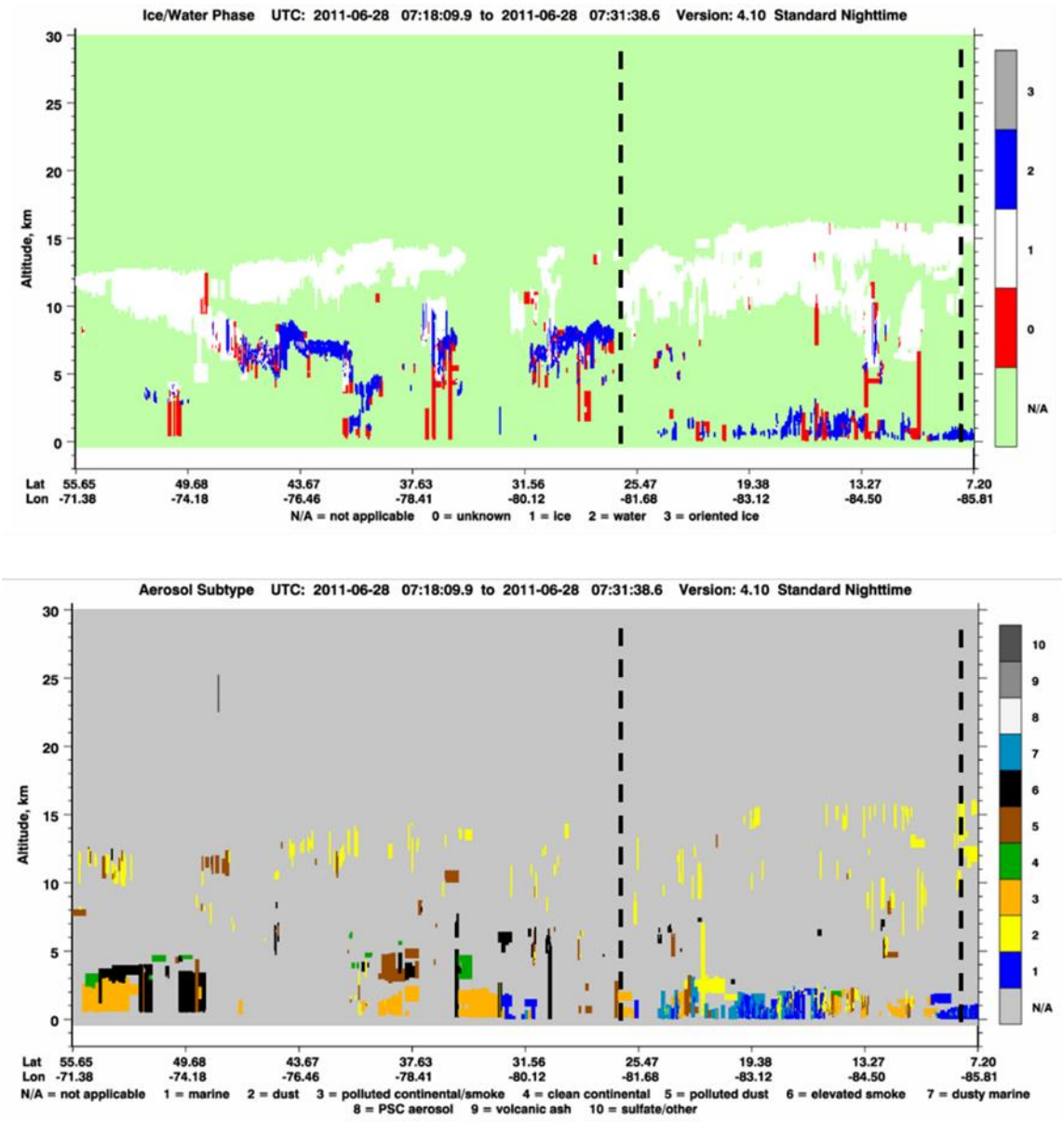

Figure 5. 52. As figure (5.51), but for profiles over Miami on June 28th, 2011.

Associated with the evolution of dust and water vapour vertical distributions over 7 days, an estimation of the impact of dust and water vapour on potential temperature at remote regions away from Africa is now possible. I have shown that the water vapour appears to be far more important than the dust although the figures (5.53) and (5.54) shows that the potential temperature structure is also aligned with dust peaks as well as water vapour peaks in concentrations. It appears that the heating rate profiles of dust and water vapour at Guadeloupe and Puerto Rico regions are consistent with maintaining the well mixed or less stability stratified potential temperature structure regions in the SAL even at these long distances from the sources. The way to explore what is actually having the impact on the structure is to perform LEM simulations by using dusty environment with wv included and compare it with using a dust profile but with non-dusty wv

profile as a reference case since that will evolve the atmosphere with the heating rates applied and then it will be possible to see which aspects of the heating rates are determining the well-mixed structures. The other possibility that neither are strong enough to drive the structure but that will be ideally tested by the LEM.

The LEM simulations were performed using the dust heating rates based on the BRSedT predictions for the flights FB604 and FB605 as well as the contributions to the heating rates from the water vapour and other trace gases, from the ECMWF, as shown in figures (5.53) and (5.54). The LEM runs are performed over 8 hours of time simulation with using the same initial SZA (i.e. SZA=63) that used in the ES radiation code for both flights FB604 and FB605. The SZA can impact the heating rates significantly reducing the heating rates and increasing the scattering upwards but for these two flights the angle is similar so comparing between these is acceptable. The dust event for the flight FB604 advects over the Guadeloupe site and the flight FB605 dusty air advects over the Puerto Rico site. LEM simulations were performed using the heating rates, including: 1) dust, water vapour and other trace gases. 2) Dust and with using non-dusty water vapour based on flight FB708 as a reference background. 3) Dust sets to zero and with using FB708 wv. 4) Runs without dust profile and with using background RB708 water vapour profile. The results are shown for the two locations after 8 hours of simulation time in figures (5.53) and (5.54). Where black lines show radiosonde observations over these destinations. Red and green lines depict potential temperature under SW and LW radiation, while total (SW+LW) radiation is shown in blue lines. The LEM results clearly show that the dust is not at levels enough to influence the atmospheric layer in the Caribbean. The water vapour, on the other hand, has enough radiative heating from SW and LW radiation and at the right levels to maintain somewhat well-mixed layers that are observed. The other gases do not influence the structure significantly. As figure (5.49) shows that dust mass loading over Guadeloupe is larger than that over Puerto Rico (see figure 5.50) as well as heating rate profiles from these figures indicate that water vapour has significant heating rates in the structure of atmosphere while other gases do not have large impact. It is evident from the results that although layer dust can be advected long distances from the African continent, the effect of the dust becomes small at distances of the Caribbean for the levels of dust studied. It is noticed from figure (5.49) that dust mass profiles corresponding with their heating rates over Guadeloupe are relatively higher than these results shown over Puerto Rico, see figure (5.50). This is expected issue since more mass loading reaches the southern Caribbean regions than southern parts of American, especially Miami.

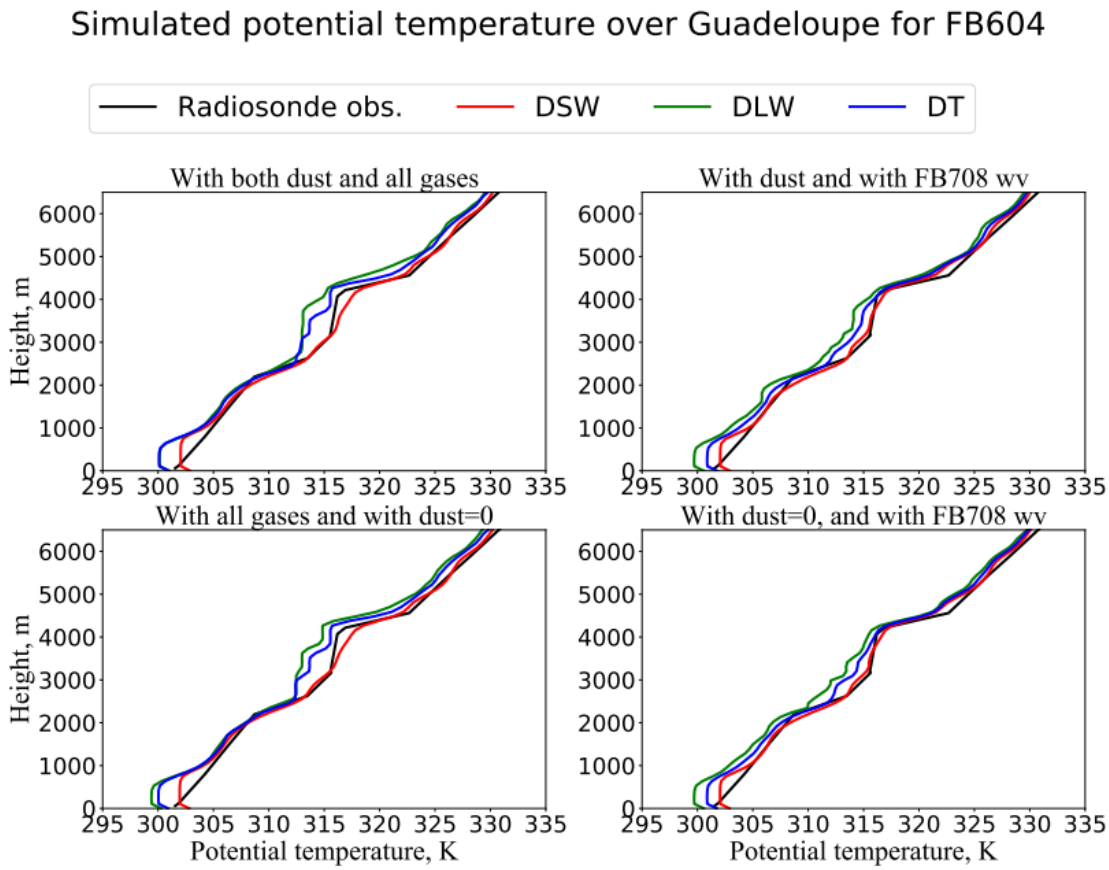

Figure 5. 53. Vertical profiles of simulated potential temperature from the LEM during 8-hour simulations at Guadeloupe location. Heating and cooling rates used in the LEM were obtained from the radiation code with using dust profiles from the BRSedT simulations predicting 7 days of dust transport across the Atlantic. Final profiles of dust mass mixing ratios at Guadeloupe from BRSedT model were based on initial profiles in the African region for flight number FB604. Top left shows the LEM results in the presence of dust, water vapour and other gases. Top right shows the LEM results with using non-dusty water vapour (FB708 wv), but with dust and other gases impact. Lower left shows the LEM results without dust impact, but with non-dusty water vapour and other gases. The lower right shows results without dust, but in the presence of other gases effect and with using non-dusty water vapour profiles. Black line indicates observation from radiosonde measurements over Guadeloupe on 28th June 2011, while red, green and blue lines indicate θ profiles from simulating dust heating rates profiles in the LEM for SW, LW and total radiation, respectively. LEM runs are performed using an initial SZA of 63 degree.

.

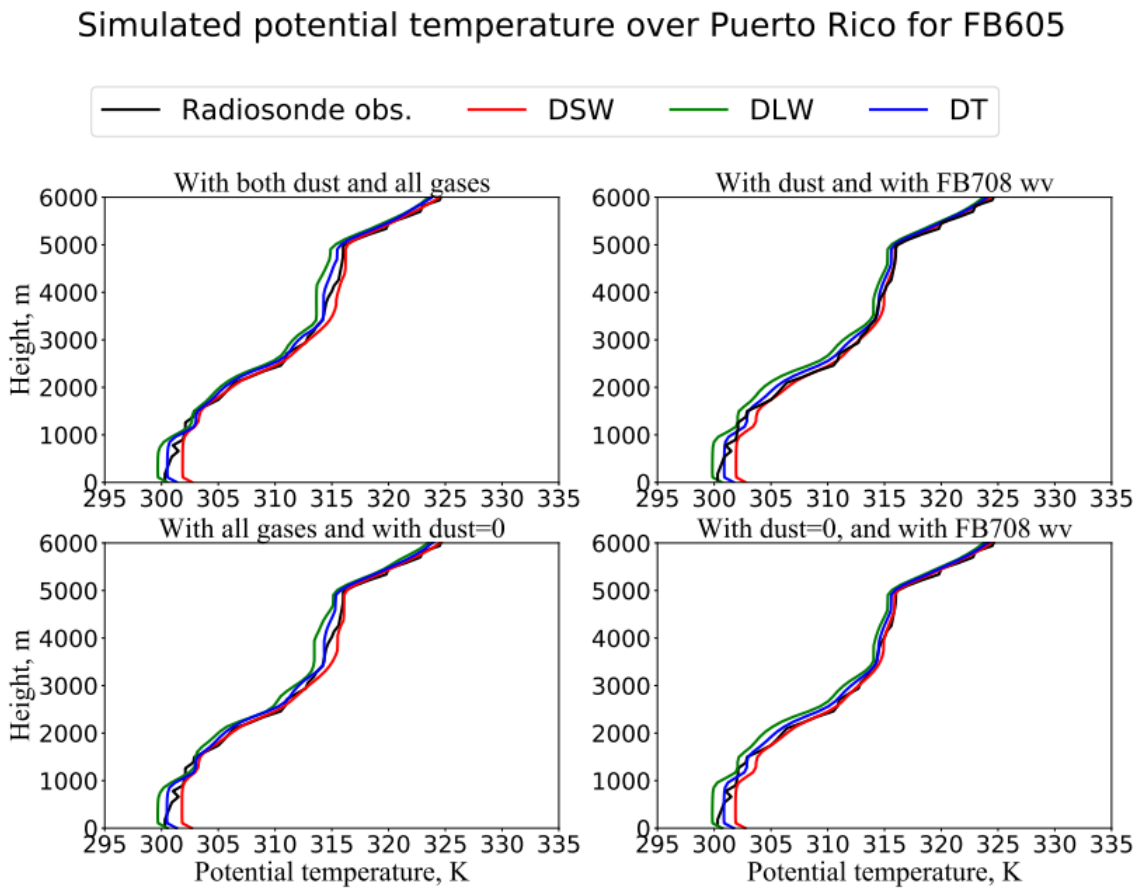

Figure 5. 54. Vertical profiles of simulated potential temperature from the LEM during 8-hour simulations at Puerto Rico. Heating and cooling rates used in the LEM were obtained from the radiation code with using dust profiles from the BRSedT simulations predicting 7 days of dust transportation across the Atlantic. Final profiles of dust mass mixing ratios at Puerto Rico from BRSedT model were based on initial profiles in the African region for flight number FB605. Top left plot shows LEM results in the presence of dust, water vapour (water vapour used based on radiosonde observations) and other gases, while top right plot shows potential temperature simulated with using dust final mass and non-dusty wv. Bottom plot shows LEM results without dust impact; left panel presents LEM results with water vapour based on radiosonde observations corresponding with flight FB605 over Puerto Rico and right panel indicates results with using non-dusty (FB708) wv and other gases. Black line indicates observation from Radiosonde measurements over Puerto Rico, while red, green and blue lines indicate θ profiles from simulating dust heating rates profiles in the LEM for SW, LW and total radiation, respectively. LEM runs are performed using an initial SZA of 63 degree.

For dust sedimented for 7 days across the Atlantic to the Caribbean, the importance of the enhanced dust outbreak water vapour effect can be investigated by running sensitivities in which the enhanced water vapour is reduced in stages to significantly (reduced by 80 %) lower levels to determine if the dust then becomes more significant. So, I selected the Puerto Rico site and ran the ES radiation code using final dust profiles and with reduced water vapour mass mixing ratios from observed levels by 10 %, 20 %, 40 %, 60 % and 80 %. Therefore, in a similar way to water vapour sensitivities in chapter 4, figure (5.55) displays the SW and LW heating rates for dust and water vapour effects over Puerto Rico associated with dust transported from Africa, initialised with the dusty flight FB605. The solid thick lines show the generated heating rates based on dust and water vapour, while dashed lines present profiles with water vapour reductions as listed above (in percentages). The thin lines indicate the heating rates for the non-dusty environment based on the FB708 water vapour profile. All runs were performed using a SZA of 63 degrees which is coincident with the initial time of flight of the observations. It is observed that SW heating rates dropped by 1 K/day associated with reducing wv by 80%, while no significant changes in LW heating rates occurred below 5.5km but it showed significant changes above this height. This implies that the reduction in SW heating rates at Caribbean is less than over Canary Islands corresponding with 80% dropping in the values of water vapour. Reducing water vapour in ES by 80% is likely to make the heating profile close to standard non-dusty water vapour, while over

the Canary Islands more than 80% reduction of water vapour is potentially needed to make heating rates similar to these profiles for non-dusty environment.

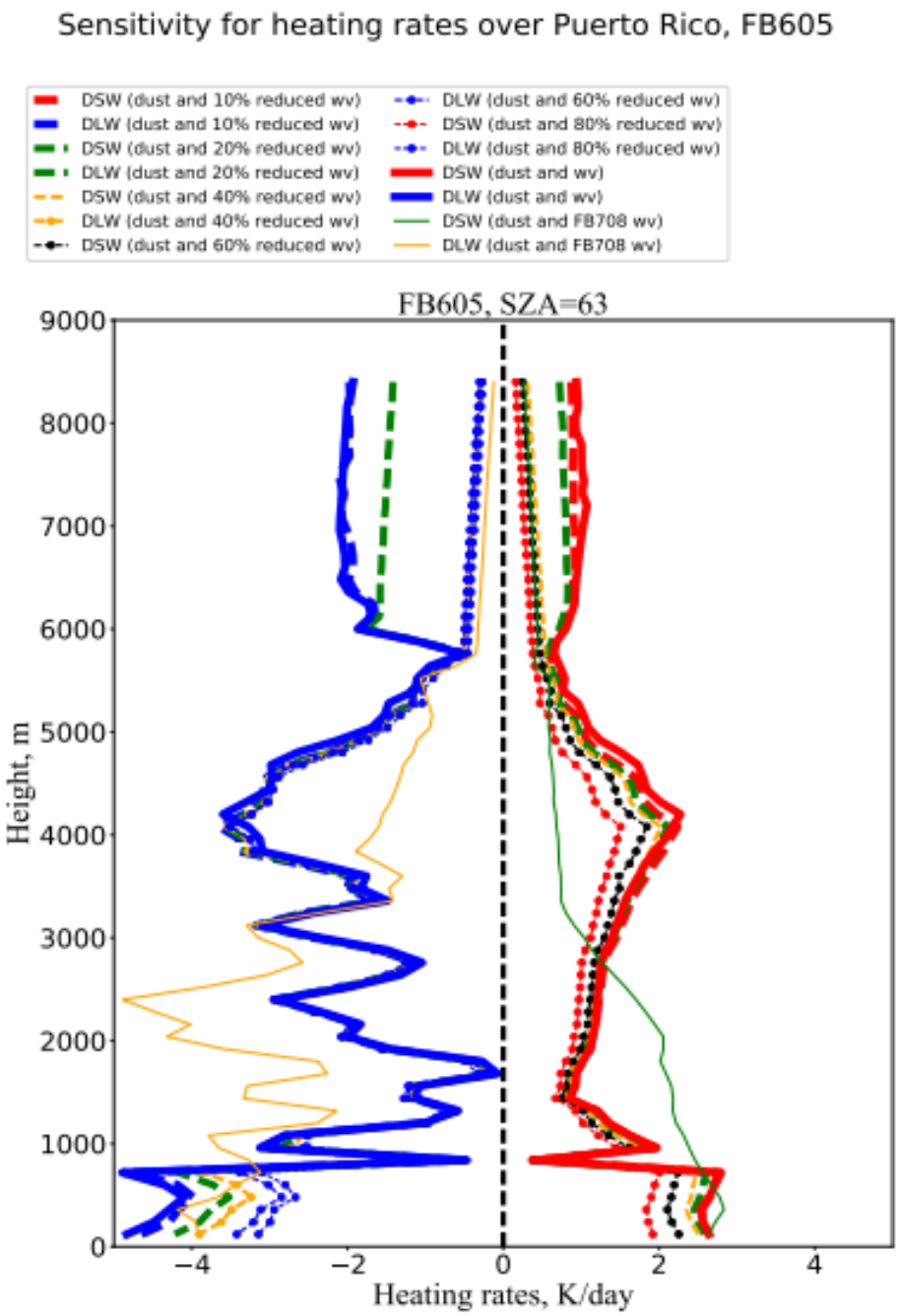

Figure 5. 55. SW and LW heating rates generated by the ES radiation model for FB605 over Puerto Rico. Solid thick red and blue lines show SW and LW heating rates with dust and wv associated with dusty flight FB605, while solid thin green and orange lines indicate heating rates for non-dusty wv based on FB708. Dashed lines show heating rates with reduced wv values by the amounts 10%, 20%, 40%, 60% and 80% from the original enhanced water vapour level. All runs were performed with SZA set to 63 degree.

5.7 Summary

This last chapter of the thesis addresses the question of whether the dust that is advected long distances across the Atlantic can maintain well-mixed layers in their profiles at large distances from the source region. To address this question, the radiosondes of profiles in the Caribbean were obtained and the dusty events from Africa that made it to the locations of the radiosonde measurements in the Caribbean showed that there appeared to be a well-mixed or at least a layer that looked to be less stably stratified than the surrounding air in the vertical. A very interesting finding was that the water vapour in the SALs were elevated compared to non-dusty conditions. This is contrary to popular understanding that the SALs are dusty and dry, but this finding was noted in the literature by Marsham et al. (2013) who observed that SAL is humid over land. Unfortunately, in the Caribbean, there were not any dust measurements to test whether the water vapour or dust was impacting the structure of the Caribbean air, so a new model to simulate the dust transport was needed. The model developed was a bin resolved dust transport model which included the effects of sedimentation and turbulent diffusion called BRSedT. Much of this chapter was about the creation and testing of this transport model BRSedT. This testing involved single process tests as well as testing performed using FENNEC flights paired up so that dust leaving Africa was measured by one flight and the arrival in the Canary Islands was measured by another flight on the next day as well as AOD comparisons with satellite observations. Sensitivities were also tested looking at variations of factors such as fall velocities in terms of shape assumptions, dust density and RI.

This all led to the final section where an assessment of what was most important for creating or maintaining the well-mixed (or less stably stratified) layers was assessed to determine if water vapour or dust was important for the Caribbean or whether the well-mixed layers were just left over structures created near Africa and no longer being maintained. LEM results showed that dust at the levels in the Caribbean were not influencing the structure by much but the water vapour during the nighttime was able to influence the layer toward being more well-mixed at least in small layers.

The main points from this chapter are the following:

- A new transport model BRSedT using ECMWF large-scale subsidence and advection as well as including sedimentation and a first order closure scheme for turbulence was developed.
- The BRSedT model was validated showing individual parcel responses for each process and then, validated using FENNEC observations from flights on the mainland African and Canary Islands accounting for advection times.
- A new approach to calculating the advection was implemented that was formulated in terms of a newly developed dust scaling factor (SF) that was calculated based on HYSPLIT

back-trajectories to estimate the fraction of dust coming from the mainland observations in the direction of the comparison destination.

- Satellite observations were used to compare the results of BRSedT for AOD which showed consistent results.
- Sensitivities to a range of factors were explored including dust density, kinematic viscosity, particle shape, etc. It is likely that density which affects the amount of mass in the distribution and hence fall velocity was more significant than altering the value of fall velocity independently.
- Aged optical properties were used to characterise the radiative properties of the dust in the Caribbean but little impact was noted; however, these optical properties were not properly representing aged optics for transport across the Atlantic. Only small changes in the optical properties were noted and I expect properly aged optical properties would vary by greater amounts.
- The BRSedT model was used to estimate the dust profiles that were transported to the Caribbean along with ECMWF reanalysis of water vapour profiles and radiosonde profiles.
- LEM simulations were used to model the evolution of the structure to determine if the dust and/or water vapour heating rates were significant enough to maintain well-mixed (or less stably stratified layers) potential temperature layers in the Caribbean.
- It was found that dust was not important for influencing well-mixed layers in the Caribbean, whereas water vapour was able progress layers towards well-mixed within small layers and especially at nighttime.
- It is possible that there is a feedback occurring in which the radiation causes the well mixed layer that then cause mixing which might sustain dust in the SAL which then feeds back to the radiation. It is clear from the work that the mixed layer is not maintained through turbulent mixing since that was relatively small but it could be established through the resolved scale mixing especially caused at nighttime (see figure 4.25) which was evident in the LEM simulations, but it would require online aerosol and radiation to verify.

6 Chapter 6: Conclusions, limitations and future work

The first section below presents the conclusions for the thesis and the second section presents the suggestions for future work.

6.1 Conclusions

Periodically, there are massive dust events from the Sahara Desert that carry huge amounts of dust from the African continent intruding into the marine environment as SALs and advecting great distances across the Atlantic Ocean to the Americas. The SALs are characterised by high levels of dust, but also, they typically have a characteristic well-mixed layer in terms of potential temperature. In this study, I was interested in what might be maintaining these characteristic well-mixed SALs. Was it the dust or were there other factors influencing it such as shear or trace gases? In addition, I was interested to know how long it would take to form a well-mixed layer if dust entered into a non-dusty stratified marine layer and whether these layers would still be maintained across the Atlantic once much of the dust had sedimented out of the atmosphere.

There are several important differences between SAL layers advecting over the marine environment compared to over land. Notably, the marine surface is a huge source of moisture that mixes into the MBL and the surface has a much lower surface albedo than typically over the African land. There are significant differences in the strength of convection and the diurnal temperature ranges and surface fluxes as well. The effects of SALs intruding into the marine atmosphere and their effects on the structure of the environment are not well understood, and thus need more analysis for observations over the ocean environment.

To investigate these SALs in the marine environment, this work was based on the FENNEC observations since FENNEC did numerous flight-based campaigns from the Canary Islands that regularly flew back and forth to and from the African continent over the ocean during 2011 and 2012. These flights provided profiles of the dusty marine environment but also, importantly, dust size distribution observations measured using PCASP, CDP, and CIP instruments. It was noted in the FENNEC observations that the well-mixed potential temperature profile of the SAL intruding into the background marine environment formed strong inversions both above and below the SAL, with a well-mixed dusty layer making up the SAL. The strong inversion at the base of the SAL is significant and would be expected to inhibit deep convective cloud development, so it is important to understand these layers since they could have significant effects on downwind clouds and thus on weather and climate.

From the FENNEC observations, not only did the SALs have high levels of dust but also it was found that the water vapour was significantly higher as well. It has been observed and studied that SALs are dry dusty layers. This led to questioning whether the dusty SAL intrusions in the marine

atmosphere could have well-mixed thermodynamic layers caused by the radiative effects of the high levels of moisture or whether the dusty layers, as expected, would have the larger effect.

In this research, the first task was to rebin the size distributions since there were procedures available to improve the accuracy of the size distributions and to take account of more appropriate refractive indexes for the region. The re-binning and conversion of scattering cross section into dust size distributions was performed for both PCASP and CDP flight instruments using a procedure originally shown by Rosenberg et al. (2012). A refractive index of 1.52+0.001i is used in this study (as was used by Ryder et al., 2013) and it was shown to be appropriate by considering the overlap between the observations in the CIP and CDP instrument results. The CIP does not depend on RI so it was a good way to ensure the RI was appropriate and consistent also with Ryder et al. (2019). The bin-resolved size distributions were used to generate dust mass profiles which were used in the ES radiation model to produce radiative heating rates that were used in the UK Met Office Large Eddy model (LEM).

The LEM model was the main model used to perform simulations of the atmosphere with the radiative effects of the dust and gases included. The aim was to assess what was causing the well-mixed structure and evolution of the marine environment with an intruding SAL. I selected two regions, one off the west coast of Africa in the region of the Canary Islands (near west Africa) and the other directly west from where the flights were landing and taking off in Africa, towards the Caribbean. Both dust and water vapour were explored in the LEM simulations through heating rates to determine what was causing the evolution of the marine atmospheric structure containing a SAL, and to compare the effects relative to other influences such as shear. Included in the LEM simulations were assessments of whether a background MA could develop a well-mixed layer if the dust intruded on a stably stratified background marine layer and how long it would take for a well-mixed layer to revert back to a stably stratified layer (typical of the background MA) if the dust was removed. This helps to understand the timescales of dust and water vapour effects on the marine atmospheric structure which has not been previously assessed.

The radiative impacts of dust and water vapour on the evolution of the dusty marine atmospheric layer over the Canary Islands was also evaluated in terms of the atmospheric stability by calculating the convective available potential energy, convective inhibition and the gradient Richardson number. Differences in these quantities are important for the downwind potential for convection and clouds. In addition to dust and water vapour radiative effects, shear was also studied to determine if it could be responsible for the well mixed layers, but the shear had little effect on the structure compared to other much more significant effects such as water vapour and dust. Shear was found to only affect the potential temperature by about 1 % in terms of the percentage change in potential temperature between shear and non-shear cases simulated by the LEM, so shear provides a low contribution to the changes in the structure of marine environment compared with water vapour effects.

Finally, I explored whether dust and water vapour would still have an important effect on the well-mixed layers on the other side of the Atlantic Ocean after transport for a week from Africa. Radiosonde profiles indicated that for locations where dust reached the Caribbean, there were somewhat well-mixed structures in the potential temperature present in the profile. Were these left-over structures or was the dust and water vapour still actively driving these structures and which was more important dust or water vapour? In order to answer these questions, it was necessary to develop a bin resolved dust transport model to provide an estimate of the dust in the Caribbean after transport from Africa.

This model was named BRSedT and included bin resolved dust transport including the effects of sedimentation and turbulent mixing. It was used to model the dust profile transport from the land out in two directions, to the Caribbean and northwest towards the Canary Islands and beyond. The amount of dust transported in each direction was scaled using a new approach that used ensembles of HYSPLIT model back trajectories to characterise the fraction of trajectories arriving at the destination originating from dusty and non-dusty locations. The scaling factor, SF, was a new approach used to estimate the fraction of the dust from a location that would transport in the direction of interest. The BRSedT model used input data of dust profiles from FENNEC observations, turbulent diffusion coefficient profiles, terminal velocities and large-scale subsidence taken from the ECMWF reanalysis data corresponding with specific latitude and longitude grid boxes as it advected over the Atlantic. The BRSedT model was validated using aircraft flight data for dust mass profiles measured during ascent/descents. This was achieved by using a profile measured in Africa on one flight and then another profile measured over the Canary Island on a different flight but timed to agree with the dust advection from Africa to the Canary Island. The BRSedT model was used to model this transport and the results were adjusted by the scaling factor, SF, to account for the amount of dust that went in the direction of the Canary Islands. The results from the validation runs were found to be in good agreement with aircraft observations, where results showed agreement within 4.9 % of total dust mass loading between flight FB604 and calculated values based on BRSedT. In addition to validation results, there is a good agreement of about 18 % of total mass loading between the BRSedT results and flight case FB611, where both validation runs were implemented with using density of dust of 2.6 g/cm^3. Comparisons of the BRSedT results with MODIS-Terra satellite observations provided in most cases very good agreement for AOD associated with large distances from Africa. The development of BRSedT then enabled dust loadings to be estimated for the Caribbean for dusty cases studied after approximately a week of transport across the Atlantic. This enabled the LEM to be run for the Caribbean region using local observations of meteorological profiles, including

water vapour, with the dust profiles predicted from the BRSedT model. A set of LEM simulations were then performed to assess whether the somewhat well-mixed layers in the Caribbean were still being influenced by the dust or water vapour, and which was more influential. A few island locations (Guadeloupe, Miami, Puerto Rico, Bahamas and Cayman Islands) were selected to understand the dust effects.

The main conclusions for this research are:

The main finding from the research is that high levels of water vapour were observed in the dusty outbreak air compared with non-dusty marine background levels of water vapour. To evaluate the relative importance of dust and water vapour radiative effects on the atmosphere, comparisons were made of the radiative effects of dusty cases associated with high outbreak levels of water vapour and these were compared to background marine environment reference water vapour levels (water vapour being switched on and off were also tested by were not realistic test). By isolating the radiative effects of dust and elevated water vapour separately, it was possible to determine that water vapour plays the most important factor in determining the well-mixed SAL structures observed and transported over the Atlantic Ocean for the cases studied. The importance of enhanced water vapour levels in dusty outbreak air has been studied over land (Evans, 2015 and Marsham et al., 2015), but in the research of this thesis it was new to observe and assess this over the marine environment and their importance for influencing the well-mixed SAL layers.

The simulation results revealed that the most important aspect was water vapour causing large longwave (LW) radiative cooling at the top of the SAL that destabilised the air and gave rise to mixing of air within the SAL, maintaining the well-mixed SAL. The SW effects tended to reduce the LW effects by somewhat diminishing the LW cooling during the day so night-time effects were most influential when SW was not active. The effects of SW and LW heating rates for dusty cases showed generally significant SW heating within the SAL and LW cooling at the top of the SAL with secondary radiative effects by the dust. Dust was noted to have some impact but limited mostly to altitudes that water vapour was less abundant (which can occur during transport through sedimentation), but it was a minor impact compared to water vapour overall. Sensitivity results showed that reducing the elevated water vapour by about 80% over the Canary Islands resulted in large reductions in SW heating rates than dust changes at the top of the SAL. Sensitivity results indicate that heating rates are more sensitive to water vapour changes than dust effects. In addition, SW heating rates are also sensitive for the Caribbean region, as shown in the sensitivity calculations by reducing the dusty outbreak water vapour down by 80%, but with a weaker effect compared to the sensitivity over the Canary Islands.

Using LEM simulations, I showed that wind shear did not have a significant impact on creating or maintaining the well-mixed layers over the Canary Islands nor for the Caribbean region, for our cases studied.

LEM studies corresponding with using literature heating rates (dust radiative properties without water vapour) illustrated that a stable layer with a SAL intrusion of dusty air would transition from a stable layer to a well-mixed layer within 8 hours after dust was introduced into a layer. This timescale has not been assessed previously. An LEM study was performed to evaluate how long it would take for a well-mixed layer to revert back into a stratified layer once the dust was removed. From our simulations, once the well-mixed profile was formed it could last for very long periods of time of at least a week with only some stabilising.

The impact of the intruding SAL on the atmospheric stability was assessed using CAPE and CIN for all locations. Relative to the non-dusty profile, CIN was larger just under the SAL and acted to inhibit convection; whereas, CAPE was increased in the SAL. These are important factors for downwind where convection may initiate and be inhibited by the CIN.

Various sensitivities were explored in this research including sensitivity of dust size distribution and dust mass profile results to dust density, fall velocities of dust, impact of refractive index on size distribution, kinematic viscosity, optical properties, aging, etc. It was found that there was significant sensitivity to these, especially fall velocity through shape considerations (spherical and non-spherical) and dust density (which affected integrated dust mass and fall velocity). The thesis findings show that the difference in the total mass of dust calculated based on BRSedT between assuming spherical and non-spherical particle shapes after 7 days of transported across the Atlantic is larger than that calculated for dust transported over 4 days towards the Canary Islands, where percentage differences for flights FB604, FB605, FB612 and FB699 are 60.05%, 83.77%, 26.1% and 95.93%, while for Canary Islands the values are 18.09%, 60.49%, 3.8% and 7.4%, respectively. Sensitivity test also shows that using fall velocity assuming a spherical shape with density of dust of 2 g/cm^3 and with viscosity of 0.000015 m^2/s provides reasonable agreement between sedimented dust and the observed dust profiles for flight measurements over the Canary Islands. It was noted that using low and high fall velocities does not provide good agreement. This can be explained by the density of dust since the current thesis determined fall velocities using a density of 2 g/cm^3, while density of dust with values of 1.5 g/cm^3 and 2.5 g/cm^3 were used for low and high fall velocity calculations. Consequently, I should consider the cases to be representative rather than exact modelling of exact conditions. Efforts have been made to reduce sensitivities or influences where possible. For example, sea salt was expected to impact on the profiles in the MBL and so an estimate was performed and subtracted from the observed aerosol

profile. The sea salt concentration was found to have a minor impact on the results of radiative effects over the Canary Islands, but may affect the MBL results over the Caribbean region, where the percentage differences in the concentration averages between dust and sea salt in those regions were about 6.5 % and 15 % within the MBL, respectively.

As mentioned, the BRSedT model was developed to enable an estimate of the dust being transported to the Caribbean so that the LEM could be used to assess whether dust and water vapour were influencing the somewhat well-mixed structures far from the African sources. The BRSedT results also showed that the turbulent diffusion could maintain dust particles even at the top of dust layer for long distances from the African land.

An assessment was performed to determine if the observed well-mixed thermodynamic structures were being maintained at long distances away from African and into the Caribbean. Caribbean observations indicated that there were partially well-mixed layers that were present during dusty outbreak days and not present on non-dusty days. It was questioned if these structures were still being driven by dust or water vapour from the outbreak? A new bin resolved quasi-Lagrangian dust transport model, BRSedT, was developed to predict the dust altitudes transported and then LEM modelling of the Caribbean was performed for 8 hours simulations. The locations studied were Guadeloupe, Bahamas, Cayman Islands, Puerto Rico, and Florida. Locations that were noted from satellite to be in the path of the dust were Guadeloupe and Puerto Rico. They both had significant portions of their profiles with somewhat mixed layers whereas all the other locations had stratified profiles. LEM simulations isolating water vapour (representative of dusty or non-dusty), dust, and other gases showed that elevated water vapour was the dominant factor that had a significant influence on the structure and once again the night-time LW cooling was the most important. Dust and water vapour at these levels in the Caribbean progress the thermodynamic profiles towards well-mixed structure but are less strong than over the Canary Islands, closer to Africa. Sensitivity results show that reducing dusty wv in the radiation by about 80% over the Canary Islands reduces SW heating rates by about 2.5 K/day, while over Puerto Rico the heating rates dropped by about 1 K/day. In addition, SW heating rates are more sensitive to the water vapour changes than dust impacts at or near the top of the SAL, while dust tended to have some degree of significance and sensitivity at the lower levels of the SAL.

6.2 Limitations

There are several limitations in this work.

- The research is based on a small set of flights over two years and only a handful of dusty cases. It is possible that the outbreaks studied are not representative of the typical conditions. This is further extended to the limited sampling of measurements in time and space in order to derive size distributions.
- The dust sedimentation was particularly sensitive to dust particle density, fall velocity dependence on particle shape and fluid kinematic viscosity, as well as the refractive index impact through altering the derived size distributions. Although steps were taken to choose the most appropriate values and test sensitivities, it is possible that the appropriate values in the future could be better constrained in the future.
- The work showed that the leading influence on the well-mixed structures was water vapour but I am unsure of the origin of the high water vapour levels in the SAL and how common they are. Based on trajectory analysis, it is possible that the history of these dust outbreaks could be long times spent over the Atlantic Ocean and then advects over the dust source region and then convection transports the water vapour to higher altitudes.
- The impact of non-sphericity on optical properties and hence heating rates was not considered in the thesis. The shape effects were, however, used to test for effects on fall velocity including the non-spherical shape assumption. The optical properties and hence the heating rates are very approximate as the shapes of dust are countless. The composition of the dust can also vary from particle to particle and change with aging which is another area that can affect results.
- The radiation was run off-line to the LEM simulations so there was no interaction between the heating rates, the motions of the air and dust and the radiative heating rates. Also, another limitation has been not modelling the dust within the LEM.
- Not having dust measurements in the Caribbean has been a significant limitation. As a consequence, the BRSedT model had to be developed to estimate the dust size distributions. The modelling using BRSedT model was a 1D quasi-Lagrangian model is approximate and is useful for estimating the possible effects of dusty layers reaching the Caribbean but measurements locally would have been better.
- The reliance of the BRSedT on various models such as ECMWF for surface fluxes and subsidence. The HYSPLIT model for advection which relies on coarse resolution models for the dynamics and crude treatments of convective motion. Finally, the assumption about dust from the continent being uniform to the values measured from the flights in order to calculate the advected amounts.

6.3 Recommendations for future work

Suggestions for future work would be the following:

1. Most important would be to assess how frequently the water vapour is high in the dust outbreaks like was observed. The role of water vapour was very important for influencing the well mixed layers and so to know how frequently these high amounts occur in dust outbreaks would be high priority. Also, to understand how the high water vapour makes it into the SAL and where the water vapour is coming from. This would be the most important follow on work from the research.
2. Research into improving the parameters of particle density, fall velocity and RI.
3. Use field campaigns in the Caribbean that measure dust size distributions to confirm the results about dusty outbreak effects affecting structure at far distances from Africa.
4. Investigate the potential of using non spherical particles to obtain the size distributions from the PCASP and CDP.
5. Use other campaigns in the Atlantic to evaluate whether the results found in this work were the same for other years.
6. Perform the study with a version of the LEM with a fully coupled radiation scheme and size resolved aerosol. This could be done by updating the LEM to handle 30+ tracers or the dust could be input into the GLOMAP model to do the aerosol tracer transport and use coupled radiation.
7. Evaluate the evolution of the dust for future climates. Use climate simulations and study the future outbreaks of dust and water vapour to see how changes to the African Easterly Jet may change over time and how this would influence the dust transport.
8. Focus on the effects of the stability changes in the atmosphere on the downwind large-scale on cloud development and storm generation (i.e. hurricanes).

References

Ackerman, S. A., & Chung, H. (1992). Radiative effects of airborne dust on regional energy budgets at the top of the atmosphere. *Journal of Applied Meteorology*, *31*(2), 223-233.

Alamirew, N.K., Todd, M.C., Ryder, C.L., Marsham, J.H. and Wang, Y. 2018. The early summertime Saharan heat low: sensitivity of the radiation budget and atmospheric heating to water vapour and dust aerosol. *Atmospheric Chemistry and Physics*, 18 (2), pp. 1241-1262.

Allen, C. J., Washington, R., and Saci, A. 2015. Dust detection from ground-based observations in the summer global dust maximum: results from Fennec 2011 and 2012 and implications for modelling and field observations. *Journal of Geophysical Research: Atmospheres*, 120 (3), pp. 897–916.

Allen, C. J., Washington, R., and Engelstaedter, S. 2013. Dust emission and transport mechanisms in the central Sahara: FENNEC ground-based observations from Bordj Badji Mokhtar, June 2011. *Journal of Geophysical Research: Atmospheres*, 118 (12), pp. 6212-6232.

Alonso-Pérez, S., Cuevas, E., Querol, X., Viana, M., & Guerra, J. C. 2007. Impact of the Saharan dust outbreaks on the ambient levels of total suspended particles (TSP) in the marine boundary layer (MBL) of the Subtropical Eastern North Atlantic Ocean. *Atmospheric Environment*, *41*(40), 9468-9480.

Alpert, P., and Ganor, E. 2001. Sahara mineral dust measurements from TOMS: Comparison to surface observations over the Middle East for the extreme dust storm, March 14–17, 1998. *Journal of Geophysical Research: Atmospheres*, 106 (D16), pp. 18275-18286.

Anderson, J. C., Wang, J., Zeng, J., Leptoukh, G., Petrenko, M., Ichoku, C., & Hu, C. (2013). Long-term statistical assessment of Aqua-MODIS aerosol optical depth over coastal regions: bias characteristics and uncertainty sources. *Tellus B: Chemical and Physical Meteorology*, *65*(1), 20805.

Ansmann, A., Petzold, A., Kandler, K., Tegen, I. N. A., Wendisch, M., Mueller, D., ... & Heintzenberg, J. 2011. Saharan Mineral Dust Experiments SAMUM–1 and SAMUM–2: what have we learned?. *Tellus B: Chemical and Physical Meteorology*, 63(4), 403-429.

Arimoto, R.R.A.B.J.C.K., Duce, R.A., Ray, B.J. and Unni, C.K. 1985. Atmospheric trace elements at Enewetak Atoll: 2. Transport to the ocean by wet and dry deposition. *Journal of Geophysical Research: Atmospheres*, 90 (D1), pp. 2391-2408.

Astitha, M., Lelieveld, J., Abdel Kader, M., Pozzer, A., & Meij, A. D. 2012. Parameterization of dust emissions in the global atmospheric chemistry-climate model EMAC: impact of nudging and soil properties. *Atmospheric Chemistry and Physics*, 12(22), 11057-11083.

Bangalath, H. K., and Stenchikov, G. 2015. Role of dust direct radiative effect on the tropical rain belt over Middle East and North Africa: A high-resolution AGCM study. *Journal of Geophysical Research: Atmospheres*, 120 (10), pp. 4564-4584.

Bellouin, N., Boucher, O., Haywood, J., and Reddy, M. S. 2005. Global estimate of aerosol direct radiative forcing from satellite measurements. *Nature*, 438 (7071), p.1138.

Bergametti, G., Gomes, L., Coudé-Gaussen, G., Rognon, P., and Le Coustumer, M. N. 1989. African dust observed over Canary Islands: Source-regions identification and transport pattern for some summer situations. *Journal of Geophysical Research: Atmospheres*, 94 (D12), pp. 14855-14864.

Bergstrom, R. W., Pilewskie, P., Schmid, B., & Russell, P. B. 2003. Estimates of the spectral aerosol single scattering albedo and aerosol radiative effects during SAFARI 2000. *Journal of Geophysical Research: Atmospheres*, 108(D13).

Birch, C. E., Parker, D. J., Marsham, J. H., and Devine, G. M. 2012. The effect of orography and surface albedo on stratification in the summertime Saharan boundary layer: Dynamics and implications for dust transport. *Journal of Geophysical Research: Atmospheres*, 117 (D5).

Bischoff, T., & Schneider, T. 2016. The equatorial energy balance, ITCZ position, and double-ITCZ bifurcations. *Journal of Climate*, 29(8), 2997-3013.

Blanchard, D. O. 1998. Assessing the vertical distribution of convective available potential energy. *Weather and Forecasting*, 13 (3), pp. 870-877.

Bogner, P. B., Barnes, G. M., & Franklin, J. L. 2000. Conditional instability and shear for six hurricanes over the Atlantic Ocean. *Weather and forecasting*, *15*(2), pp.192-207.

Bristow, C. S., Hudson-Edwards, K. A., and Chappell, A. 2010. 'Fertilizing the Amazon and equatorial Atlantic with West African dust'. *Geophysical Research Letters*, 37 (14).

Broccoli, A. J., Dahl, K. A., & Stouffer, R. J. 2006. Response of the ITCZ to Northern Hemisphere cooling. *Geophysical Research Letters*, *33*(1).

Brown, A. R. 1999. The sensitivity of large-eddy simulations of shallow cumulus convection to resolution and sub-grid model. *Quarterly Journal of the Royal Meteorological Society*, 125 (554), pp. 469-482.

Burpee, R. W. 1974. Characteristics of North African easterly waves during the summers of 1968 and 1969. *Journal of the Atmospheric Sciences*, 31(6), pp.1556-1570.

Cabello, M., Orza, J. A. G., Dueñas, C., Liger, E., Gordo, E., and Cañete, S. 2016. Back-trajectory analysis of African dust outbreaks at a coastal city in southern Spain: Selection of starting heights and assessment of African and concurrent Mediterranean contributions. *Atmospheric Environment*, 140, pp. 10-21.

Carlson, T.N. and Benjamin, S.G. 1980. Radiative heating rates for Saharan dust. *Journal of the Atmospheric Sciences*, 37 (1), pp. 193-213.

Carlson, T. N. 2016. The Saharan Elevated Mixed Layer and its Aerosol Optical Depth. *The Open Atmospheric Science Journal.* [Online]. 10 (1). [Accessed 19 July 2016]. Available from: https://benthamopen.com/FULLTEXT/TOASCJ-10-26.

Carrillo, J., Guerra, J. C., Cuevas, E., & Barrancos, J. 2016. Characterization of the marine boundary layer and the trade-wind inversion over the sub-tropical North Atlantic. Boundary-layer meteorology, 158(2), 311-330.

Camenen, B. 2007. Simple and general formula for the settling velocity of particles. *Journal of Hydraulic Engineering*, 133 (2), 229–233.

Chen, S. H., Wang, S. H., and Waylonis, M. 2010. Modification of Saharan air layer and environmental shear over the eastern Atlantic Ocean by dust-radiation effects. *Journal of Geophysical Research: Atmospheres*, 115 (D21), pp. 1984–2012.

Chouza, F., Reitebuch, O., Benedetti, A. and Weinzierl, B. 2016. Saharan dust long-range transport across the Atlantic studied by an airborne Doppler wind lidar and the MACC model. *Atmospheric Chemistry and Physics*, 16 (18).

Colarco, P. R., Toon, O. B., and Holben, B. N. 2003. Saharan dust transport to the Caribbean during PRIDE: 1. Influence of dust sources and removal mechanisms on the timing and magnitude of downwind aerosol optical depth events from simulations of in situ and remote sensing observations. *Journal of Geophysical Research: Atmospheres*, 108 (D19).

Cuesta, J., Marsham, J. H., Parker, D. J., and Flamant, C. 2009. Dynamical mechanisms controlling the vertical redistribution of dust and the thermodynamic structure of the West Saharan atmospheric boundary layer during summer. *Atmospheric Science Letters*, 10 (1), pp. 34-42.

De Boer BSc, S., Siebesma, A. P., and de Roode, S. R. 2010. Scale Dependence of Parameterizations for Shallow Cumulus Clouds. Master's thesis, Department of Multi-Scale Physics, Faculty of Applied Sciences, Delft University of Technology.

Denjean, C., Caquineau, S., Desboeufs, K., Laurent, B., Maille, M., Quiñones Rosado, M., ... & Formenti, P. 2015. Long-range transport across the Atlantic in summertime does not enhance the hygroscopicity of African mineral dust. *Geophysical Research Letters*, 42(18), 7835-7843.

Dentener, F. J., Carmichael, G. R., Zhang, Y., Lelieveld, J., and Crutzen, P. J. 1996. Role of mineral aerosol as a reactive surface in the global troposphere. *Journal of Geophysical Research: Atmospheres*, 101 (D17), pp. 22869-22889.

Dickinson, R. E., & Cicerone, R. J., 1986. Future global warming from atmospheric trace gases. *nature*, 319(6049), 109.

Dubovik, O., Holben, B., Eck, T. F., Smirnov, A., Kaufman, Y. J., King, M. D., ... & Slutsker, I. 2002. Variability of absorption and optical properties of key aerosol types observed in worldwide locations. *Journal of the atmospheric sciences*, 59(3), 590-608.

Doronzo, D. M., Khalaf, E. A., Dellino, P., de Tullio, M. D., Dioguardi, F., Gurioli, L., Mele, D., Pascazio, G., and Sulpizio, R. 2015. Local impact of dust storms around a suburban building in arid and semi-arid regions: numerical simulation examples from Dubai and Riyadh, Arabian Peninsula. *Arabian Journal of Geosciences*, 8 (9), pp. 7359-7369.

Dunion, J. P., & Velden, C. S. 2004. The impact of the Saharan air layer on Atlantic tropical cyclone activity. *Bulletin of the American Meteorological Society*, *85*(3), 353-366.

Edwards, J. M. and Slingo, A. 1996. Studies with a flexible new radiation code. I: Choosing a configuration for a large-scale model. *Quarterly Journal of the Royal Meteorological Society*, 122, pp. 689-719.

Edwards, J. M. 2007. Oceanic latent heat fluxes: Consistency with the atmospheric hydrological and energy cycles and general circulation modeling. *Journal of Geophysical Research: Atmospheres*, 112(D6).

Engelstaedter, S., Tegen, I., and Washington, R. 2006. North African dust emissions and transport. *Earth-Science Reviews*, 79 (1), pp. 73-100.

Engelstaedter, S., & Washington, R. 2007. Atmospheric controls on the annual cycle of North African dust. *Journal of Geophysical Research: Atmospheres*, *112*(D3).

Evan, A. T., Flamant, C., Lavaysse, C., Kocha, C., & Saci, A. 2015. Water vapor–forced greenhouse warming over the Sahara Desert and the recent recovery from the Sahelian drought. *Journal of Climate*, 28(1), 108-123.

Falke, S. R., Husar, R. B., and Schichtel, B. A. 2001. Fusion of SeaWiFS and TOMS satellite data with surface observations and topographic data during extreme aerosol events. *Journal of the Air and Waste Management Association*, 51 (11), pp. 1579-1585.

Feltz, W. F., Smith, W. L., Howell, H. B., Knuteson, R. O., Woolf, H., and Revercomb, H. E. 2003. Near-continuous profiling of temperature, moisture, and atmospheric stability using the Atmospheric Emitted Radiance Interferometer (AERI). *Journal of Applied Meteorology*, 42 (5), pp. 584-597.

Feng, S., and Fu, Q. 2013. Expansion of global drylands under a warming climate. Atmos. *Chem. Phys*, 13 (19), pp. 10-081.

Fontaine, B., & Janicot, S. 1992. Wind-field coherence and its variations over West Africa. *Journal of Climate*, 5(5), 512-524.

Formenti, P., Elbert, W., Maenhaut, W., Haywood, J., & Andreae, M. O. 2003. Chemical composition of mineral dust aerosol during the Saharan Dust Experiment (SHADE) airborne campaign in the Cape Verde region, September 2000. *Journal of Geophysical Research: Atmospheres*, 108(D18).

Formenti, P. 2011. Interactive comment on "Airborne observations of mineral dust over Western Africa in the summer monsoon season: spatial and vertical variability of physico-chemical and optical properties" by P. Formenti et al. *Atmos. Chem. Phys. Discuss*., 11, C956–C959.

Fouquart, Y., Bonnel, B., Brogniez, G., Buriez, J. C., Smith, L., Morcrette, J. J., & Cerf, A. 1987. Observations of Saharan aerosols: Results of ECLATS field experiment. Part II: Broadband radiative characteristics of the aerosols and vertical radiative flux divergence. *Journal of climate and applied meteorology*, 26(1), 38-52.

Garcia-Carreras, L., Parker, D. J., Marsham, J. H., Rosenberg, P. D., Brooks, I. M., Lock, A. P., Marenco, F., Mcquaid, J. B., and Hobby, M. 2015. The turbulent structure and diurnal growth of the Saharan atmospheric boundary layer. *Journal of the Atmospheric Sciences*. [Online]. 72 (2), pp. 693-713. [Accessed 3 February 2015]. Available from: https://doi.org/10.1175/JAS-D-13-0384.1.

Gasteiger, J., Groß, S., Sauer, D., Haarig, M., Ansmann, A., & Weinzierl, B. 2017. Particle settling and vertical mixing in the Saharan Air Layer as seen from an integrated model, lidar, and in situ perspective. *Atmospheric Chemistry and Physics*, *17*(1), 297-311.

Gasteiger, J., Wiegner, M., Gross, S., Freudenthaler, V., Toledano, C., Tesche, M., & Kandler, K. 2011. Modelling lidar-relevant optical properties of complex mineral dust aerosols. *Tellus B: Chemical and Physical Meteorology*, *63*(4), 725-741.

Ginoux, P. 2003. Effects of nonsphericity on mineral dust modeling. *Journal of Geophysical Research: Atmospheres*, *108*(D2).

Giménez, J., Pastor, C., Castañer, R., Nicolás, J., Crespo, J., and Carratalá, A. 2010. Influence of Saharan dust outbreaks and atmospheric stability upon vertical profiles of size-segregated aerosols and water vapor. *Atmospheric Environment*, 44 (3), pp. 338-346.

Gleeson, E., Toll, V., Nielsen, K. P., Rontu, L., & Mašek, J. 2015. Effects of aerosols on solar radiation in the ALADIN-HIRLAM NWP system. *Atmospheric Chemistry & Physics Discussions*, 15(22).

Gong, S. L., Barrie, L. A., & Blanchet, J. P. 1997. Modeling sea-salt aerosols in the atmosphere: 1. Model development. *Journal of Geophysical Research: Atmospheres*, 102(D3), 3805-3818.

Goudie, A., and Middleton, N. J. 2006. 'Desert dust in the global system'. *Springer Science and Business Media*. Germany.

Goudie, A. S., and Middleton, N. J. 2001. Saharan dust storms: nature and consequences. *Earth-Science Reviews*, 56 (1), pp. 179-204.

Griffin, D. W. 2007. Atmospheric movement of microorganisms in clouds of desert dust and implications for human health. *Clinical microbiology reviews*, 20 (3), pp. 459-477.

Gross, A., Goren, T., Pio, C., Cardoso, J., Tirosh, O., Todd, M.C., Rosenfeld, D., Weiner, T., Custódio, D. and Angert, A. 2015. Variability in sources and concentrations of Saharan dust phosphorus over the Atlantic Ocean. *Environmental Science and Technology Letters*, 2 (2), pp. 31-37.

Guichard, F., Parsons, D., & Miller, E. 2000. Thermodynamic and radiative impact of the correction of sounding humidity bias in the tropics. *Journal of climate*, 13(20), 3611-3624.

Guo, H., Liu, Y., Daum, P. H., Senum, G. I., & Tao, W. K. 2008. Characteristics of vertical velocity in marine stratocumulus: comparison of large eddy simulations with observations. *Environmental Research Letters*, 3(4), 045020.

https://nsidc.org/cryosphere/seaice/processes/albedo.html, accessed Sept 26th, 2018.

Harrison, S. P., Kohfeld, K. E., Roelandt, C., and Claquin, T. 2001. The role of dust in climate changes today, at the last glacial maximum and in the future. *Earth-Science Reviews*, 54 (1), pp. 43-80.

Haywood, J. M., Francis, P. N., Glew, M. D., and Taylor, J. P. 2001. Optical properties and direct radiative effect of Saharan dust: A case study of two Saharan dust outbreaks using aircraft data. *Journal of Geophysical Research: Atmospheres*, 106 (D16), pp. 18417-18430.

Haywood, J., Francis, P., Osborne, S., Glew, M., Loeb, N., Highwood, E., Tanre´, D., Myhre, G., Formenti, P., and Hirst, E. 2003. Radiative properties and direct radiative effect of Saharan dust measured by the C-130 aircraft during SHADE: 1. Solar spectrum. *Journal of Geophysical Research: Atmospheres*, 108 (D18), pp. 1984–2012.

Haywood, J. M., Allan, R. P., Culverwell, I., Slingo, T., Milton, S., Edwards, J., & Clerbaux, N. 2005. Can desert dust explain the outgoing longwave radiation anomaly over the Sahara during July 2003?. *Journal of Geophysical Research: Atmospheres*, 110(D5).

Heald, C. L., Ridley, D. A., Kroll, J. H., Barrett, S. R. H., Cady-Pereira, K. E., Alvarado, M. J., & Holmes, C. D. 2014. Contrasting the direct radiative effect and direct radiative forcing of aerosols.

Heinold, B., Tegen, I., Schepanski, K., and Hellmuth, O. 2008. Dust radiative feedback on Saharan boundary layer dynamics and dust mobilization. *Geophysical Research Letters*, 35 (20).

Heinold, B., Schepanski, K., Gieseler, D. and Ulrich, M. 2017, April. Mixing and Deposition of Saharan Dust during Transatlantic Transport. *In EGU General Assembly Conference Abstracts*, 19, p. 5334.

Hill, A. A., Dobbie, S., and Yin, Y. 2008. The impact of aerosols on non-precipitating marine stratocumulus. I: Model description and prediction of the indirect effect. *Quarterly Journal of the Royal Meteorological Society*, 134 (634), pp. 1143-1154.

Hill, A. A., and Dobbie, S. 2008. The impact of aerosols on non-precipitating marine stratocumulus. II: The semi-direct effect. *Quarterly Journal of the Royal Meteorological Society*, 134 (634), pp. 1155-1165.

Holton, J.R. and Hakim, G.J., 2012. An introduction to dynamic meteorology (Vol. 88). Academic press.

Holtslag, A. A. M., & Boville, B. A. 1993. Local versus nonlocal boundary-layer diffusion in a global climate model. *Journal of Climate*, *6*(10), 1825-1842.

Hsu, N.C., Herman, J.R. and Weaver, C. 2000. Determination of radiative forcing of Saharan dust using combined TOMS and ERBE data. *Journal of Geophysical Research: Atmospheres*, 105 (D16), pp. 20649-20661.

Huang, J., Wang, T., Wang, W., Li, Z., and Yan, H. 2014. Climate effects of dust aerosols over East Asian arid and semiarid regions. *Journal of Geophysical Research: Atmospheres*, 119 (19). pp. 11-398.

Huang, J., Fu, Q., Su, J., Tang, Q., Minnis, P., Hu, Y., and Zhao, Q. 2009. Taklimakan dust aerosol radiative heating derived from CALIPSO observations using the Fu-Liou radiation model with CERES constraints. *Atmospheric Chemistry and Physics*, 9 (12), pp. 4011-4021.

Huneeus, N., Schulz, M., Balkanski, Y., Griesfeller, J., Prospero, M. J., Kinne, S., Prospero, J., Bauer, S., Boucher, O., Chin, M., Dentener, F., and Diehl, T. 2011. Global dust model intercomparison in AeroCom phase I. *Atmospheric Chemistry and Physics*, 11, pp. 7781-7816.

Hu, R.M. and Sokhi, R.S. 2009. Light scattering and absorption properties of dust particles retrieved from satellite measurements. *Journal of Quantitative Spectroscopy and Radiative Transfer*, 110 (14-16), pp. 1698-1705.

Inomata, Y., Igarashi, Y., Chiba, M., Shinoda, Y. and Takahashi, H. 2009. Dry and wet deposition of water-insoluble dust and water-soluble chemical species during spring 2007 in Tsukuba, Japan. *Atmospheric Environment*, 43 (29), pp. 4503-4512.

Córdoba-Jabonero, C., Andrey-Andres, J., Gomez, L., Adame, J. A., Sorribas, M., Navarro-Comas, M., ... & Gil-Ojeda, M. 2016. Vertical mass impact and features of Saharan dust intrusions derived from ground-based remote sensing in synergy with airborne in-situ measurements. *Atmospheric Environment*, 142, 420-429.

Córdoba-Jabonero, C., Sicard, M., Ansmann, A., Águila, A. D., & Baars, H. (2018). Separation of the optical and mass features of particle components in different aerosol mixtures by using POLIPHON retrievals in synergy with continuous polarized Micro-Pulse Lidar (P-MPL) measurements. *Atmospheric Measurement Techniques*, *11*(8), 4775-4795.

Jacobson, M.Z., 2004. Climate response of fossil fuel and biofuel soot, accounting for soot's feedback to snow and sea ice albedo and emissivity. *Journal of Geophysical Research: Atmospheres*, 109(D21).

Janicot, S., Kamga, F., Lafore, J. P., Biasutti, M., Knippertz, P., Taylor, C., & Thorncroft, C. 2015. Key research and prediction challenges for West and Central Africa. Special Issue on Monsoons: Advancing understanding of monsoon variability and improving prediction, 10.

Jeričević, A., & Večenaj, Ž. 2009. Improvement of vertical diffusion analytic schemes under stable atmospheric conditions. *Boundary-layer meteorology*, *131*(2), 293-307.

Jickells, T. D., An, Z. S., Andersen, K. K., Baker, A. R., Bergametti, G., Brooks, N., Cao, J., Boyd, P., Duce, R., Hunter, K., Kubilay, N., LaRoche, J., Liss, P., Mahowald, N., Prospero, J., Ridgwell, A., Tegen, I., and Torres, R. 2005. Global iron connections between desert dust, ocean biogeochemistry, and climate. *Science*, 308 (5718), pp. 67-71.

Ji, Z., Wang, G., Pal, J. S., and Yu, M. 2016. Potential climate effect of mineral aerosols over West Africa. Part I: model validation and contemporary climate evaluation. *Climate dynamics*, 46 (3-4), pp. 1223-1239.

Ji, Z., Wang, G., Yu, M., and Pal, J. S. 2018. Potential climate effect of mineral aerosols over West Africa: Part II—contribution of dust and land cover to future climate change. *Climate Dynamics*, 50 (7-8), pp. 2335-2353.

Jochum, M., Malanotte-Rizzoli, P., & Busalacchi, A. 2004. Tropical instability waves in the Atlantic Ocean. Ocean Modelling, 7(1-2), pp. 145-163.

Johnson, B. T., and Osborne, S. R. 2011. Physical and optical properties of mineral dust aerosol measured by aircraft during the GERBILS campaign. *Quarterly Journal of the Royal Meteorological Society*, 137 (658), pp. 1117-1130.

Jones, D. R. 1953. Note on observed vertical wind shear at low levels over the ocean. *Bulletin of the American Meteorological Society*, *34*(9), 393-396.

Kaly, F., Marticoréna, B., Chatenet, B., Rajot, J.L., Janicot, S., Niang, A., Yahi, H., Thiria, S., Maman, A., Zakou, A. and Coulibaly, B.S., 2015. Variability of mineral dust concentrations over West Africa monitored by the Sahelian Dust Transect. Atmospheric Research, 164, pp.226-241.

Karyampudi, V. M., Palm, S. P., Reagen, J. A., Fang, H., Grant, W. B., Hoff, R. M., ... & Melfi, S. H. 1999. Validation of the Saharan dust plume conceptual model using lidar, Meteosat, and ECMWF data. *Bulletin of the American Meteorological Society*, 80(6), 1045-1076.

Kaufman, Y. J., Koren, I., Remer, L. A., Tanré, D., Ginoux, P., and Fan, S. 2005. Dust transport and deposition observed from the Terra-Moderate Resolution Imaging Spectroradiometer (MODIS) spacecraft over the Atlantic Ocean. *Journal of Geophysical Research: Atmospheres*, 110 (D10), pp. 1984–2012.

Kaufman, Y. J., Koren, I., Remer, L. A., Rosenfeld, D., and Rudich, Y. 2005b. The effect of smoke, dust, and pollution aerosol on shallow cloud development over the Atlantic Ocean. *Proceedings of the National Academy of Sciences of the United States of America*, 102 (32), pp. 11207-11212.

Kellogg, C. A., and Griffin, D. W. 2006. Aerobiology and the global transport of desert dust. *Trends in ecology and evolution*, 21 (11), pp. 638-644.

Kienast, S. S., Winckler, G., Lippold, J., Albani, S., and Mahowald, N. M. 2016. 'Tracing Dust Input to the Global Ocean using Thorium Isotopes in Marine Sediments: ThoroMap'. *Global Biogeochemical Cycles*.

Kim, K.H., Kabir, E. and Kabir, S. 2015. A review on the human health impact of airborne particulate matter. *Environment international*, 74, pp. 136-143.

Kleb, M. M., Chen, G., Ferrare, R. A., Zhang, H., Thornhill, K. L., Slusher, D. L., ... & Anderson, B. E. 2011. Observations of Saharan dust microphysical and optical properties from the Eastern Atlantic during NAMMA airborne field campaign.

Knippertz, P., and Stuut, J., W., 2014. Mineral dust: On Composition, Morphology, and Size Distribution of Airborne Mineral Dust, pp.15-49.

Knippertz, P., Tesche, M., Heinold, B., Kandler, K., Toledano, C. and Esselborn, M., 2011. Dust mobilization and aerosol transport from West Africa to Cape Verde—a meteorological overview of SAMUM–2. Tellus B*: Chemical and Physical Meteorology*, 63(4), pp.430-447.

Koepke, P., Gasteiger, J., & Hess, M. 2015. Optical properties of desert aerosol with non-spherical mineral particles: data incorporated to OPAC. *Atmospheric Chemistry and Physics*, *15*(10), 5947-5956.

Koren, I., Kaufman, Y. J., Washington, R., Todd, M. C., Rudich, Y., Martins, J. V., and Rosenfeld, D. 2006. The Bodélé depression: a single spot in the Sahara that provides most of the mineral dust to the Amazon forest. *Environmental Research Letters*, 1 (1), p. 014005.

Kok, J. F., Parteli, E. J., Michaels, T. I., & Karam, D. B. 2012. The physics of wind-blown sand and dust. *Reports on progress in Physics*, 75(10), 106901.

Lacagnina, C., Hasekamp, O. P., Bian, H., Curci, G., Myhre, G., Noije, T., ... & Zhang, K. 2015. Aerosol single-scattering albedo over the global oceans: Comparing PARASOL retrievals with AERONET, OMI, and AeroCom models estimates. *Journal of Geophysical Research: Atmospheres*, 120(18), 9814-9836.

Lafore, J. P., Flamant, C., Giraud, V., Guichard, F., Knippertz, P., Mahfouf, J. F., ... & Williams, E. R. 2010. Introduction to the AMMA Special Issue on 'Advances in understanding atmospheric processes over West Africa through the AMMA field campaign'. *Quarterly Journal of the Royal Meteorological Society*, *136*(S1), 2-7.

Lashof, D. A., & Ahuja, D. R., 1990. Relative contributions of greenhouse gas emissions to global warming. *Nature*, 344(6266), 529.

Lau, K. M., Kim, K. M., Sud, Y. C., & Walker, G. K. 2009. A GCM study of responses of the atmospheric water cycle of West Africa and the Atlantic to Saharan dust radiative forcing.

Lebel, T., Parker, D.J., Flamant, C., Bourlès, B., Marticoréna, B., Mougin, E., Peugeot, C., Diedhiou, A., Haywood, J.M., Ngamini, J.B. and Polcher, J., 2010. The AMMA field campaigns: multiscale and multidisciplinary observations in the West African region. *Quarterly Journal of the Royal Meteorological Society*, 136(S1), pp.8-33.

Lee, I. Y. 1983. Simulation of transport and removal processes of the Saharan dust. *Journal of Climate and Applied Meteorology*, *22*(4), 632-639.

Lemaître, C., Flamant, C., Cuesta, J., Raut, J. C., Chazette, P., Formenti, P., and Pelon, J. 2010. Radiative heating rates profiles associated with a springtime case of Bodélé and Sudan dust transport over West Africa. *Atmospheric Chemistry and Physics*, 10 (17), pp. 8131-8150.

Lenschow, D. H., Lothon, M., Mayor, S. D., Sullivan, P. P., & Canut, G. 2012. A comparison of higher-order vertical velocity moments in the convective boundary layer from lidar with in situ measurements and large-eddy simulation. Boundary-layer meteorology, 143(1), 107-123.

Li, J., & Osada, K. 2007. Preferential settling of elongated mineral dust particles in the atmosphere. *Geophysical research letters*, 34(17).

Li, F., Vogelmann, A. M., and Ramanathan, V. 2004. Saharan dust aerosol radiative forcing measured from space. *Journal of Climate*, 17 (13), pp. 2558-2571.

Liou, K. N. 2002. An introduction to atmospheric radiation. *Elsevier*.

Liou, K. N. 1992. Radiation and cloud processes in the atmosphere. Theory, observation, and modeling.

Liu, R., He, R., Cui, X. and Ma, L.Q. 2018. Impact of particle size on distribution, bioaccessibility, and cytotoxicity of polycyclic aromatic hydrocarbons in indoor dust. *Journal of hazardous materials.* [Online]. 357, pp. 341-347. [Accessed 25 January 2018]. Available from: https://doi.org/10.1016/j.jhazmat.2018.05.058.

Loeb, N.G. and Manalo-Smith, N. 2005. Top-of-atmosphere direct radiative effect of aerosols over global oceans from merged CERES and MODIS observations. *Journal of Climate*, 18 (17), pp. 3506-3526.

Mallet, M., Tulet, P., Serça, D., Solmon, F., Dubovik, O., Pelon, J., Pont, V. and Thouron, O. 2009. Impact of dust aerosols on the radiative budget, surface heat fluxes, heating rate profiles and convective activity over West Africa during March 2006. *Atmospheric Chemistry and Physics*, 9 (18), pp. 7143-7160.

Mahowald, N. M., Baker, A. R., Bergametti, G., Brooks, N., Duce, R. A., Jickells, T. D., Kubilay, N., Prospero, J., and Tegen, I. 2005. Atmospheric global dust cycle and iron inputs to the ocean. *Global biogeochemical cycles*, 19 (4).

Manners, J. 2015. Socrates technical guide suite of community radiative transfer codes based on edwards and slingo. In Tech. Rep., Met Office, FitzRoy Rd, Exeter EX1 3PB.

Maring, H., Savoie, D. L., Izaguirre, M. A., Custals, L., and Reid, J. S. 2003. Mineral dust aerosol size distribution change during atmospheric transport. *Journal of Geophysical Research: Atmospheres*, 108 (D19).

Maring, H., Savoie, D. L., Izaguirre, M. A., McCormick, C., Arimoto, R., Prospero, J. M., & Pilinis, C. (2000). Aerosol physical and optical properties and their relationship to aerosol composition in the free troposphere at Izana, Tenerife, Canary Islands, during July 1995. *Journal of Geophysical Research: Atmospheres*, *105*(D11), 14677-14700.

Marsham, J. H., Dobbie, S., & Hogan, R. J. 2006. Evaluation of a large-eddy model simulation of a mixed-phase altocumulus cloud using microwave radiometer, lidar and Doppler radar data. Quarterly Journal of the Royal Meteorological Society: *A journal of the atmospheric sciences, applied meteorology and physical oceanography*, 132(618), 1693-1715.

Marsham, J.H., Parker, D.J., Todd, M.C., Banks, J.R., Brindley, H.E., Garcia-Carreras, L., Roberts, A.J. and Ryder, C.L. 2016. The contrasting roles of water and dust in controlling daily variations in radiative heating of the summertime Saharan heat low. *Atmospheric Chemistry and Physics*, 16 (5), pp. 3563-3575.

Marsham, J. H., Hobby, M., Allen, C. J. T., Banks, J. R., Bart, M., Brooks, B. J., ... & Martins, J. V. 2013. Meteorology and dust in the central Sahara: Observations from Fennec supersite-1 during the June 2011 Intensive Observation Period. *Journal of Geophysical Research: Atmospheres*, *118*(10), 4069-4089.

Marticorena, B., and Bergametti, G. 1995. Modeling the atmospheric dust cycle: 1. Design of a soil-derived dust emission scheme. *Journal of Geophysical Research: Atmospheres*, 100 (D8), pp. 16415-16430.

Marticorena, B., Chatenet, B., Rajot, J. L., Bergametti, G., Deroubaix, A., Vincent, J., ... & Koné, I. 2017. Mineral dust over west and central Sahel: Seasonal patterns of dry and wet deposition fluxes from a pluriannual sampling (2006–2012). *Journal of Geophysical Research: Atmospheres*, *122*(2), 1338-1364.

Matsuki, A., Schwarzenboeck, A., Venzac, H., Laj, P., Crumeyrolle, S., and Gomes, L. 2010. Cloud processing of mineral dust: direct comparison of cloud residual and clear sky particles during AMMA aircraft campaign in summer (2006). *Atmospheric Chemistry and Physics*, 10 (3), pp. 1057-1069.

Mbourou, G. N. T., Bertrand, J. J., & Nicholson, S. E. 1997. The diurnal and seasonal cycles of wind-borne dust over Africa north of the equator. *Journal of Applied Meteorology*, 36(7), 868-882.

McConnell, C. L., Highwood, E. J., Coe, H., Formenti, P., Anderson, B., Osborne, S., S. Nava K. Desboeufs, G. Chen M. A. J. & Harrison, .2008. Seasonal variations of the physical and optical characteristics of Saharan dust: Results from the Dust Outflow and Deposition to the Ocean (DODO) experiment. *Journal of Geophysical Research: Atmospheres*, 113(D14).

McConnell, C. L., Formenti, P., Highwood, E. J., & Harrison, M. A. J. 2010. Using aircraft measurements to determine the refractive index of Saharan dust during the DODO Experiments. *Atmospheric Chemistry and Physics*, *10*(6), 3081-3098.

McQuaid, J., Ryder, C. L., Flamant, C., Washington, R., Brindley, H., Highwood, E. J., and Woolley, A. 2013. Overview and Highlights of Airborne Observations over the Sahara during Fennec 2011 and 2012.

Menéndez, I., Diaz-Hernandez, J.L., Mangas, J., Alonso, I. and Sánchez-Soto, P.J., 2007. Airborne dust accumulation and soil development in the North-East sector of Gran Canaria (Canary Islands, Spain). *Journal of Arid Environments*, 71 (1), pp. 57-81.

Müller, T., Schladitz, A., Massling, A., Kaaden, N., Kandler, K., & Wiedensohler, A. (2009). Spectral absorption coefficients and imaginary parts of refractive indices of Saharan dust during SAMUM-1. *Tellus B: Chemical and Physical Meteorology*, *61*(1), 79-95.

Azorin-Molina, C., Menendez, M., McVicar, T. R., Acevedo, A., Vicente-Serrano, S. M., Cuevas, E., ... & Chen, D. 2018. Wind speed variability over the Canary Islands, 1948–2014: focusing on trend differences at the land–ocean interface and below–above the trade-wind inversion layer. *Climate Dynamics*, 50(11-12), 4061-4081.

Velasco-Merino, C., Mateos, D., Toledano, C., Prospero, J. M., Molinie, J., Euphrasie-Clotilde, L., ... & de Frutos, A. M. 2018. Impact of long-range transport over the Atlantic Ocean on Saharan

dust optical and microphysical properties based on AERONET data. *Atmospheric Chemistry and Physics*, 18(13), 9411-9424.

Monin, A. S, and Yaglom A. M., 1975. Statistics Fluid Mechanics (Cambridge, MA: MIT Press) p 683.

Monkam, D. 2002. Convective available potential energy (CAPE) in Northern Africa and tropical Atlantic and study of its connections with rainfall in Central and West Africa during Summer 1985. *Atmospheric research*, 62 (1-2), pp. 125-147.

Montgomery, R. B. 1947. Viscosity and thermal conductivity of air and diffusivity of water vapor in air. *Journal of Meteorology*, 4(6), 193-196.

Moulin, C., Lambert, C.E., Dulac, F. and Dayan, U. 1997. Control of atmospheric export of dust from North Africa by the North Atlantic Oscillation. *Nature*, 387 (6634), p. 691.

Meloni, D., Di Sarra, A., Di Iorio, T., and Fiocco, G. 2005. Influence of the vertical profile of Saharan dust on the visible direct radiative forcing. *Journal of Quantitative Spectroscopy and Radiative Transfer*, 93 (4), pp. 397-413.

Meloni, D., Junkermann, W., di Sarra, A., Cacciani, M., De Silvestri, L., Di Iorio, T., Estellés, V., Gómez-Amo, J.L., Pace, G. and Sferlazzo, D.M. 2015. Altitude-resolved shortwave and longwave radiative effects of desert dust in the Mediterranean during the GAMARF campaign: Indications of a net daily cooling in the dust layer. *Journal of Geophysical Research: Atmospheres*, 120 (8), pp. 3386-3407.

Myhre, G., Grini, A., Haywood, J. M., Stordal, F., Chatenet, B., Tanré, D., ... & Isaksen, I. S. 2003. Modeling the radiative impact of mineral dust during the Saharan Dust Experiment (SHADE) campaign. *Journal of Geophysical Research: Atmospheres*, 108(D18).

Newburgh, R. 2002. Conceptual difficulties with rates of change, or Zeno redux. *Physics education*, 37(2), 147.

Nicklin, K. J., Challinor, A., & Tompkins, A. 2011. The use of seasonal forecasts in a crop failure early warning system for West Africa. In *AGU Fall Meeting Abstracts*.

Nicholson, S.E., Nash, D.J., Chase, B.M., Grab, S.W., Shanahan, T.M., Verschuren, D., Asrat, A., Lézine, A.M. and Umer, M. 2013. Temperature variability over Africa during the last 2000 years. *The Holocene*, 23 (8), pp. 1085-1094.

Osada, H., 2014. Dynamical rigidity of stochastic Coulomb systems in infinite-dimensions. arXiv preprint arXiv:1405.6123.

Osborne, S. R., Johnson, B. T., Haywood, J. M., Baran, A. J., Harrison, M. A. J., & McConnell, C. L. 2008. Physical and optical properties of mineral dust aerosol during the Dust and Biomass-burning Experiment. *Journal of Geophysical Research: Atmospheres*, 113(D23).

Otto, S., Reus, M. D., Trautmann, T., Thomas, A., Wendisch, M., and Borrmann, S. 2007. Atmospheric radiative effects of an in situ measured Saharan dust plume and the role of large particles. *Atmospheric Chemistry and Physics*, 7 (18), pp. 4887-4903.

Parker, D. J., & Diop-Kane, M. (Eds.). 2017. Meteorology of tropical West Africa*: The forecasters' handbook*. John Wiley & Sons.

Parker, D.J., Fink, A., Janicot, S., Ngamini, J.B., Douglas, M., Afiesimama, E., Agusti-Panareda, A., Beljaars, A., Dide, F., Diedhiou, A. and Lebel, T. 2008. The AMMA radiosonde program and its implications for the future of atmospheric monitoring over Africa. *Bulletin of the American Meteorological Society*, 89 (7), pp. 1015-1028.

Parker, D. J., Burton, R. R., Diongue-Niang, A., Ellis, R. J., Felton, M., Taylor, C. M., ... & Tompkins, A. M. 2005. The diurnal cycle of the West African monsoon circulation. *Quarterly Journal of the Royal Meteorological Society: A journal of the atmospheric sciences, applied meteorology and physical oceanography*, *131*(611), 2839-2860.

Péré, J. C., Rivellini, L., Crumeyrolle, S., Chiapello, I., Minvielle, F., Thieuleux, F., ... & Popovici, I. 2018. Simulation of African dust properties and radiative effects during the 2015 SHADOW campaign in Senegal. *Atmospheric Research*, 199, 14-28.

Pinker, R. T., Bentamy, A., Katsaros, K. B., Ma, Y., & Li, C. 2014. Estimates of net heat fluxes over the Atlantic Ocean. *Journal of Geophysical Research: Oceans*, 119(1), 410-427.

Pleavin, T. D. 2013. Large eddy simulations of Arctic stratus clouds.

Prospero, J. M., Ginoux, P., Torres, O., Nicholson, S. E., and Gill, T. E. 2002. Environmental characterization of global sources of atmospheric soil dust identified with the Nimbus 7 Total Ozone Mapping Spectrometer (TOMS) absorbing aerosol product. *Reviews of geophysics*, 40 (1), pp. 2-1.

Prospero, J. M., and Lamb, P. J. 2003. African droughts and dust transport to the Caribbean: Climate change implications. *Science*, 302 (5647), pp. 1024-1027.

Prospero, J.M., Barrett, K., Church, T., Dentener, F., Duce, R.A., Galloway, J.N., Levy, H., Moody, J. and Quinn, P. 1996. Atmospheric deposition of nutrients to the North Atlantic Basin. In Nitrogen Cycling in the North Atlantic Ocean and its Watersheds, *Springer, Dordrecht*. 35 (1), pp. 27-73.

Prospero, J. M., Bullard, J. E., and Hodgkins, R. 2012. High-latitude dust over the North Atlantic: Inputs from Icelandic proglacial dust storms. *Science*, 335 (6072), pp. 1078-1082.

Prospero, J. M. 1981. Arid regions as sources of mineral aerosols in the marine atmosphere. *Geological Society of America Special Papers*, 186, pp. 71-86.

Prospero, J.M. and Mayol-Bracero, O.L. 2013. Understanding the transport and impact of African dust on the Caribbean basin. *Bulletin of the American Meteorological Society*, 94 (9), pp. 1329-1337.

Prospero, J. M., and Carlson, T. N. 1972. Vertical and areal distribution of Saharan dust over the western equatorial North Atlantic Ocean. *Journal of Geophysical Research*, 77 (27), pp. 5255-5265.

Prospero, J.M. and Nees, R.T. 1986. Impact of the North African drought and El Nino on mineral dust in the Barbados trade winds. *Nature*, 320 (6064), p. 735.

Prospero, J. M. 1979. Mineral and sea salt aerosol concentrations in various ocean regions. *Journal of Geophysical Research: Oceans*, *84*(C2), 725-731.

Quijano, A.L., Sokolik, I.N. and Toon, O.B., 2000. Radiative heating rates and direct radiative forcing by mineral dust in cloudy atmospheric conditions. *Journal of Geophysical Research: Atmospheres*, 105(D10), pp.12207-12219.

Rap A., Scott CE., Spracklen, DV., Forster, PM., Carslaw, KS., Schmidt, A., Mann, G., Bellouin, N. 2013. Natural aerosol direct and indirect radiative effects, *Geophysical Research Letters*, 40, pp. 3297-3301.

Reid, J.S., Kinney, J.E., Westphal, D.L., Holben, B.N., Welton, E.J., Tsay, S.C., Eleuterio, D.P., Campbell, J.R., Christopher, S.A., Colarco, P.R. and Jonsson, H.H., 2003. Analysis of measurements of Saharan dust by airborne and ground-based remote sensing methods during the Puerto Rico Dust Experiment (PRIDE). *Journal of Geophysical Research: Atmospheres*, 108(D19).

Remer, L.A., Kaufman, Y.J., Tanré, D., Mattoo, S., Chu, D.A., Martins, J.V., Li, R.R., Ichoku, C., Levy, R.C., Kleidman, R.G. and Eck, T.F. 2005. The MODIS aerosol algorithm, products, and validation. *Journal of the atmospheric sciences*, 62 (4), pp. 947-973.

Remer, L.A., Kleidman, R.G., Levy, R.C., Kaufman, Y.J., Tanré, D., Mattoo, S., Martins, J.V., Ichoku, C., Koren, I., Yu, H. and Holben, B.N. 2008. Global aerosol climatology from the MODIS satellite sensors. *Journal of Geophysical Research: Atmospheres*, 113 (D14).

Rittmeister, F., Ansmann, A., Engelmann, R., Skupin, A., Baars, H., Kanitz, T., and Kinne, S. 2017. Profiling of Saharan dust from the Caribbean to western Africa–Part 1: Layering structures and optical properties from shipborne polarization/Raman lidar observations. *Atmospheric Chemistry and Physics*, 17 (21), p. 12963.

Rocha-Lima, A., Vanderlei Martins, J., Remer, L. A., Todd, M., Marsham, J. H., Engelstaedter, S., ... & Washington, R. 2018. A detailed characterization of the Saharan dust collected during the Fennec campaign in 2011: in situ ground-based and laboratory measurements. *Atmospheric Chemistry and Physics*, *18*, 1023-1043.

Rodríguez González, S., Alastuey, A., Alonso-Pérez, S., Querol, X., Cuevas Agulló, E., Abreu Afonso, J., Viana, M., Pérez, N., Pandolfi, M. and Rosa, J.D.D.L., 2011. Transport of desert dust mixed with North African industrial pollutants in the subtropical Saharan Air Layer. *Atmospheric Chemistry and Physics*. [Online]. 11(13), pp. 6663-6685. [Accessed 12 January 2011]. Available from: http://hdl.handle.net/20.500.11765/416.

Rodríguez, S., Torres, C., Guerra, J. C., & Cuevas, E. (2004). Transport pathways of ozone to marine and free-troposphere sites in Tenerife, Canary Islands. *Atmospheric Environment*, *38*(28), 4733-4747.

Romano, S., and Perrone, M. R. 2016. 'Mineral Dust Impact on Short-and Long-Wave Radiation and Comparison with Ceres Measurements'. *In EPJ Web of Conferences*. *EDP Sciences.* 119, p. 08005.

Rosenberg, P. D., Dean, A. R., Williams, P. I., Dorsey, J. R., Minikin, A., Pickering, M. A., and Petzold, A. 2012. Particle sizing calibration with refractive index correction for light scattering optical particle counters and impacts upon PCASP and CDP data collected during the Fennec campaign. *Atmospheric Measurement Techniques*, 5 (5), pp. 1147-1163.

Roux, F. 1985. Retrieval of thermodynamic fields from multiple-Doppler radar data using the equations of motion and the thermodynamic equation. *Monthly weather review*, 113(12), 2142-2157.

Rosenfeld, D., Rudich, Y., and Lahav, R. 2001. Desert dust suppressing precipitation: A possible desertification feedback loop. *Proceedings of the National Academy of Sciences*, 98 (11), pp. 5975-5980.

Ryder, C.L., Highwood, E.J., Rosenberg, P.D., Trembath, J., Brooke, J.K., Bart, M., Dean, A., Crosier, J., Dorsey, J., Brindley, H. and Banks, J. 2013. Optical properties of Saharan dust aerosol and contribution from the coarse mode as measured during the Fennec 2011 aircraft campaign. *Atmospheric Chemistry and Physics*, 13 (1), pp. 303-325.

Ryder, C. L., Highwood, E. J., Lai, T. M., Sodemann, H., & Marsham, J. H. 2013a. Impact of atmospheric transport on the evolution of microphysical and optical properties of Saharan dust. Geophysical Research Letters, 40(10), 2433-2438.

Ryder, C.L., McQuaid, J.B., Flamant, C., Rosenberg, P.D., Washington, R., Brindley, H.E., Highwood, E.J., Marsham, J.H., Parker, D.J., Todd, M.C. and Banks, J.R. 2015. Advances in understanding mineral dust and boundary layer processes over the Sahara from Fennec aircraft observations. *Atmospheric Chemistry and Physics*, 15 (14), pp. 8479-8520.

Ryder, C., Marenco, F., Brooke, J., Estelles, V., Cotton, R., Formenti, P., ... & Rosenberg, P. 2018. Coarse-mode mineral dust size distributions, composition and optical properties from AER-D aircraft measurements over the tropical eastern Atlantic.

Ryder, C. L., Highwood, E. J., Walser, A., Seibert, P., Philipp, A., & Weinzierl, B. 2019. Coarse and giant particles are ubiquitous in saharan dust export regions and are radiatively significant over the sahara. *Atmospheric Chemistry and Physics*, *19*, 15353-15376.

Saxby, J., Beckett, F., Cashman, K., Rust, A., & Tennant, E. 2018. The impact of particle shape on fall velocity: Implications for volcanic ash dispersion modelling. *Journal of Volcanology and Geothermal Research*, *362*, 32-48.

Schepanski, K., Heinold, B. and Tegen, I. 2017. Harmattan, Saharan heat low, and West African monsoon circulation: modulations on the Saharan dust outflow towards the North Atlantic. *Atmospheric Chemistry and Physics*, 17 (17), p. 10223.

Schumann, U. and Gerz, T. 1995. Turbulent mixing in stably stratified shear flows. *Journal of Applied Meteorology*, 34 (1), pp. 33-48.

Schutz, L., Jaenicke, R., and Pietrek, H. 1981. Saharan dust transport over the North Atlantic Ocean. *Geological Society of America Special Papers*, 186, pp. 87-100.

Seinfeld, J. H., & Pandis, S. N. 2016. *Atmospheric chemistry and physics: from air pollution to climate change*. John Wiley & Sons.

Shao, Y. 2001. A model for mineral dust emission. *Journal of Geophysical Research: Atmospheres*, 106 (D17), pp. 20239-20254.

Shi, Z., Bonneville, S., Krom, M.D., Carslaw, K.S., Jickells, T.D., Baker, A.R. and Benning, L.G. 2011. Iron dissolution kinetics of mineral dust at low pH during simulated atmospheric processing. *Atmospheric Chemistry and Physics*, 11 (3), pp. 995-1007.

Sodemann, H., Lai, T.M., Marenco, F., Ryder, C.L., Flamant, C., Knippertz, P., Rosenberg, P., Bart, M. and Mcquaid, J.B. 2015. Lagrangian dust model simulations for a case of moist convective dust emission and transport in the Western Sahara region during Fennec/LADUNEX. *Journal of Geophysical Research: Atmospheres*, 120 (12), pp. 6117-6144.

Sokolik, I.N. and Toon, O.B. 1996. Direct radiative forcing by anthropogenic airborne mineral aerosols. *Nature*, 381 (6584), p. 681.

Sokolik, I.N., Winker, D.M., Bergametti, G., Gillette, D.A., Carmichael, G., Kaufman, Y.J., Gomes, L., Schuetz, L. and Penner, J.E. 2001. Introduction to special section: Outstanding problems in quantifying the radiative impacts of mineral dust. *Journal of Geophysical Research: Atmospheres*, 106 (D16), pp. 18015-18027.

Solmon, F., Elguindi, N., & Mallet, M. 2012. Radiative and climatic effects of dust over West Africa, as simulated by a regional climate model. Climate Research, 52, 97-113.

Song, Q., Zhang, Z., Yu, H., Kato, S., Yang, P., Colarco, P., ... & Ryder, C. L. 2018. Net radiative effects of dust in the tropical North Atlantic based on integrated satellite observations and in situ measurements. *Atmospheric Chemistry and Physics*, 18(15), 11303-11322.

Spracklen, D.V., Pringle, K.J., Carslaw, K.S., Chipperfield, M.P. and Mann, G.W. 2005. A global off-line model of size-resolved aerosol microphysics: II. Identification of key uncertainties. *Atmospheric Chemistry and Physics*, 5 (12), pp. 3233-3250.

Steeneveld, G. J., Wokke, M. J. J., Groot Zwaaftink, C. D., Pijlman, S., Heusinkveld, B. G., Jacobs, A. F. G., & Holtslag, A. A. M. 2010. Observations of the radiation divergence in the surface layer and its implication for its parameterization in numerical weather prediction models. *Journal of Geophysical Research: Atmospheres*, 115(D6).

Stein, A. F., Draxler, R. R., Rolph, G. D., Stunder, B. J., Cohen, M. D., & Ngan, F. 2015. NOAA's HYSPLIT atmospheric transport and dispersion modeling system. Bulletin of the American Meteorological Society, 96(12), 2059-2077.

Stull, R. B. 2012. An introduction to boundary layer meteorology (Vol. 13). Springer Science & Business Media.

Sud, Y. C., and Fennessy, M. 1982. A study of the influence of surface albedo on July circulation in semi-arid regions using the glas GCM. *Journal of Climatology*, 2 (2), pp. 105-125.

Sultan, B., & Janicot, S. 2003. The West African monsoon dynamics. Part II: The "preonset" and "onset" of the summer monsoon. *Journal of climate*, 16(21), 3407-3427.

Sun, D., Lau, K. M., & Kafatos, M. 2008. Contrasting the 2007 and 2005 hurricane seasons: Evidence of possible impacts of Saharan dry air and dust on tropical cyclone activity in the Atlantic basin. *Geophysical Research Letters*, *35*(15).

Sun, D., Lau, W. K. M., Kafatos, M., Boybeyi, Z., Leptoukh, G., Yang, C., & Yang, R. 2009. Numerical simulations of the impacts of the Saharan air layer on Atlantic tropical cyclone development. *Journal of Climate*, 22(23), 6230-6250.

Takemura, T., Nakajima, T., Dubovik, O., Holben, B. N., & Kinne, S. 2002. Single-scattering albedo and radiative forcing of various aerosol species with a global three-dimensional model. *Journal of Climate*, 15(4), 333-352.

Tanaka, T.Y. and Chiba, M., 2006. A numerical study of the contributions of dust source regions to the global dust budget. *Global and Planetary Change*, 52(1), pp.88-104.

Tao, D., & Zhang, F. 2018. Effect of Sea-Surface Temperature and Ambient Moisture on the Formation and Predictability of Tropical Cyclones Under Vertical Wind Shear: An Ensemble Predictability Perspective. *In 33rd Conference on Hurricanes and Tropical Meteorology. AMS*.

Taylor, J. A. 1982. Climatic variations and variability: Facts and theories, Edited by A. Berger, D. Reidel, 1981. Price: $87.50.

Tegen, I., Bierwirth, E., Heinold, B., Helmert, J., and Wendisch, M. 2010. Effect of measured surface albedo on modeled Saharan dust solar radiative forcing. *Journal of Geophysical Research: Atmospheres*, 115 (D24), pp. 1984–2012.

Tegen, I., Werner, M., Harrison, S. P., and Kohfeld, K. E. 2004. Relative importance of climate and land use in determining present and future global soil dust emission. *Geophysical Research Letters*, 31 (5).

Tegen, I., and Fung, I. 1994. Modeling of mineral dust in the atmosphere: Sources, transport, and optical thickness. *Journal of Geophysical Research: Atmospheres*, 99 (D11), pp. 22897-22914.

Tetzlaff, G. 1983. Albedo of the Sahara. Cologne University Satellite Measurement of Radiation Budget Parameters. pp. 60–63.

Todd, M. C., Allen, C. T., Bart, M., Bechir, M., Bentefouet, J., Brooks, B. J., ... & Engelstaedter, S. 2013. Meteorological and dust aerosol conditions over the western Saharan region observed at Fennec Supersite-2 during the intensive observation period in June 2011. *Journal of Geophysical Research: Atmospheres*, 118(15), 8426-8447.

Torge, A., Macke, A., Heinold, B., and Wauer, J. 2011. Solar radiative transfer simulations in Saharan dust plumes: particle shapes and 3-D effect. *Tellus B*, 63 (4), pp. 770-780.

Torres, O., Bhartia, P. K., Herman, J. R., Sinyuk, A., Ginoux, P., and Holben, B. 2002. A long-term record of aerosol optical depth from TOMS observations and comparison to AERONET measurements. *Journal of the Atmospheric Sciences*, 59 (3), pp. 398-413.

Trzeciak, T. M., Garcia-Carreras, L., & Marsham, J. H. 2017. Cross-Saharan transport of water vapor via recycled cold pool outflows from moist convection. *Geophysical research letters*, 44(3), 1554-1563.

Tsikerdekis, A., Zanis, P., Steiner, A.L., Solmon, F., Amiridis, V., Marinou, E., Katragkou, E. and Karacostas, T.S. 2017. Simulated Dust Over the Sahara and Mediterranean with a Regional Climate Model (RegCM4). *In Perspectives on Atmospheric Sciences*, pp. 615-620. Springer, Cham.

Valenzuela, A., Costa, M. J., Guerrero-Rascado, J. L., Bortoli, D., and Olmo, F. J. 2017. Solar and thermal radiative effects during the 2011 extreme desert dust episode over Portugal. *Atmospheric Environment*, 148, pp. 16-29

Van der Does, M., Knippertz, P., Zschenderlein, P., Harrison, R. G., & Stuut, J. B. W. 2018. The mysterious long-range transport of giant mineral dust particles. *Science advances*, *4*(12), eaau2768.

Van Der Does, M., Korte, L. F., Munday, C. I., Brummer, G. J. A., & Stuut, J. B. W. 2016. Particle size traces modern Saharan dust transport and deposition across the equatorial North Atlantic. *Atmospheric Chemistry & Physics*, *16*(21).

Velasco-Merino, C., Mateos, D., Toledano, C., Prospero, J. M., Molinie, J., Euphrasie-Clotilde, L., ... & Frutos, A. M. D. 2018. Impact of long-range transport over the Atlantic Ocean on Saharan dust optical and microphysical properties based on AERONET data. *Atmospheric Chemistry and Physics*, 18(13), 9411-9424.

Viana, M., Querol, X., Alastuey, A., Cuevas, E. and Rodrıguez, S. 2002. Influence of African dust on the levels of atmospheric particulates in the Canary Islands air quality network. *Atmospheric Environment*, 36 (38), pp. 5861-5875.

Vittorio Barale. 2010. Oceanography from Space: Revisited. Springer, ISBN 978-90-481-8680-8.

Wallace, J. M., & Hobbs, P. V. 2006. Atmospheric science: an introductory survey (Vol. 92). Elsevier.

Wang, Z., Zhang, H., Jing, X., & Wei, X. 2013. Effect of non-spherical dust aerosol on its direct radiative forcing. *Atmospheric research*, *120*, 112-126.

Wang, C., Tang, B. H., Wu, H., Tang, R., & Li, Z. L. 2017. Estimation of Downwelling Surface Longwave Radiation under Heavy Dust Aerosol Sky. *Remote Sensing*, 9(3), 207.

Weaver, C. J., Ginoux, P., Hsu, N. C., Chou, M. D., & Joiner, J. 2002. Radiative forcing of Saharan dust: GOCART model simulations compared with ERBE data. *Journal of the atmospheric sciences*, 59(3), 736-747.

Weinzierl, B., Sauer, D., Esselborn, M., Petzold, A., Veira, A., Rose, M., ... & Gross, S. 2011. Microphysical and optical properties of dust and tropical biomass burning aerosol layers in the Cape Verde region—an overview of the airborne in situ and lidar measurements during SAMUM-2. *Tellus B: Chemical and Physical Meteorology*, *63*(4), 589-618.

Weinzierl, B., Ansmann, A., Prospero, J. M., Althausen, D., Benker, N., Chouza, F., ... & Gasteiger, J. 2017. The Saharan aerosol long-range transport and aerosol–cloud-interaction experiment: overview and selected highlights. *Bulletin of the American Meteorological Society*, 98(7), 1427-1451.

White, R. P., and Nackoney, J. 2003. Drylands, people, and ecosystem goods and services: a web-based geospatial analysis. *World Resources Institute*. [Online]. PDF version. [Accessed 30 January 2012]. Available from: http://pdf. wri. org/drylands. pdf.

Wiscombe, W. J. (1980). Improved Mie scattering algorithms. Applied optics, 19(9), 1505-1509.

Wong, S., and Dessler, A. E. 2005. Suppression of deep convection over the tropical North Atlantic by the Saharan Air Layer. *Geophysical research letters*, 32 (9).

World Health Organization. 1999. The world health report: 1999: making a difference. World Health Organization.

Yi, B., Hsu, C. N., Yang, P., & Tsay, S. C. 2011. Radiative transfer simulation of dust-like aerosols: Uncertainties from particle shape and refractive index. *Journal of aerosol science*, 42(10), 631-644.

Yue, H., He, C., Zhao, Y., Ma, Q., and Zhang, Q. 2017. The brightness temperature adjusted dust index: An improved approach to detect dust storms using MODIS imagery. *International journal of applied earth observation and geoinformation*, 57, pp. 166-176.

Yu, H., Chin, M., Yuan, T., Bian, H., Remer, L.A., Prospero, J.M., Omar, A., Winker, D., Yang, Y., Zhang, Y. and Zhang, Z. 2015. The fertilizing role of African dust in the Amazon rainforest: A first multiyear assessment based on data from Cloud-Aerosol Lidar and Infrared Pathfinder Satellite Observations. *Geophysical Research Letters*, 42 (6), pp. 1984-1991.

Zipser, E.J., Twohy, C.H., Tsay, S.C., Thornhill, K.L., Tanelli, S., Ross, R., Krishnamurti, T.N., Ji, Q., Jenkins, G., Ismail, S. and Hsu, N.C. 2009. The Saharan air layer and the fate of African easterly waves—NASA's AMMA field study of tropical cyclogenesis. *Bulletin of the American Meteorological Society*, 90 (8), pp. 1137-1156.

Zhao, C., Liu, X., Leung, L.R., Johnson, B., McFarlane, S.A., Gustafson Jr, W.I., Fast, J.D. and Easter, R. 2010. The spatial distribution of mineral dust and its shortwave radiative forcing over North Africa: modeling sensitivities to dust emissions and aerosol size treatments. *Atmospheric Chemistry and Physics*, 10 (18), pp. 8821-8838.

Zhao, C., Liu, X., Ruby Leung, L., and Hagos, S. 2011. Radiative impact of mineral dust on monsoon precipitation variability over West Africa. *Atmospheric Chemistry and Physics*, 11 (5), pp. 1879-1893.

Zhang, R. J. 1989. Sediment Dynamics in Rivers. Beijing: *Water Resources Press*.

Zhang, Y. C., Rossow, W. B., and Lacis, A. A. 1995. Calculation of surface and top of atmosphere radiative fluxes from physical quantities based on ISCCP data sets: 1. Method and sensitivity to input data uncertainties. *Journal of Geophysical Research: Atmospheres* (1984–2012), 100 (D1), pp. 1149-1165.

Zhang, L., Li, Q.B., Gu, Y., Liou, K.N. and Meland, B. 2013. Improved estimate of global dust radiative forcing using a coupled chemical transport-radiative transfer model. *Atmospheric Chemistry and Physics Discussions*, 13 (1).

Zhang, Y., Li, Z., Zhang, Y., Li, D., Qie, L., Che, H., & Xu, H. 2017. Estimation of aerosol complex refractive indices for both fine and coarse modes simultaneously based on AERONET remote sensing products. *Atmospheric Measurement Techniques*, *10*(9), 3203.

Zhiyao, S., Tingting, W., Fumin, X., and Ruijie, L. 2008. A simple formula for predicting settling velocity of sediment particles. *Water Science and Engineering*, 1 (1), pp. 37-43.

Zhu, A., Ramanathan, V., Li, F., and Kim, D. 2007. Dust plumes over the Pacific, Indian, and Atlantic oceans: Climatology and radiative impact. *Journal of Geophysical Research: Atmospheres*, 112 (D16), pp. 1984–201.

Appendix

Appendix A

This appendix shows ensemble backward and forward trajectories obtained from HYSPLIT model runs over the African land and Canary Islands. The sources of air mass trajectories used for BRSedT model over the Canary Islands and Puerto Rico regions are also shown. This appendix presents the profiles of dust mass loading corresponding with dust heating rates that derived by ES radiation model. In addition, the vertical contributions of CAPE and CIN calculations based on LEM results for Otto et al. (2007) and Zhu et al. (2007) will be shown here. All results shown in appendix including, profiles, calculations and figures are represented as a complementary result to the current thesis work.

A1. HYSPLIT backward trajectories

Backward trajectories are shown over Canary Islands with heights of 2220, 3060 and 5100 m to investigate the consistency in air mass sources between study region and dusty event cases.

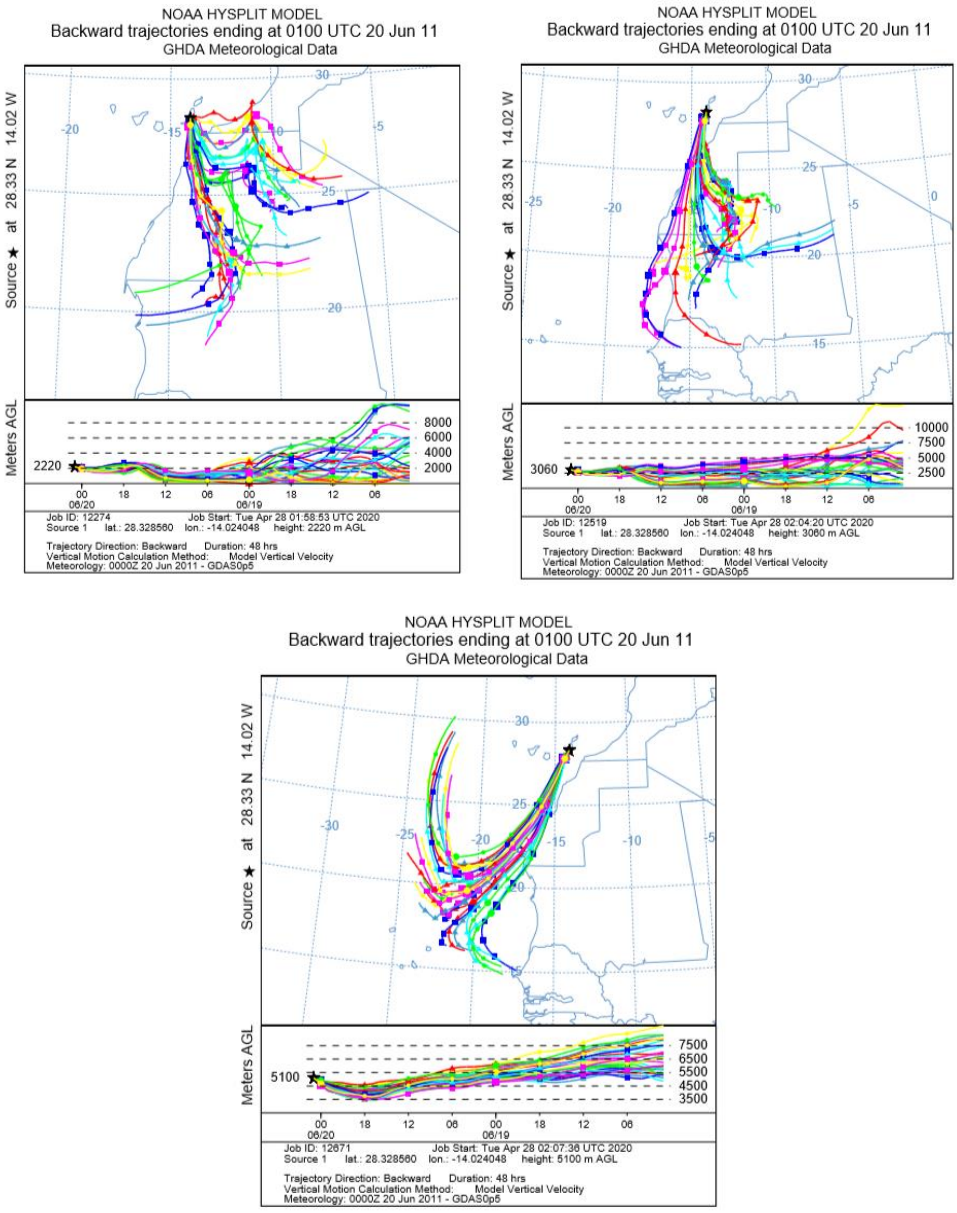

Figure A1. 1. Backward trajectories from NOAA HYSPLIT model during June 2011 with various height ranges (2220 m, 3060 m, and 5100 m). The ensemble trajectories are obtained by running the HYSPLIT model at 0.5 degree given output for every 6 hours and with a time duration 48 hours over Fuerteventura (Canary Islands). The model was started at 28.2 latitude and -14.02 longitude at the Canary Islands. Runs show backward air mass sources of the dust event for flight number FB604.

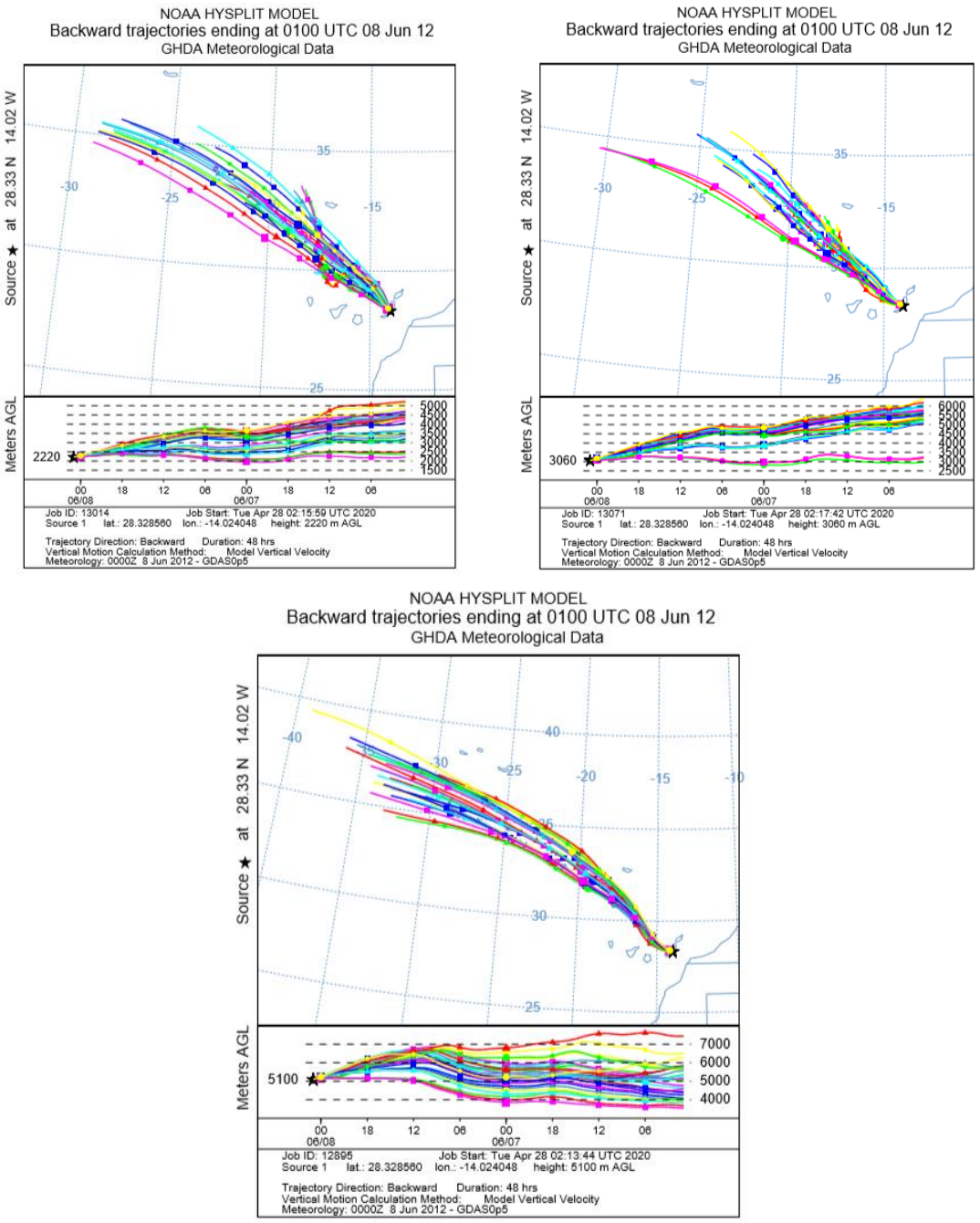

Figure A1. 2. As figure (A1.1), but for non-dust case (FB700).

A2. HYSPLIT forward trajectories

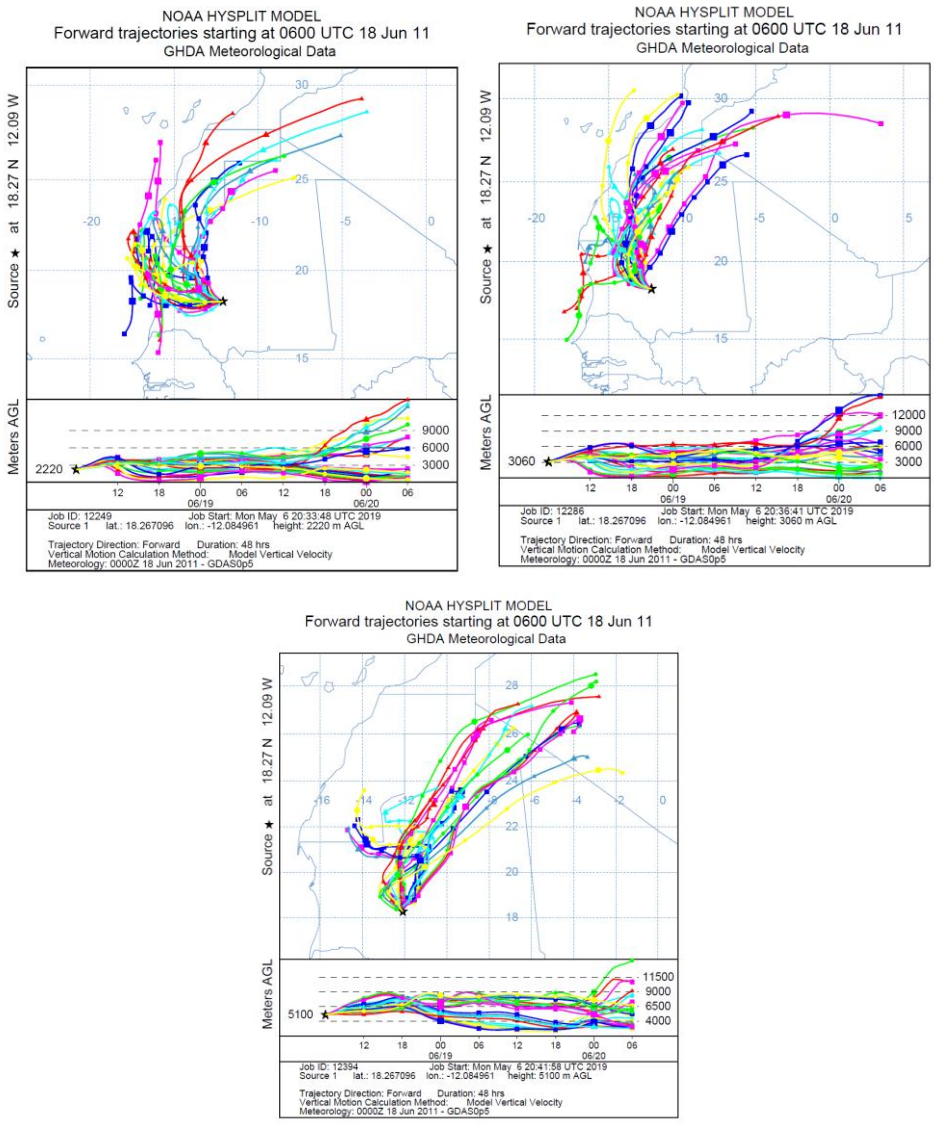

Figure A2. 1. Forward trajectories from NOAA HYSPLIT model during June 2011 with various height ranges 2220 m, 3060 m, and 5100 m. The ensemble trajectories are obtained by running the HYSPLIT model at 0.5 degree with providing output every 6 hours and with time duration of 48 hours over Fuerteventura (Canary Islands). The model runs start at 18.2 latitude and -12.08 longitude at western Saharan. Runs show forward air mass sources of the dust event for flight number FB604.

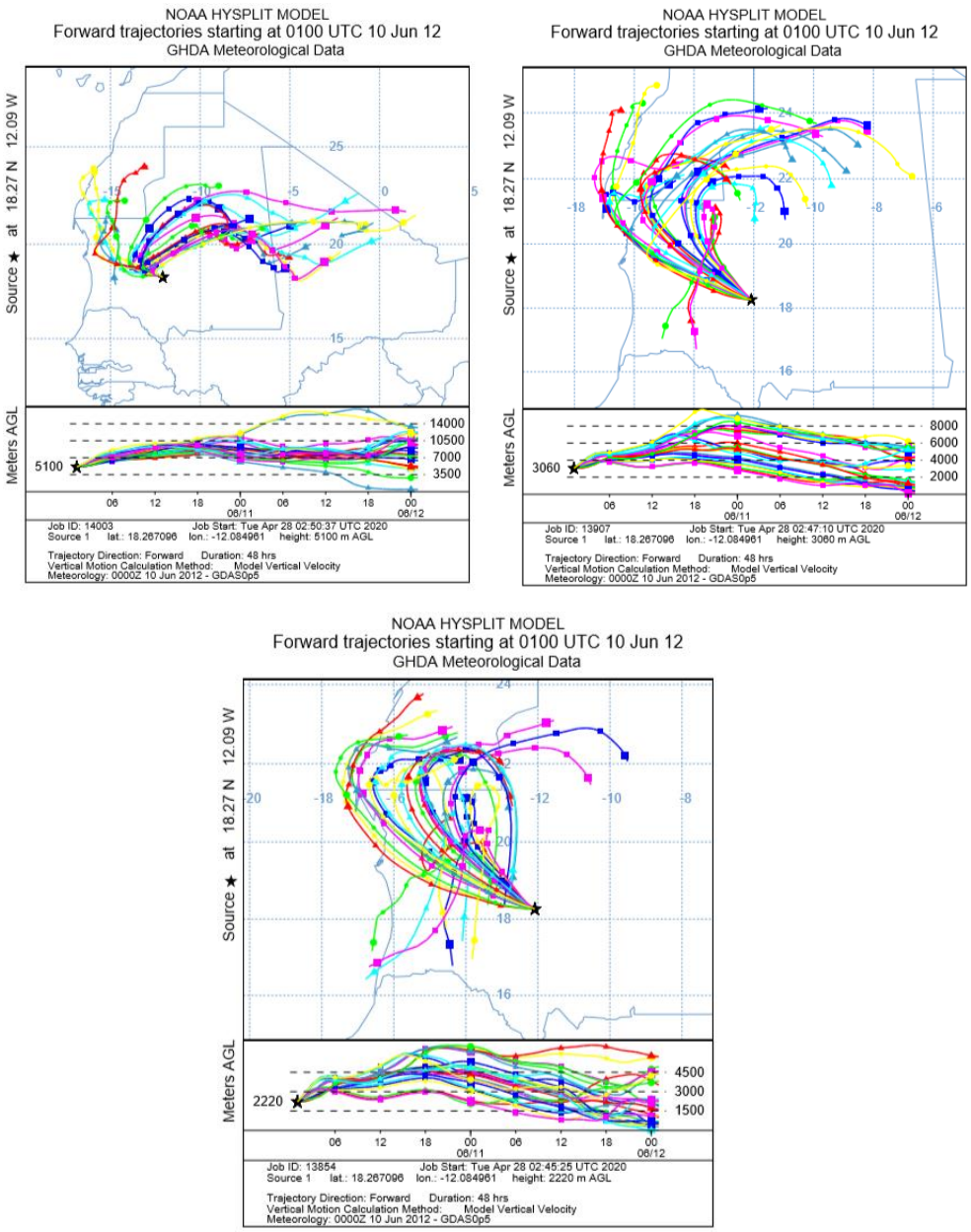

Figure A2. 2. As figure (A2.1), but for non-dust event, FB700.

A3. Heating rates with dust mass loading profiles.

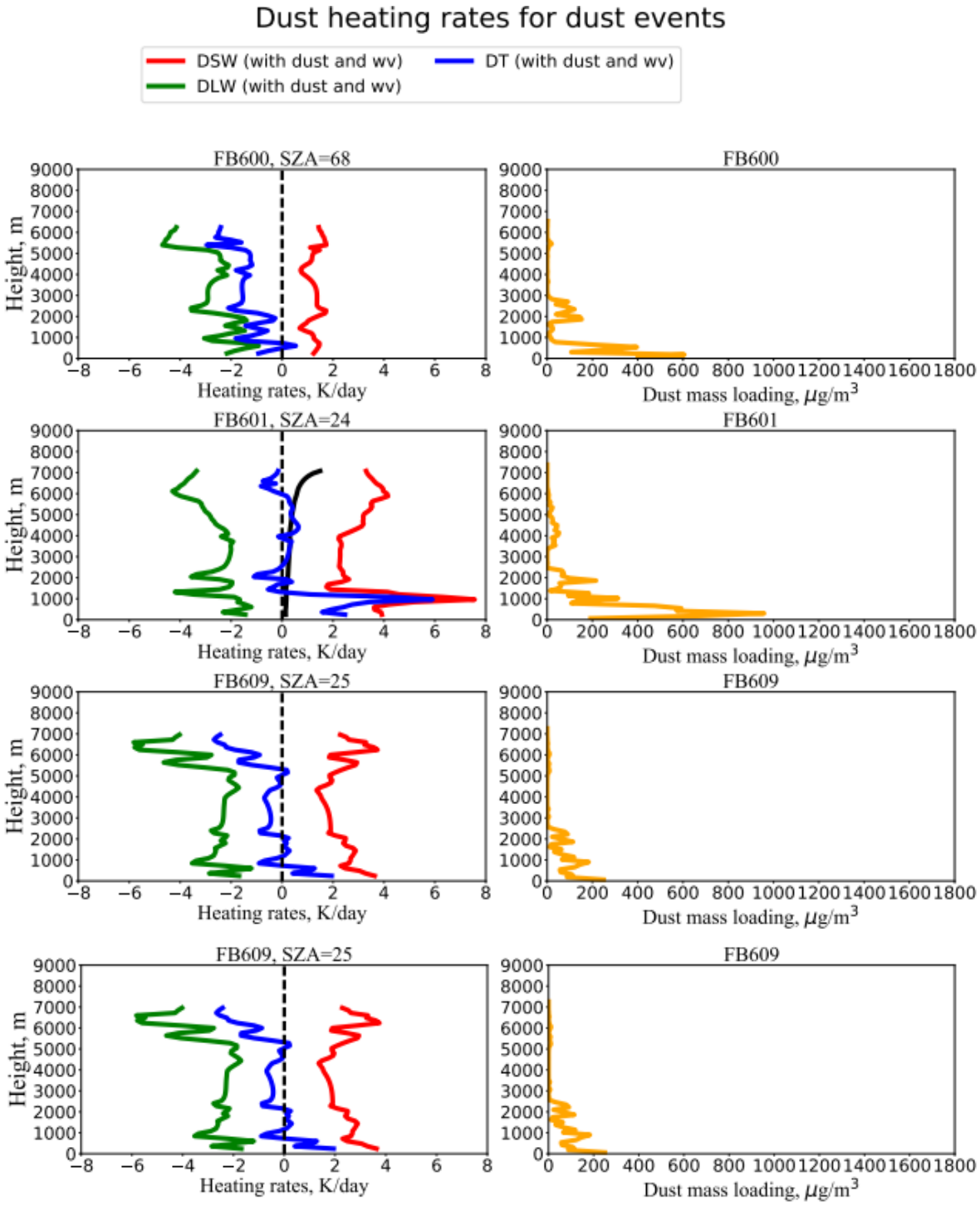

Figure A3. 1. Profiles of heating rates in units of K/day and mass concentration in units of μg/m^3 over the study region. All profiles were derived with using RI=1.53+0.001i (value based on Ryder et al., 2013). Runs for FB600, FB601, FB609 and FB611.

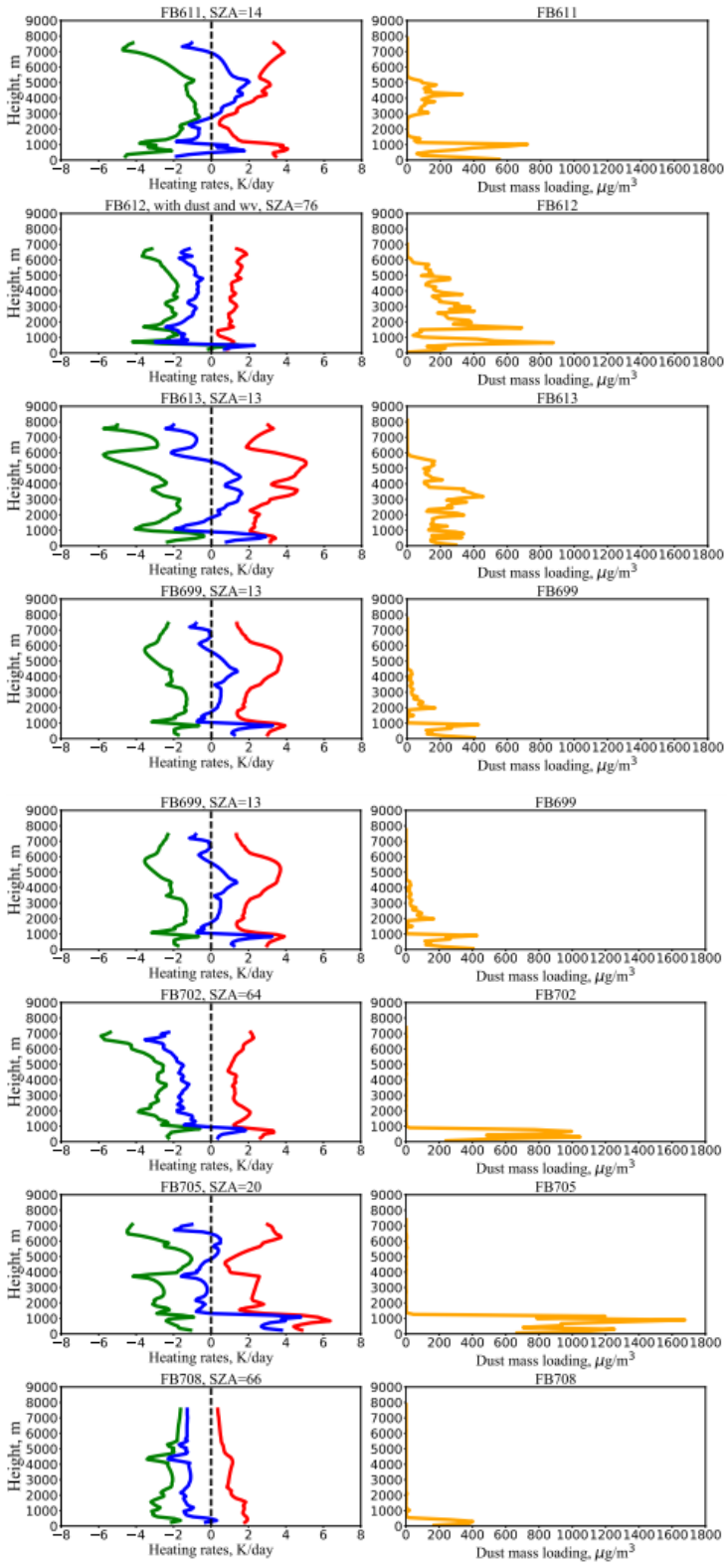

Figure A3. 2. As figure (A3.1), but for more flight cases.

A4. Potential temperature and virtual potential temperature profiles associated with dust mass loading.

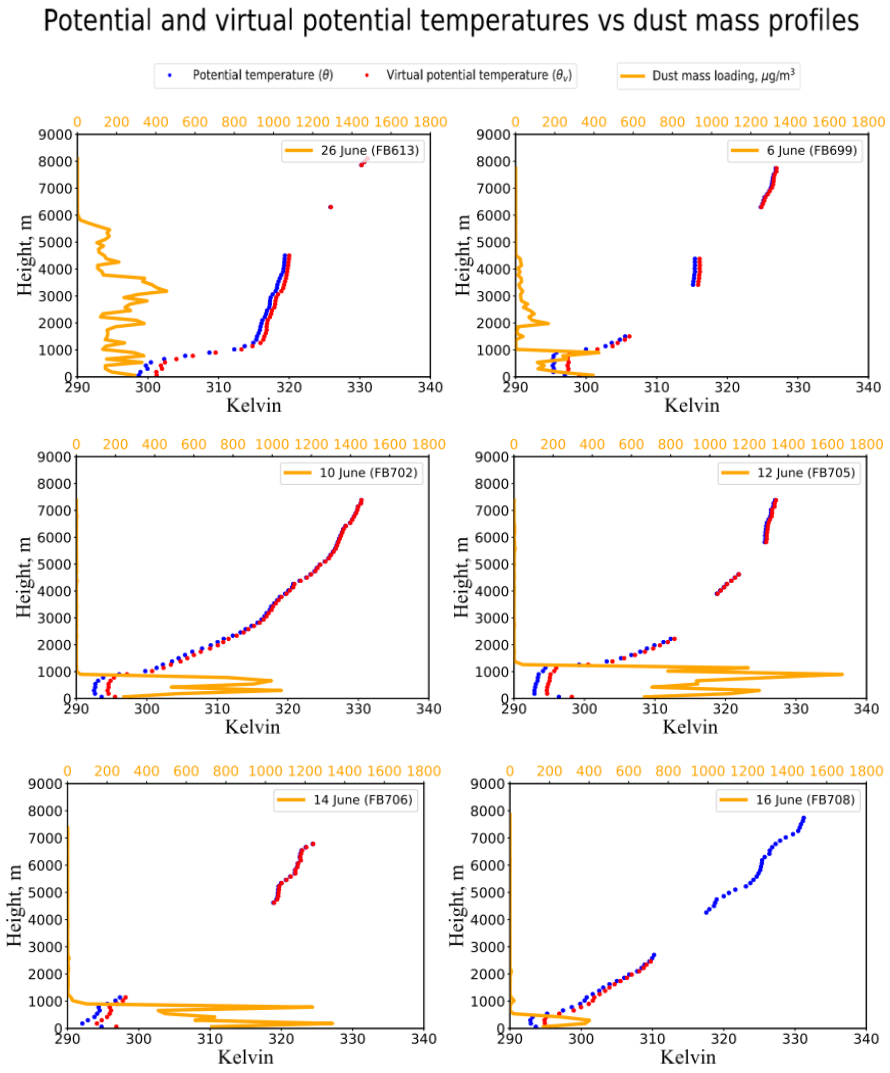

Figure A4. 1. Profile of potential (θ) and virtual potential (θ_v) temperatures vs dust mass loading from FENNEC observations for flights FB613, FB699, FB702, FB705, FB706 and FB708. Blue and red dotted lines refer to θ and θ_v in units of Kelvin, while orange line shows dust mass loading in units of $\mu g/m^3$. Virtual potential temperature in all cases are slightly higher than potential temperature up to 1 km due to large moisture, and thus it will be considered in stability calculations for CAPE and CIN factors. In some cases, slightly larger amounts of water present within the marine environment SAL. This is surprising since dusty layers are often considered to be dry. The gap in the profiles of potential temperature was interpolated linearly to be ready as input data in the model simulation.

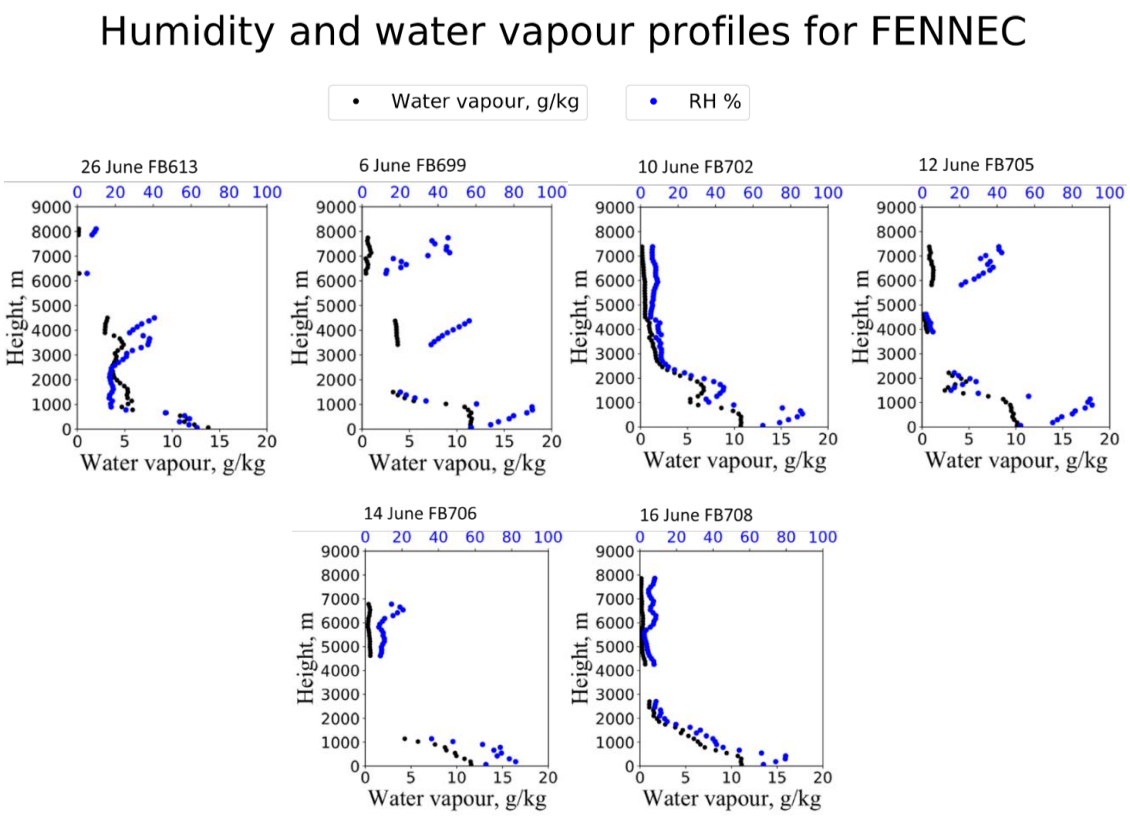

Figure A4. 2. Profiles of water vapour mass mixing ratio in units of g/kg and relative humidity (RH %) calculated from FENNEC observations for flights FB613, FB699, FB702, FB705, FB706 and FB708. Large amount of water vapour was observed within the transported Sahara dust. Evan (2015) and Marsham et al. (2016) state that water vapour over the Sahara has a larger impact on the radiative effects than the dust layer, and therefore, quantification dust outbreaks must include both the dust and the elevated water vapour. Categories of dust events are coincident with these profiles of potential temperatures. The gap in the profiles of water vapour was interpolated linearly to be ready as input data in the model simulation.

Table A4- 1. Mean and standard deviation (SD) of wv mixing ratios (g/kg) for BL, IL, SAL and FA layers.

a

FB604	BL	IL	SAL	FA
[3]Mean	7.15	5.02	4.14	0.70
SD	2.54	0.03	0.97	0.39

b

FB605	BL	IL	SAL	FA
Mean	7.48	5.72	2.69	0.67
SD	1.51	0.14	0.91	0.12

c

FB611	BL	IL	SAL	FA
Mean	11.2	4.21	2.23	1.25
SD	2.04	1.41	0.89	0.43

d

FB612	BL	IL	SAL	FA
Mean	9.01	3.56	3.22	2.06
SD	2.80	1.41	0.61	0.02

e

FB700	BL	IL	SAL	FA
Mean	11.3	10	2.45	0.38
SD	0.82	0.32	2.31	0.09

f

FB702	BL	IL	SAL	FA
Mean	10.24	5.87	1.87	0.27
SD	0.72	0.48	1.91	0.08

g

FB705	BL	IL	SAL	FA
Mean	9.78	7.68	1.62	1.01
SD	0.24	1.82	1.17	0.16

h

FB708	BL	IL	SAL	FA
Mean	9.82	5.72	0.98	0.19
SD	1.48	0.75	0.97	0.07

[3] Statistics (Mean and SD) in all tables stated above are computed for water vapour mass mixing ratios.

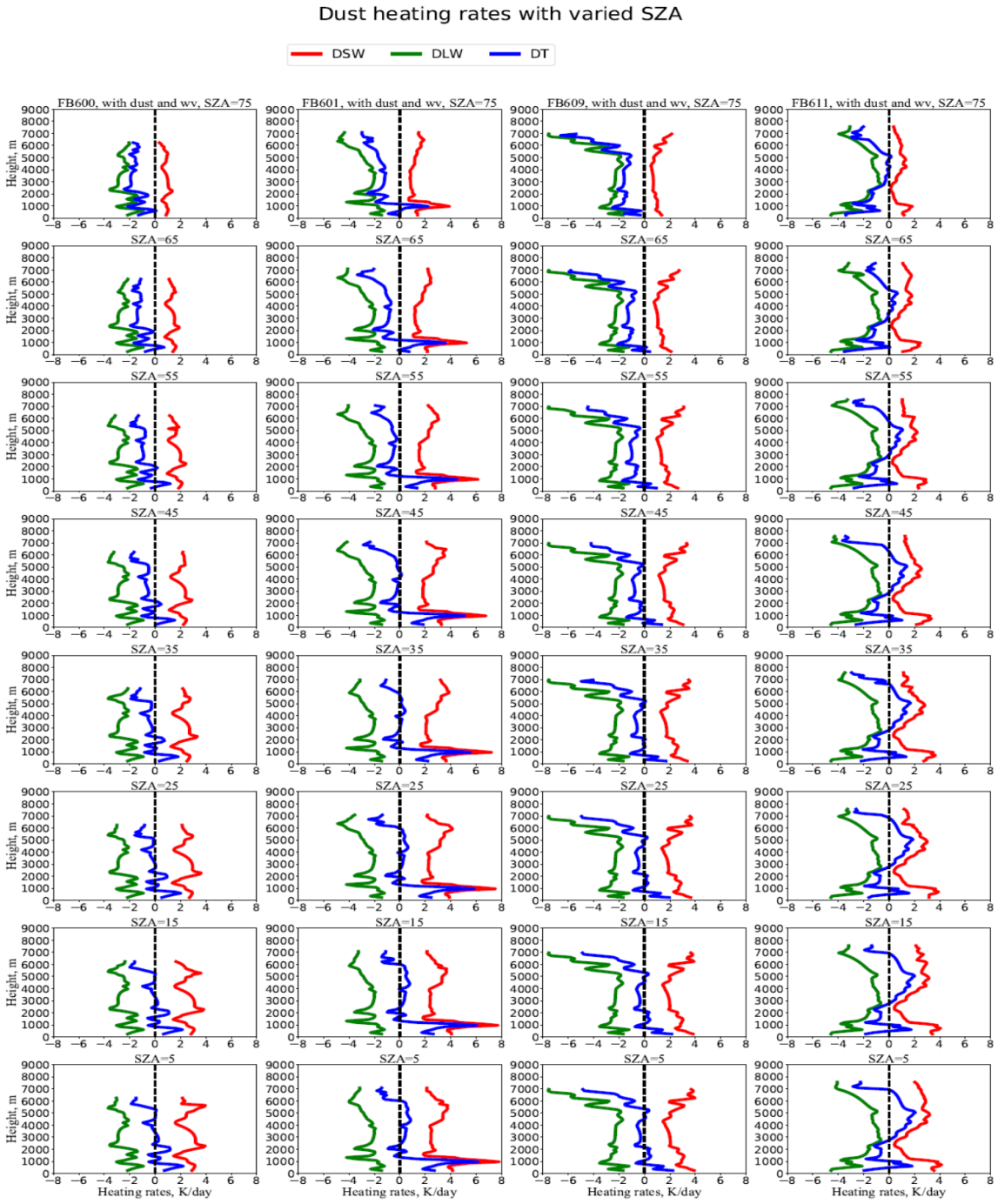

Figure A4. 3. Dust heating rates with using a variation in Solar Zenith Angles (SZA) for flights FB600, FB601, FB609 and FB611. Heating rate profiles were simulated for SW (red line), LW (green line) and Total (blue lines) radiation based on values of SZA initializing from morning until afternoon time, see table (2-6).

A4. 4. Ensemble backward and forward trajectories for BRSedT transport model: Canary Islands, case study FB604

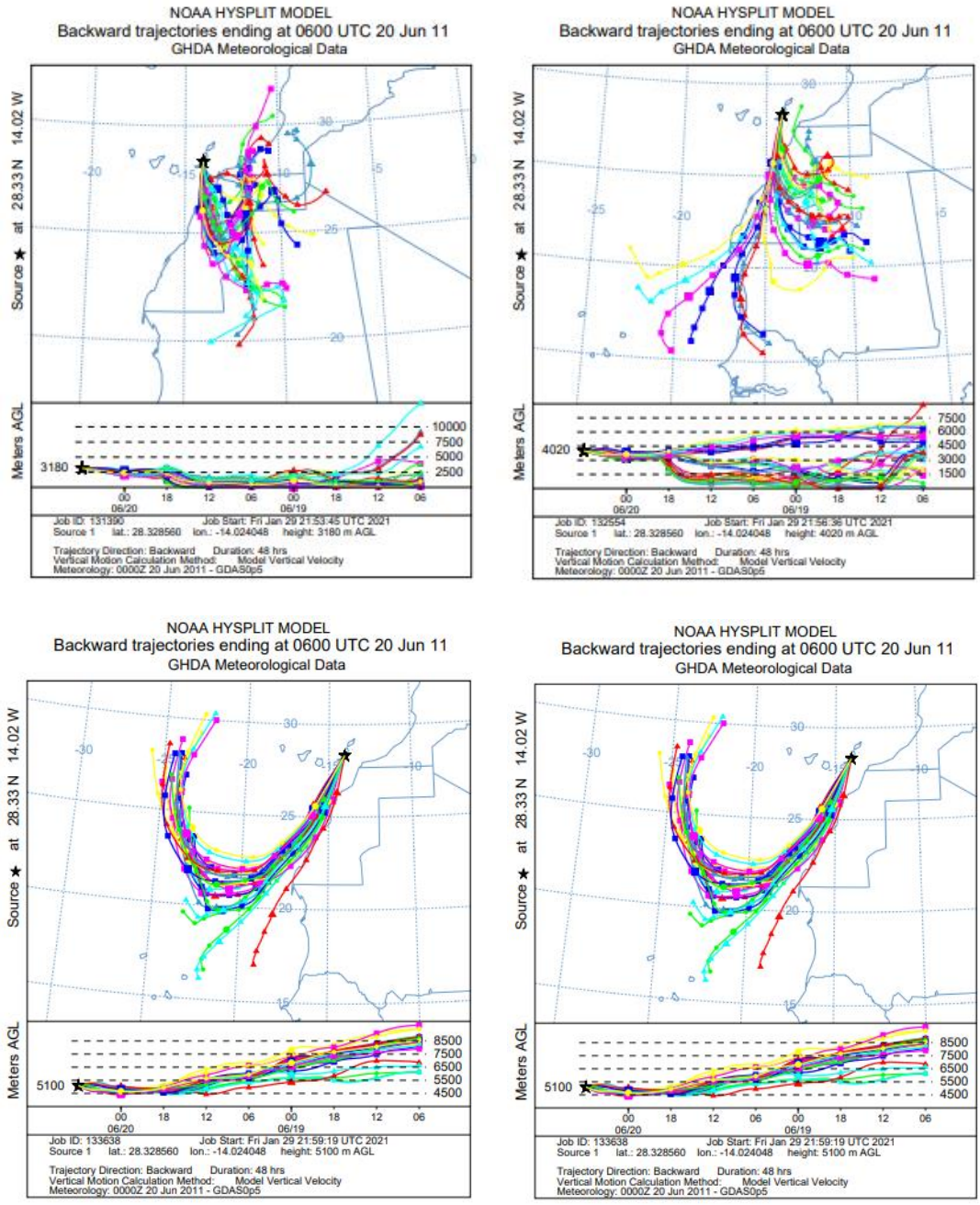

Figure A4. 4. Backward trajectories from NOAA HYSPLIT model during June 2011 with various height ranges 1020 m, 3060 m, 5100 m and 6060 m. The ensemble trajectories are obtained by running the HYSPLIT model at 0.5 degree with given result every 6 hours and with a time duration 48 hours over Fuerteventura (Canary Islands). The model was started at 28.3285 latitude and -14.0240 longitude at the Canary Islands. Runs show backward air mass sources of the dust event for flight number FB604

A4.5. Case study FB605

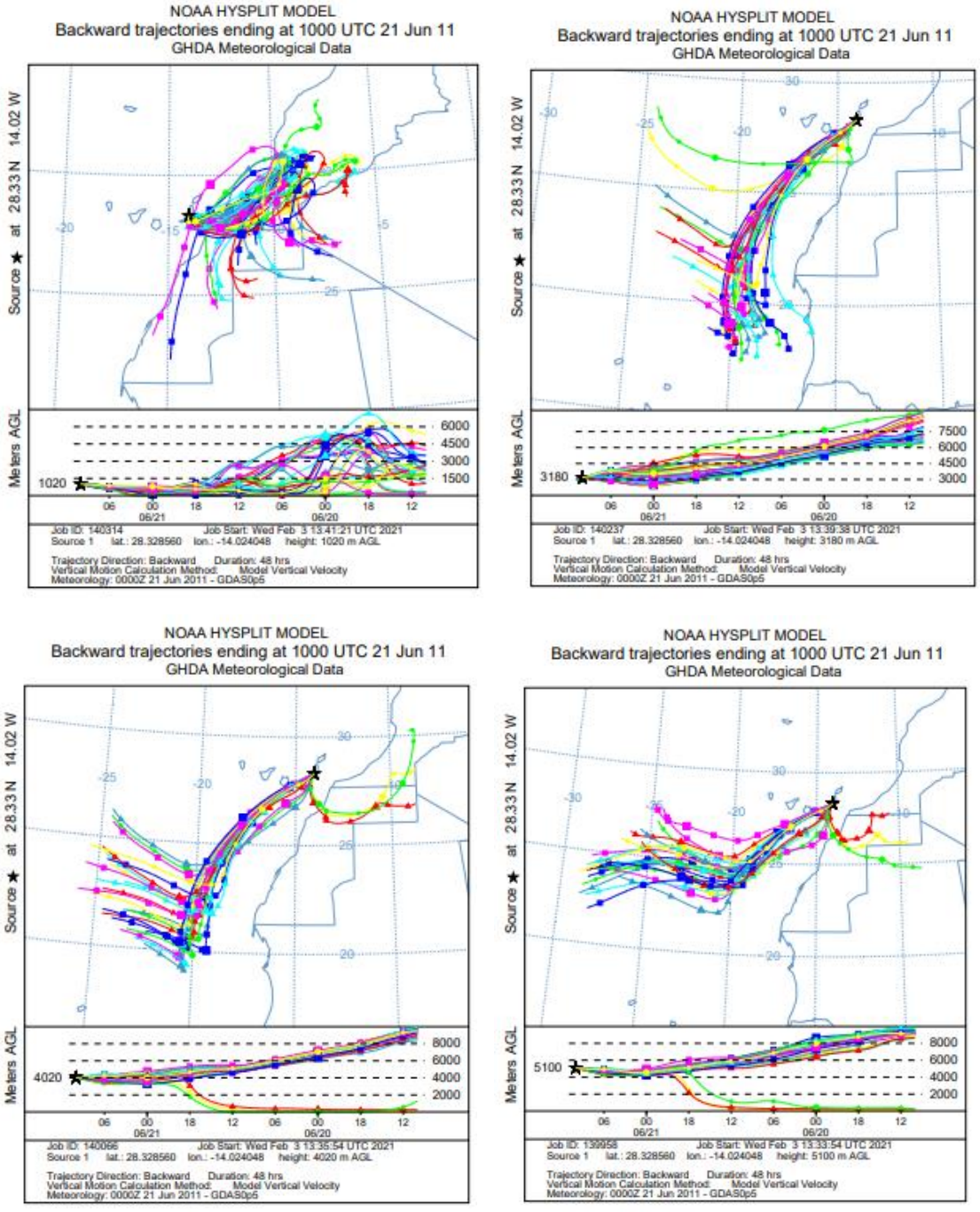

Figure A4. 5. As figure (A4.4), but for backward trajectories associated with flight FB605.

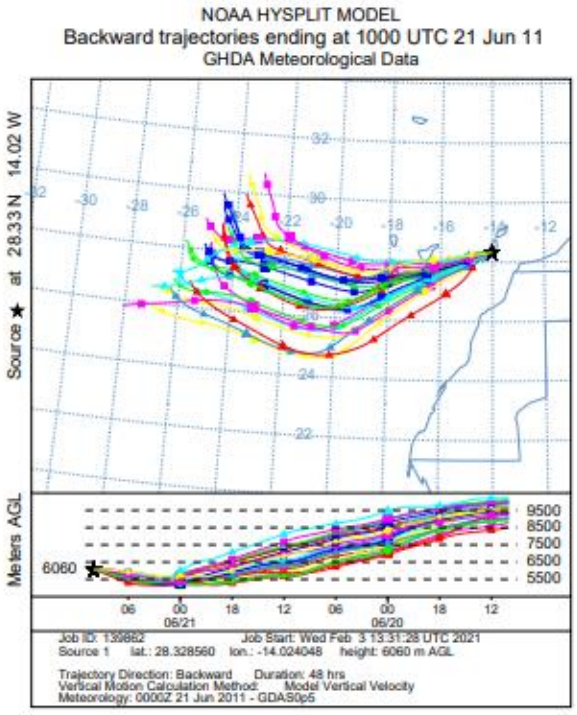

Figure A4. 6. As figure (A4.5), except for height 6060m.

A4.7. Case study FB612

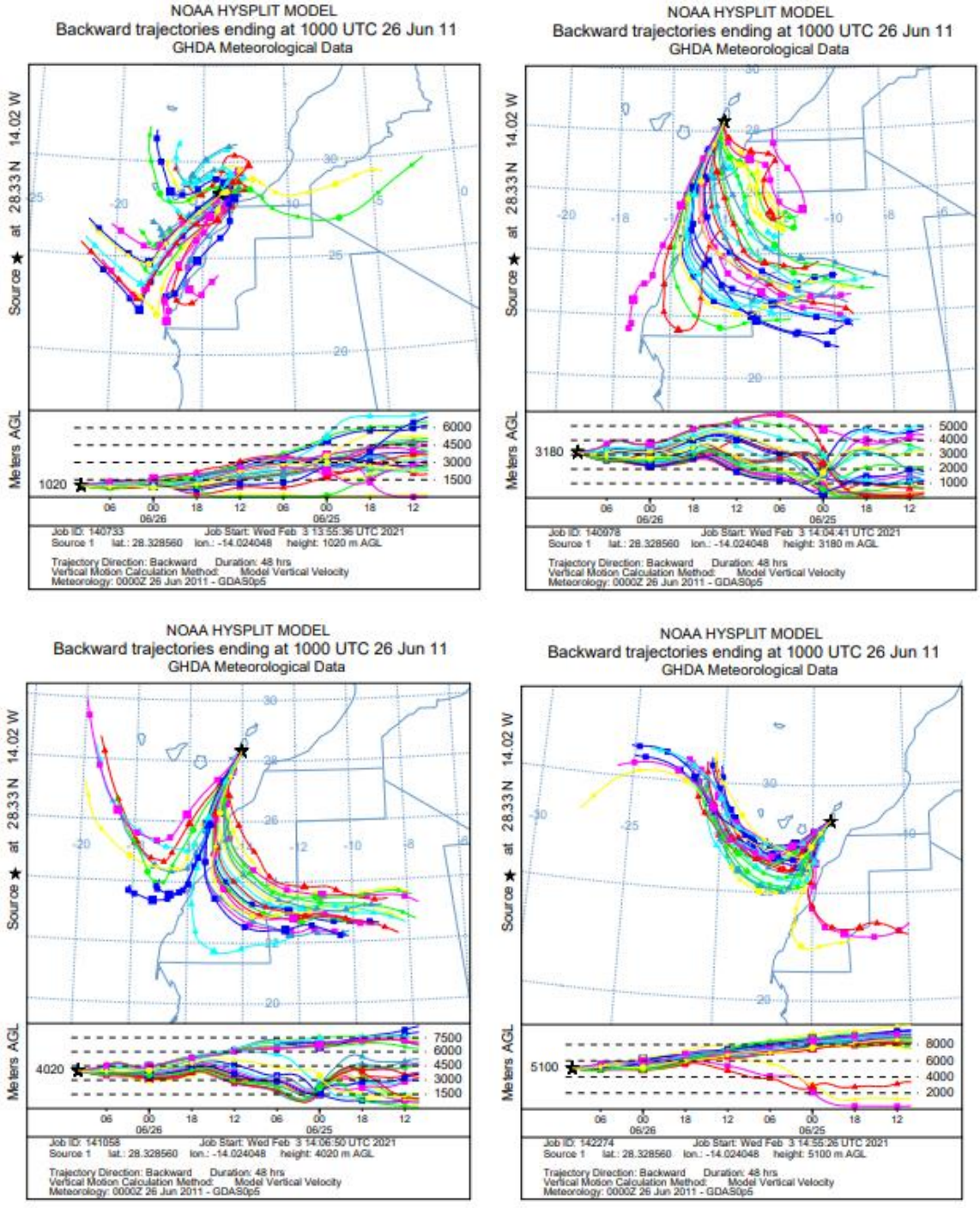

Figure A4. 7. As figure (A4.5), but for flight FB612.

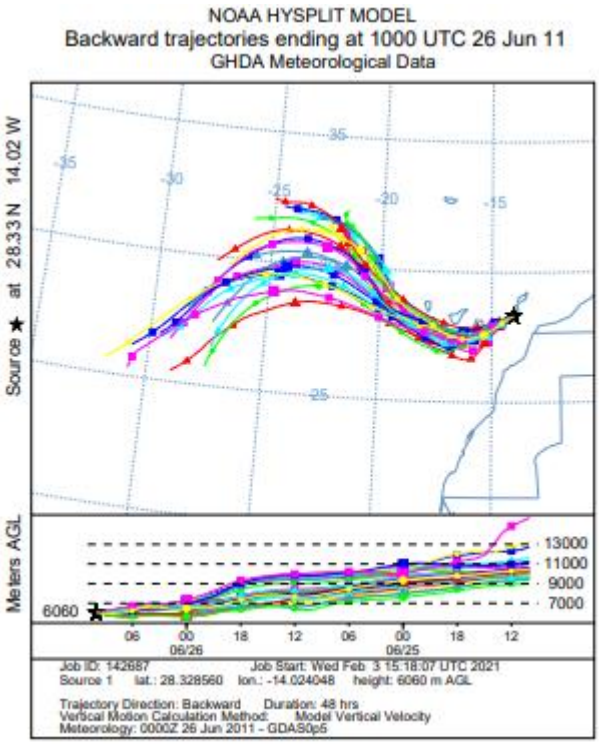

Figure A4. 8. As figure (A4.7), except for height 6060m.

A4.9. Case study FB699

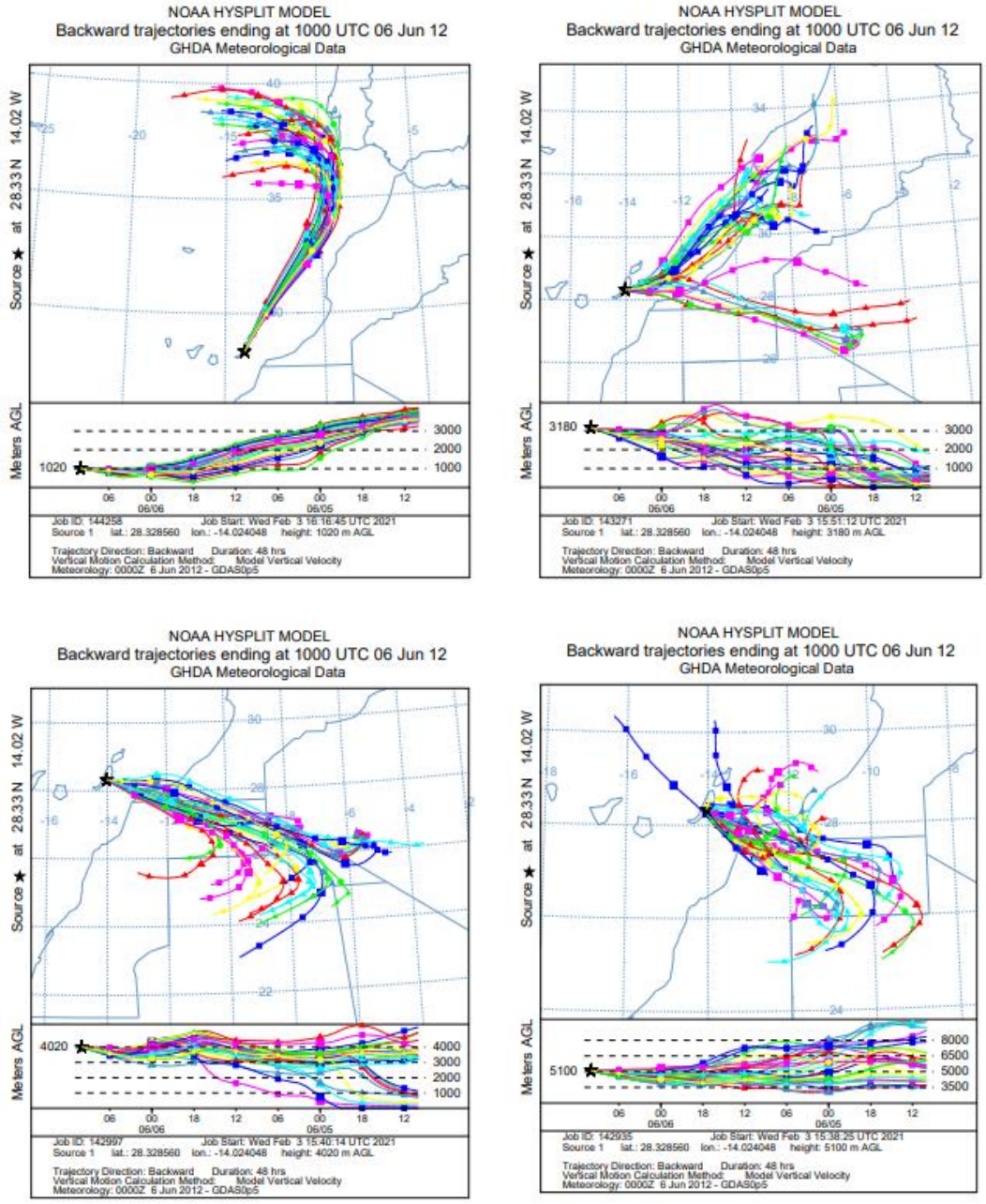

Figure A4. 9. As figure (A4.7), but for flight FB699

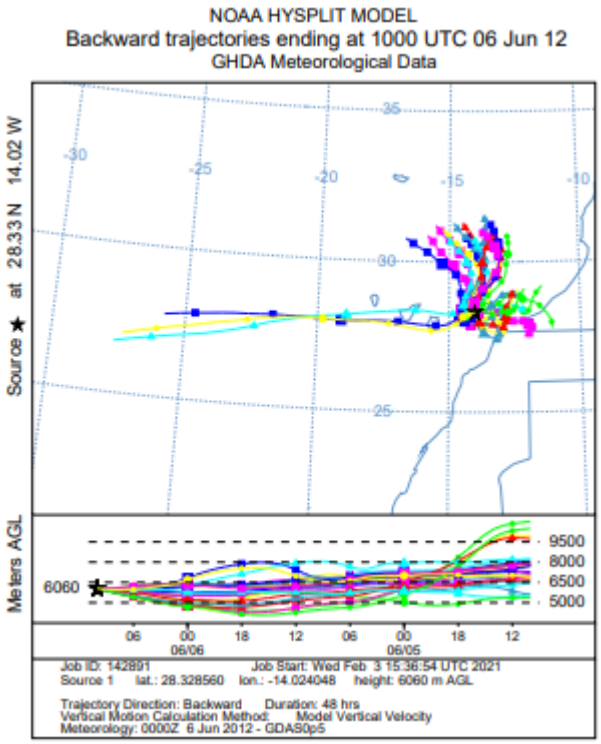

Figure A4. 10. As figure (A4.9), except for height 6060m.

A4.11. Puerto Rico: backward trajectories coincident with flight FB604

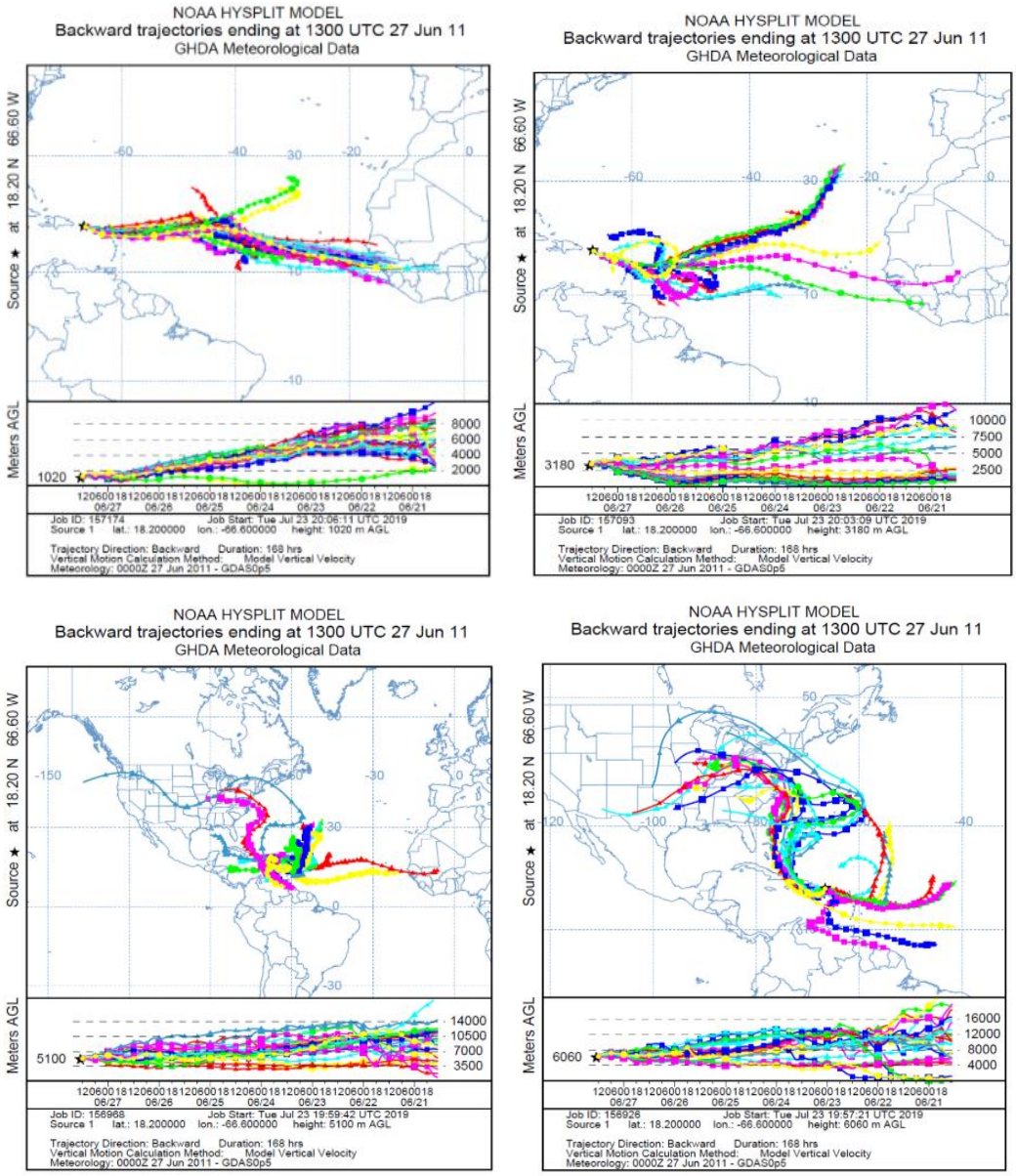

Figure A4. 11. Backward trajectories from NOAA HYSPLIT model during June 2011 with various height ranges 1020 m, 3060 m, 5100 m and 6060 m. The ensemble trajectories are obtained by running the HYSPLIT model at 0.5 degree with given result every 6 hours and with a time duration 168 hours over Puerto Rico (Caribbean site). The model was started at 18.2 latitude and -66.60 longitude at the Canary Islands. Runs show backward air mass sources of the dust event for flight number FB604

.

A4.12. Case study FB605

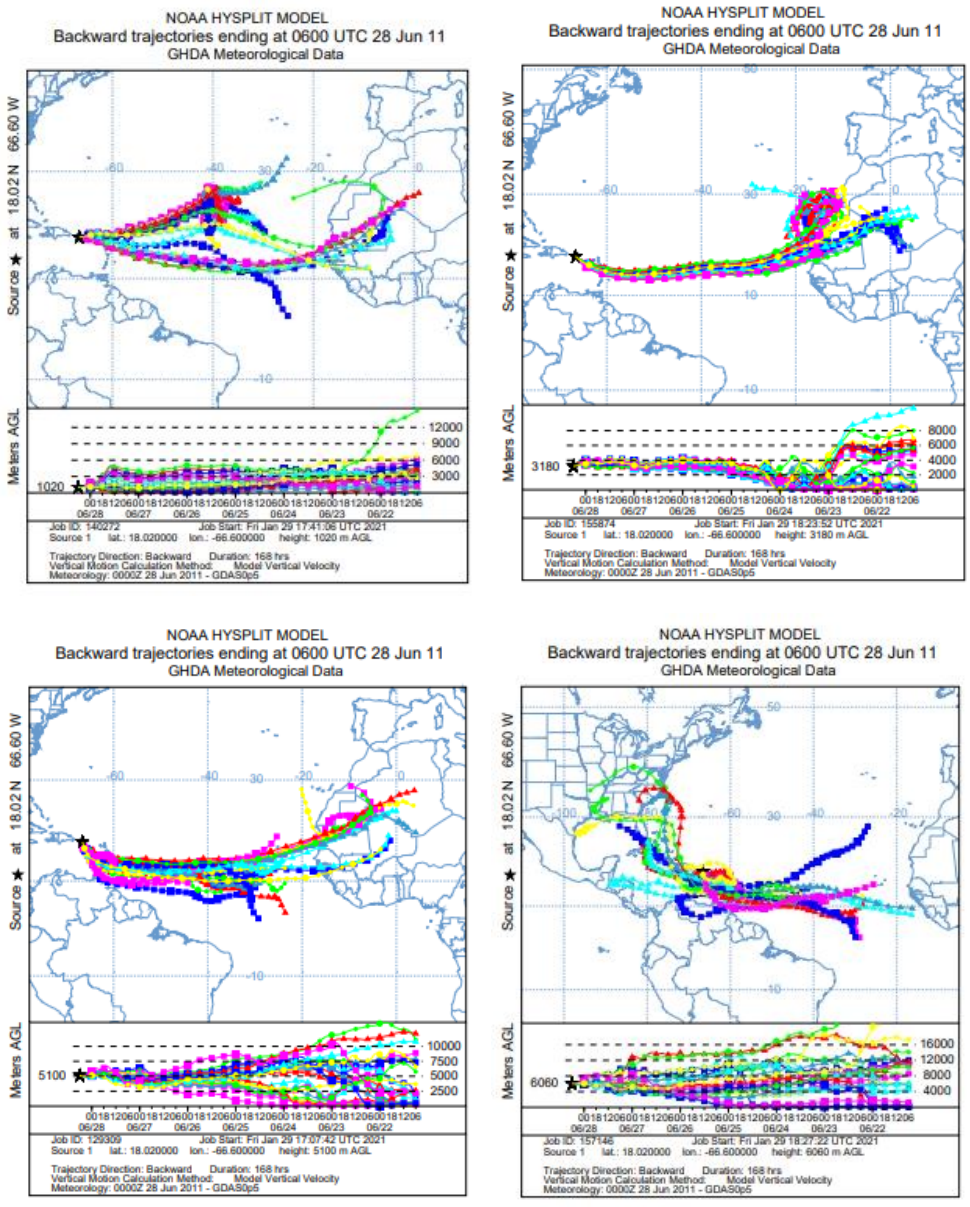

Figure A4. 12. As figure (A4.11), but for flight FB605.

A4.13. Case study FB612

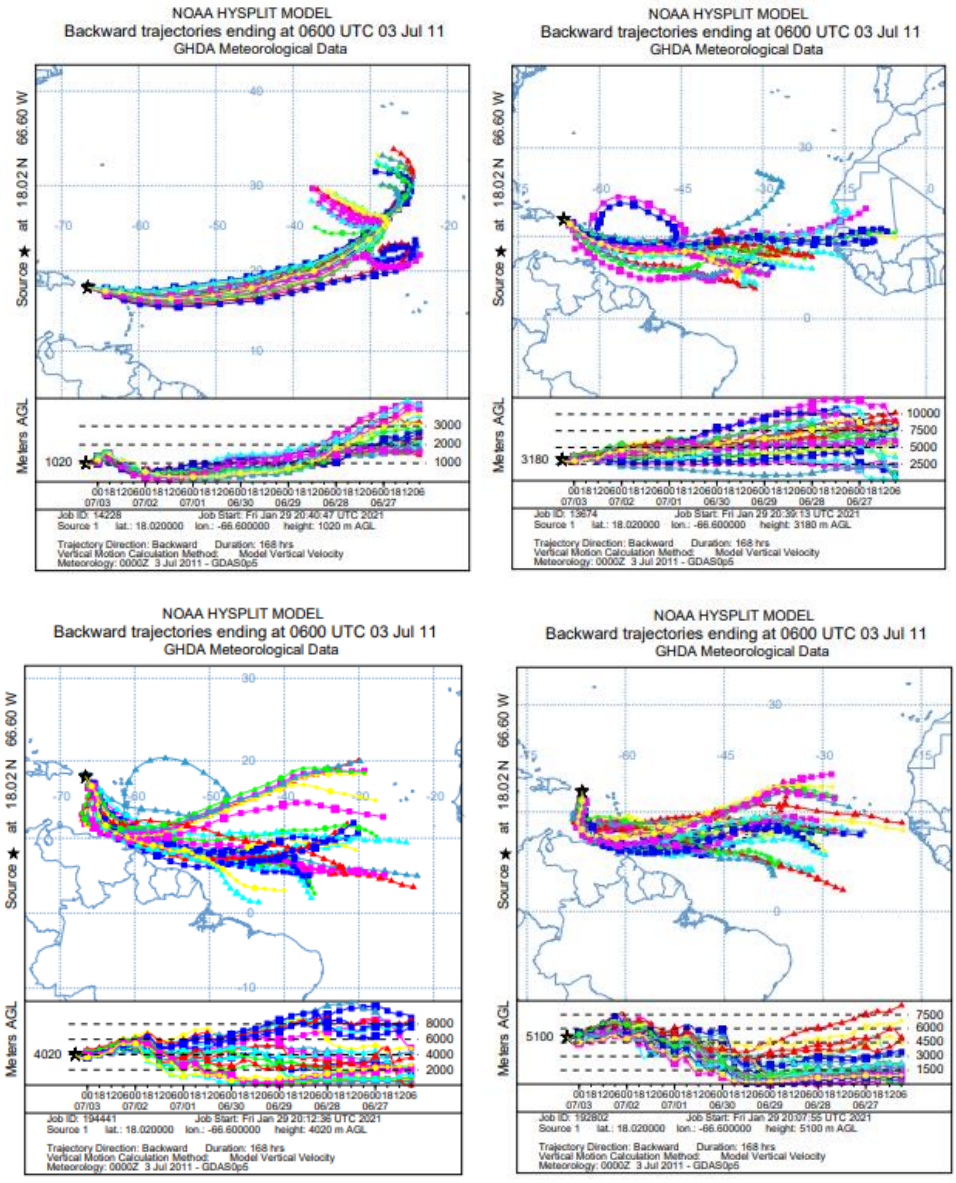

Figure A4. 13. As figure (A4.12), but for flight FB612.

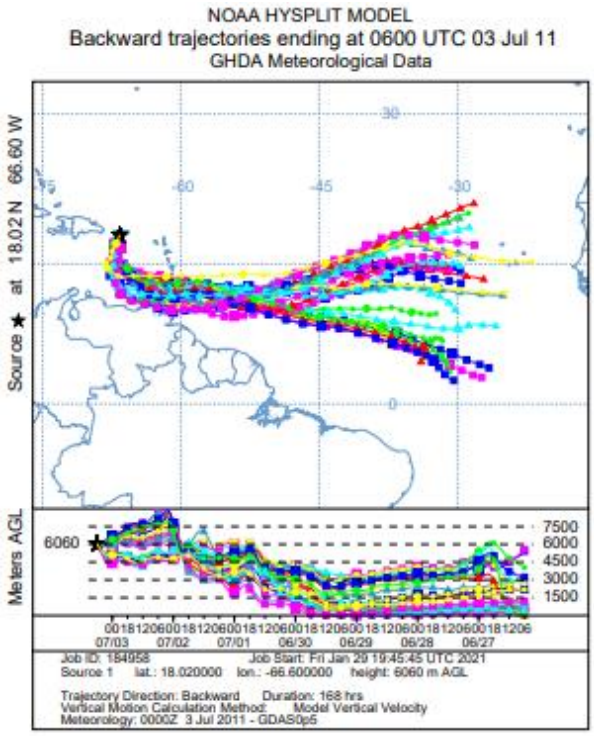

Figure A4. 14. As figure (A4.13), except for height 6060m.

A4.15. Case study FB699

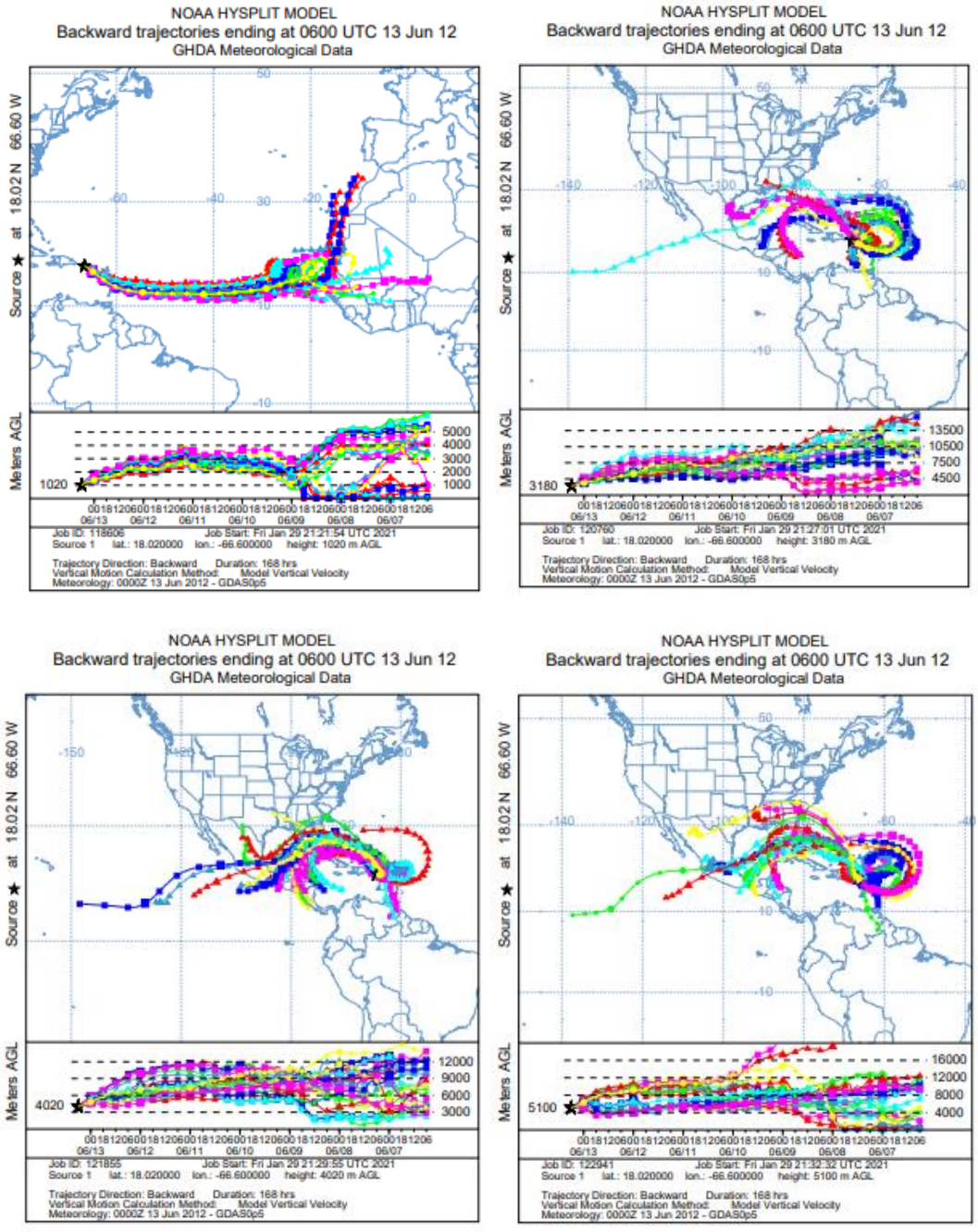

Figure A4. 15. As figure (A4.13), but for flight FB699.

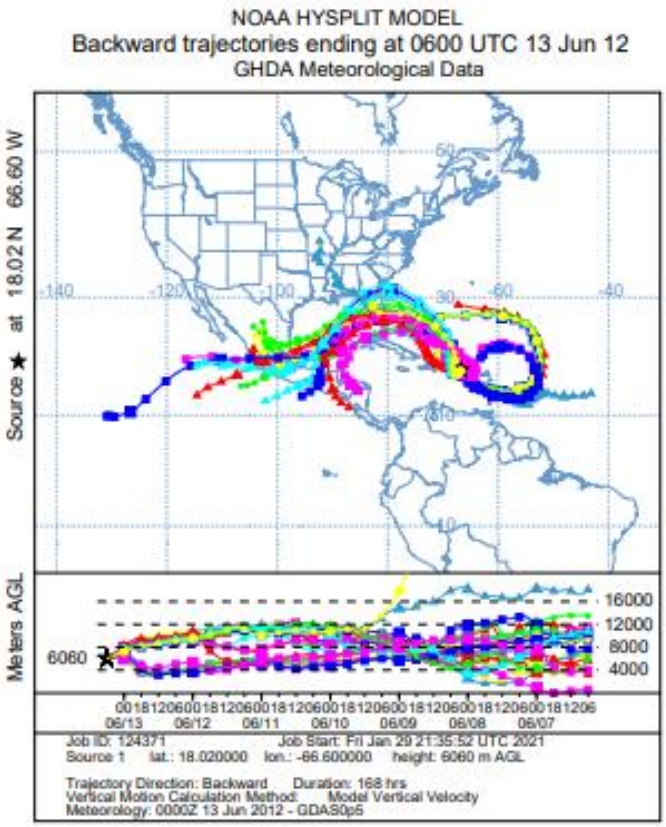

Figure A4. 16. As figure (A4.15), except for height 6060m.

A4.17. Forward trajectories

For forward trajectories, I show only plots for flight FB604 since thesis results are focused on backward trajectories for calculating scaling factor, SF.

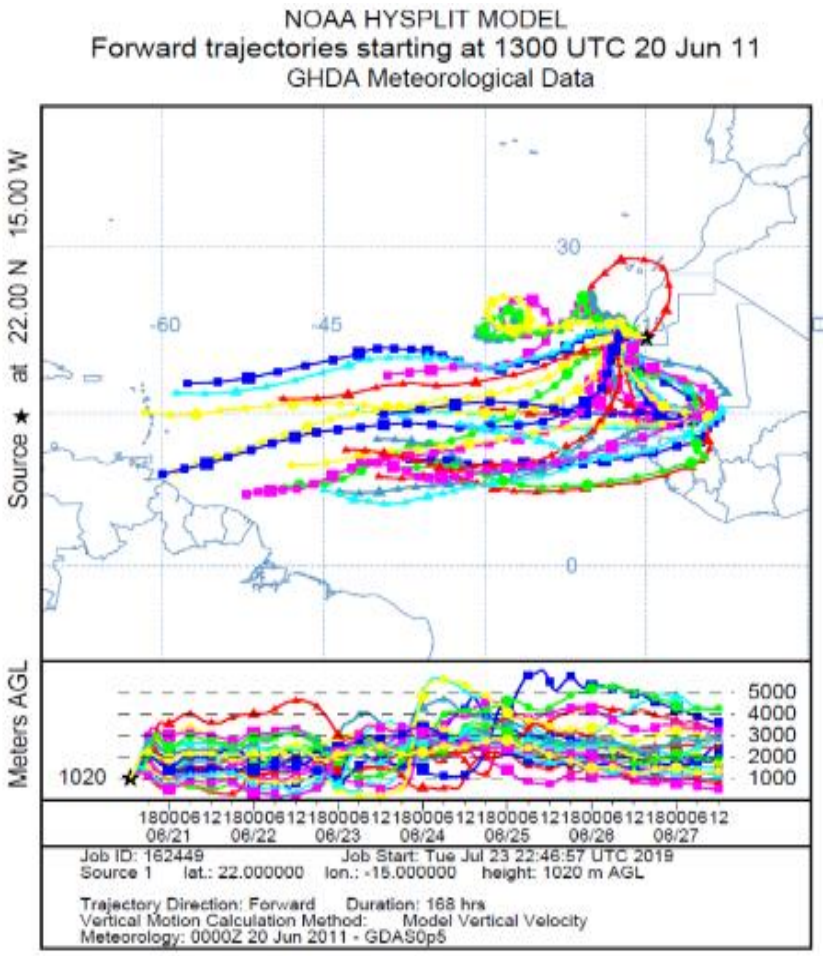

Figure A4. 17. Forward trajectories from NOAA HYSPLIT model during June 2011 with height 1020 m. The ensemble trajectories are obtained by running the HYSPLIT model at 0.5 degree every 6 hours and with time duration of 168 hours over the African coastline. The model runs start at 22.0 latitude and -15.0 longitude at western Saharan. Runs show forward air mass sources of the dust event for flight number FB604.

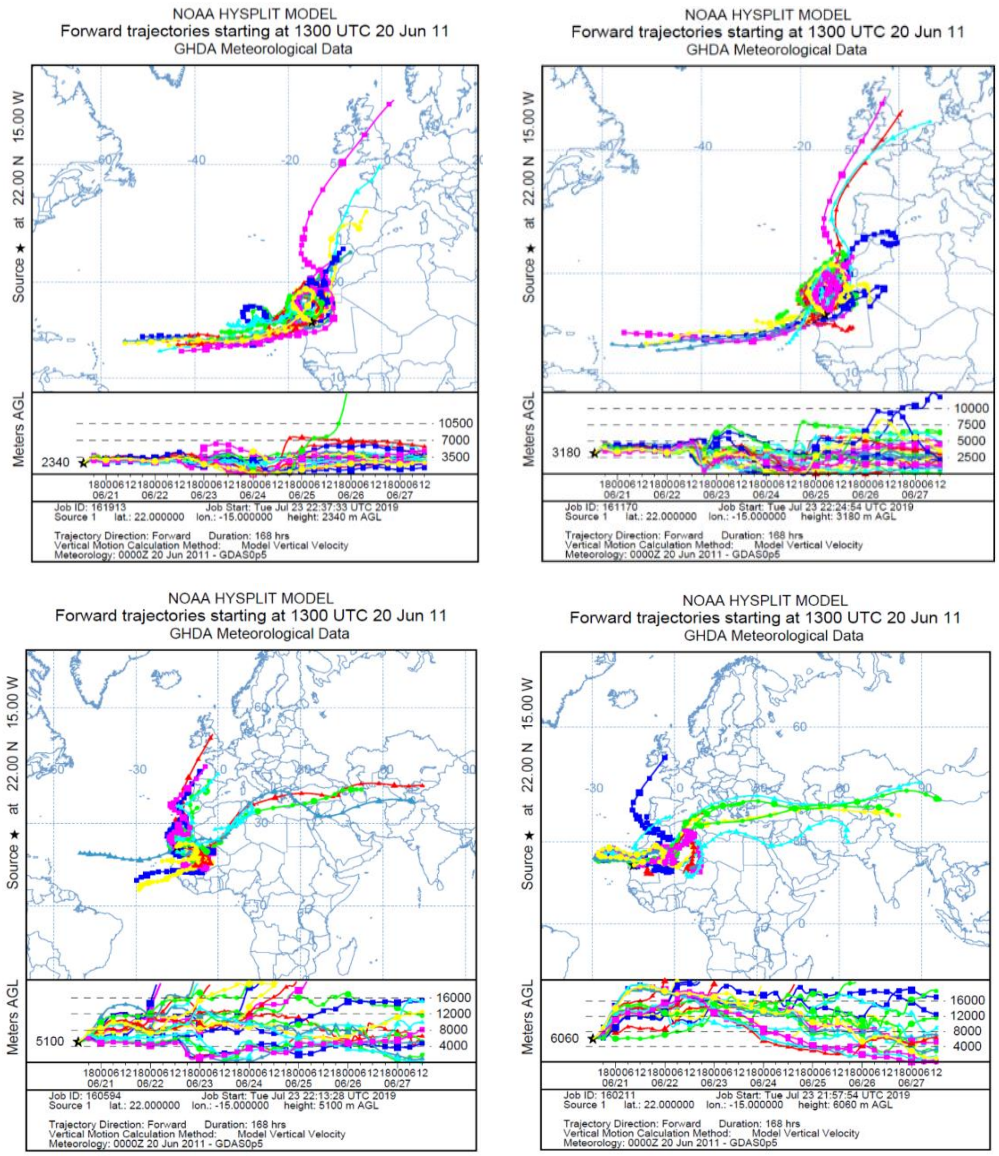

Figure A4. 18. As figure (A4.17), but for more heights including 2340 m,3180 m, 5100 m and 6060 m

.

Appendix B

B1. Turbulent diffusion and dust mass profiles toward the Canary Islands

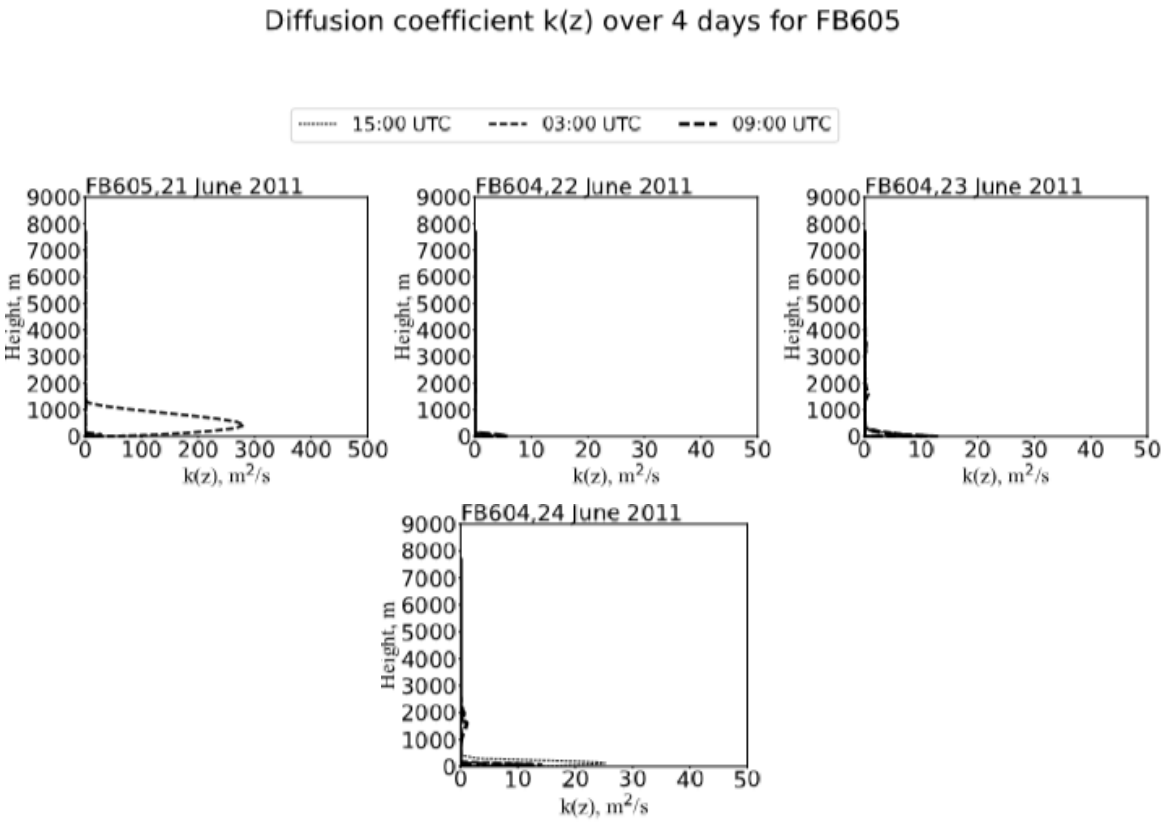

Figure B1. 1. Calculated vertical turbulent diffusion coefficient profiles (kz, m^2/s) at three different selected times; 1500, 0300 and 0900 UTC over 4 days over the Canary Islands. Turbulent diffusion coefficients are calculated based on local-diffusive scheme from Holtslag and Boville, (1993) and Jeričević et al. (2009). Turbulent diffusion calculation is for FB605.

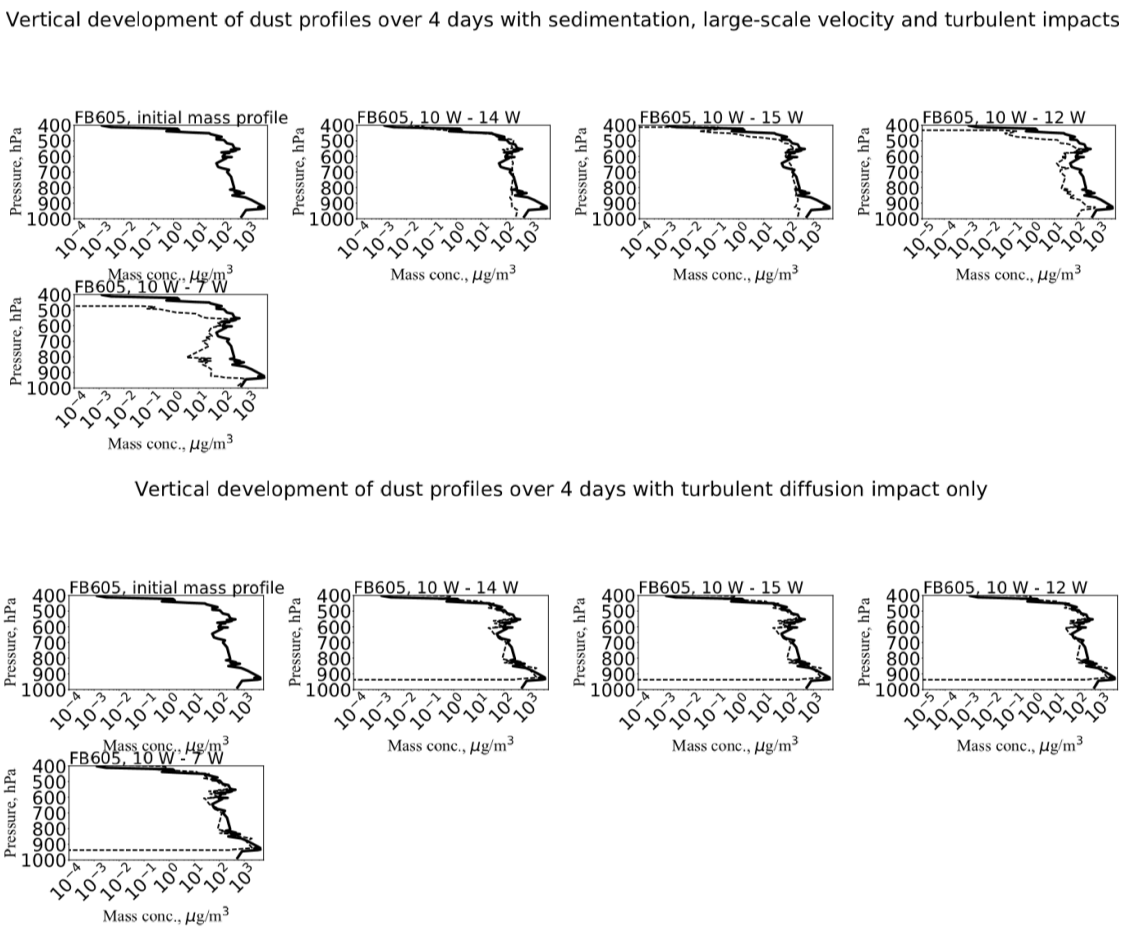

Figure B1. 2. Dust mass concentrations (μg/m^3) calculated from the BRSedT model over 4 days over the Canary Islands for case FB605. Solid lines indicate the initial profiles of dust mass over the African land, whereas dashed lines show the evolution of the mass in the model associated with sedimentation, large-scale process and turbulent diffusion impact. Top two rows indicate results with including all processes impact, while plots underneath present turbulent diffusion impact only. The plots from top left to bottom right specify the results from the African land to Caribbean.

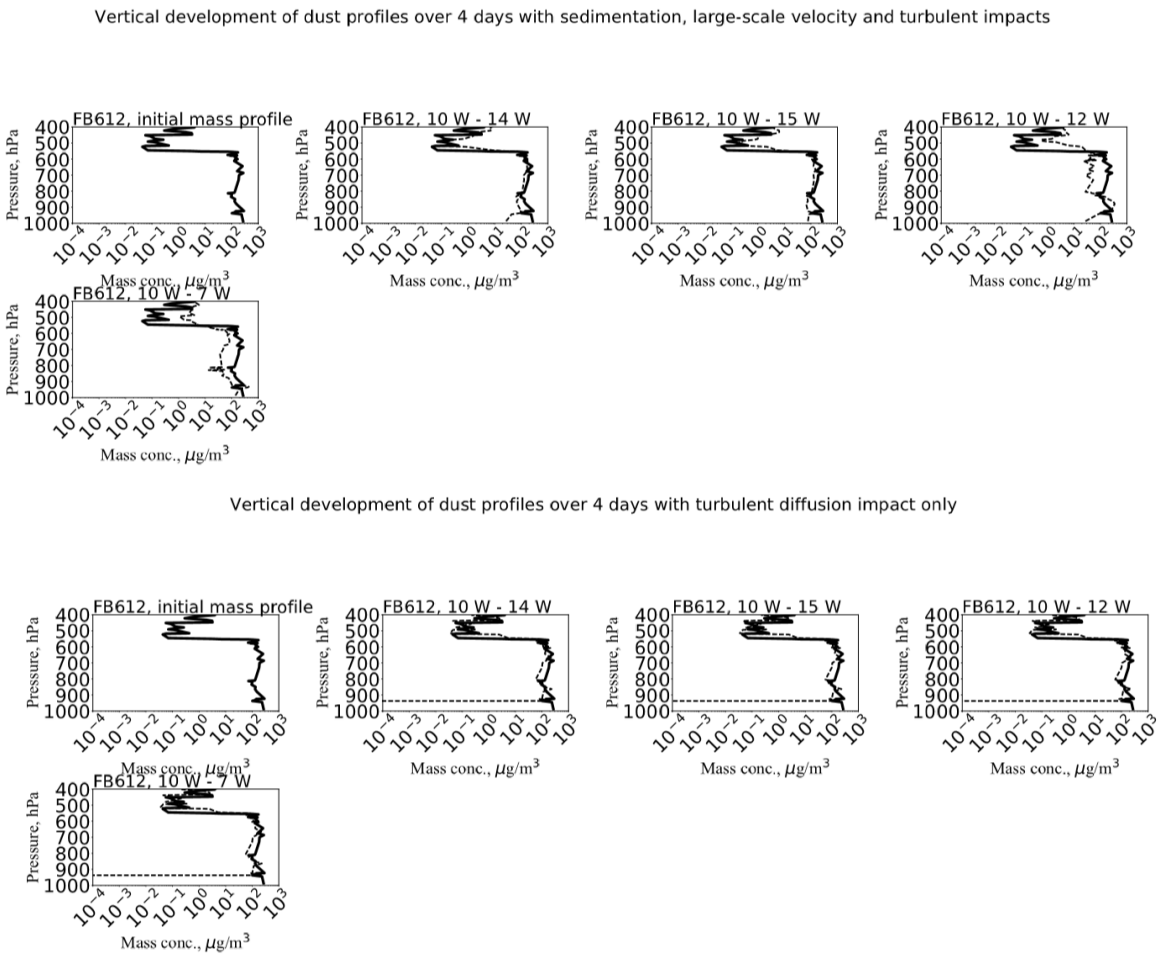

Figure B1. 3. As figure (B1.2), but for flight FB612.

B2. Sedimentation and turbulence model (BRSedT)

```
      include 'headernew.dat'
      real*8 w(numlay), nr(numlay,numbins),vt(numbins),z(numlay,numbins)
      real*8 srf(numbins), c(numlay), bgc(nsub)
      real*8 a1, a2, dt,nw,dz,bt
      real*8 cbefore,cafter
      real*8 intmass(numlay), pi, vol1, vol2, r(numbins), denf
      real*8 zm,zas(numlay,numbins)
      real*8 tmp,sz(numlay,numbins)
      real*8 snr(numlay,numbins),totmass
      real*8 beforesnr(numlay,numbins)
      real*8 rdum1, tm,newdt,tmax,ct,updatetime
      integer idum1, idum2, ibg
      integer i, i2, i3, b,t,nt,ilay(numlay,numbins),itrig
      integer s(numlay,numbins),silay(numlay,numbins)

c     set some paramters
      ibg=0         ! use the below-grid diffusion coefficients, ibg=0 yes, ibg=1 no
      itrig=0       ! 0 means dt is fine, 1 means dt needs changing
      dt=1.0        ! timestep this is adjusted according to diffcoef maximum value in each 3hrs
      tmax=604800.    ! max time in sec
      updatetime=3.00D0*3600.00D0 ! the time between updates
      bt=3          ! used for testing output of one bin, bt
      cbefore=0.   ! conservation before
      cafter=0.    ! conservation after
      do b=1,numbins
       srf(b)=0.0  ! Initialise the surface values
      enddo

c     open input and output files
      open(87,file='w.dat')          ! large scale w
      open(88,file='vt.dat')         ! fall velocities
      open(89,file='nr.dat')         ! size dist n(r)
      open(24,file='initial.dat')
      open(25,file='output.dat',access='append')
      open(26,file='srf.dat')
      open(27,file='output2.dat',access='append')
      open(28,file='maxdiffcoef.dat')
      open(55,file='inputrad.dat')
      open(60,file='massinitial.dat')
      open(62,file='diffcoef.dat')               ! diffusion coeffs
      open(97,file='srftime.dat')
      open(57,file='massfinal.dat')


c     read in the data
      do i=1,numlay
       do b=1,numbins
        read(89,*) z(i,b),a2,nr(i,b)
        if (i .eq. 1) then  ! vt values are only a function of b so no i loop
         read(88,*) a2,vt(b)
         read(88,*)a2
        endif
       enddo
      enddo
c     calculate the mass to start with and output it.
      pi=3.141592654
      denf=2. ! this needs to be density of dust plus other factors
      do b=1,numbins
       read(55,*)r(b)
```

```
      r(b)=r(b)/2.
     enddo
     totmass=0.
     do i=1,numlay
      intmass(i)=0. ! initialise
      do b=2,numbins
       vol1=(4./3.)*pi*(r(b)*r(b)*r(b))
       vol2=(4./3.)*pi*(r(b-1)*r(b-1)*r(b-1))
       intmass(i)=intmass(i)+0.5*(vol1*nr(i,b)+vol2*nr(i,b-1))*denf
     &  *((2.*r(b))-(2.*r(b-1)))
      enddo
      write(60,*) intmass(i)
      totmass=totmass+intmass(i)
     enddo
     write(60,*) 'total mass at time=0 is ',totmass
c    cal conservation quantity
     do i=1,numlay
      do b=1,numbins
       cbefore=cbefore+nr(i,b)
      enddo
     enddo
     do b=1,numbins
      cbefore=cbefore+srf(b)
     enddo
c    print out nr and srf before timestep
     do b=1,numbins
      write(24,*) '0 ','0 ',b,' 0. ',srf(b)
      do i=1,numlay
       write(24,*) '0. ',i,b,z(i,b),nr(i,b)
      enddo
     enddo
c****** Entering the time step loop ***************************************
c    advect/sed the dust.  i,b refers to the initial dust and its height
c    changes are tracked in z(i,b) rather than i and b
c    this is a Lagrangian tracking scheme

     ct=0.00000D0
     dt=1.D0
     tm=0.D0

c    Main loop in time starts here
 10  if (tm .lt. tmax) then     ! loop time index

 20   continue
c     reduce the timestep if necessary if itrig is set to 1 below
      if (itrig .eq. 1) then ! dt is too large
       dt=dt/2.D0 ! reduce the timestep by a half
       print *, 'dt was reduced to a half ',dt
       itrig=0  ! reset the trigger
      endif

c     input and output call every 3 hrs. Input latest diff coeff and w
c     and output the snapshot of the atmosphere
      if (tm .ge. (ct*updatetime) then
       ct=ct+1.00000D0  ! increment tracker up by 1
       call updatesub(bgc,w,c)  ! read in w and c for next three hours
       read(28,*) idum1,idum2,rdum3,newdt
       print *,'readingn',idum1,idum2,rdum1,newdt
       dt=newdt
       print *,'timestep updated to ',dt,' and total time is ',tm
       do i=1,numlay
        do b=1,numbins
         if (i.eq.1) write(27,*) '0 ','0 ',b,' 0. ',srf(b)
```

```
          if (i.eq.1) write(97,*) tm,b,srf(b)
          write(27,*) tm,i,b,z(s(i,b),b),nr(s(i,b),b),s(i,b)
         enddo
        enddo
       endif

c      now advance the dust with sed and large-scale dynamics
       do i=1,numlay
        do b=1,numbins
         call findlay(z(i,b),ilay(i,b))
         nw=w(ilay(i,b))-vt(b)

         z(i,b)=z(i,b)+nw*dt ! the net effect of sed/wind is net wind,
                             ! nw the distance it travels is nw*dt in m.
c        use findlay again so that ilay is up-to-date for the turbulence scheme.
         call findlay(z(i,b),ilay(i,b))
        enddo
       enddo

c      Turbulence scheme prep

c      sz will be sorted and s will track mapping of sz and z.
       do b=1,numbins
        do i=1,numlay
         sz(i,b)=z(i,b)
         s(i,b)=i
        enddo
       enddo

c      This bit of code below sorts the z heights into order.
c      s provides the connection between the ordered heights and original heights
c      Define the integer array to hold locations
       do b=1,numbins
        do i=1,numlay-1
         do i2=i+1,numlay
          if (sz(i,b) .gt. sz(i2,b) ) then
           tmp    = sz(i,b)
           sz(i,b) = sz(i2,b)
           sz(i2,b)= tmp
           tmp    = s(i,b)
           s(i,b) = s(i2,b)
           s(i2,b)= tmp
          endif
         enddo
        enddo
       enddo
c      create a new nr array to hold the values of nr in order with
c      ascending z.
c      put the values of snr just before the turbulence in a holding
c      array called beforesnr so I can compare after with before
       do b=1,numbins
        do i=1,numlay
         snr(i,b)=nr(s(i,b),b)
         silay(i,b)=ilay(s(i,b),b)
         beforesnr(i,b)=snr(i,b)
        enddo
       enddo

c****** Turbulence call ***************************************************
       call turbulence(sz,snr,c,bgc,dt,silay,itrig,ibg)

       if (itrig .eq. 1) goto 20  ! timestep dt is too large so reduce
```

```
c      pass the updated values from the turbulence held in snr back to nr
       do b=1,numbins
        do i=1,numlay
         nr(s(i,b),b)=snr(i,b)
        enddo
       enddo


c      update the time

       tm=tm+dt ! tm is the actual time

       goto 10
      endif ! timestep loop

c     check if the dust reaches the surface
      do i=1,numlay
       do b=1,numbins
        if (z(i,b) .le. 0.0) then  ! surface has been reached.
         srf(b)=srf(b)+nr(i,b)
         nr(i,b)=0.0              ! the dust is now in the surface
         z(i,b)=0.0
        endif
       enddo
      enddo

      do b=1,numbins
       write(26,*) b,srf(b)
       write(25,*) '0 ','0 ',b,' 0. ',srf(b)
       do i=1,numlay
        write(25,*) tmax,i,b,z(s(i,b),b),nr(s(i,b),b),s(i,b)
       enddo
      enddo

      do i=1,numlay
       do b=1,numbins
        if (i.eq.1) write(27,*) '0 ','0 ',b,' 0. ',srf(b)
        write(27,*) tmax,i,b,z(s(i,b),b),nr(s(i,b),b),s(i,b)
       enddo
      enddo

c     calculate the integrated mass for output
      pi=3.141592654
      denf=2. ! this needs to be density of dust plus other factors
      do i=1,numlay
       intmass(i)=0. ! initialise
       do b=2,numbins
        vol1=(4./3.)*pi*(r(b)*r(b)*r(b))
        vol2=(4./3.)*pi*(r(b-1)*r(b-1)*r(b-1))
        intmass(i)=intmass(i)+0.5*(vol1*nr(i,b)+vol2*nr(i,b-1))*denf
     &  *((2.*r(b))-(2.*r(b-1)))
       enddo
      write(56,*) intmass(i)*0.4
      enddo
      close(55)

c     cal conservation quantity
      do i=1,numlay
       do b=1,numbins
        cafter=cafter+nr(i,b)
       enddo
      enddo
      do b=1,numbins
```

```
      cafter=cafter+srf(b)
     enddo

     print *, 'Conservation before is ',cbefore
     print *, 'Conservation after  is ',cafter

c    end of program
     stop
     end

c******** end of program ***************************************************

     subroutine updatesub(bgc,w,c)
c    this subroutine reads in the newest w, c, and bgc values every 3 hrs
     include 'headernew.dat'
     integer i
     real*8 bgc(nsub),w(numlay),c(numlay)
     do i=1,nsub
      read(62,*) a1,bgc(i)    ! read in the below-grid w 20 layer from the surface to 300m
      print *, 'bgc ',i,a1,bgc(i)
     enddo
     do i=1,numlay-1

      read(87,*) a1,w(i)      ! read in time varying w. Must vary with dt
      read(62,*) a1,c(i)      ! read in time varying diffusion coeffcients
      if (c(i) .lt. 0.00001) c(i)=0.001
      print *, 'c and w ',i,a1,c(i),w(i)
     enddo
     c(numlay)=c(numlay-1) ! c only goes up to 66 layers so set the 67th to the 66th
     read(87,*) a1,w(numlay)

     print *, 'c and w ',numlay,a1,c(numlay),w(numlay)
     return
     end

     subroutine bgfindlay(z,ilay1,zbg)
c    find out what layer the z is at now that it has been sed
     include 'headernew.dat'

     real*8 z,zb(0:nsub),zbg
     integer ilay1,i
     zb(0)=0.
c    establish the layer interfaces
     do i=1,nsub-1
      zb(i)=zb(i-1)+10.
     enddo
     zb(nsub)=300.

c    search to find out where z(i,b) is now
     do i=1,nsub
      if (z .lt. zb(i) .and. z .gt. zb(i-1)) then
       ilay1=i ! sets ilay1=1 if in lowest layer up to top layer at 300m
       zbg=zb(i)
      endif
     enddo
     return
     end
     subroutine findlay(z,ilay1)
c    find out what layer the z is at now that it has been sed
     include 'headernew.dat'

     real*8 z,zb(0:numlay)
     integer ilay1,i
```

```
      zb(0)=0.
      zb(1)=300.
c     establish the layer interfaces
      do i=2,numlay
       zb(i)=zb(i-1)+120.
      enddo
c     search to find out where z(i,b) is now
      if (z .le. zb(0)) then ! into the ground
      ! fine to set these also equal to overlap as will have same val.
       ilay1=0
      elseif (z .ge. zb(numlay)) then ! above the top layer so set to 61 layer
       ilay1=numlay
      endif
      do i=1,numlay
       if (z .lt. zb(i) .and. z .gt. zb(i-1)) then
        ilay1=i ! sets ilay1=1 if in lowest layer up to top layer ilay1=61
       endif
      enddo
      return
      end

      subroutine turbulence(tz,tnr,dc,bgc,dt,tilay,itrig,ibg)
c     Turbulent dispersion of aerosol
      include 'headernew.dat'
      real*8 tz(numlay,numbins),tnr(numlay,numbins)
      real*8 dc(numlay) ! turb diff coef which can vary with height
      real*8 diffz(numlay,numbins),diffnr(numlay,numbins)
      real*8 flux(numlay,numbins),difft,bgc(nsub)
      real*8 dt,zbg,dca
      integer i,b,up(numlay,numbins),tilay(numlay,numbins)
      integer itrig,iequal,ilay1,ibg

c     set some paramters
      iequal=0 ! assuming the parcels are not at the same heights

c     calculate the turbulent diffusion flux
c     don't update nr yet since fluxes all need to be
c     determined first before moving nr around.

c     check for equal heights and mix the amounts evenly
      do b=1,numbins
       do i=1,numlay-1
        diffz(i,b)=tz(i+1,b)-tz(i,b)
        if (diffz(i,b) .eq. 0.00000D0) then
         tnr(i,b)  =(tnr(i,b)+tnr(i+1,b))/2.
         tnr(i+1,b)=tnr(i,b)
         iequal=1 ! they are at the same heights and were equalised
        endif
       enddo
      enddo

c     calculation of the turbulent flux
      do b=1,numbins
       do i=1,numlay-1
        if (tilay(i,b) .ne. 0) then
         diffz(i,b)=tz(i+1,b)-tz(i,b)
         diffnr(i,b)=tnr(i+1,b)-tnr(i,b)
         if (diffnr(i,b) .gt. 0.000000000D0) then
          up(i,b)=-1 ! indicates flux is down from i+1 to i
         elseif (diffnr(i,b) .lt. 0.000000000000D0) then
          up(i,b)=1 ! indicates flux is up from i to i+1
         else
          up(i,b)=0 ! flux is zero so no change
```

```
      endif
      difft=dt
      if (diffz(i,b) .eq. 0.00000000000D0) then
       up(i,b)=2 !special code to indicate z values are equal
      endif

c      note the flux below has no neg sign since handled by 'up' array
      if (up(i,b) .ne. 2) then

       if (ibg .eq. 0) then ! use the below grid diffusion coefs.
        if (tilay(i,b) .eq. 1 .and. tilay(i+1,b) .eq. 1) then ! both layers in the bg layer
         call bgfindlay(tz(i,b),ilay1,zbg)
         flux(i,b)=abs(bgc(ilay1)*diffnr(i,b)*difft/diffz(i,b))

        elseif (tilay(i,b) .eq. 1  .and. tilay(i+1,b) .ge. 2) then
         call bgfindlay(tz(i,b),ilay1,zbg)
         dca=0.5*(bgc(ilay1)+dc(tilay(i+1,b)))  ! average the two diff coefs
         flux(i,b)=abs(dca*diffnr(i,b)*difft/diffz(i,b))

        else ! normal case where both layers are above 300m
         flux(i,b)=abs(dc(tilay(i,b))*diffnr(i,b)*difft/diffz(i,b))
        endif
       else ! don't use the diffusion coefs below-grid
         flux(i,b)=abs(dc(tilay(i,b))*diffnr(i,b)*difft/diffz(i,b))
       endif
c      perform a timestep check.  If the flux would equalise in one
c      timestep then it is too large a flux. If it goes half way to
c      equalising in one step it is too large.
       if (flux(i,b) .gt. abs(diffnr(i,b)/4.)) then
        print *,'Flux too large at ',i,b,' so reduce dt'
        print *, i,b,tnr(i,b),tnr(i+1,b),diffnr(i,b),flux(i,b),
     &    abs(diffnr(i,b)/2)
        print *, 'i b tnri tnri+1 diffnr flux absdiffnr'
        itrig=1 ! indicates the dt needs reducing.
        goto 30 ! exit this subroutine without updating the dust
       endif
      else
       flux(i,b)=0.000000000D0
      endif
     endif
    enddo
   enddo
c   now update the nr values by moving the flux around.
c   (now apply the changes to nr but make sure that you check
c   to see if pos or neg to apply in the layer or the one above)
   do b=1,numbins
    do i=1,numlay-1
     if (tilay(i,b) .ne. 0) then  ! Don't shift around flux in the ground.
      if (up(i,b).eq.1) then ! transfer from i to i+1
       tnr(i+1,b)=tnr(i+1,b)+flux(i,b)
       tnr(i,b)  =tnr(i,b)  -flux(i,b)
      elseif (up(i,b).eq.-1) then  ! transfer from i+1 to i
       tnr(i,b)  =tnr(i,b)  +flux(i,b)
       tnr(i+1,b)=tnr(i+1,b)-flux(i,b)
      else  ! no flux transfer
       ! no flux to move so do nothing
      endif
     endif
    enddo
   enddo
30  continue
   return
   end
```